

UNCLASSIFIED

AD NUMBER
AD875449
NEW LIMITATION CHANGE
TO Approved for public release, distribution unlimited
FROM Distribution authorized to U.S. Gov't. agencies and their contractors; Critical Technology; AUG 1970. Other requests shall be referred to Commander, Air Force Materials Laboratory, Wright-Patterson AFB, OH 45433.
AUTHORITY
AFML ltr, 8 May 1974

THIS PAGE IS UNCLASSIFIED

AD 875449

AFML-TR-70-108
Volume III

20
100
ck

AD No. _____
DDC FILE COPY

DEVELOPMENT OF ENGINEERING DATA FOR ADVANCED COMPOSITE MATERIALS

Volume III
Anisotropic Plate Characterization
Bending, Dynamics, Stability

B. E. Kaminski
The Fort Worth Division of General Dynamics Corporation

TECHNICAL REPORT AFML-TR-70-108, Vol. III

August 1970

OCT 16 1970

This document is subject to special export controls and each transmittal to foreign governments or foreign nationals may be made only with prior approval of the Air Force Materials Laboratory (MAC), Wright-Patterson Air Force Base, Ohio 45433

Air Force Materials Laboratory
Air Force Systems Command
Wright-Patterson Air Force Base, Ohio

DEVELOPMENT OF ENGINEERING DATA
FOR ADVANCED COMPOSITE MATERIALS

Volume III Anisotropic Plate Characterization -
Bending, Dynamics, Stability

B. E. Kaminski

This document is subject to special export controls and each transmittal to foreign governments or foreign nationals may be made only with prior approval of the Air Force Materials Laboratory, Wright-Patterson Air Force Base, Ohio 45433.

F O R E W O R D

The Fort Worth Division of General Dynamics, prime contractor, and subcontractor Illinois Institute of Technology Research Institute have completed a 26-month program to develop reliable engineering data on the application of advanced composites to aircraft structure.

The work was performed under Air Force Contract F33615-68-C-1474, "Development of Engineering Data for Advanced Composite Materials" under the sponsorship of the Air Force Materials Laboratory, Air Force Systems Command, Wright-Patterson Air Force Base, Ohio. Mr. R. L. Rapson, MACM, was the Air Force Project Engineer. Mr. P. D. Shockey of the Fort Worth Division of General Dynamics was the overall program manager. Mr. K. E. Hofer directed the work conducted by Illinois Institute of Technology Research Institute (IITRI).

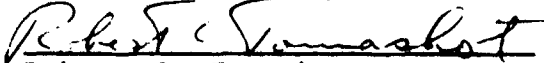
This final report is divided into three volumes as follows:

Volume I	Static and Thermophysical Properties
Volume II	Fatigue and Dynamic Characteristics
Volume III	Anisotropic Plate Characterization - Bending, Dynamics, Stability

The work reported in this volume, Volume III, is the characterization of the behavior of flat plates fabricated with an advanced composite material. Transverse, uniaxial, biaxial, and diagonal tension loading configurations were used to study the small deflection and post-buckling behaviors.

Various personnel from the Fort Worth Division of General Dynamics supported the work reported herein. In particular, Dr. J. E. Ashton made valuable contributions with his criticism and advice concerning various technical aspects of the program. Mr. M. S. Howeth has been responsible for the documentation of the program. The manuscript was released by the author in January 1970 for publication as a technical report.

This report has been reviewed and is approved.


Robert C. Tomashot
Technical Area Manager
Advanced Composites Division

A B S T R A C T

The program to develop engineering data for the Narmco 5505 boron-epoxy material system included an experimental investigation of the small deflection and post-buckling behaviors of flat plates fabricated with that system. Analytical predictions of the behaviors of the test plates were made utilizing an anisotropic plate analysis. The results of this investigation and analysis are documented in this volume. Detailed descriptions of the specimens, equipment, and procedures are also presented.

This abstract is subject to special export controls and each transmittal to foreign governments or foreign nationals may be made only with prior approval of the Air Force Materials Laboratory (MAC), Wright-Patterson Air Force Base, Ohio 45433.

T A B L E O F C O N T E N T S

<u>Section</u>		<u>Page</u>
I	INTRODUCTION	1
II	SUMMARY	3
III	METHOD OF ANALYSIS	5
IV	SPECIMENS, EQUIPMENT, AND PROCEDURES	9
	4.1 Description of Specimens	9
	4.2 Fixtures and Equipment	17
	4.3 Test Procedures	33
	4.4 Fixture Calibration	40
	4.5 Uniaxial Buckling Results	42
V	TRANSVERSE LOAD STUDY	55
VI	BIAXIAL LOAD STUDY	115
VII	NATURAL FREQUENCY STUDY	131
VIII	DIAGONAL TENSION STUDY	157
IX	ULTIMATE LOAD OBSERVATIONS	175
X	CONCLUSIONS	191
APPENDIX I	SOUTHWELL'S METHOD	193
APPENDIX II	UNIAXIAL BUCKLING DATA	199
APPENDIX III	BIAXIAL BUCKLING DATA	225
	REFERENCES	319

L I S T O F I L L U S T R A T I O N S

<u>Figure</u>		<u>Page</u>
1	Boron Composite Panels	10
2	Cross-Section of Tapered Panel 19A	13
3	Thickness Measurement Locations, Compression Panels	14
4	Thickness Measurement Locations, Shear Panels	14
5	Compression Frame with Panel Installed and Upper Head Removed	19
6	Compression Setup Installed in 200,000-Pound Universal Test Machine	20
7	Top View of Compression Frame Showing Panel in Clamped Support	21
8	Top View of Compression Frame Showing Panel in Knife Edge Support	22
9	Basic Compression Frame Modified for Lateral Loads	23
10	Top View of Modified Compression Frame Showing Panel in Clamped Edge Support and Pressure Bag Installed	24
11	Pressure Monitoring Equipment	25
12	Lateral Load - Uniaxial Compression Setup	26
13	Biaxial Loading Geometry	27
14	Typical Biaxial Test Setup Without Dial Indicators	28
15	Load Actuator Locations	29
16	Dial Indicator Locations	30
17	Dynamic Vibration Test Setup	31

LIST OF ILLUSTRATIONS (Continued)

<u>Figure</u>		<u>Page</u>
18	Dynamic Vibration Monitoring Circuit Equipment	32
19	Shear Panel Test Installation	34
20	Shear Panel Instrumentation	35
21	Edge Member Effect on Clamped-Clamped Boundary Condition	36
22	Plots of Amplitude Ratio and Phase Angle	39
23	Test Configuration and Coordinate Reference	41
24	Deflection vs Lateral Load, Clamped-Clamped Conditions, Aluminum Panel 3	43
25	Deflection vs Lateral Load, Clamped-Simple Conditions, Aluminum Panel 3	44
26	Buckling Results, Clamped-Clamped and Clamped-Simple	45
27	Frequency vs Stress Resultant, Clamped-Clamped Conditions	46
28	Frequency vs Stress Resultant, Clamped-Simple Conditions	47
29	Buckling Results - Elastic Restraints	50
30	Buckling Results - Ideal Boundaries	51
31	Pressure Imprint Study, Clamped-Simple Conditions, Steel Panel	57
32	Deflection vs Lateral Load, Clamped-Clamped Condition, Steel Panel	58
33	Deflection vs Lateral Load, Clamped-Clamped Condition, Panel No. 2	59

LIST OF ILLUSTRATIONS (Continued)

<u>Figure</u>		<u>Page</u>
34	Deflection vs Lateral Load, Clamped-Simple Condition, Panel No. 2	60
35	Deflection vs Lateral Load, Clamped-Clamped Condition, Panel No. 3	61
36	Deflection vs Lateral Load, Clamped-Simple Condition, Panel No. 3	62
37	Deflection vs Lateral Load, Clamped-Clamped Condition, Panel No. 5	63
38	Deflection vs Lateral Load, Clamped-Clamped Condition, Panel No. 5, Turned 90°	64
39	Deflection vs Lateral Load, Clamped-Simple Condition, Panel No. 5	65
40	Deflection vs Lateral Load, Clamped-Simple Condition, Panel No. 5, Turned 90°	66
41	Deflection vs Lateral Load, Clamped-Clamped Condition, Panel No. 7	67
42	Deflection vs Lateral Load, Clamped-Simple Condition, Panel No. 7	68
43	Deflection vs Lateral Load, Clamped-Clamped Condition, Panel No. 9	69
44	Deflection vs Lateral Load, Clamped-Simple Condition, Panel No. 9	70
45	Deflection vs Lateral Load, Clamped-Clamped Condition, Panel No. 12	71
46	Deflection vs Lateral Load, Clamped-Simple Condition, Panel No. 12	72
47	Deflection vs Lateral Load, Clamped-Clamped Condition, Panel No. 16	73

LIST OF ILLUSTRATIONS (Continued)

<u>Figure</u>		<u>Page</u>
48	Deflection vs Lateral Load, Clamped-Simple Condition, Panel No. 16	74
49	Deflection vs Lateral Load, Clamped-Clamped Condition, Panel No. 19A	75
50	Deflection vs Lateral Load, Clamped-Clamped Condition, Panel No. 19A, Turned 90°	76
51	Deflection vs Lateral Load, Clamped-Simple Condition, Panel No. 19A	77
52	Deflection vs Lateral Load, Clamped-Simple Condition, Panel No. 19A, Turned 90°	78
53	Data Reduction, Steel Panel Clamped-Clamped Condition	80
54	Combined Uniaxial and Lateral Loadings, Steel Panel, Clamped-Clamped Condition	82
55	Data Reduction, Steel Panel, Clamped-Simple Condition	83
56	Combined Uniaxial and Lateral Loadings, Steel Panel, Clamped-Simple Condition	84
57	Combined Uniaxial and Lateral Loadings, Panel No. 2, Clamped-Clamped Condition	85
58	Combined Uniaxial and Lateral Loadings, Panel No. 2, Clamped-Simple Condition	86
59	Combined Uniaxial and Lateral Loadings, Panel No. 3, Clamped-Clamped Condition	87
60	Combined Uniaxial and Lateral Loadings, Panel No. 3, Clamped-Simple Condition	88
61	Combined Uniaxial and Lateral Loadings, Panel No. 5, Clamped-Clamped Condition	89

LIST OF ILLUSTRATIONS (Continued)

<u>Figure</u>		<u>Page</u>
62	Combined Uniaxial and Lateral Loadings, Panel No. 5, Clamped-Clamped Condition, Turned 90°	90
63	Combined Uniaxial and Lateral Loadings, Panel No. 5, Clamped-Simple Condition	91
64	Combined Uniaxial and Lateral Loadings, Panel No. 5, Clamped-Simple Condition, Turned 90°	92
65	Combined Uniaxial and Lateral Loadings, Panel No. 7, Clamped-Clamped Condition	93
66	Combined Uniaxial and Lateral Loadings, Panel No. 7, Clamped-Simple Condition	94
67	Combined Uniaxial and Lateral Loadings, Panel No. 9, Clamped-Clamped Condition	95
68	Combined Uniaxial and Lateral Loadings, Panel No. 9, Clamped-Simple Condition	96
69	Combined Uniaxial and Lateral Loadings, Panel No. 12, Clamped-Clamped Condition	97
70	Combined Uniaxial and Lateral Loadings, Panel No. 12, Clamped-Simple Condition	98
71	Combined Uniaxial and Lateral Loadings, Panel No. 16, Clamped-Clamped Condition	99
72	Combined Uniaxial and Lateral Loadings, Panel No. 16, Clamped-Simple Condition	100
73	Combined Uniaxial and Lateral Loadings, Panel No. 19A, Clamped-Clamped Condition	101
74	Combined Uniaxial and Lateral Loadings, Panel No. 19A, Clamped-Clamped Condition, Turned 90°	102

LIST OF ILLUSTRATIONS (Continued)

<u>Figure</u>		<u>Page</u>
75	Combined Uniaxial and Lateral Loadings, Panel No. 19A, Clamped-Simple Condition	103
76	Combined Uniaxial and Lateral Loadings, Panel No. 19A, Clamped-Simple Condition, Turned 90°	104
77	Shapes of Natural Modes of Vibration	108
78	RA5 Solution Study	112
79	Mode Shape Study	113
80	Biaxial Compression Interaction Curve for Aluminum Panel No. 1	117
81	Biaxial Compression Interaction Curve for Panel No. 2	118
82	Biaxial Compression Interaction Curve for Panel No. 3	119
83	Biaxial Compression Interaction Curve for Panel No. 5	120
84	Biaxial Compression Interaction Curve for Panel No. 7	121
85	Biaxial Compression Interaction Curve for Panel No. 9	122
86	Biaxial Compression Interaction Curve for Panel No. 12	123
87	Biaxial Compression Interaction Curve for Panel No. 16	124
88	Biaxial Compression Interaction Curve for Panel No. 19A	125
89	Natural Frequency vs Compressive Stress, Aluminum Panel No. 1, Clamped-Clamped	133

LIST OF ILLUSTRATIONS (Continued)

<u>Figure</u>		<u>Page</u>
90	Natural Frequency vs Compressive Stress, Aluminum Panel 1, Clamped-Simple	134
91	Natural Frequency vs Compressive Stress, Panel 2, Clamped-Clamped	135
92	Natural Frequency vs Compressive Stress, Panel 2, Clamped-Simple	136
93	Natural Frequency vs Compressive Stress, Panel 3, Clamped-Clamped	137
94	Natural Frequency vs Compressive Stress, Panel 3, Clamped-Simple	138
95	Natural Frequency vs Compressive Stress, Panel 5, Clamped-Clamped	139
96	Natural Frequency vs Compressive Stress, Panel 5, Clamped-Simple	140
97	Natural Frequency vs Compressive Stress, Panel 5, Turned 90 ^o , Clamped-Clamped	141
98	Natural Frequency vs Compressive Stress, Panel 5, Turned 90 ^o , Clamped-Simple	142
99	Natural Frequency vs Compressive Stress, Panel 7, Clamped-Clamped	143
100	Natural Frequency vs Compressive Stress, Panel 7, Clamped-Simple	144
101	Natural Frequency vs Compressive Stress, Panel 9, Clamped-Clamped	145
102	Natural Frequency vs Compressive Stress, Panel 9, Clamped-Simple	146
103	Natural Frequency vs Compressive Stress, Panel 12, Clamped-Clamped	147

LIST OF ILLUSTRATIONS (Continued)

<u>Figure</u>		<u>Page</u>
104	Natural Frequency vs Compressive Stress, Panel 12, Clamped-Simple	148
105	Natural Frequency vs Compressive Stress, Panel 16, Clamped-Clamped	149
106	Natural Frequency vs Compressive Stress, Panel 16, Clamped-Simple	150
107	Natural Frequency vs Compressive Stress, Panel 19A, Clamped-Clamped	151
108	Natural Frequency vs Compressive Stress, Panel 19A, Clamped-Simple	152
109	Natural Frequency vs Compressive Stress, Panel 19A, Turned 90°, Clamped-Clamped	153
110	Natural Frequency vs Compressive Stress, Panel 19A, Turned 90°, Clamped-Simple	154
111	Load-Deflection Curves for Shear Panels 1 and 801	158
112	Shear Panel 1 (+45-45-45+45)	159
113	Shear Panel 801 (-45+45+45-45)	160
114	Shear Panel Strain Gauge Locations	162
115	Load-Deflection Curves, Shear Panel 1A	163
116	Load-Deflection Curves, Shear Panel 801A	164
117	Load-Deflection Curves for Shear Panels 3 and 803	165
118	Shear Panel 3 (+0+90+90+0)	166
119	Shear Panel 803 (+90+0+0+90)	168
120	Load-Deflection Curves for Shear Panels 5, 805, and 807	169

LIST OF ILLUSTRATIONS (Continued)

<u>Figure</u>		<u>Page</u>
121	Shear Panel 5 (+60+0-60-60+0+60)	172
122	Shear Panel 805 (-60+0+60+60+0-60)	173
123	Shear Panel 807 (+60-60+0+0-60+60)	174
124	Load-Deflection Curve for Panel 3	177
125	Load-Deflection Curve for Panel 9	178
126	Strain Gauge Locations, Ultimate Load Tests	181
127	Load Distribution Results, Panel 3	182
128	Load Distribution Results, Panel 9	183
129	Load-Deflection Curve for Panel 12	185
130	Load-Deflection Curve for Panel 13	186
131	Load-Deflection Curve for Panel 14	187
132	Load-Deflection Curve for Panel 16	188
133	Load-Deflection Curve for Panel 21	189
134	Biaxial Load-Deflection Curves for Aluminum Panel 3	195
135	Southwell Plots for Aluminum Panel 3, $P_y = 5960$ lbs.	196
136	Southwell Plot for Aluminum Panel 3, $N_x/N_y = .304$	197
137	Load Deflection Curve and Southwell Plots for the Unit Isotropic Plate, $P_y = 40$ lbs.	198
138	Southwell Plot for Aluminum Panel 3, Clamped-Clamped	200
139	Southwell Plot for Aluminum Panel 3, Clamped-Simple	201

LIST OF ILLUSTRATIONS (Continued)

<u>Figure</u>		<u>Page</u>
140	Load-Deflection Curve and Southwell Plot for Steel Panel, Clamped-Clamped	202
141	Load-Deflection Curve and Southwell Plot for Steel Panel, Clamped-Simple	203
142	Load-Deflection Curve and Southwell Plot for Panel No. 2, Clamped-Clamped	204
143	Load-Deflection Curve and Southwell Plot for Panel No. 2, Clamped-Simple	205
144	Load-Deflection Curve and Southwell Plot for Panel No. 3, Clamped-Clamped	206
145	Load-Deflection Curve and Southwell Plot for Panel No. 3, Clamped-Simple	207
146	Load-Deflection Curve and Southwell Plot for Panel No. 5, Clamped-Clamped	208
147	Load-Deflection Curve and Southwell Plot for Panel No. 5, Clamped-Clamped, Turned 90°	209
148	Load-Deflection Curve and Southwell Plot for Panel No. 5, Clamped-Simple	210
149	Load-Deflection Curve and Southwell Plot for Panel No. 5, Clamped-Simple, Turned 90°	211
150	Load-Deflection Curve and Southwell Plot for Panel No. 7, Clamped-Clamped	212
151	Load-Deflection Curve and Southwell Plot for Panel No. 7, Clamped-Simple	213
152	Load-Deflection Curve and Southwell Plot for Panel No. 9, Clamped-Clamped	214
153	Load-Deflection Curve and Southwell Plot for Panel No. 9, Clamped-Simple	215

LIST OF ILLUSTRATIONS (Continued)

<u>Figure</u>		<u>Page</u>
154	Load-Deflection Curve and Southwell Plot for Panel No. 12, Clamped-Clamped	216
155	Load-Deflection Curve and Southwell Plot for Panel No. 12, Clamped-Simple	217
156	Load-Deflection Curve and Southwell Plot for Panel No. 16, Clamped-Clamped	218
157	Load-Deflection Curve and Southwell Plot for Panel No. 16, Clamped-Simple	219
158	Load-Deflection Curve and Southwell Plot for Panel No. 19A, Clamped-Clamped	220
159	Load-Deflection Curve and Southwell Plot for Panel No. 19A, Clamped-Clamped, Turned 90°	221
160	Load-Deflection Curve and Southwell Plot for Panel No. 19A, Clamped-Simple	222
161	Load-Deflection Curve and Southwell Plot for Panel No. 19A, Clamped-Simple, Turned 90°	223
162	Load-Deflection Curves for Aluminum Panel No. 1	226
163	Southwell Plot for Aluminum Panel No. 1, $N_y/N_x = 0.0068$	227
164	Southwell Plot for Aluminum Panel No. 1, $N_y/N_x = 0.053$	228
165	Southwell Plot for Aluminum Panel No. 1, $N_y/N_x = 0.110$	229
166	Southwell Plot for Aluminum Panel No. 1, $N_y/N_x = 0.239$	230
167	Southwell Plot for Aluminum Panel No. 1, $N_y/N_x = 0.402$	231
168	Southwell Plot for Aluminum Panel No. 1, $N_y/N_x = 0.627$	232

LIST OF ILLUSTRATIONS (Continued)

<u>Figure</u>		<u>Page</u>
169	Load-Deflection Curve and Southwell Plot for Aluminum Panel No. 1, $N_y/N_x = 1.000$	233
170	Load Deflection Curves for Panel No. 2	234
171	Southwell Plot for Panel No. 2, $N_y/N_x = 0$	235
172	Southwell Plot for Panel No. 2, $N_y/N_x = .015$	236
173	Southwell Plot for Panel No. 2, $N_y/N_x = .133$	237
174	Southwell Plot for Panel No. 2, $N_y/N_x = .319$	238
175	Southwell Plot for Panel No. 2, $N_y/N_x = .445$	239
176	Southwell Plot for Panel No. 2, $N_y/N_x = .531$	240
177	Southwell Plot for Panel No. 2, $N_y/N_x = .634$	241
178	Southwell Plot for Panel No. 2, $N_y/N_x = .774$	242
179	Load-Deflection Curves for Panel No. 3	243
180	Load-Deflection Curve and Southwell Plot for Panel No. 3, $N_y/N_x = 123.0$	244
181	Southwell Plot for Panel No. 3, $N_y/N_x = .0081$	245
182	Southwell Plot for Panel No. 3, $N_y/N_x = .086$	246
183	Southwell Plot for Panel No. 3, $N_y/N_x = .171$	247
184	Southwell Plot for Panel No. 3, $N_y/N_x = .244$	248
185	Southwell Plot for Panel No. 3, $N_y/N_x = .367$	249
186	Southwell Plot for Panel No. 3, $N_y/N_x = .475$	250
187	Southwell Plot for Panel No. 3, $N_y/N_x = .532$	251
188	Load-Deflection Curve and Southwell Plot for Panel No. 3, $N_y/N_x = 1.000$	252

LIST OF ILLUSTRATIONS (Continued)

<u>Figure</u>		<u>Page</u>
189	Load-Deflection Curves for Panel No. 5	253
190	Southwell Plot for Panel No. 5, $N_y/N_x = .0079$	254
191	Southwell Plot for Panel No. 5, $N_y/N_x = .043$	255
192	Southwell Plot for Panel No. 5, $N_y/N_x = .101$	256
193	Southwell Plot for Panel No. 5, $N_y/N_x = .140$	257
194	Southwell Plot for Panel No. 5, $N_y/N_x = .158$	258
195	Load-Deflection Curves for Panel No. 5, Turned 90°	259
196	Southwell Plot for Panel No. 5, $N_y/N_x = 47.250$	260
197	Southwell Plot for Panel No. 5, $N_y/N_x = 4.620$	261
198	Southwell Plot for Panel No. 5, $N_y/N_x = 2.350$	262
199	Southwell Plot for Panel No. 5, $N_y/N_x = 1.703$	263
200	Southwell Plot for Panel No. 5, $N_y/N_x = 1.255$	264
201	Southwell Plot for Panel No. 5, $N_y/N_x = 1.060$	265
202	Load Deflection Curves for Panel No. 7	266
203	Southwell Plot for Panel No. 7, $N_y/N_x = 0$	267
204	Southwell Plot for Panel No. 7, $N_y/N_x = .021$	268
205	Southwell Plot for Panel No. 7, $N_y/N_x = .212$	269
206	Southwell Plot for Panel No. 7, $N_y/N_x = .312$	270
207	Southwell Plot for Panel No. 7, $N_y/N_x = .376$	271
208	Southwell Plot for Panel No. 7, $N_y/N_x = .448$	272
209	Southwell Plot for Panel No. 7, $N_y/N_x = .509$	273

LIST OF ILLUSTRATIONS (Continued)

<u>Figure</u>		<u>Page</u>
210	Southwell Plot for Panel No. 7, $N_y/N_x = .614$	274
211	Southwell Plot for Panel No. 7, $N_y/N_x = .787$	275
212	Load Deflection Curves for Panel No. 9	276
213	Southwell Plot for Panel No. 9, $N_y/N_x = 0$	277
214	Southwell Plot for Panel No. 9, $N_y/N_x = .013$	278
215	Southwell Plot for Panel No. 9, $N_y/N_x = .089$	279
216	Southwell Plot for Panel No. 9, $N_y/N_x = .201$	280
217	Southwell Plot for Panel No. 9, $N_y/N_x = .364$	281
218	Southwell Plot for Panel No. 9, $N_y/N_x = .475$	282
219	Southwell Plot for Panel No. 9, $N_y/N_x = .643$	283
220	Southwell Plot for Panel No. 9, $N_y/N_x = .867$	284
221	Load Deflection Curves for Panel 12	285
222	Southwell Plot for Panel No. 12, $N_y/N_x = 0$	286
223	Southwell Plot for Panel No. 12, $N_y/N_x = .004$	287
224	Southwell Plot for Panel No. 12, $N_y/N_x = .125$	288
225	Southwell Plot for Panel No. 12, $N_y/N_x = .306$	289
226	Southwell Plot for Panel No. 12, $N_y/N_x = .406$	290
227	Southwell Plot for Panel No. 12, $N_y/N_x = .537$	291
228	Southwell Plot for Panel No. 12, $N_y/N_x = .762$	292
229	Load Deflection Curves for Panel No. 16	293
230	Southwell Plot for Panel No. 16, $N_y/N_x = 0$	294

LIST OF ILLUSTRATIONS (Continued)

<u>Figure</u>		<u>Page</u>
231	Southwell Plot for Panel No. 16, $N_y/N_x = .008$	295
232	Southwell Plot for Panel No. 16, $N_y/N_x = .062$	296
233	Southwell Plot for Panel No. 16, $N_y/N_x = .139$	297
234	Southwell Plot for Panel No. 16, $N_y/N_x = .240$	298
235	Southwell Plot for Panel No. 16, $N_y/N_x = .405$	299
236	Southwell Plot for Panel No. 16, $N_y/N_x = .517$	300
237	Southwell Plot for Panel No. 16, $N_y/N_x = .678$	301
238	Load-Deflection Curves for Panel 19A	302
239	Southwell Plot for Panel No. 19A, $N_y/N_x = .047$	303
240	Southwell Plot for Panel No. 19A, $N_y/N_x = .194$	304
241	Southwell Plot for Panel No. 19A, $N_y/N_x = .335$	305
242	Southwell Plot for Panel No. 19A, $N_y/N_x = .428$	306
243	Southwell Plot for Panel No. 19A, $N_y/N_x = .560$	307
244	Southwell Plot for Panel No. 19A, $N_y/N_x = .678$	308
245	Southwell Plot for Panel No. 19A, $N_y/N_x = 1.00$	309
246	Southwell Plot for Panel No. 19A, $N_y/N_x = 1.00$, Turned 90°	310
247	Load-Deflection Curves for Panel No. 19A, Turned 90°	311
248	Southwell Plot for Panel No. 19A, $N_y/N_x = 1.448$	312
249	Southwell Plot for Panel No. 19A, $N_y/N_x = 1.759$	313
250	Southwell Plot for Panel No. 19A, $N_y/N_x = 2.171$	314

LIST OF ILLUSTRATIONS (Continued)

<u>Figure</u>		<u>Page</u>
251	Southwell Plot for Panel No. 19A, $N_y/N_x = 3.214$	315
252	Southwell Plot for Panel No. 19A, $N_y/N_x = 5.611$	316
253	Southwell Plot for Panel No. 19A, $N_y/N_x = 17.769$	317

L I S T O F T A B L E S

<u>Table</u>		<u>Page</u>
I	Laminate Orientation of Boron Compression Panels	11
II	Laminate Orientation of Boron Shear Panels	12
III	Compression Panel Thickness Measurements	15
IV	Shear Panel Thickness Measurements	16
V	Buckling Results	49
VI	Panel No. 5 Buckling Comparison	53
VII	Uniaxial Edge Load and Transverse Pressure Tests	56
VIII	Biaxial Compressive Load Tests	116
IX	Critical Buckling Loads, Biaxial Compression	126
X	Natural Frequency Tests	132
XI	Ultimate Load Tests	176
XII	Load Distribution Study, Panel 3	179
XIII	Load Distribution Study, Panel 9	180

SECTION I
INTRODUCTION

The overall objective under AF Contract F33615-68-C-1474 was to provide a source of reliable advanced composite engineering property data to enhance the high-confidence design of primary aircraft structures. The program spanned 26 months and was composed of the following basic technical tasks:

1. Work Area I - Design Allowables
2. Work Area II - Structural Elements.

Data gathering and fabrication efforts also spanned the entire program.

The design allowable effort was devoted to determining and establishing statistically significant static design allowables for a boron-reinforced epoxy matrix composite material system. In addition, the material response to various dynamic loading configurations and certain physical characteristics of the material were determined.

The structural element effort was devoted to additional characterization of the behavior of flat plates fabricated with advanced composite materials. Transverse, uniaxial, biaxial, and diagonal tension loading configurations were used to study small deflection and post-buckling behaviors.

The area of work covered in this volume is the anisotropic plate evaluation - bending, dynamics, and stability. The primary objective was to determine the small deflection and post-buckling behaviors of boron-epoxy flat plates subjected to transverse, uniaxial, biaxial, and diagonal tension loading configurations. These studies were conducted to verify an existing anisotropic plate analysis. A secondary objective was to observe the mode of failure of laminated anisotropic flat plates under uniaxial compression and shear.

S E C T I O N I I

S U M M A R Y

An experimental investigation of the behavior of boron-epoxy flat plates is presented. The behaviors studied were (1) normal deflections due to transverse loads and transverse loads combined with uniaxial compression, (2) stability under biaxial compressive loads, (3) inplane load effects on the natural modes of vibration, (4) uniaxial compressive modes of failure, and (5) the diagonal tension behavior of thin panels. Boundary conditions considered were either clamped-clamped or clamped-simple.

Analytical predictions have been presented for the plates tested. These predictions were obtained using the Anisotropic Plate Analysis Computer Program RA5. An attempt was made to express the actual experimental boundary conditions analytically using data obtained from isotropic plates.

A comparison of the analytical and experimental results verifies that the Anisotropic Plate Analysis Computer Program RA5 is an accurate analytical tool for predicting the response of boron-epoxy composite plates to various load conditions.

SECTION III
METHOD OF ANALYSIS

Analytical predictions of the static and dynamic response of each of the plates tested in this program have been made. These predictions are based on the Anisotropic Plate Analysis method (Computer Program RA5) described in Reference 1. A brief description of the method is given below.

The method of solution is the Ritz method, which involves the minimization of a linear theory energy expression.

The potential energy due to bending of a plate can be written as follows (Reference 2):

$$V = \frac{1}{2} \iint_A [M]^T [k] \, dx dy, \quad (1)$$

where

$$[M] = \begin{bmatrix} M_x \\ M_y \\ M_{xy} \end{bmatrix} = \text{plate bending and twisting moments} \quad (2)$$

and

$$[k] = \begin{bmatrix} k_{xx} \\ k_{yy} \\ k_{xy} \end{bmatrix} = - \begin{bmatrix} W(x,y),_{xx} \\ W(x,y),_{yy} \\ 2W(x,y),_{xy} \end{bmatrix} = \text{plate curvatures}, \quad (3)$$

where a comma denotes partial differentiation.

The deflection is assumed in a series:

$$W(x,y) = \sum_{m=1}^p \sum_{n=1}^q a_{mn} X_m(x) Y_n(y) \quad (4)$$

where $X_m(x)$ and $Y_n(y)$ are functions that satisfy the boundary conditions of a rectangular plate at the edges $x = 0, a$ and $y = 0, b$. The coefficients a_{mn} are parameters which are determined by minimizing the energy expressions.

The potential energy of the inplane loads (with respect to bending deflections) is the same for both isotropic and anisotropic plates. It is given by the following expression in orthogonal cartesian coordinates (Reference 3):

$$U = - \frac{1}{2} \iint_A [N_x W(x,y)_{,x}^2 + N_y W(x,y)_{,y}^2 + 2N_{xy} W(x,y)_{,x} W(x,y)_{,y}] dx dy \quad (5)$$

where N_x , N_y , and N_{xy} are the inplane stress resultants. For the stability analysis, the basic principle used is the principle of stationary potential energy. The condition for equilibrium is

$$V + \lambda U = \text{stationary value}, \quad (6)$$

where λ is an arbitrary multiplier of the inplane loads.

By using the assumed series (equation 4) for the deflection, the condition (equation 6) becomes an ordinary maximum-minimum problem in the $p \times q$ variables a_{mn} . The problem can be stated as follows:

$$\frac{\partial(V + \lambda U)}{\partial a_{ik}} = 0 \quad (7)$$

The basic principle used in the analysis of the deflections, moments, and shears due to lateral (and inplane) loads is also the principle of stationary potential energy and in this case, where body forces have been neglected, is equivalent to the condition that the variation of the internal potential energy is equal to the variation of the work of the applied loads (Reference 2). By using the assumed series (equation 4) for the deflection, this variational problem again becomes an ordinary maximum-minimum problem in the $p \times q$ variables a_{mn} and can be stated as follows:

$$\frac{\partial V}{\partial a_{ik}} + \frac{\partial U}{\partial a_{ik}} = \frac{\partial Q}{\partial a_{ik}}, \quad (8)$$

where Q is the work of the applied loads. Q is given as follows:

$$Q = \int_0^b \int_0^a \bar{q}W(x,y) dx dy , \quad (9)$$

where

\bar{q} = distributed load.

The basic principle used in the dynamic analysis is Hamilton's Principle:

$$V + U - T = \text{stationary value}, \quad (10)$$

where V and U are as defined above and T is the kinetic energy of the plate vibrating at an angular frequency ω . T is given by the following expression (Reference 3):

$$T = \frac{1}{2} \omega^2 \rho h \int_0^b \int_0^a W(x,y)^2 dx dy . \quad (11)$$

Substituting expression (4) into V , U , and T , the condition (10) again becomes an ordinary maximum-minimum problem in $p \times q$ variables a_{mn} :

$$\frac{\partial V}{\partial a_{ik}} + \frac{\partial U}{\partial a_{ik}} = \frac{\partial T}{\partial a_{ik}} . \quad (12)$$

SECTION IV
SPECIMENS, EQUIPMENT,
AND PROCEDURES

Descriptions of the test specimens, test equipment, and test procedures used in this program are presented on the following pages. An attempt was made to express the actual experimental boundary conditions analytically using isotropic control panels. The results of this effort are discussed.

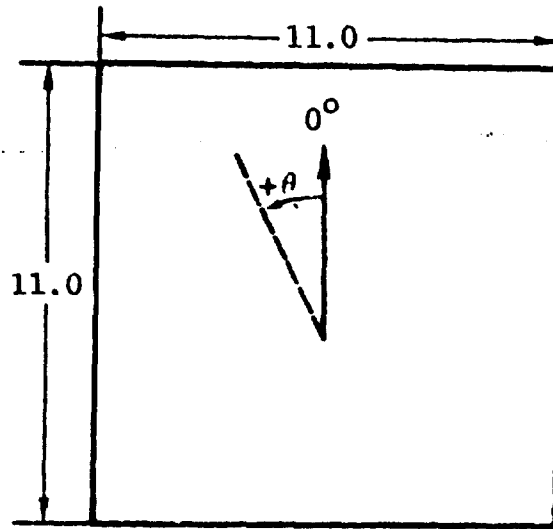
4.1 DESCRIPTION OF SPECIMENS

Twenty-three panels were evaluated in the test program; 11 were compression specimens and nine were shear panels made of boron-epoxy composite with various patterns of fiber orientation; the remaining three panels, which served as isotropic control specimens, were either aluminum or steel. Two of the isotropic panels and 10 of the 11 compression specimens had been used previously for a buckling study sponsored by the Air Force Materials Laboratory, under Contract No. AF33(615)-5257 (Reference 4).

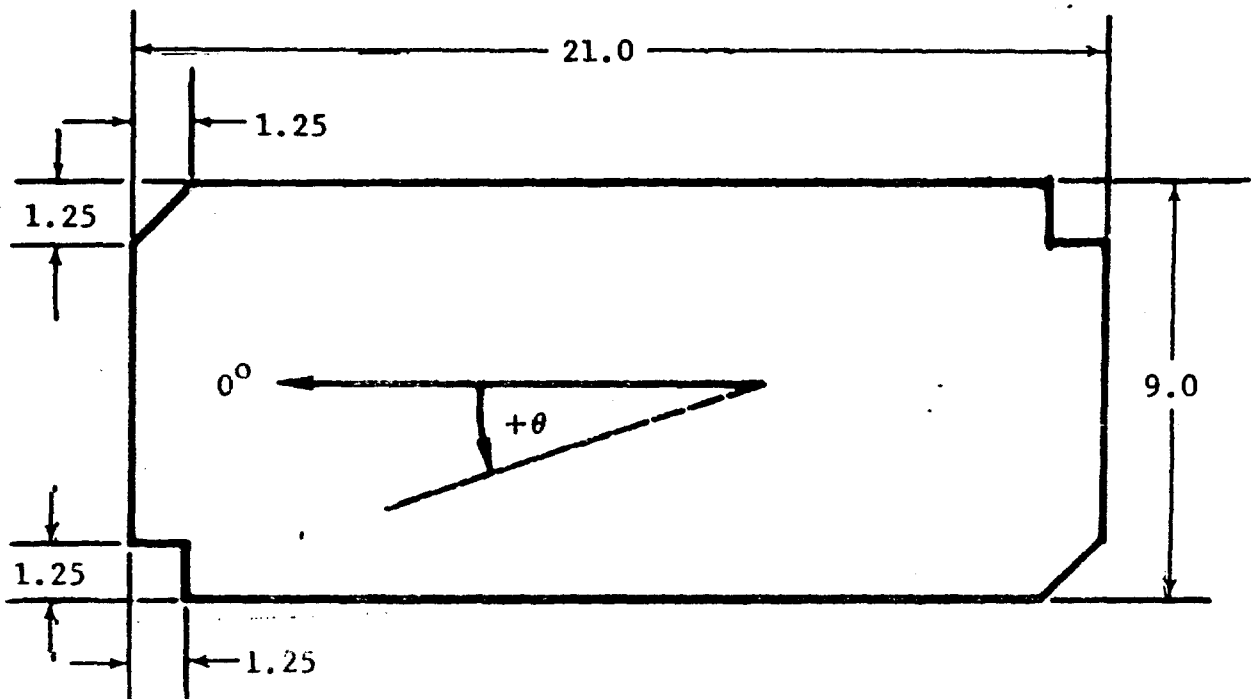
The configurations of the compression and shear panels are shown in Figure 1. The direction from 0-degree of each layer is shown in Tables I and II. In the case of the tapered plate, Panel 19A, the thicker of the two uniform edges was at the base of the test fixture. All panels had a constant number of plies over the area with the exception of Panel 19A, which was tapered from 19 layers at one end to 10 layers at the opposite end as shown in Figure 2.

The average thickness of each panel was determined by a standard procedure. Thickness measurements were made for each compression panel at the points shown in Figure 3 and for each shear panel at the points shown in Figure 4 and then averaged to obtain the tabulated values shown in Tables I and II. The tabulated thickness values are presented in Tables III and IV.

All composite panels were fabricated of Narmco 5505 boron-epoxy preimpregnated tape by the fabrication process described in Reference 5. Panel 2 was fabricated from two 10-ply unidirectional panels orientated at ± 45 -degrees. The two 10-ply plates were bonded together with Shell Epon 828 (60 parts by weight) and General Mills Versamid 115 (40 parts by weight) to form the single 20-ply



a. Compression



b. Shear

Figure 1 Boron Composite Panels

Table I LAMINATE ORIENTATION OF BORON COMPRESSION PANELS
(In Degrees)

Panel	Layer No.																				Average Thickness Inches
	1	2	3	4	5	6	7	8	9	10	11	12	13	14	15	16	17	18	19	20	
2	+45	+45	+45	+45	+45	+45	+45	+45	+45	+45	-45	-45	-45	-45	-45	-45	-45	-45	-45	-45	0.112
3	0	90	0	90	0	90	0	90	0	90	0	90	0	90	0	90	0	90	0	90	0.102
5	0	0	0	0	0	0	0	0	0	0	0	0	0	0	0	0	0	0	0	0	0.098
7	+45	+45	+45	+45	+45	+45	+45	+45	+45	+45	+45	+45	+45	+45	+45	+45	+45	+45	+45	+45	0.097
9	+45	-45	+45	-45	+45	-45	+45	-45	+45	-45	+45	-45	+45	-45	+45	-45	+45	-45	+45	-45	0.105
12	0	0	+45	-45	0	0	+45	-45	0	0	0	-45	+45	0	0	-45	+45	0	0	0	0.112
13	+30	-30	+30	-30	+30	-30	+30	-30	+30	-30	+30	-30	+30	-30	+30	-30	+30	-30	+30	-30	0.111
14	+30	-30	+30	-30	+30	-30	+30	-30	+30	-30	+30	-30	+30	-30	+30	-30	+30	-30	+30	-30	0.111
16	0	+45	90	-45	0	+45	90	-45	0	-45	90	+45	0	-45	90	+45	0	-45	90	+45	0.084
19A	+45	+45	+45	+45	+45	+45	+45	+45	+45	+45	+45	+45	+45	+45	+45	+45	+45	+45	+45	+45	0.107-0.051
21	0	0	0	0	0	0	0	0	0	0	0	0	0	0	0	0	0	0	0	0	0.103
Aluminum 1																					0.127
Aluminum 3																					0.127
Steel																					0.038

Table II LAMINATE ORIENTATION OF BORON SHEAR PANELS
(In Degrees)

Panel No.	Layer Number						Average Thickness (in.)
	1	2	3	4	5	6	
1	+45	-45	-45	+45			0.022
1A	+45	-45	-45	+45			0.022
3	0	90	90	0			0.023
5	+60	0	-60	-60	0	+60	0.034
801	-45	+45	+45	-45			0.022
801A	-45	+45	+45	-45			0.023
803	90	0	0	90			0.023
805	-60	0	+60	+60	0	-60	0.034
807	+60	-60	0	0	-60	+60	0.033

SMD1347

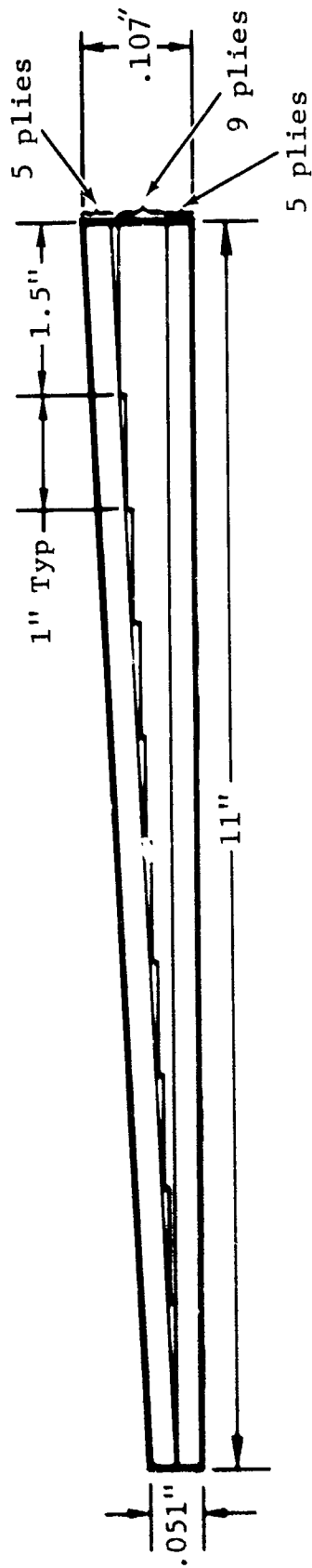


Figure 2 Cross-Section of Tapered Panel 19A

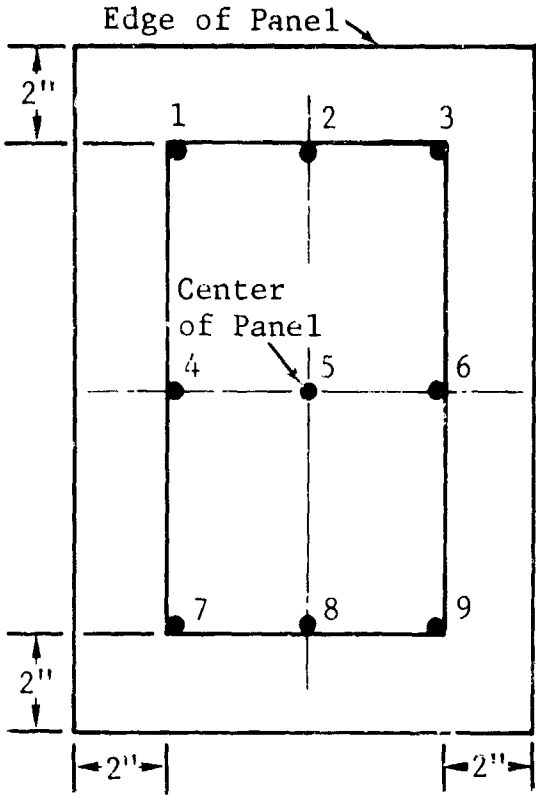


Figure 3 Thickness Measurement Locations, Compression Panels

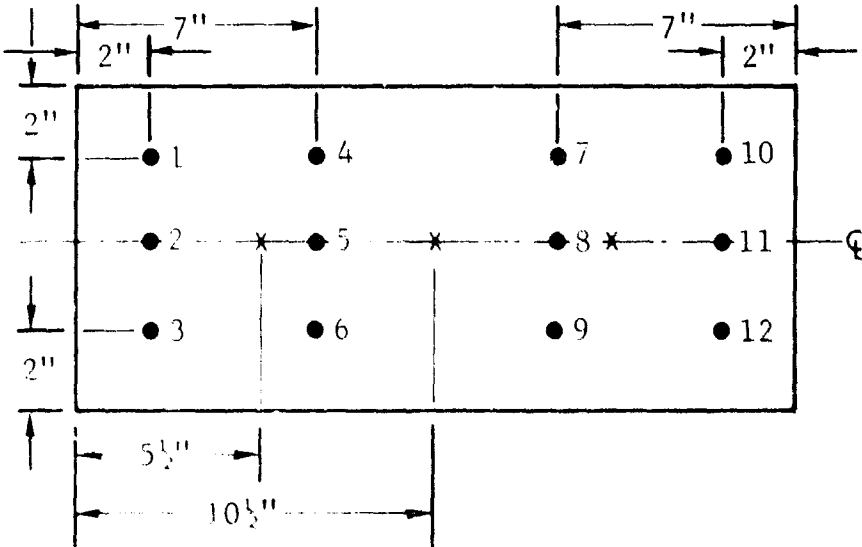


Figure 4 Thickness Measurement Locations, Shear Panels

Table III COMPRESSION PANEL THICKNESS MEASUREMENTS

Panel	Thickness Measurements, Inches									Average Thickness (in.)
	1	2	3	4	5	6	7	8	9	
2	0.111	0.111	0.109	0.111	0.112	0.114	0.113	0.113	0.113	0.112
3	0.099	0.101	0.103	0.104	0.103	0.102	0.102	0.101	0.103	0.102
5	0.101	0.100	0.098	0.097	0.098	0.096	0.097	0.099	0.098	0.098
7	0.095	0.095	0.097	0.098	0.097	0.100	0.099	0.096	0.099	0.097
9	0.104	0.106	0.105	0.106	0.106	0.106	0.105	0.106	0.105	0.110
12	0.112	0.111	0.113	0.111	0.113	0.113	0.114	0.113	0.112	0.112
13	0.111	0.111	0.110	0.111	0.112	0.112	0.112	0.113	0.111	0.111
14	0.111	0.112	0.112	0.111	0.111	0.110	0.111	0.110	0.111	0.111
16	0.084	0.085	0.084	0.085	0.084	0.084	0.085	0.085	0.084	0.084
19A	0.096	0.096	0.094	0.076	0.076	0.075	0.060	0.061	0.056	-
21	0.102	0.103	0.103	0.102	0.103	0.103	0.103	0.102	0.103	0.103
Aluminum 1	0.127	0.127	0.127	0.127	0.127	0.127	0.127	0.127	0.127	0.127
Aluminum 3	0.127	0.127	0.127	0.127	0.127	0.127	0.127	0.127	0.127	0.127
Steel	0.088	0.088	0.088	0.088	0.088	0.088	0.088	0.088	0.088	0.088

Table IV SHEAR PANEL THICKNESS MEASUREMENT

Panel No.	Thickness, Inches												Average	
	1	2	3	4	5	6	7	8	9	10	11	12		
1	0.021	0.023	0.021	0.021	0.023	0.021	0.021	0.022	0.021	0.021	0.022	0.021	0.022	0.022
1A	0.023	0.023	0.023	0.023	0.023	0.022	0.022	0.022	0.022	0.022	0.022	0.023	0.022	0.022
3	0.023	0.023	0.022	0.023	0.023	0.023	0.022	0.023	0.023	0.023	0.023	0.024	0.023	0.023
5	0.035	0.033	0.034	0.033	0.033	0.033	0.035	0.033	0.034	0.033	0.035	0.034	0.035	0.034
801	0.022	0.022	0.022	0.022	0.023	0.022	0.022	0.022	0.022	0.022	0.022	0.022	0.022	0.022
801A	0.022	0.023	0.022	0.023	0.023	0.022	0.022	0.023	0.023	0.023	0.023	0.023	0.023	0.023
803	0.024	0.023	0.023	0.023	0.023	0.022	0.022	0.024	0.023	0.022	0.022	0.022	0.022	0.023
805	0.035	0.034	0.033	0.034	0.034	0.034	0.033	0.035	0.034	0.033	0.033	0.034	0.033	0.034
807	0.033	0.033	0.034	0.034	0.033	0.033	0.033	0.033	0.033	0.033	0.033	0.033	0.033	0.033

unsymmetrical $+45^\circ$ plate. The two-stage operation was necessary to avoid the temperature-induced curvatures that occur when an unsymmetrical plate is cooled from the cure temperatures. The panels to be used for ultimate load tests were infrared inspected for defects. None were found.

4.2 FIXTURES AND EQUIPMENT

The compression panels were installed in the compression fixture (shown in Figure 5), which had previously been used for a buckling study sponsored by the Air Force Materials Laboratory, under Contract No. AF33(615)-5257 (Reference 4). The complete setup was mounted in the 200,000-pound test machine as shown in Figure 6. The sides of the plates were held either by clamped supports (Figure 7) or by knife edge supports (Figure 8). After the edges were secured, the panels measured 10 x 10 inches inside the frame.

The basic compression fixture was modified to accommodate lateral loads as shown in Figure 9. Lateral load was applied to the flat plate by means of a square pressure bag (Figure 10) sandwiched between the boron panel and an aluminum supporting plate. Pressure in the bag was monitored using the manometer shown in Figure 11. Deflection readings were recorded using five Federal dial indicators (Figure 12) located at the center and the diagonal quarter points of the plate.

For biaxial compressive loads, the basic compression fixture was modified to accommodate four hydraulic load actuators (two on either side) located as shown in Figure 13. A typical test setup is shown in Figure 14. In Figure 15 the location of all four actuators is shown relative to the test fixture. The actuators were pressurized using an Edison Multi-Channel Load Converter until preselected actuator loads were reached. Loads carried by the hydraulic actuators were monitored via strain gauges bonded to the shaft of each actuator as shown in Figure 14. Deflection readings were recorded by use of five Federal dial indicators located at the center and centerline quarter points of the panels. The dial indicators are shown positioned in Figure 16.

The test setup used to determine the natural frequencies of the compression panels is shown in Figures 17 and 18. The shaker and monitoring equipment are listed below:

1. Phase Meter
Action Laboratories Incorporated, Model 329BSD
2. Log Voltmeter - Converter
Houston Instrument Corporation, Model HLVC-150

3. Master Control
Spectral Dynamics, Model SD23A
4. Dynamic Analyzer
Spectral Dynamics, Model SD101A
5. Log Frequency Converter
Houston Instrument Corporation, Model HLFC-120
6. XYY' Recorder
Electro Instruments, Model 580
7. Oscillator Power Supply
Consolidated Engineering Corporation, Model 2-105
8. Amplifier
Consolidated Engineering Corporation, Model 1-113B
9. Displacement Acceleration Selector
Ling, Model DA-10-B
10. Servo Control Amplifier
Ling, Model S-10-B
11. Servo D and G Amplifier
Ling, Model S-11-D
12. Charge Amplifier
Endevco, Model 2710A
13. Logarithmic Converter
Moseley, Model 60B
14. Electronic Counter
Hewlett-Packard, Model 521A
15. Amplifier
McIntosh, Model M1-200
16. Sweep Oscillator
Spectral Dynamics, Model SD104A-5
17. Accelerometer
Endevco, Model 2222A
18. Vibration Exciter
General Dynamics

SMD4009

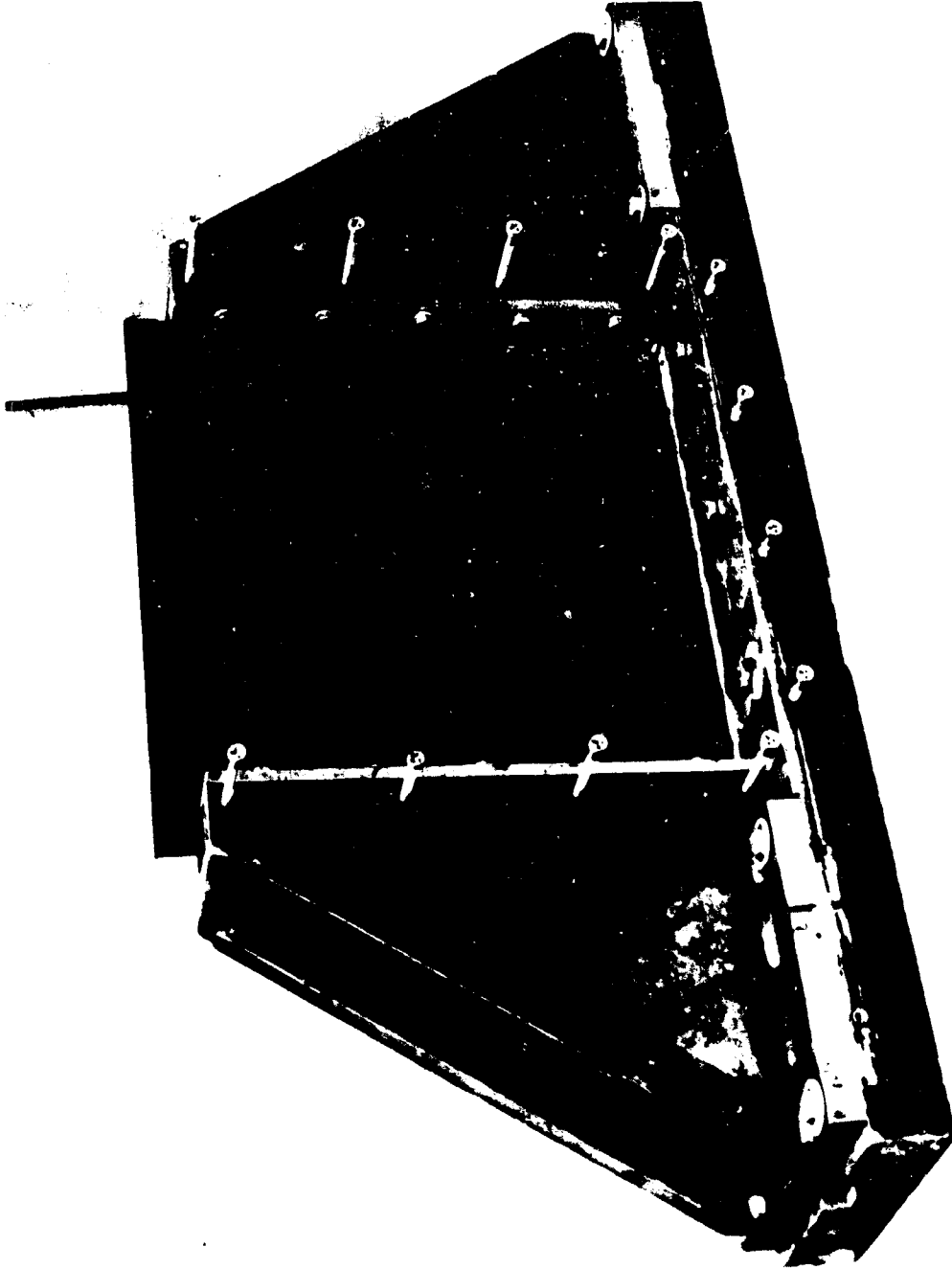


Figure 5 Compression Frame with Panel Installed and Upper Head Removed

SMD4010



Figure 6 Compression Setup Installed in 200,000 Pound Universal Test Machine

SMD4011



Figure 7 Top View of Compression Frame Showing Panel in Clamped Support

SMD4012

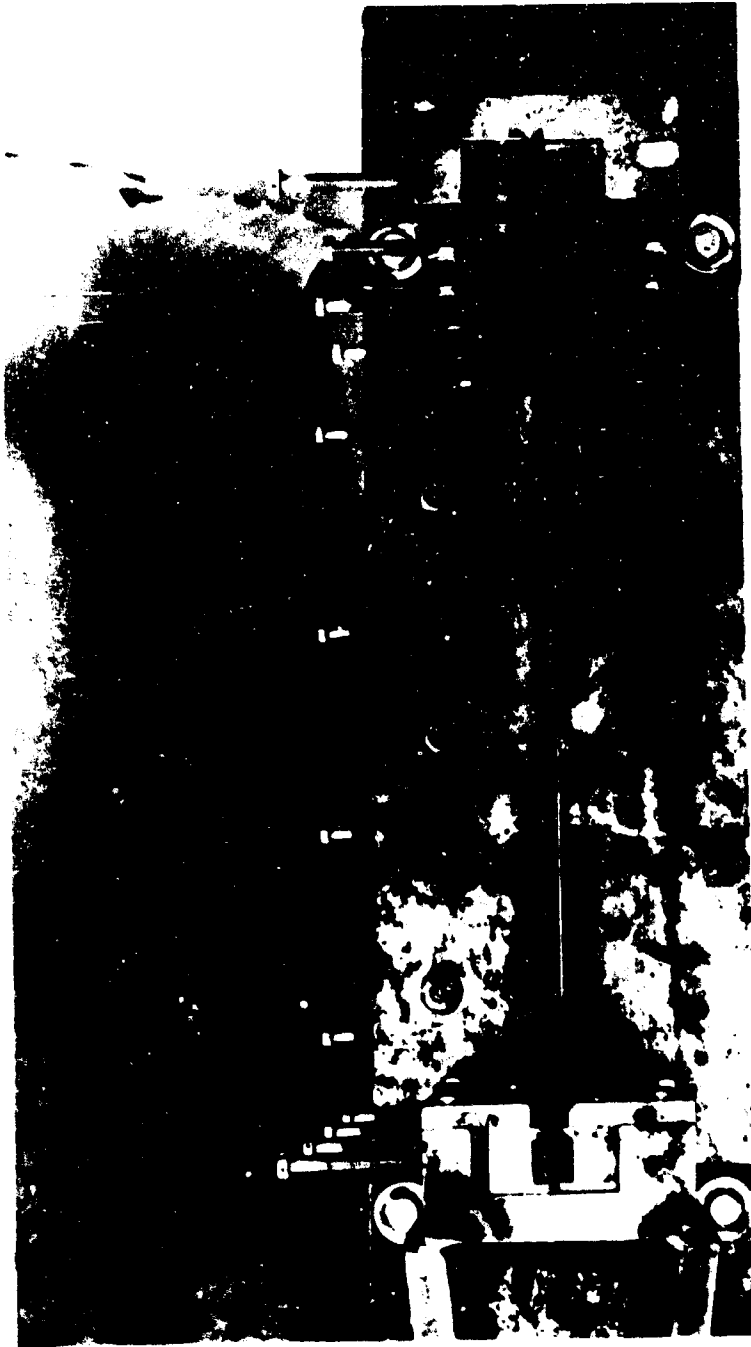


Figure 8 Top View of Compression Frame Showing Panel in Knife Edge Support

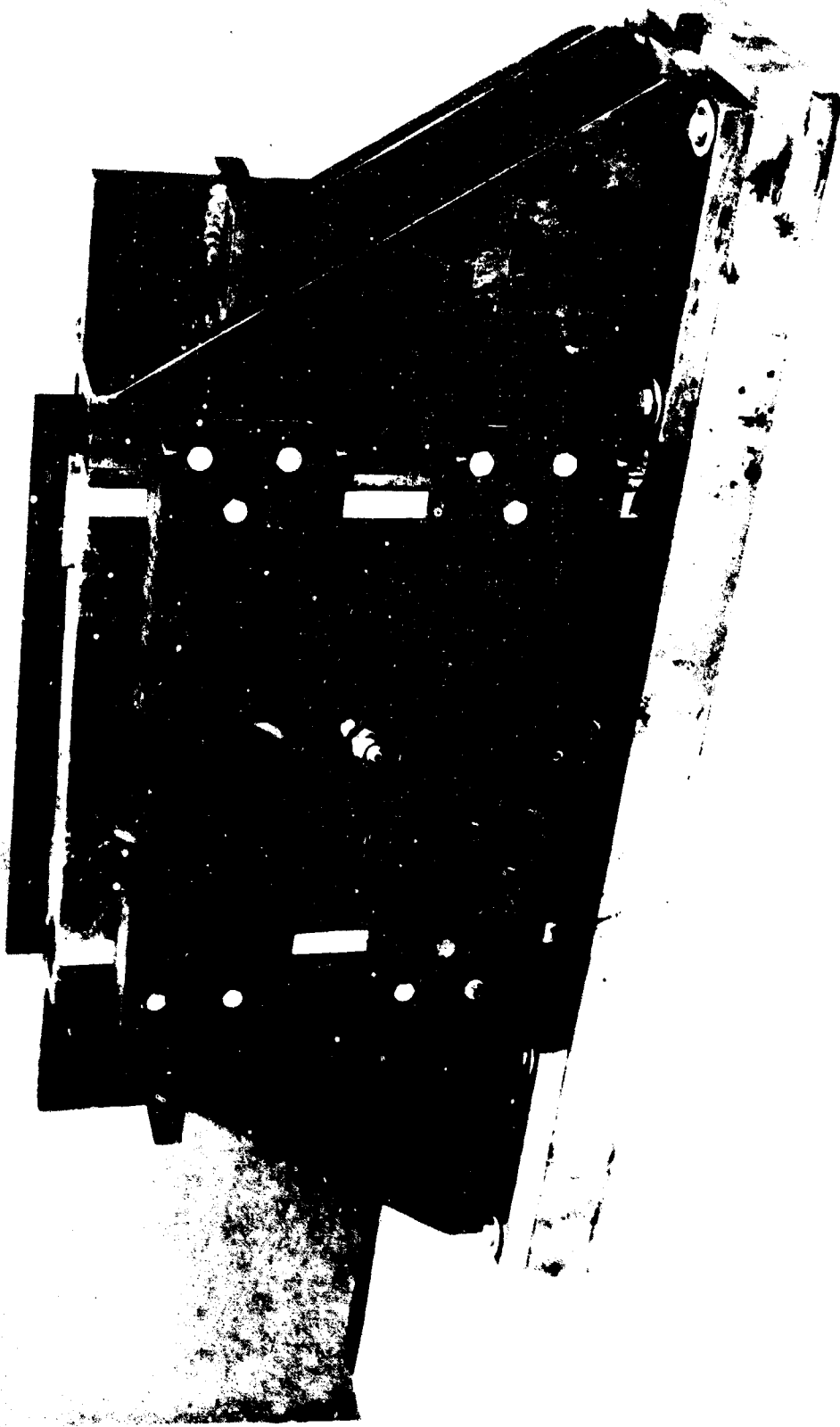


Figure 9 Basic Compression Frame Modified for Lateral Loads

SMD3942

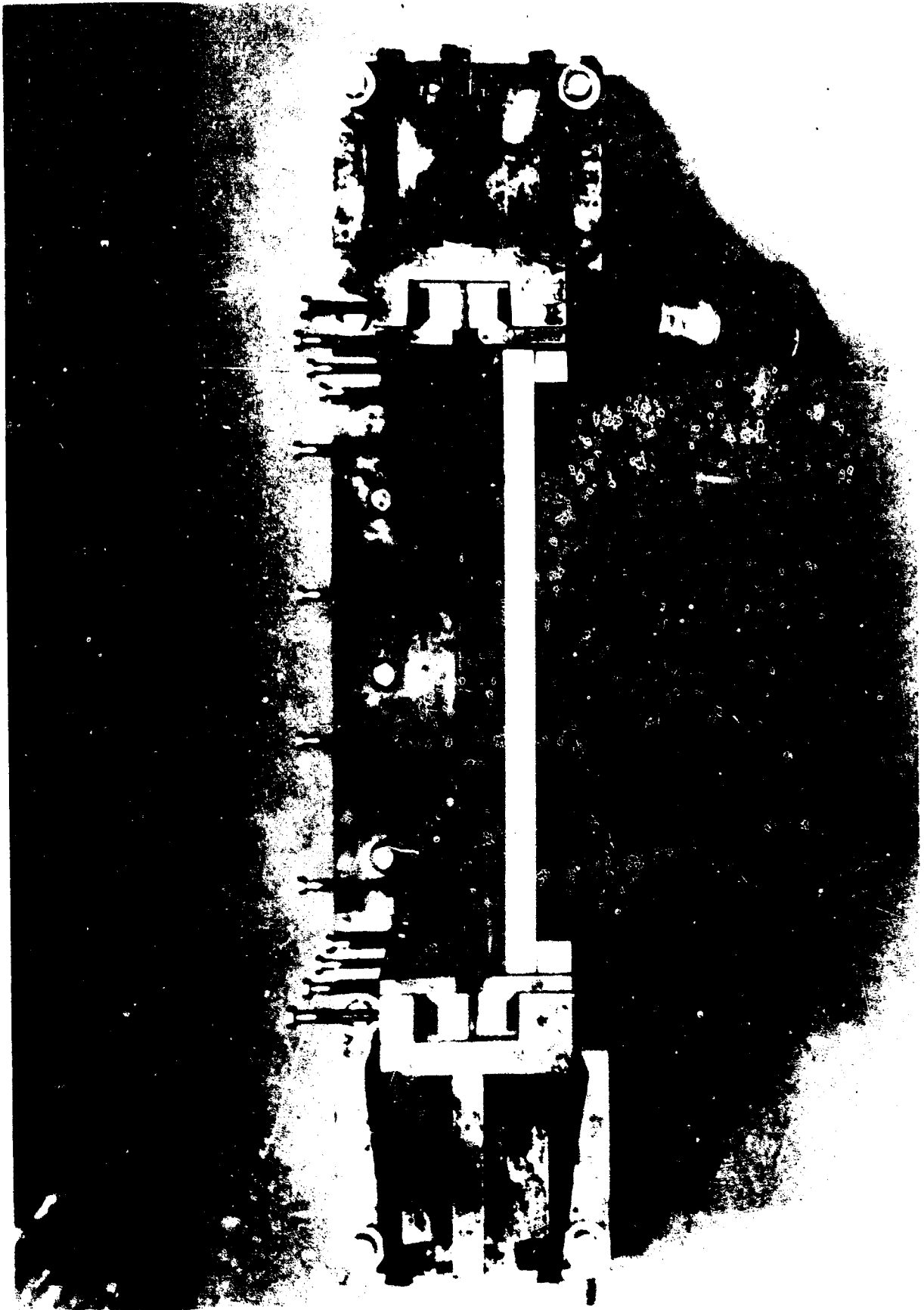


Figure 10 Top View of Modified Compression Frame Showing Panel
in Clamped Edge Support and Pressure Bag Installed

SMD3943

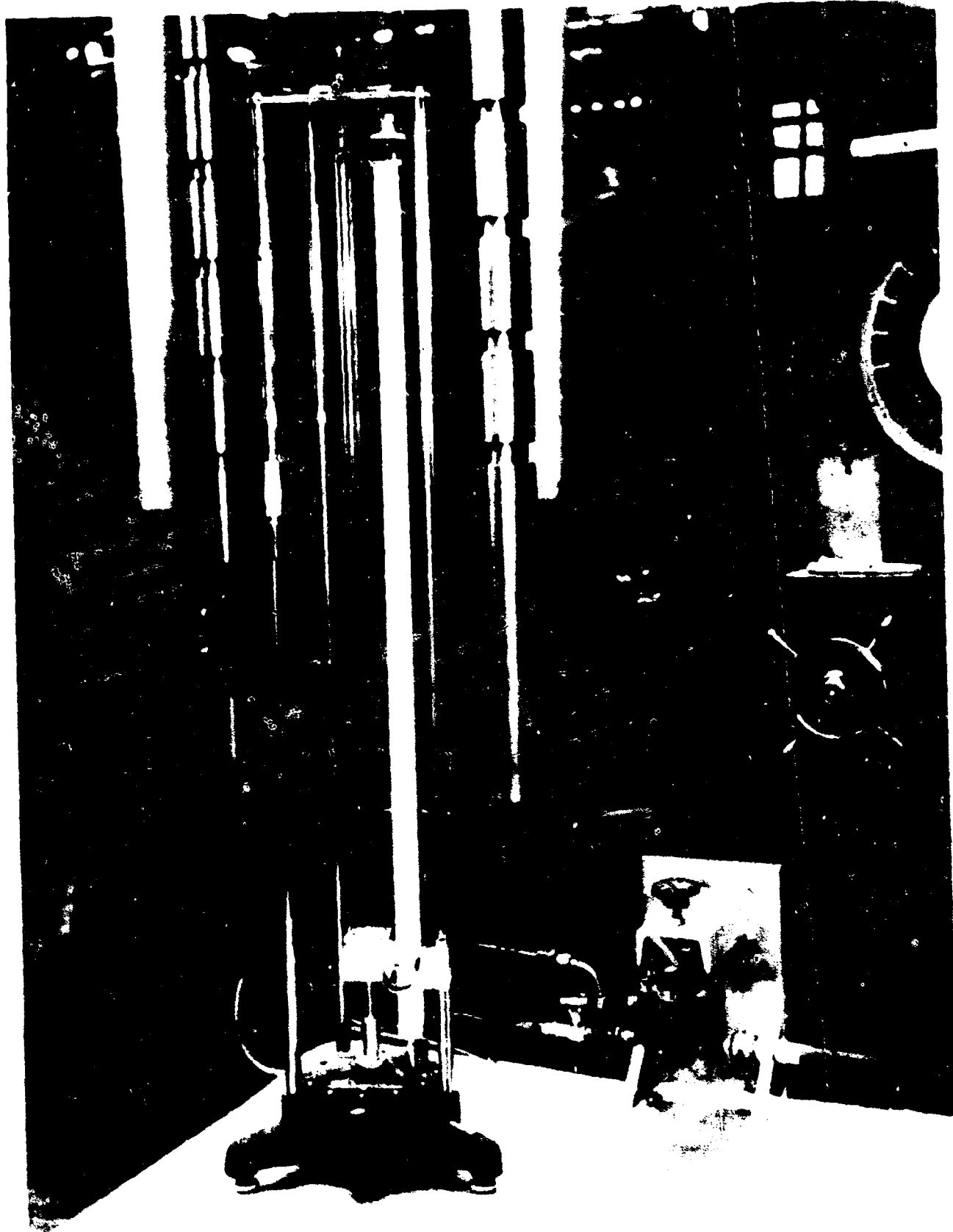


Figure 11 Pressure Monitoring Equipment

SMD3944

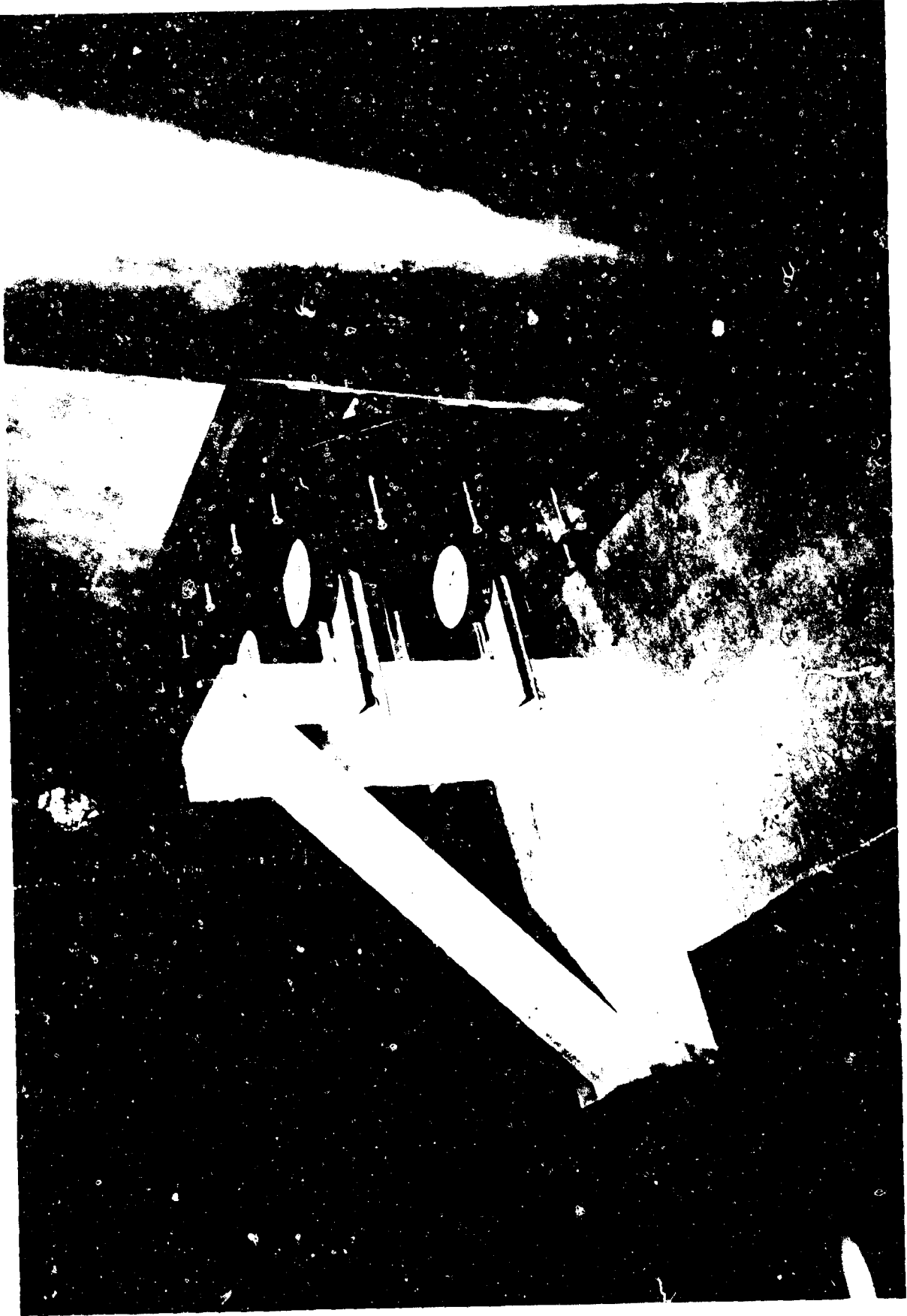


Figure 12 Lateral Load - Uniaxial Compression Setup

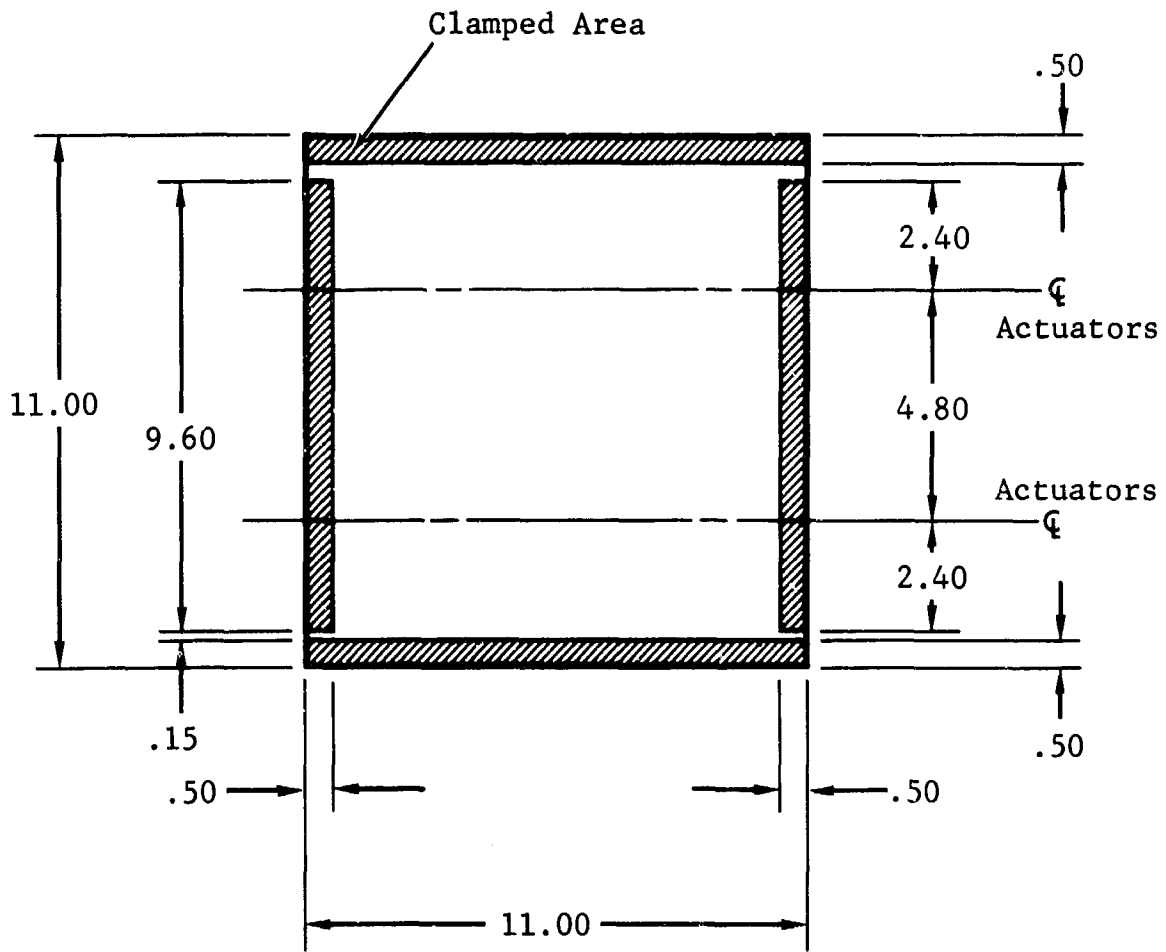


Figure 13 Biaxial Loading Geometry

SMD 3265

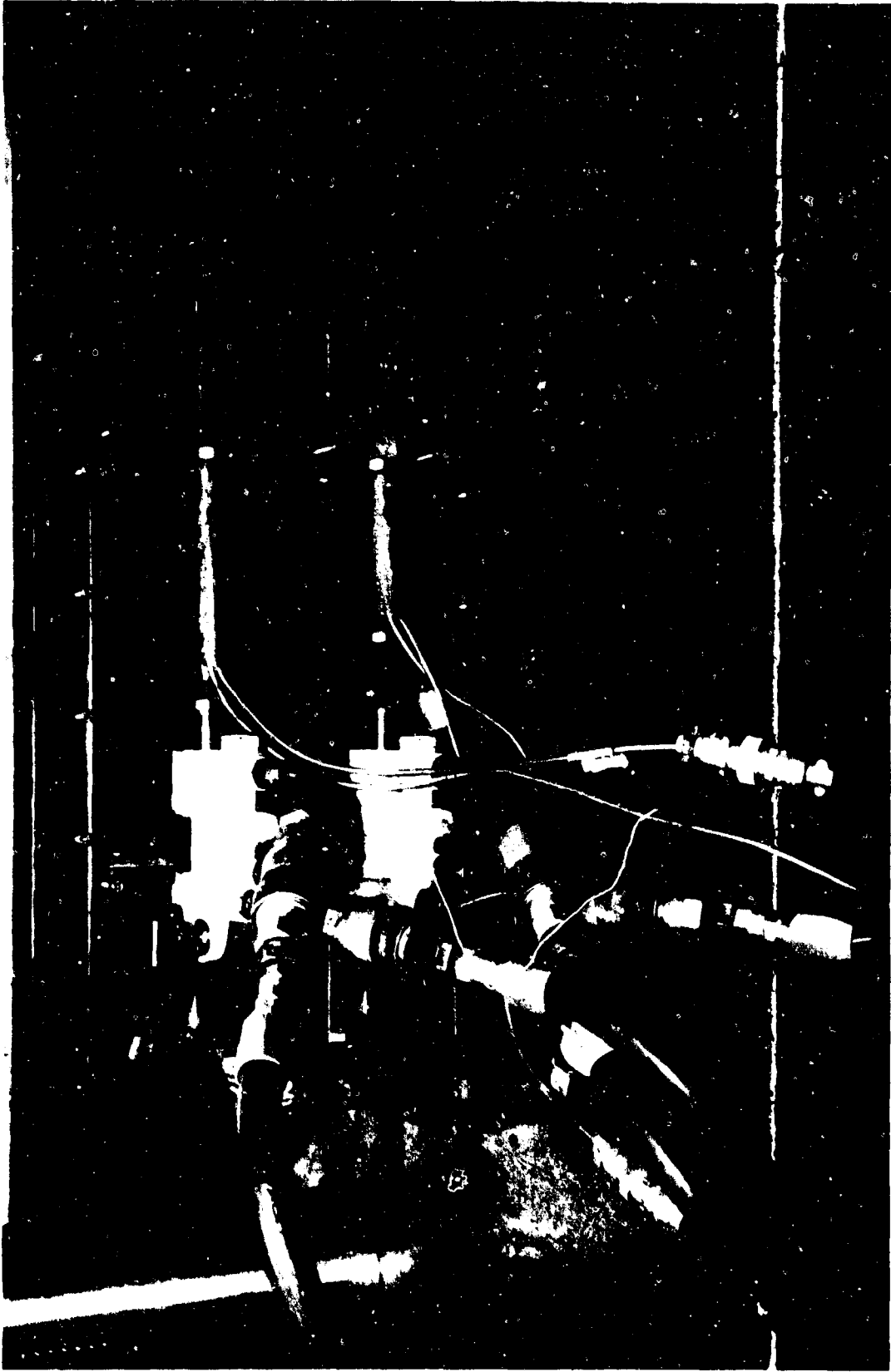


Figure 14 Typical Biaxial Test Setup Without Dial Indicators

SMD 3266

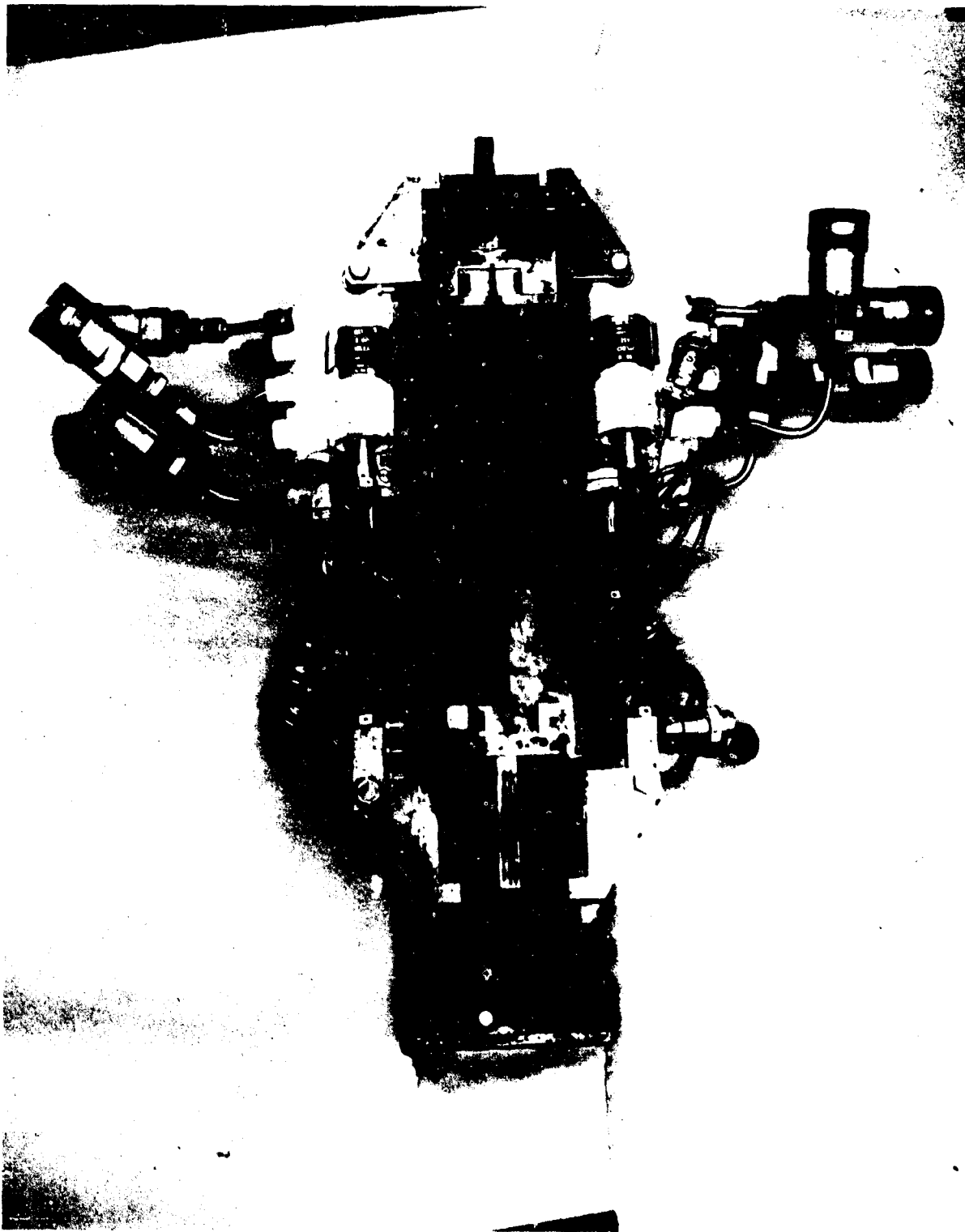


Figure 15 Load Actuator Locations

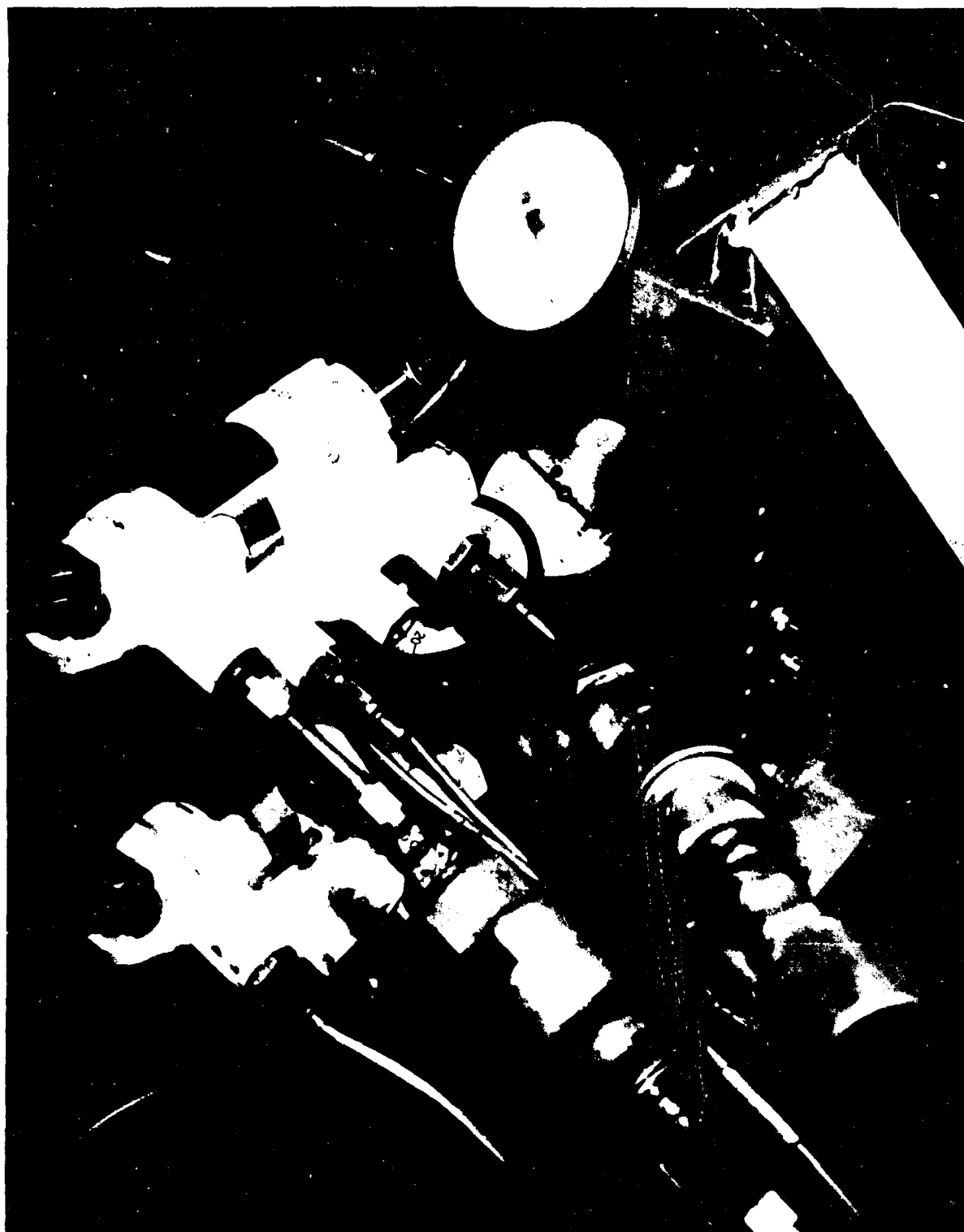


Figure 16 Dial Indicator Locations

SMD 3302

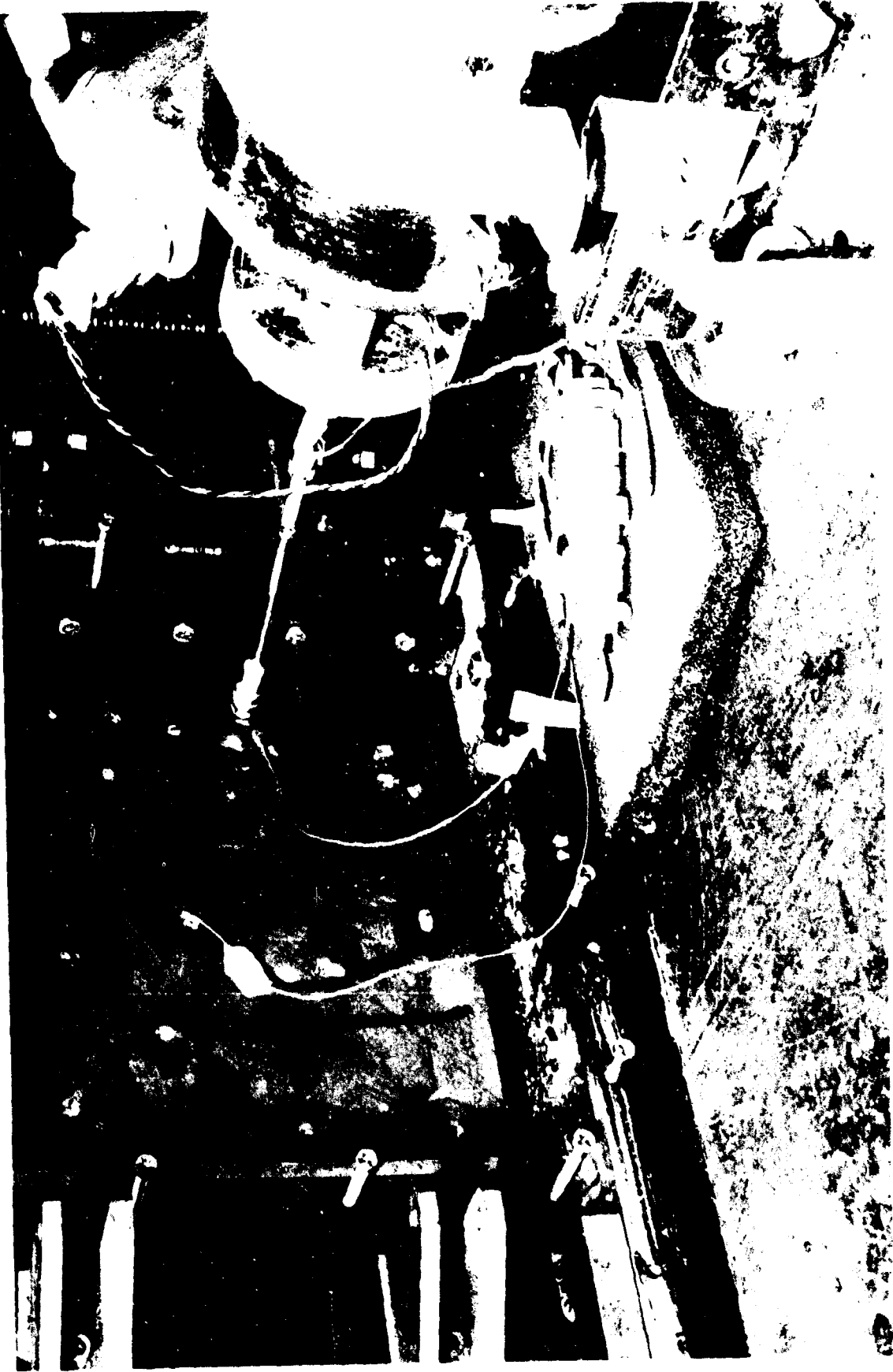


Figure 17 Dynamic Vibration Test Setup

SMD 3303

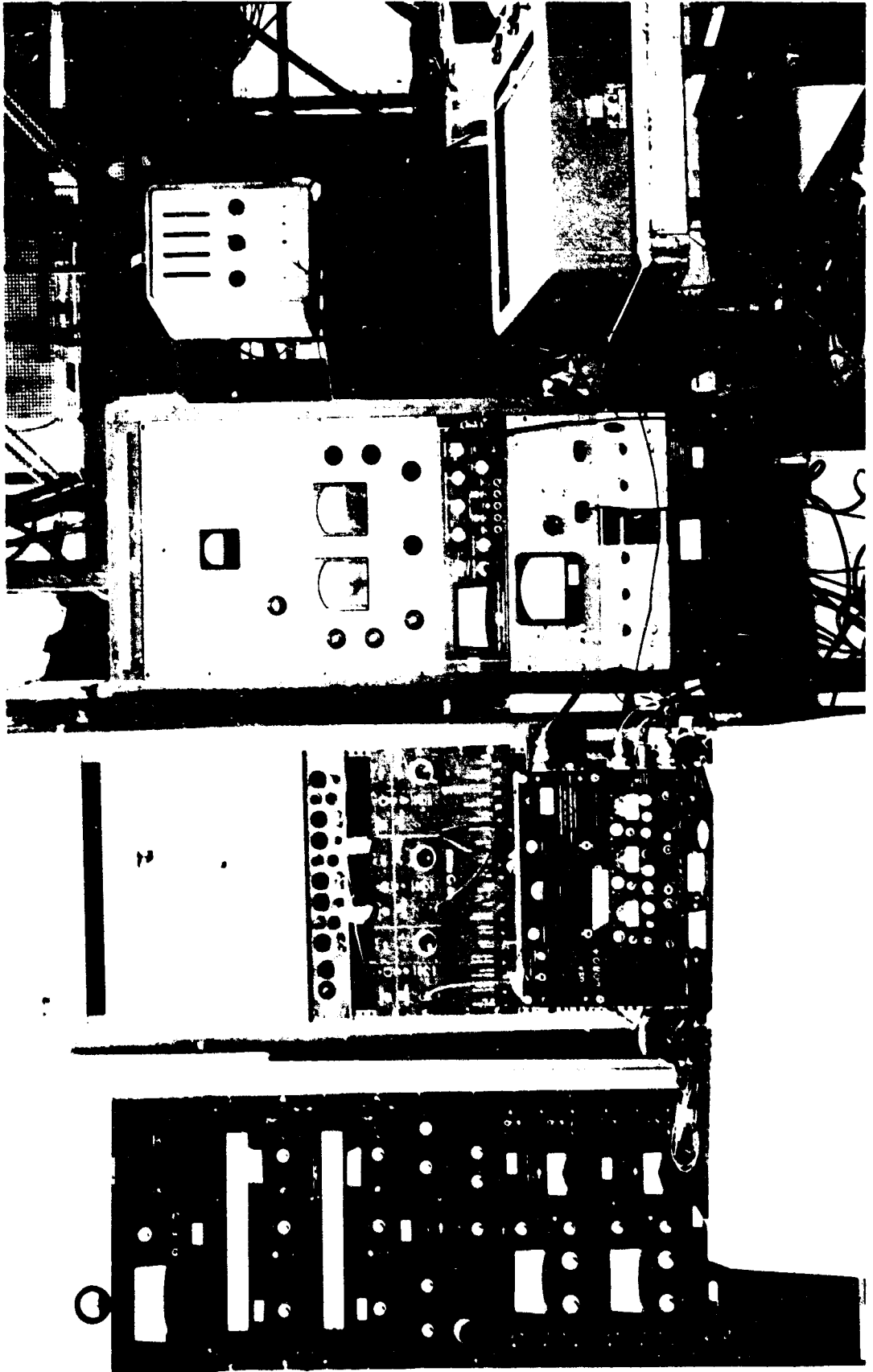


Figure 18 Dynamic Vibration Monitoring Circuit Equipment

The shear frame, Figure 19, consisted of two sets of two pin-connected legs which were bonded to the shear panel. A special jig was designed to serve as a holding fixture for the bonding operation and as a means of transporting and holding the panel and frame until they were installed in the test machine (Figure 19). The jig was required to prevent premature damage to the thin shear panels due to the massive picture-frame fixture used. Three Federal dial indicators were used to monitor deflections as shown in Figure 20. Location of the indicators on the panels is shown by an "X" in Figure 4.

4.3 TEST PROCEDURES

In preparation for the inplane compression tests, each panel was taped on all four edges with two layers of Scotch 549 Teflon tape. Use of the tape reduced the induced lateral shear forces between the loaded edges of the plate and the loadhead, as well as tension and compression reactions in the edge supports, and shear-load transfer to the side supports.

The upper portion of the loading frame was attached to the middle head of the loading machine and the lower portion rested on the load table. Shim stock was used to maintain parallelism between the upper and lower head of ± 0.003 inch over the 11-inch test length.

For the clamped-clamped condition, these general steps were followed: (1) The panel was inserted in the fixture, and the pressure bolts which force the four clamping bars against the panel were tightened. (2) The assembly was lifted from the table using the loadhead, which allowed the bottom to swing free, thus aligning the head and base as it was lowered to the table again. (3) Maintaining a 100-pound edge load, the dial indicators were positioned against the plate and adjusted to indicate zero deflection.

The results of a study of the effect of side-support clamping force on the buckling load of a steel panel are shown in Figure 21. The experimental buckling loads were determined using Southwell's method (Reference 6), that is, the critical buckling load is given to be the inverse of the slope of the linear portion of the deflection/load versus deflection curve. As indicated in Figure 21, the critical buckling load increased with increased pressure of the side support screws. In one particular case (not shown) with the screws wrench tight, the experimental buckling value obtained (22,800 lbs) was higher than predicted using ideal boundary conditions (20,000 lbs).



Figure 19 Shear Panel Test Installation

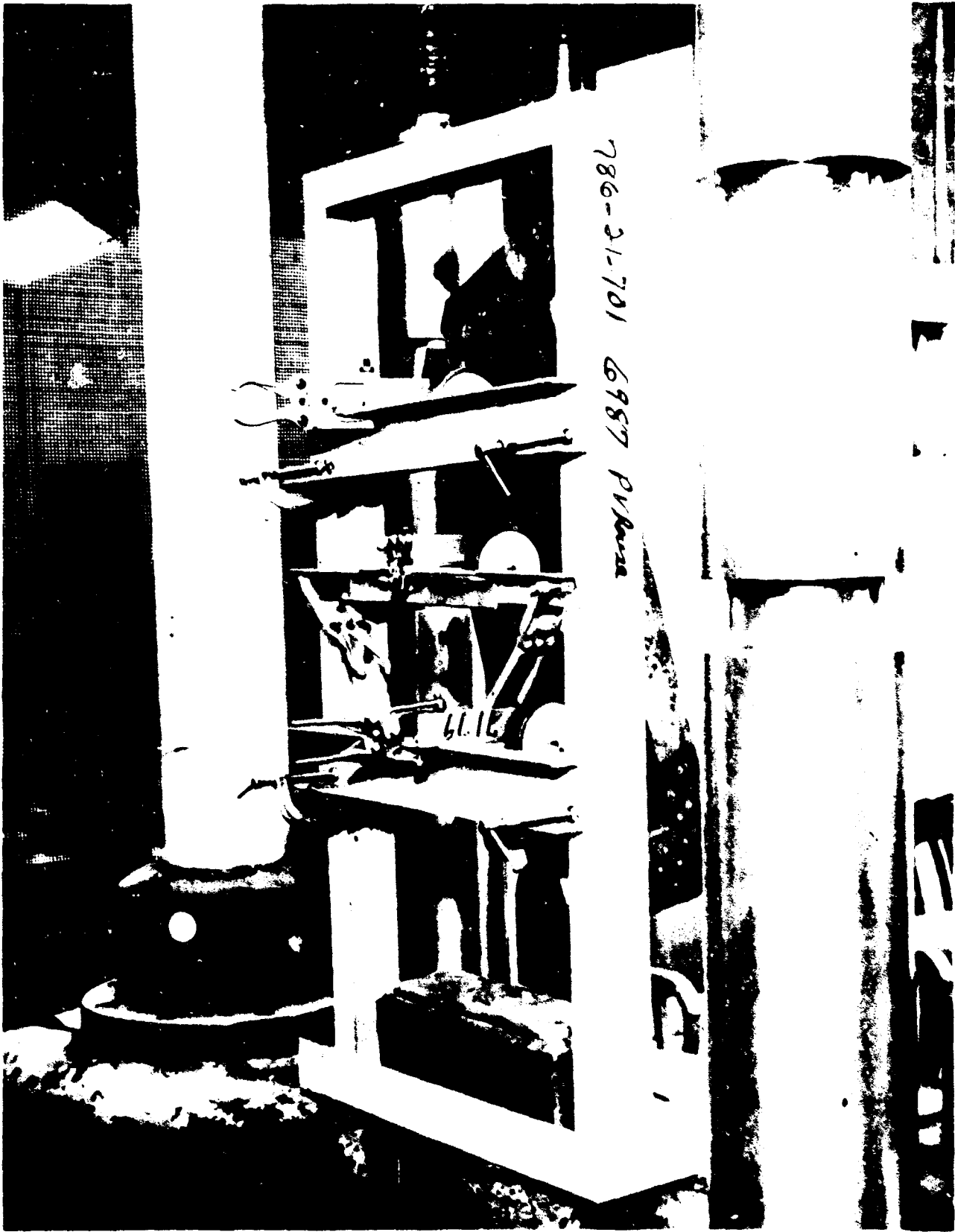


Figure 20 Shear Panel Instrumentation

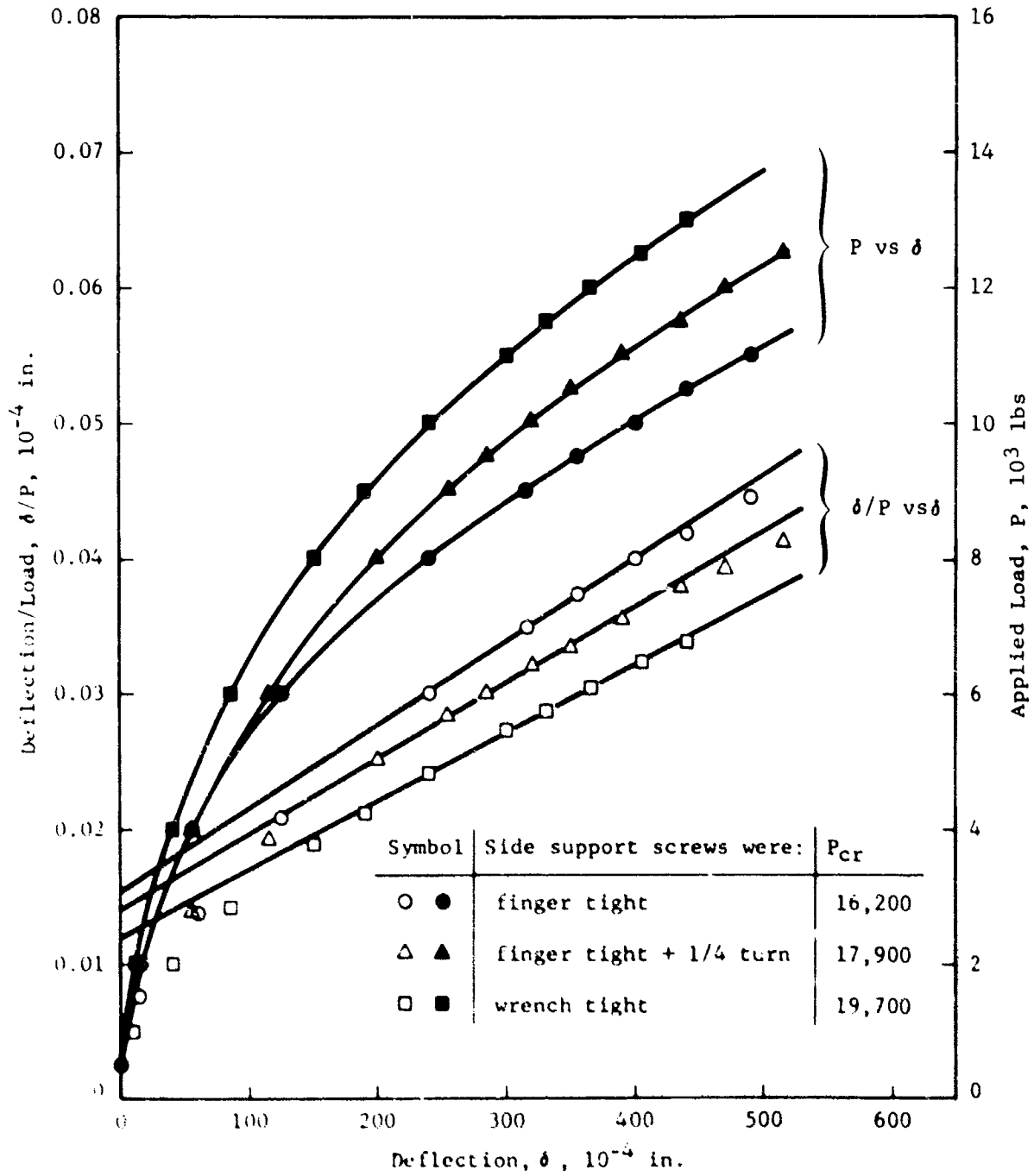


Figure 21 Edge Member Effect on Clamped-Clamped Boundary Condition

An inquiry into the test procedure used in the Reference 4 study indicated that the present condition of side-support, i.e., screws finger tight plus one-quarter turn, closely approximated the reported procedure. This technique was used throughout the current program for the clamped-clamped boundary condition.

For the clamped-simple test condition, the same procedure was followed except the side clamps were rotated as shown in Figure 8 and the side support tightening bolts were left only finger tight.

After the panel had been installed in the compression fixture, each of the applied loads was exercised in order to seat the panel. In the discussion that follows the load exerted by the test machine will be referred to as P_x , that exerted by the hydraulic actuators as P_y , and that by the pressure bag as q .

Initially the panel was loaded in increments of P_x , usually 500 to 1000 pounds, and the dial indicators were monitored until a maximum deflection of half the panel thickness was reached. The load, P_x , was then dropped to 100 pounds to ascertain a zero shift. After readjustment to zero, the exercise was repeated. When the system returned satisfactorily to zero, the second load (if present) was exercised.

For the case of a lateral load, q , the pressure was initially increased until the maximum recorded deflection was half the panel thickness. The pressure was then dropped to 0.2 psi and the dial gauges were adjusted to indicate zero deflection. The exercise was repeated until the system returned satisfactorily to zero. The panel was then ready for a data run. Deflections were recorded for increasing values of q and P_x . A minimum of two data runs was performed in each test configuration.

For the biaxial test condition, the same procedure was followed except that a zero was established at P_x and P_y equal to 100 pounds. Load-deflection data for the combined loads were obtained by setting P_y to a predetermined value and increasing P_x . Experimental buckling loads were determined using Southwell's method. The technique selected for calculating the critical buckling load via Southwell's method was to divide the deflection by the sum of the axial loads. Two other techniques that were attempted lead to inaccurate buckling loads. All three techniques are described in greater detail in Appendix I.

For the natural frequency study, once the panel was seated in the fixture by exercising P_x , an electromagnetic shaker and two accelerometers were bonded to the panel using Eastman 910

adhesive. Subsequent steps in the procedure were to define an artificial zero point at P_x equal to 100 pounds, make a frequency sweep between 50 and 1400 hz, and identify the first four natural modes of panel vibration. The edge load was then increased and held constant while the frequencies of the established modes were recorded. At least four load increments were made at each position; then the shaker was moved to another position and the cycle was repeated. Movement of the shaker was required to determine its effect on modal shapes and natural frequencies.

When excited at a natural resonant frequency, a panel will vibrate in a characteristic mode shape. Shapes are usually visualized either by sprinkling a loose material on the surface of the panel or by using a grid pattern and a stroboscope. The loose material method could not be used in these tests because of the vertical positioning of the panel, and an attempt to use the grid pattern and stroboscope method failed because the amplitudes were too small to be visualized. Therefore, it was necessary to use an indirect method to determine the mode shapes.

An accelerometer was bonded to the panel adjacent to the shaker as shown in Figure 17. This accelerometer is referred to subsequently as the input accelerometer. A second accelerometer was bonded to a predetermined point on the panel. This accelerometer is referred to as either the output or roving accelerometer. Signals from both accelerometers provided plots of amplitude ratio (output/input) versus frequency and of phase angle versus frequency. Concurrent use of these plots determined the natural frequencies, which were read on an electronic counter. Because inherent damping in the system shifted the resonance peaks to the left, thus lowering the recorded frequency, the experimental frequencies reported are those associated with the phase angle plots. This behavior is shown graphically in Figure 22.

Actual mode shapes were determined by using the roving accelerometer. The setup is such that any two points on a vibrating plate at resonance are either in phase or 180 degrees out of phase. If the two points are on the same side of a nodal line, they are in phase. If one point represents input (force) and the other output (displacement), the phase angle is 90 degrees. If the two points are on opposite sides of a nodal line, they are 180 degrees out of phase with each other, and the phase angle is then 270 degrees. Therefore, mode shapes were defined by recording the location of the roving accelerometer and the associated phase angle.

In the ultimate load study, the test procedure and data runs were the same as in the compression panel tests, except that the

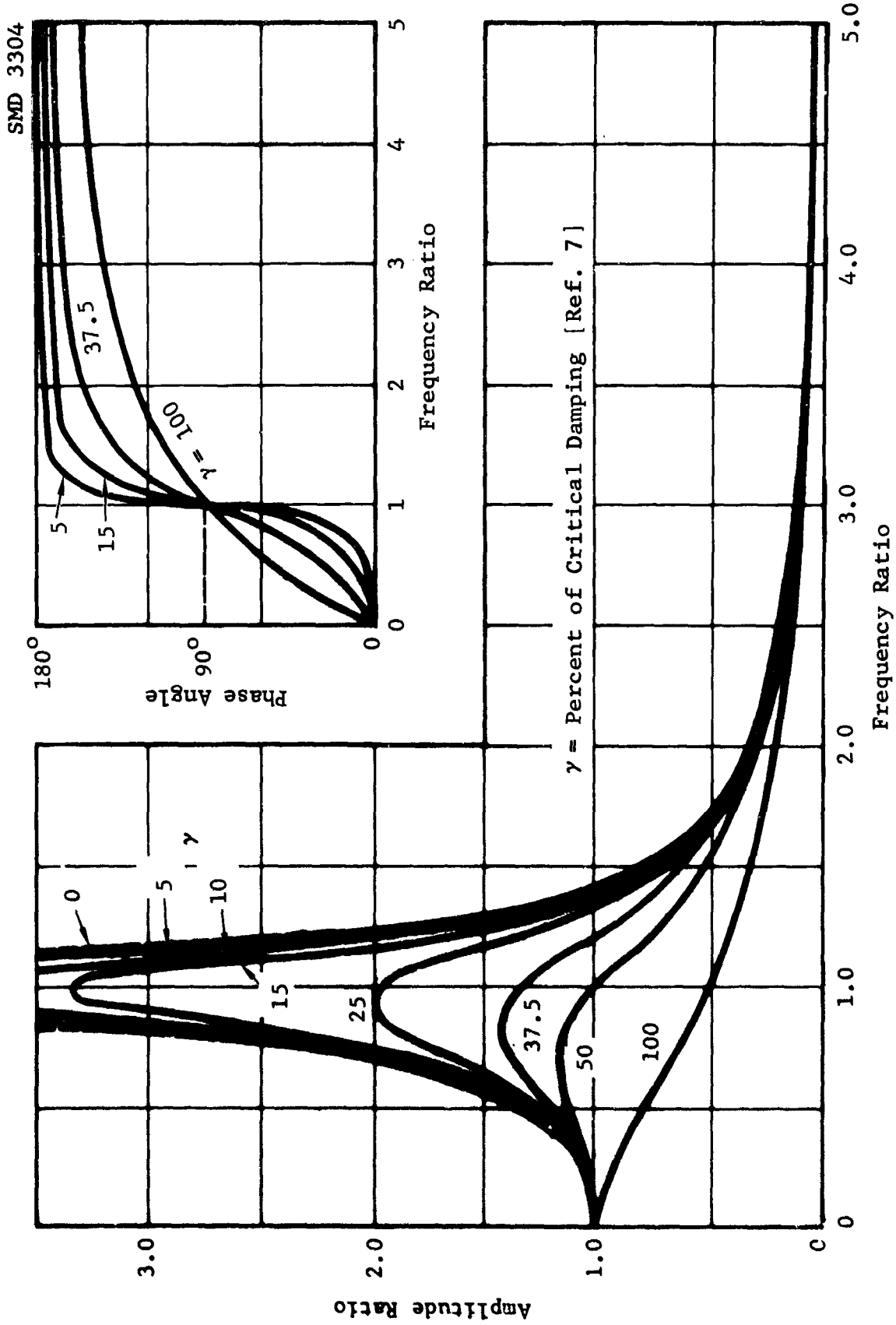


Figure 22 Plots of Amplitude Ratio and Phase Angle

panels were loaded to failure. Each panel was infrared inspected after test for areas of delamination.

In the shear test, the frame assembly and holding fixture were installed in the test machine (Figure 19). The holding fixture was then removed and the external load increased to 50 pounds. At this load the dial indicators were adjusted to read zero deflection. The data runs were performed in the same way as those in the compression panel tests, except the panel was loaded to failure. Each panel was infrared inspected after test for areas of delamination.

Two of the nine shear panels were load-cycled prior to failure. The test procedure was to cycle a panel 100 times to an applied load approximately five times its critical buckling load. On the one-hundredth cycle, the panel was loaded to failure.

4.4 FIXTURE CALIBRATION

For the current test program, an attempt has been made to express the actual experimental boundary conditions analytically using isotropic data from Reference 4 and data generated under the present contract.

An analysis of the buckling data (Reference 1) indicated that the clamped-clamped boundary condition results were about 90 percent of the idealized condition, while the clamped-simple boundary conditions averaged approximately the same as the idealized condition. The averaging effect was attributed to the condition that the simple supports were subject to a small degree of fixity. Results from dynamic tests performed on the same plates and in the same fixture (Reference 8) supported the conclusion that these trends were due to the fact that the actual boundary conditions imposed experimentally were slightly different from the idealized conditions.

In computer program RA5 (Reference 1), elastic restraint of the panel edges is controlled by a constant which relates the slope along an edge to its curvature. For the case of a simple support the constant is equal to zero; as it increases positively, elastic restraint is applied. The clamped condition is reached when the constant becomes infinite.

The constants and reference system used in the RA5 procedure are defined in Figure 23, an illustration of a typical panel subjected to uniaxial load. Selection of the elastic restraint

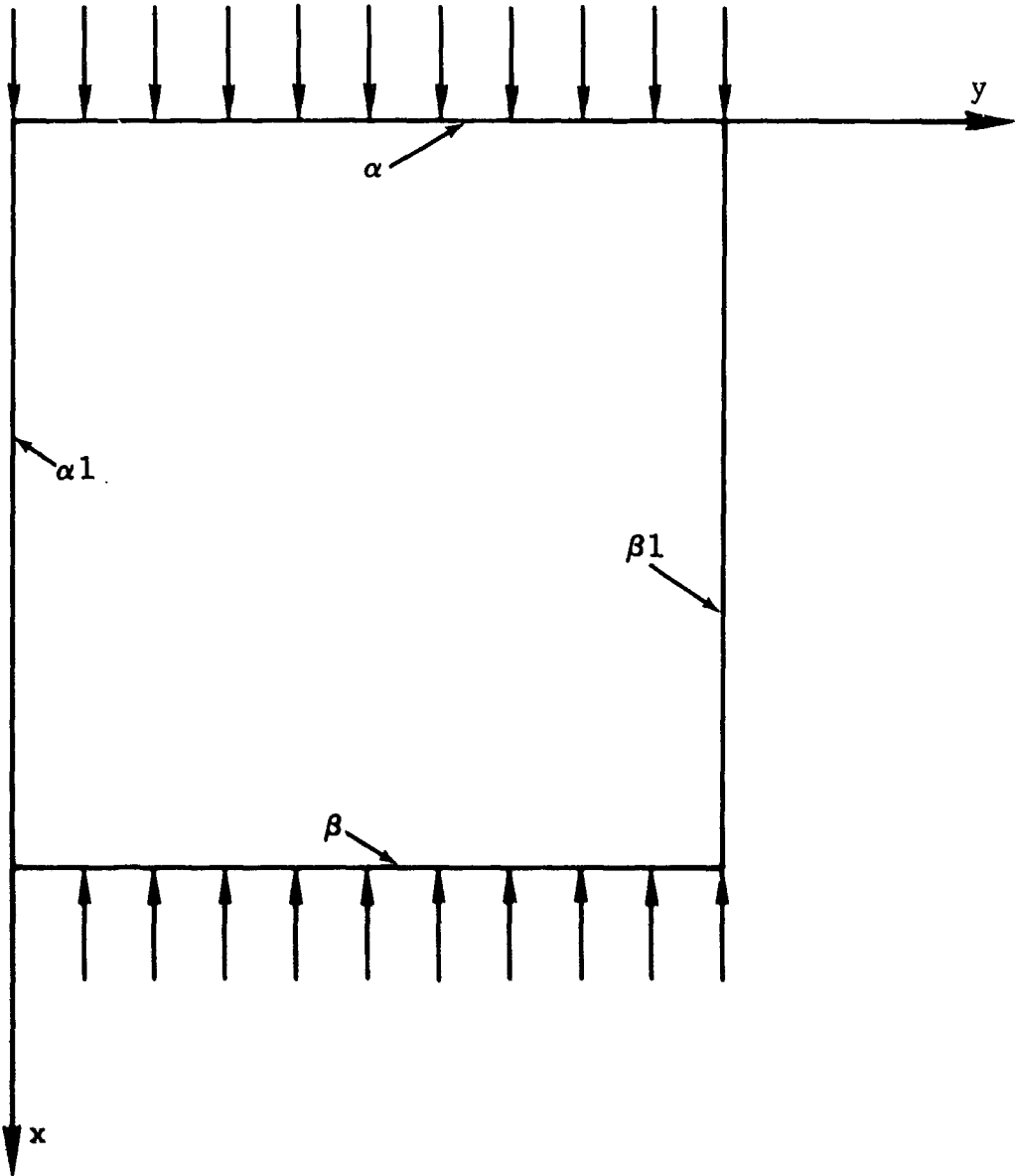


Figure 23 Test Configuration and Coordinate Reference

constants ($\alpha, \beta, \alpha_1, \beta_1$) was an iterative process. Factors considered were natural frequency, buckling load, and maximum deflection under lateral load. Figures 24 and 25 are plots of deflection versus lateral load for the clamped-clamped and clamped-simple conditions, respectively. These test data were obtained under this contract. Buckling results from Reference 4 are presented in Figure 26. Plots of natural frequency versus edge load, obtained from Reference 8, are presented in Figures 27 and 28 for the clamped-clamped and clamped-simple conditions, respectively.

Test data obtained with clamped-clamped edge supports indicated that the fully fixed condition should be relaxed. After several iterations, the value $\alpha = \beta = \alpha_1 = \beta_1 = 21.0$ was selected as the best fit for the data. The new buckling results indicate that a higher value would be preferable. However, an increase in α is undesirable based on the results of natural frequency and deflection versus applied load. A review of the corrected results indicates that a best value for the elastic restraint has been selected. In a similar manner the elastic restraint constants for the clamped-simple edge supports were set at $\alpha = \beta = 21.0$ and $\alpha_1 = \beta_1 = 1.0$.

Plots of deflection and frequency versus applied load indicate a tendency for the test data to approach the ideal conditions for both clamped-clamped and clamped-simple edge supports with increasing load. The buckling results, which require a higher degree of elastic restraint for better agreement, were calculated in the vicinity of these higher loads; therefore, it appears that the degree of edge fixity may be a function of increasing load.

On the basis of this investigation, it has been concluded that boundary conditions of elastic restraint represent the actual supports better than the idealized conditions and thus the elastic boundary restraint factors have been used to evaluate the data from the boron panels.

4.5 UNIAXIAL BUCKLING RESULTS

Although the critical uniaxial buckling loads for the flat plates of this study (with the exception of Panel 19A (tapered, $+45^\circ$) and the steel panel) were reported in Reference 4, the tests were repeated for two reasons: (1) the plates may have been accidentally damaged in the interim period between test programs and (2) since the elastic boundary constraint factors were determined from data obtained from Reference 4, it was necessary to ensure that the test techniques of both programs were identical.

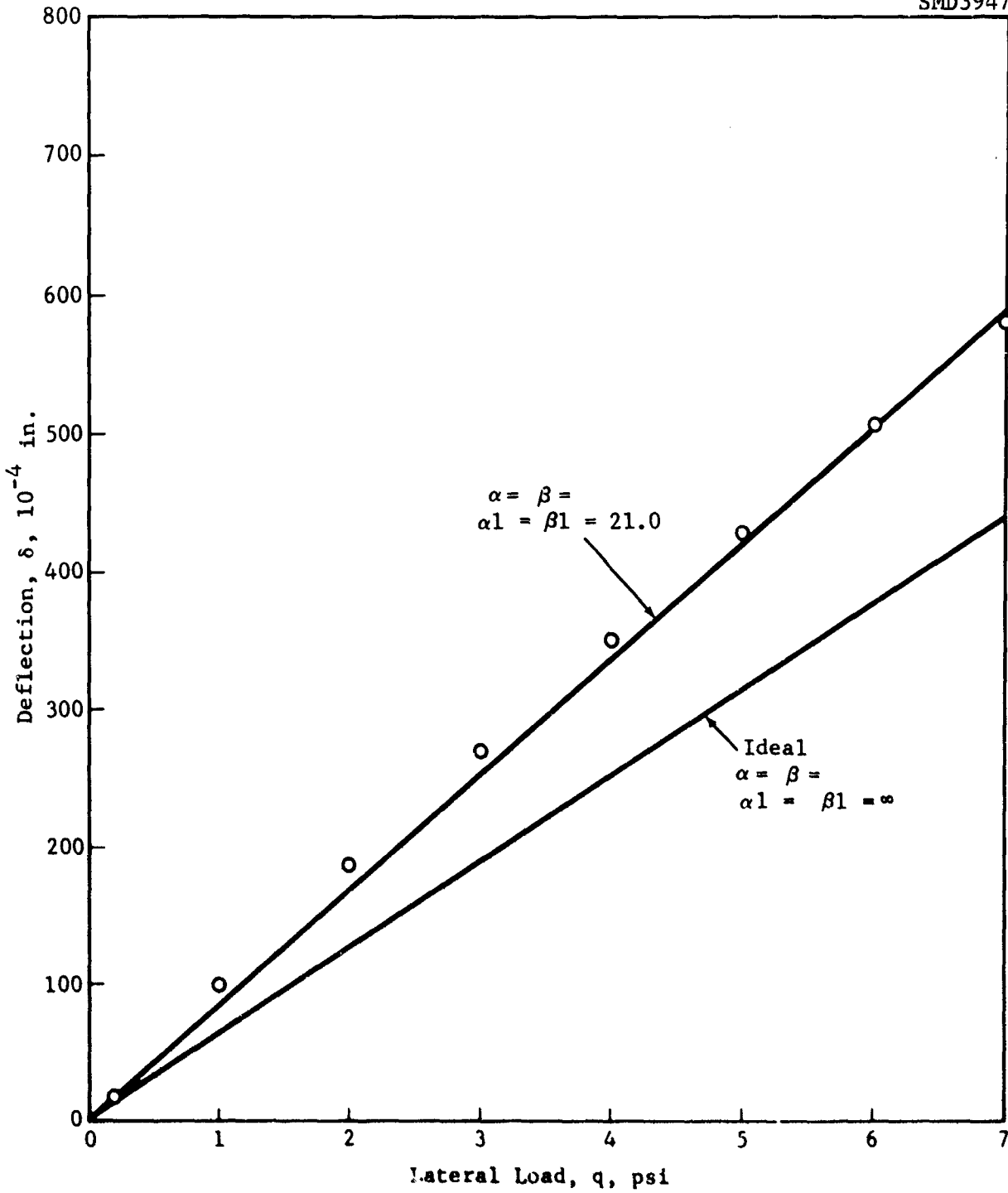


Figure 24 Deflection vs Lateral Load, Clamped-Clamped Conditions, Aluminum Panel 3

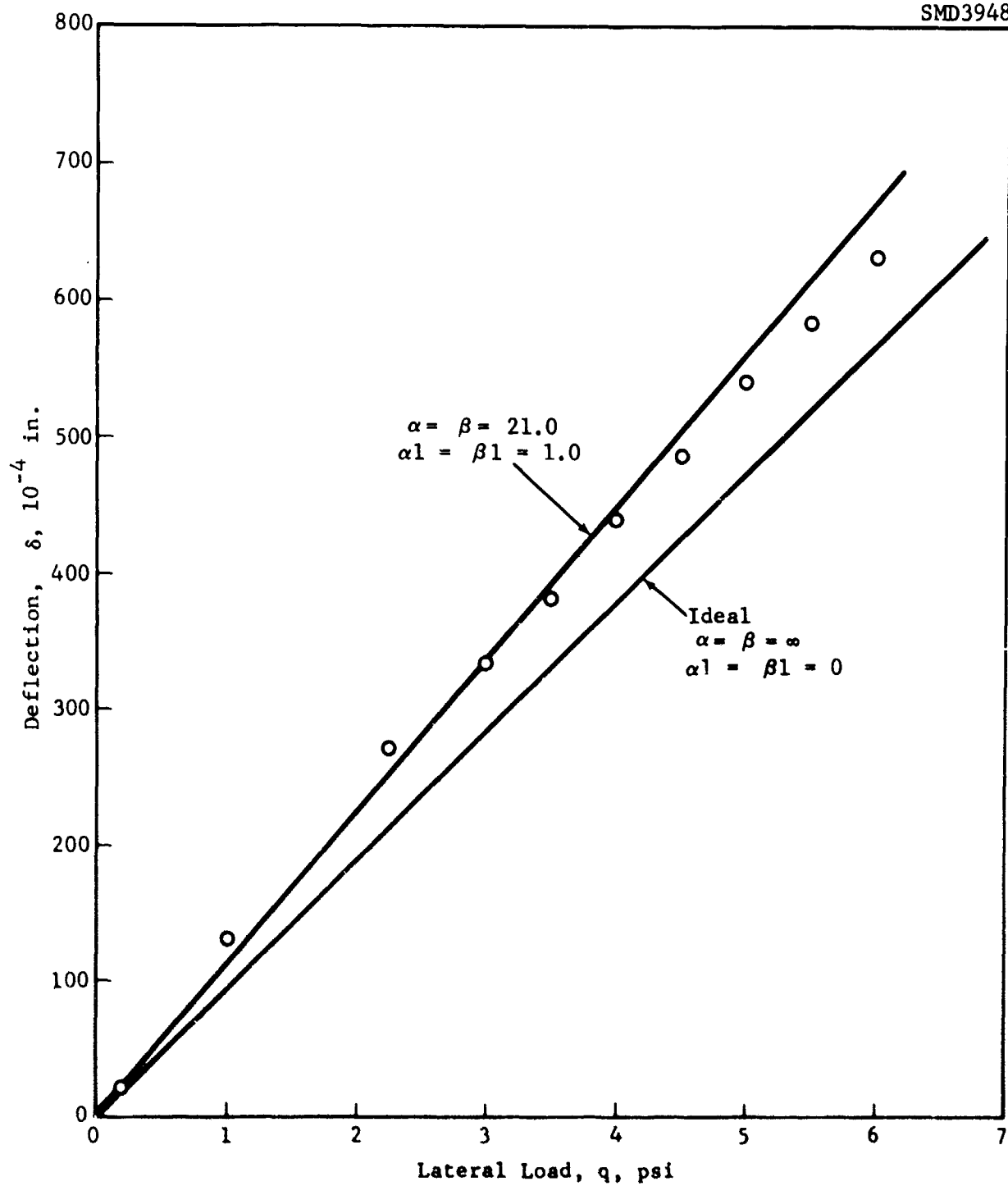


Figure 25 Deflection vs Lateral Load, Clamped-Simple Conditions, Aluminum Panel 3

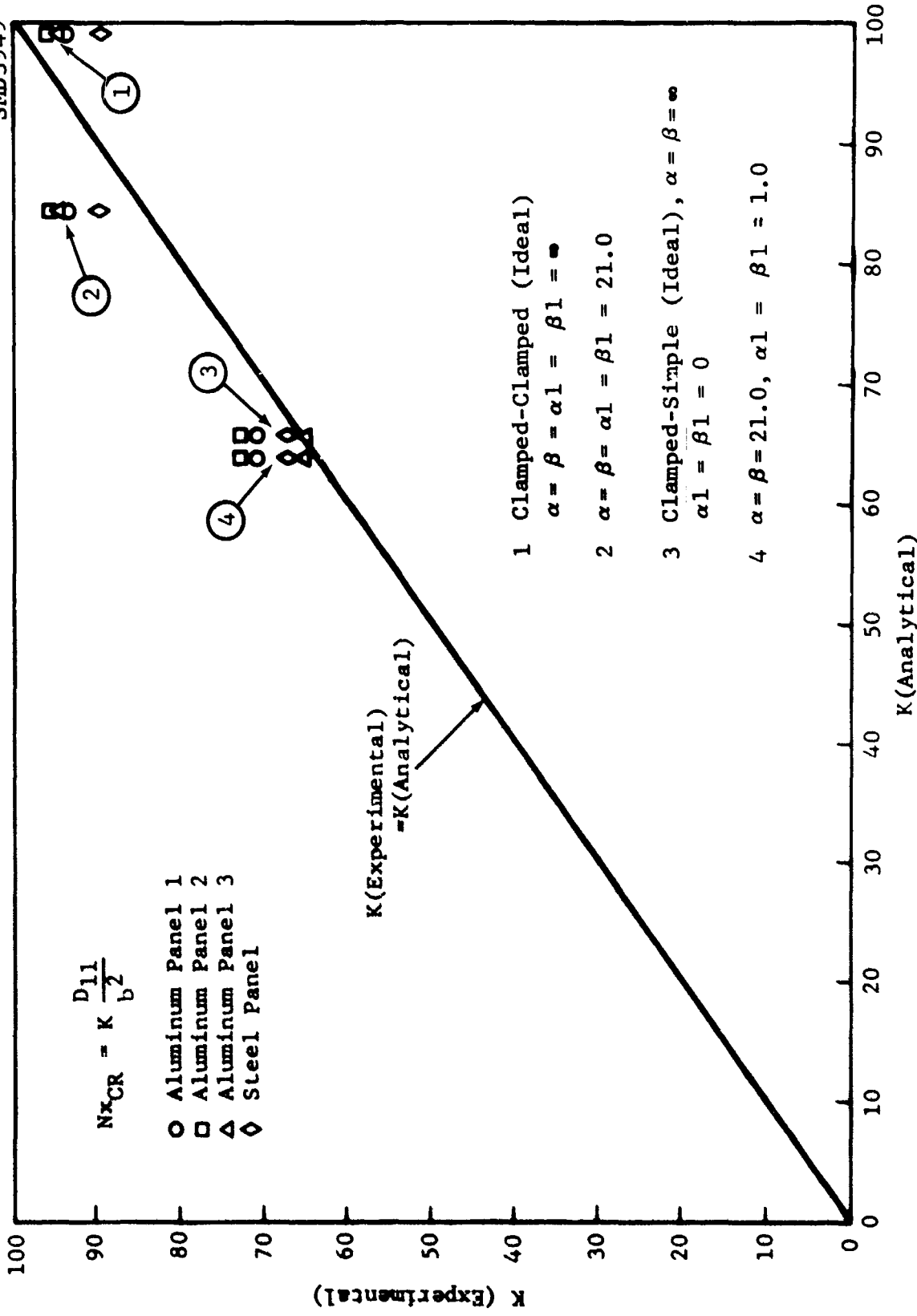


Figure 26 Buckling Results, Clamped-Clamped and Clamped-Simple

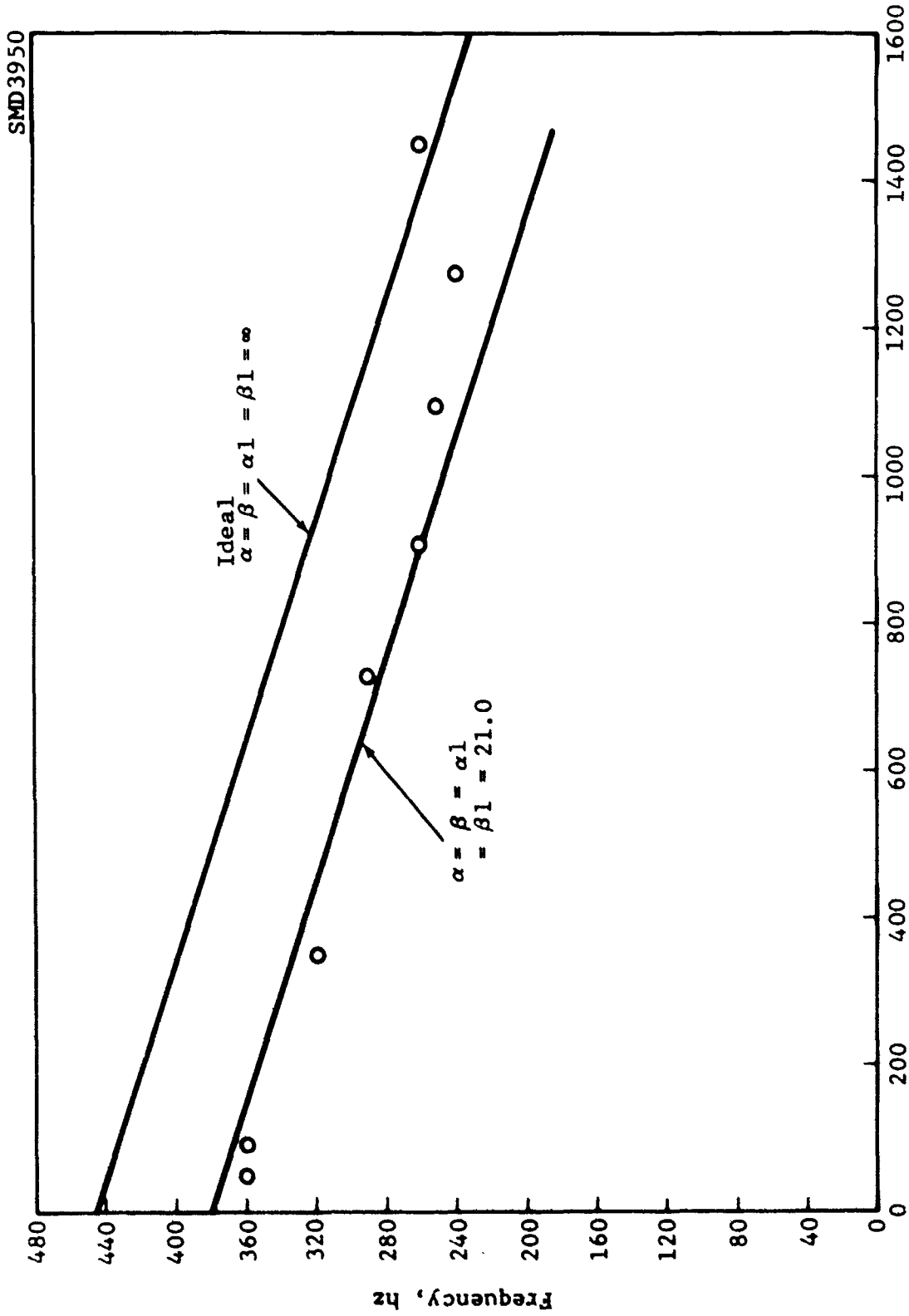


Figure 27 Frequency vs Stress Resultant, Clamped-Clamped Conditions

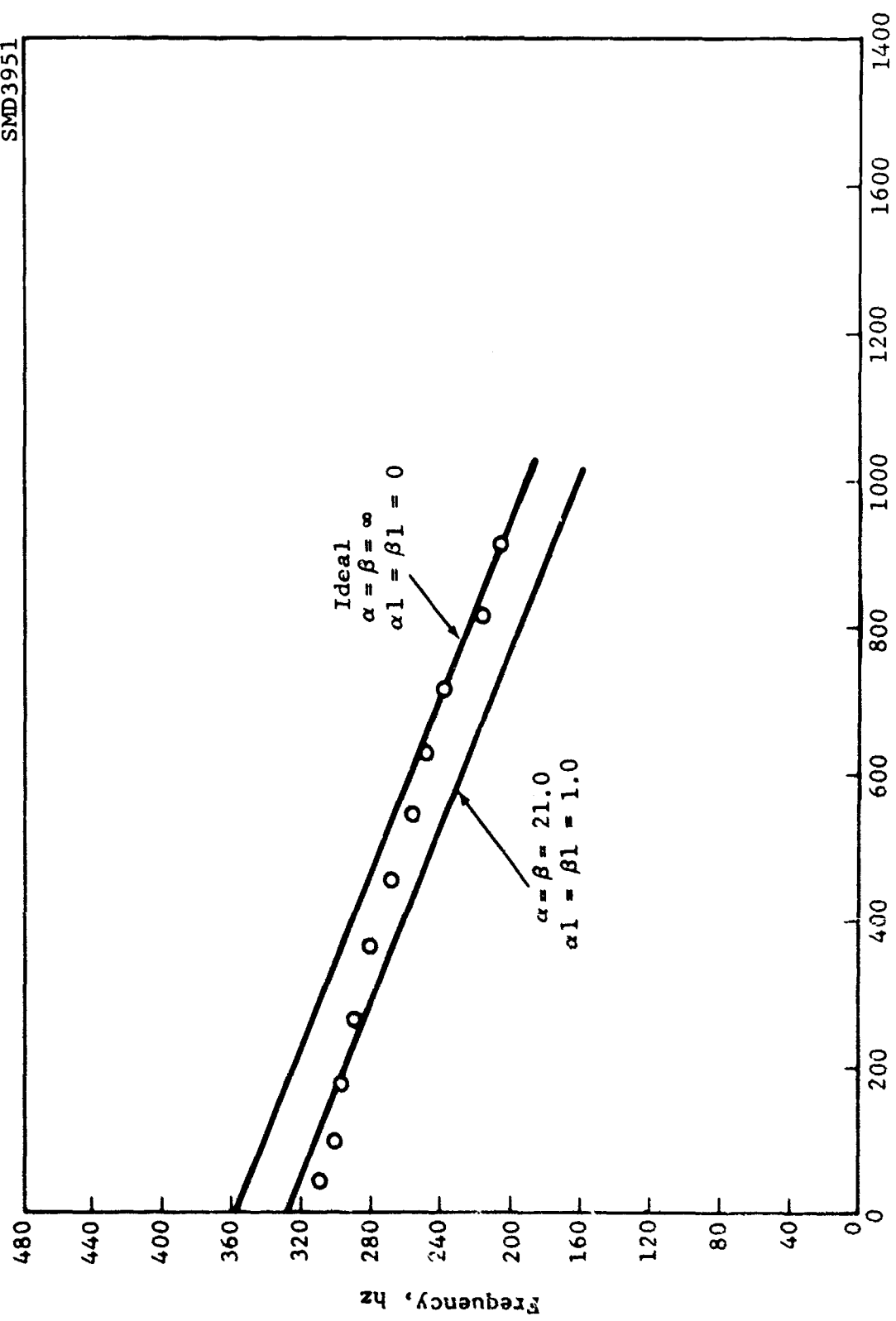


Figure 28 Frequency vs Stress Resultant, Clamped-Simple Conditions

Inputs to computer program RA5 are plate thickness, dimensions, ply-orientation, boundary conditions, and ply-properties. Panel thicknesses and orientations are listed in Table I. Plate 19A, which was tapered stepwise along the load direction, was analyzed as a linearly tapered plate. For Panel 2 (the unsymmetrical $+45^\circ$ panel), the analysis was conducted using the "reduced bending stiffness matrix" suggested in Reference 10.

The inplane stress resultants were assumed to be uniformly distributed along the panel edges. For Panel 19A (tapered, $+45^\circ$) the stress resultants along the tapered edge were assumed to vary linearly.

The ply properties used in the analysis were obtained from General Dynamics sandwich beam tests. For a nominal ply thickness of 0.0053 inch, the following input properties were used:

$$E_1 = 31.0 \times 10^6 \text{ psi}$$

$$E_2 = 3.0 \times 10^6 \text{ psi}$$

$$G_{12} = 1.1 \times 10^6 \text{ psi}$$

$$\nu_{12} = 0.22$$

These ply properties were modified for the actual ply thicknesses by multiplying E_1 and E_2 by the ratio of nominal thickness to the actual thickness.

Properties used for the aluminum panels were

$$E = 10.5 \times 10^6 \text{ psi}, \nu = 0.33,$$

and for the steel (PH 15-7 Mo) panel

$$E = 30.0 \times 10^6 \text{ psi}, \nu = 0.28.$$

The results of the uniaxial buckling study are presented in Table V, where they are compared with the results of the analytical predictions for elastically restrained boundaries. The same values are shown graphically in Figure 29 where N_x (experimental) is plotted versus N_x (analytical). Agreement between theory and experiment is good, with the exception of the unidirectional plate, Panel 5. In Figure 30, the experimental data have been plotted against the analytical predictions for ideal boundary conditions (from Reference 4). Not shown are the unsymmetrical plate, Panel 2, and the tapered plate, Panel 19A. A comparison of Figures 29 and 30 substantiates the assumption of elastic restraint on the boundaries. The load-

Table V BUCKLING RESULTS

Panel	Fiber Orientation	Load Direction*	Boundary Condition**	Critical Buckling Load, N_x		Double Mode	
				Experimental	Analytical	Experimental	Analytical
Al. 3			CC	2075	1716		
			CS	1447	1304		
Steel			CC	1580	1615		
			CS	1280	1226		
2	Unsym. $\pm 45^\circ$	0°	CC	627	652		
		0°	CS	522	516		
3	$0^\circ/90^\circ$	0°	CC	1230	1061		
		0°	CS	921	796		
5	0°	0°	CC	1070	996		
		90°	CC	397	440		X
		0°	CS	1210	941		
		90°	CS	365	305		X
7	$\pm 45^\circ$	0°	CC	593	567		
		0°	CS	486	477	X	
9	$\pm 45^\circ$	0°	CC	1050	1110		
		0°	CS	809	699		
12	$0^\circ/\pm 45^\circ$	0°	CC	1410	1301		
		0°	CS	1340	1162		
16	$0^\circ/\pm 45^\circ/90^\circ$	0°	CC	627	575		
		0°	CS	506	459		
19A	Tapered $\pm 45^\circ$	0°	CC	238	240		
		90°	CC	260	275		
		0°	CS	214	206		
		90°	CS	215	230		

Notes: * Orientation with respect to the arbitrary 0° axis

** CC: Unloaded edges clamped; CS: Unloaded edges simply supported.

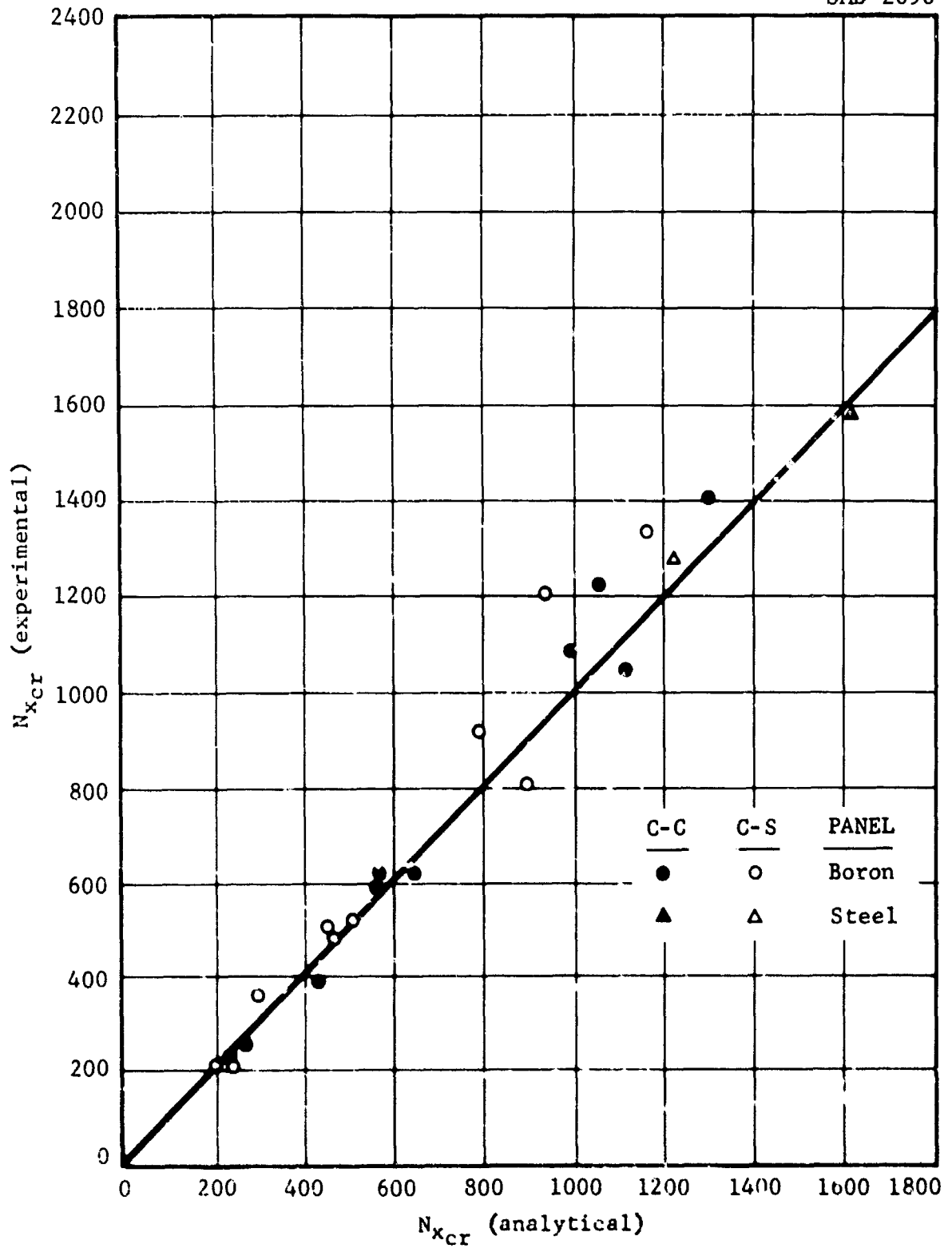


Figure 29 Buckling Results - Elastic Restraints

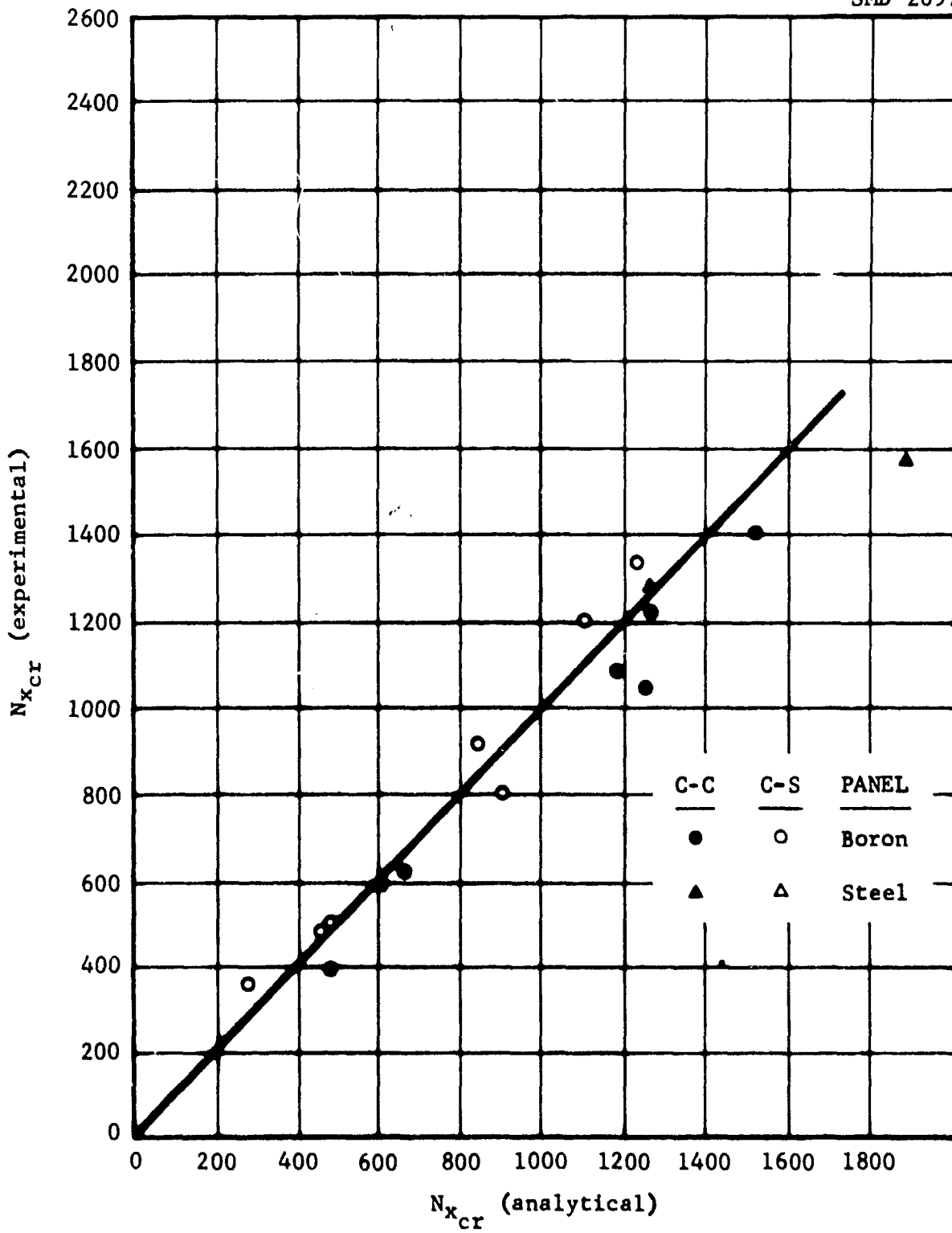


Figure 30 Buckling Results - Ideal Boundaries

deflection curves and Southwell plots used in obtaining the buckling results are presented in Appendix II.

When Panel 5 (0°) was tested with clamped-simple boundary conditions, the observed mode shape for the 90-degree load direction was the first mode, while the predicted shape was a double mode. This discrepancy was also noted in Reference 4. In Table VI the experimental buckling loads, N_x , obtained for the four test conditions of Panel 5, are compared with the analytical results where the boundary conditions were either elastically restrained or ideal. With the exception of the 90-degree load direction, clamped-clamped boundary conditions, the results indicate that the panel acted stiffer than anticipated. This behavior is also confirmed by the data in Reference 4.

The discrepancies observed are probably due primarily to two effects. First, it was shown in Reference 4 that the panel is very sensitive to the assumed value of E_2 . In fact, it was found that when using $E_2 = 3.4 \times 10^6$ psi, the predicted buckling mode was the first, which agrees with the experiment. Secondly, the panel is very sensitive to the degree of moment fixity at the boundaries because of the great difference in stiffness in the longitudinal and transverse directions.

Table VI PANEL NO. 5 BUCKLING COMPARISON

Boundary Condition	Load Direction	Experimental	N_x cr Elastic Restraint	Ideal
CS	0°	1210	941	1120
CS	90°	365	305	283
CC	0°	1090	996	1180
CC	90°	397	440	480

SECTION V

TRANSVERSE LOAD STUDY

The purpose of the experimental program described was to determine the normal deflections of 10 flat plates (orientation as variables) subject to transverse load and transverse load combined with uniaxial compression and to compare the test data with the analytical predictions of computer program RA5. The boundary conditions considered were fully-clamped plates and plates clamped on the compressed edges and simply supported on the sides.

The boron panels selected for the study and the configurations tested are enumerated in Table VII. Panel thicknesses and orientations were presented in Table I. The isotropic control panel was steel. The input properties used for the RA5 analysis were described in subsection 4.5.

Prior to testing, an investigation of the pressure system, which involved the imprint of the pressure bag on the control panel, was conducted. It had been assumed that the bag while under uniform internal pressure transmitted a uniform lateral load to the plate, i.e., the bag stiffness was assumed to be negligible. In Figure 31 the deflection-versus-lateral load data obtained using the bag are compared with data obtained using a sealed compartment for clamped-simple boundaries. The results indicate no adverse effects due to the bag. Data obtained for clamped-clamped boundaries are presented in Figure 32.

From the theory of plates, the deflection-versus-lateral load data were anticipated to be linear to half the plate thickness, or 0.044-inch for the steel panel. The data presented in Figure 32 appeared to become nonlinear at deflections less than 0.040 inch, or slightly lower than expected. Upon removal from the test fixture, the steel panel was found to have an initial imperfection in the form of a slight curvature amounting to a maximum normal displacement of 0.030 inch. The addition of an inplane load normal to the applied variable load essentially increases the initial imperfection. Thus, before a load-deflection curve can be obtained (from which a buckling load may be calculated), plate deflections are of the magnitude $t/2$. Past experience has shown that this situation leads to an overestimation of the buckling load.

Figures 33 through 52 are plots of deflection versus lateral load for the boron panels. Agreement between experiment and analysis is good, with the exception of the unidirectional plate, Panel 5.

Table VII UNIAXIAL EDGE LOAD AND TRANSVERSE PRESSURE TESTS

Panel No.	Orientation (degree)	Clamped-Clamped		Clamped-Simple	
		0° Config.	90° Config.	0° Config.	90° Config.
2	Unsymmetrical +45	X		X	
3	0/90	X		X	
5	0	X	X	X	X
7	+45	X		X	
9	+45	X		X	
12	0/+45	X		X	
16	0/+45/90	X		X	
19A	Tapered +45	X	X	X	X
Steel	--	X		X	

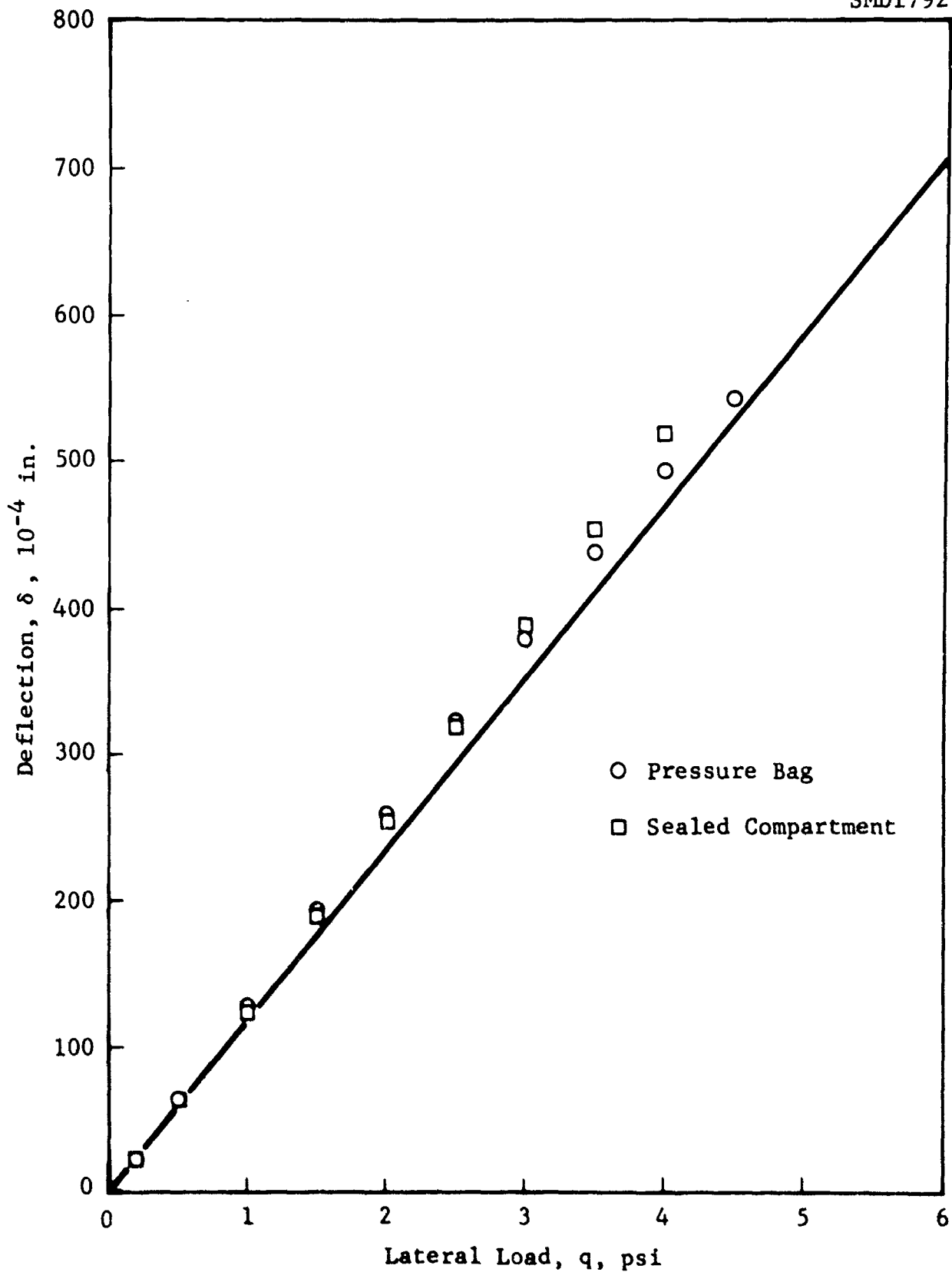


Figure 31 Pressure Imprint Study, Clamped-Simple Conditions, Steel Panel

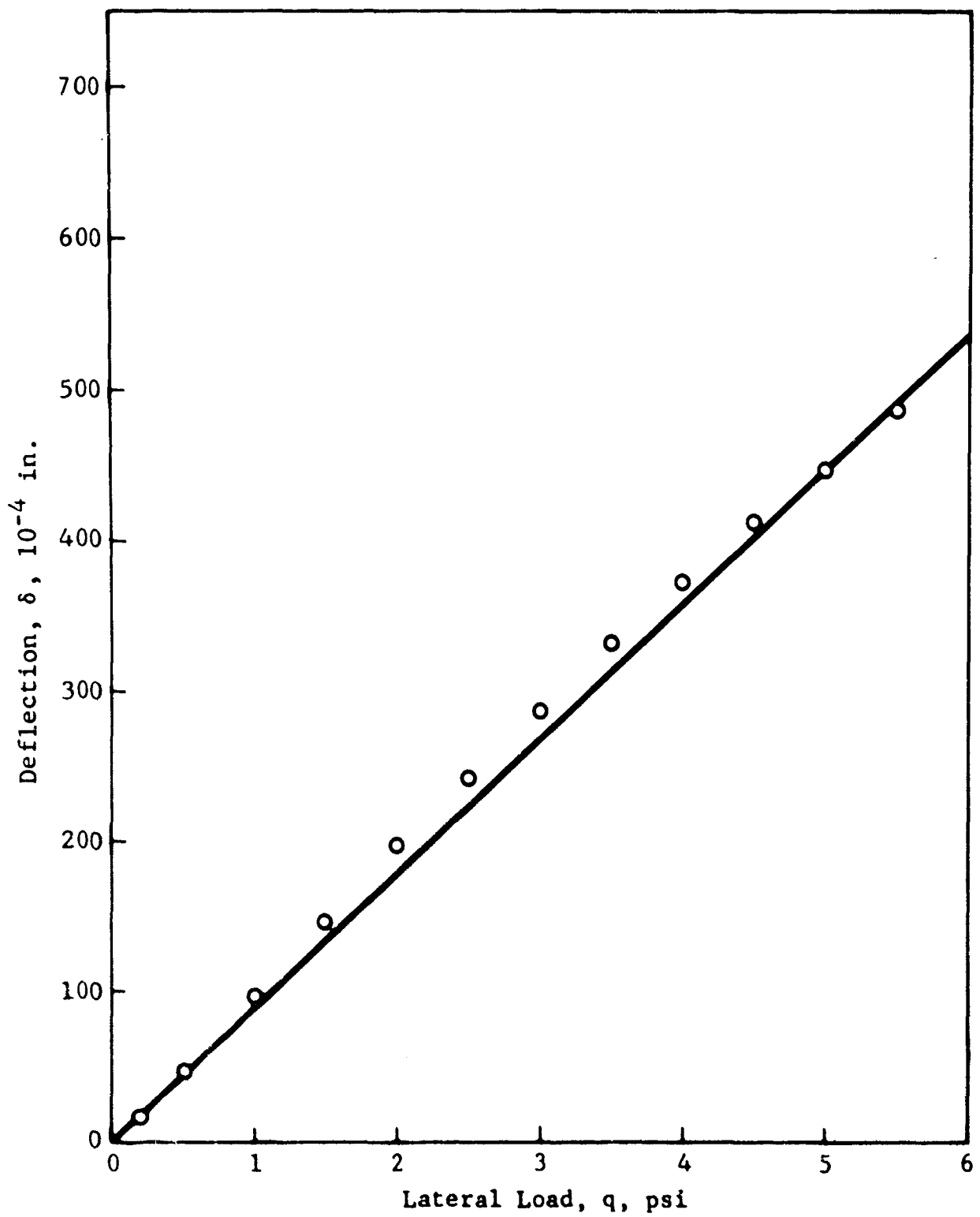


Figure 32 Deflection vs Lateral Load, Clamped-Clamped Condition, Steel Panel

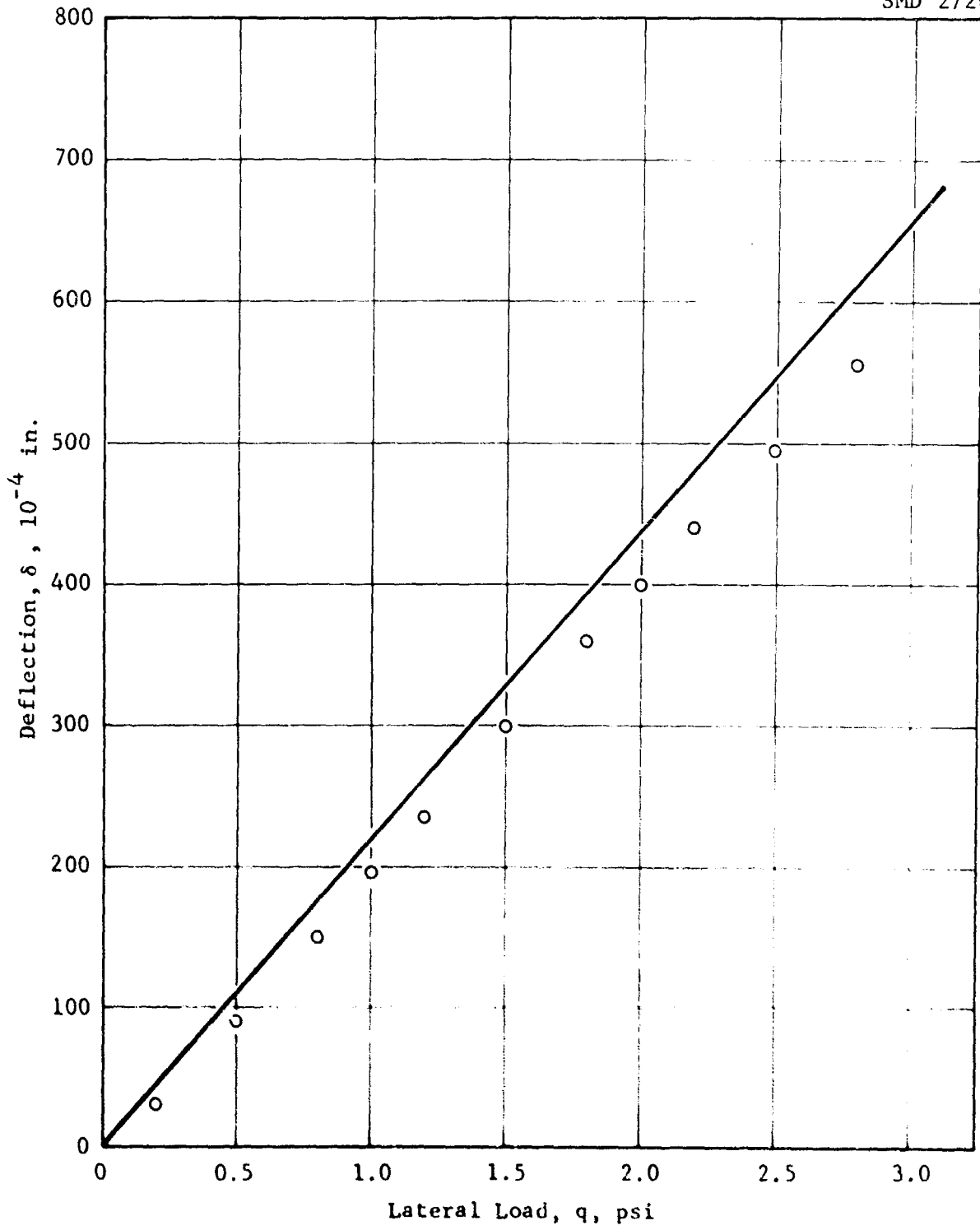


Figure 33 Deflection vs Lateral Load, Clamped-Clamped Condition, Panel No. 2

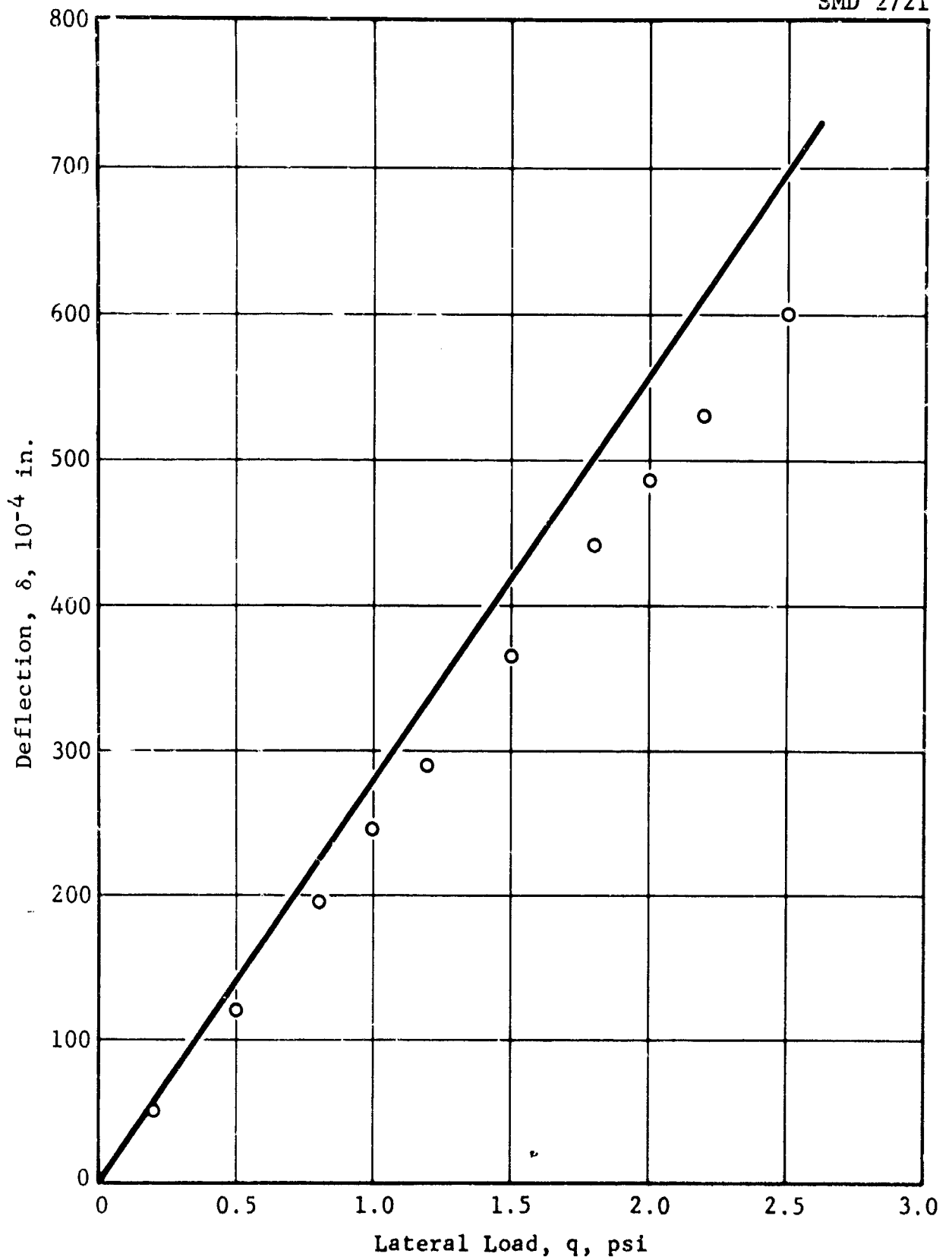


Figure 34 Deflection vs Lateral Load, Clamped-Simple Condition, Panel No. 2

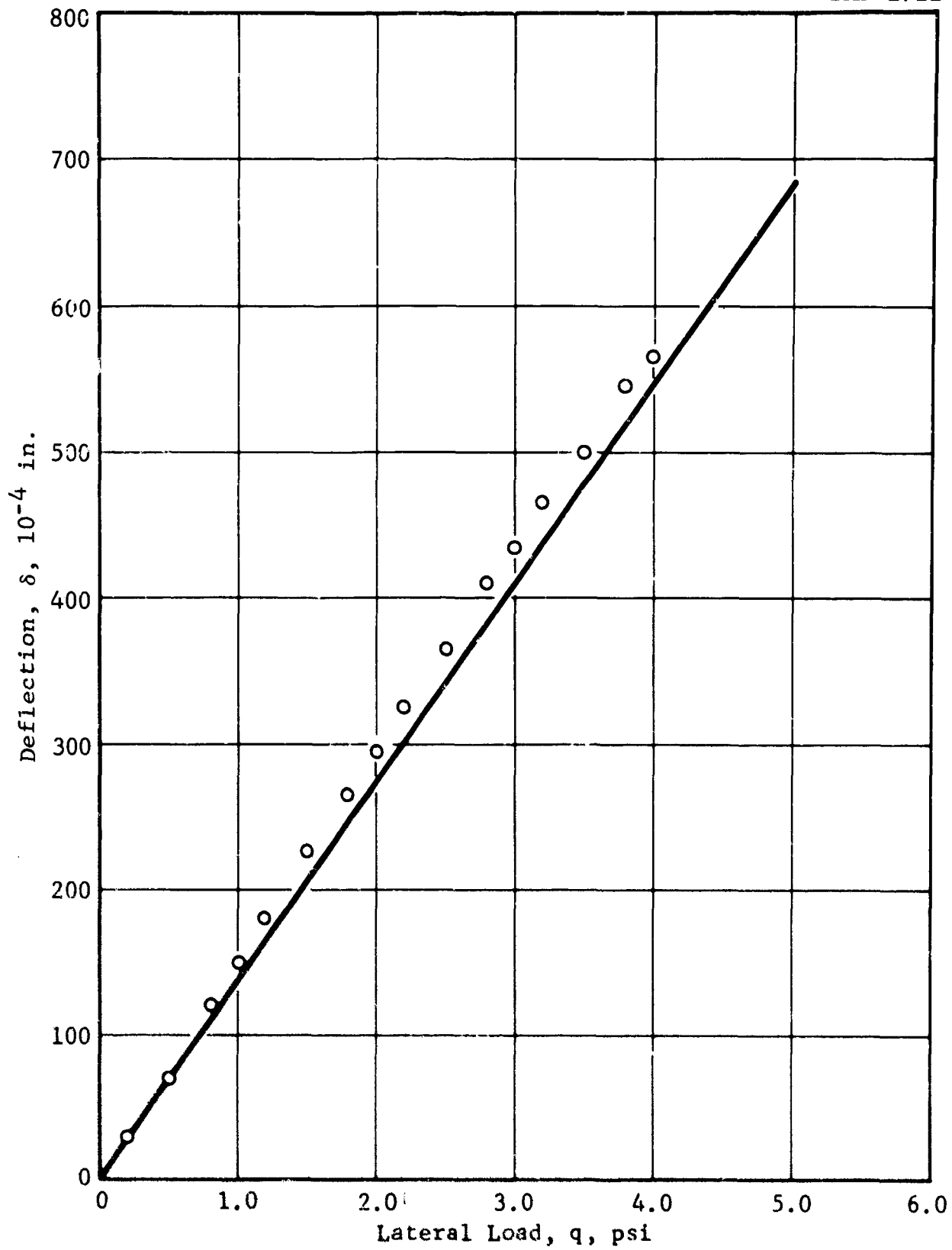


Figure 35 Deflection vs Lateral Load, Clamped-Clamped Condition, Panel No. 3

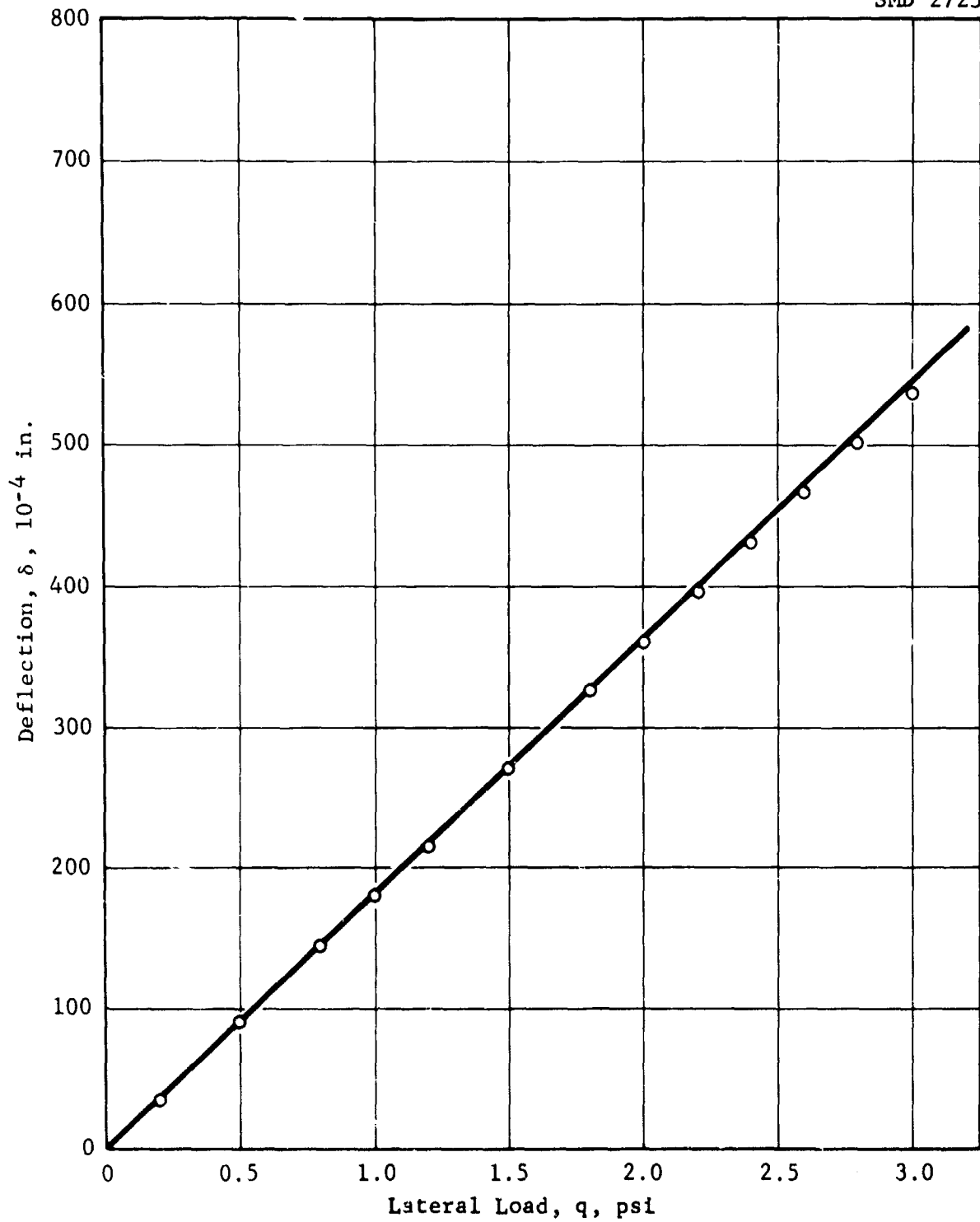


Figure 36 Deflection vs Lateral Load, Clamped-Simple Condition, Panel No. 3

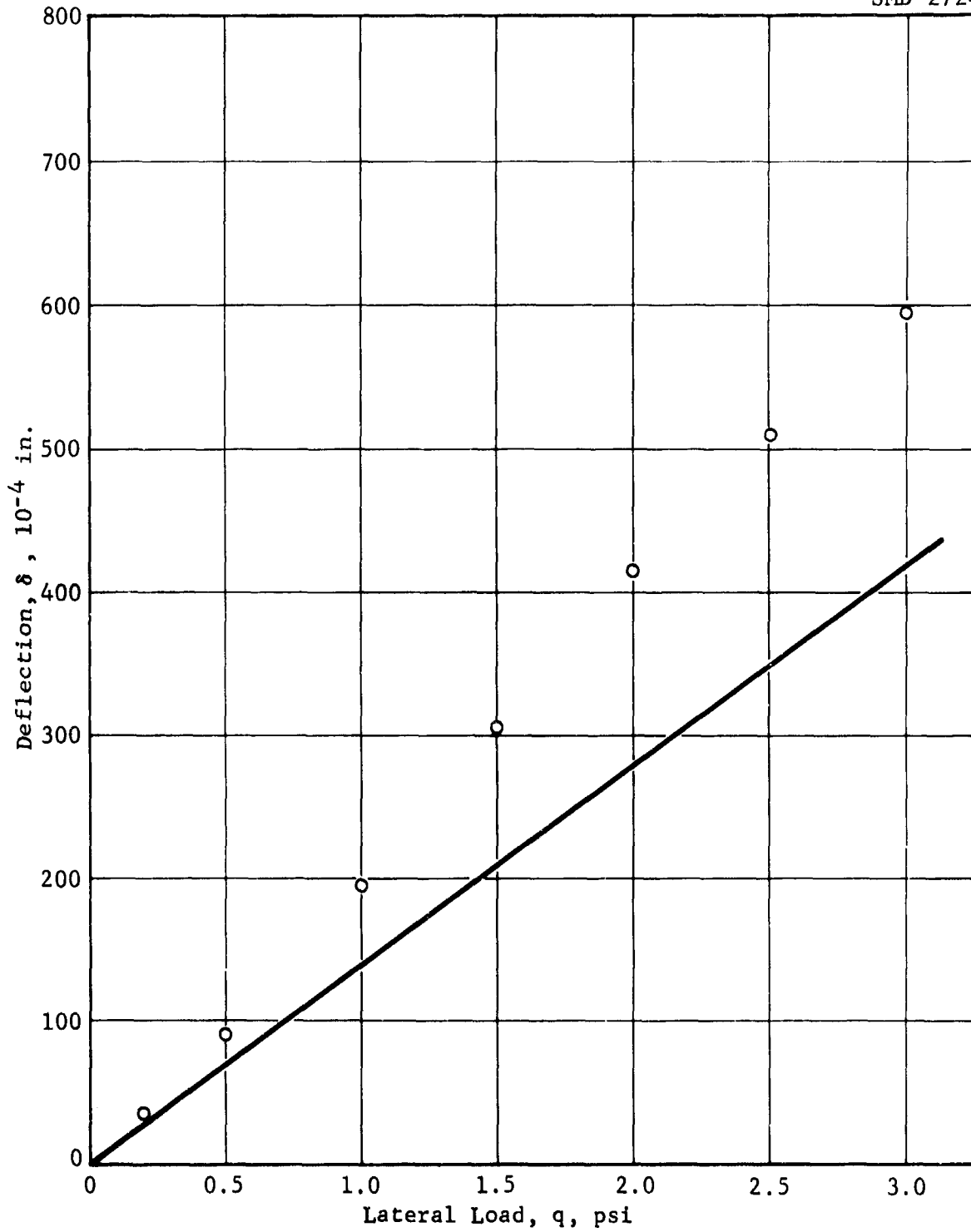


Figure 37 Deflection vs Lateral Load, Clamped-Clamped Condition,
Panel No. 5

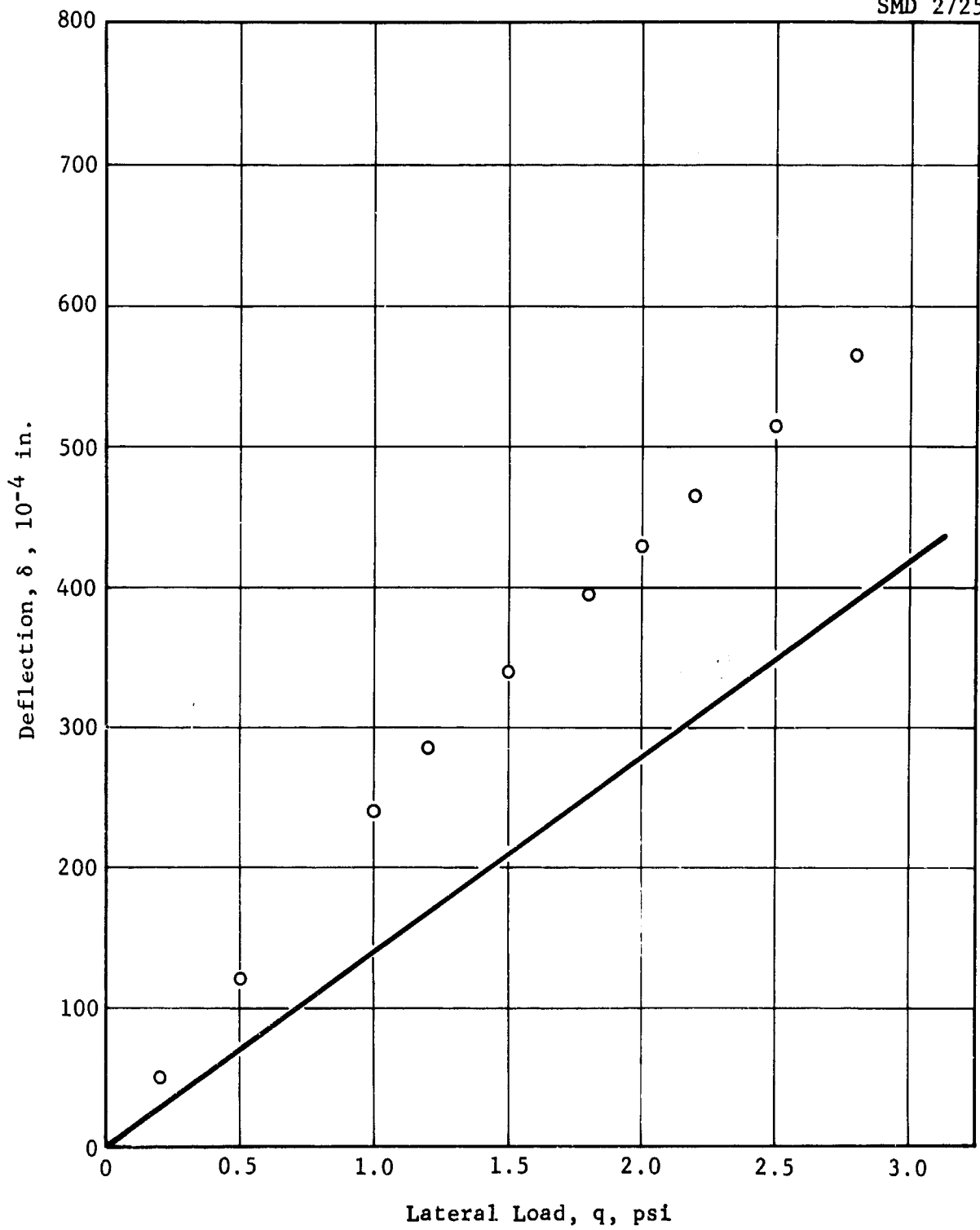


Figure 38 Deflection vs Lateral Load, Clamped-Clamped Condition, Panel No. 5, Turned 90°

SMD 2726

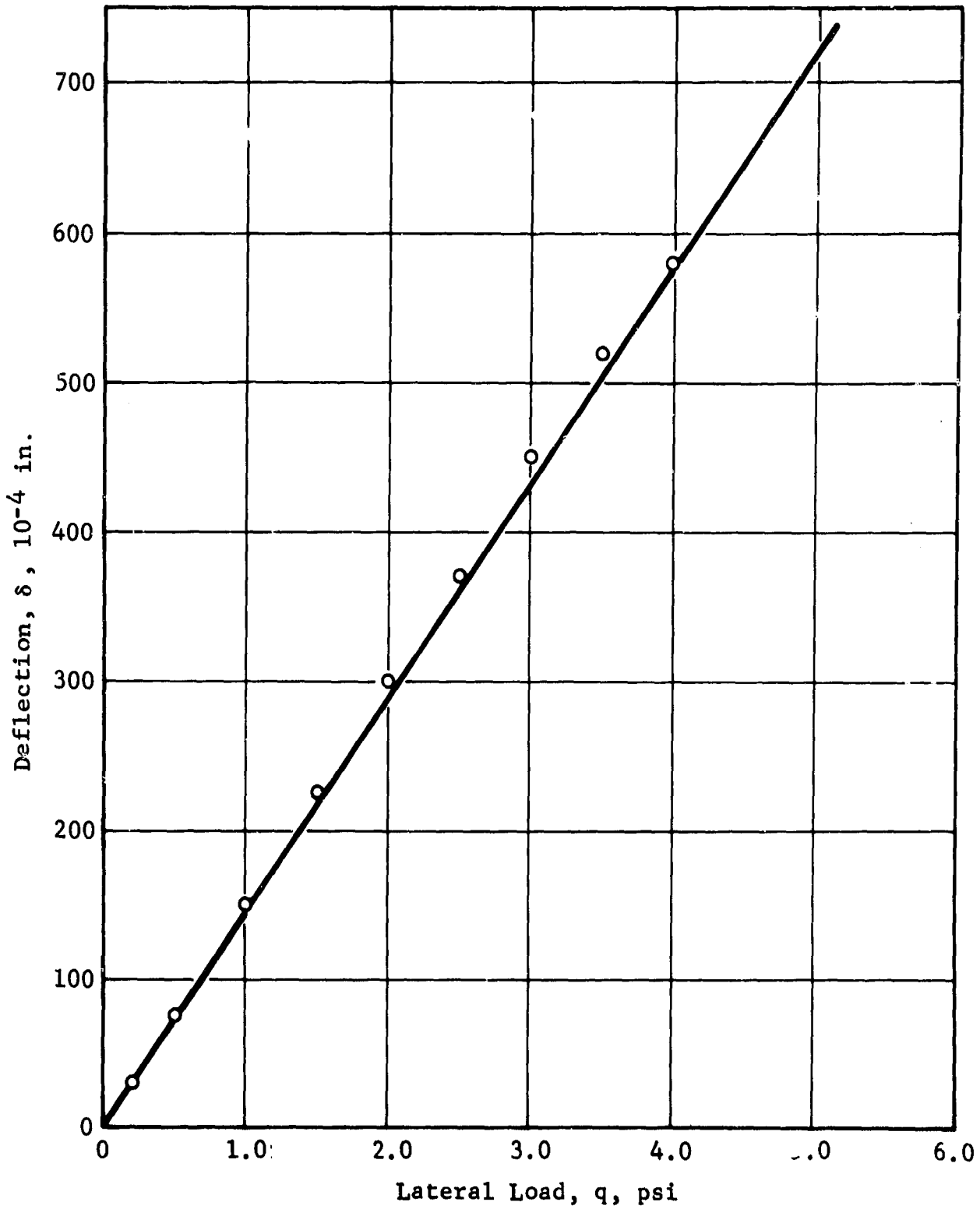


Figure 39 Deflection vs Lateral Load, Clamped-Simple Condition, Panel No. 5

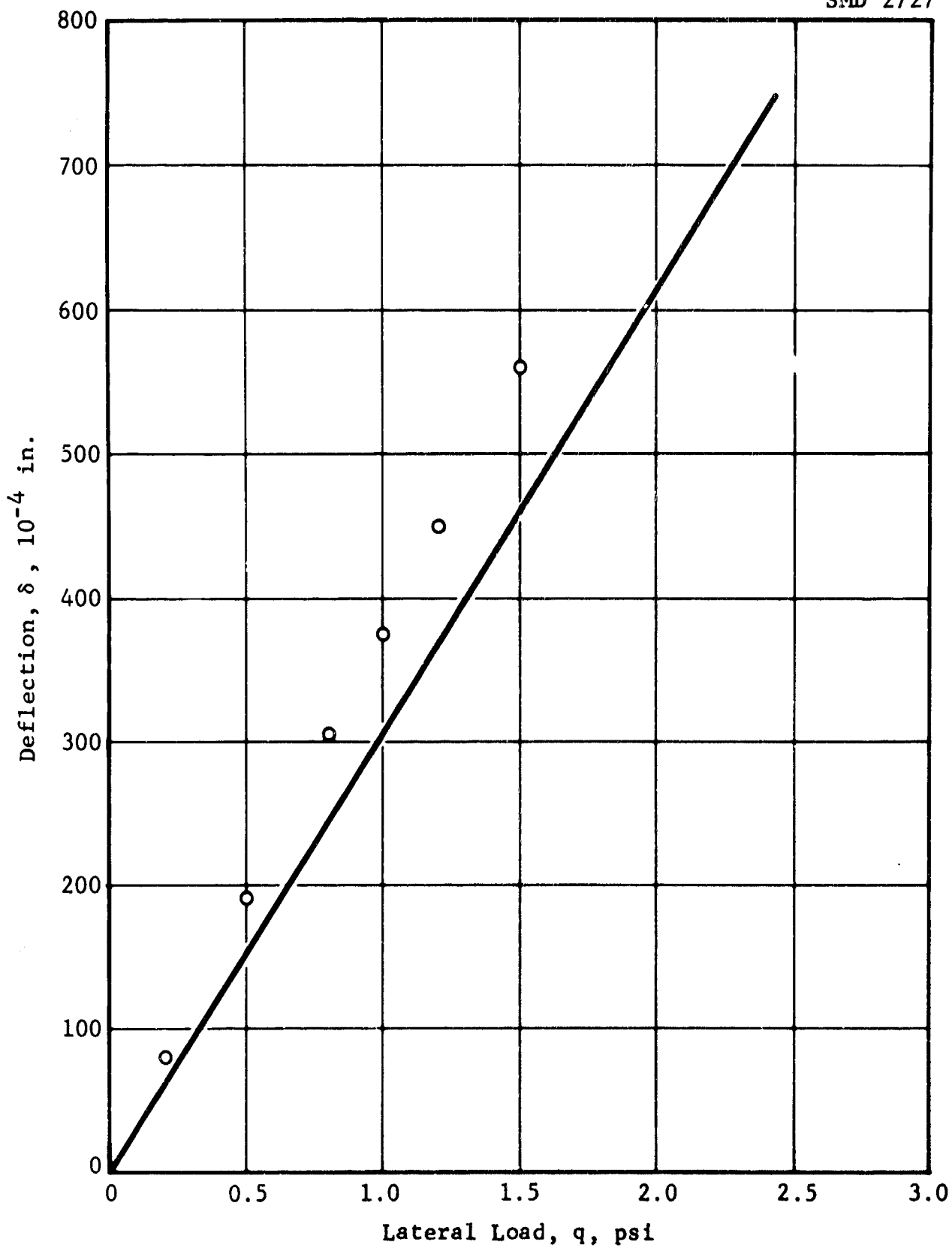


Figure 40 Deflection vs Lateral Load, Clamped-Simple Condition, Panel No. 5, Turned 90°

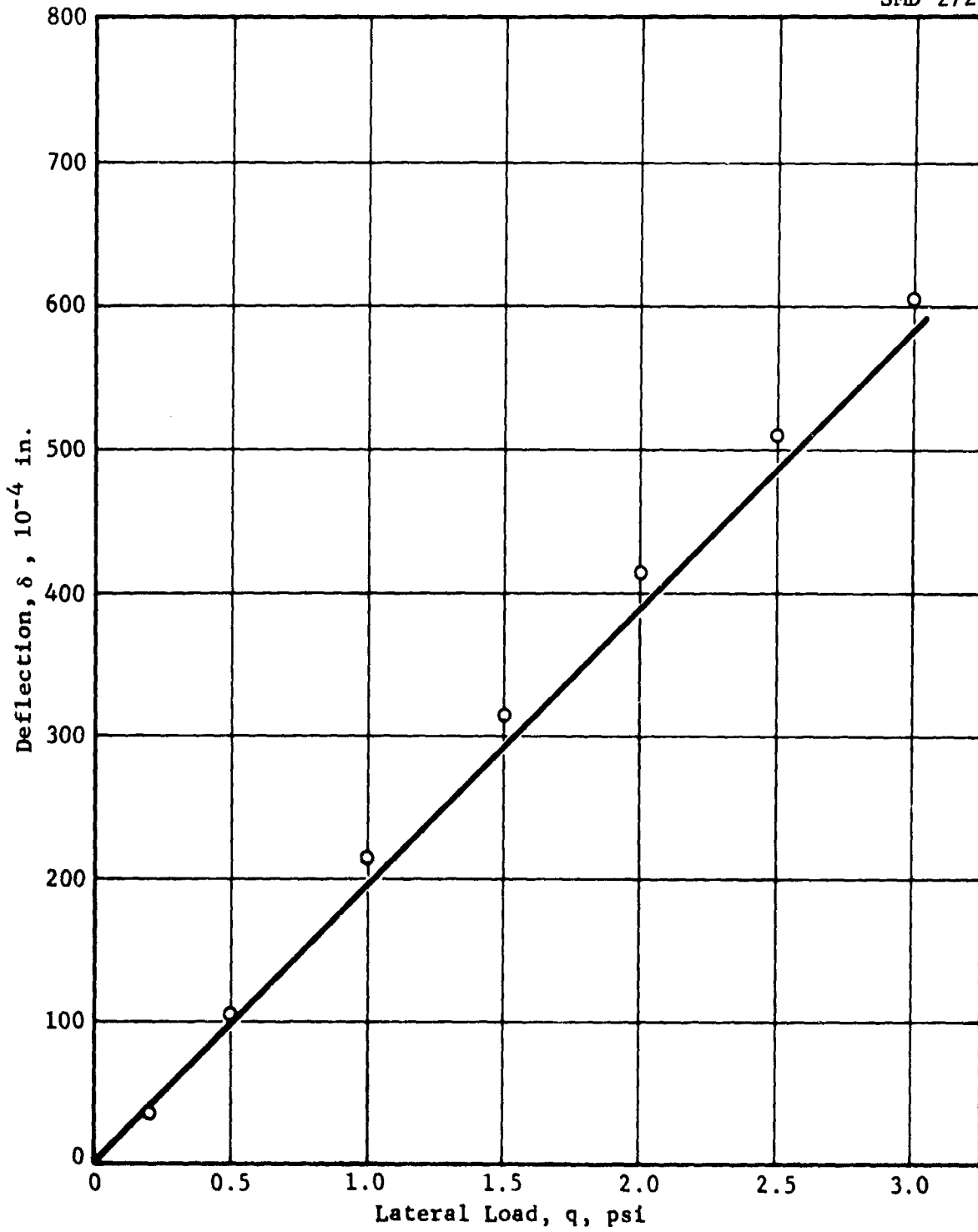


Figure 41 Deflection vs Lateral Load, Clamped-Clamped Condition,
Panel No. 7

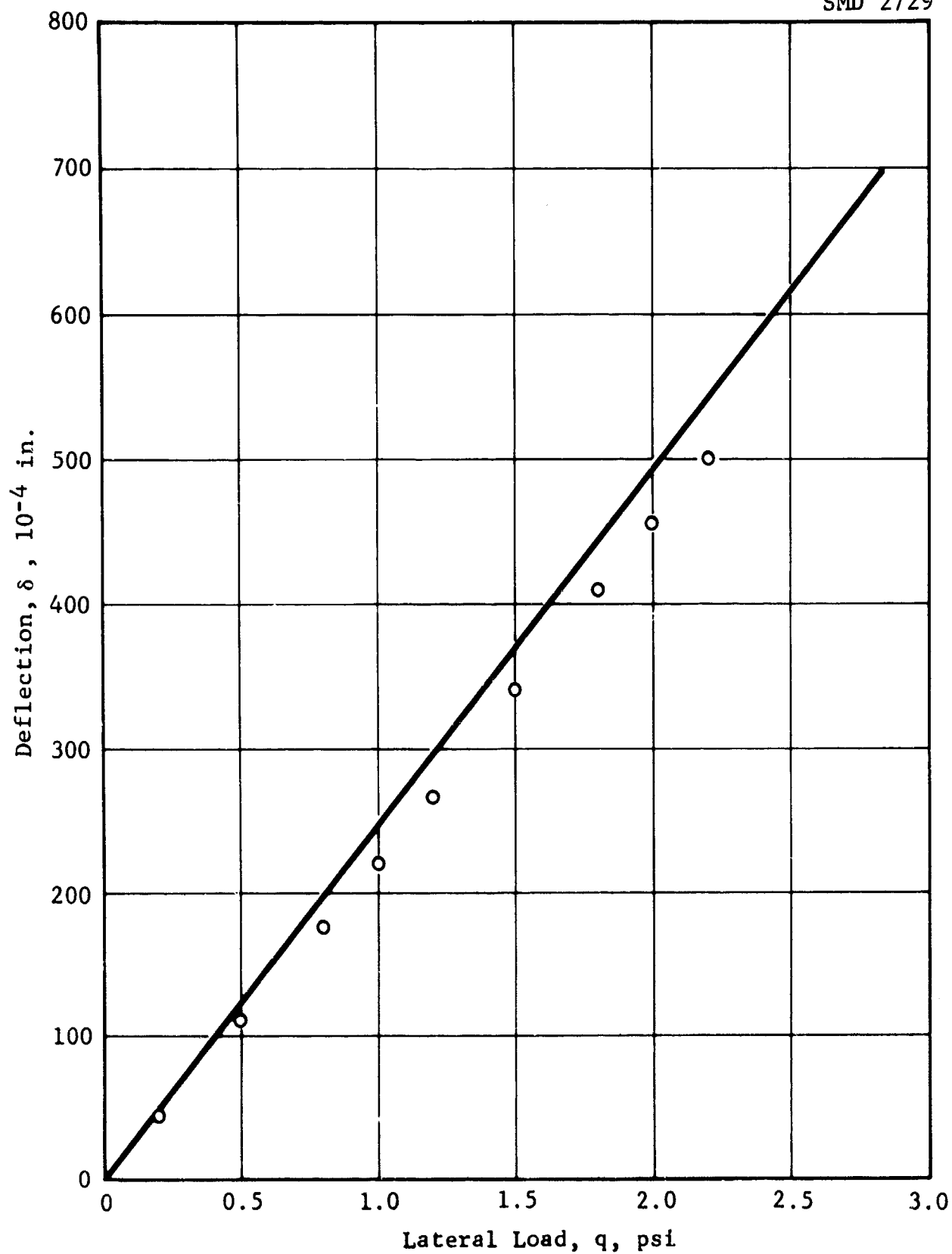


Figure 42 Deflection vs Lateral Load, Clamped-Simple Condition, Panel No. 7

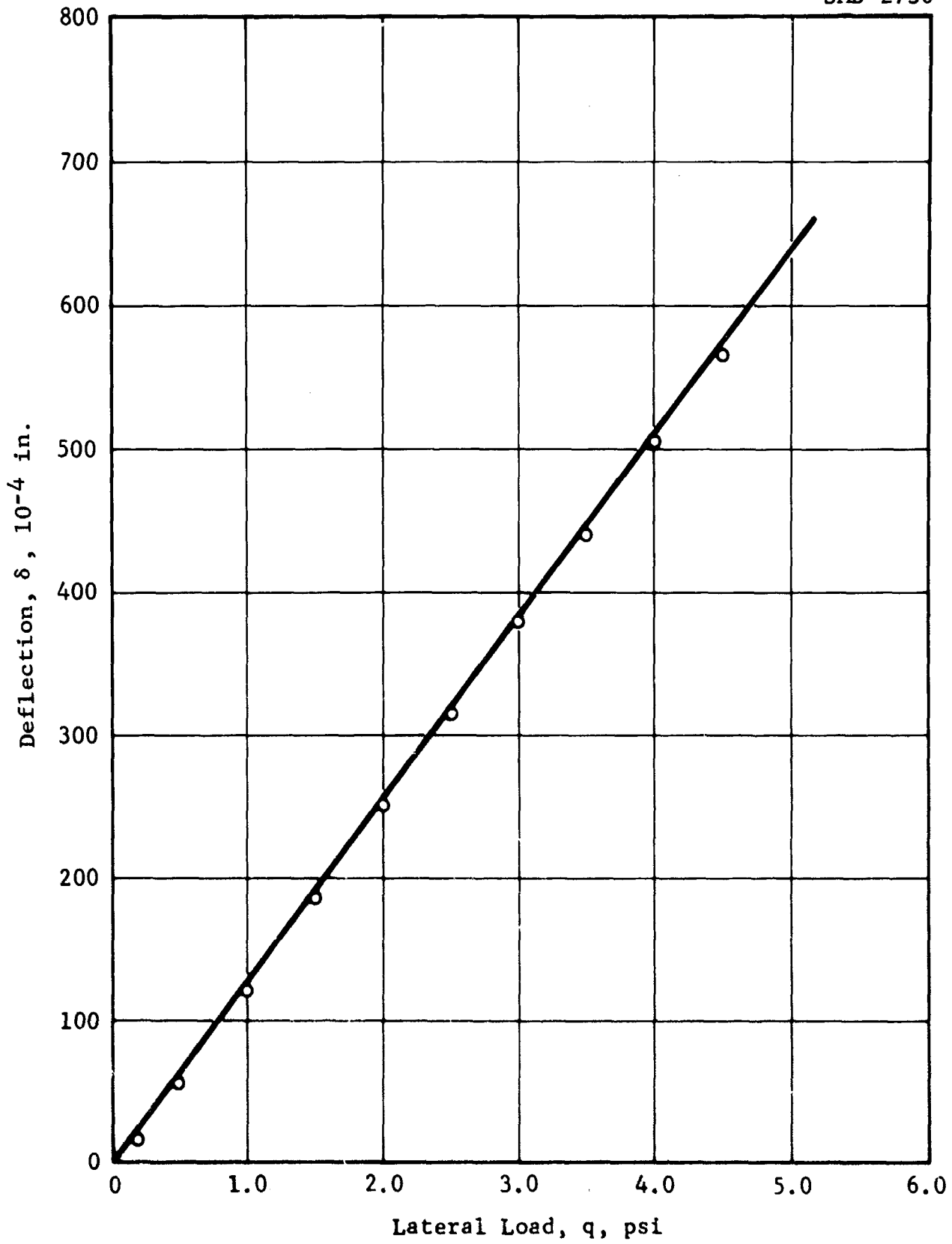


Figure 43 Deflection vs Lateral Load, Clamped-Clamped Condition, Panel No. 9

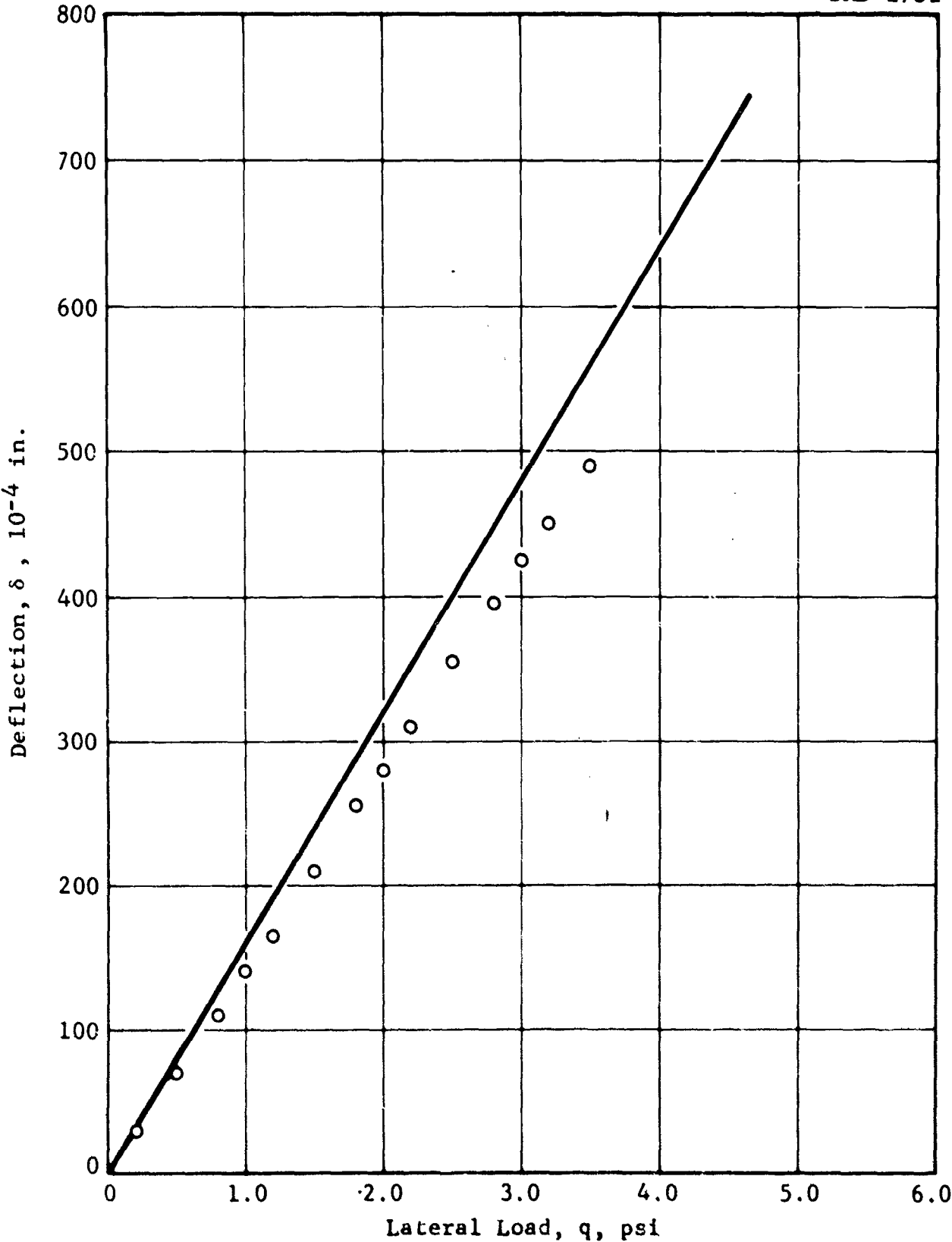


Figure 44 Deflection vs Lateral Load, Clamped-Simple Condition, Panel No. 9

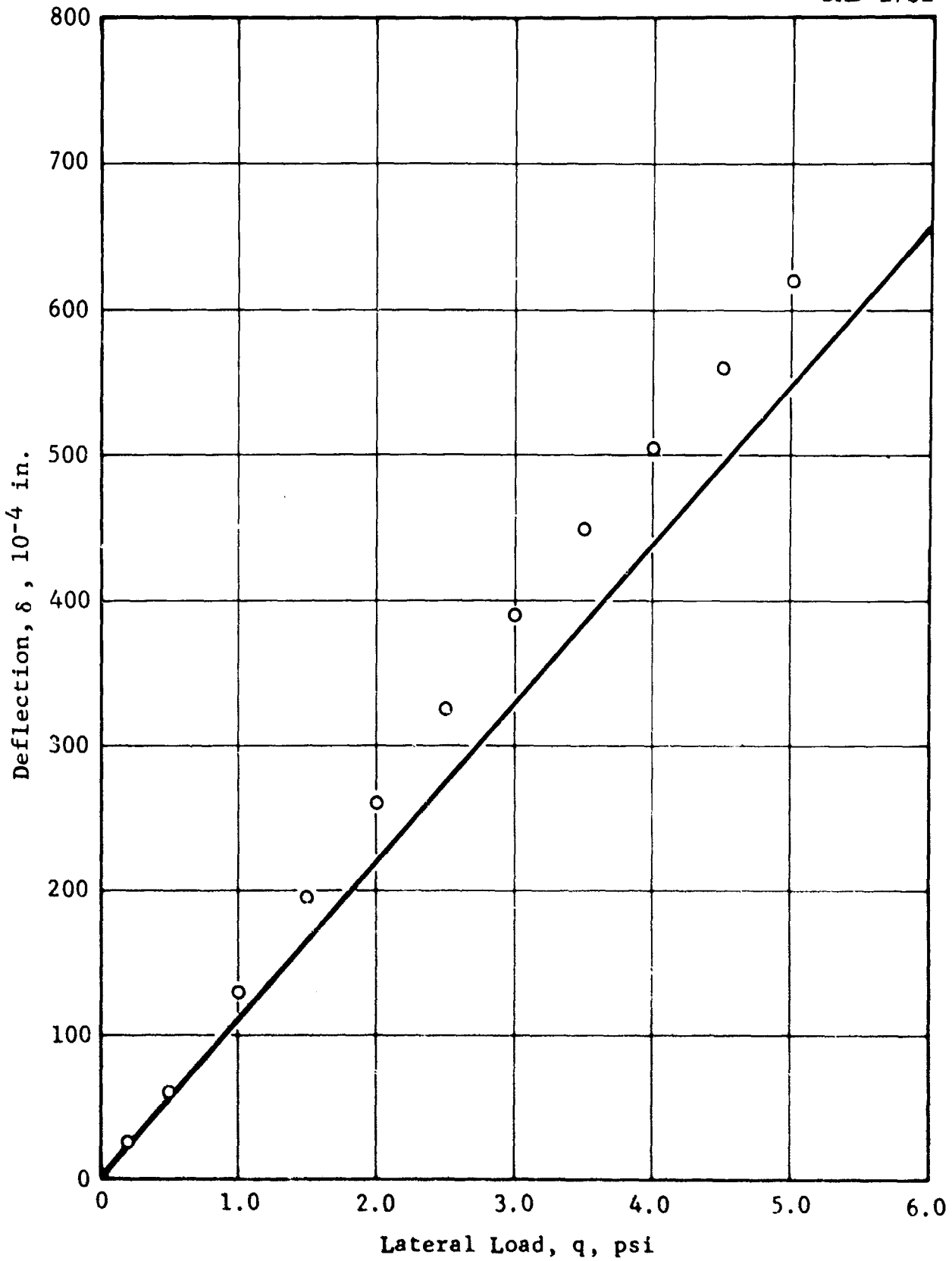


Figure 45 Deflection vs Lateral Load, Clamped-Clamped Condition,
Panel No. 12

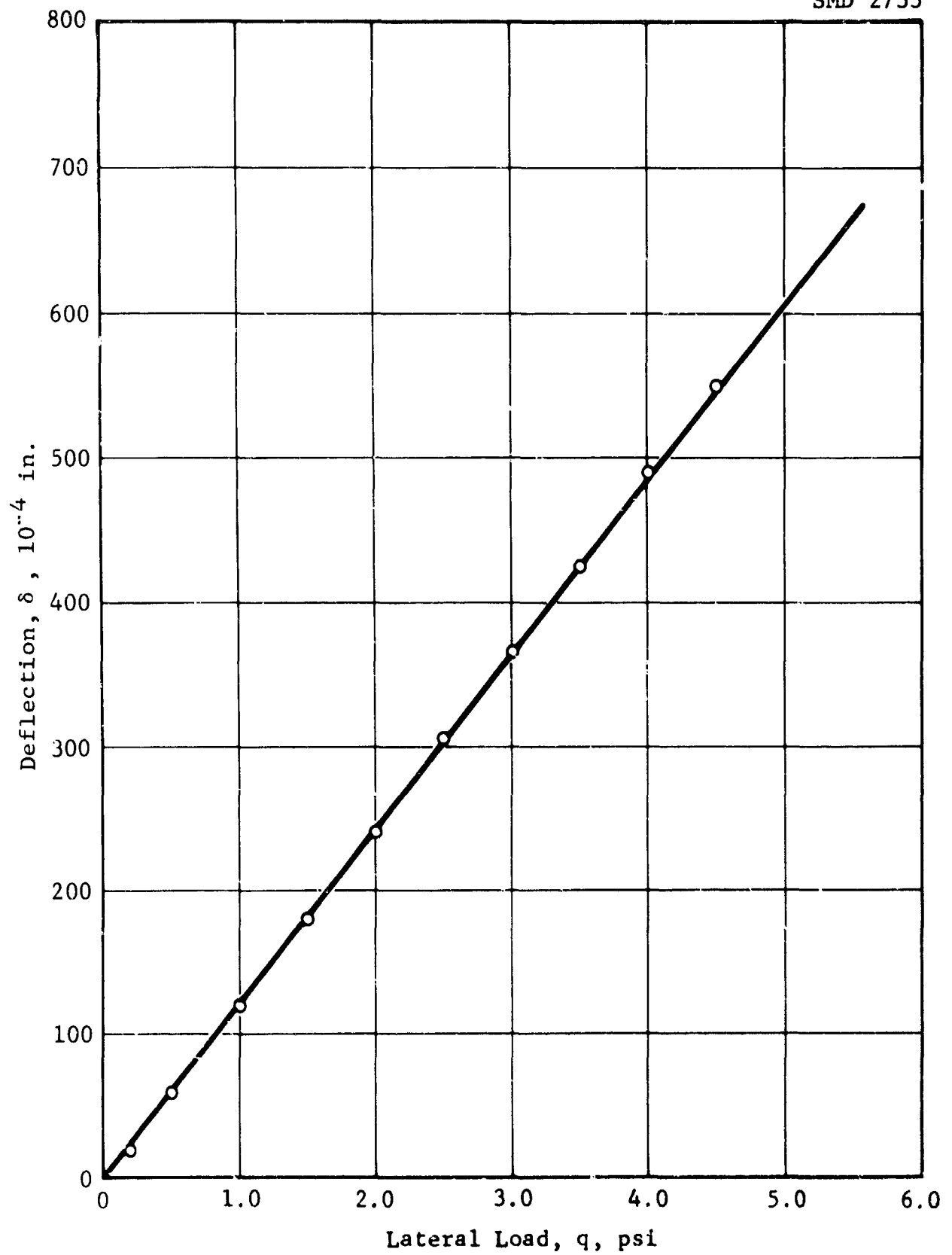


Figure 46 Deflection vs Lateral Load, Clamped-Simple Condition, Panel No. 12

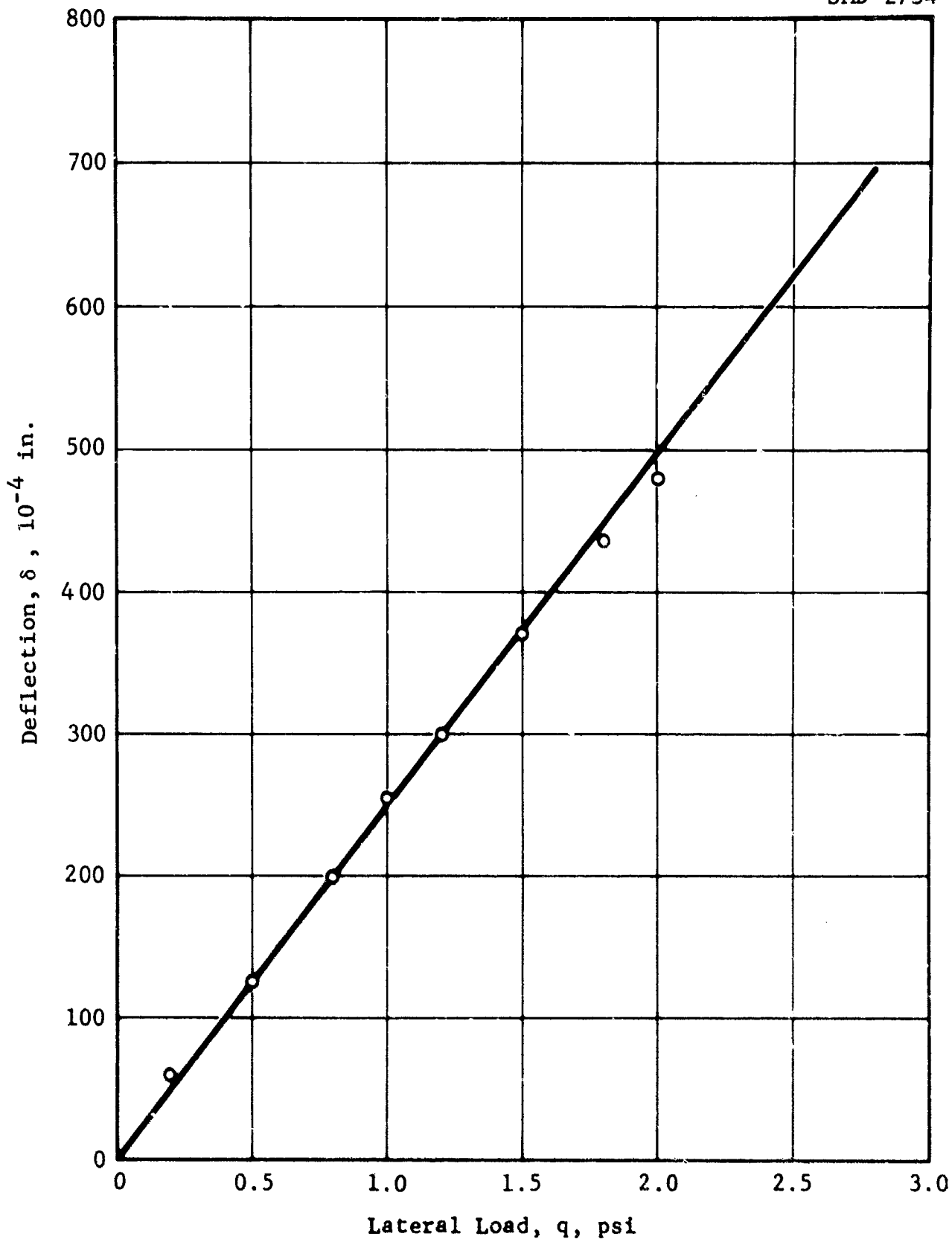


Figure 47 Deflection vs Lateral Load, Clamped-Clamped Condition, Panel No. 16

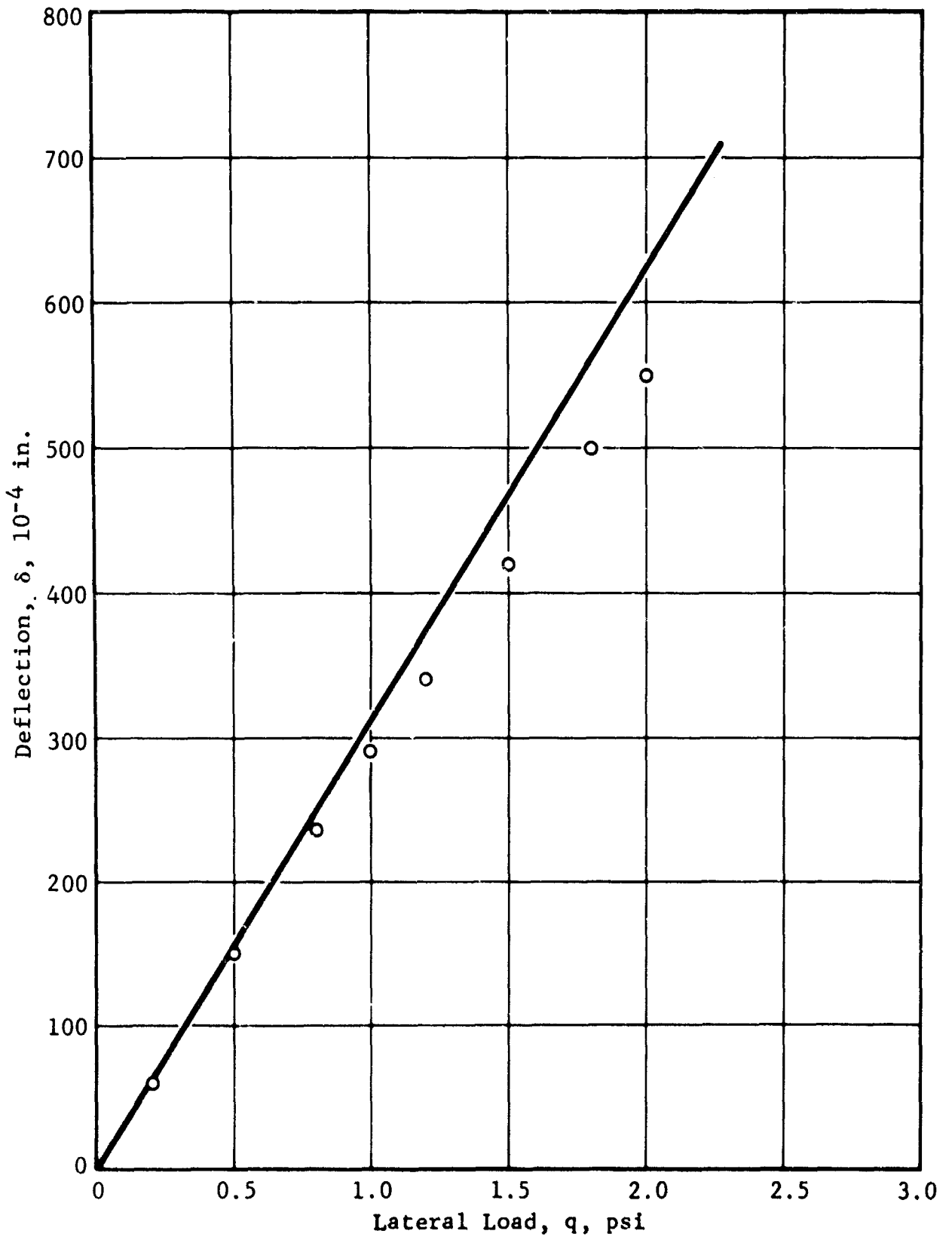


Figure 48 Deflection vs Lateral Load, Clamped-Simple Condition, Panel No. 16

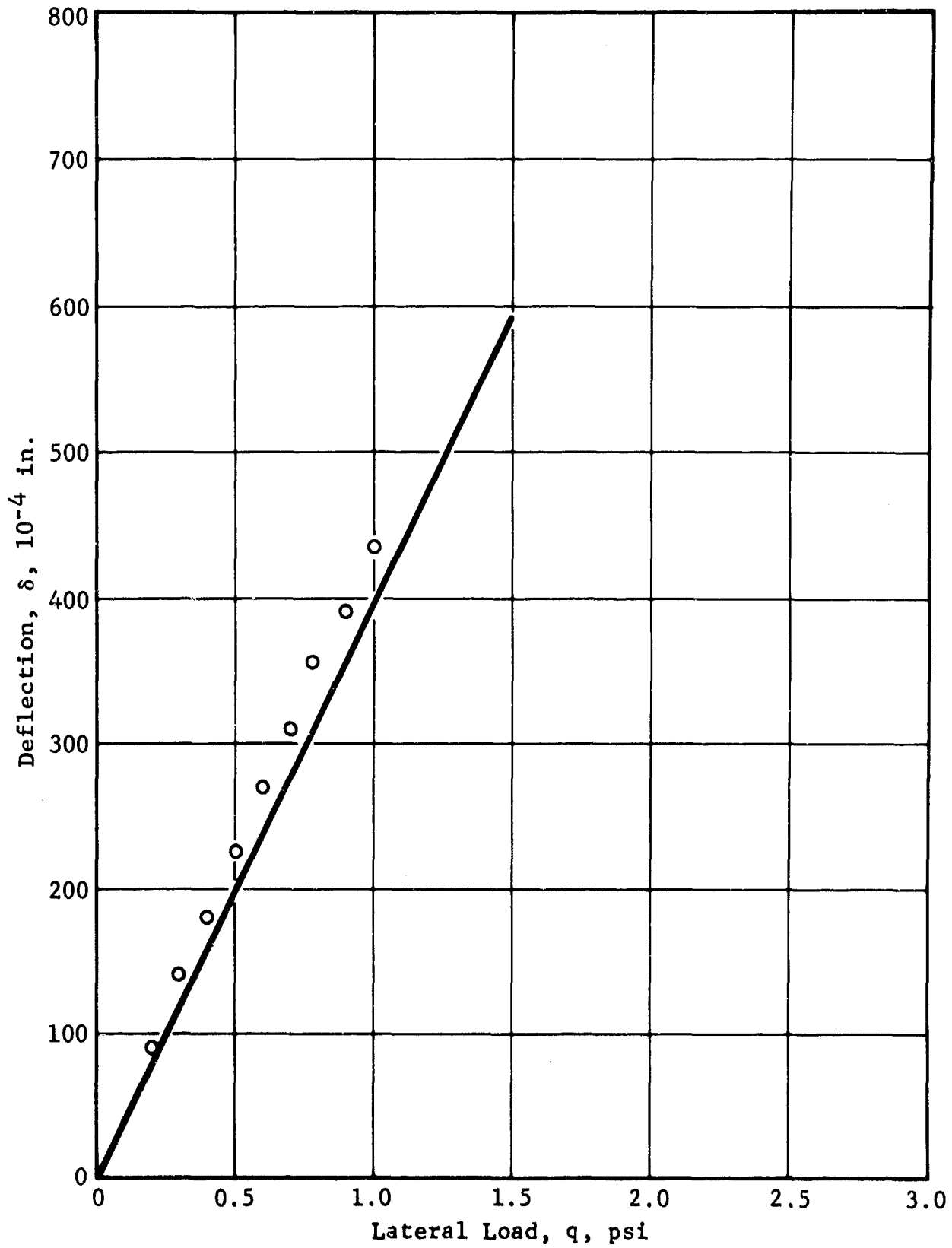


Figure 49 Deflection vs Lateral Load, Clamped-Clamped Condition, Panel No. 19A

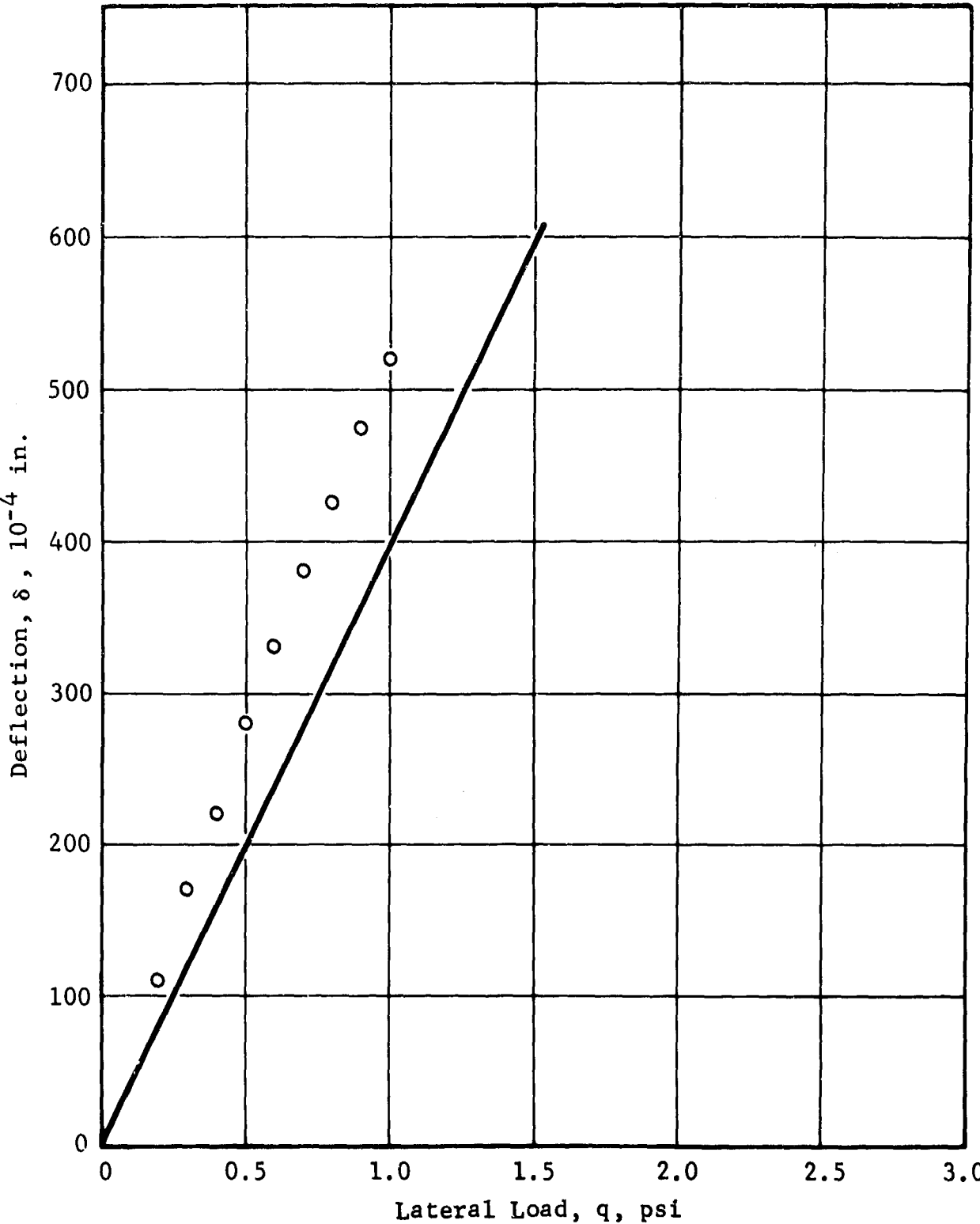


Figure 50 Deflection vs Lateral Load, Clamped-Clamped Condition, Panel No. 19A, Turned 90°

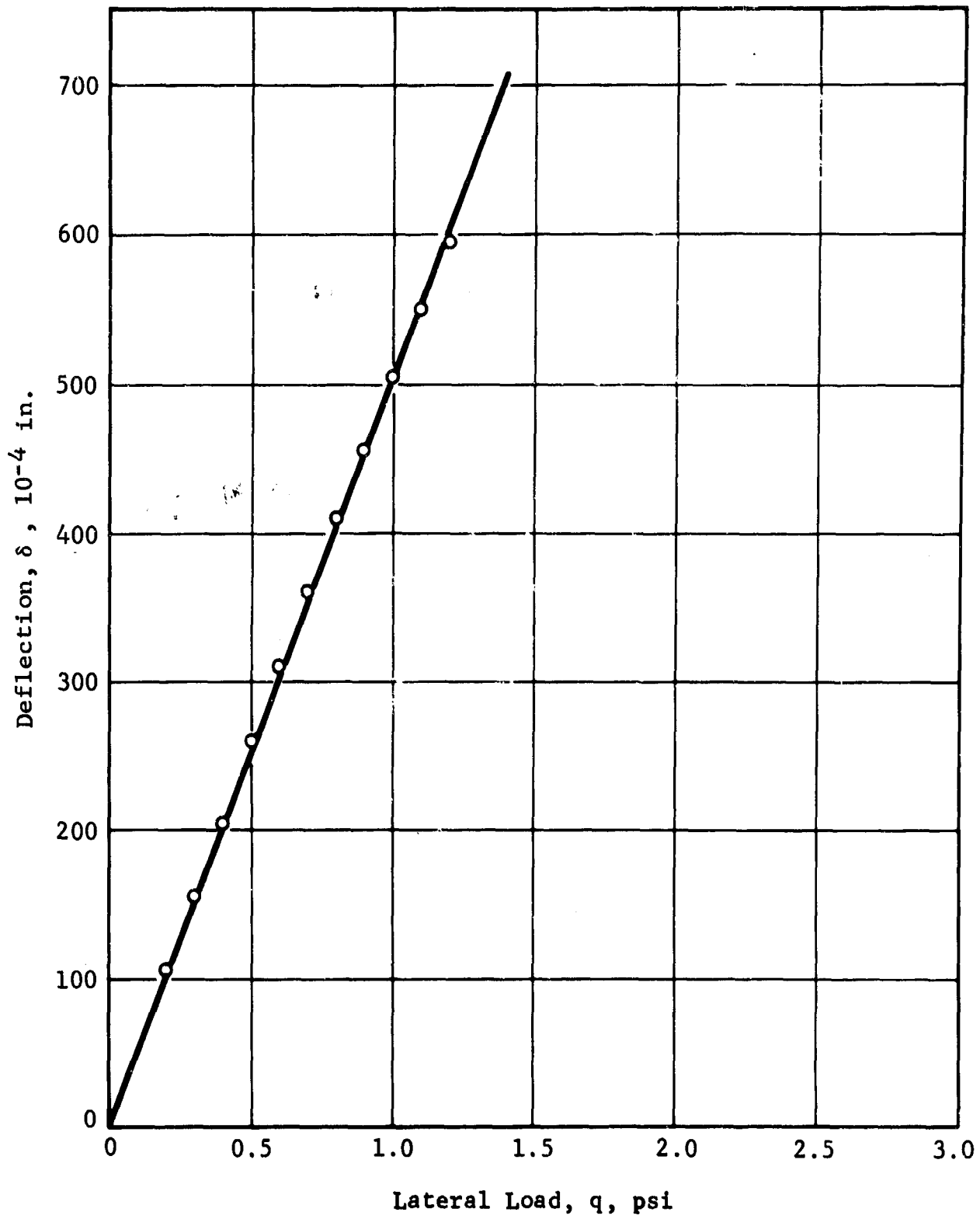


Figure 51 Deflection vs Lateral Load, Clamped-Simple Condition, Panel No. 19A

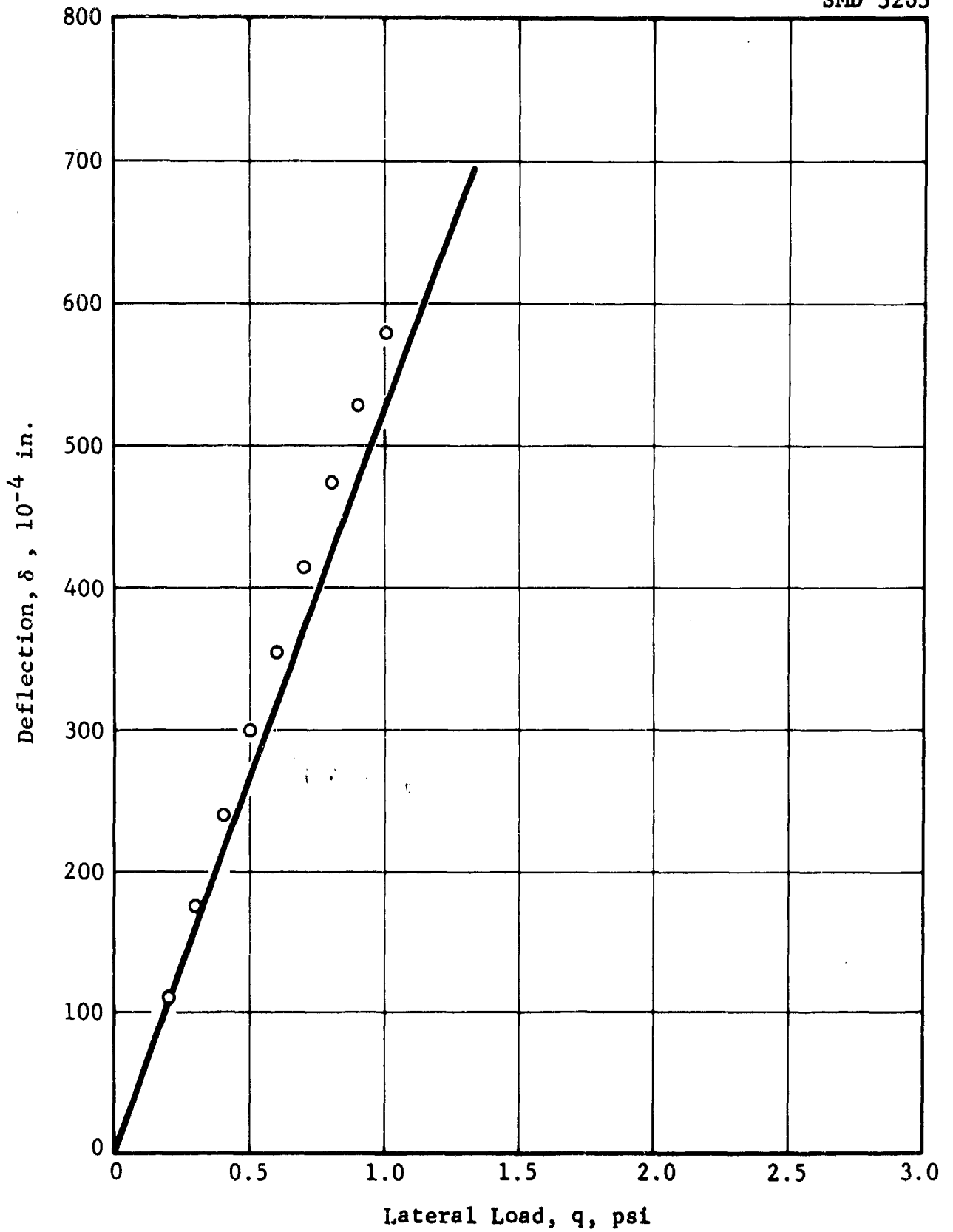


Figure 52 Deflection vs Lateral Load, Clamped-Simple Condition, Panel No. 19A, Turned 90°

The lateral load data for the clamped-clamped boundary condition tends generally to be slightly higher than the analytical predictions, indicating that the elastic restraint constants ($\alpha = \beta = \alpha_1 = \beta_1 = 21.0$) should be lowered. Buckling results (Figure 29) indicate that higher values would be preferable. This tradeoff of elastic restraint constants corresponds to that noted in subsection 4.4. Data for the clamped-simple boundary condition agree quite well with the analytical predictions.

For Panel 5 (0°) with clamped-clamped boundary conditions, data obtained for a lateral load should be the same for the 0- and 90- degree test configurations. Referring to Figures 37 and 38, a comparison of the test data indicates that, within scatter, this condition was obtained. However, correlation between experiment and theory is poor even though the clamped-clamped data for all panels tended to be higher than the analytical predictions. Correlation of the data with the analytical predictions for clamped-simple boundary conditions (Figures 39 and 40) is excellent for the 0-degree configuration and fair for the 90-degree configuration.

In general, when Panel 5 (0°) was subjected to a lateral load, it acted less stiff than anticipated. This behavior contradicts that observed in the buckling study discussed previously.

For tests under combined loads (lateral plus uniaxial), it was assumed that superposition of loads was valid. The combined loads data for the steel panel with clamped-clamped boundary conditions are depicted in Figure 53. To evaluate the test data, it is necessary to consider the correlation of test data with analysis when lateral pressure is acting alone and when the effect of initial imperfections is removed.

When the deflections obtained from the lateral load study (Figure 32) were replotted (open triangles) in Figure 53 with the deflections (open circles) from the combined loads study, a comparison showed that the deflections from the two tests were consistent and slightly above the predicted values for a zero applied edge load. Proper evaluation of the combined loads data would require identical experimental and analytical deflections at zero edge load. Since test scatter makes it impossible to get such agreement, the load-deflection curves for increasing levels of pressure are discussed without reference to their initial points.

The data shown for 0.2 psi in Figure 53 do not agree with the analytical predictions; better agreement is obtained as pressures are increased. It will be shown later that this agreement is only a coincidence due to two compensating factors. The lack of agreement between experiment and analysis is due to initial imperfections

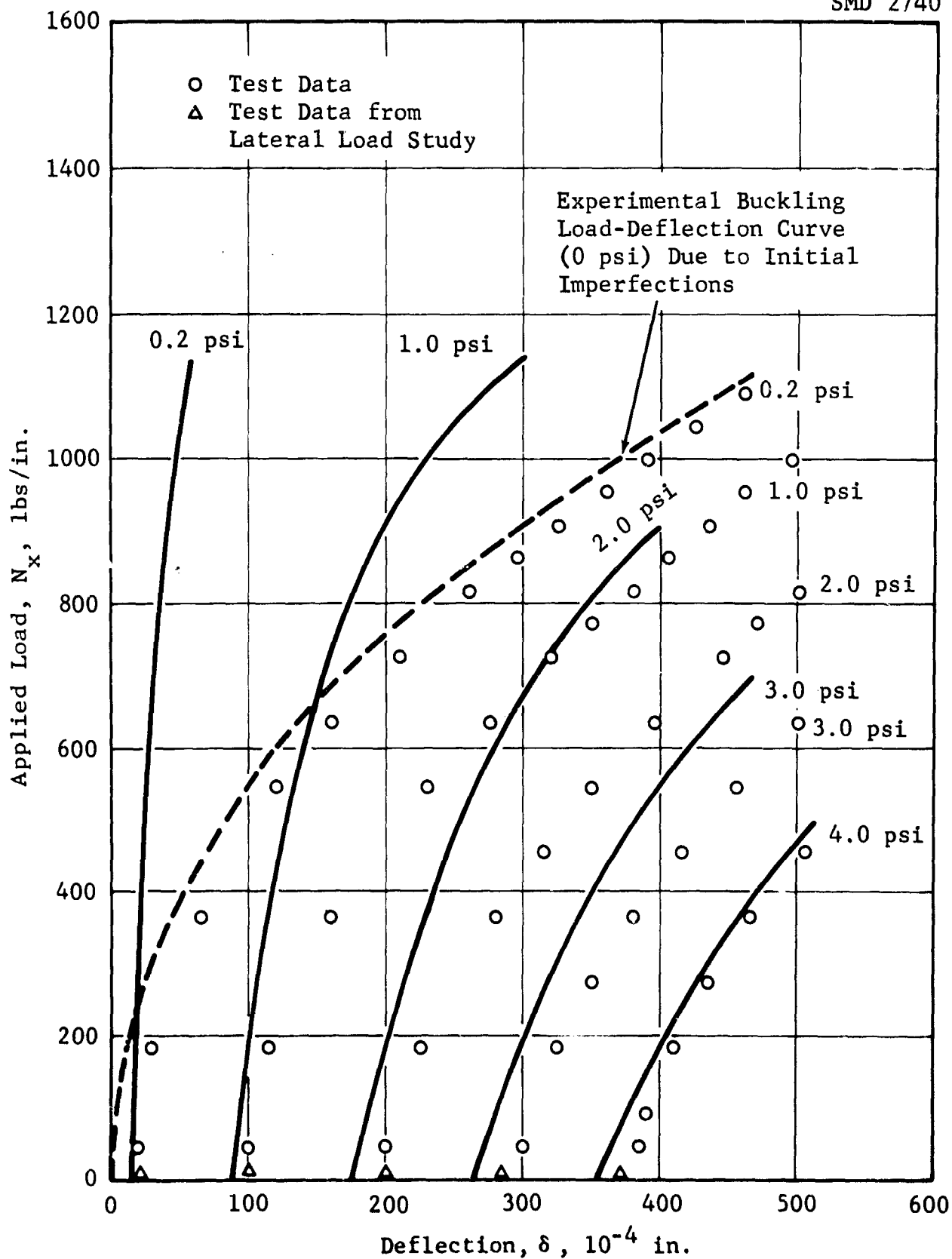


Figure 53 Data Reduction, Steel Panel Clamped-Clamped Condition

in the plate. These imperfections are the same as those encountered in a buckling test. To illustrate this, the buckling load-deflection curve for clamped-clamped boundaries (Figure 140) has been superimposed on Figure 53.

Since the analysis does not account for the deflections due to initial imperfections (i.e., the plate is assumed to be perfectly flat), these deflections were subtracted from the combined loads test data. The test data plotted in Figure 53 have been replotted in Figure 54 with the above correction. Adjusted data for the clamped-clamped boundary conditions show that the linear theory predictions of the behavior of the steel panel are accurate within the area enclosed by the dashed line. Beyond this region, the panel has begun to stiffen due to membrane forces. This behavior is not as obvious in the rough data (Figure 53).

If the linear theory limit line (Figure 54) were superimposed on the rough data (Figure 53), it would show that the steel panel stiffens before the deflection reaches the theoretical limit of $t/2$ (0.044 inch for the steel panel). This limit has been established for an ideal plate having no initial imperfections. The above behavior can be explained by the slight curvature in the steel panel (noted earlier), which introduced membrane forces at a measured deflection lower than $t/2$. Thus, what appeared to be a correlation of test data with analysis at 4.0 psi in Figure 53 is in reality a nullification of the deflection due to initial imperfections by the increased stiffening due to membrane forces.

The preceding discussion of the steel panel with clamped-clamped boundaries is supported by the data obtained with the clamped-simple condition as shown by Figures 55 and 56. The load-deflection curves for combined loads should also be reviewed without reference to the agreement of their initial points with the analytical predictions.

Combined loads data for the boron panels are presented in Figures 57 through 76. The load-deflection curves have been corrected as discussed above for the steel panel. With the exception of the unidirectional plate, Panel 5, agreement is generally good.

Panels 2, 7, and 9 (unsym $\pm 45^\circ$, all $+45^\circ$, sym $\pm 45^\circ$, respectively) exhibited excellent agreement with their analytical predictions for both the clamped-clamped and clamped-simple boundary conditions. The clamped-clamped data for Panel 3 ($0^\circ/90^\circ$) and Panel 12 ($0^\circ/\pm 45^\circ$), presented in Figures 59 and 69, show an apparent trend to deviate from the analytical predictions with increasing

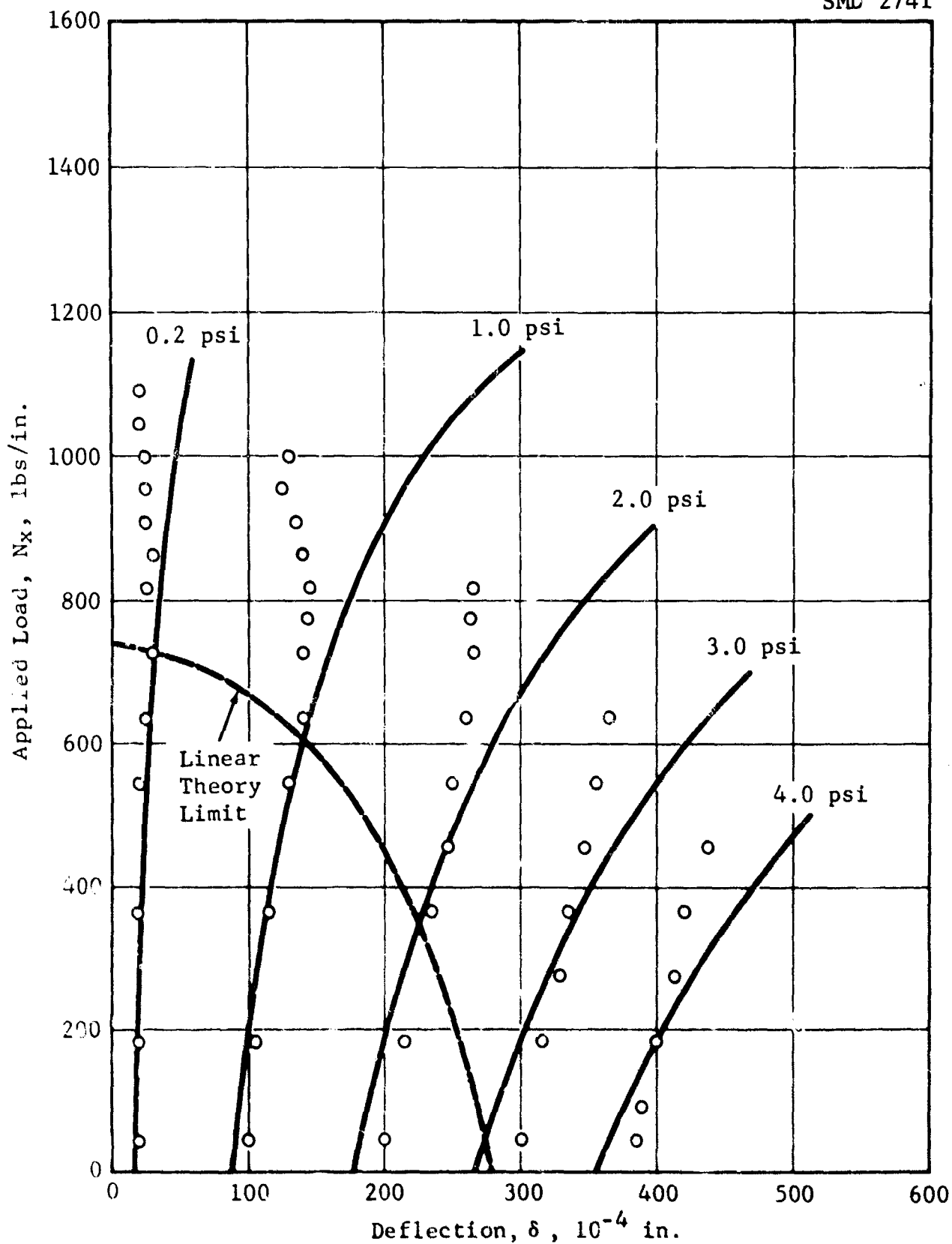


Figure 54 Combined Uniaxial and Lateral Loadings, Steel Panel, Clamped-Clamped Condition

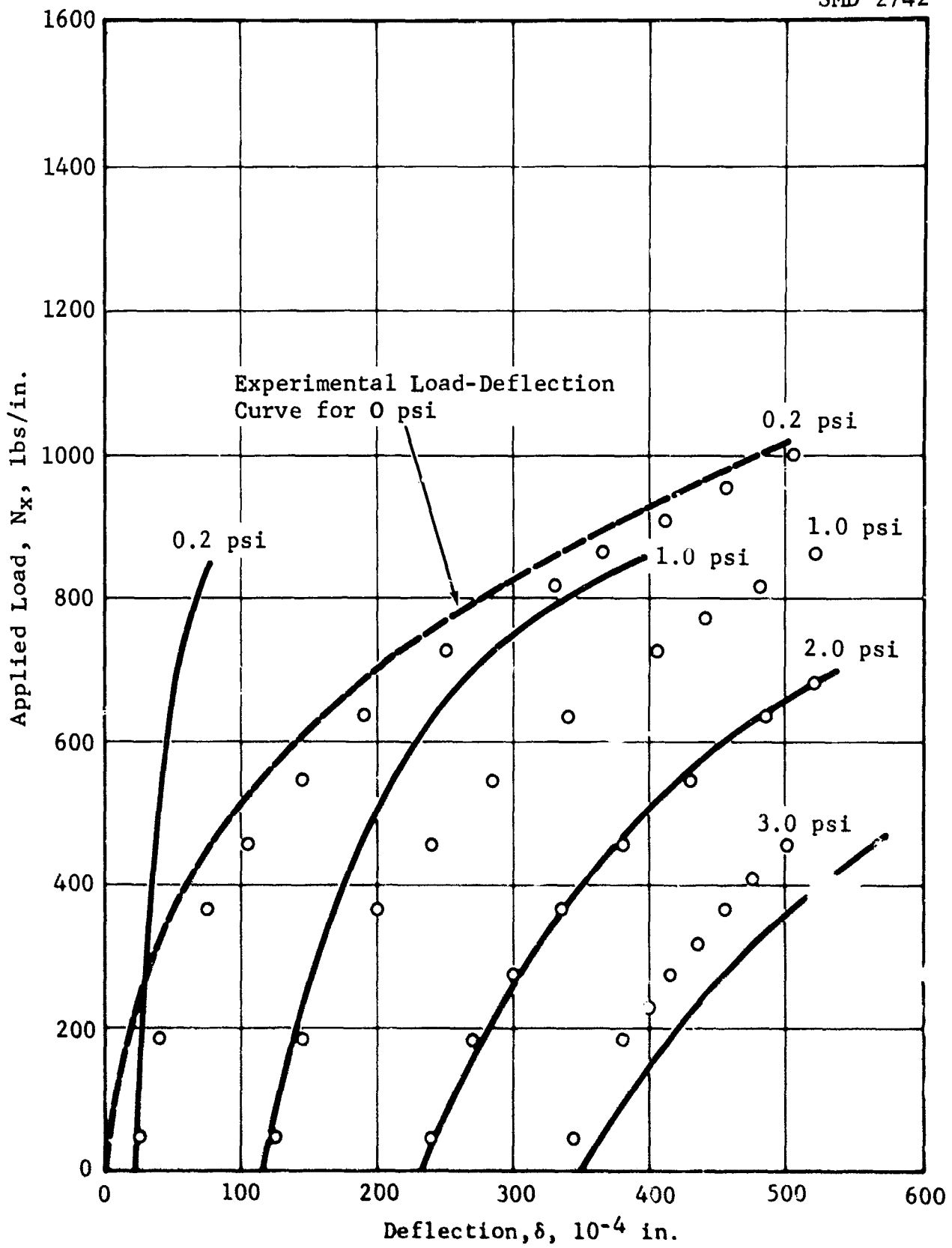


Figure 55 Data Reduction, Steel Panel, Clamped-Simple Condition

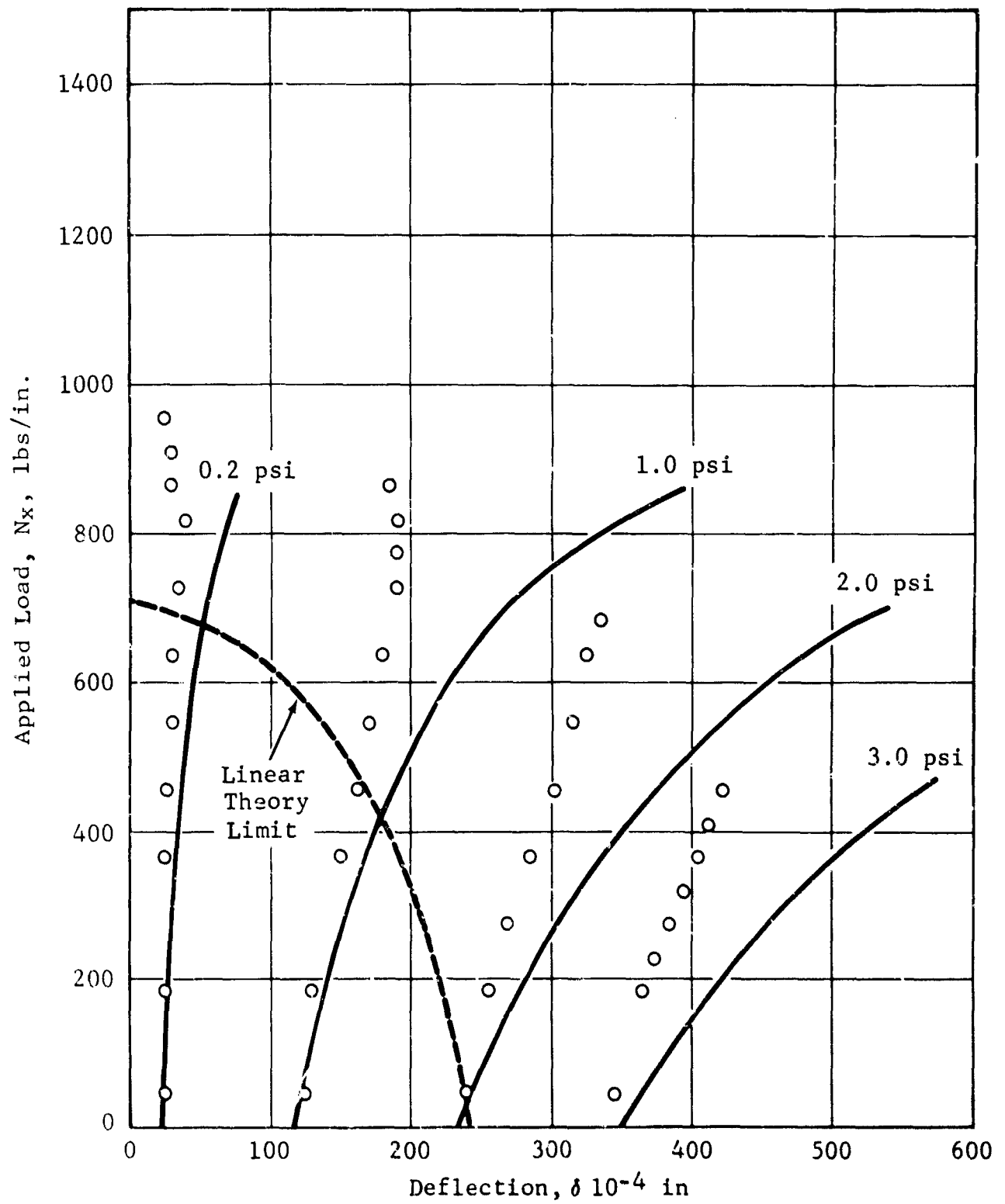


Figure 56 Combined Uniaxial and Lateral Loadings, Steel Panel, Clamped-Simple Condition

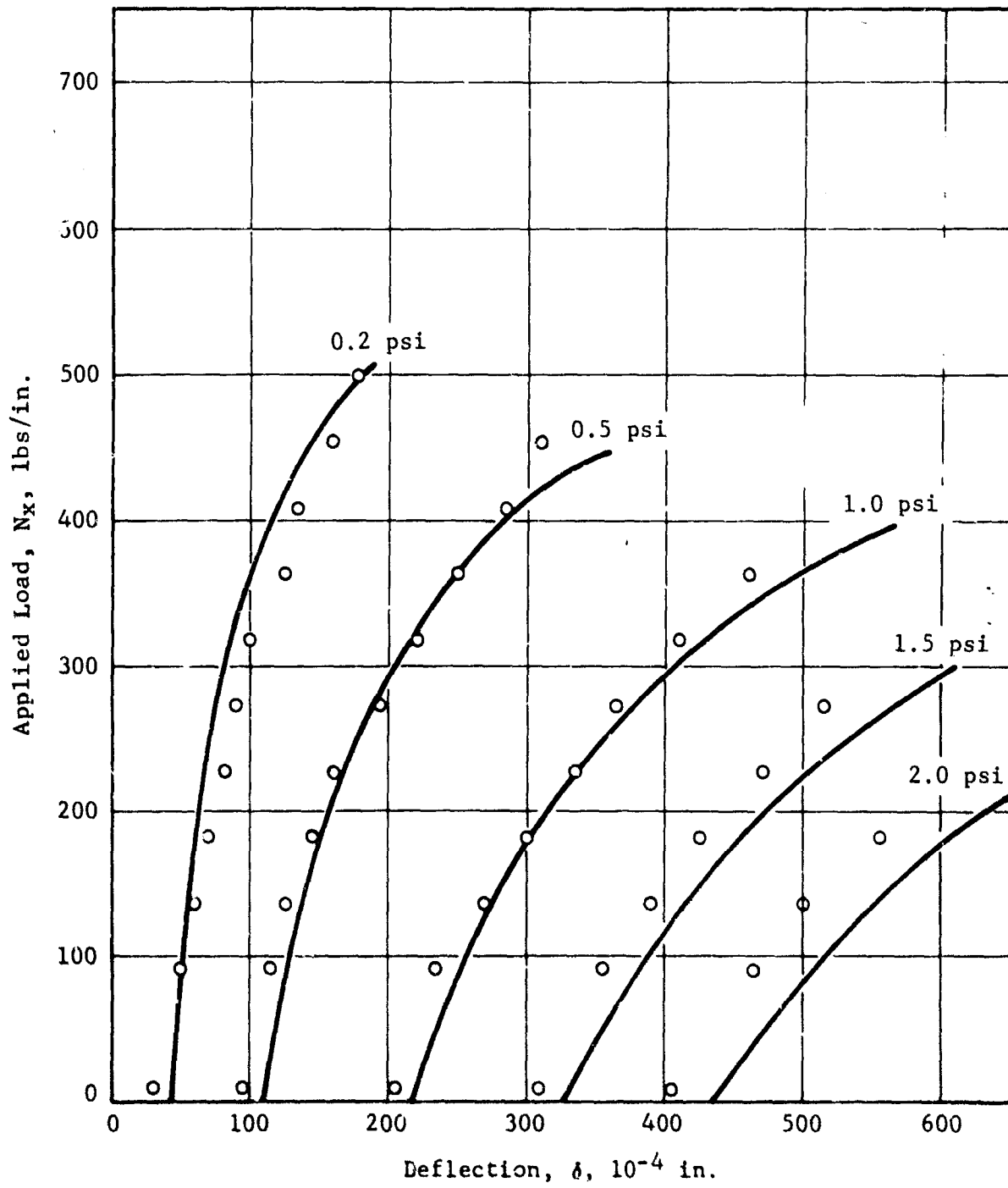


Figure 57 Combined Uniaxial and Lateral Loadings, Panel No. 2, Clamped-Clamped Condition

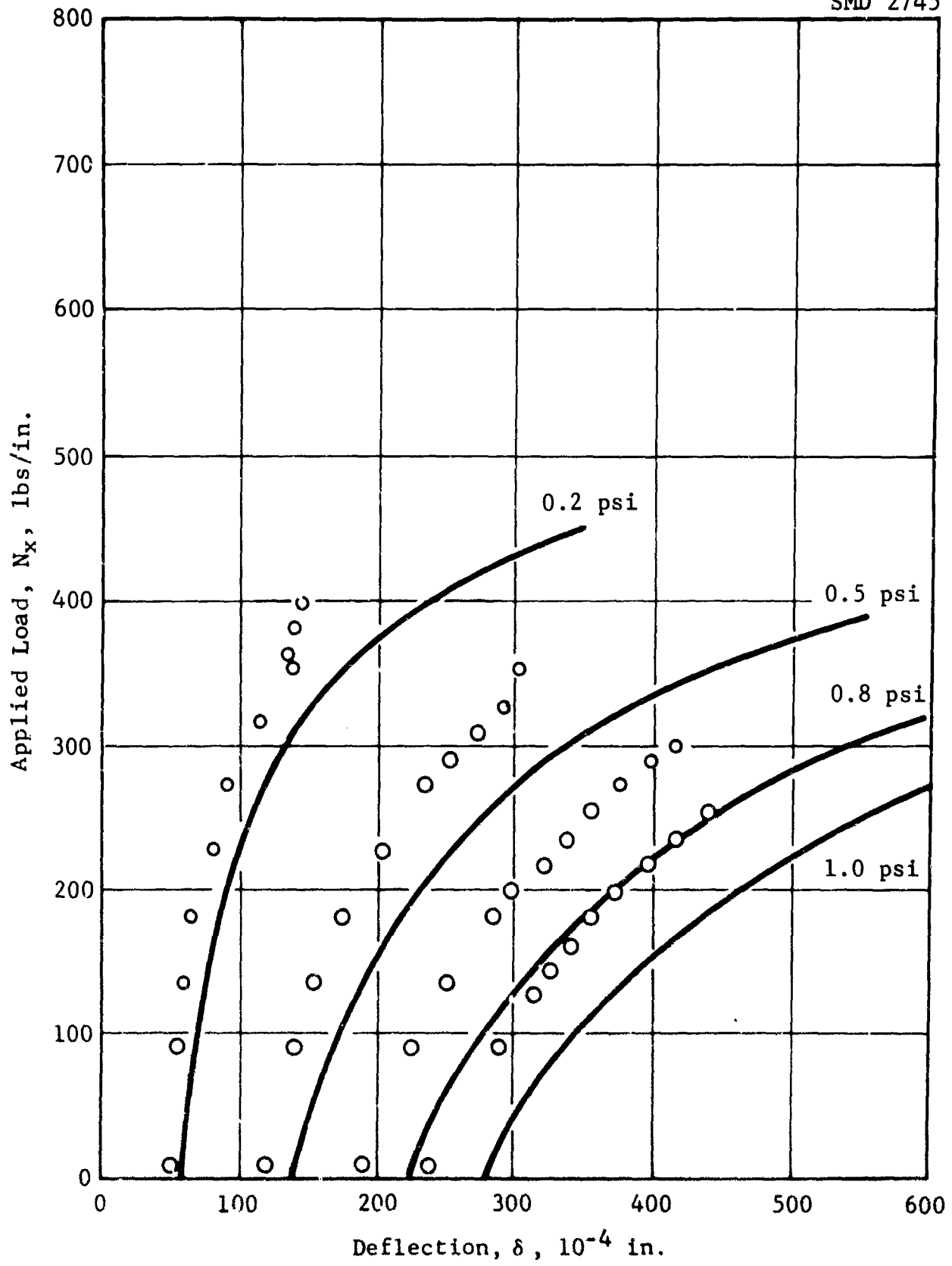


Figure 58 Combined Uniaxial and Lateral Loadings, Panel No. 2, Clamped-Simple Condition

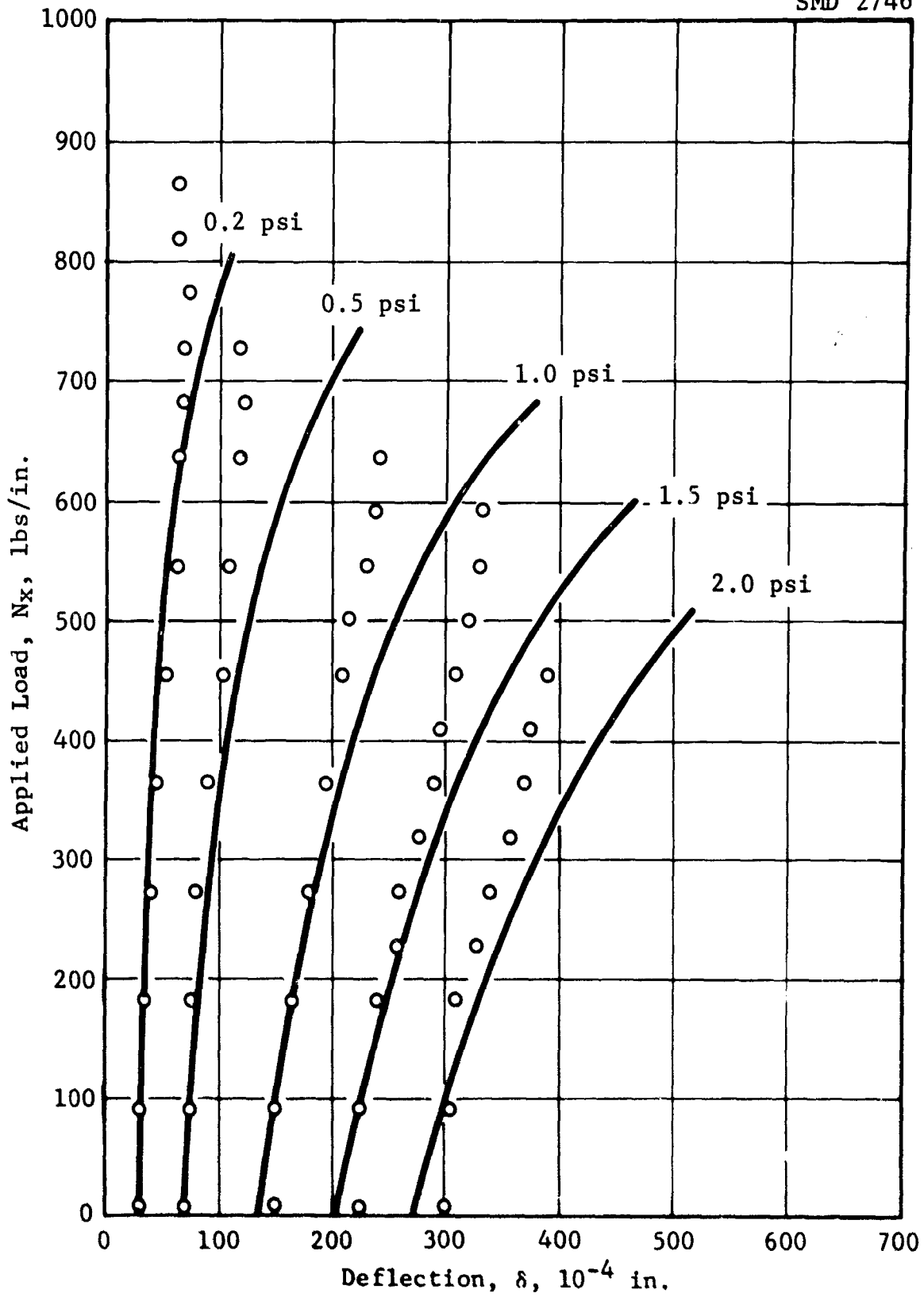


Figure 59 Combined Uniaxial and Lateral Loadings, Panel No. 3, Clamped-Clamped Condition

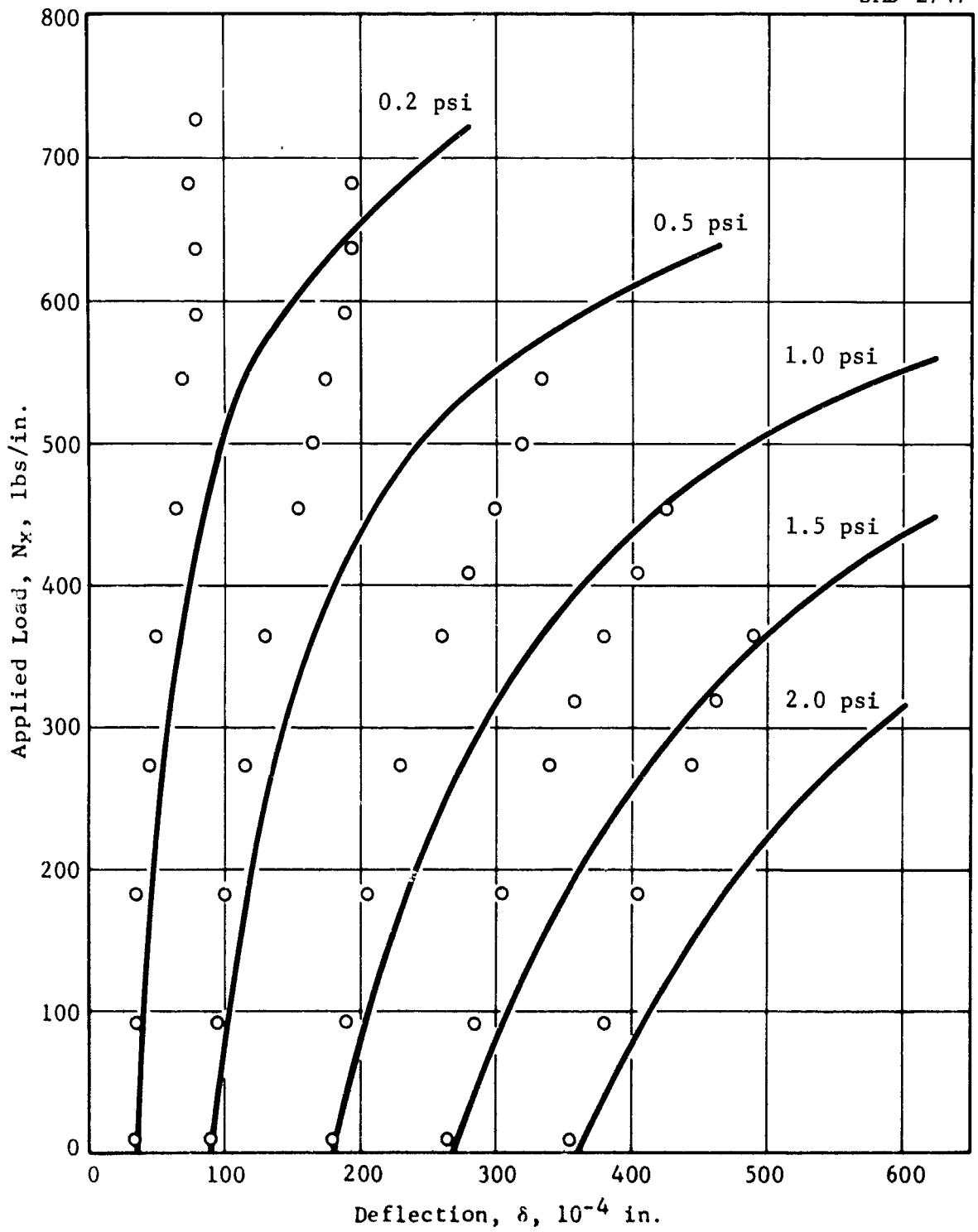


Figure 60 Combined Uniaxial and Lateral Loadings, Panel No. 3, Clamped-Simple Condition

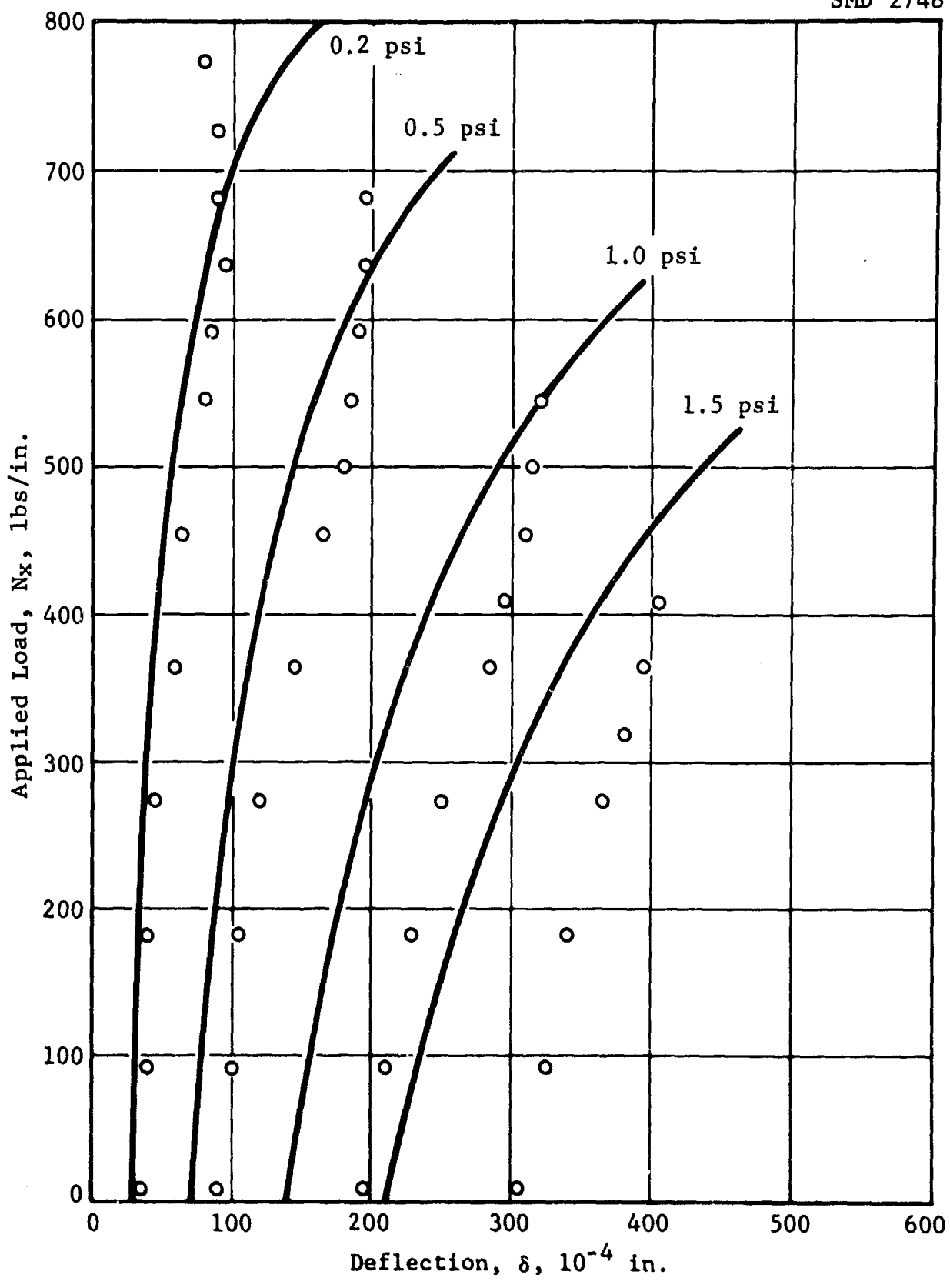


Figure 61 Combined Uniaxial and Lateral Loadings, Panel No. 5, Clamped-Clamped Condition

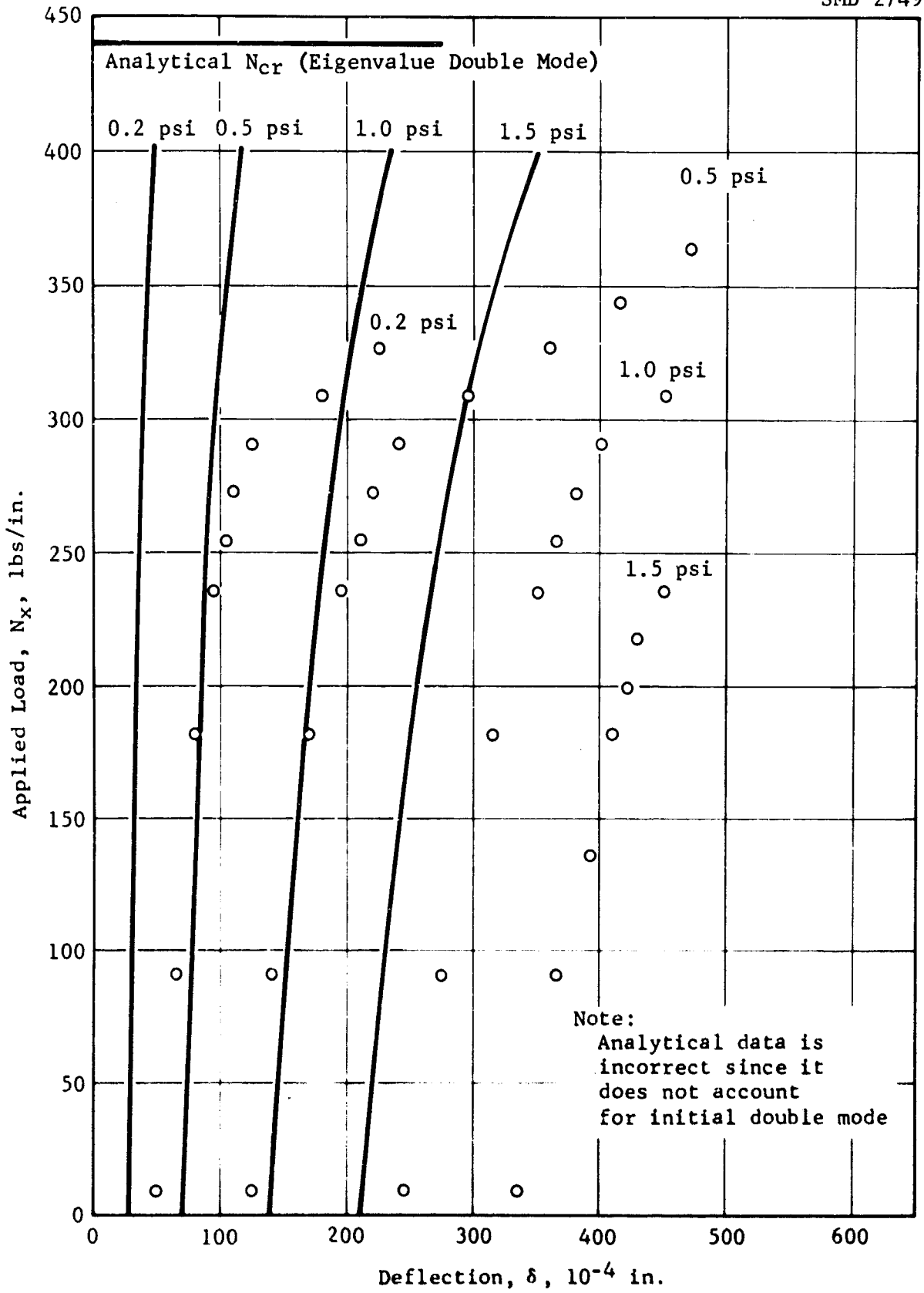


Figure 62 Combined Uniaxial and Lateral Loadings, Panel No. 5, Clamped-Clamped Condition, Turned 90°

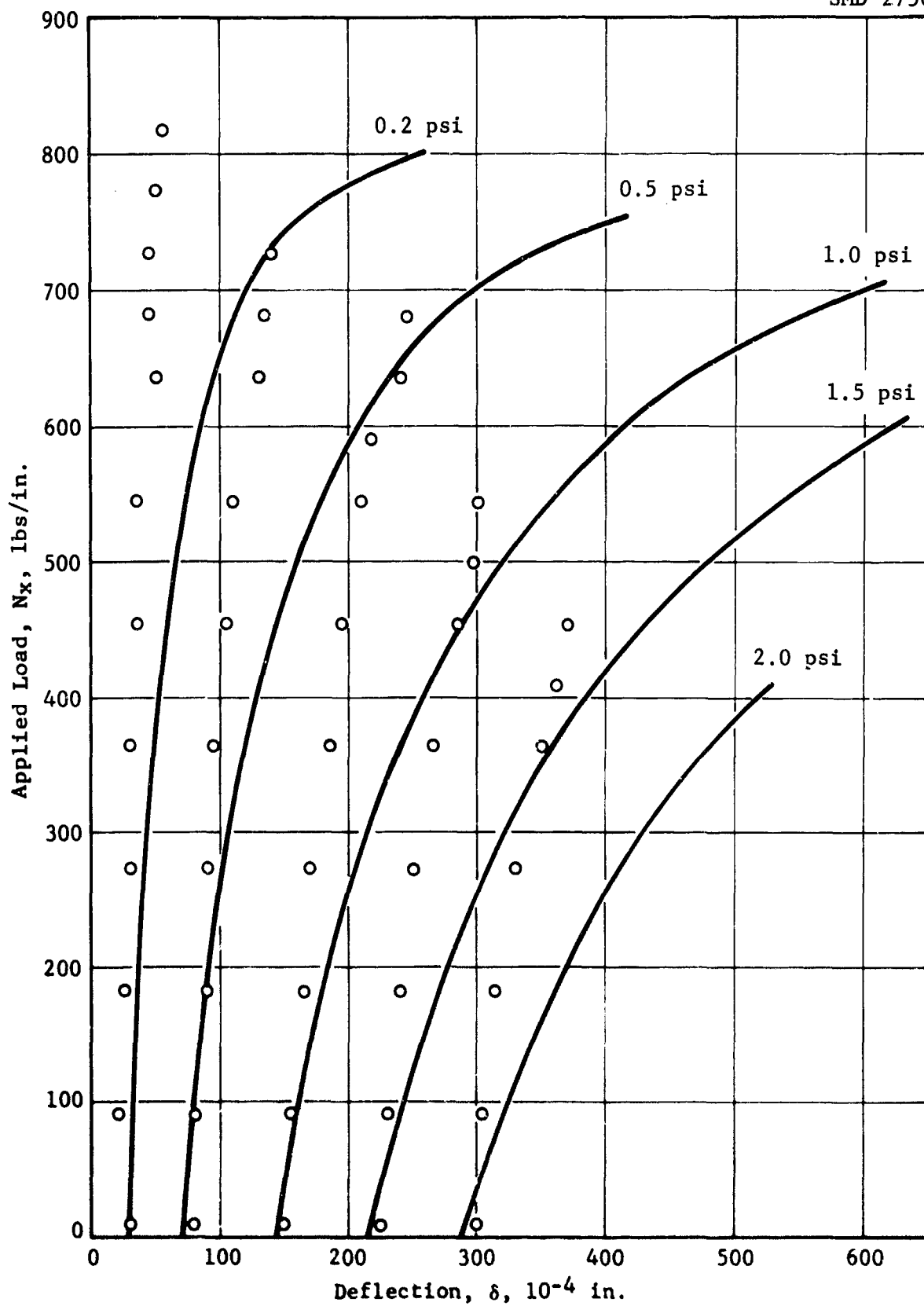


Figure 63 Combined Uniaxial and Lateral Loadings, Panel No. 5, Clamped-Simple Condition

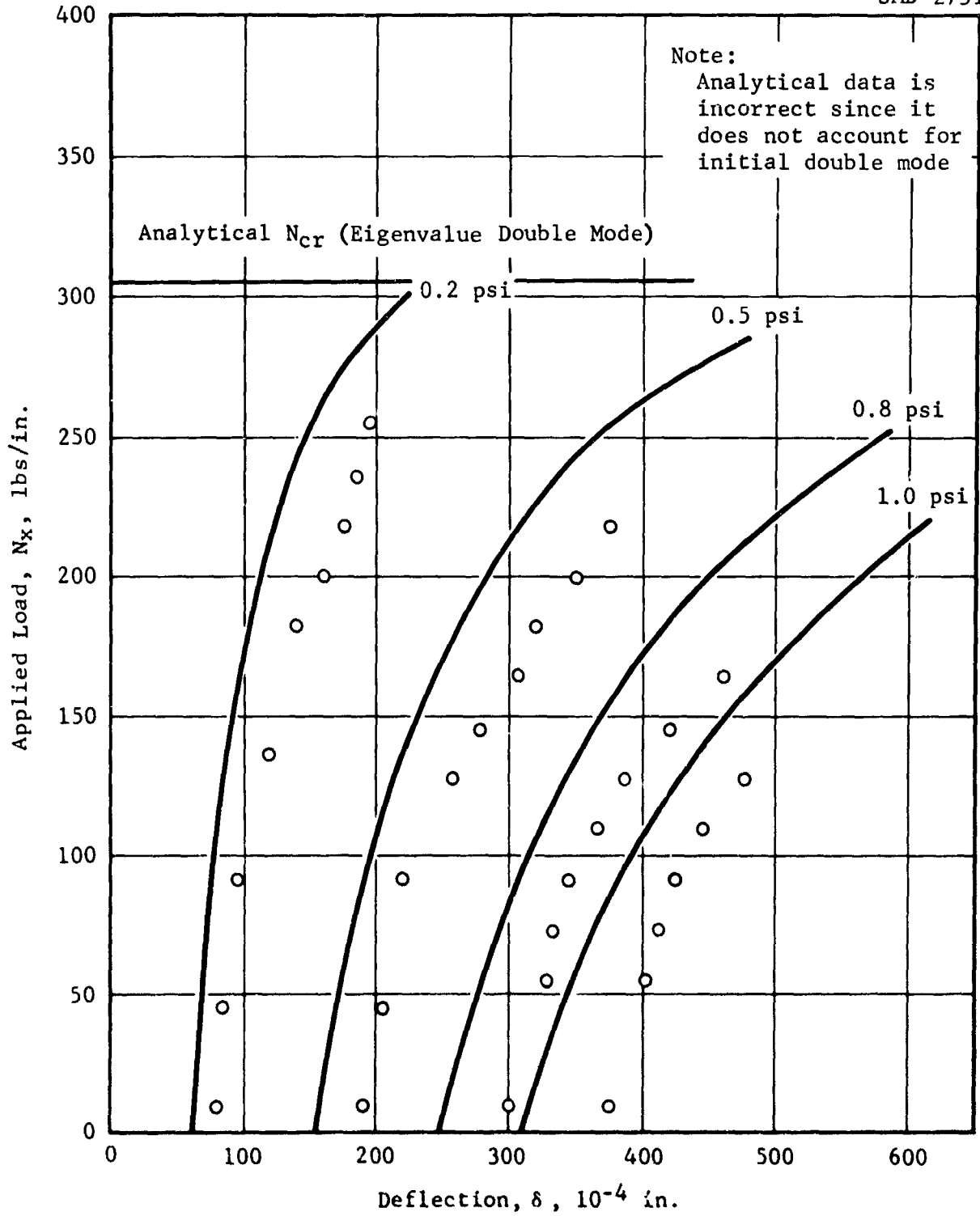


Figure 64 Combined Uniaxial and Lateral Loadings, Panel No. 5, Clamped-Simple Condition, Turned 90°

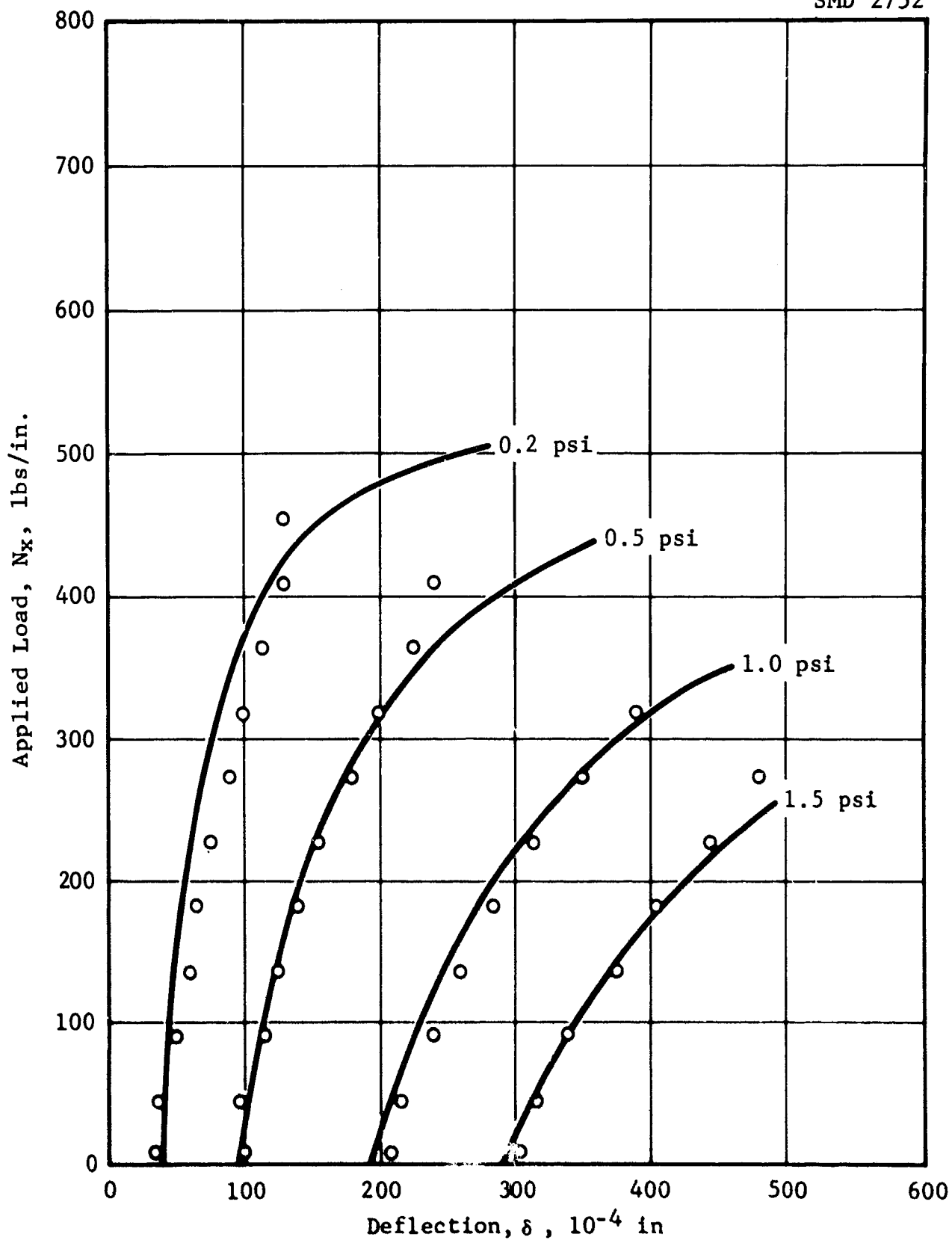


Figure 65 Combined Uniaxial and Lateral Loadings, Panel No. 7, Clamped-Clamped Condition

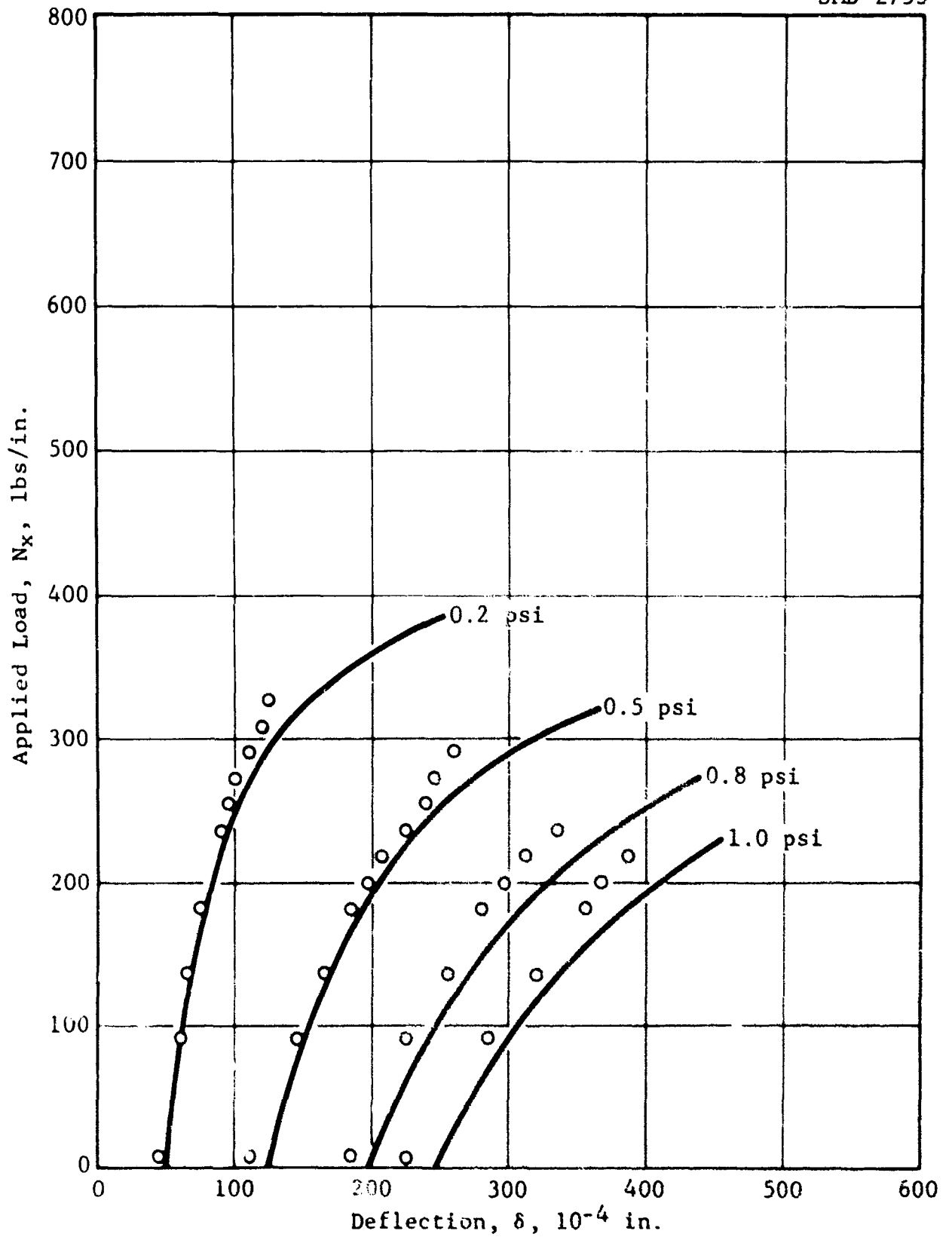


Figure 66 Combined Uniaxial and Lateral Loadings, Panel No. 7
Clamped-Simple Condition

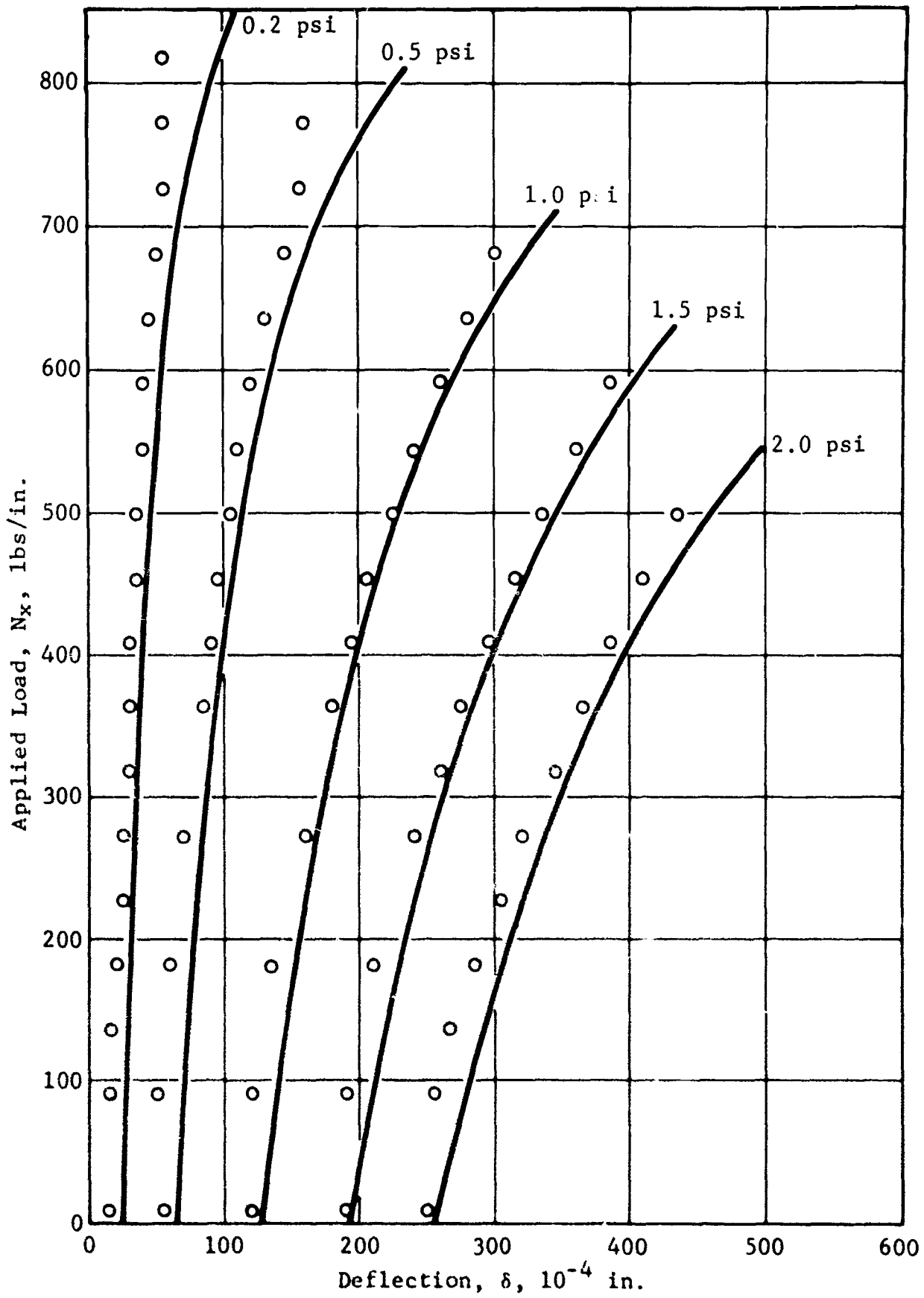


Figure 67 Combined Uniaxial and Lateral Loadings, Panel No. 9
Clamped-Clamped Condition

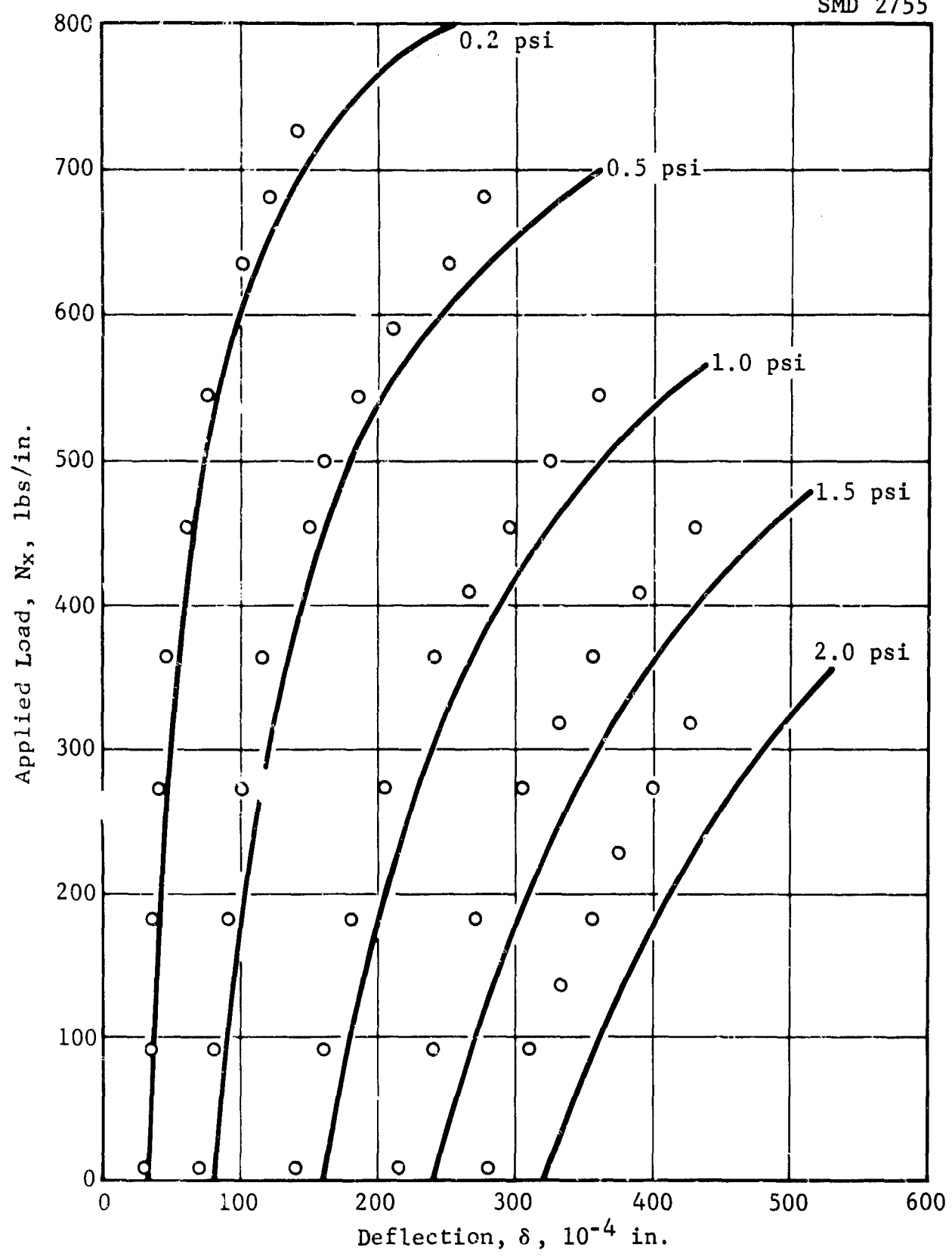


Figure 68 Combined Uniaxial and Lateral Loadings, Panel No. 9, Clamped-Simple Condition

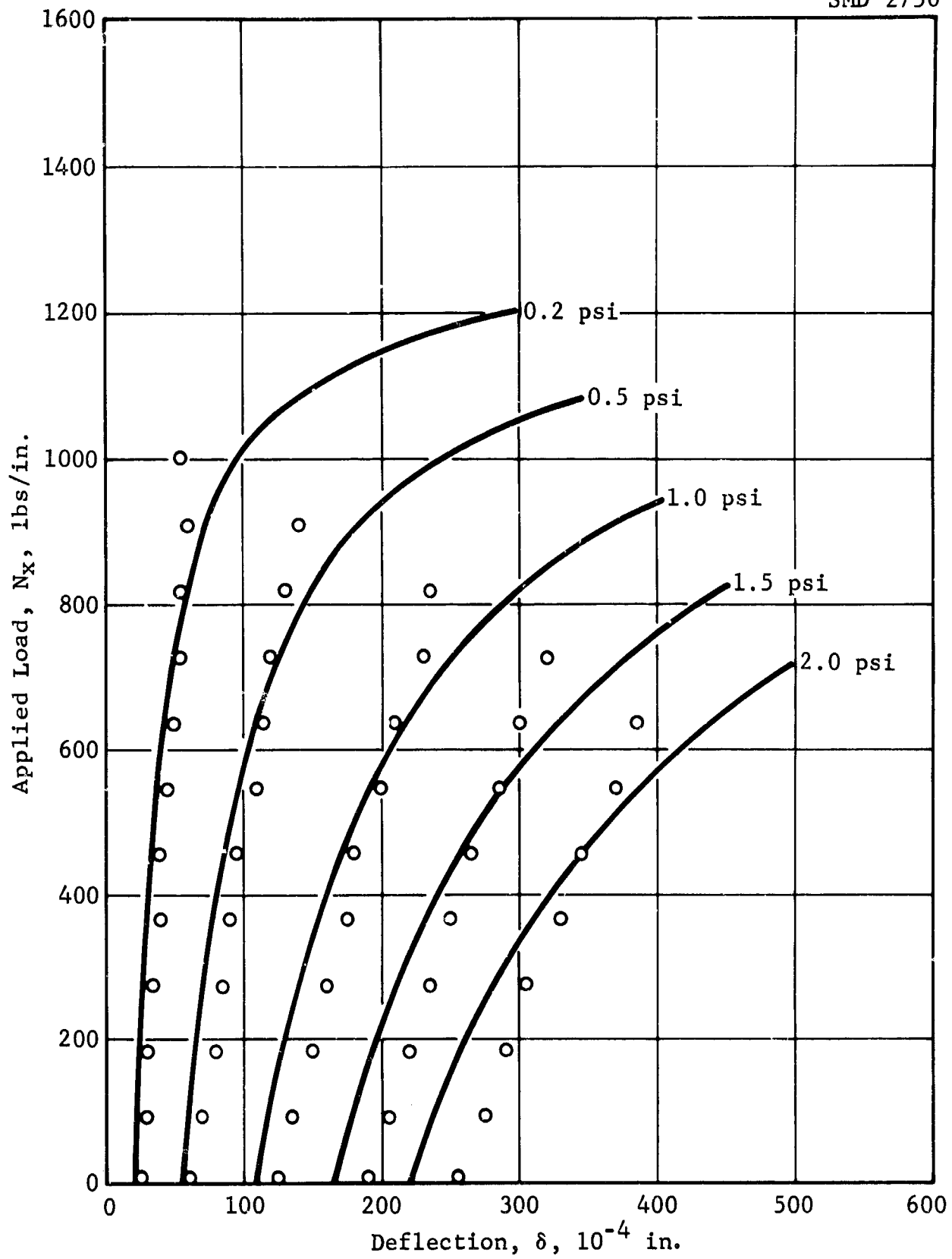


Figure 69 Combined Uniaxial and Lateral Loadings, Panel No. 12, Clamped-Clamped Condition

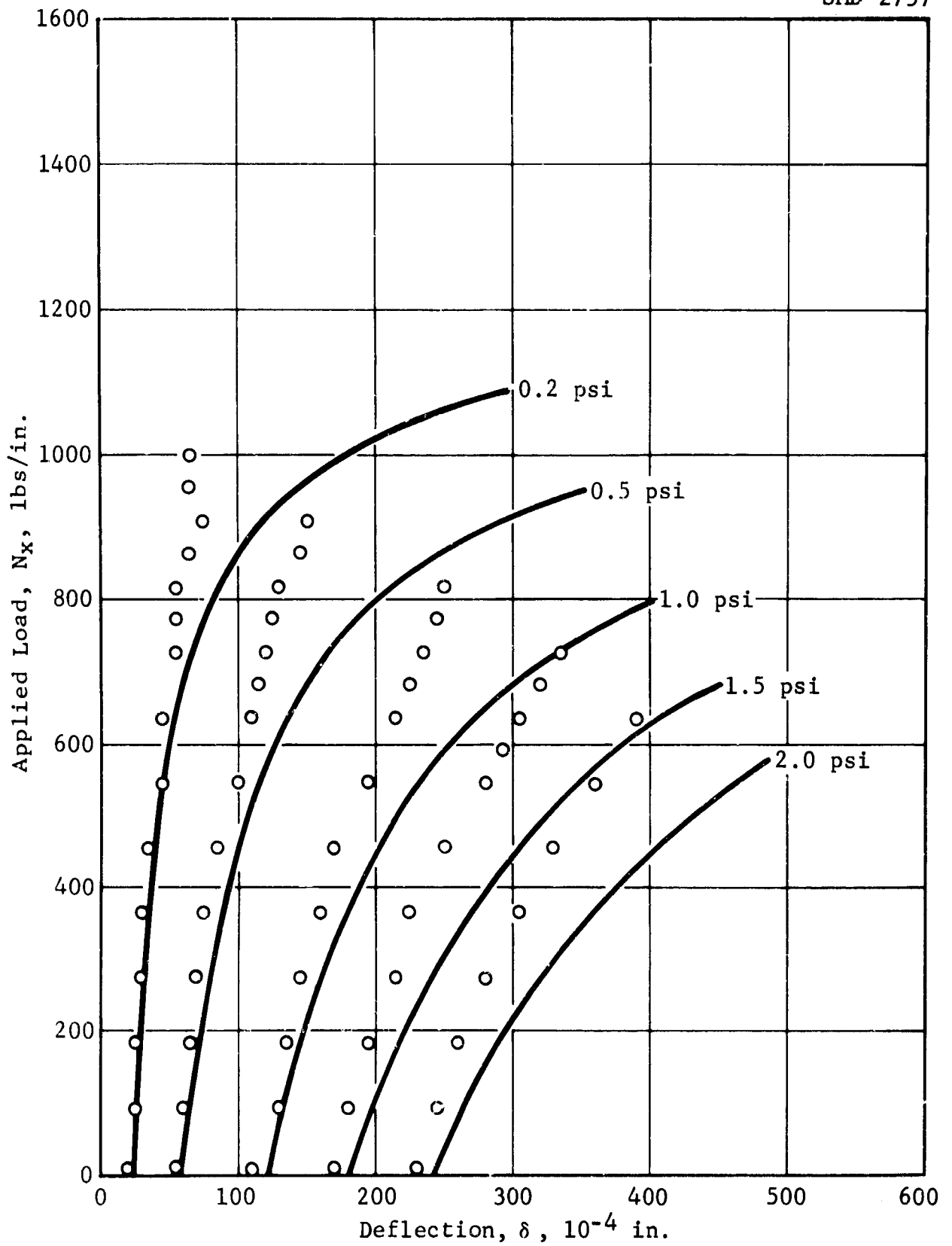


Figure 70 Combined Uniaxial and Lateral Loadings, Panel No. 12, Clamped-Simple Condition

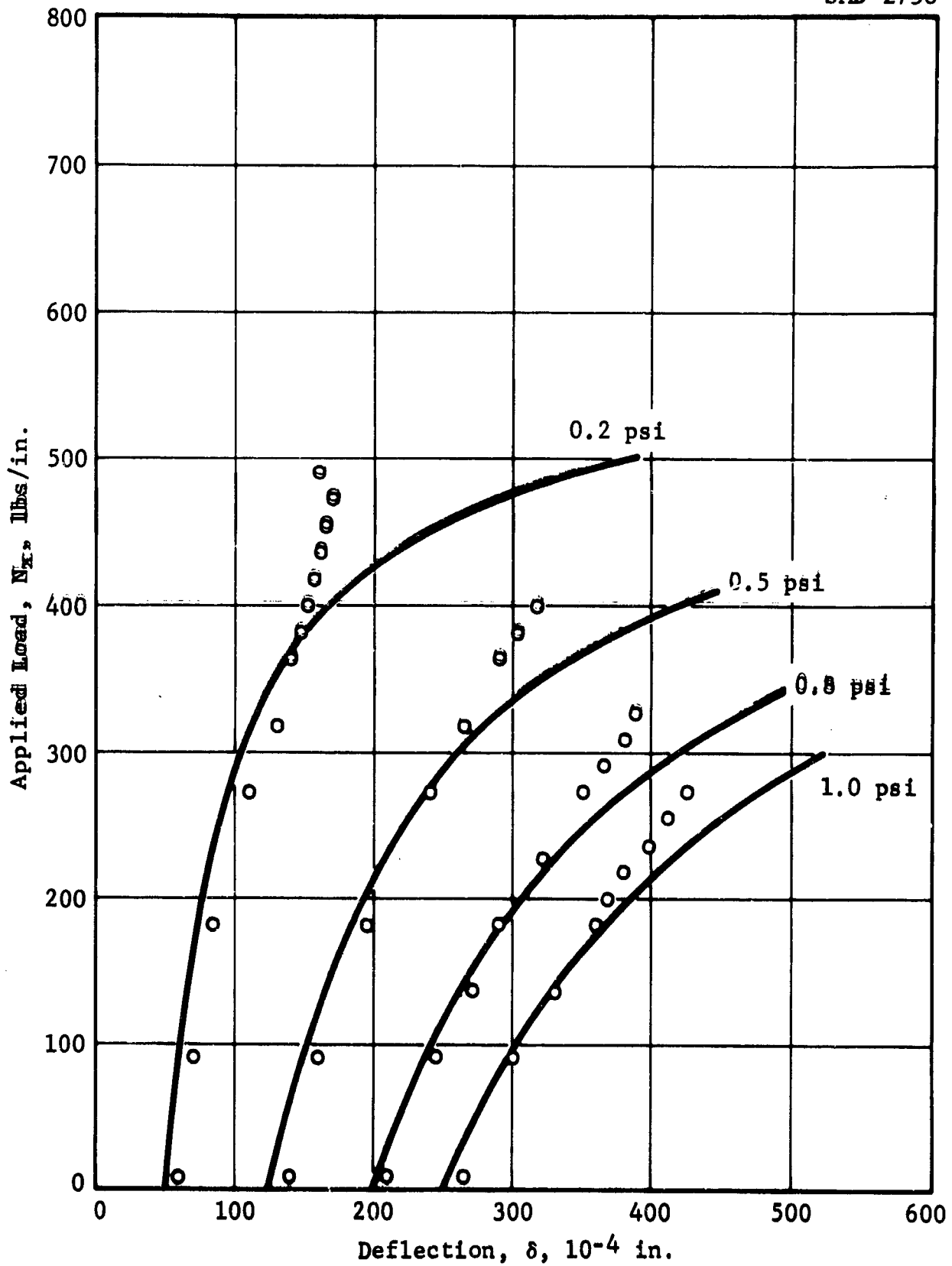


Figure 71. Combined Uniaxial and Lateral Loadings, Panel No. 16, Clamped-Clamped Condition

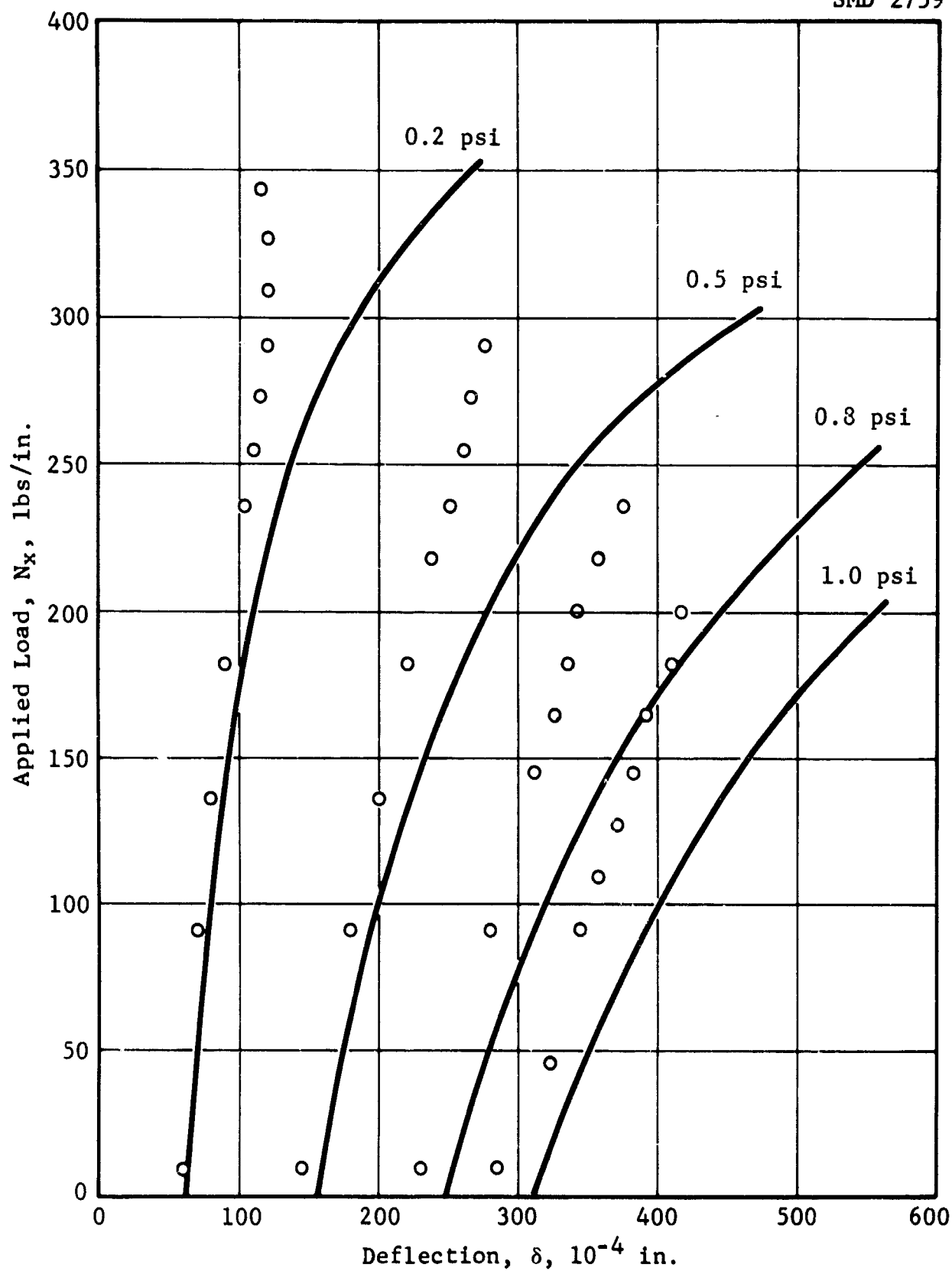


Figure 72 Combined Uniaxial and Lateral Loadings, Panel No. 16, Clamped-Simple Condition

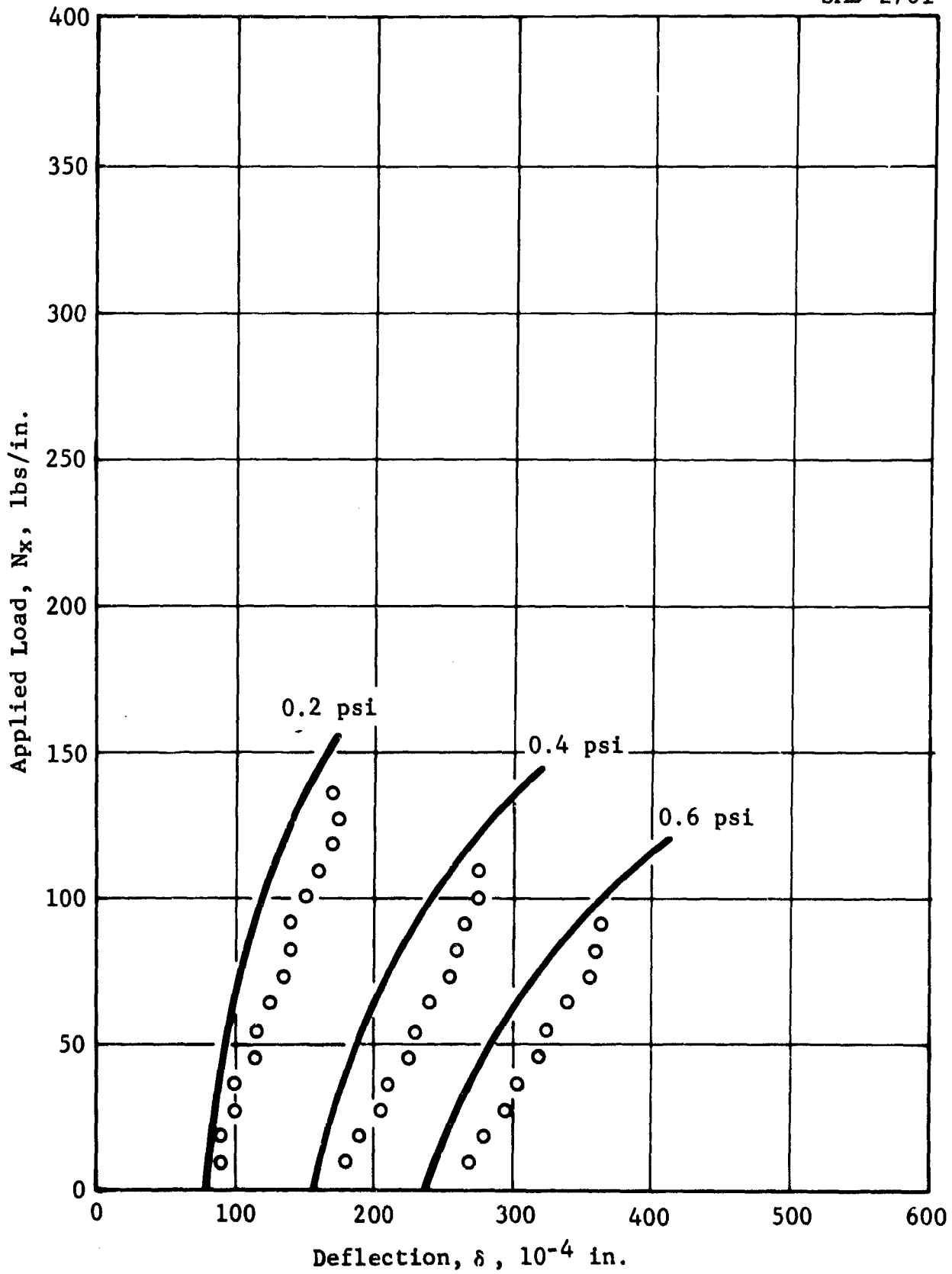


Figure 73 Combined Uniaxial and Lateral Loadings, Panel No. 19A, Clamped-Clamped Condition

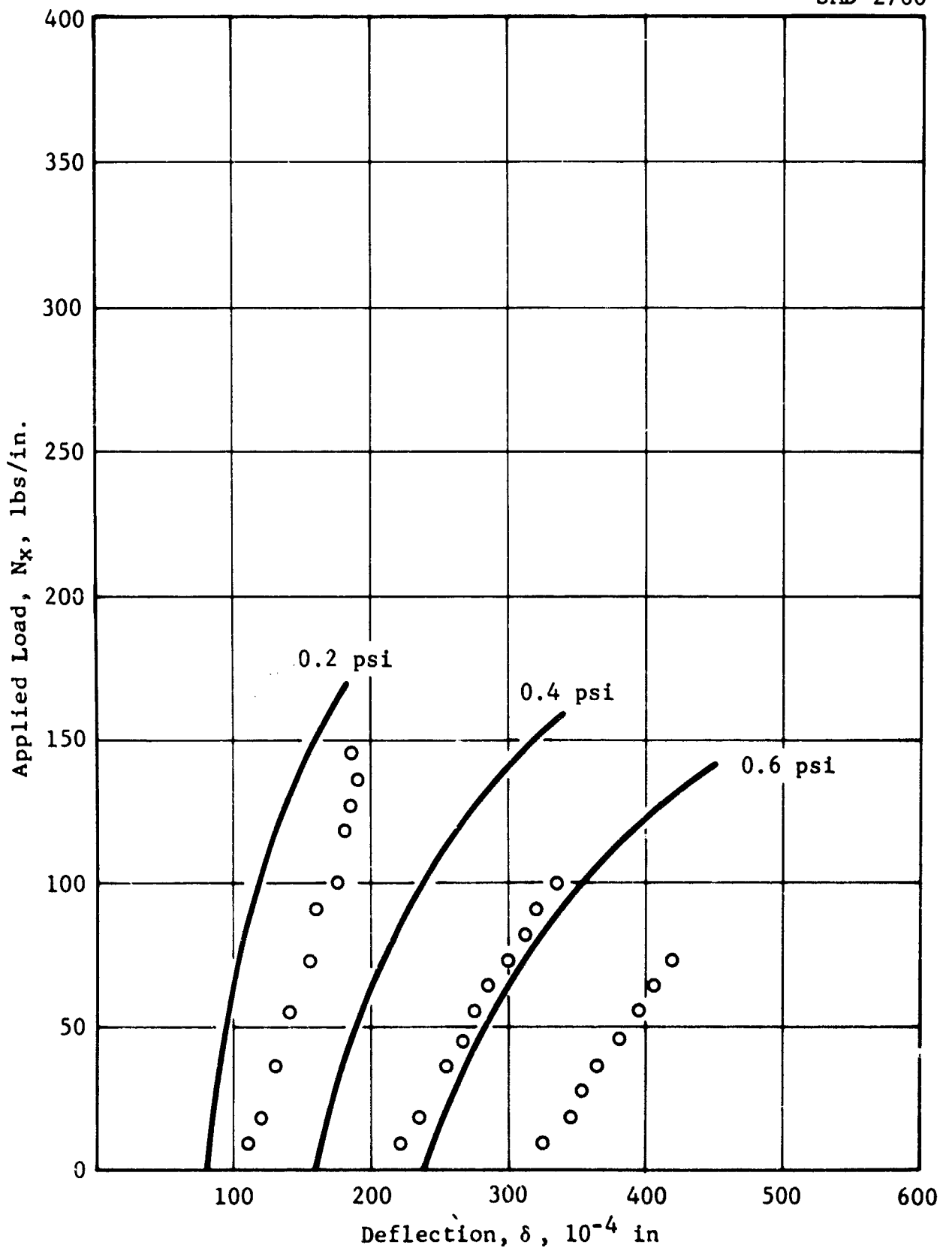


Figure 74 Combined Uniaxial and Lateral Loadings, Panel No. 19A, Clamped-Clamped Condition, Turned 90°

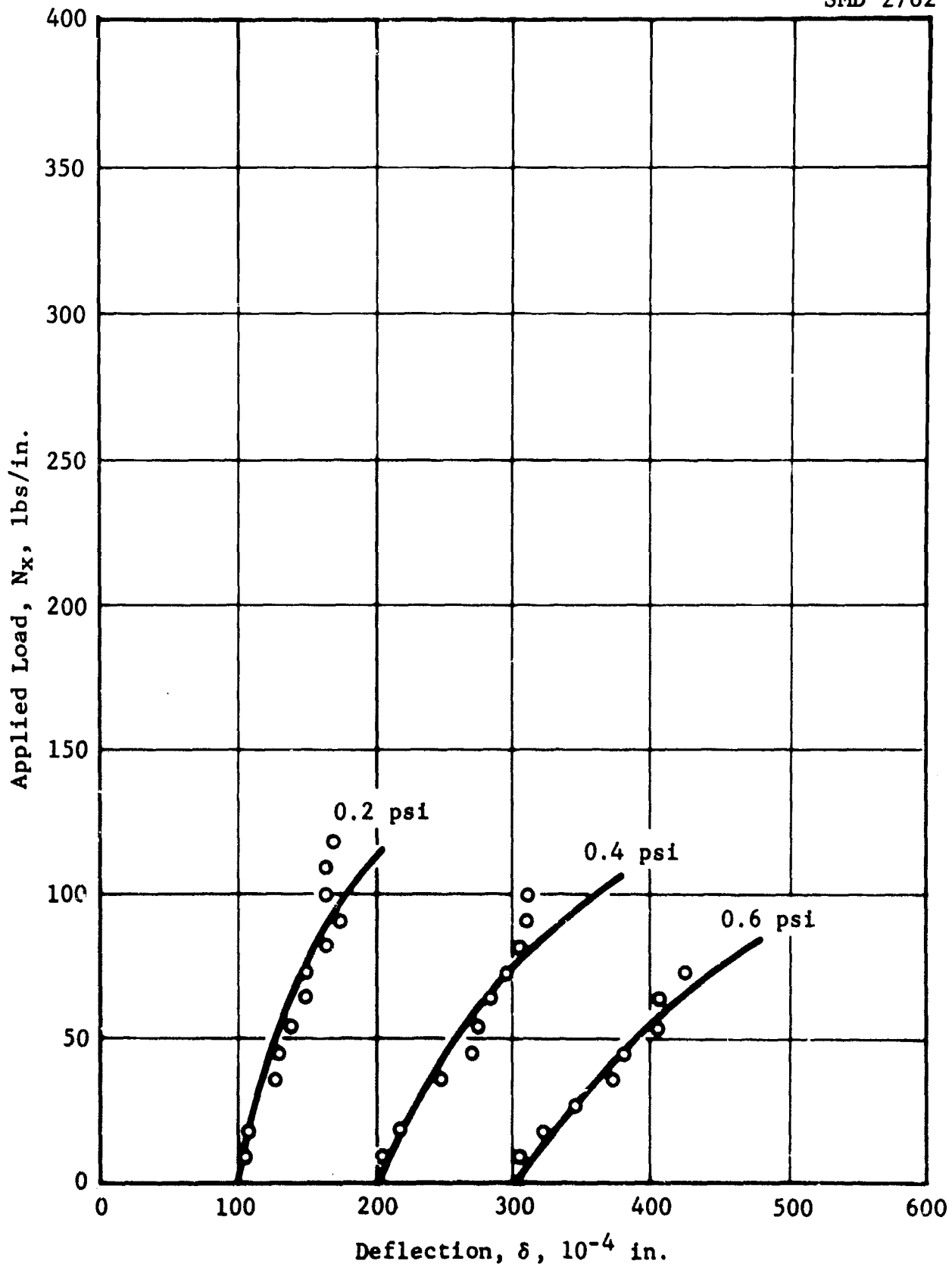


Figure 75 Combined Uniaxial and Lateral Loadings, Panel No. 19A, Clamped-Simple Condition

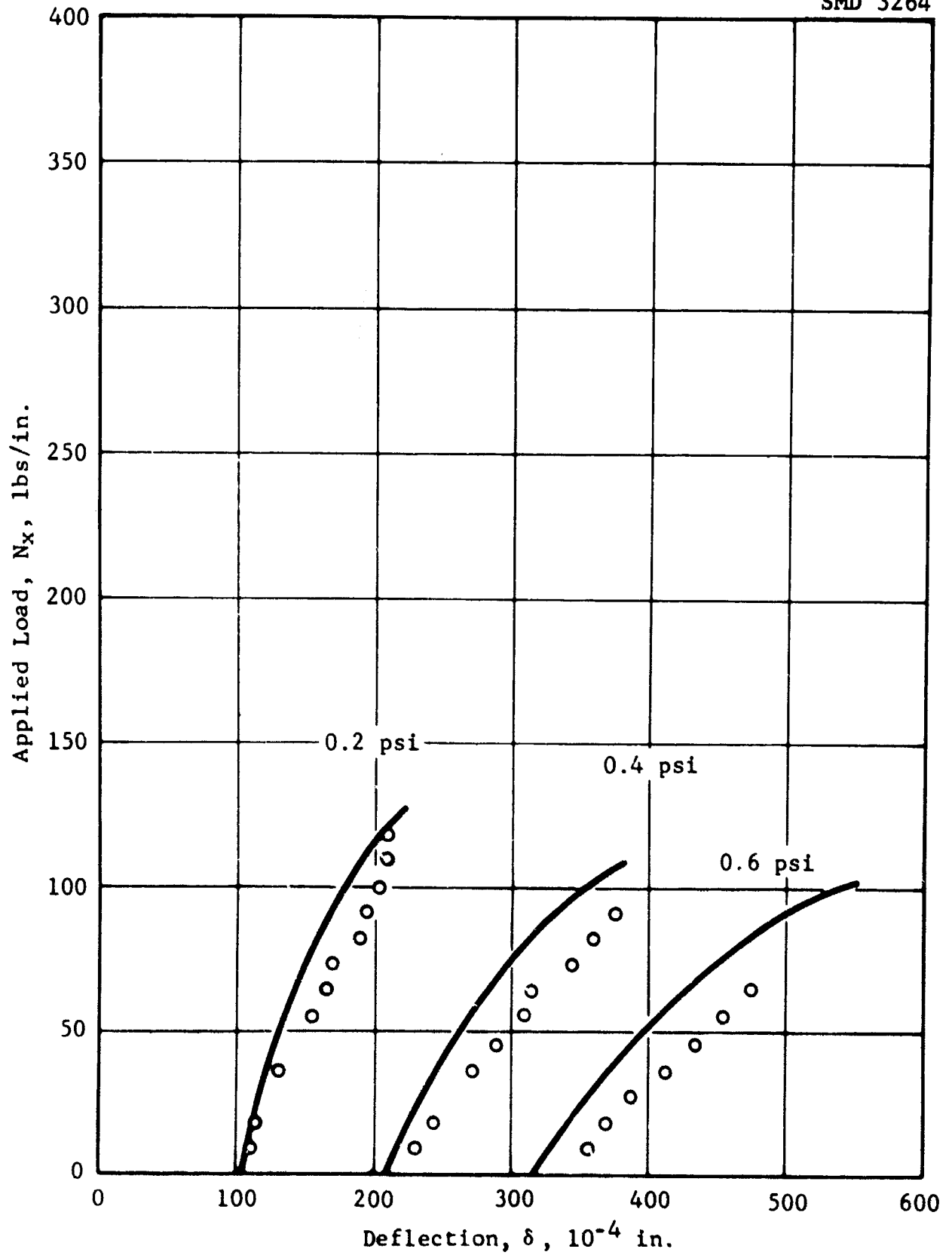


Figure 76 Combined Uniaxial and Lateral Loadings, Panel No. 19A, Clamped-Simple Condition, Turned 90°

pressure, i.e., the experimental data appear to indicate a plate that is stiffer than expected. This apparent stiffness should not be confused with that due to membrane forces which occurs at higher inplane load levels. The stiffening trend is more pronounced for the clamped-simple boundaries (Figures 60 and 70). Agreement of the experimental data for Panel 16 (quasi-isotropic) with the analytical predictions was good.

In view of the assumptions made as to thickness, stiffness and load distribution along the edge of the tapered plate, Panel 19A (discussed in subsection 4.5), the data obtained for combined loads agree quite well with the analytical predictions. The effects of membrane stiffening can be seen in each configuration tested (Figures 73 through 76). The scatter in the test data is attributed to the sensitivity of the test machine and instrumentation at the low test loads.

The unidirectional plate, Panel 5, when tested in the 0-degree configuration (i.e., fibers aligned with the inplane load), behaved in a manner similar to that of Panels 3 ($0^\circ/90^\circ$) and 12 ($0^\circ/+45^\circ$), i.e., the experimental data indicated a panel stiffer than predicted.

When Panel 5 (0°) was tested in the 90-degree configuration, a unique situation occurred. Tested with clamped-clamped boundaries and zero pressure, the panel initially maintained a single-mode deflected shape. This behavior was attributed to initial imperfections. At the applied load $N_x = 273$ lb/in., the maximum deflection, which had been located at the center of the panel, shifted to a quarter point, creating a double-mode shape. As noted previously, the analytical deflected shape for buckling was the double mode. For a lateral load of 0.2 psi, the shift in maximum deflection began at $N_x = 309$ lb/in., and a fully formed double-mode shape was finally observed at 364 lb/in. At 0.5 psi, only a skewed single-mode shape was observed. For 1.0 and 1.5 psi, the symmetric single-mode predominated. The interesting point here is that although the analysis predicted a double-mode shape for zero pressure, a single mode was predicted when a uniform lateral load was applied. By referring to Figure 62, it can be seen that the experimental load-deflection curves do not agree with those of the analysis. Furthermore a comparison of the analytical load-deflection curves with the analytical buckling value shows that the curves will become asymptotic to a buckling value above the double-mode eigenvalue. This is more easily seen by noting that the predicted deflections for the 90-degree configuration are approximately the same as those for the 0-degree configuration (Figure 61). It seems probable that the experimental load-deflection curves would approach the experimental double-mode

eigenvalue ($N_{cr} = 397 \text{ lb/in.}$) if it were not for the effects of the initial imperfections and the membrane forces.

For the 90-degree configuration with clamped-simple boundaries, Panel 5 (0°) retained a single-mode deflected shape regardless of the pressure level tested. The predicted shapes were a double mode for zero pressure and single modes for all other pressure levels. Analytical solutions and experimental data are presented in Figure 64. Again, the analytical load-deflection curves appear asymptotically to approach a buckling value above the double mode eigenvalue. It is difficult to state whether or not the experimental and analytical load-deflection curves correlate well because of the closeness of the eigenvalues.

To understand why the analysis failed to predict the proper mode shape, it is necessary to review the mathematical formulation of the problem. The basic principle used in the analysis is that of stationary potential energy:

$$V + U - Q = \text{stationary value} \quad (13)$$

where Q is the work of the applied transverse loads. This becomes an ordinary maximum-minimum problem in coefficients a_{mn} when stated as

$$\frac{\partial V}{\partial a_{ik}} + \frac{\partial U}{\partial a_{ik}} = \frac{\partial Q}{\partial a_{ik}} \quad (14)$$

with deflection $w(x, y)$ expressed in the form

$$w(x, y) = \sum_{m=1}^p \sum_{n=1}^q a_{mn} X_m(x) Y_n(y) \quad (15)$$

Functions $X_m(x)$ and $Y_n(y)$ are beam mode functions satisfying the boundary conditions and are of the form

$$Z_j(z) = C_1 \cosh(\alpha_j z) + C_2 \cos(\alpha_j z) + C_3 \sinh(\alpha_j z) + C_4 \sin(\alpha_j z). \quad (16)$$

The coefficient α_j is the square root of the natural frequency of the j^{th} beam mode. The first four beam mode shapes for various

boundary conditions are illustrated in Figure 77. Substitution of Equation (15) into (14) yields

$$\frac{\partial V}{\partial a_{ik}} = \sum_{m=1}^p \sum_{n=1}^q d_{ikmn} a_{mn} \quad (17)$$

where d_{ikmn} is a function of the stiffness matrix D and integrals of the form

$$\int_0^1 \frac{\partial^r Z_m(z)}{\partial z^r} \frac{\partial^s Z_n(z)}{\partial z^s} dz \quad (18)$$

and

$$\frac{\partial U}{\partial a_{ik}} = - \sum_{m=1}^p \sum_{n=1}^q e_{ikmn} a_{mn} \quad (19)$$

where e_{ikmn} is a function of the inplane stress resultants N_x , N_y and N_{xy} and integrals of the form given by Equation (18). Indices p and q determine the number of beam mode shapes to be included in the analysis. The first seven modes were used in the subject analysis. The work Q of the applied pressure is given as follows:

$$Q = \int_0^b \int_0^a \bar{q} w(x,y) dx dy, \quad (20)$$

where \bar{q} is the uniform lateral load. Therefore,

$$\frac{\partial Q}{\partial a_{ik}} = \bar{q} ab \int_0^1 X_i(x) dx \int_0^1 Y_k(y) dy. \quad (21)$$

Substitution of Equations (18), (19) and (21) into Equation (14) produces a set of linear algebraic equations for the coefficients a_{ik} . This set of equations can be expressed in matrix form as

$$[F - G] [C] = [\bar{S}], \quad (22)$$

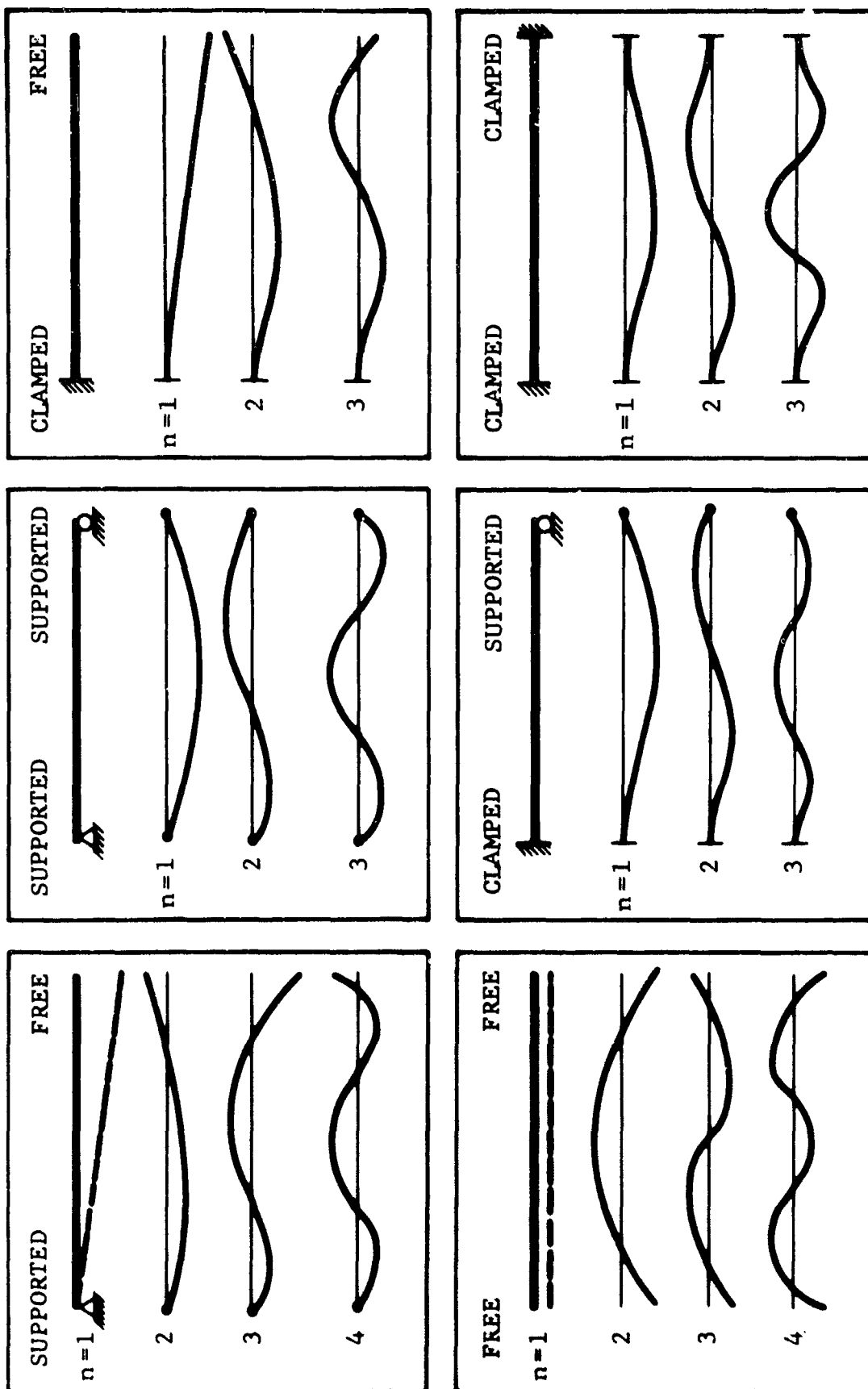


Figure 77 Shapes of Natural Modes of Vibration

where

$$f_{jl} = d_{ikmn}$$

$$g_{jl} = e_{ikmn}$$

$$c = a_{mn}$$

$$\bar{s}_j = \bar{q} a b \int_0^1 X_i(x) dx \int_0^1 Y_k(y) dy$$

$$j = (i - 1) q + k$$

$$l = (m - 1) q + n$$

The coefficients a_{ik} are then calculated from

$$[C] = [F - G]^{-1} [\bar{S}]. \quad (23)$$

It is at this point that the analysis fails to predict the proper deflected shape. Because a symmetric (uniform) lateral load has been applied to the plate, the only nonzero elements in the vector $[\bar{S}]$ are those due to the symmetric beam mode shapes. For example, if all of the available beam mode shapes are included in the clamped-clamped plate (i.e., let $p = q = 7$), then

\bar{s}_1	$i = k = 1$
\bar{s}_2	$i = 1, k = 2$
\bar{s}_3	$i = 1, k = 3$
.	.
.	.
.	.
\bar{s}_6	$i = 1, k = 6$
\bar{s}_7	$i = 1, k = 7$
\bar{s}_8	$i = 2, k = 1$
\bar{s}_9	$i = 2, k = 2$
.	.
.	.
.	.

$$\bar{s}_{48} \quad i = 6, k = 6$$

$$\bar{s}_{49} \quad i = 6, k = 7,$$

where the indices i and k determine the beam mode shapes to be used in evaluating \bar{s}_j . By referring to Figure 77, it can be seen that

$$\int_0^1 X_i(x) dx \neq 0 \quad \text{for } i = 1, 3, 5$$

$$= 0 \quad \text{for } i = 2, 4, 6$$

and

$$\int_0^1 Y_k(y) dy \neq 0 \quad \text{for } k = 1, 3, 5, 7$$

$$= 0 \quad \text{for } k = 2, 4, 6.$$

Obviously, then the only products

$$\int_0^1 X_i(x) dx \int_0^1 Y_k(y) dy$$

that are nonzero are those corresponding to symmetric beam modes.

The elements of the matrix $[F - G]$ are, in general, nonzero and are obtained by integrating the product of two beam mode shapes (see Equation 18). Because the buckling results for the 90-degree configuration of Panel 5 (0°) indicated an antisymmetric mode, it is clear that the unsymmetric elements of $[F - G]$ predominated when the inverse of that matrix was obtained. For the case of combined loads, these unsymmetric terms are multiplied by the zeros of $[\bar{S}]$ leaving only the symmetric terms in $[F - G]^{-1}$ to calculate the coefficients a_{ik} .

Once the coefficients a_{ik} are determined, the deflections are immediately calculated using Equation (15). Thus, any load-deflection curve generated for a perfectly symmetric lateral load must become asymptotic to the smallest eigenvalue corresponding to a symmetric buckling mode. In particular, the predicted load-deflection curve will become asymptotic to the correct buckling load if, and only if, the predicted buckling mode shape is symmetric.

Since the unique problem experienced with Panel 5 (0°) may arise for other plates, a method has been proposed which will provide an approximate load-deflection curve for any antisymmetric

buckling mode. Consider an isotropic rectangular plate 12 inches wide, 18 inches long, and having the following stiffness matrix:

$$[D] = \begin{bmatrix} 21800 & 5890 & 0 \\ 5890 & 21800 & 0 \\ 0 & 0 & 4910 \end{bmatrix} .$$

For all four sides simply supported, predicted buckling results indicate that the critical load corresponds to the second mode eigenvalue, i.e., the buckled shape is antisymmetric. When a uniform lateral load ($q_0 = 0.25$ psi) is added to the problem, the load-deflection curve shown in Figure 78 is obtained. The curve asymptotically approaches the buckling load corresponding to the first mode eigenvalue. This trend is confirmed by a plot of the deflections along the panel center line as shown in Figure 79. The symmetric shape occurs for all levels of N_x .

When an unsymmetric lateral load of the form

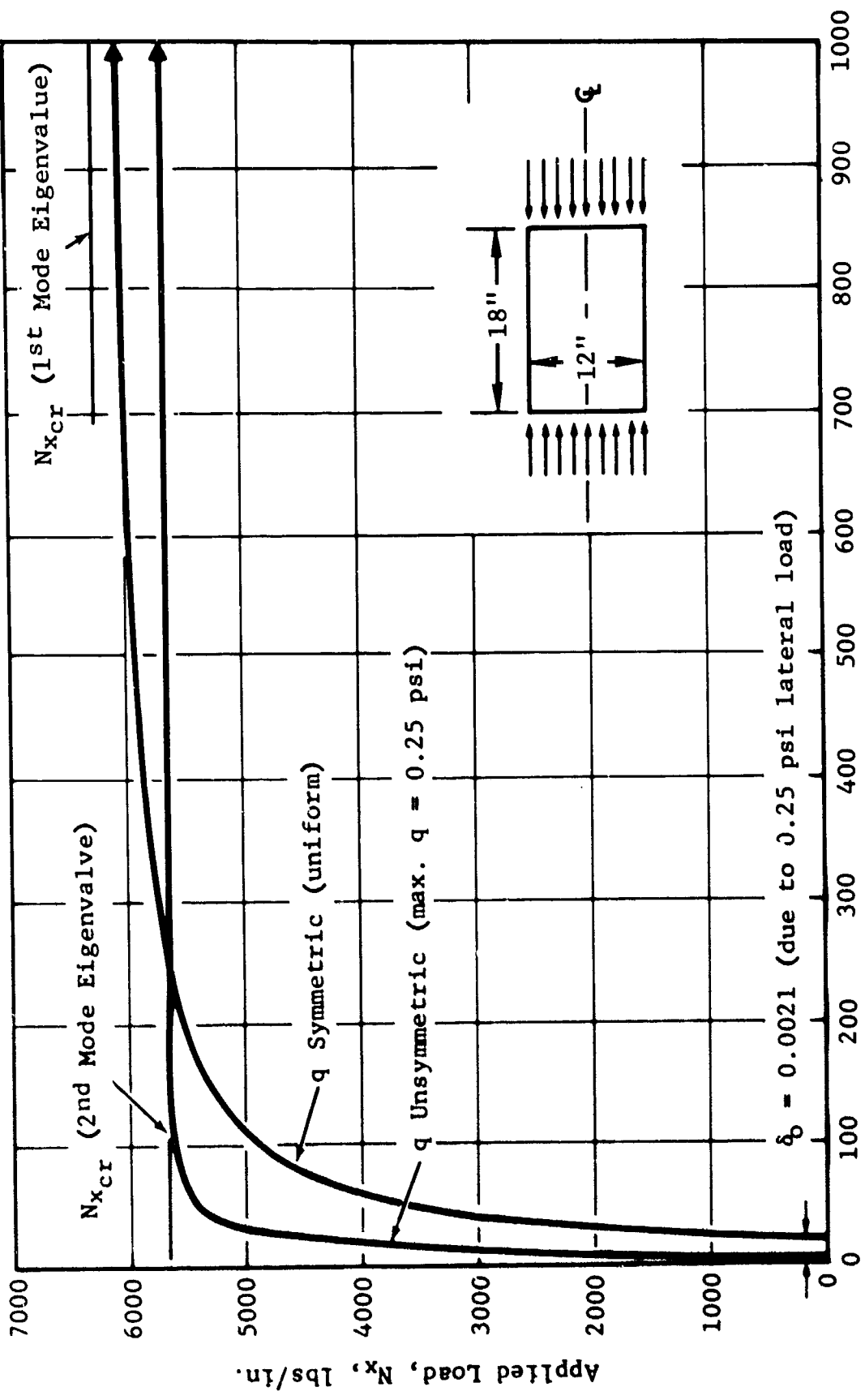
$$q = q_0 \left(\frac{x}{a}\right) \left(\frac{y}{b}\right)$$

is applied, the load-deflection curve that is obtained asymptotically approaches the proper buckling load as shown in Figure 78. In addition, the deflected shape changes from an unsymmetric single mode to an unsymmetric double mode as N_x is increased. This behavior is similar to that noted for the 90-degree configuration of Panel 5 (0°) with clamped-clamped boundaries.

The deflection corresponding to zero N_x for the unsymmetric lateral load is less than that for the symmetric load. By choosing a different form for the unsymmetric pressure distribution, these two points can be made to agree within experimental accuracy.

What has happened analytically for the case of the unsymmetric load is that the zeros of $[S]$ no longer exist and, therefore, the unsymmetric elements of $[F - G]^{-1}$ were allowed to dominate in predicting the deflected shape.

The situation incurred with Panel 5 (0°) can be alleviated by adding a small, unsymmetrical load to the perfectly symmetrical load assumed for the analysis. This method was first used in Reference 9. In this manner, the unsymmetric load will act in a manner similar to that of the initial imperfections existing in



Deflection, δ , 10^{-4} in.

Figure 78. RA5 Solution Study

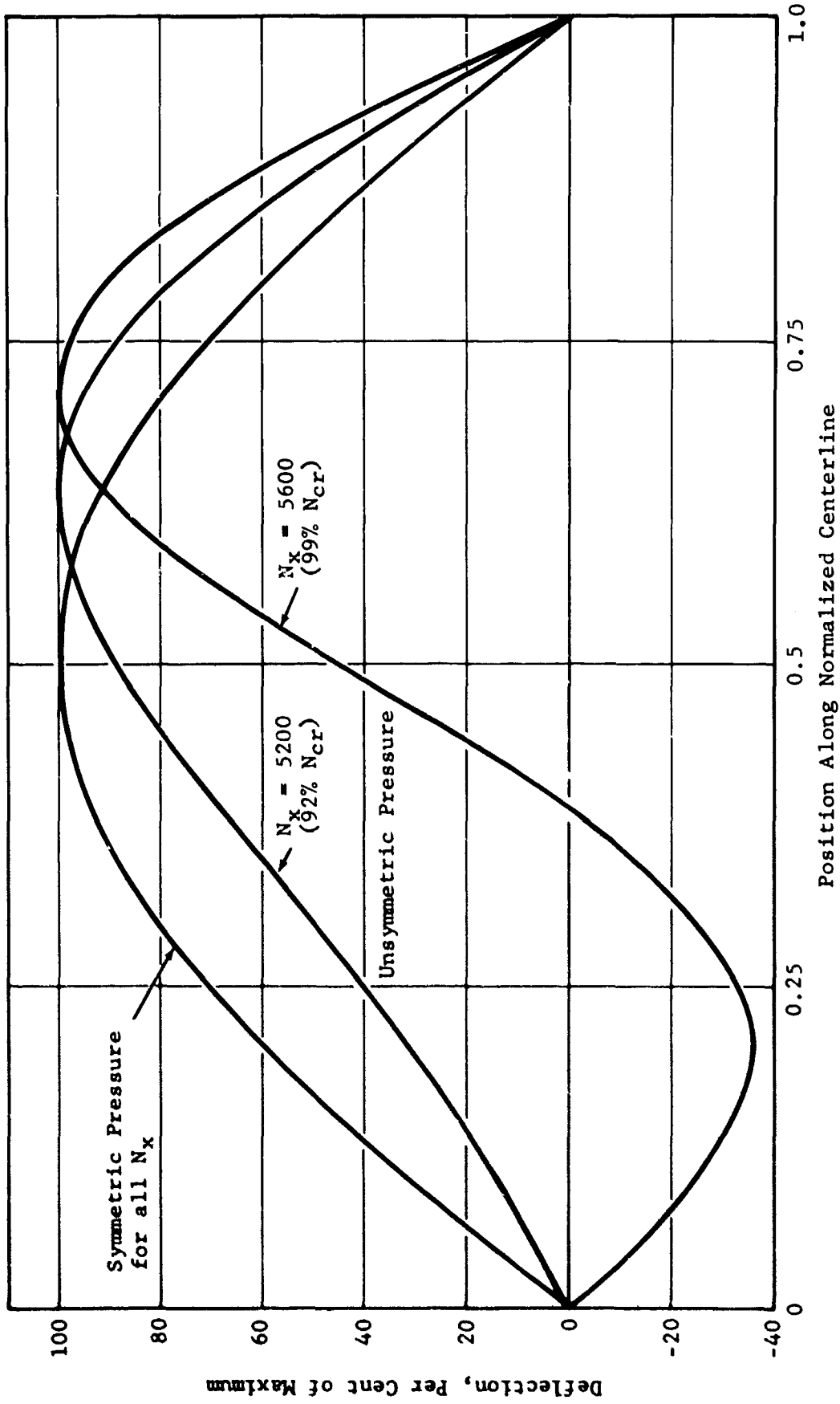


Figure 79 Mode Shape Study

the real plate. For example, if the working pressure is 14.00 psi let the perturbing pressure be 0.01 psi; then assuming a pressure distribution

$$q = q_0 \left[1 + (.01) \left(\frac{x}{a} \right) \left(\frac{y}{b} \right) \right] ,$$

the maximum pressure would be 14.01 psi. The unsymmetrical component of the total pressure distribution is sufficient to eliminate the zeros of $[\delta]$ but not large enough to affect the deflection due to the uniform lateral load alone.

SECTION VI
BIAXIAL LOAD STUDY

Interaction curves were developed for the 10 flat plates (orientation as variables) subjected to biaxial compressive loads and these were compared with the analytical predictions of computer program RA5. Fully-clamped plates were considered.

The boron panels selected for the study and the configurations tested are identified in Table VIII. Panel thicknesses and orientations were established in Table I. The isotropic control panel selected was aluminum Panel 1. The input properties used for the RA5 analysis were described in subsection 4.5.

The interaction curves for the aluminum control panel and the boron plates are presented in Figures 80 through 88. A summary of the buckling values is presented in Table IX. The load-deflection curves and Southwell plots used in obtaining the test data are presented in Appendix III. As shown in Figure 80, the test data for the aluminum panel is slightly higher than the analytical predictions based on elastic restraint on the boundaries. This behavior corresponds to that described in subsection 4.4. To maintain a stress ratio, N_x/N_y , equal to one, both values (N_x and N_y) were increased simultaneously. Also shown on the interaction curve are an analytical curve assuming ideal boundary conditions and test data from Reference 4.

A comparison of the test data for Panels 2 (Unsym $+45^\circ$), 7 ($+45^\circ$) and 9 ($\pm 45^\circ$), presented in Figures 81, 84, and 85, shows excellent agreement with the analytical predictions. The general tendency of the data from Panels 12 ($0^\circ/+45^\circ$) and 16 ($0^\circ/\pm 45^\circ/90^\circ$), presented in Figures 86 and 87, is good.

The interaction curve for Panel 3 ($0^\circ/90^\circ$) is shown in Figure 82. Although the uniaxial buckling loads calculated from the biaxial data were in good agreement with the analytical predictions, the biaxial points were not. In fact, most of the data points appear to be above those of an analytical curve if ideal boundary conditions were assumed. The data from Panel 5 (0°) agree well with the predicted uniaxial buckling values N_x and N_y but not with the biaxial predictions, as shown in Figure 83.

Table VIII BIAXIAL COMPRESSIVE LOAD TESTS

Panel Number	Orientation (degrees)	Test Configuration	
		0°	90°
2	Unsymmetrical ± 45	x	
3	0/90	x	
5	0	x	x
7	+ 45	x	
9	± 45	x	
12	0/ ± 45	x	
16	0/ ± 45 /90	x	
19A	Tapered ± 45	x	x
Aluminum 1	-	x	

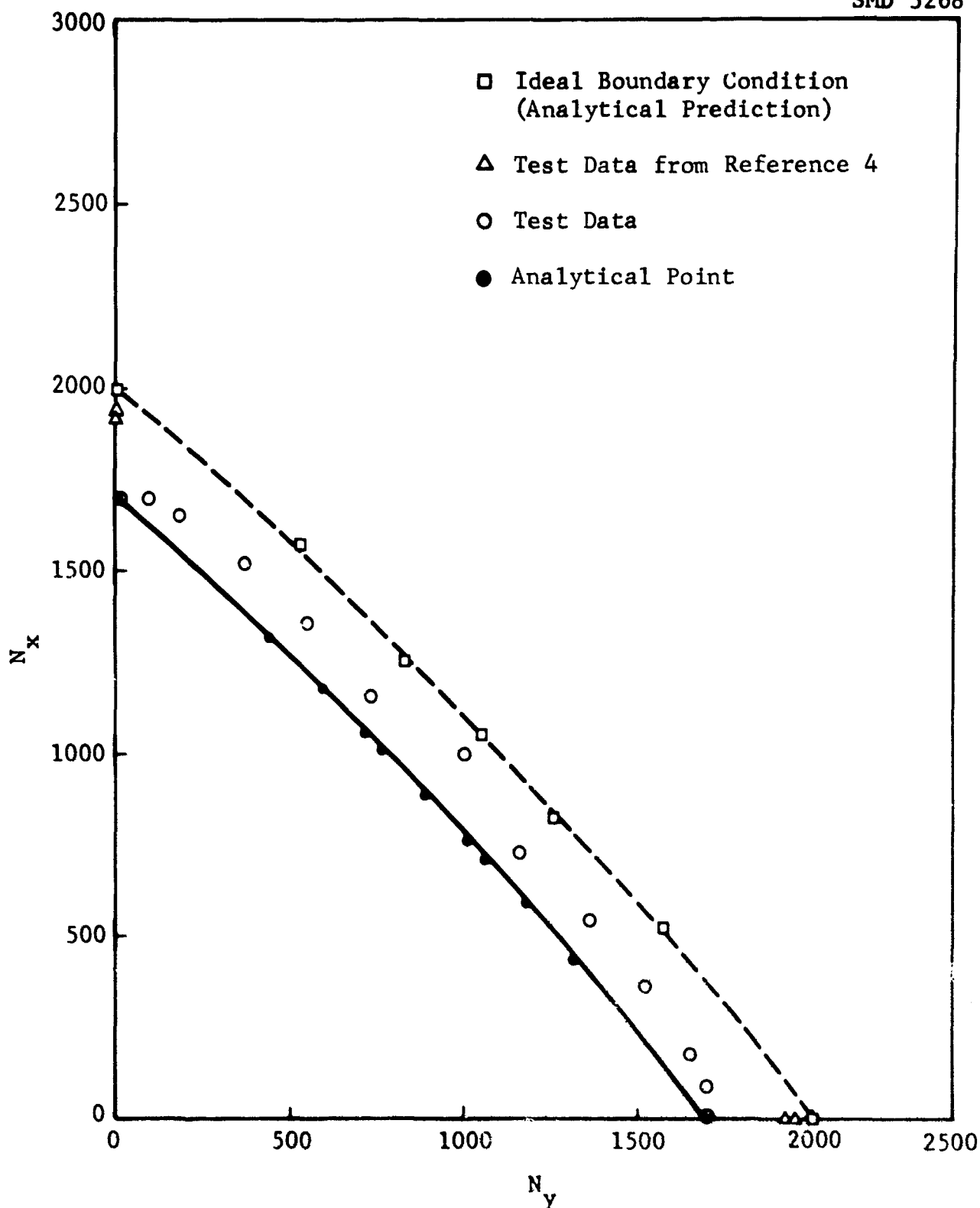


Figure 80 Biaxial Compression Interaction Curve
for Aluminum Panel No. 1

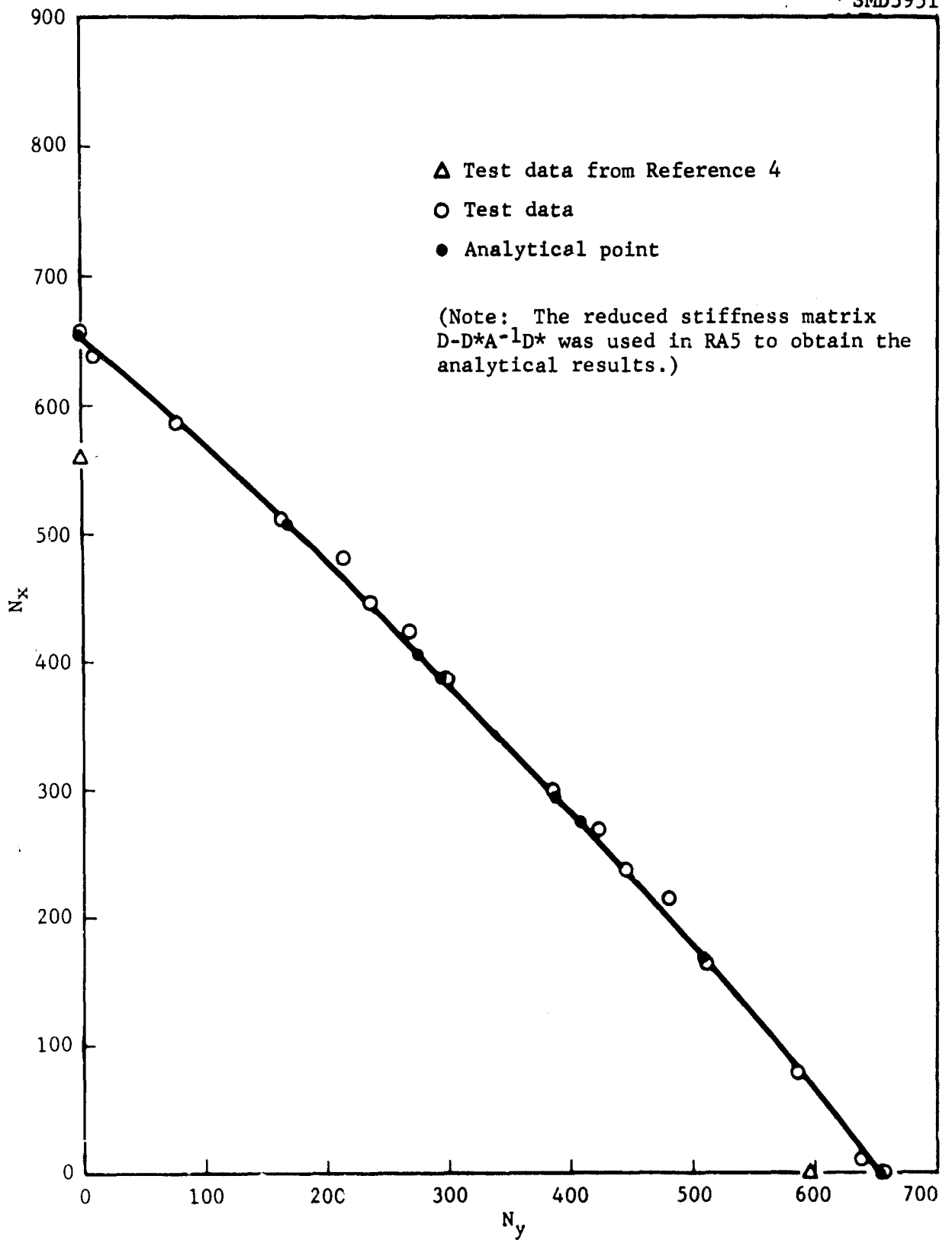


Figure 81 Biaxial Compression Interaction Curve for Panel No. 2

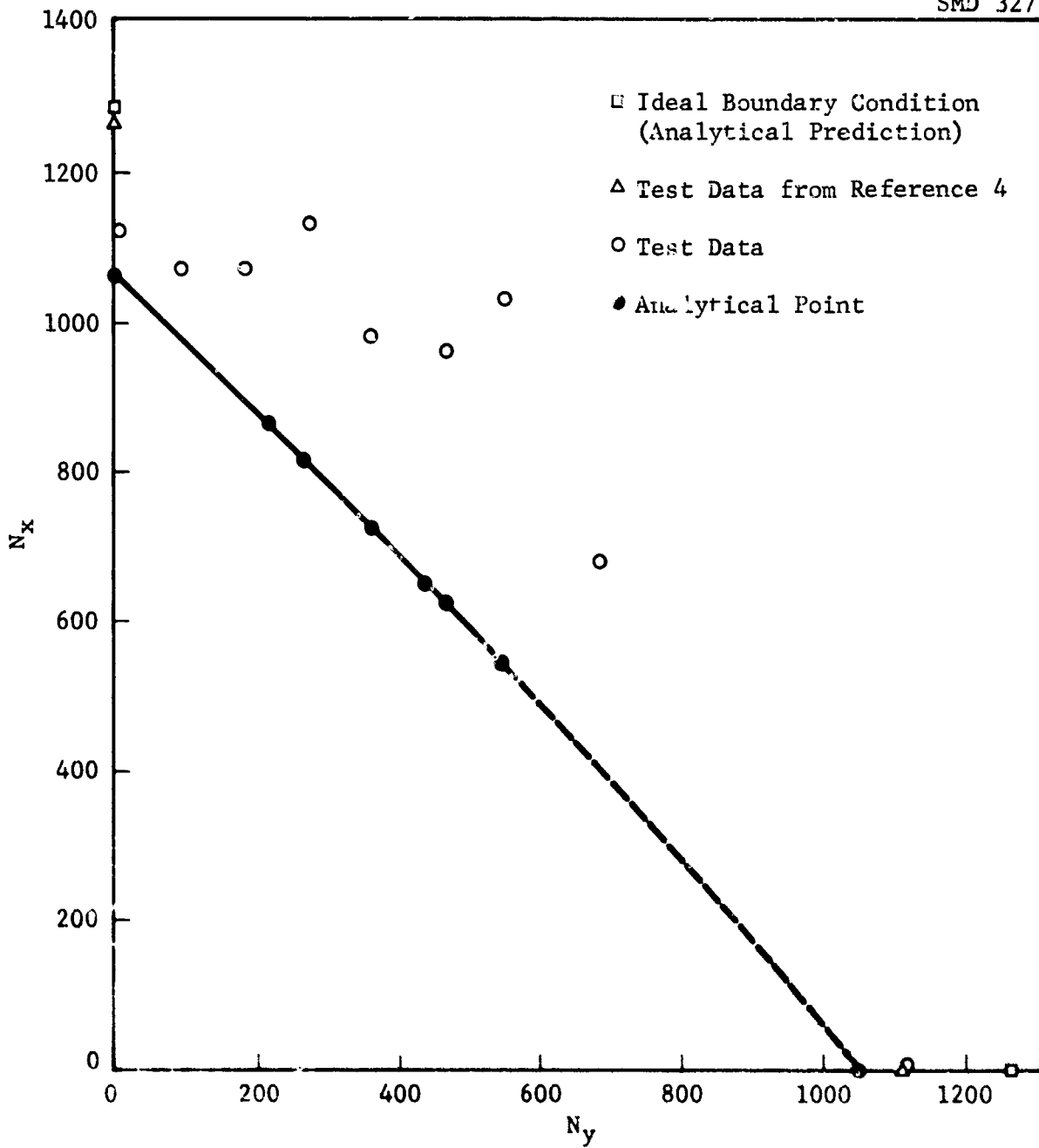


Figure 82 Biaxial Compression Interaction Curve for Panel No. 3

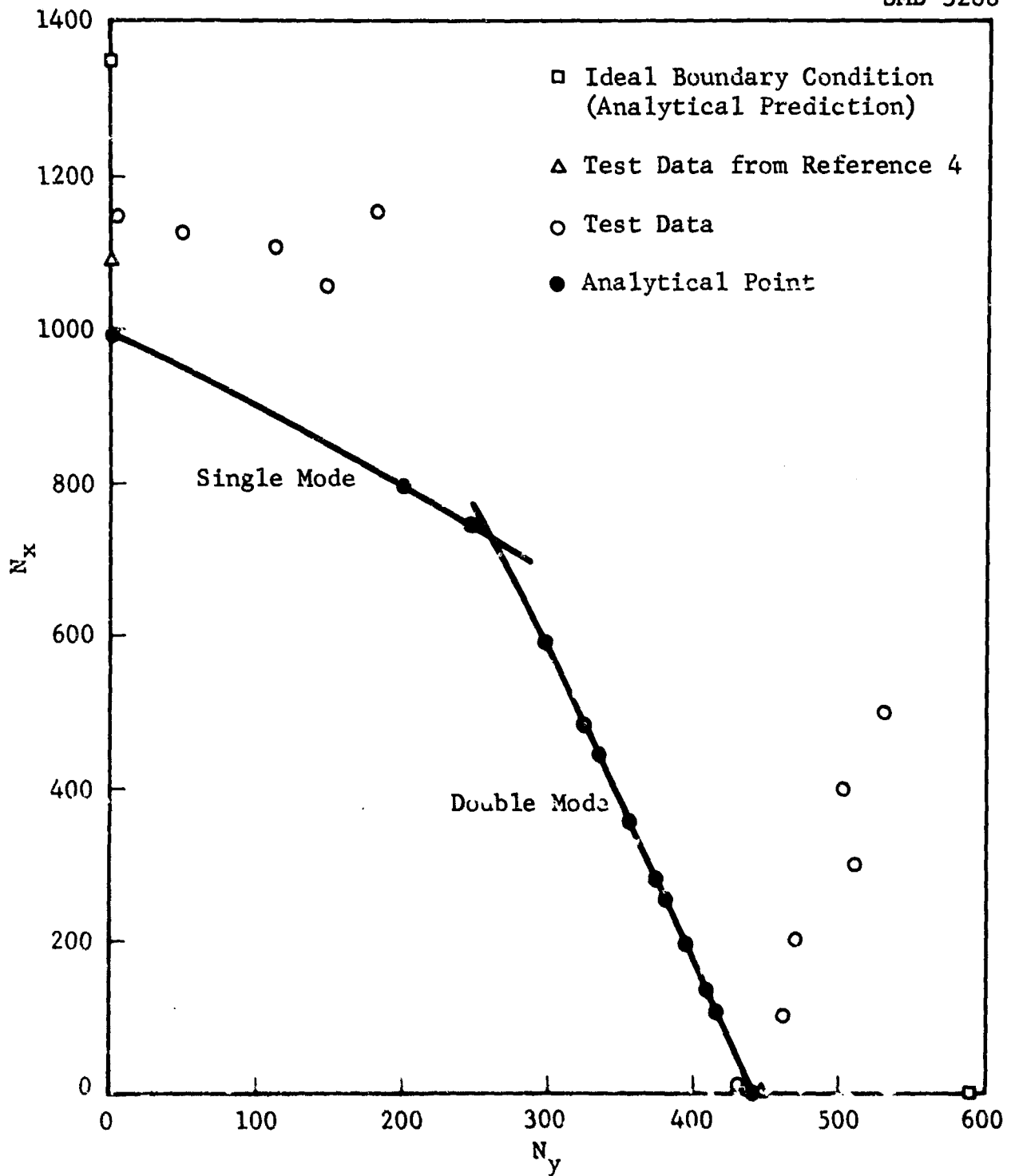


Figure 83 Biaxial Compression Interaction Curve for Panel No. 5

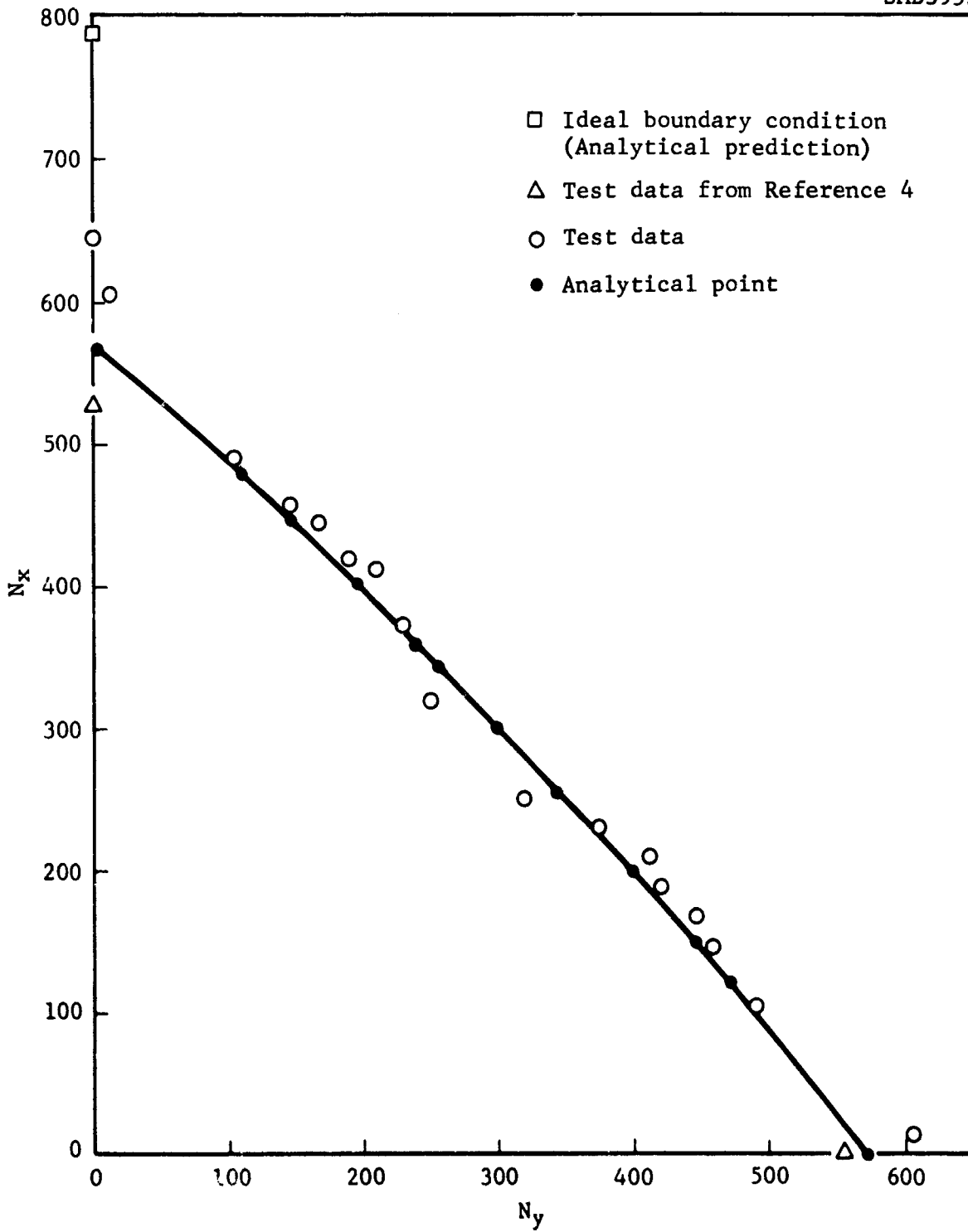


Figure 84 Biaxial Compression Interaction Curve for Panel No. 7

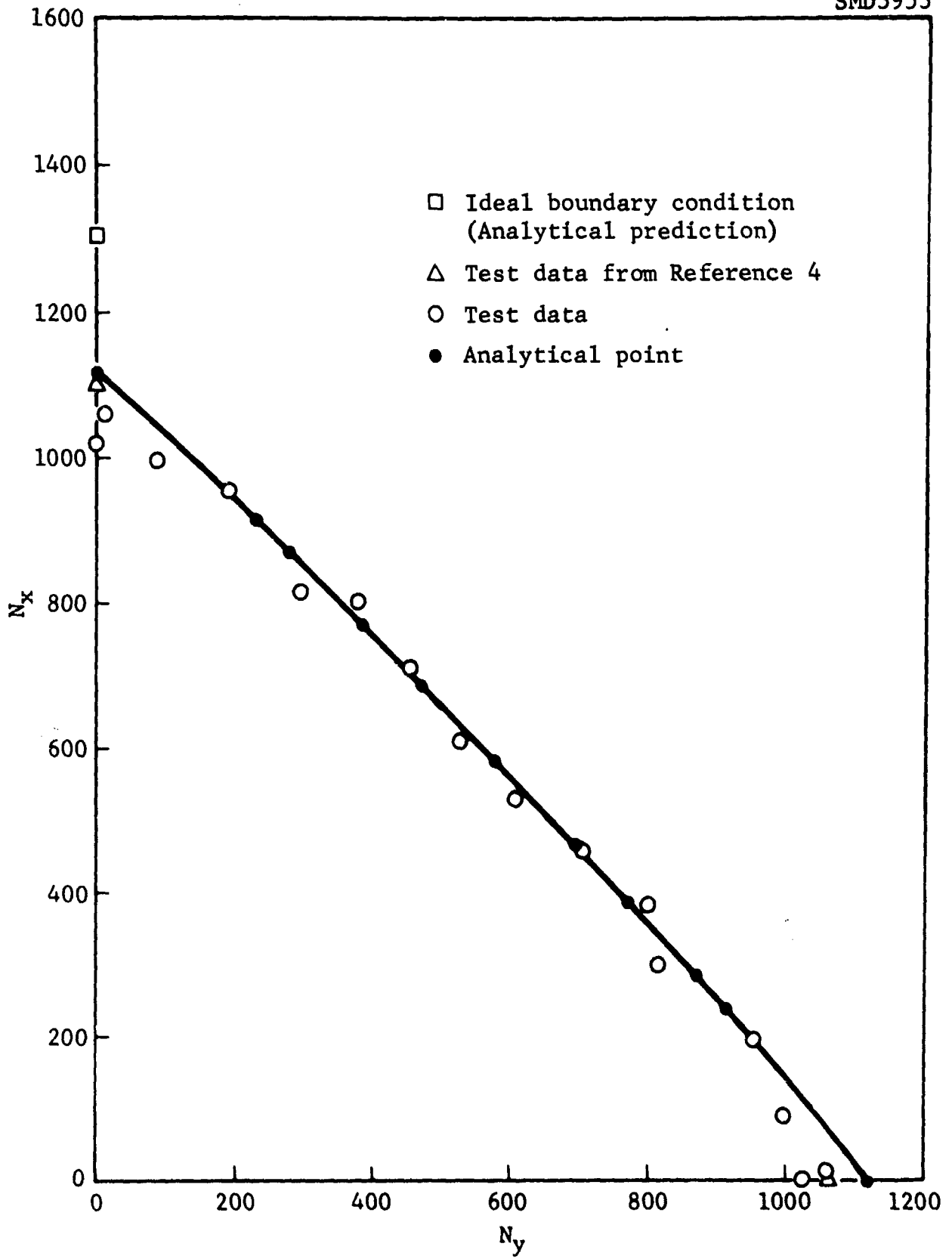


Figure 85 Biaxial Compression Interaction Curve for Panel No. 9

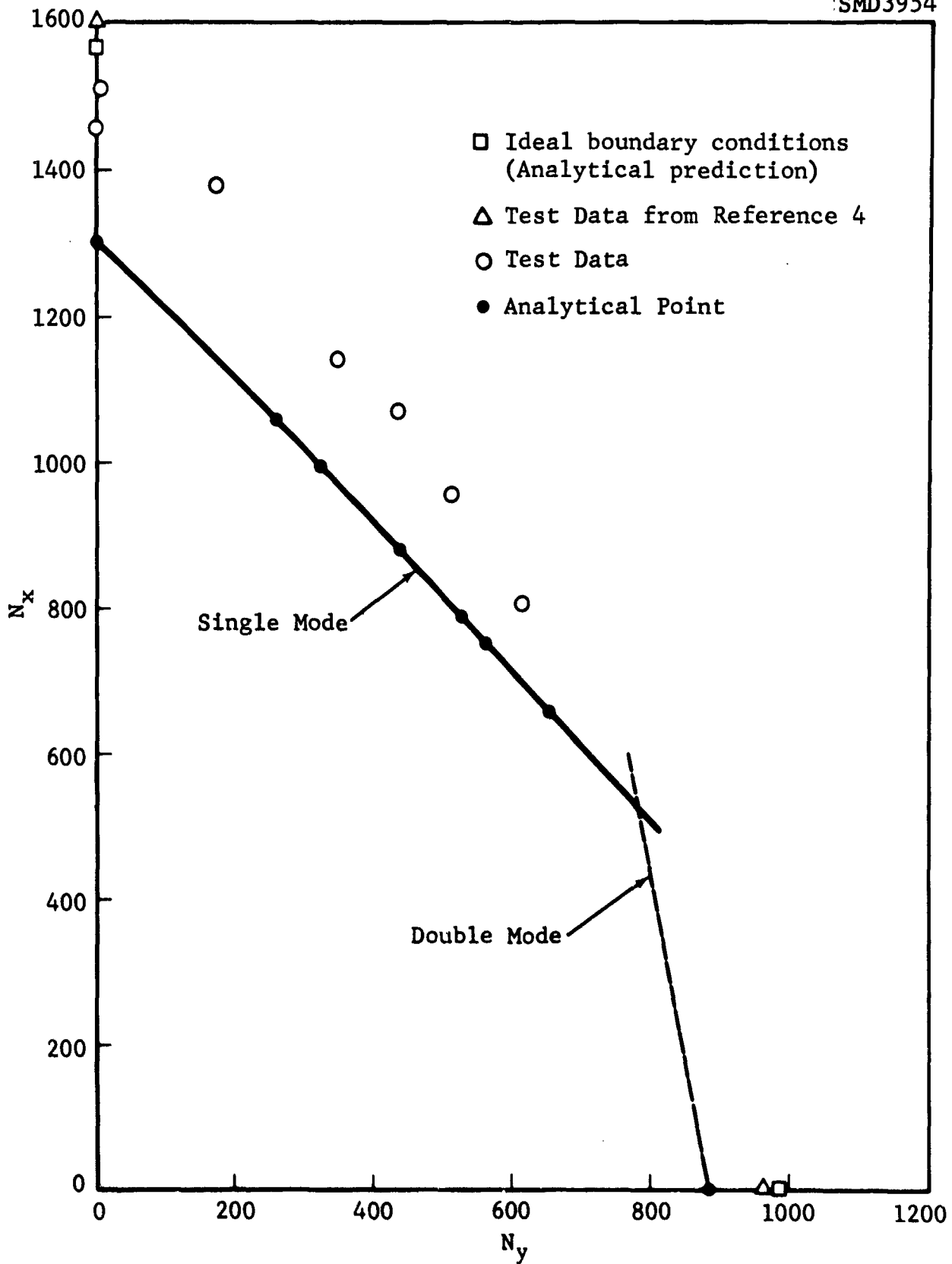


Figure 86 Biaxial Compression Interaction Curve for Panel No. 12

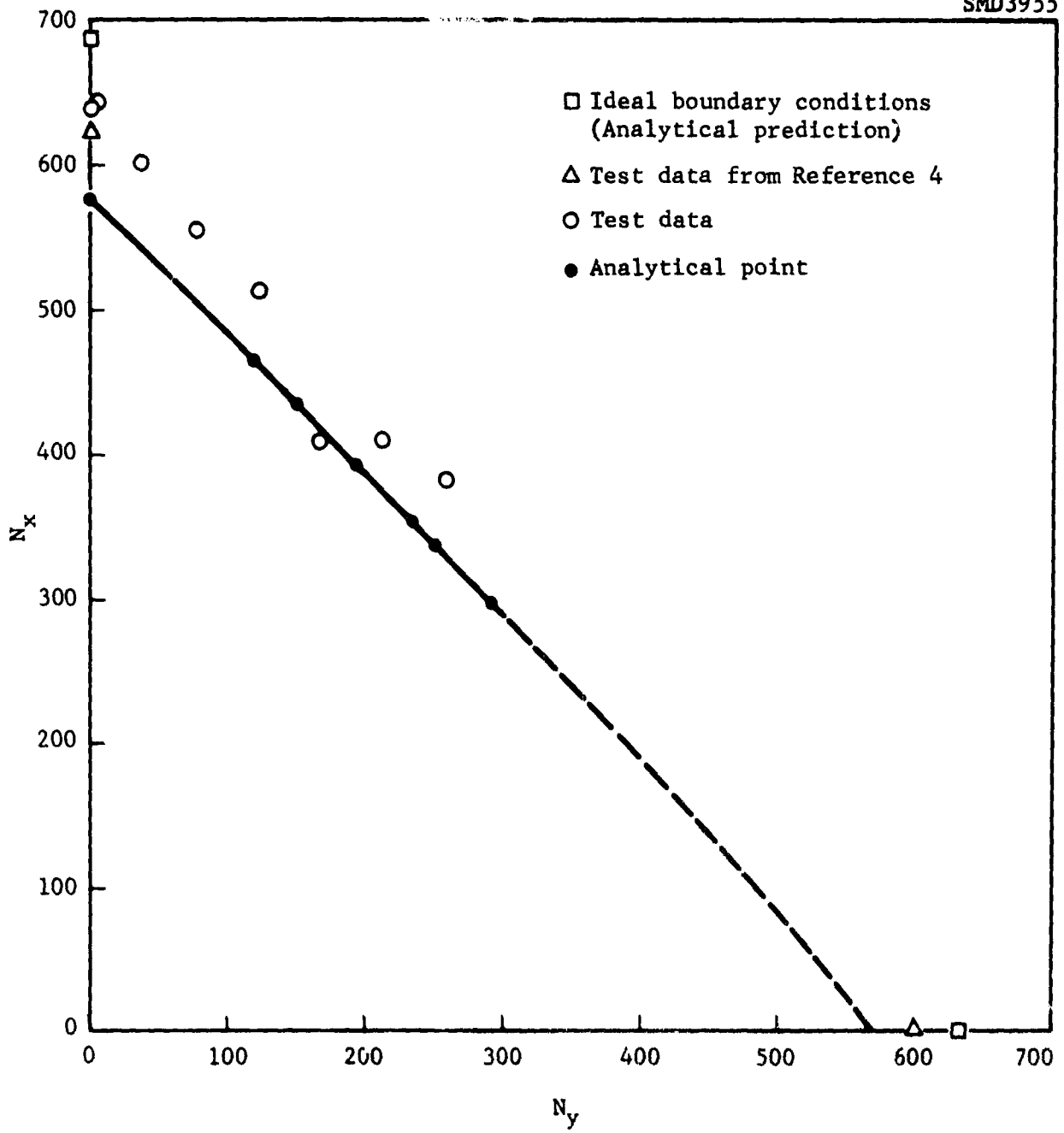


Figure 87 Biaxial Compression Interaction Curve for Panel No. 16

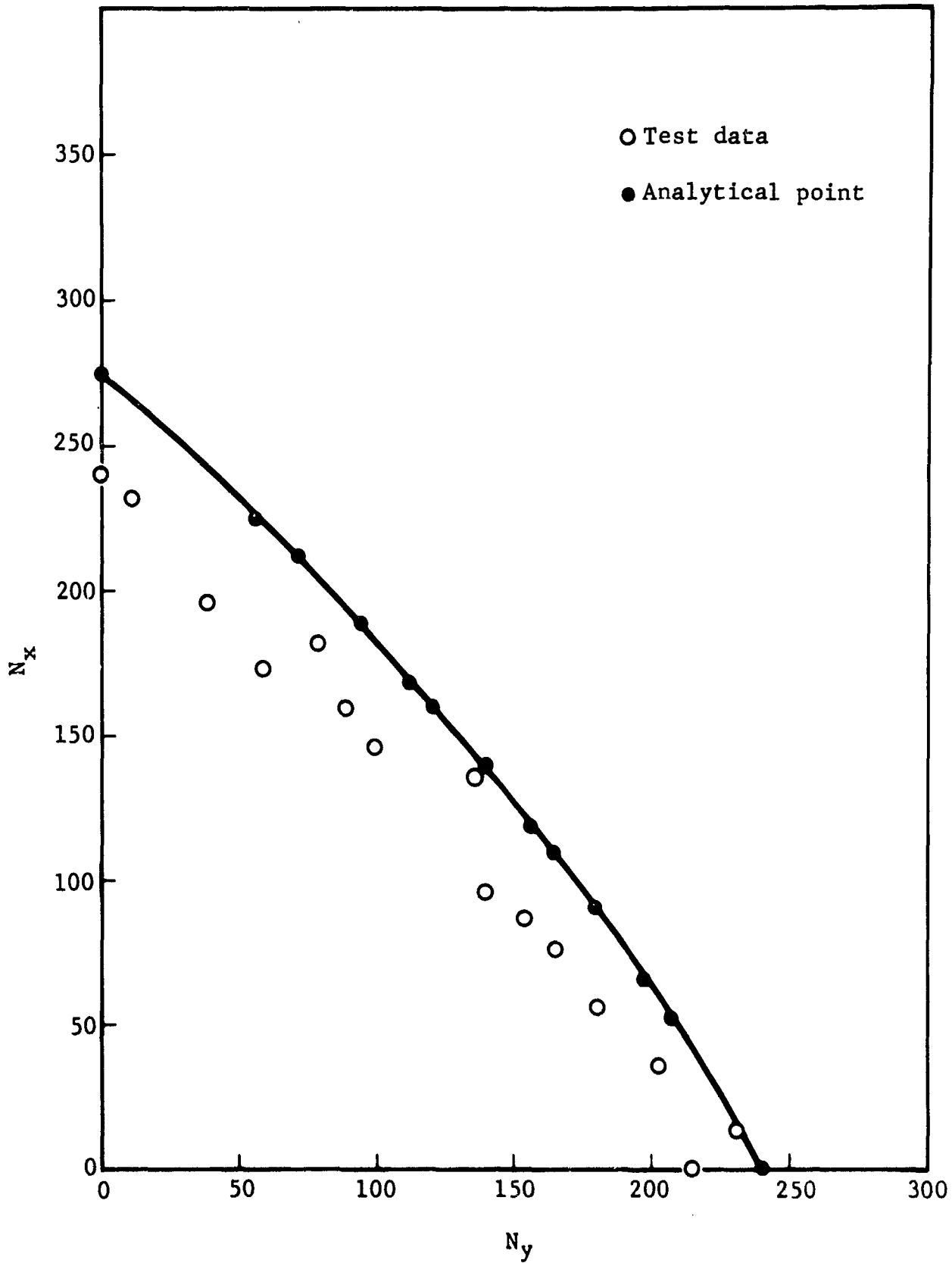


Figure 88 Biaxial Compression Interaction Curve for Panel No. 19A

Table IX CRITICAL BUCKLING LOADS, BIAXIAL COMPRESSION

Panel Number	Orientation	Test Config*	Critical Buckling Load (Pounds)		
			P _x	P _y	
Aluminum 1	--	0°	18,700	127	
			18,700	992	
			18,160	1,993	
			16,750	3,996	
			15,500	6,008	
			12,750	8,006	
			11,000**	11,000**	
2	Unsym. +45	0°	7,180	0	
			7,020	108	
			6,440	856	
			5,620	1,792	
			5,290	2,244	
			4,890	2,596	
			4,250	3,388	
3	0/90	0°	12,360	99	
			11,770	1,007	
			11,760	2,010	
			12,400	3,024	
			10,750	4,000	
			10,550	5,015	
			11,300	6,006	
			7,485**	7,485**	
100	12,270				
5	0	0°	12,660	101	
			12,450	535	
			12,210	1,228	
			11,630	1,626	
			12,720	2,005	
			4,730	100	
	90°			5,080	1,100
				5,170	2,200
				5,630	3,300
				5,530	4,400
				5,830	5,500

NOTES: * Orientation with respect to the arbitrary 0° axis.
 *** P_x and P_y were increased simultaneously at a ratio of N_x/N_y = 1.0.

Table IX CRITICAL BUCKLING LOADS, BIAXIAL COMPRESSION (Continued)

Panel Number	Orientation	Test Config*	Critical Buckling Load (Pounds)	
			P _x	P _y
7	+45	0°	7,100	0
			6,680	130
			5,390	1,138
			5,030	1,610
			4,890	1,838
			4,610	2,067
			4,530	2,305
			4,100	2,520
			3,500	2,753
9	+45	0°	11,260	0
			11,660	115
			10,940	976
			10,480	2,110
			8,960	3,262
			8,800	4,181
			7,780	5,002
			6,700	5,800
12	0/+45	0°	16,020	0
			16,600	66
			15,230	1,900
			12,550	3,835
			11,770	4,777
			10,490	5,637
			8,870	6,765
16	0/+45/90	0°	7,030	0
			7,080	58
			6,610	412
			6,110	848
			5,650	1,355
			4,510	1,833
			4,510	2,336
4,200	2,853			

NOTE: * Orientation with respect to the arbitrary 0° axis.

Table IX CRITICAL BUCKLING LOADS, BIAXIAL COMPRESSION (Continued)

Panel Number	Orientation	Test Config*	Critical Buckling Load (Pounds)	
			P _x	P _y
19A	Tapered +45	0°	2,550	116
			2,160	424
			1,900	641
			2,000	858
			1,730	969
			1,605	1,085
			1,535**	1,535**
		90°	2,540	142
			2,220	396
			1,980	622
			1,820	839
			1,680	956
			1,530	1,061
			1,490**	1,490**

NOTES: * Orientation with respect to the arbitrary 0° axis.

** P_x and P_y were increased simultaneously at a ratio of N_x/N_y = 1.0.

As discussed in subsection 4.5, the poor agreement between the predicted and observed response of Panel 5 (0°) under biaxial loading is probably due primarily to two effects: (1) the assumed value of E_2 and (2) the great difference in stiffness values in the longitudinal and transverse directions. However, there appears to be no simple explanation for the behavior of Panel 3 ($0^\circ/90^\circ$).

The interaction curve for Panel 19A (tapered $+45^\circ$) is presented in Figure 88. The test data were lower than the analytical predictions, which may be due to the fact that the actual edge conditions on the tapered plate are even less fixed than those of the other panels.

SECTION VII
NATURAL FREQUENCY STUDY

The purpose of the natural frequency study was to determine the natural modes of vibration of 10 flat plates (orientation as variables) at four different levels of uniaxial compression loading and to compare the test data with the analytical predictions of computer program RA5. The boundary conditions considered were fully-clamped plates and plates clamped on the compressed edges and simply supported on the sides.

Boron panels selected for the study and the configurations tested are enumerated in Table X. Panel thicknesses and orientations were presented in Table I. The isotropic control panel selected was aluminum Panel 1. Input properties used for the RA5 analysis were described in subsection 4.5. The required mass density for boron is

$$\rho = 0.000192 \text{ lb-sec}^2/\text{in.}^4,$$

and that for aluminum is

$$\rho = 0.002667 \text{ lb-sec}^2/\text{in.}^4.$$

In Figures 89 through 110 the experimental and analytical frequencies are plotted against edge load for each test condition. Analytical solutions were obtained for each of the test conditions using the RA5 and assuming elastically restrained boundaries. The illustrations on the right of each figure are the predicted mode shapes; node lines are indicated by solid lines.

The experimental data obtained for the fully clamped aluminum panel agree well with the analytical predictions. As shown in Figure 89, for zero edge load, four separate mode shapes were established experimentally even though a double root was predicted.

For the condition of clamped-simple boundaries, the analysis predicted that the curves for the second and third modes would intersect. Experimentally, the third (horizontal) mode was lost above the point of intersection as shown in Figure 90.

The effect of the shaker on modal shape and frequency was negligible. For comparative purposes, test data from Reference 8, which was obtained by monitoring the free vibration of the

Table X NATURAL FREQUENCY TESTS

Panel No.	Orientation	Clamped-Clamped		Clamped-Simple	
		0° Config	90° Config	0° Config	90° Config
2	Unsymmetrical +45	X		X	
3	0/90	X		X	
5	0	X	X	X	X
7	+45	X		X	
9	+45	X		X	
12	0/+45	X		X	
16	0/+45/90	X		X	
19A	Tapered +45	X	X	X	X
Aluminum 1	-	X		X	

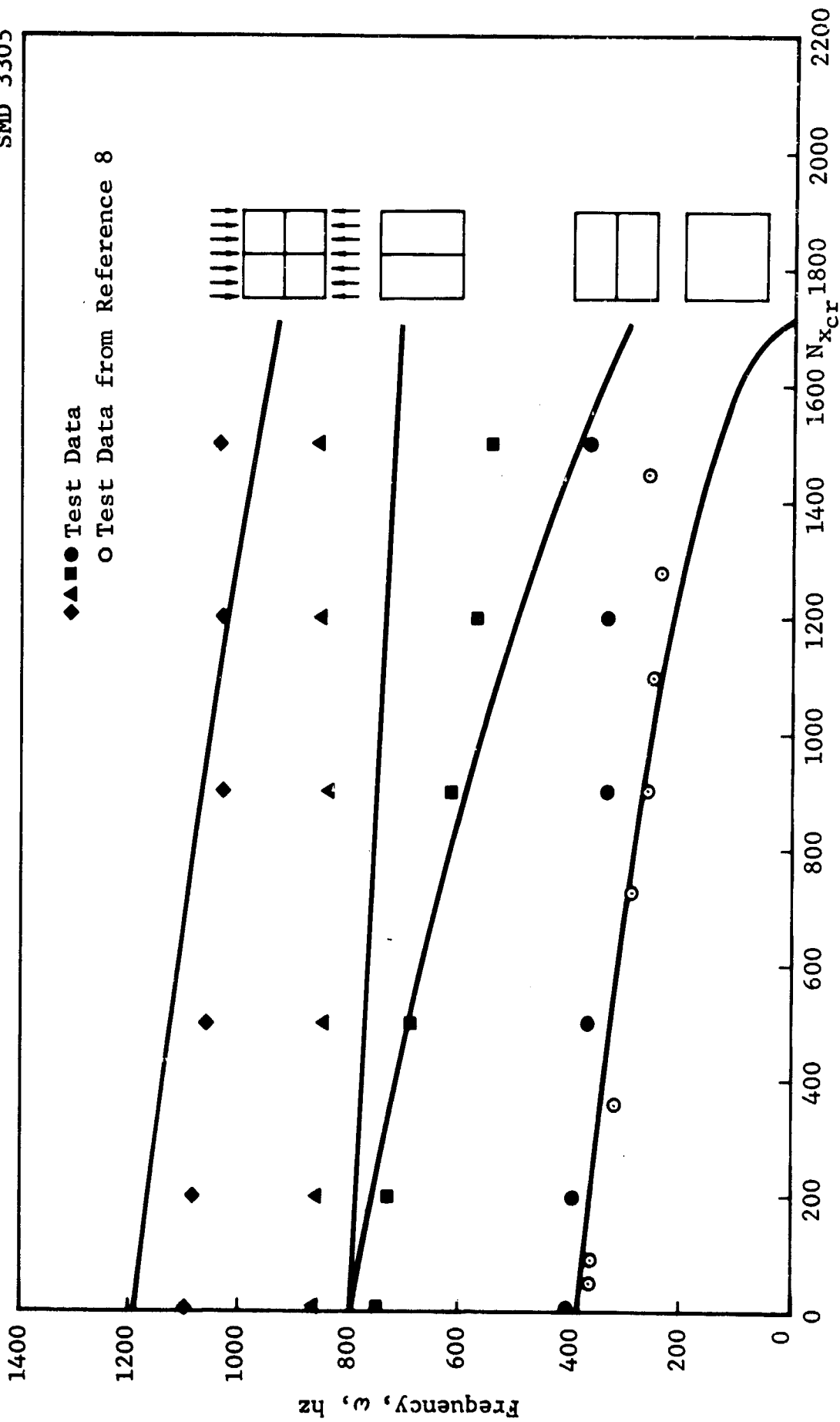


Figure 89 Natural Frequency vs Compressive Stress, Aluminum Panel No. 1, Clamped-Clamped

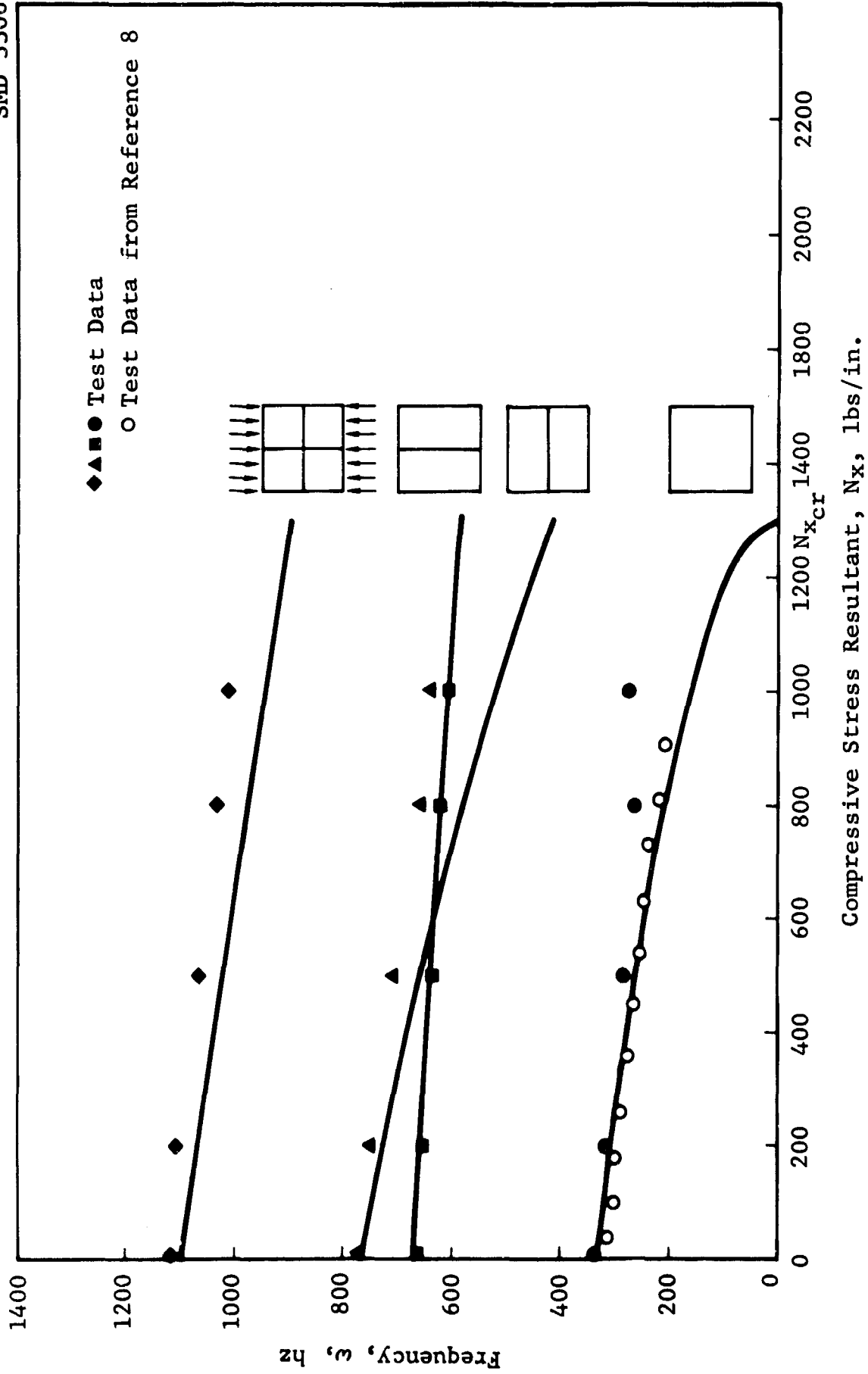
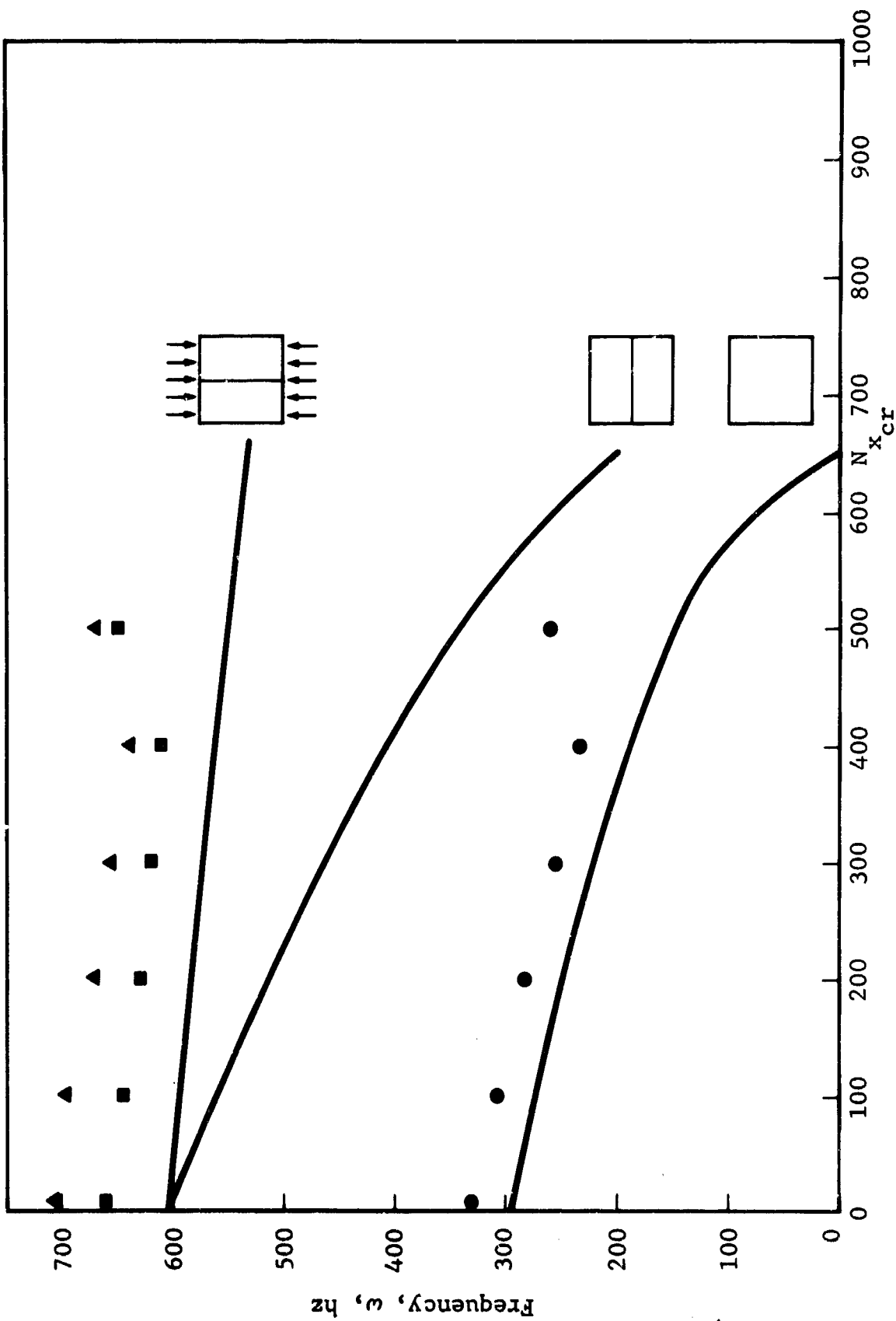
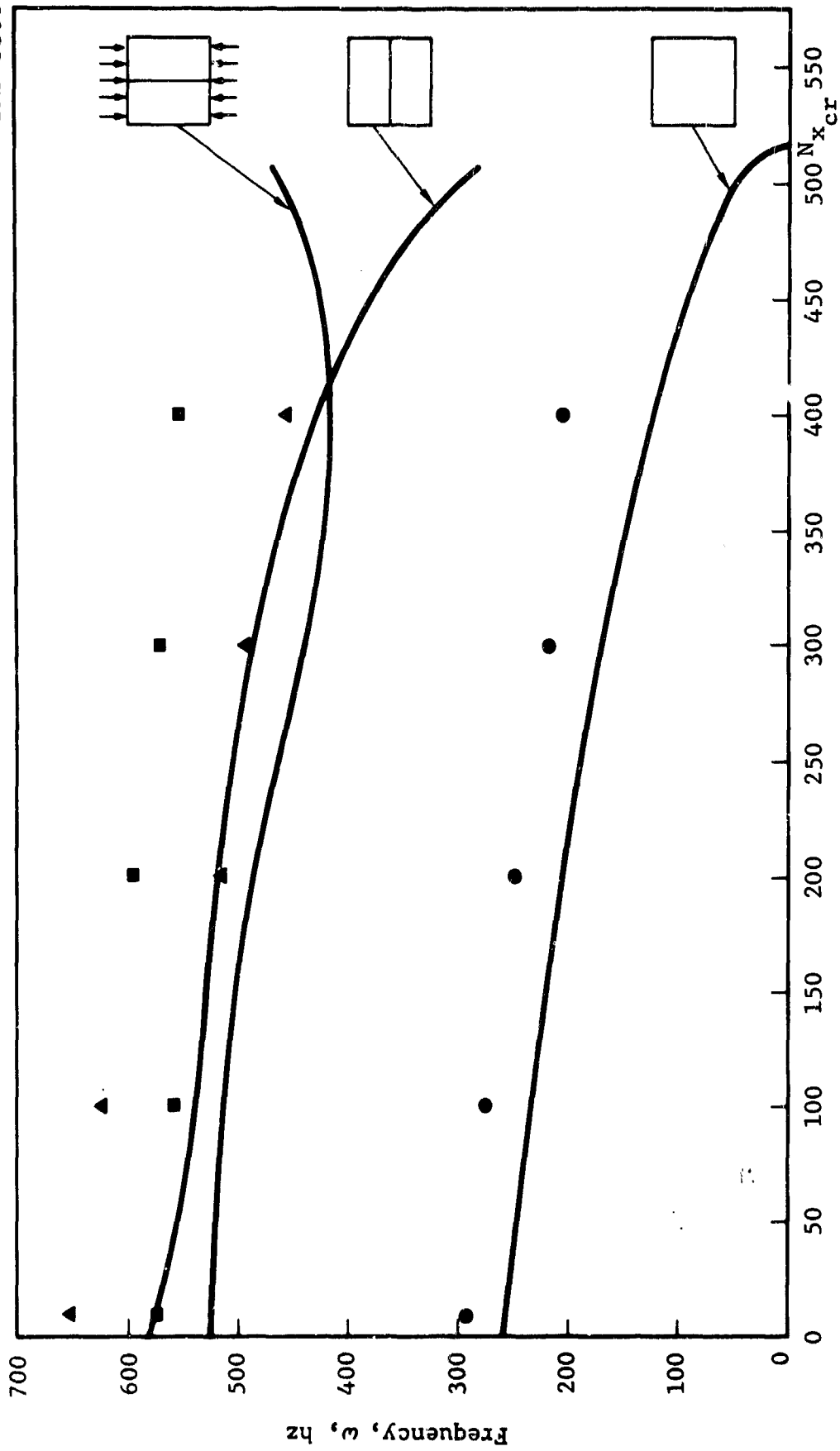


Figure 90 Natural Frequency vs Compressive Stress, Aluminum Panel 1, Closed Form



Compressive Stress Resultant, N_x , lbs/in.
 Figure 91 Natural Frequency vs Compressive Stress, Panel 2,
 Clamped-Clamped

SMD 3308



Compressive Stress Resultant, N_x , lbs/in.

Figure 92 Natural Frequency vs Compressive Stress, Panel 2, Clamped-Simple

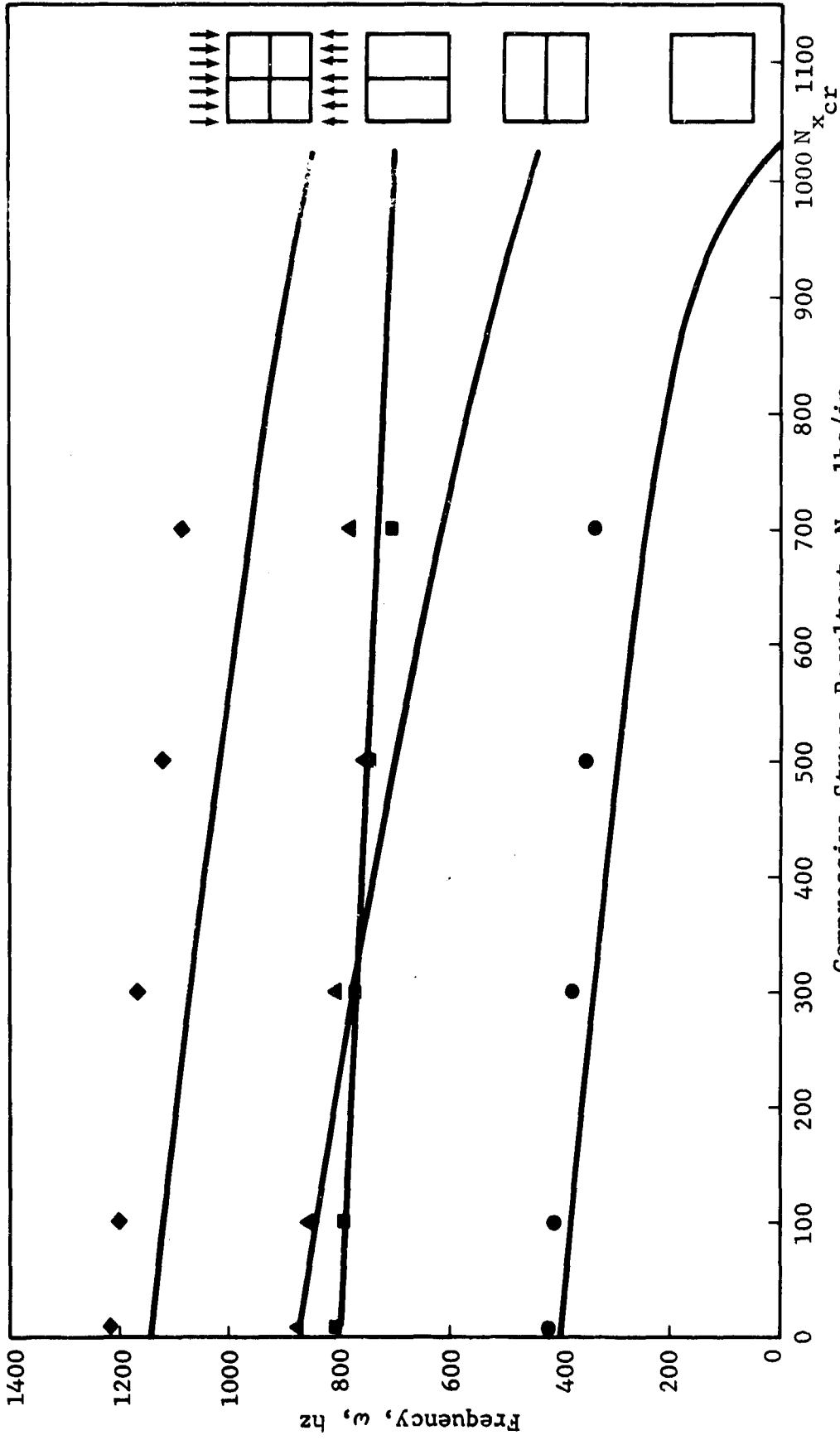


Figure 93 Natural Frequency vs Compressive Stress, Panel 3, Clamped-Clamped

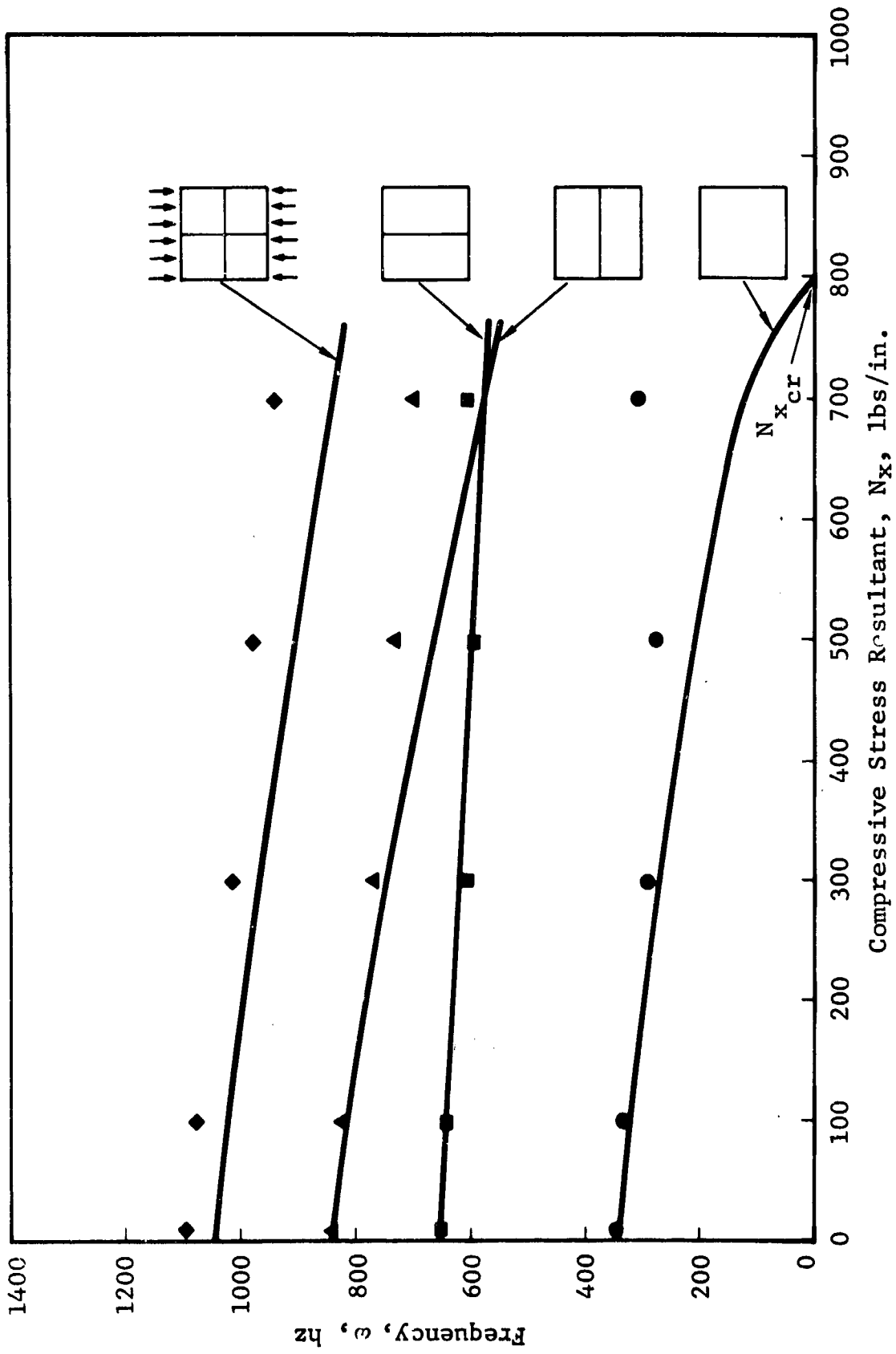


Figure 94 Natural Frequency vs Compressive Stress, Panel 3, Clamped-Simple

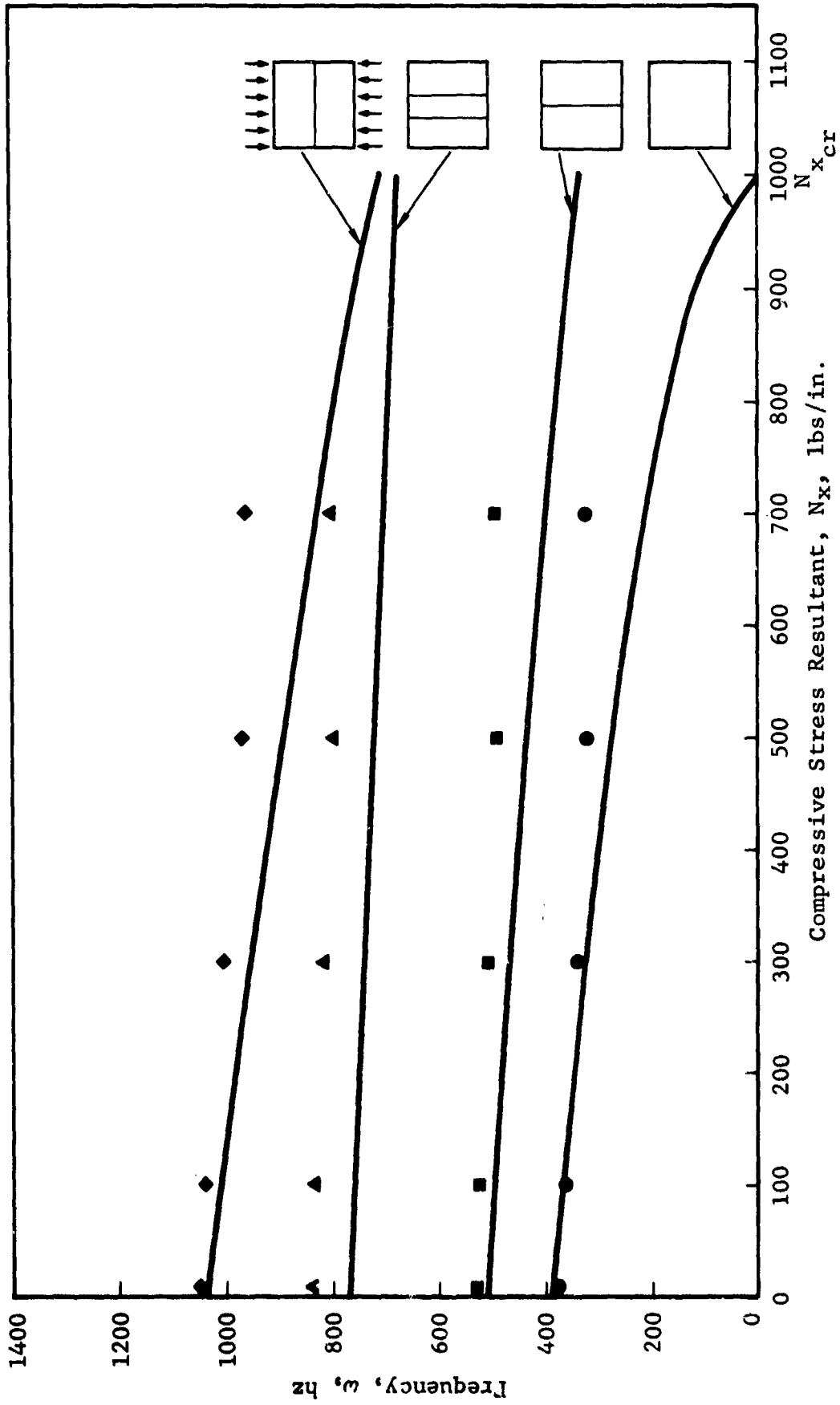


Figure 95 Natural Frequency vs Compressive Stress, Panel 5, Clamped-Clamped

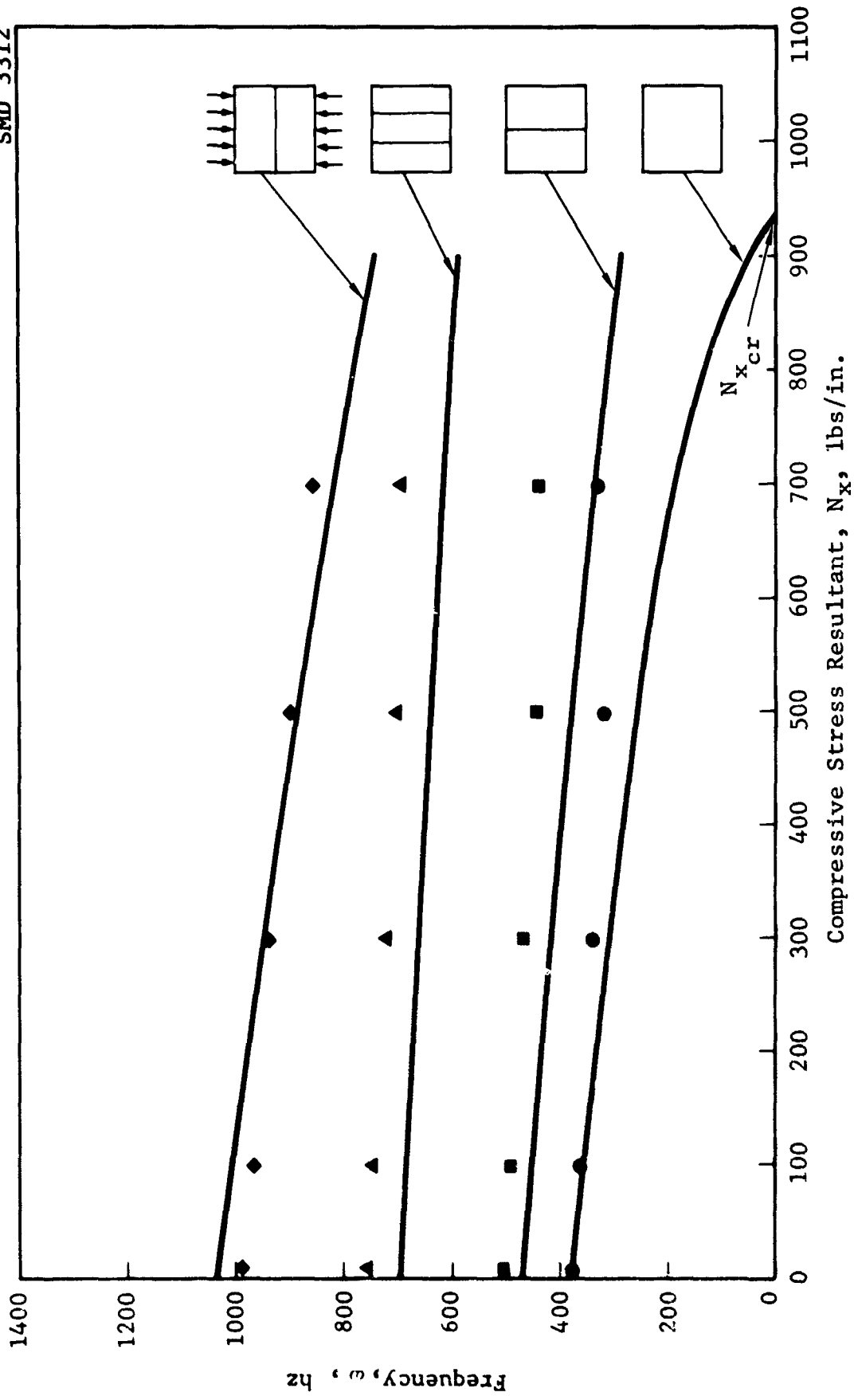


Figure 96 Natural Frequency vs Compressive Stress, Panel 5, Clamped-Simple

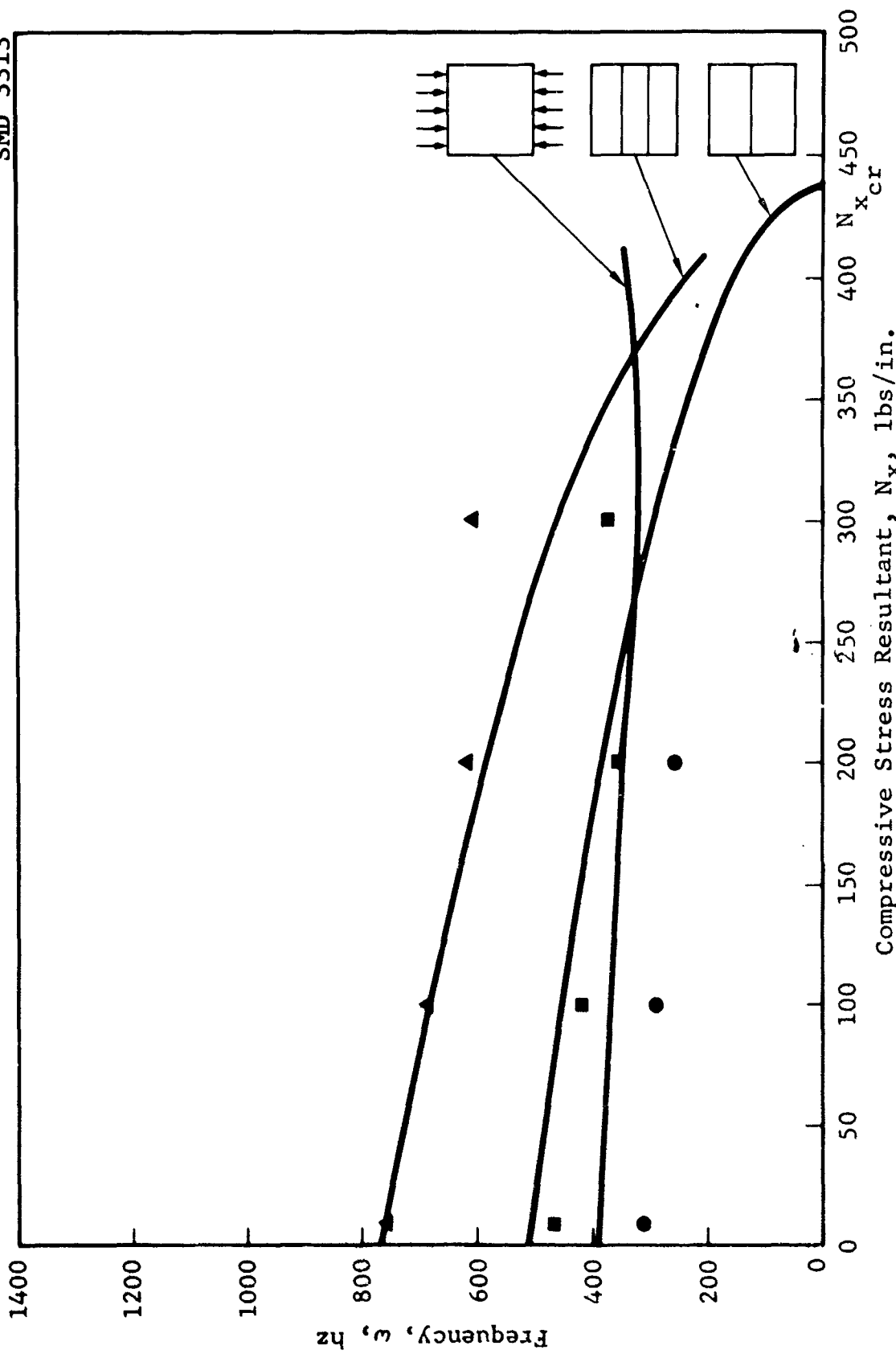


Figure 97 Natural Frequency vs Compressive Stress, Panel 15, Turned 90°, Clamped-Clamped

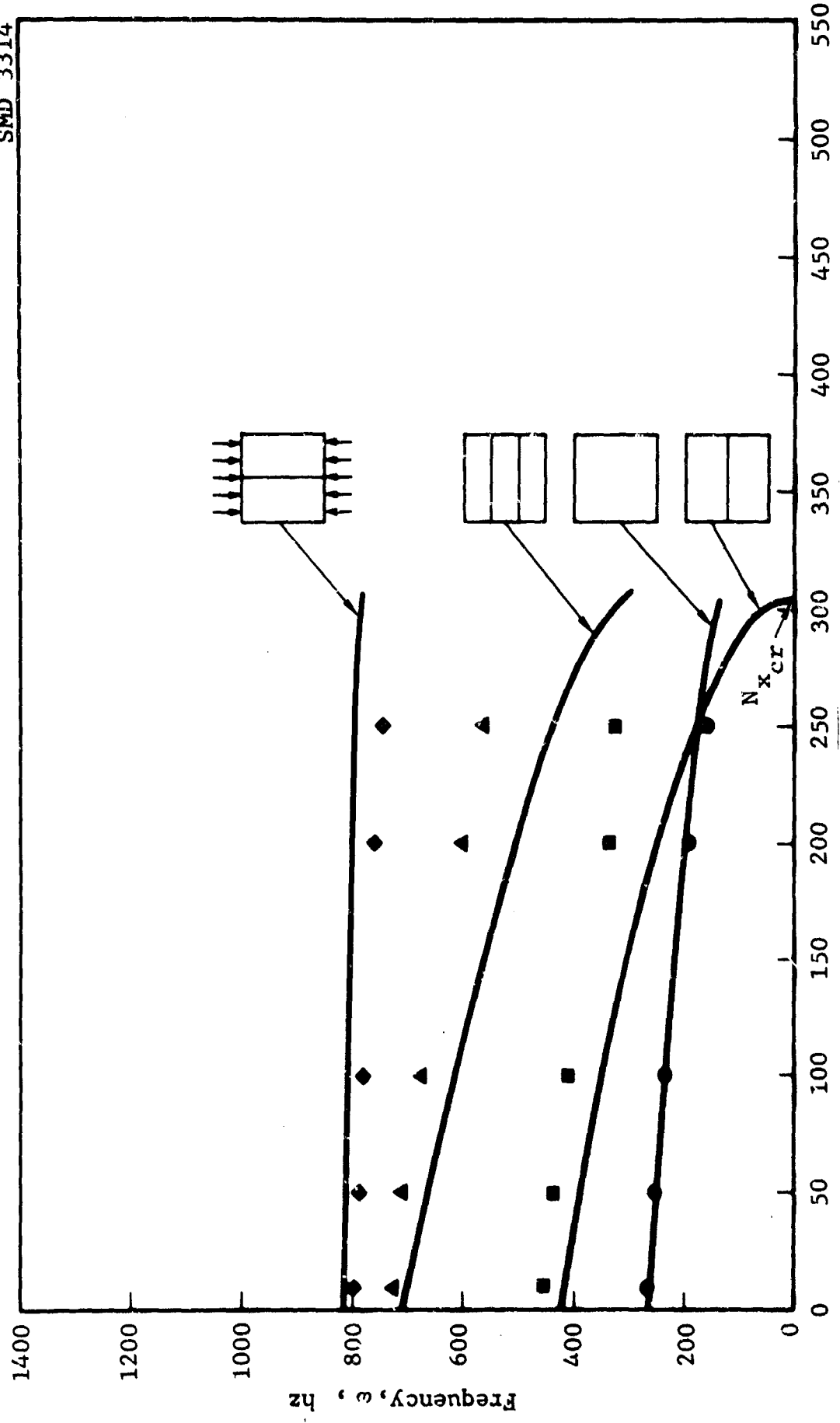


Figure 98 Natural Frequency vs Compressive Stress, Panel 5, Turned 90°, Clamped-Simple

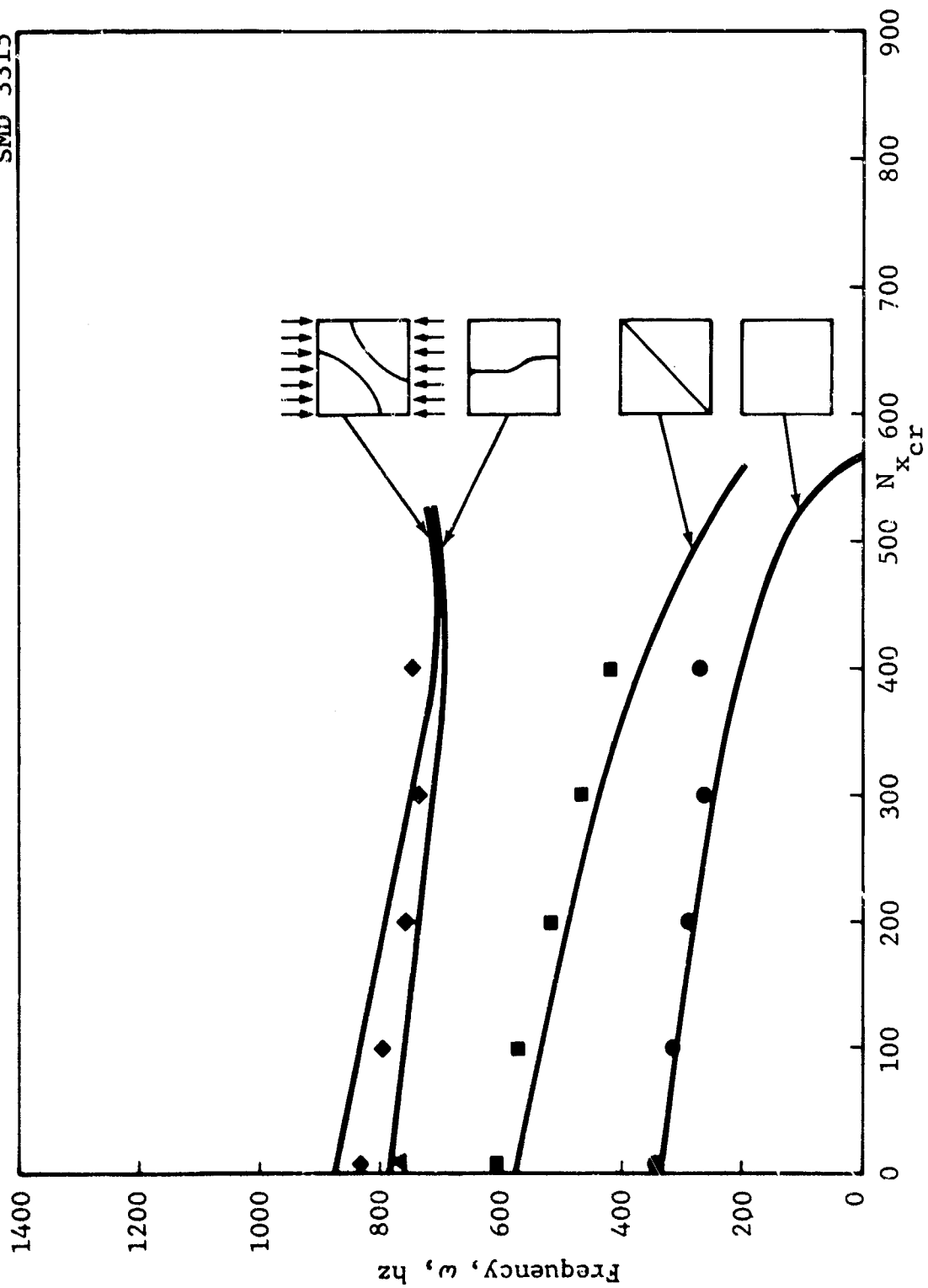


Figure 99 Natural Frequency vs Compressive Stress, Panel 7, Clamped-Clamped

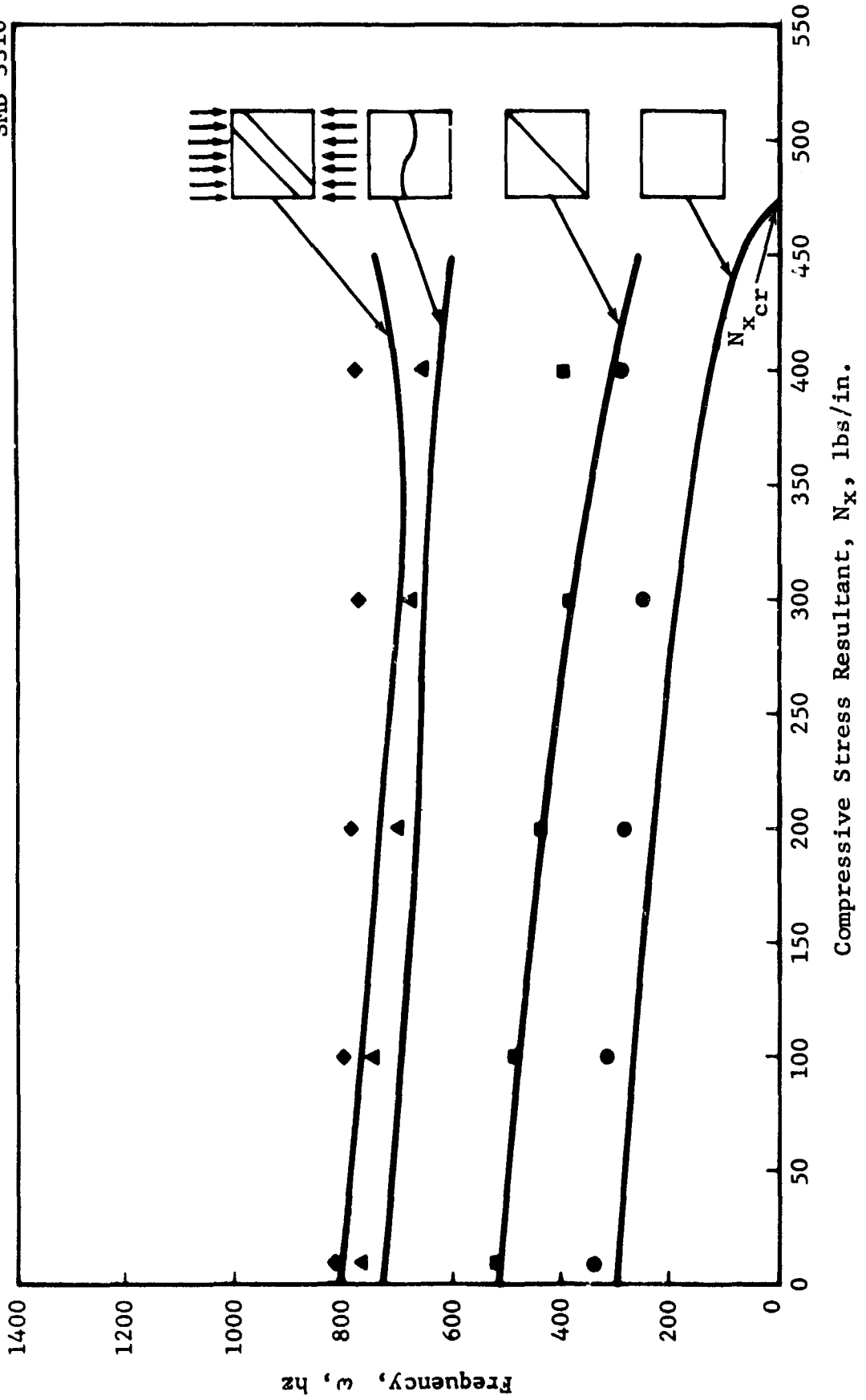


Figure 100 Natural Frequency vs Compressive Stress, Panel 7, Clamped-Simple

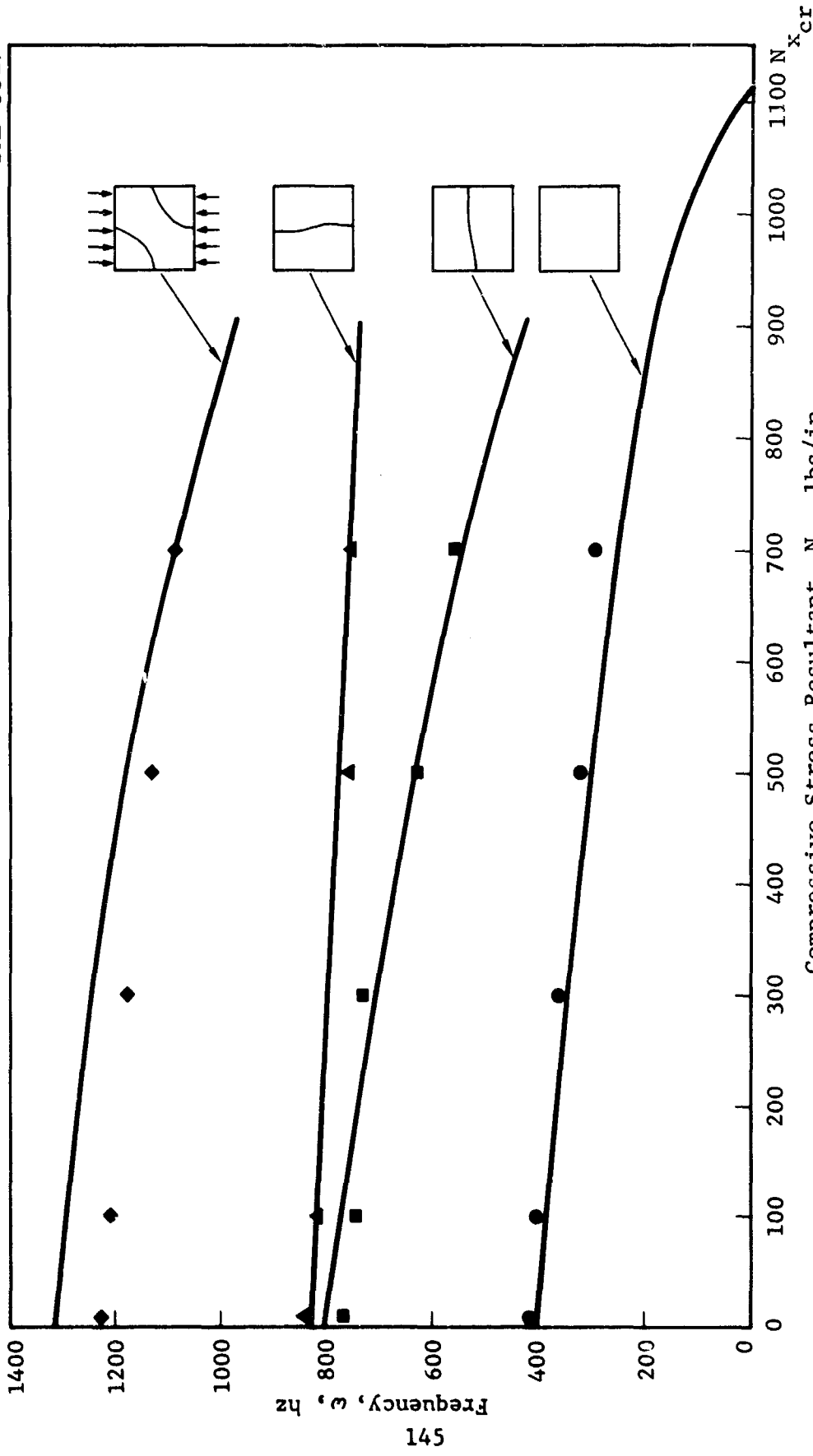


Figure 101 Natural Frequency vs Compressive Stress, Panel 9, Clamped-Clamped

SMD 3318

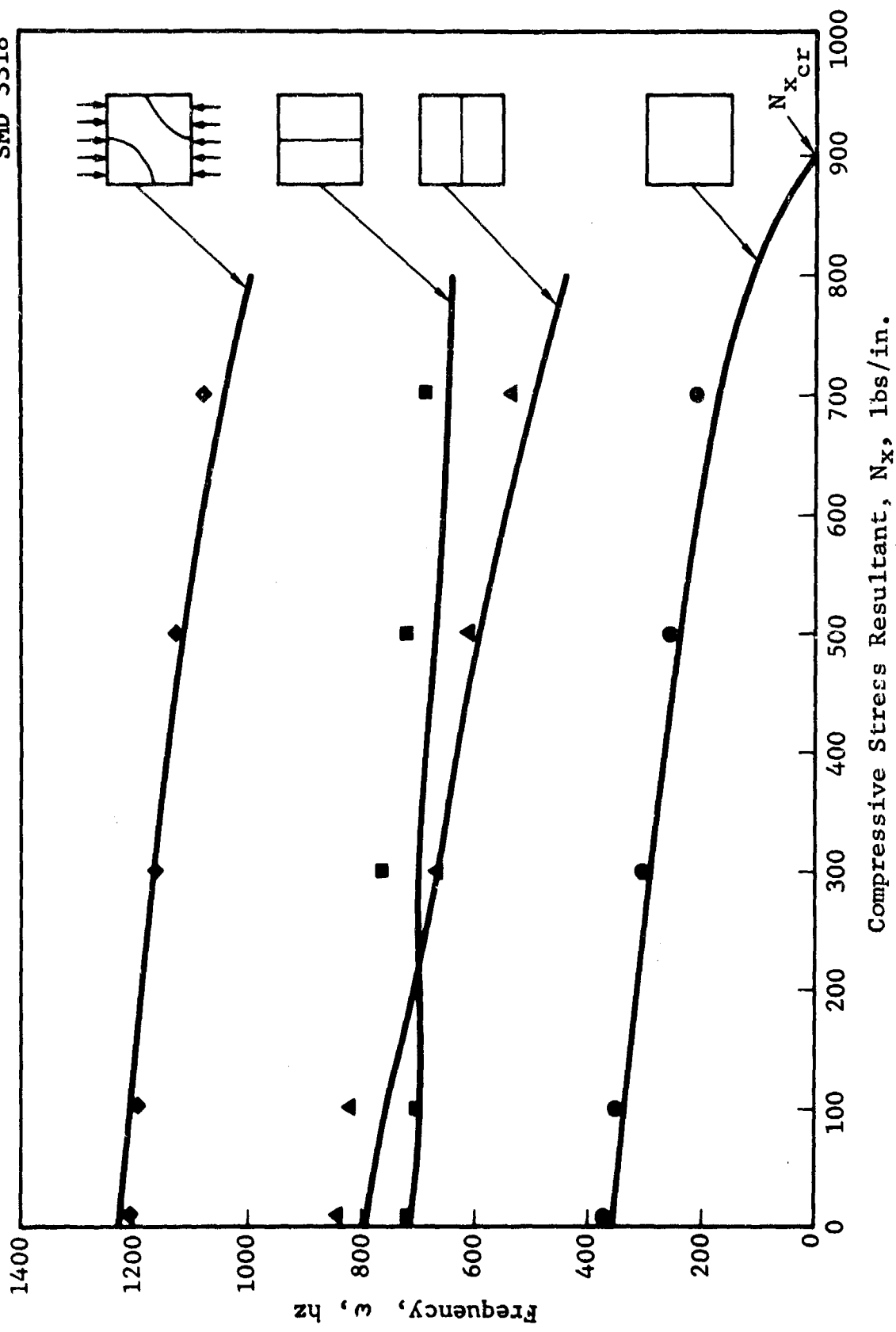
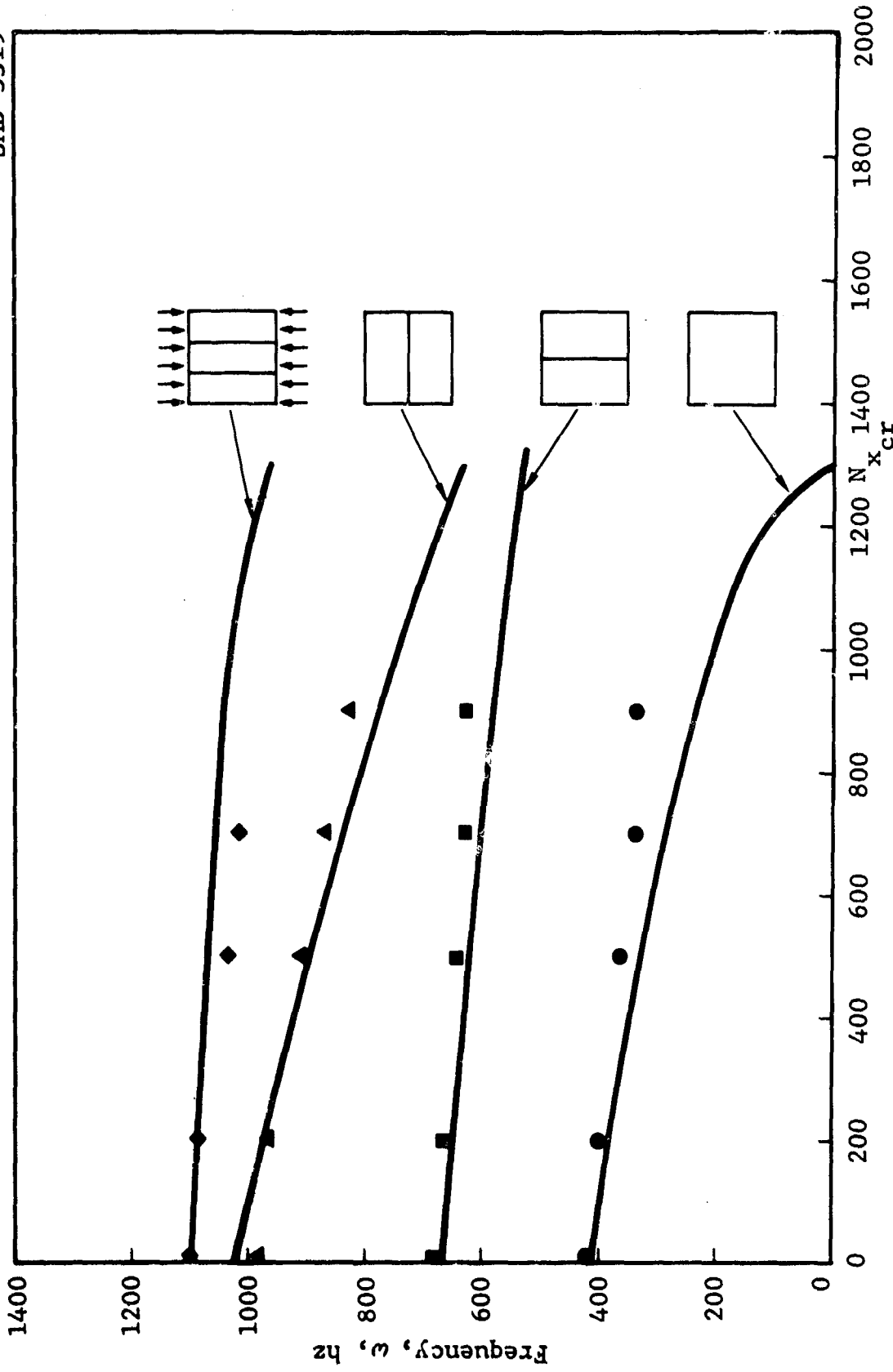


Figure 102 Natural Frequency vs Compressive Stress, Panel 9, Clamped-Simple



Compressive Stress Resultant, N_x , lbs/in.
 Figure 103 Natural Frequency vs Compressive Stress, Panel 12,
 Clamped-Clamped

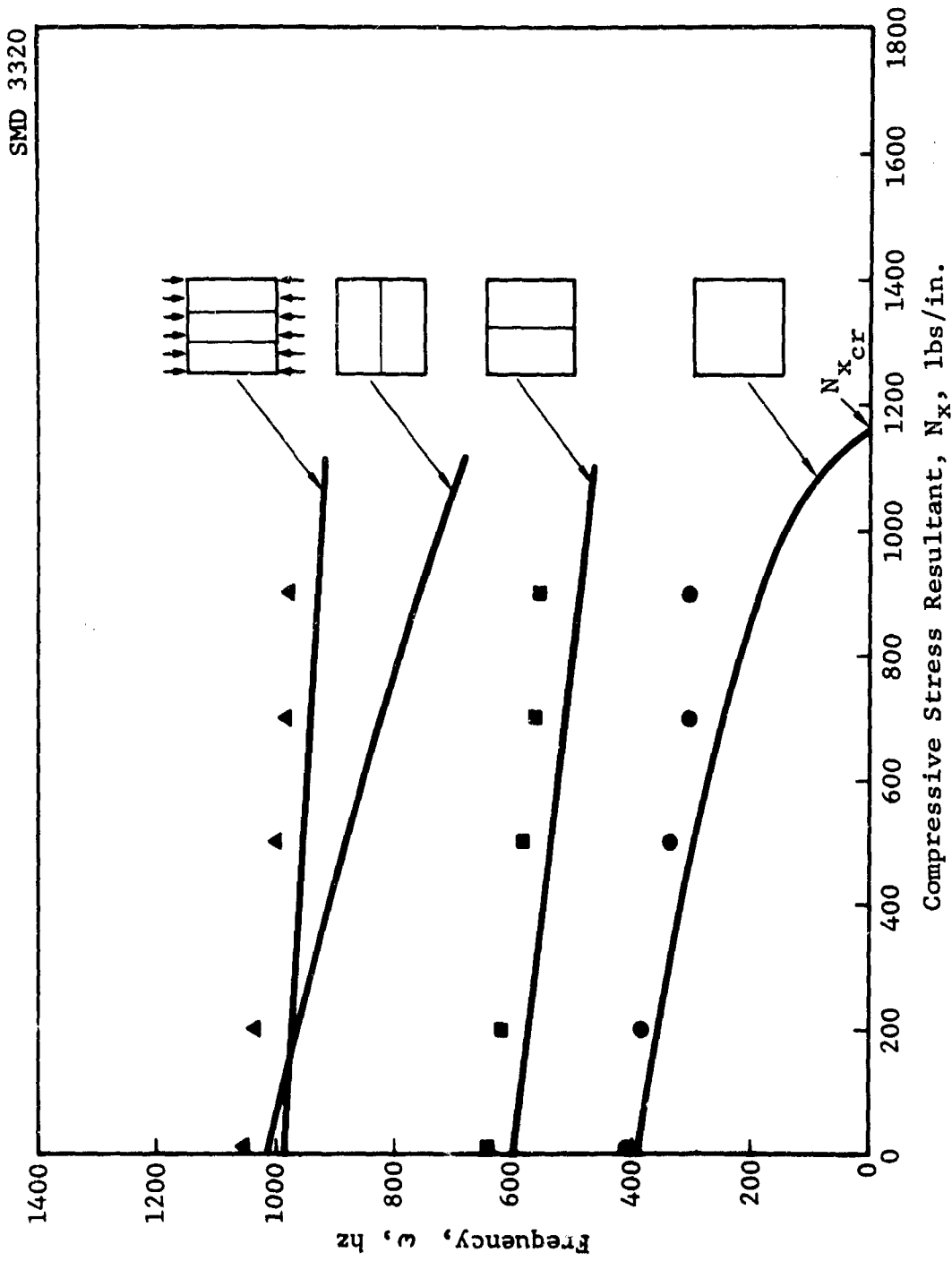
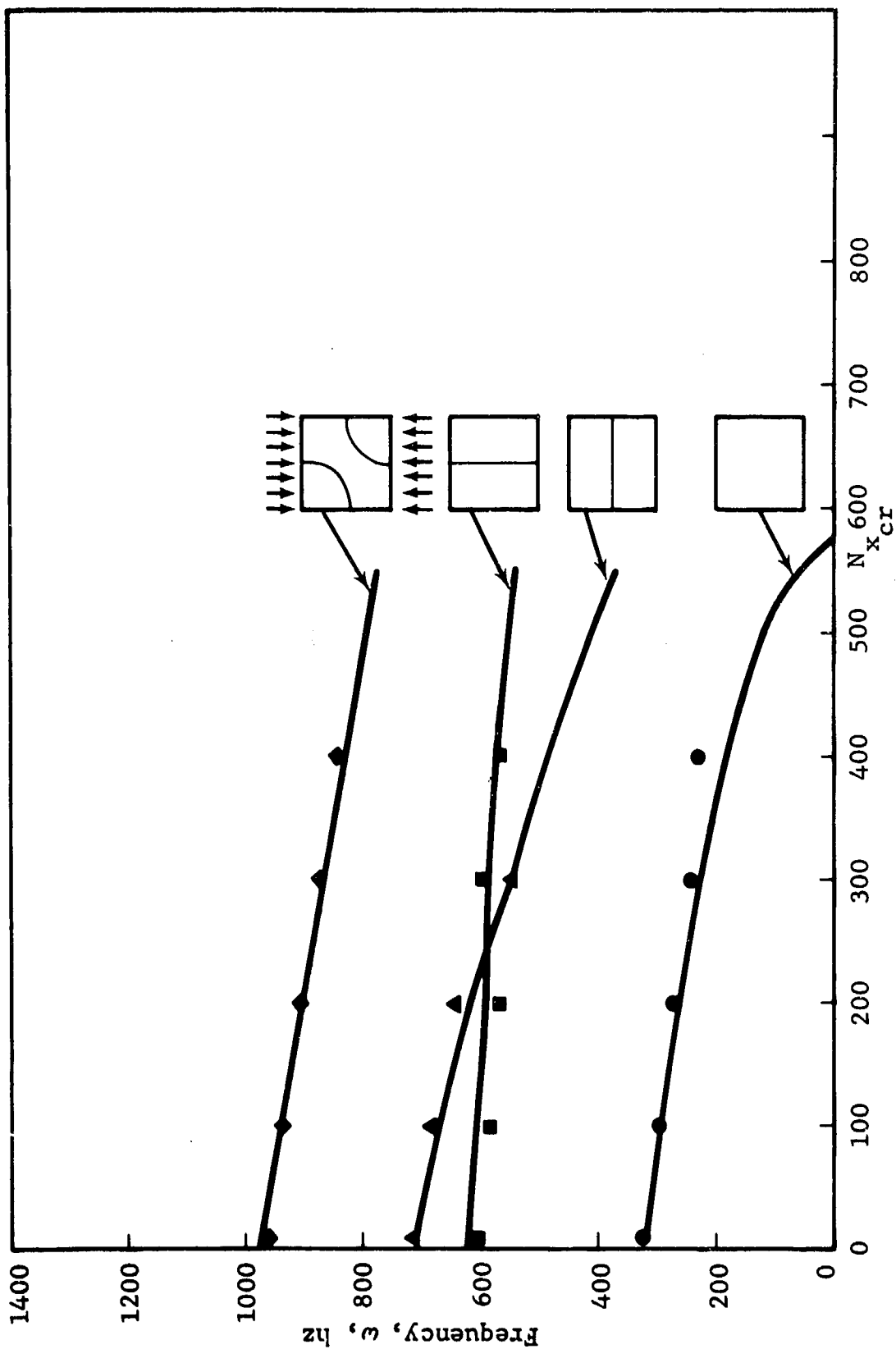


Figure 104 Natural Frequency vs Compressive Stress, Panel 12, Clamped-Simple



Compressive Stress Resultant, N_x , lbs/in.
 Figure 105 Natural Frequency vs Compressive Stress, Panel 16,
 Clamped-Clamped

SMD 3322

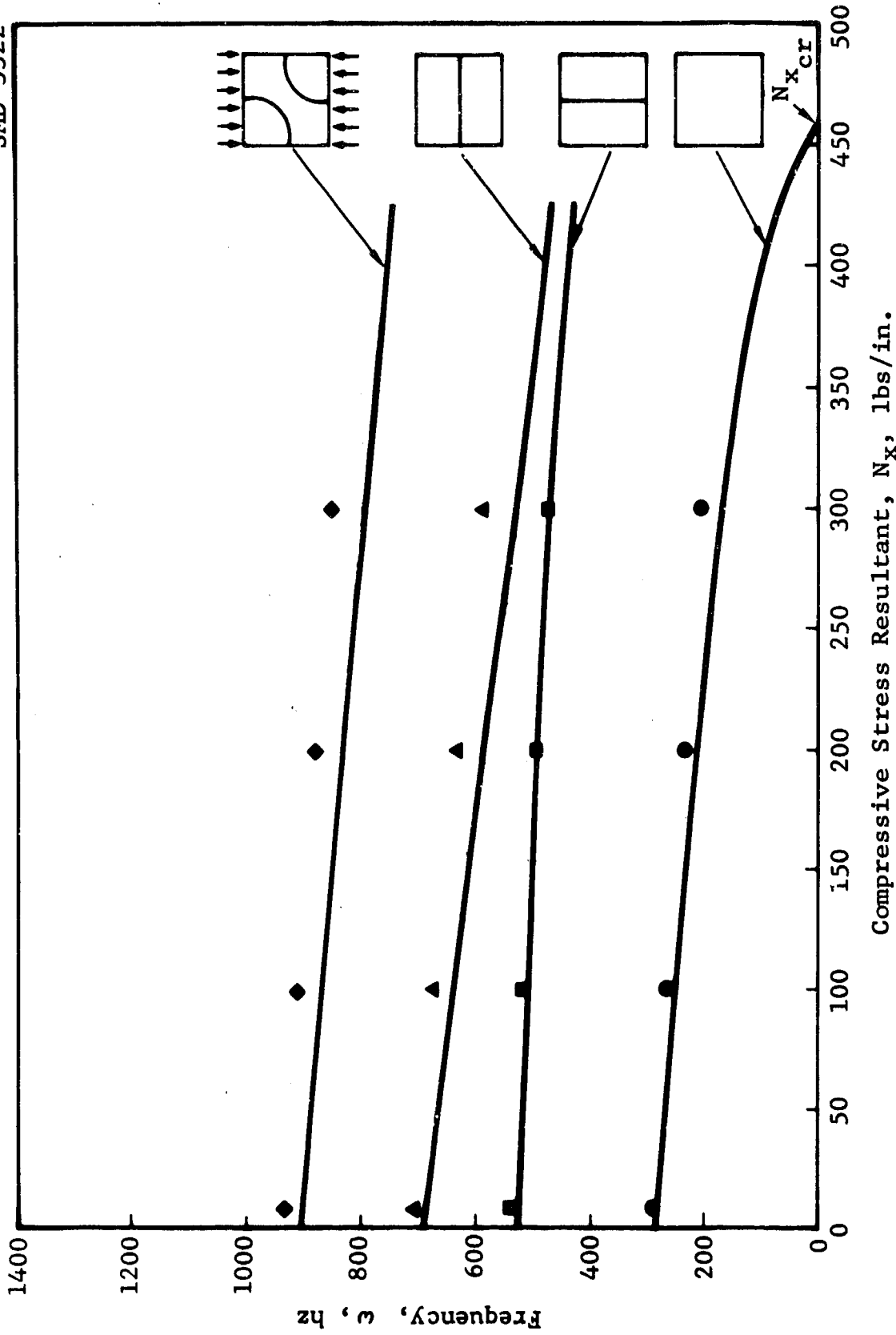


Figure 106 Natural Frequency vs Compressive Stress, Panel 16, Clamped-Simple

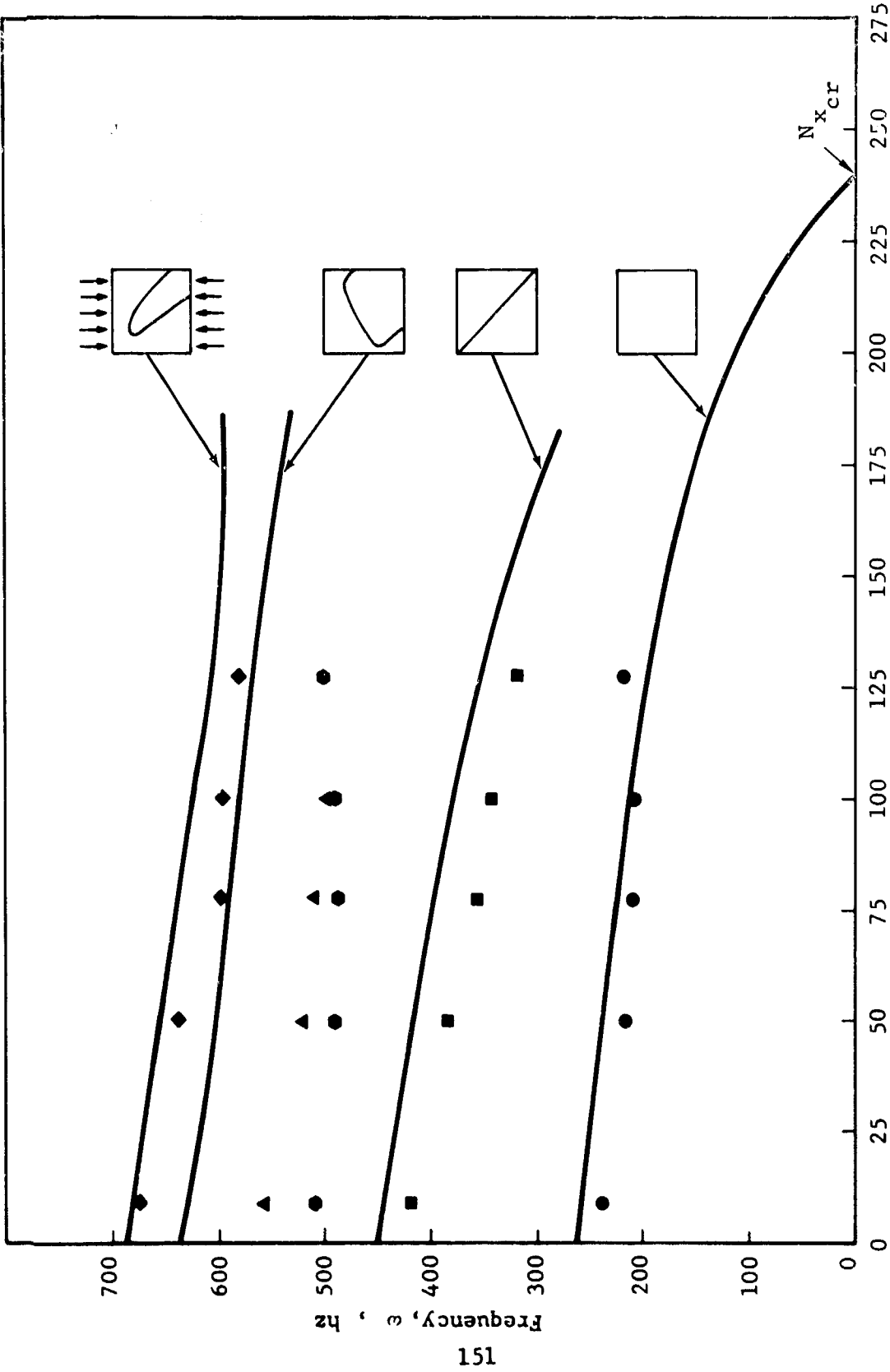


Figure 107 Natural Frequency vs Compressive Stress, Panel 19A, Clamped-Clamped

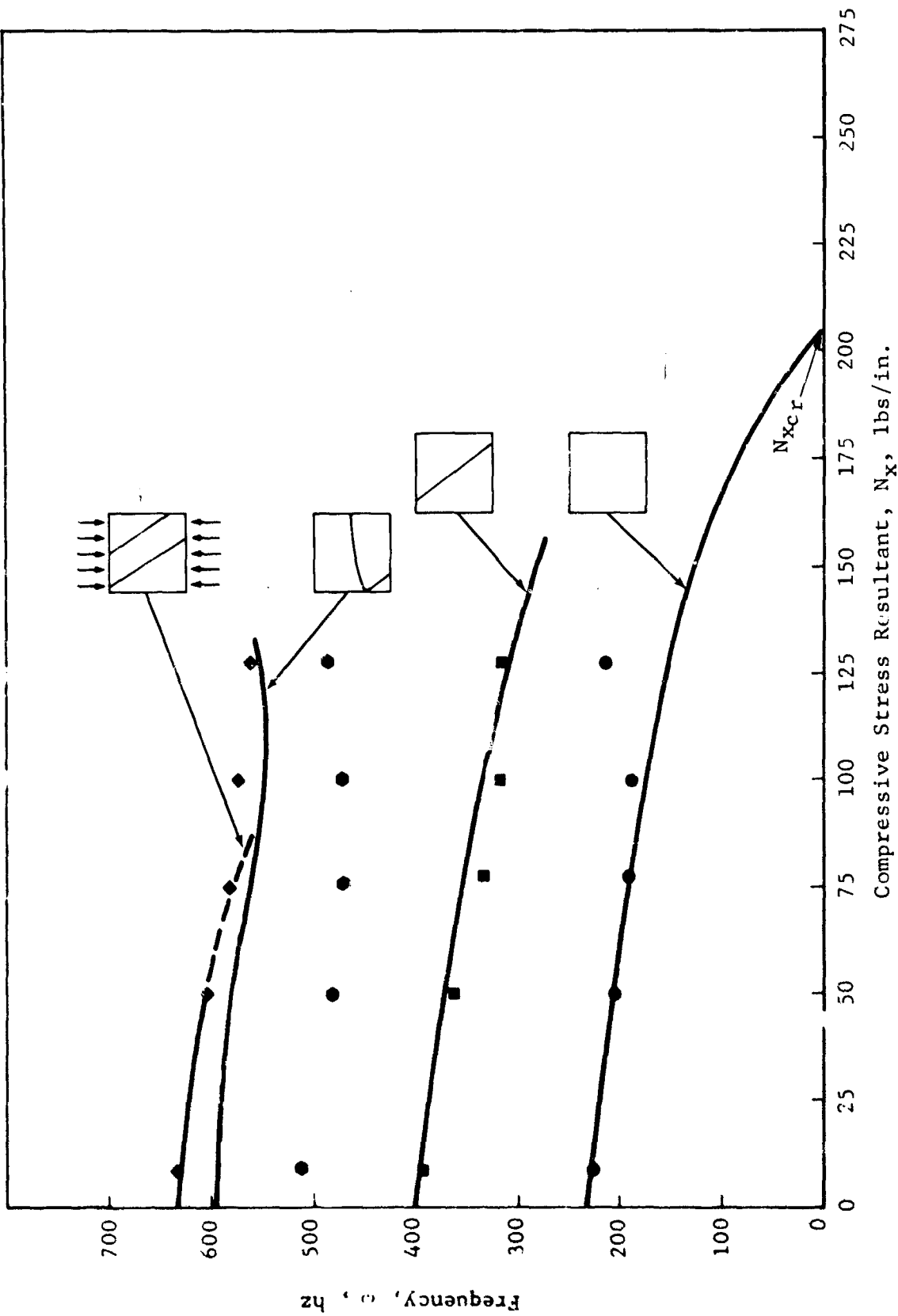


Figure 108 Natural Frequency vs Compressive Stress, Panel 19A, Clamped-Simple

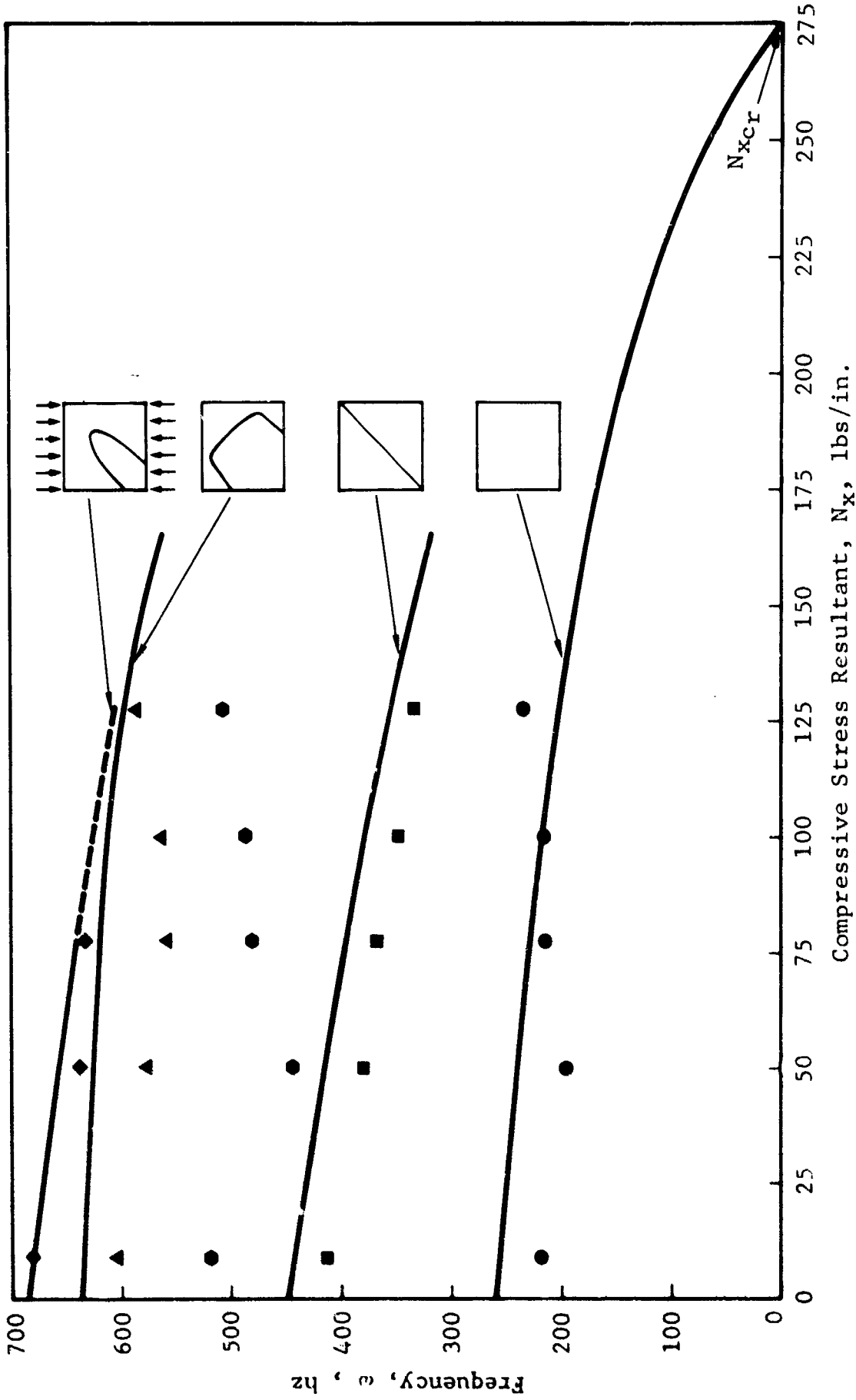


Figure 109 Natural Frequency vs Compressive Stress, Panel 19A, Turned 90°, Clamped-Clamped

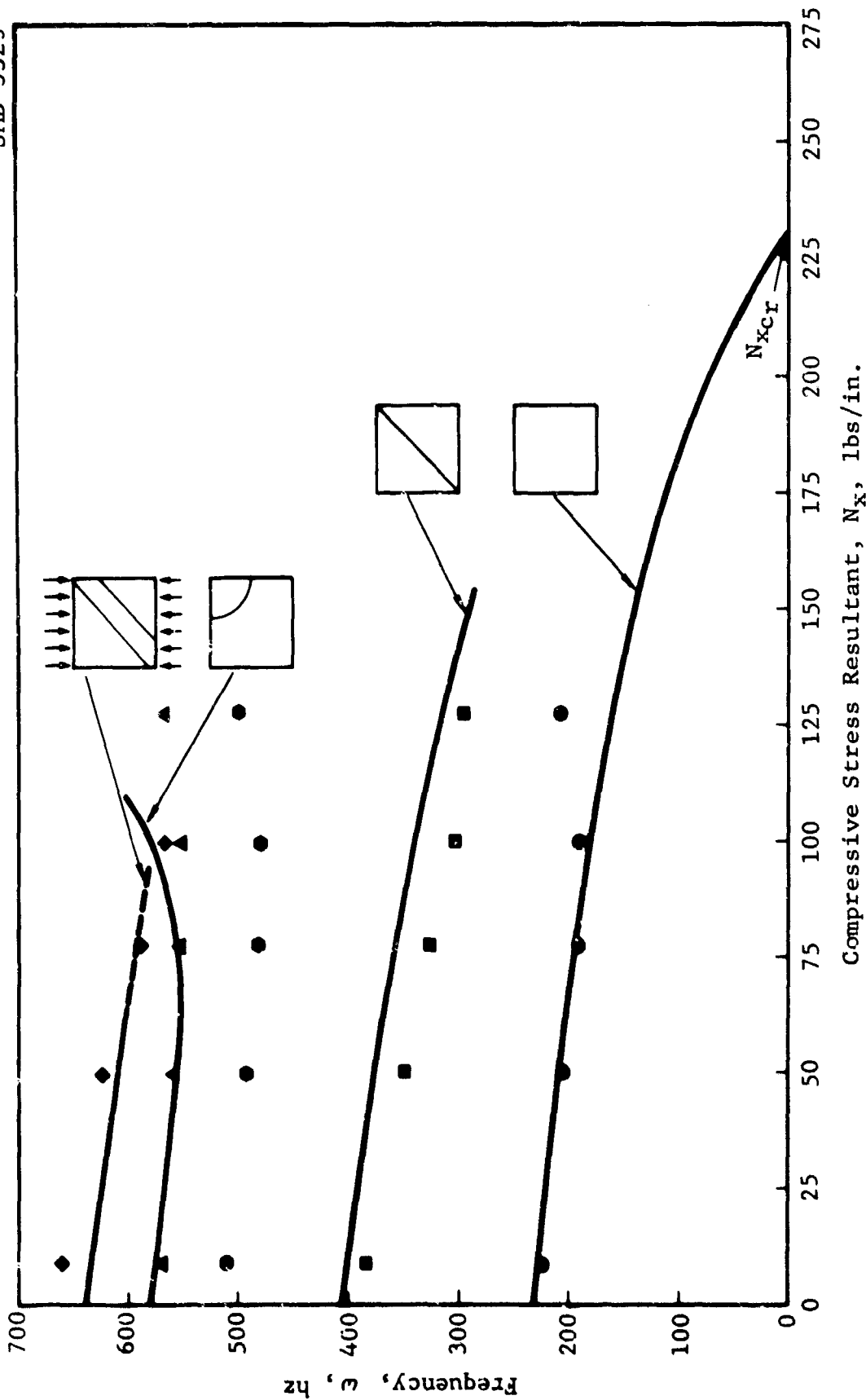


Figure 110 Natural Frequency vs Compressive Stress, Panel 19A, Turned 90°, Clamped-Simple

aluminum panel, has been added to Figures 89 and 90. Agreement between the two sets of data is good.

Correlation between test data and analysis (using the "reduced bending stiffness" approach) for Panel 2 (Unsym $+45^\circ$) was good for the fundamental mode for both boundary conditions as shown in Figures 91 and 92. For the clamped-clamped condition, the second mode was never obtained; instead, a skewed third (vertical) mode appeared. For the clamped-simple condition, the predicted second and third modes crossed over at a higher edge load than observed. A possible explanation may be the closeness of the analytically predicted modes.

Test data for Panel 3 ($0^\circ/90^\circ$) agreed well with the analysis. As shown in Figure 93, the horizontal mode was not lost after the analytical crossover of the second and third modes. Data from both boundary conditions of Panel 5 (0°) also agreed well with the analysis for both test orientations; however, the horizontal mode was again lost for the case of clamped-clamped boundaries, 90-degree test orientation, as illustrated in Figure 97. The data obtained for Panel 7 ($+45^\circ$) are presented in Figures 99 and 100. For the fully clamped condition, all four natural frequencies were obtained for zero edge load. However, for successive loadings, the vertical mode was not obtained. A possible explanation is the closeness of the third and fourth modes as shown in Figure 99. The clamped-simple data (Figure 100) show that the third and fourth modes were observed for all values of N_x even though the two modes were close analytically.

Data from Panel 9 ($+45^\circ$) show excellent agreement with the analytical predictions. Note that the horizontal mode was not lost after crossover of the second and third modes as shown in Figure 102. Excellent agreement was also obtained for Panel 12 ($0^\circ/+45^\circ$). However, for the case of clamped-simple boundaries the horizontal mode (Figure 104) was never obtained.

The data for Panel 16 ($0^\circ/+45^\circ/90^\circ$) are presented in Figures 105 and 106. Note that for the fully fixed boundary condition the horizontal mode was eventually lost even though crossover of the vertical and horizontal modes was observed.

Data obtained for the tapered plate (Panel 19A) are shown in Figures 107 through 110. For one of the clamped-clamped condition (Figure 107), it appears that a shift of the third mode occurred. The shaker may have affected the complicated mode form creating a skewed third mode. A distinct mode, which had not been predicted,

was obtained experimentally between the second and third analytical modes. This mode is represented by the solid, hexagonal points. When the panel was turned 90 degrees, the analysis for the fourth mode did not converge above 75 lbs/in. Experimentally, the fourth mode was coincidentally lost above the same value of N_x . In addition, the unidentified mode was again observed.

When clamped-simple boundaries were used, the analysis did not converge on the fourth mode above the same value of N_x for either position of the panel. For the 0-degree orientation, the third mode was never found experimentally.

The unidentified experimental mode appears again in Figures 108 and 110. Since it is possible that the mode may either have been created by the test technique or may not have been predicted by the analysis due to the assumptions made regarding panel stiffness and/or load distribution, no conclusion can be made as to the validity of the unidentified mode shape.

In the comparisons presented, the agreement between experiment and analysis is generally good for small values of the inplane compressive loading. However, as the compressive loading is increased, a load is reached where the experimentally determined frequencies begin to increase while the analytically predicted frequencies decrease. Generally this divergence between the analysis and experiment begins when the edge load reaches the vicinity of one-half the static buckling load. Previous testing of these panels (Reference 4) indicates that the deflections due to initial curvatures and load eccentricities are generally nearing one-half the plate thickness of this load; consequently, the membrane behavior of the plates should begin to be important. The linear analysis, of course, does not include the large deflection effects, and a zero fundamental frequency is predicted at the static buckling load. No conclusion has been made regarding the disappearance of the horizontal mode in certain instances because of the lack of pattern in this behavior.

SECTION VIII

DIAGONAL TENSION STUDY

One objective of the experimental program was to determine the postbuckling or diagonal tension behavior of nine thin boron-epoxy shear panels having an aspect ratio of 3:1 and then to compare the test data with the analytically predicted buckling loads of computer program RA5. Boundary conditions considered were ideally clamped plates ($\alpha = \beta = \alpha_1 = \beta_1 = \infty$).

Panel thicknesses and orientations were presented in Table II. The input properties used for the RA5 analysis were described in subsection 4.5.

Experimental results are presented in Figures 111, 115, 116, 117, and 120 as plots of applied load versus maximum deflection. These figures are supplemented by photographs showing the deformed surface at various levels of applied load and also the mode of failure. A direct comparison between the curves cannot be made because maximum deflections were used to generate the plots and the location of the point of maximum deflection was not common to all the panels. Also the recorded maximum deflections are only relative maximums.

As shown in Figure 111, the maximum deflections recorded for Panels 1 and 801 were approximately seven times the maximum panel thickness. Failing loads (5890 and 5450 pounds, respectively) were approximately eight times greater than the highest critical buckling load. Dashed horizontal lines in Figure 111 indicate a snap-through of the panels from one buckled shape to another. The first occurrence of the snap-through agrees well with the predicted critical buckling loads. Irregularities in the load-deflection curves may be due to rigid body displacements caused by gradual failure of the panels.

Failure of Panel 1 initiated with cracks at the unpinned corners of the frame and continued as a gradual tearing process (see Figure 112). Initial failure of Panel 801 occurred at the pinned corners of the frame as shown by the photograph sequence in Figure 113. Note the crack growth from Figure 113d to 113e, and also note that the failed panel (Figure 113f) has cracks in all four corners.

To establish whether or not repeated loading has an effect on failing load and deflection, two panels (Panels 1A and 801A)

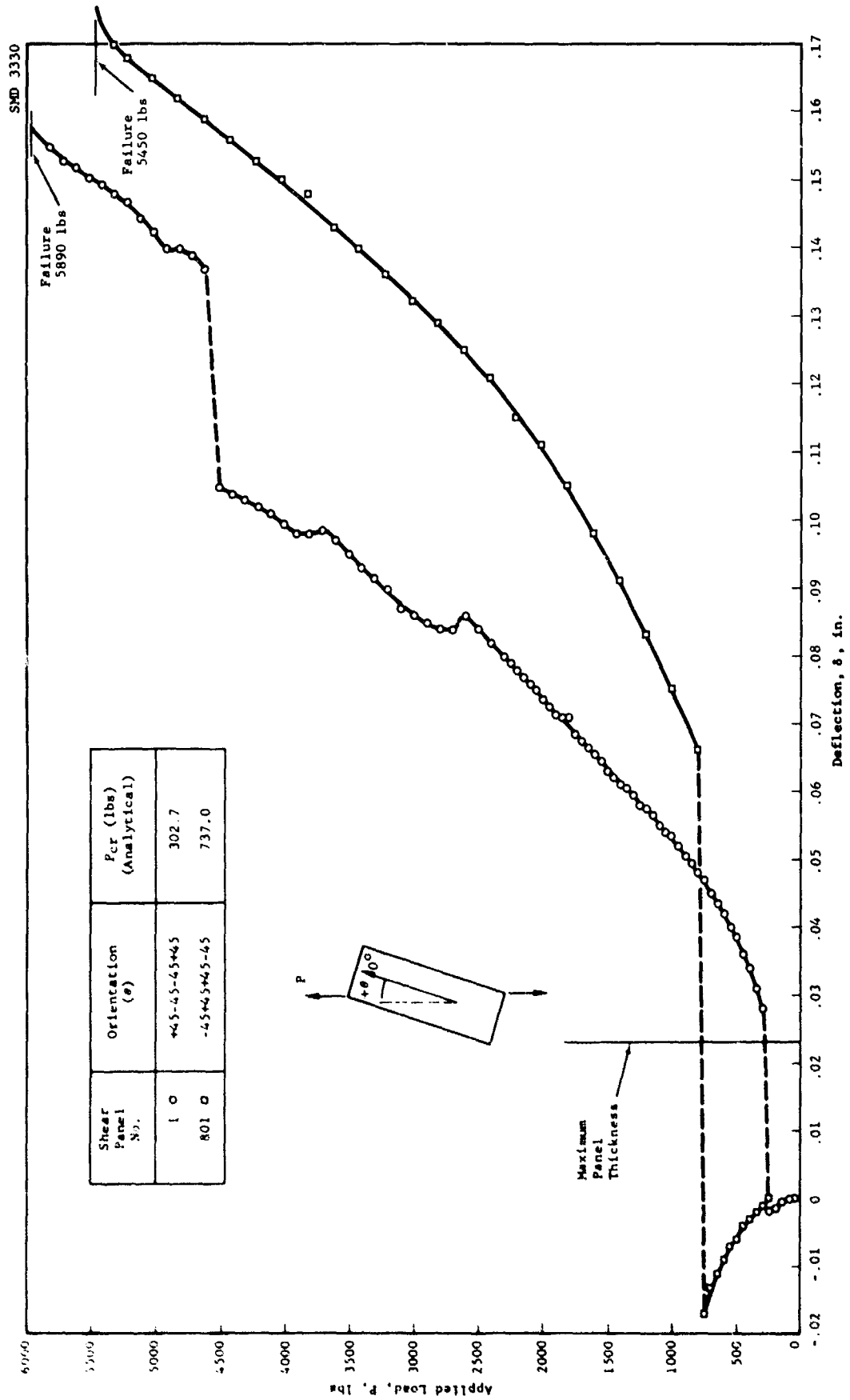


Figure 11i Load-Deflection Curves for Shear Panels 1 and 801

SMD 3331

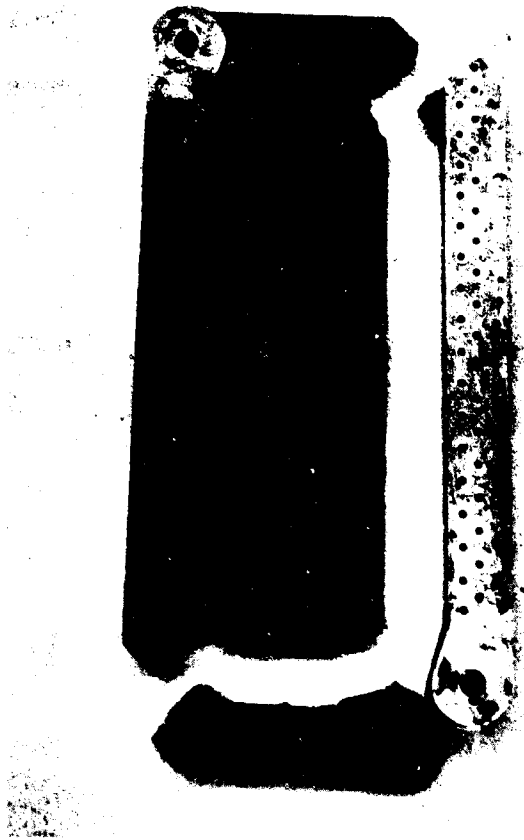
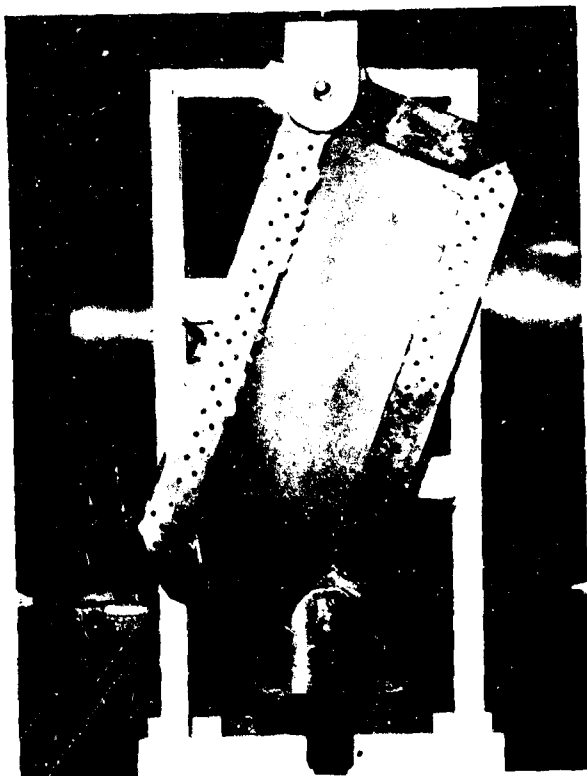


Figure 112 Shear Panel 1 (+45-45-45+45)



(a) P = 1200 lbs



(b) P = 4000 lbs



(c) P = 5000 lbs



(d) P = 5300 lbs

Figure 113 Shear Panel 801 (-45+45+45-45)

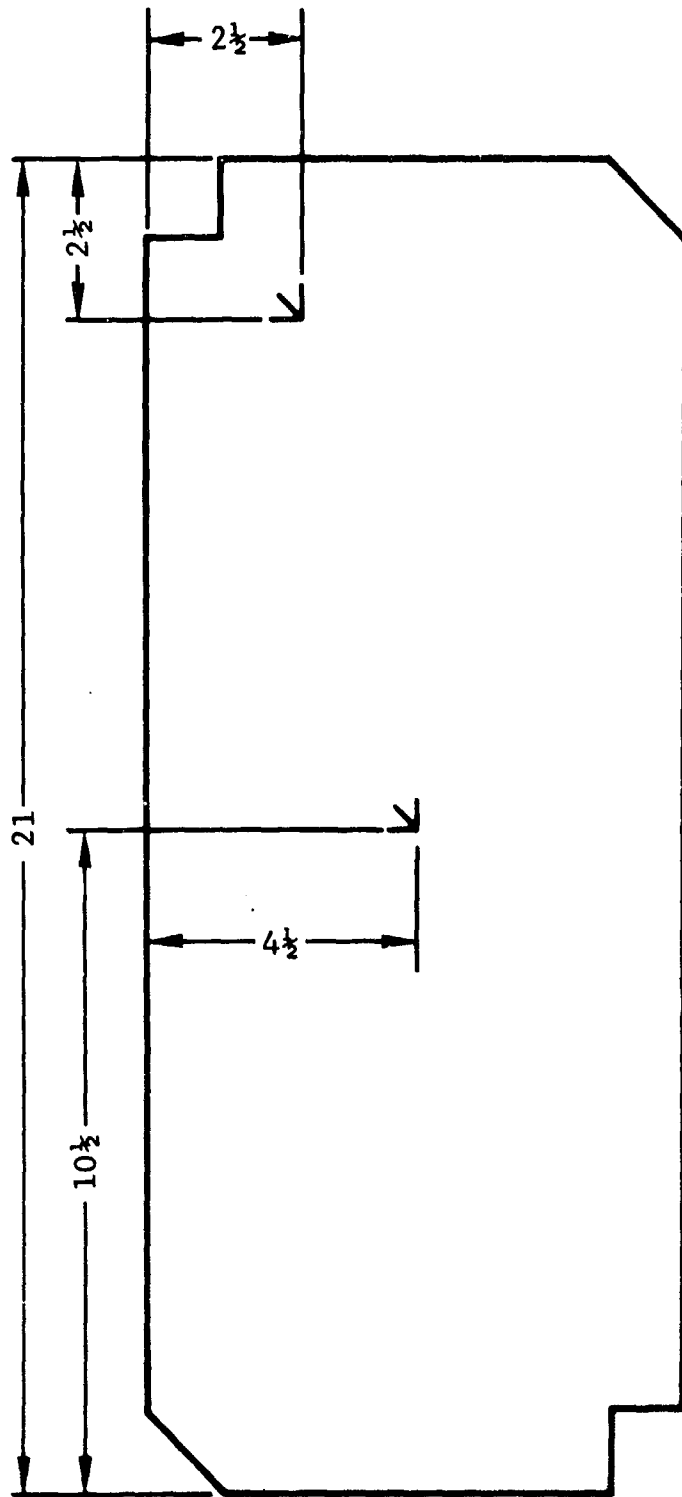


(e) $P = 5400$ lbs



(f) Failed, $P = 5450$ lbs

Figure 113 Shear Panel 801 (-45+45+45-45) (Cont'd)



Notation: ∇ Back-to-back rosettes

Figure 114 Shear Panel Strain Gauge Locations

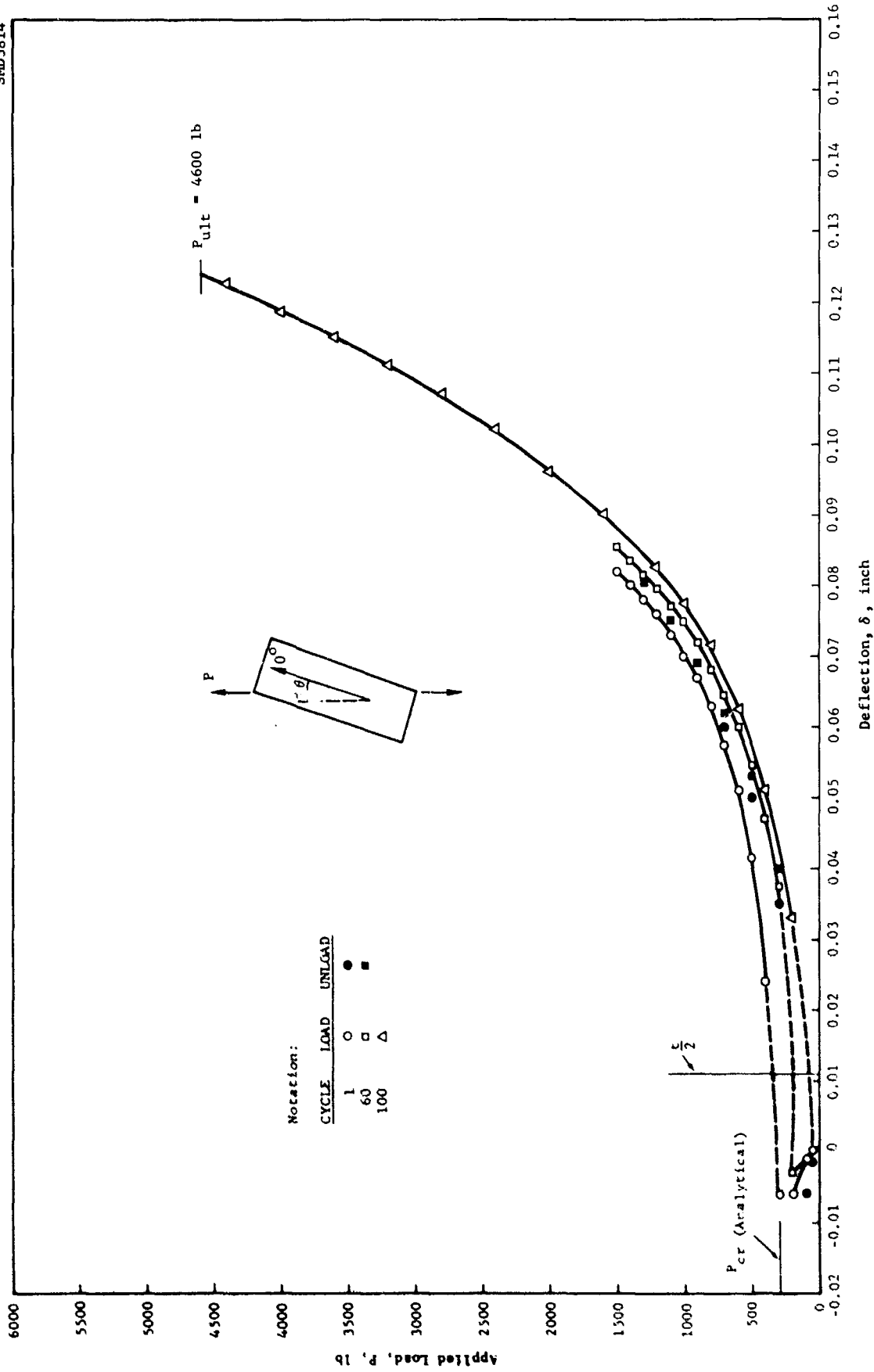


Figure 115 Load-Deflection Curves, Shear Panel 1A

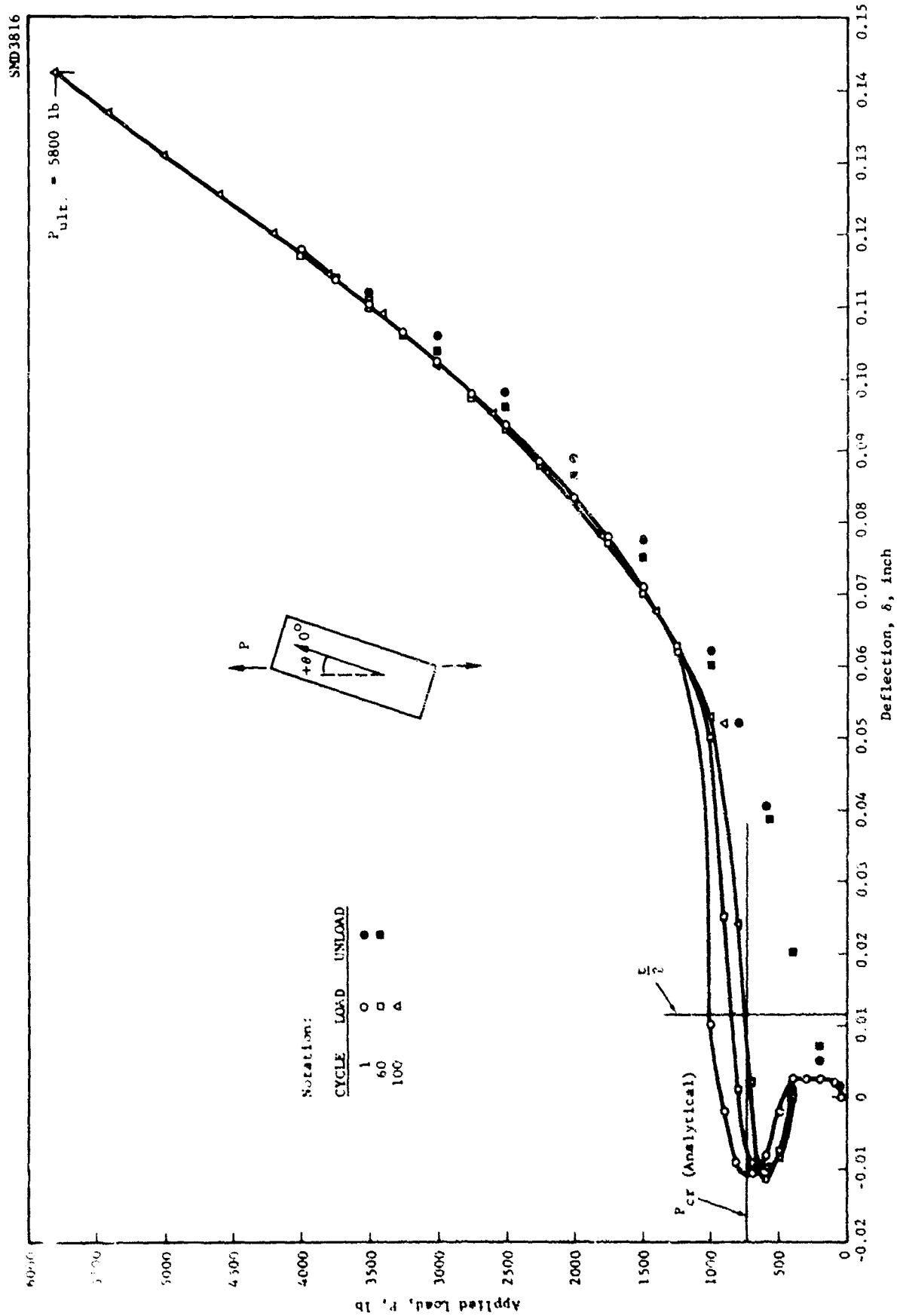


Figure 116 Load-Deflection Curves, Shear Panel 801A

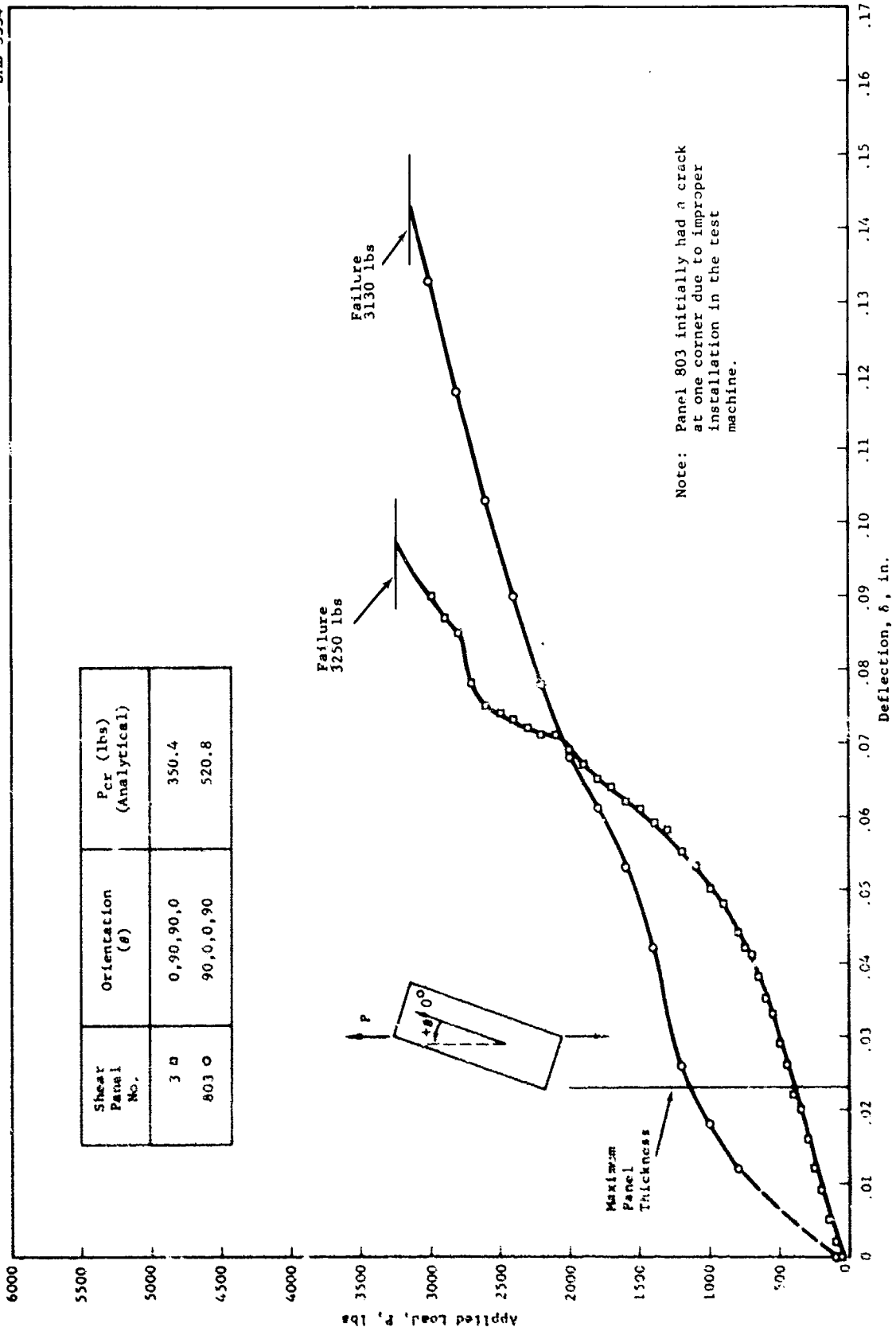
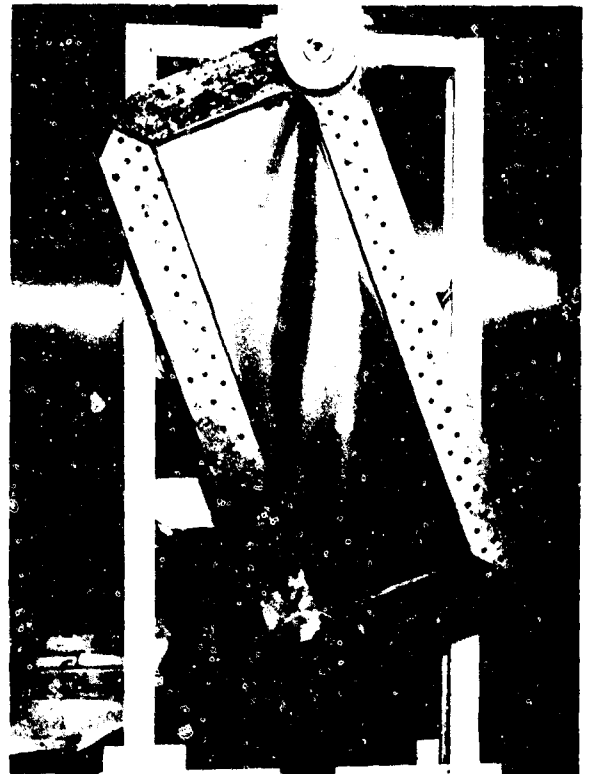


Figure 117 Load-Deflection Curves for Shear Panels 3 and 803



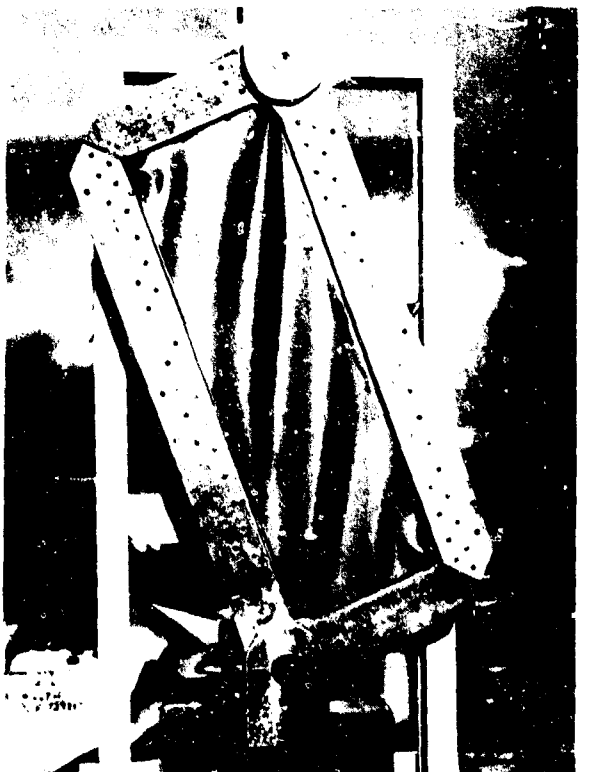
(a) $P = 2000$ lbs



(b) $P = 2700$ lbs



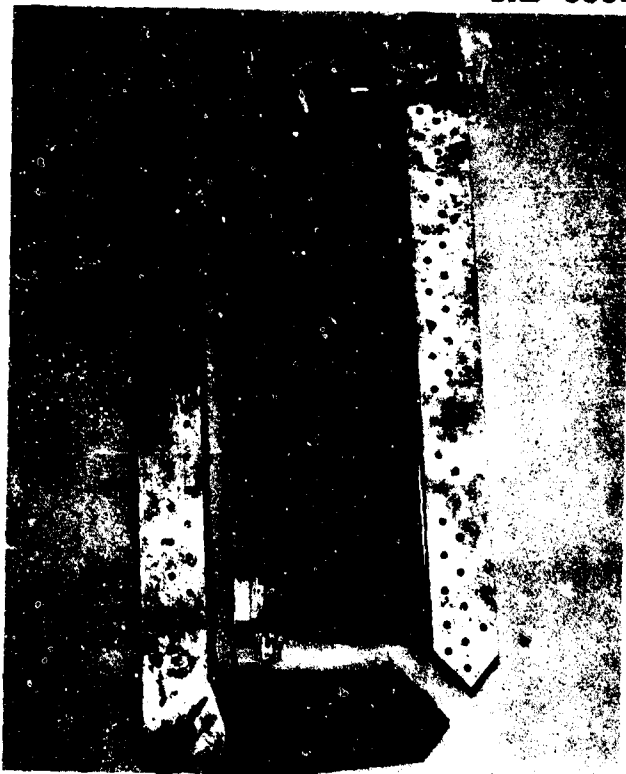
(c) $P = 2900$ lbs



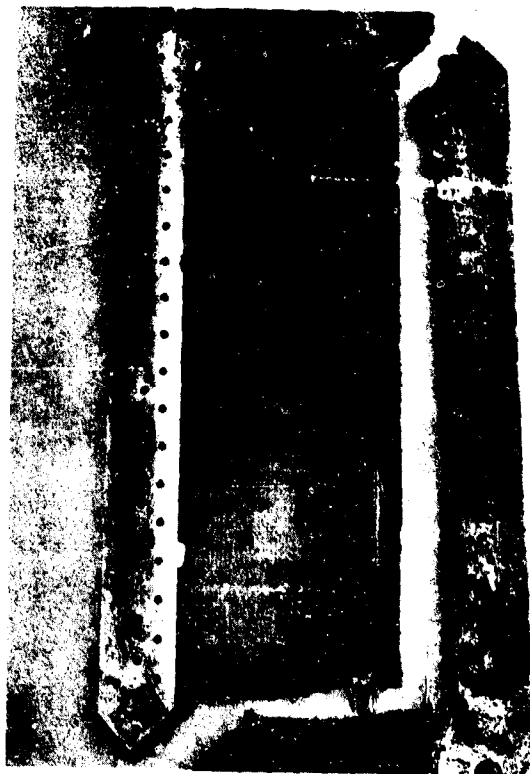
(d) $P = 3100$ lbs

Figure 118 Shear Panel 3 (+0+90+90+0)

SMD 3338



(e) Front View

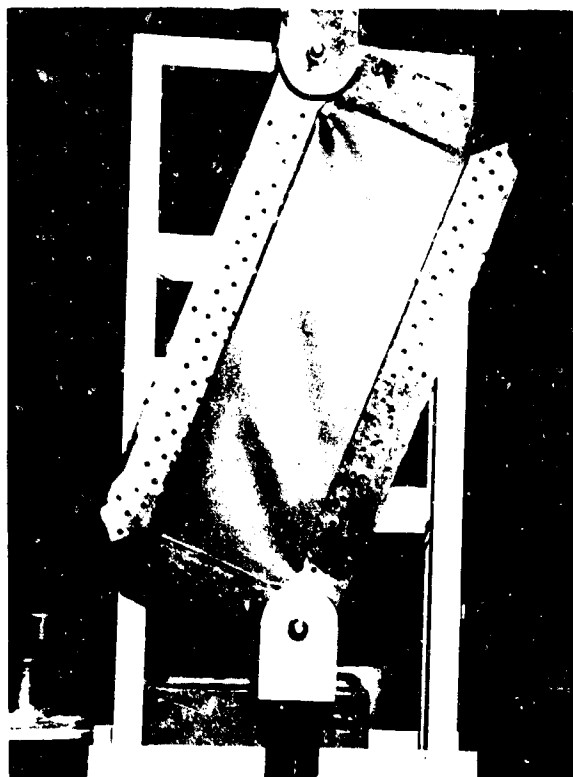


(f) Rear View

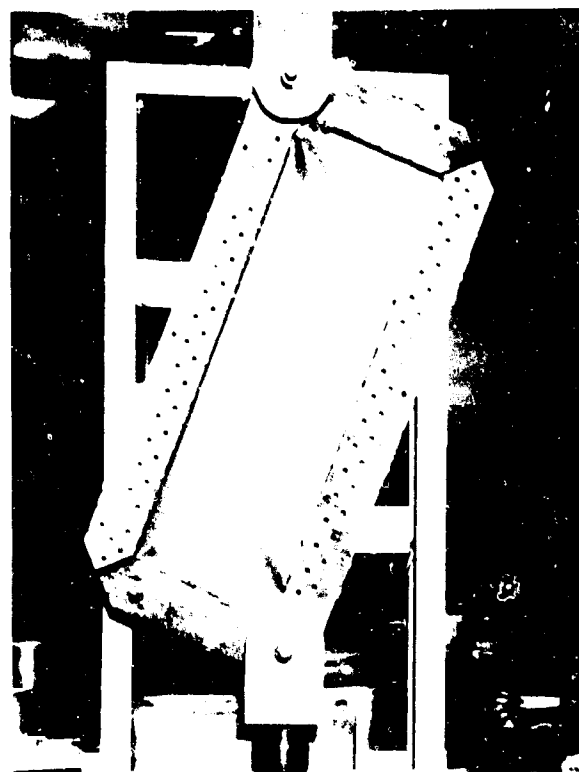
Figure 11 8 Shear Panel 3 (+0+90+90+0) (Cont'd)



(a) Initial Crack



(b) P = 2200 lbs



(c) P = 3000 lbs



(d) Failed, 3130 lbs

Figure 119 Shear Panel 803 (+90+0+0+90)

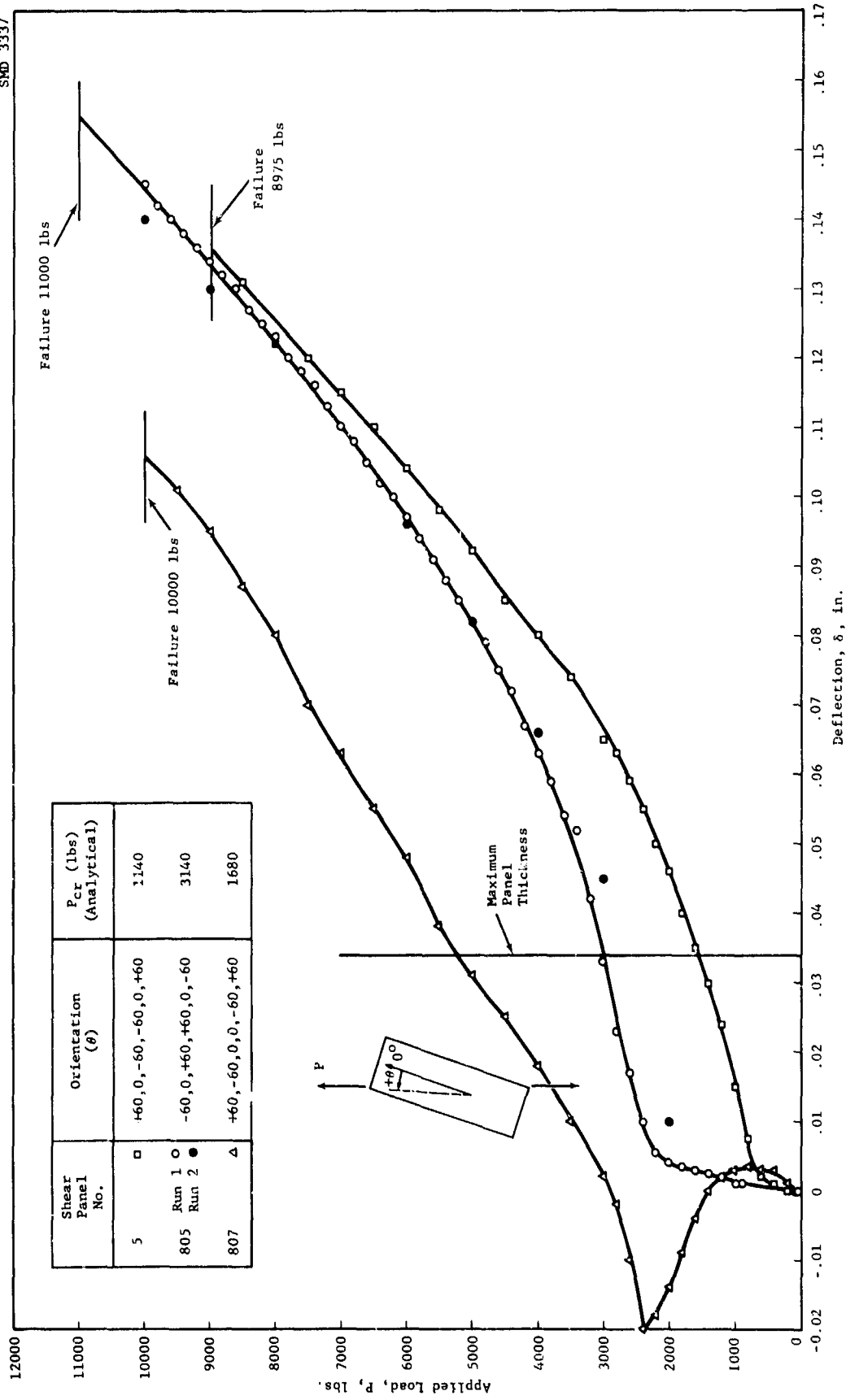


Figure 120 Load-Deflection Curves for Shear Panels 5, 805, and 807

were cycled to an applied load approximately five times their respective buckling loads. Each panel was strain gauged to ascertain the amount of accumulative damage. Strain gauges were located as shown in Figure 114.

Panel 1A was cycled 100 times to an applied load of 1500 pounds, approximately five times its critical buckling load. On the one-hundredth cycle, the panel was loaded to failure. Maximum normal deflection recorded was 0.1225 inch and maximum applied load was 4600 pounds. Failure initiated at the unpinned corners of the panel. Post-failure infrared inspection indicated no evidence of delamination. The strain gauge data indicated that the strains were well below the limit design values implying that initial failure was caused by stress concentrations. Load-deflection curves (Figure 115) of the first, sixtieth and one-hundredth cycles show a slight shift to the right. The load-deflection curve for Panel 1 (Figure 111) indicated a snap-through of the panel from one deformed shape to another at an applied load of 4600 pounds with failure occurring at 5890 pounds. It is possible that the cyclic panel failed while attempting a snap-through into a new deformed shape.

Panel 801A was cycled 100 times to an applied load of 4000 pounds, which is approximately 5.5 times its critical buckling load, and failed on the one-hundredth cycle. Maximum normal deflection recorded was 0.1425 inch and maximum applied load was 5800 pounds. Failure initiated at the unpinned corners of the panel. Strain gauge data taken at one of the pinned corners and at the center of the panel indicated that the strains were below limit design values, implying that the initial failure was caused by stress concentrations. Load-deflection curves of the first, sixtieth, and one-hundredth cycles indicate differences in the shape of the curves below 1250 pounds although they were identical above that value, as shown in Figure 116. The failing load of 5800 pounds compares favorably with those of Panels 1 and 801 (5890 and 5450 pounds, respectively). Infrared inspection of Panel 801A (as well as Panel 1A) indicated no evidence of delamination.

The load-deflection curves for Panels 3 and 803 are presented in Figure 117. Panel 803 was accidentally cracked at the upper, unpinned corner (Figure 119a) during handling. However, the panel sustained a load greater than six times its buckling load and a deflection six times greater than the maximum panel thickness. Failure of the panel initiated at the corner opposite the crack as shown by the sequence of photographs in Figure 119. Panel 3 failed approximately at the same load as Panel 803 but with a maximum deflection only four times greater than the maximum panel thickness. Photographs of the failed panel (Figures 118e and 118f) show a

delamination of the outer plies. The delamination was probably caused by a combination of the tearing action of the failure and the extremely distorted panel shape (Figure 118d). Infrared inspection of both panels indicated no evidence of delamination other than that visually observed.

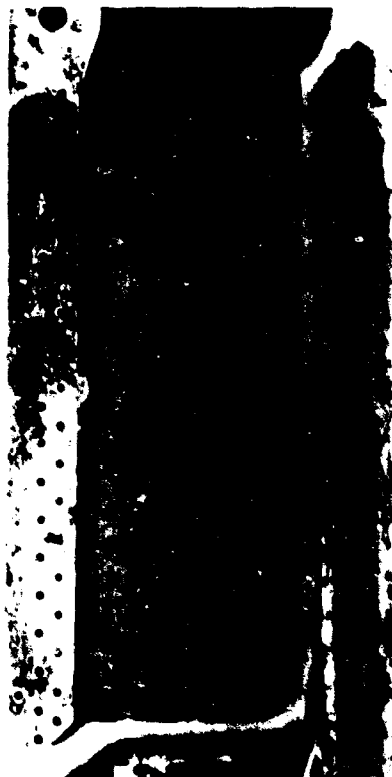
Panels 5, 805, and 807 were thicker (0.034 vs. 0.023 in.) than the previous panels and thus the diagonal tension buckling mode did not develop as well, as shown by Figures 121, 122, and 123. The failing loads averaged 10,000 pounds or approximately three times the critical buckling load. Maximum recorded deflections ranged from 0.101 to 0.145 inch or approximately four times greater than the maximum panel thickness.

The first panel of this sequence to be tested, Panel 805, was initially loaded to 10,000 pounds (solid dots in Figure 120) and then unloaded. Dial gauges were returned to zero and the panel reloaded to failure, which occurred at 11,000 pounds. Infrared inspection of all panels indicated no evidence of delamination.

SMD 3339



(a) $P = 8000$ lbs



(b) Failed, $P = 8975$

Figure 121 Shear Panel 5 (+60+0-60-60+0+60)

SMD 3340



(a) P = 7600 lbs



(b) Failed, 11000 lbs

Figure 122 Shear Panel 805 (-60+0+60+60+0-60)



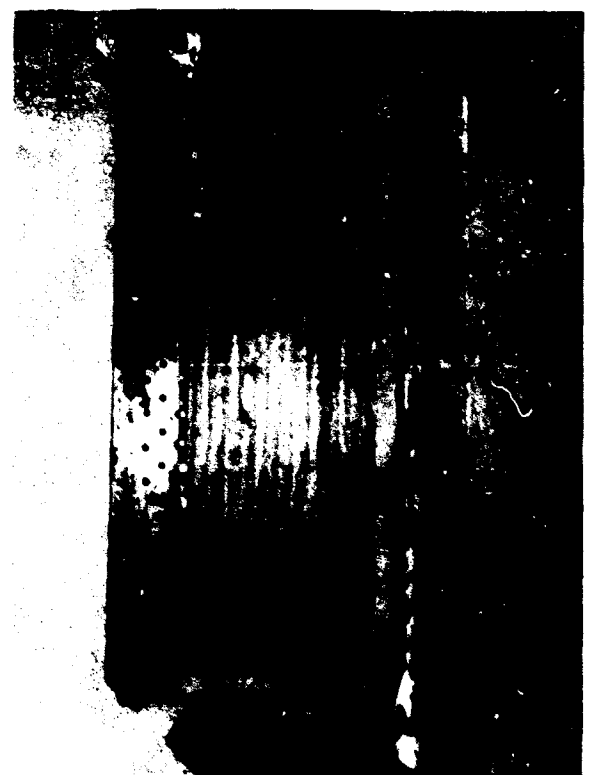
(a) P = 6500 lbs



(b) P = 7500 lbs



(c) P = 9500 lbs



(d) Failed, P = 10000 lbs

Figure 123 Shear Panel 807 (+60-60+0+0-60+60)

S E C T I O N I X

U L T I M A T E L O A D O B S E R V A T I O N S

The purpose of the ultimate load experimental program was to observe the uniaxial compressive mode of failure for boron-epoxy plates. The boundary condition considered was fully-clamped edges. The boron panels used in the study and the configurations tested are detailed in Table XI. Panel thicknesses and orientations were presented in Table I.

Initially only two panels, Panels 3 ($0^{\circ}/90^{\circ}$) and 9 ($+45^{\circ}$), were tested to ultimate in the compression fixture. Each panel was strain gauged to provide information on the inplane load distribution along the compressed edge and along one of the sides. Normal deflections were recorded from dial gauges as in the past.

Panel 9 ($+45^{\circ}$) was selected to determine if sufficient clearance existed between the loading head and the side supports. Panel 3 ($0^{\circ}/90^{\circ}$) was selected to determine if a valid failure mode could be obtained without damage to the fixture.

Panel 3 failed at an applied load of 21,000 pounds, approximately twice its buckling load. Maximum recorded deflection was 0.258 inch as compared to the panel thickness of 0.102 inch. The load-deflection curve is shown in Figure 124. Failure occurred at the top grip of the fixture.

Panel 9 ($+45^{\circ}$) could not be loaded to failure. At a load of approximately 13,000 pounds, the compression head of the test fixture came in contact with the side supports. This caused artificial stiffening of the load-deflection curve (Figure 125). Maximum deflection, recorded at 13,000 pounds, was 0.279 inch.

Instrumentation of Panels 3 ($0^{\circ}/90^{\circ}$) and 9 ($+45^{\circ}$) consisted of back-to-back strain-gauge rosettes located as shown in Figure 126. The resulting inplane load distributions for several levels of applied load, P_x , are summarized in Tables XII and XIII. The load N_x obtained from the strain gauge data is compared with the assumed load distribution (shown by dashed horizontal lines) in Figures 127 and 128.

The load deflection curves (Figures 124 and 125) indicate that the applied load, P_x , corresponding to the limiting maximum

Table XI ULTIMATE LOAD TESTS

Panel Number	Orientation (Degrees)	Test Configurations	
		0°	90°
3	0/90	x	
9	<u>±</u> 45	x	
12	0/ <u>±</u> 45	x	
13	<u>±</u> 30		x
14	<u>±</u> 30	x	
16	0/ <u>±</u> 45/90	x	
21	0		x

SMD3819

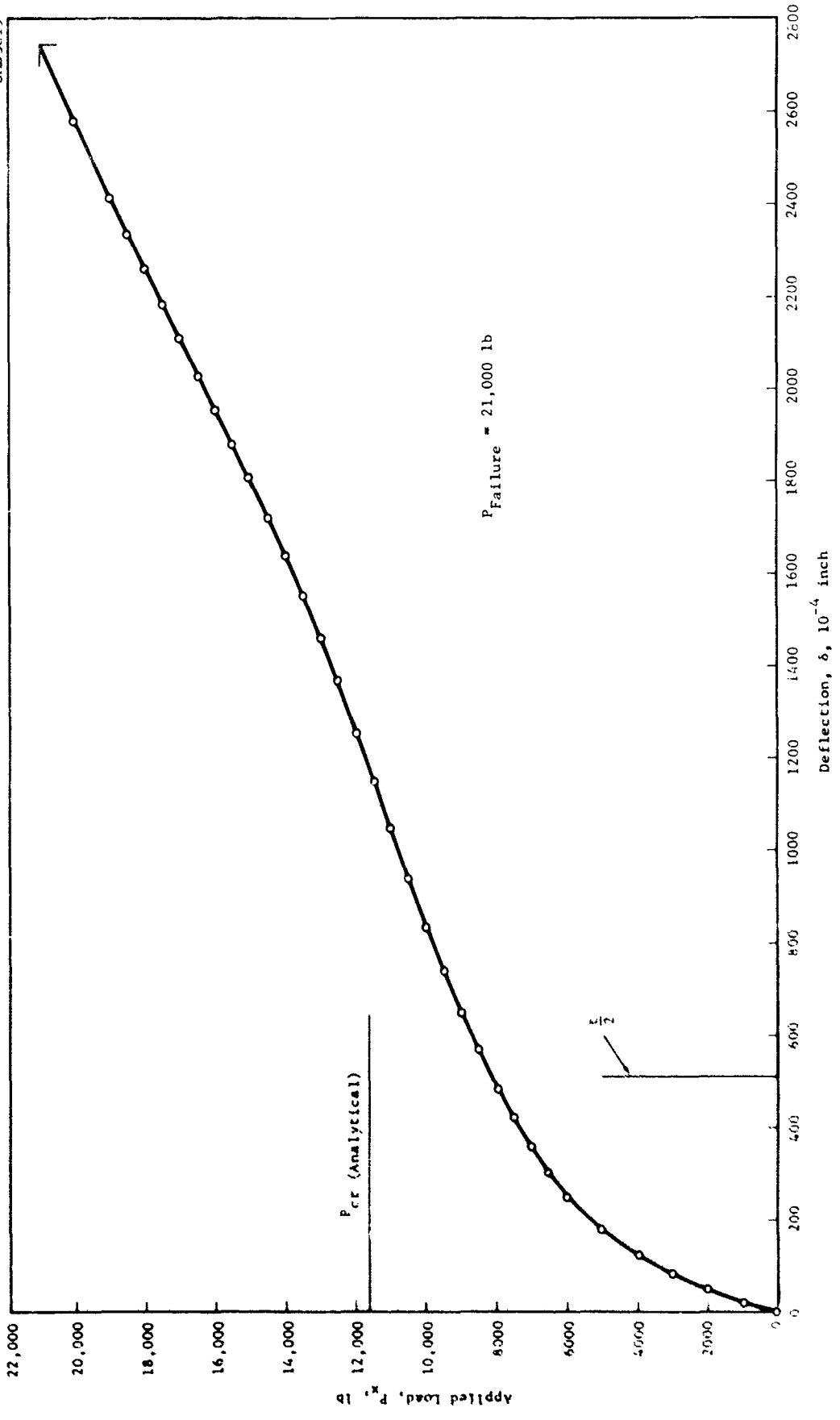


Figure 124 Load-Deflection Curve for Panel 3

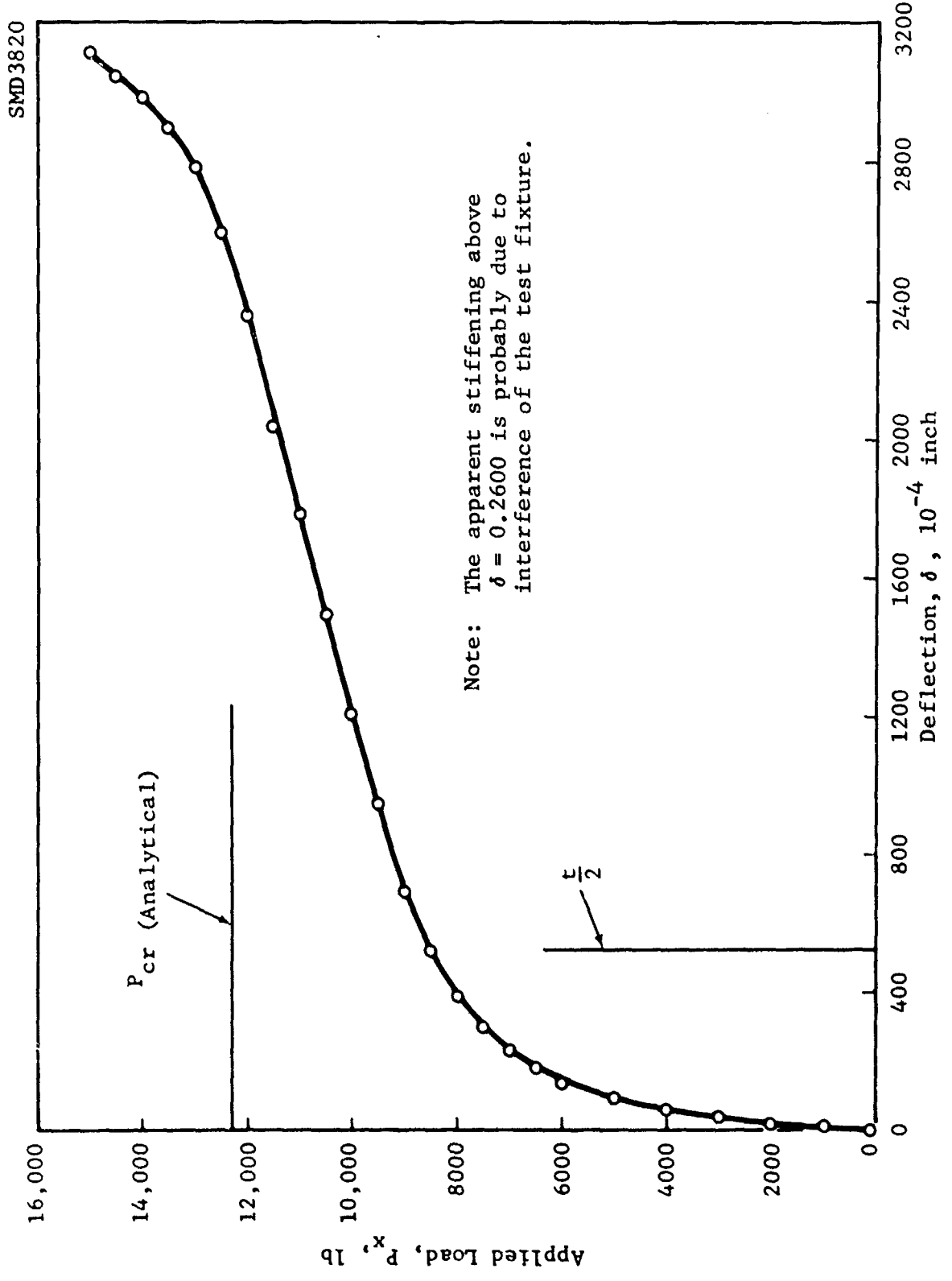


Figure 125 Load-Deflection Curve for Panel 9

Table XII LOAD DISTRIBUTION STUDY, PANEL 3

Applied P_x	Position	N_y	N_x	N_{xy}
- 1000	A	- 19.6	- 40.5	- 8.8
	B	- 8.0	- 65.4	1.5
	C	- 8.5	- 79.8	- 5.6
	D	- 5.8	- 148.4	11.9
- 4000	A	- 30.7	- 185.5	- 30.6
	B	- 29.1	- 283.0	1.6
	C	- 11.7	- 394.4	- 28.4
	D	- 5.9	- 616.4	36.2
- 8000	A	- 50.7	- 699.5	- 35.0
	B	- 55.2	- 537.0	0.2
	C	- 12.3	- 687.2	- 60.5
	D	0.7	-1098.7	48.6
-12000	A	-102.1	-1232.8	- 46.0
	B	-126.6	- 700.6	4.5
	C	- 19.5	- 967.5	-102.7
	D	- 93.6	-1711.3	59.5
-20000	A	-208.8	-2583.2	-106.0
	B	-326.4	- 726.5	1.1
	C	- 40.6	-1510.5	-169.3
	D	227.4	-2981.9	- 19.6

Table XIII LOAD DISTRIBUTION STUDY, PANEL 9

Applied P_x	Position	N_y	N_x	N_{xy}
- 1000	A	- 14.6	- 177.2	38.3
	B	3.0	- 91.4	3.5
	C	- 15.6	- 74.7	- 0.9
	D	- 14.0	- 63.2	4.4
- 4000	A	20.2	- 488.6	116.6
	B	53.6	- 422.3	8.7
	C	24.9	- 397.4	- 11.3
	D	12.5	- 386.9	33.1
- 8000	A	93.0	- 947.0	368.1
	B	117.8	- 847.7	0.9
	C	104.1	- 839.6	- 175.8
	D	93.4	- 815.8	64.4
-12000	A	243.8	-1541.8	1627.4
	B	- 37.7	-1222.7	- 60.9
	C	226.3	-1345.6	1153.1
	D	551.7	-1708.6	178.4

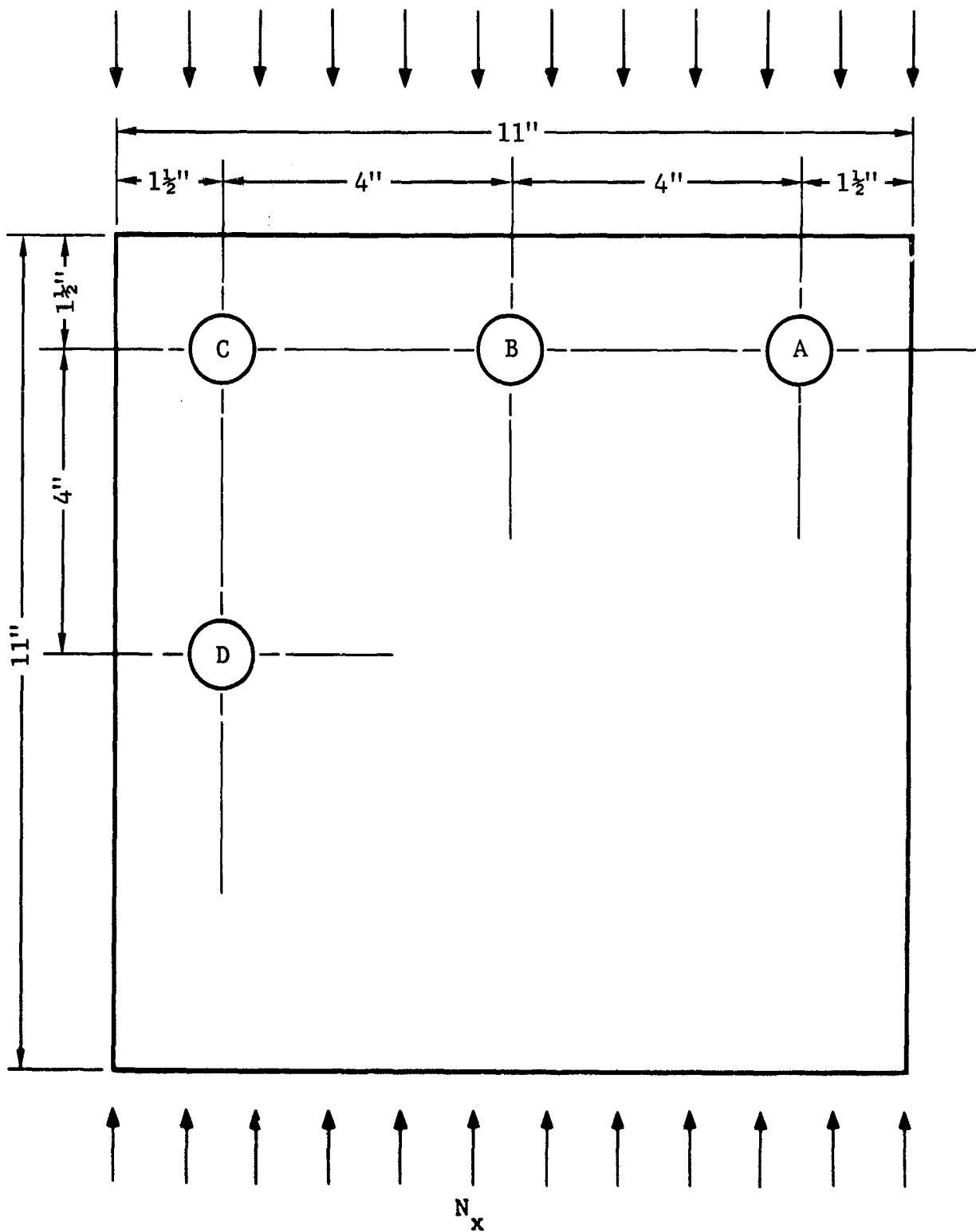


Figure 126 Strain Gauge Locations, Ultimate Load Tests

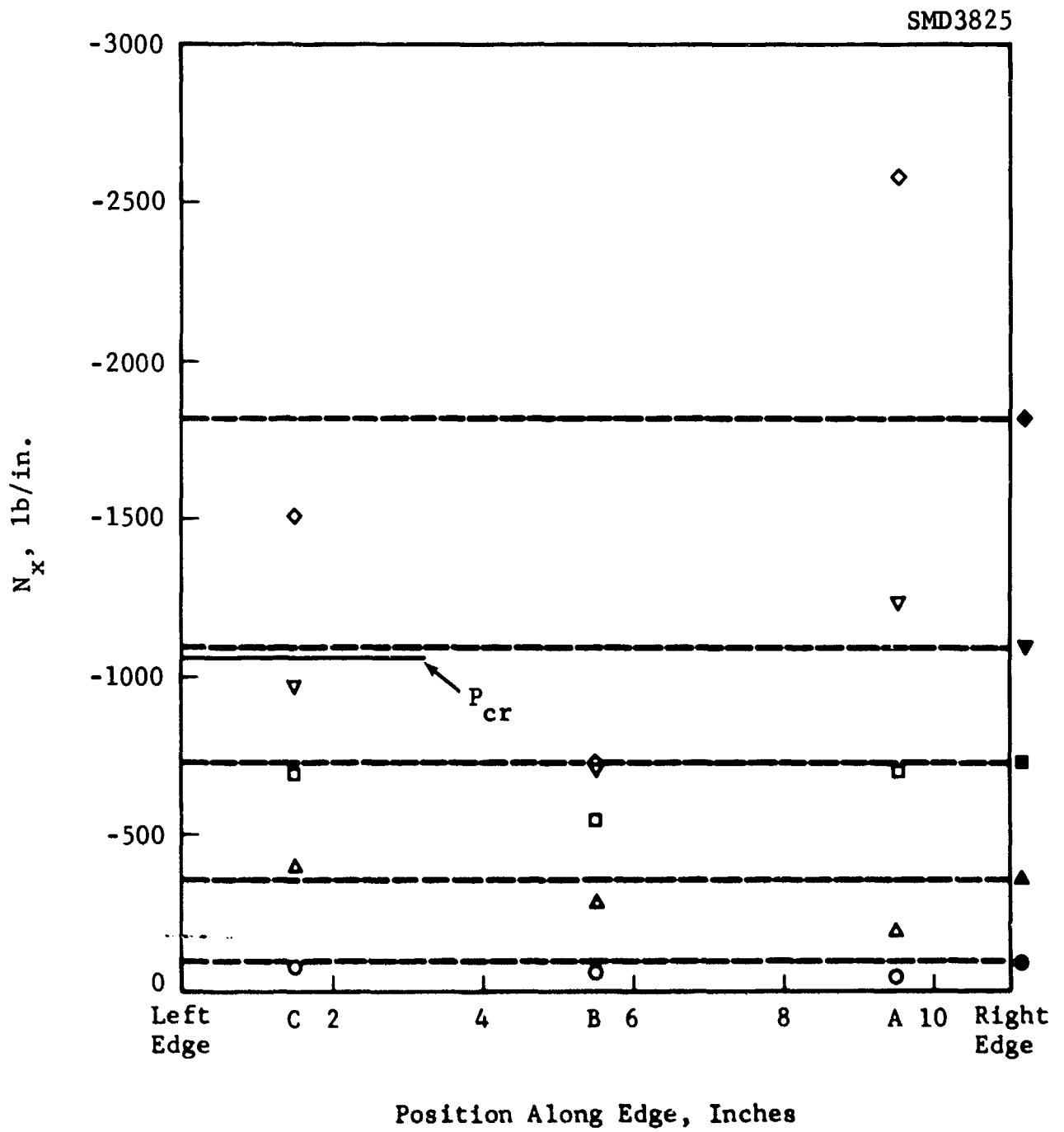


Figure 127 Load Distribution Results, Panel 3

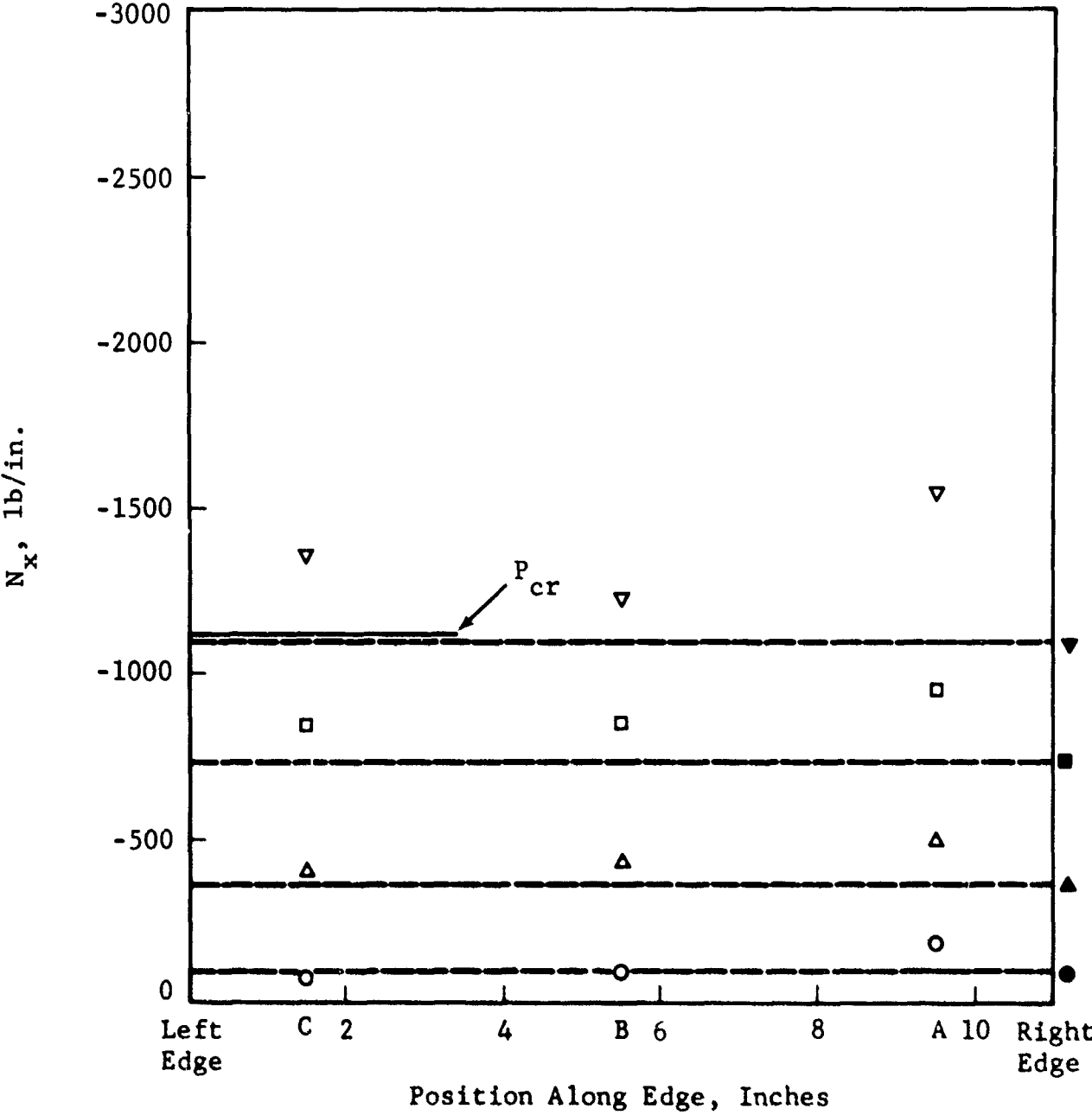


Figure 128 Load Distribution Results, Panel 9

deflection ($t/2$) for either panel was approximately 8000 pounds ($N_x = 727$ lbs/in.). Referring again to Figures 127 and 128, the resultant load distributions exhibit good agreement with the assumed distribution below the value of 727 lbs/in. and tend to peak near the side supports above that value. The peaking of the load above the linear theory limit (set by $t/2$) is caused by the normal deflection of the panels. Where the normal deflections are the greatest, the plate can carry little or no additional load due to its curvature. However, the edges of the plate do carry an increasing amount of stress because they are constrained by the edge supports.

A comparison of positions C and D for Panel 9 ($+45^\circ$) shows good agreement, while a similar comparison for Panel 3 ($0^\circ/90^\circ$) does not. The results must therefore be considered inconclusive.

Panel 12 ($0^\circ/+45^\circ$) failed at an applied load of 26,300 pounds, approximately twice its buckling load of 14,300 pounds. Maximum recorded deflection was 0.285 inch as compared to the panel thickness of 0.112 inch. Failure occurred in the test section parallel to the outer, 0-degree fibers. An initial failure occurred at a load of 23,500 pounds near the left support causing a shift in the load-deflection curve (Figure 129).

Panel 13 ($+30^\circ$), tested as a $+60^\circ$ laminate, could not be loaded to failure because of the interference of the test fixture. The panel did reach a load of 14,500 pounds (Figure 130), which is slightly above its buckling load of 10,550 pounds. Maximum recorded deflection was 0.238 inch as compared to the panel thickness of 0.111 inch.

Panel 14 ($+30^\circ$) failed at an applied load of 21,000 pounds ($P_{cr} = 14,000$ pounds) and a maximum deflection of 0.406 inch ($t = 0.111$) as shown in Figure 131. Failure occurred parallel to the outer fibers midway down the plate adjacent to the left support. The failure extended approximately 3.5 inches inward.

As shown in Figure 132, Panel 16 ($0^\circ/+45^\circ/90^\circ$) failed at an applied load of 14,750 pounds ($P_{cr} = 6320$ pounds) and a maximum deflection of 0.270 inch ($t = 0.084$). The failing mode was crushing of the lower, right-hand corner of the panel.

Panel 21 (0°), tested as an all 90° laminate, failed at the lower clamp at a load of 8250 pounds ($P_{cr} = 5100$ pounds) and a maximum deflection of 0.145 inch ($t = 0.103$). The double mode, which corresponds to the buckling mode, was present until panel failure. The load-deflection curve for this panel is shown in Figure 133.

SMD3829

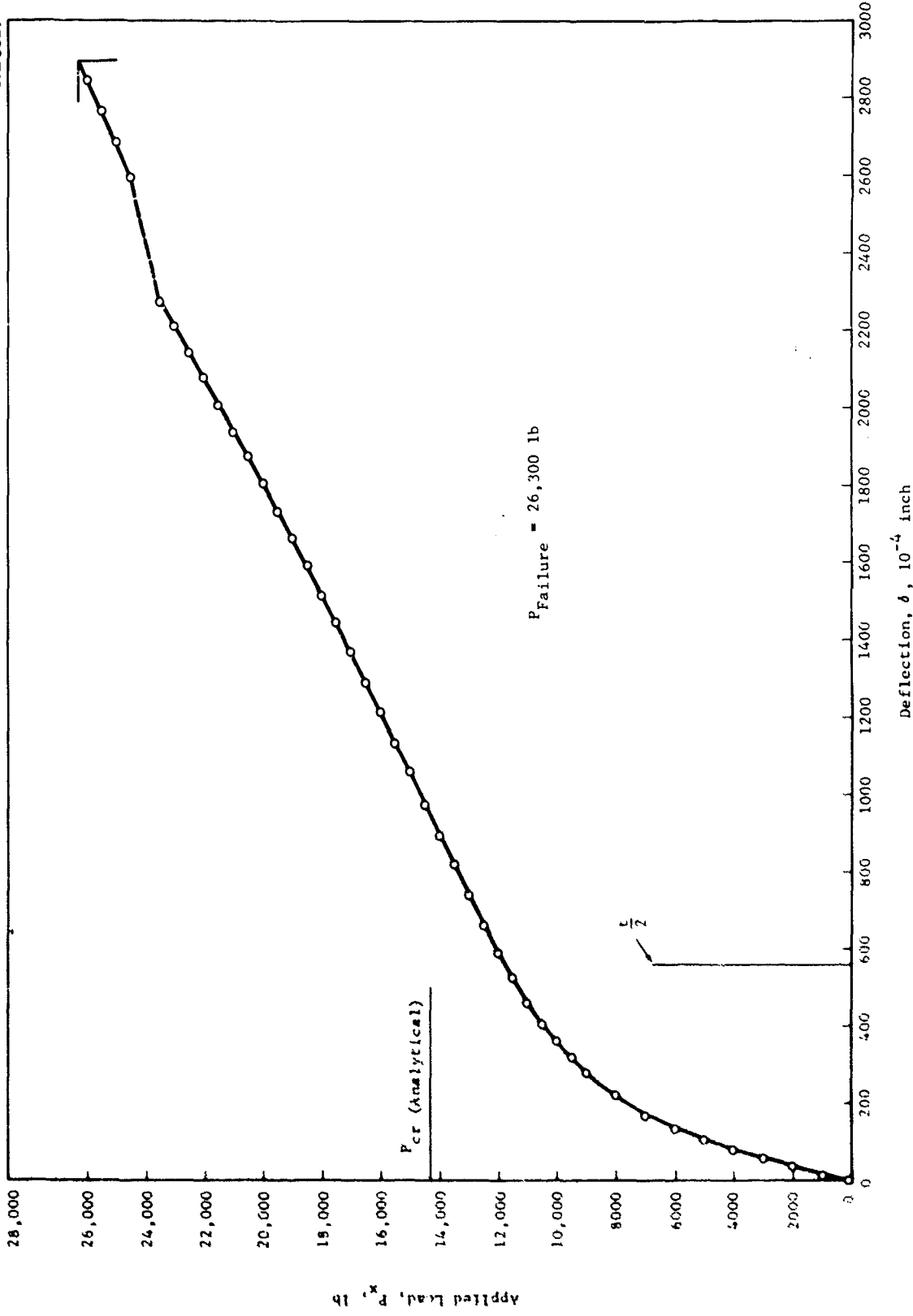


Figure 129 Load-Deflection Curve for Panel 12

SMD3832

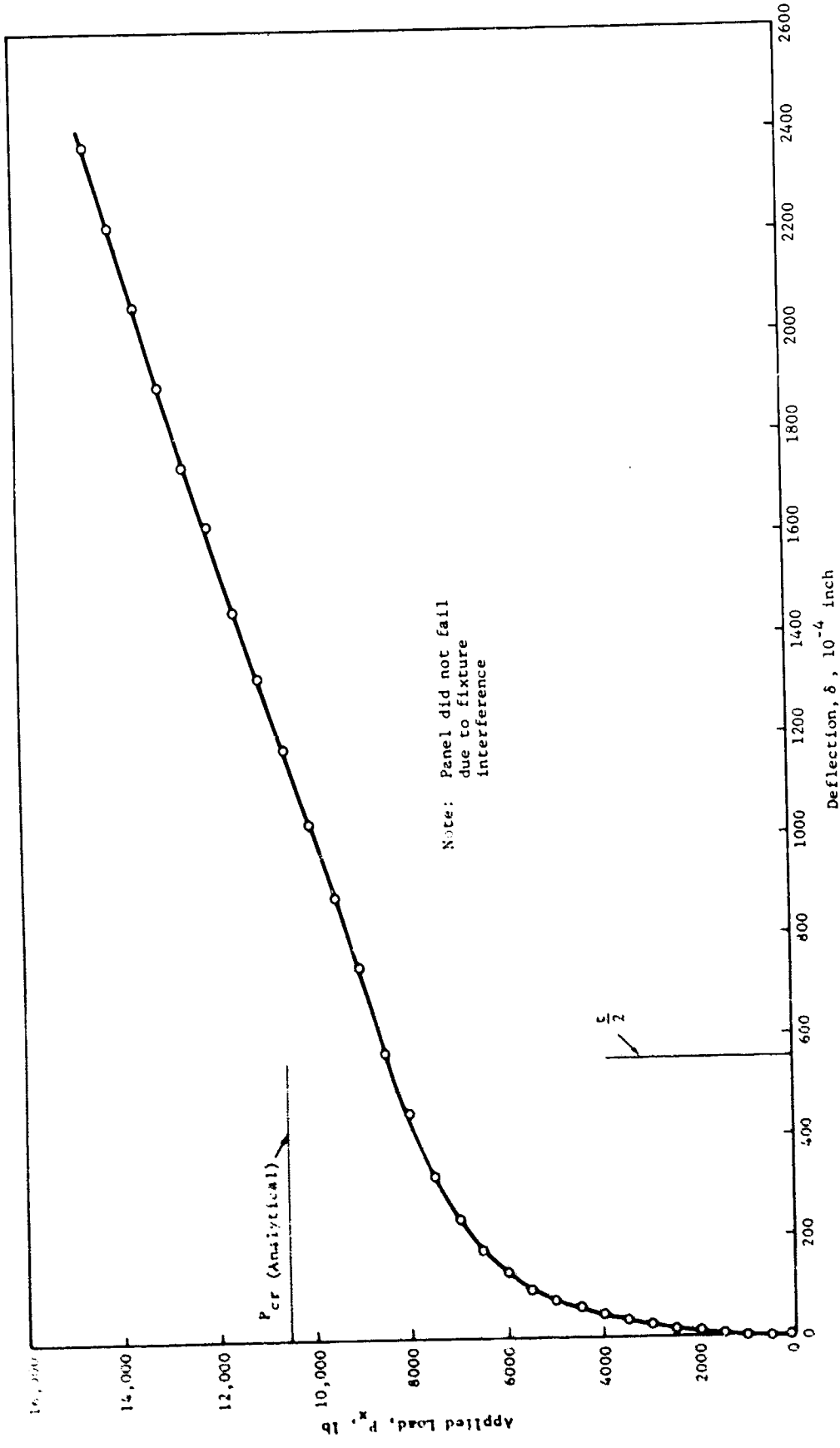


Figure 130 Load-Deflection Curve for Panel 13

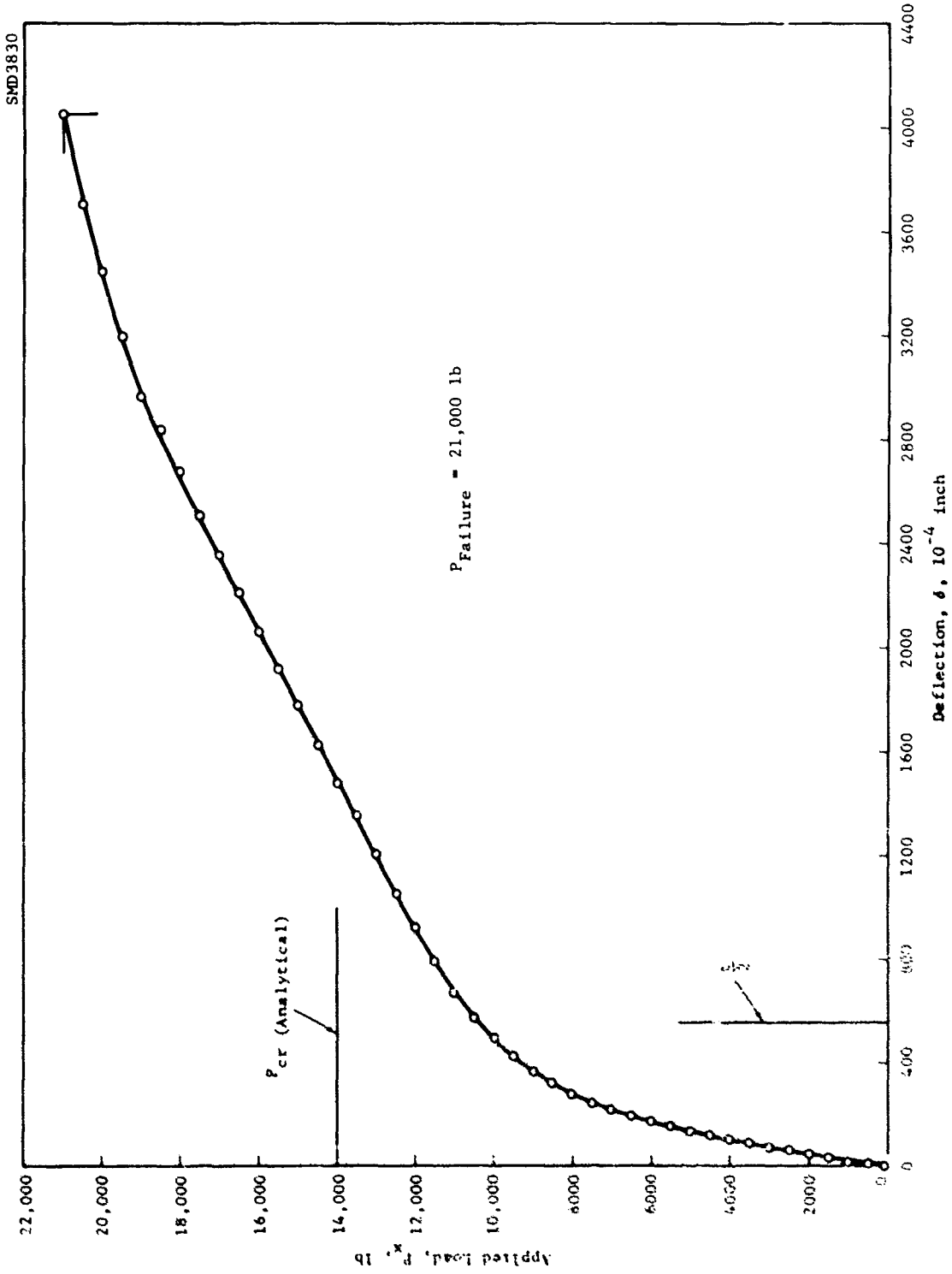


Figure 131 Load-Deflection Curve for Panel 14

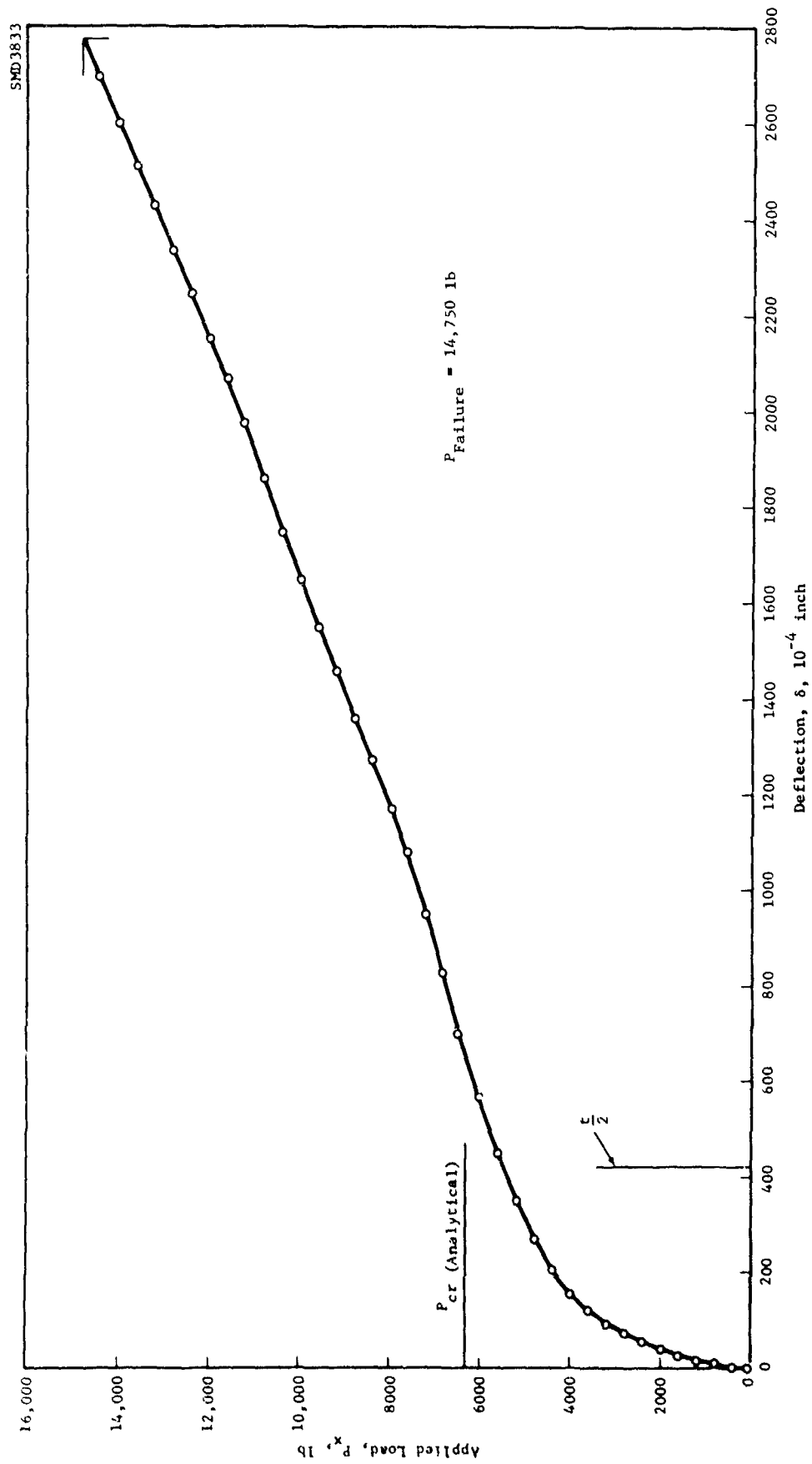


Figure 132 Load-Deflection Curve for Panel 16

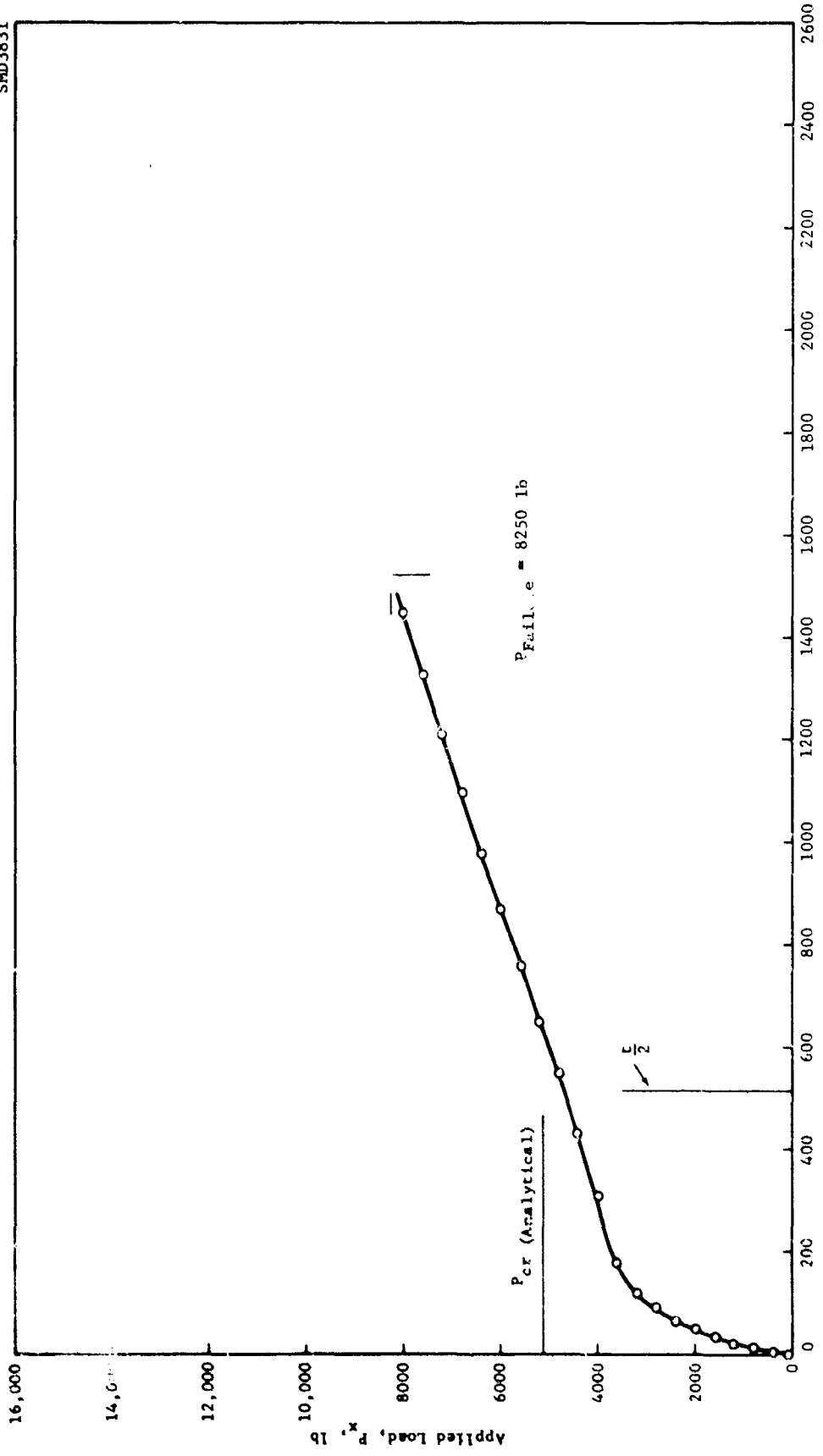


Figure 133 Load-Deflection Curve for Panel 21

Of the seven panels tested, only two (Panels 12 ($0^\circ/\underline{+45^\circ}$) and 14 ($+30^\circ$)) provided satisfactory failures. These two panels and Panel 16 ($0^\circ/\underline{+45^\circ}/90^\circ$) were subjected to infrared inspection. The results indicated no delamination except in the immediate areas of failure, i.e., cracks parallel to the outer, 0-degree fibers for Panel 12; cracks parallel to the outer fibers adjacent to left support for Panel 14; and a crushing of the lower, right-hand corner for Panel 16.

SECTION X
CONCLUSIONS

The results obtained from the experimental program and comparisons with the analytical predictions permit several significant conclusions regarding the small deflection and post-buckling behaviors of flat boron-epoxy plates and the predictions of the Anisotropic Plate Analysis, computer program RA5.

An attempt was made to express the actual experimental boundary conditions analytically using isotropic plate data. The experimental results from the boron panels indicated that the degree of elastic restraint established for the boundary conditions was essentially correct.

In general, experimental results from the transverse load study confirmed the analytical predictions for both loading conditions, lateral load and lateral load combined with uniaxial compression. The second load condition supports the assumption that superposition of loads is valid for composite materials.

Because of the effect of initial imperfections, the prediction of anisotropic plate behavior subject to lateral and inplane loads using linear theory should be restricted to deflections less than the theoretical limit of $t/2$ (as are isotropic plates). It was also found that load-deflection curves that become asymptotic to incorrect eigenvalues could be predicted if the lateral load was assumed perfectly symmetric. A method has been proposed to alleviate this situation.

Experimental results from the biaxial load study generally confirmed the analytical predictions. Agreement between the analytical and experimental results of the natural frequency study was excellent until the compressive load reached approximately one-half of the buckling load. At that load, deflections due to initial curvatures and load eccentricities approach one-half the plate thickness, and consequently the membrane behavior of the plates becomes important.

Results from the post-buckling study on the shear panels showed that the panels sustained loads many times greater than their buckling loads and deflections several times greater than their thicknesses. The results also indicated that the failing load for a given laminate was not severely affected by the

lay-up sequence. Finally, infrared inspection of all the shear panels produced no evidence to indicate that delamination was a primary failure mode for thin laminates taken into the diagonal tension buckling region.

The post-buckling study on the boron-epoxy compression panels showed that their load-deflection behavior above the critical buckling load was similar to that of isotropic panels. In addition, infrared inspection of three failed plates indicated no delamination except in the immediate areas of their failures.

A P P E N D I X I

S O U T H W E L L ' S M E T H O D

The critical buckling load can be determined by using a method recommended by R. V. Southwell (Reference 6) and described briefly as follows:

Southwell has shown that near the critical buckling load the relationship between the deflections, externally applied load, and the critical buckling load can be expressed as:

$$\delta = \frac{a_1}{\frac{P_{cr}}{P} - 1} \quad (24)$$

where

δ = deflection

a_1 = constant

P = applied load

P_{cr} = critical buckling load.

Rewriting Equation (24) in a more usable form,

$$\frac{\delta}{P} P_{cr} - \delta = a_1 \quad , \quad (25)$$

it is apparent that a plot of δ/P versus δ should yield a straight line (near the critical buckling load). Furthermore, the slope of this line is equal to $1/P_{cr}$.

Care must be used in selecting the region in which the Southwell hypothesis applies. Points on the δ/P versus δ plots corresponding to a maximum deflection greater than one-half the plate's thickness cannot be used (membrane stiffening action begins to become important) and points well below the buckling region will also not follow a straight line relationship (Reference 11).

For a state of biaxial compression, it appears obvious that one should obtain the critical buckling load by applying Southwell's method to a crossplot of load-deflection curves, such as those shown in Figure 134, for a given stress ratio N_x/N_y . To do so without prior knowledge of the range of P_y required to produce an accurate Southwell plot would require many curves.

An alternative procedure is to assume that the predetermined load P_y detracts from the stiffness of the panel and the problem reduces to one of experimentally determining the uniaxial buckling load of an equivalent plate with reduced stiffness. An initial attempt using this method resulted in a gross overestimation of the buckling load. For example, consider the load-deflection curve (Figure 134) for P_y equal to 5960 pounds; the corresponding Southwell plot is shown in the upper portion of Figure 135, where the predicted buckling load P_{xcr} was found to be 49,000 pounds.

Southwell's method can, however, be used to predict the critical buckling load if one divides the deflection by the sum of the corresponding axial loads. A Southwell plot using this procedure, bottom portion of Figure 135, results in a predicted buckling load P_{xcr} of 19,640 pounds. The corresponding stress ratio N_x/N_y is 0.304. The Southwell plot obtained by crossplotting the load-deflection curves (Figure 134) for a stress ratio of 0.304 is shown in Figure 136. The predicted buckling load was 19,000 pounds.

Since all three procedures appear analytically valid, an investigation was conducted to ascertain the cause of the differences in the buckling values. The study was performed using a unit isotropic panel with an applied lateral load of 1 psi and an axial load P_y of 40 pounds. Plate stiffness, D , was arbitrarily set at 1.0 pound-inch and Poisson's ratio at 0.3. The analytical load-deflection curve and Southwell plots using the two alternative methods are shown in Figure 137. Identical buckling load predictions ($P_{xcr} = 65.5$ lb) were obtained. The reason for the differences in the buckling values of the aluminum plate lies in the location of the data points of the Southwell plots. In Figure 137, the straight line for δ/P_x passes through the asymptote using only two points, while that for the aluminum plate data (Figure 135) passed through the apparent asymptote. The procedure utilizing $\delta/(P_x + P_y)$ permits more points of the load-deflection curve to fall in line for the Southwell plot as shown by the example in Figure 137. The experimental aluminum Southwell plot (Figure 135) generated in the same manner exhibited an identical trend.

A study of Figure 135 indicates that when the method employing δ/P_x is used, the deflections approach half the plate thickness before the Southwell plot becomes linear. These large deflections result in a stiffening due to the induced inplane restraint and thus a lower slope for the Southwell plot and an overestimation of the buckling load. Based upon this conclusion, a decision was made to plot $\delta/(P_x + P_y)$ versus δ for the biaxial compression tests. The straight line region was determined graphically, emphasizing the larger deflections, but keeping the maximum deflection below half the plate thickness.

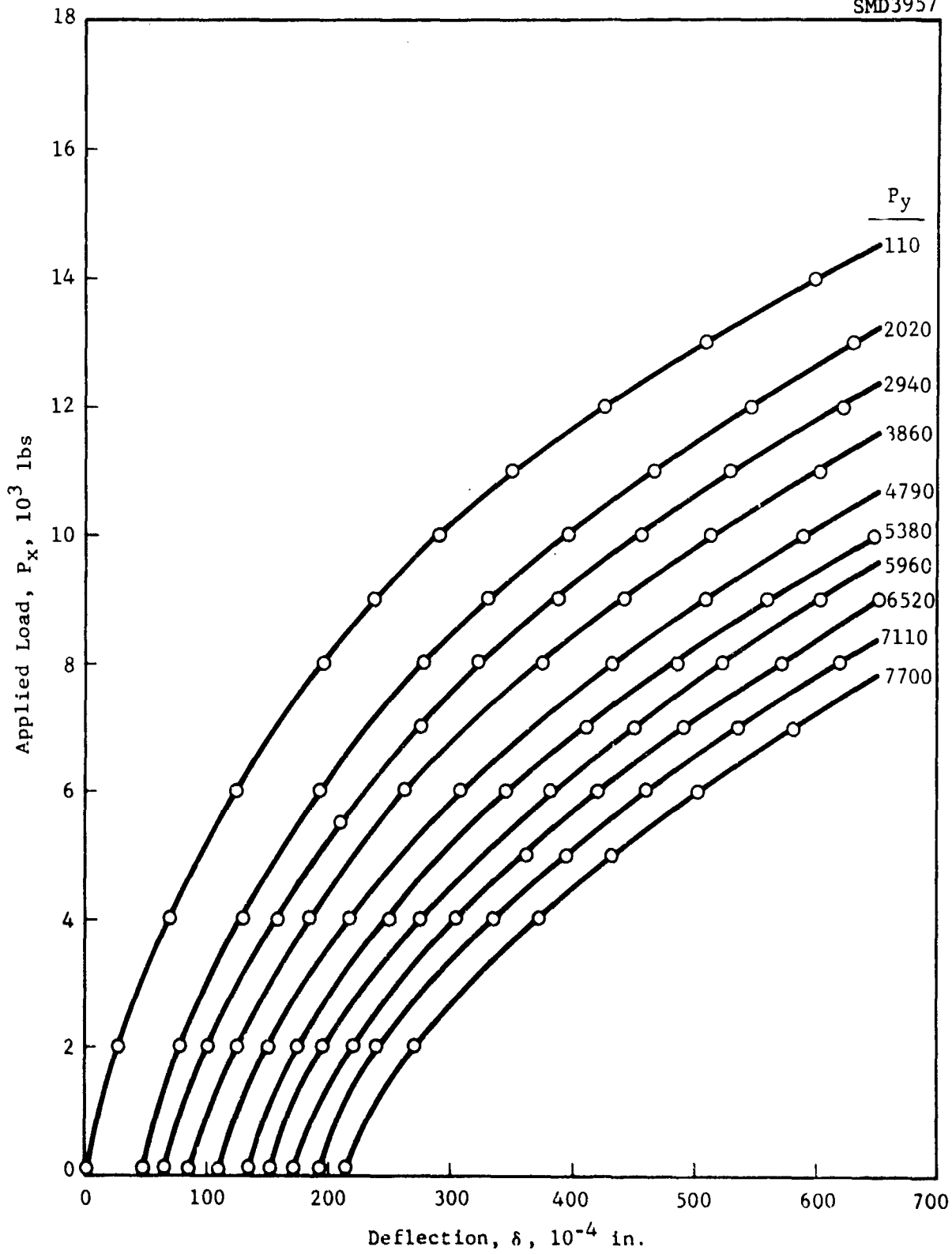


Figure 134 Biaxial Load-Deflection Curves for Aluminum Panel 3

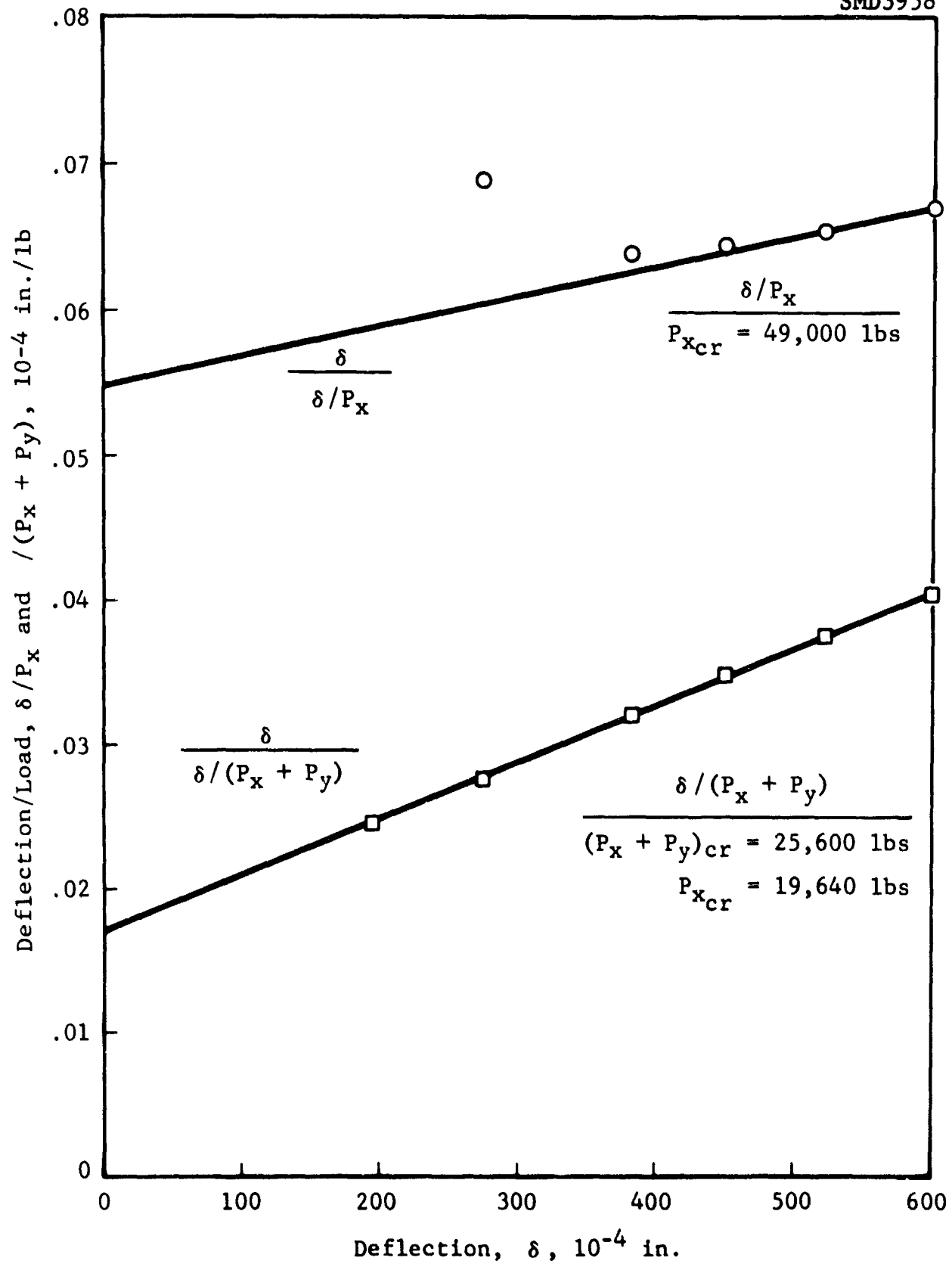


Figure 135 Southwell Plots for Aluminum Panel 3, $P_y = 5960$ lbs

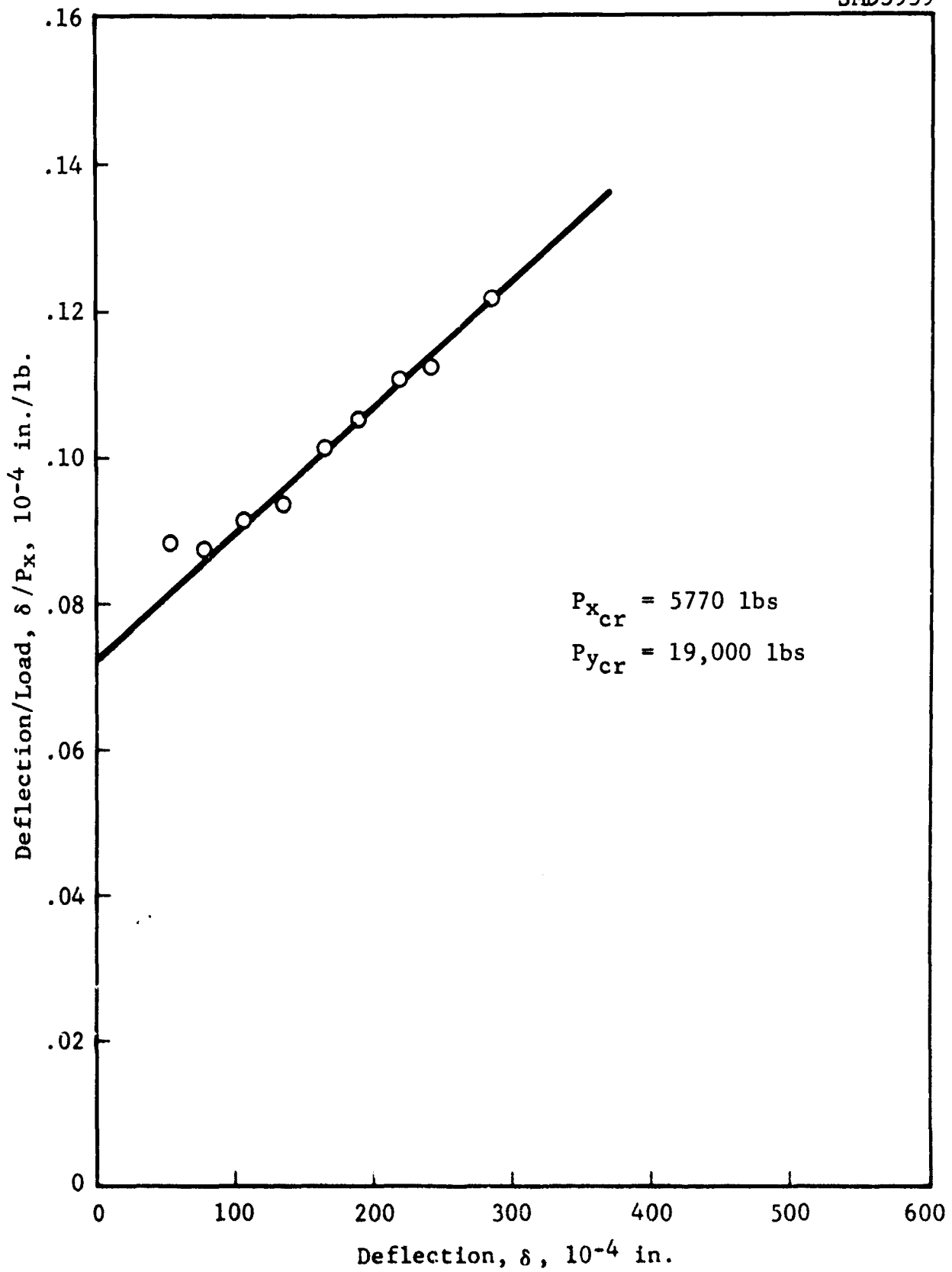


Figure 136 Southwell Plot for Aluminum Panel 3, $N_x/N_y = .304$

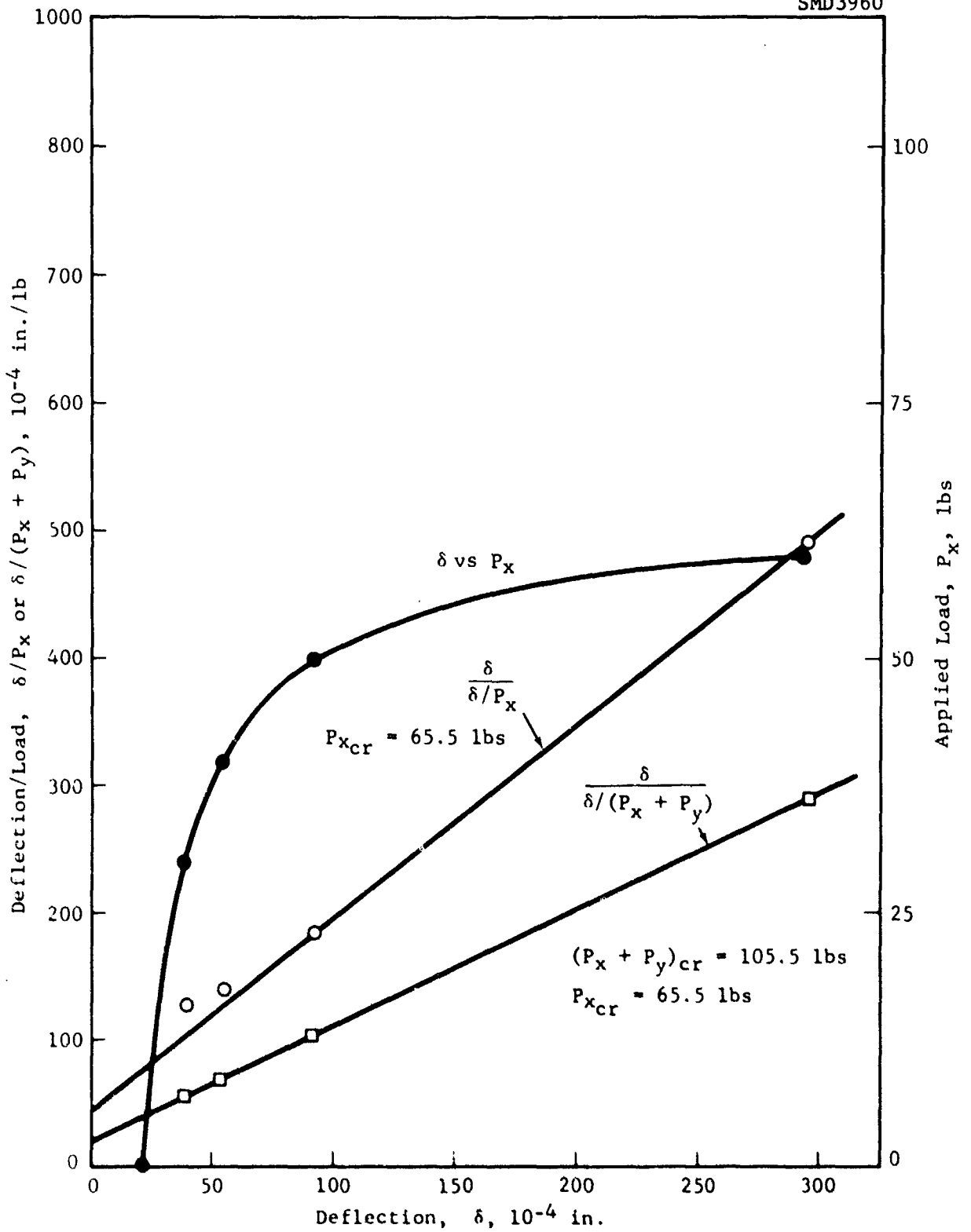


Figure 137 Load Deflection Curve and Southwell Plots for the Unit Isotropic Plate, $P_y = 40$ lbs.

A P P E N D I X I I
U N I A X I A L B U C K L I N G D A T A

The load-deflection curves and Southwell plots used to generate the uniaxial buckling data described in subsection 4.5 and summarized in Table V are presented in this appendix as Figures 138 through 161.

SMD3961

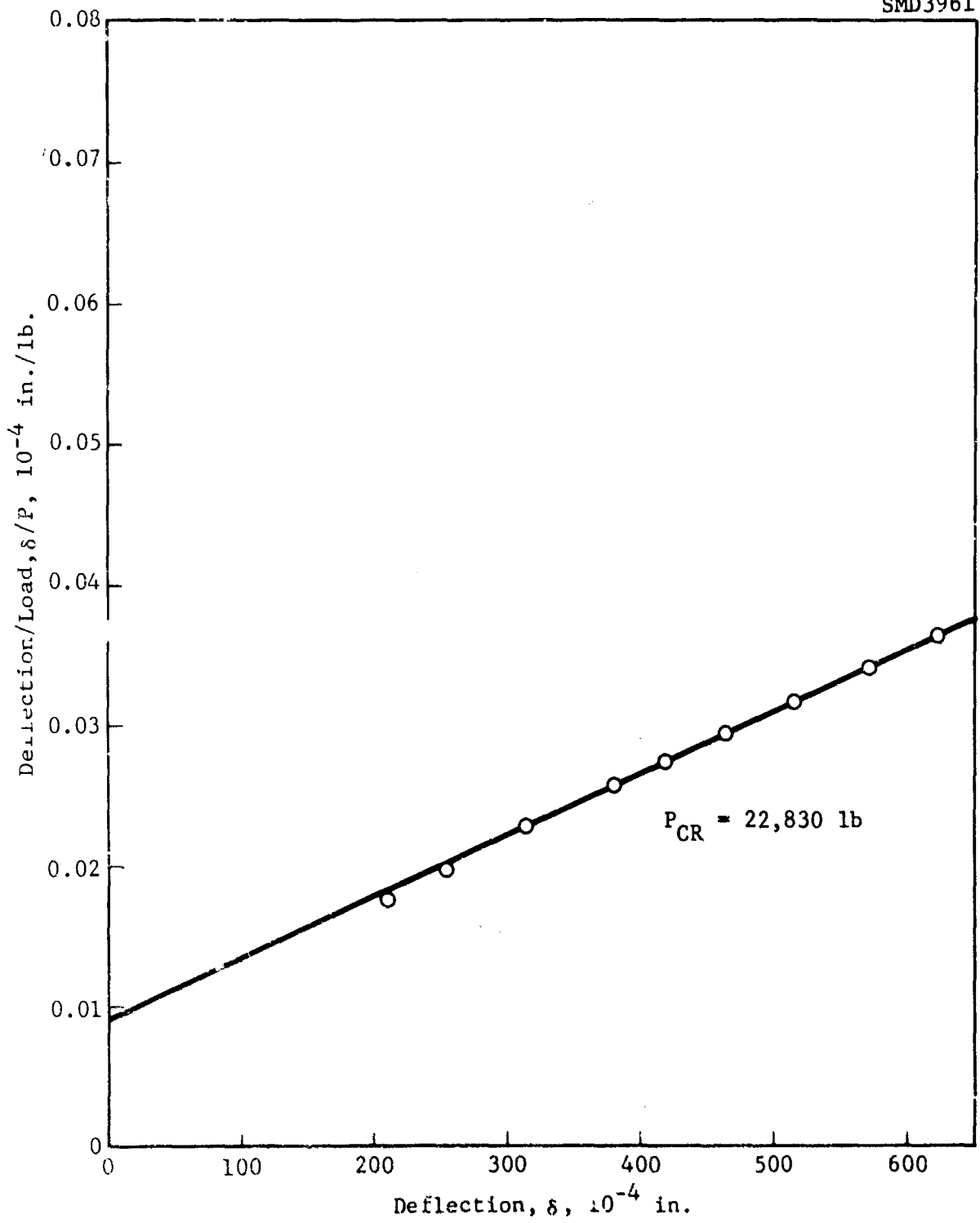


Figure 138 Southwell Plot for Aluminum Panel 3, Clamped-Clamped

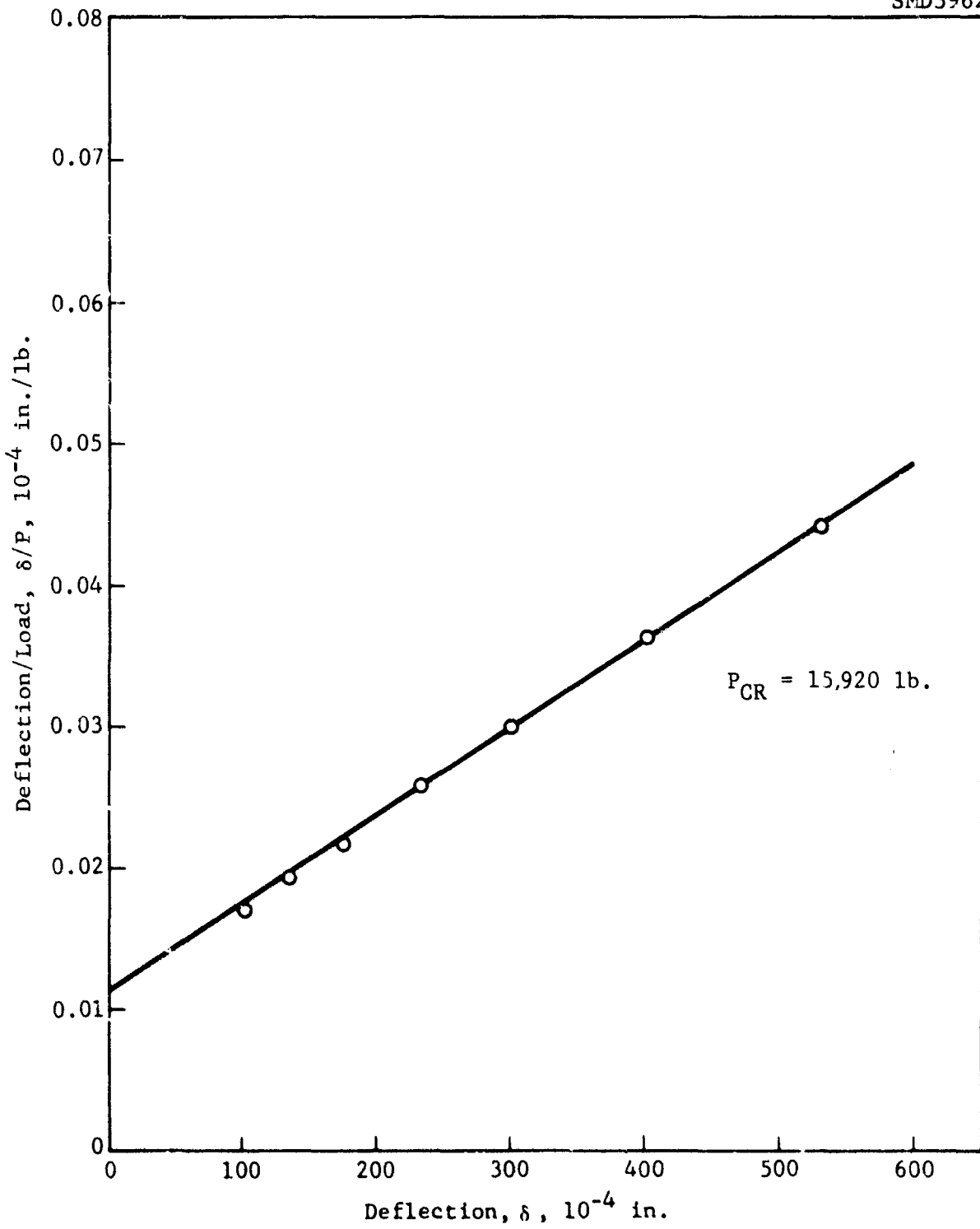


Figure 139 Southwell Plot for Aluminum Panel 3, Clamped-Simple

SMD 2698

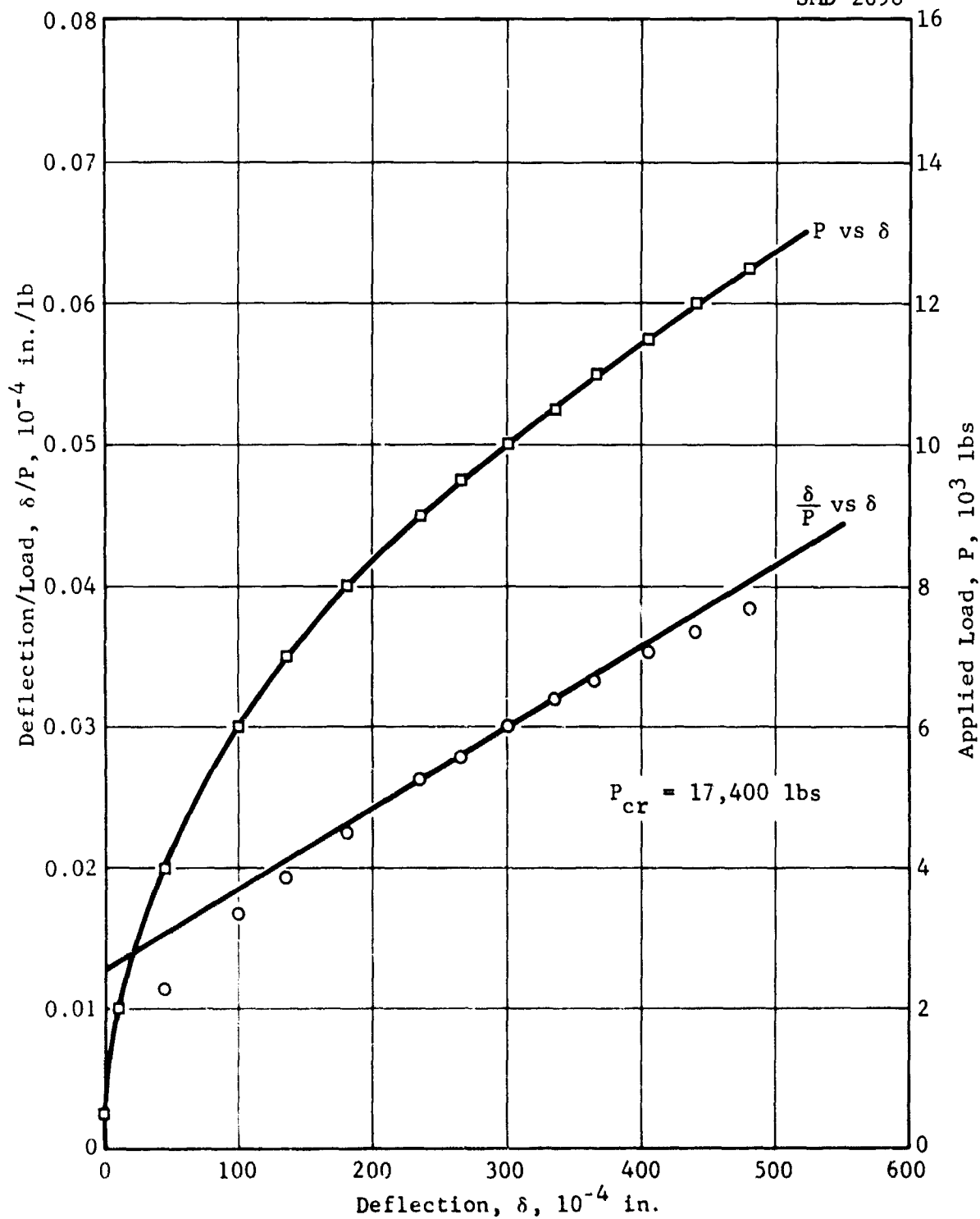


Figure 140 Load-Deflection Curve and Southwell Plot for Steel Panel, Clamped-Clamped

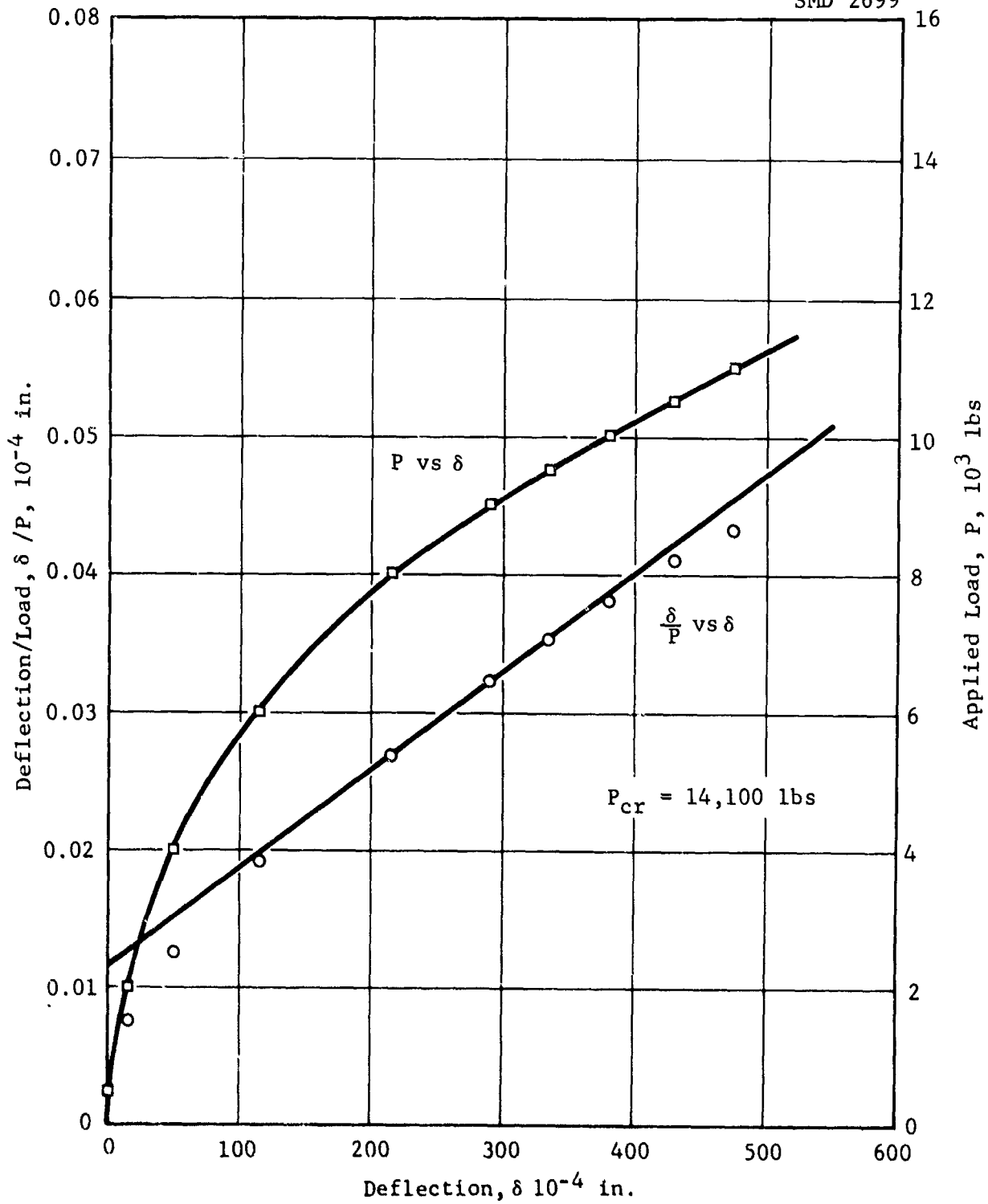


Figure 141 Load-Deflection Curve and Southwell Plot for Steel Panel, Clamped-Simple

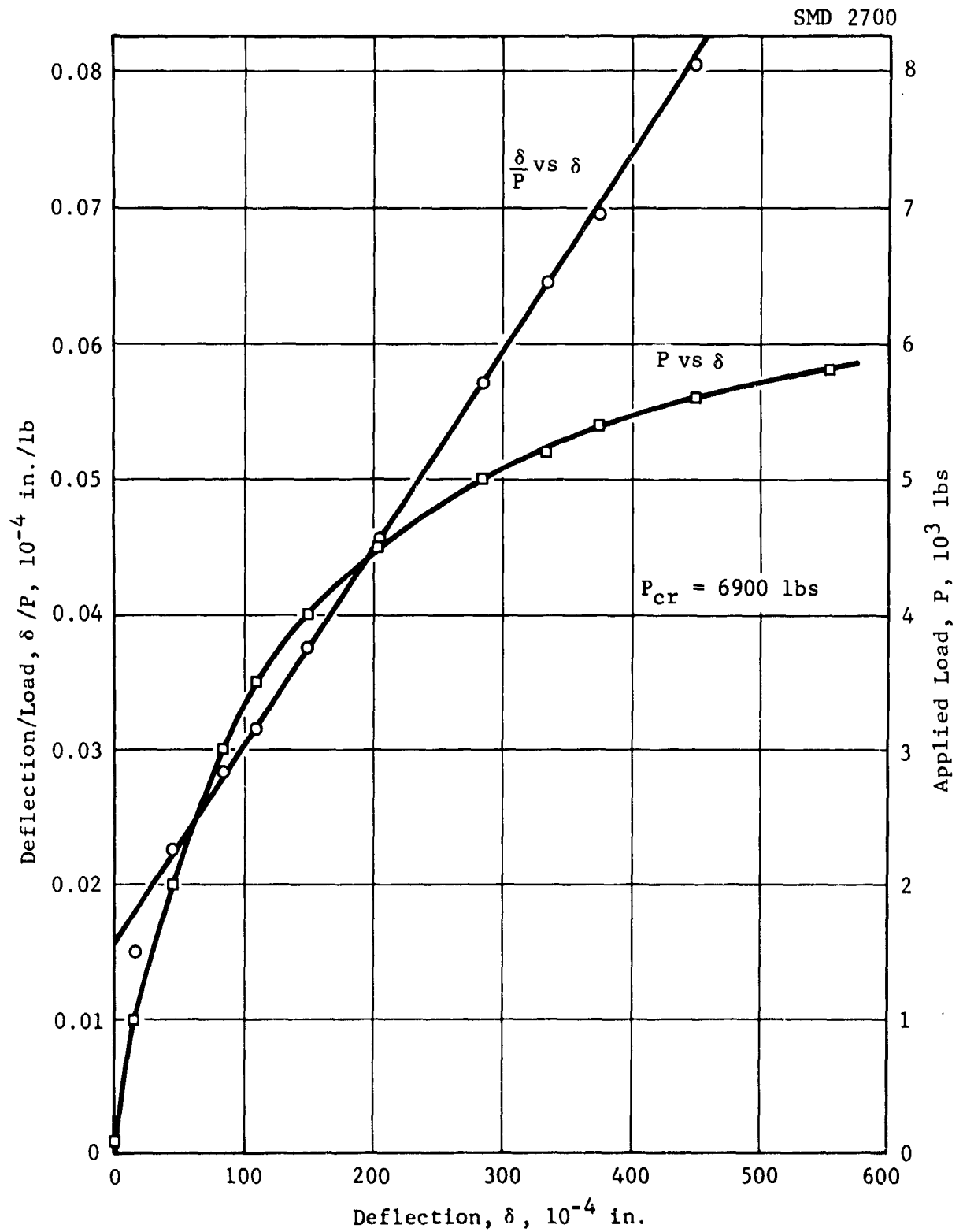


Figure 142 Load-Deflection Curve and Southwell Plot for Panel No. 2, Clamped-Clamped

SMD 2701

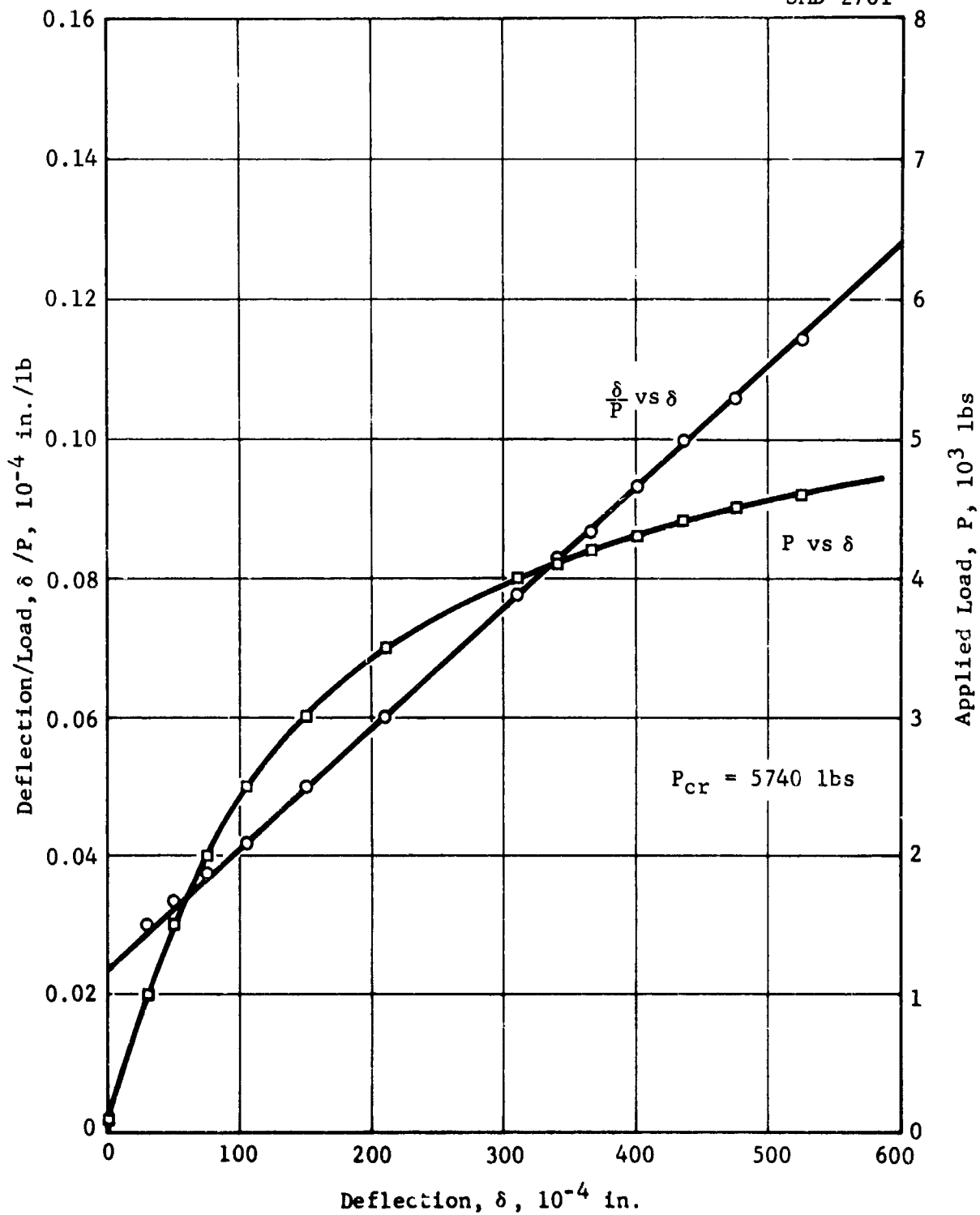


Figure 143 Load-Deflection Curve and Southwell Plot for Panel No. 2, Clamped-Simple

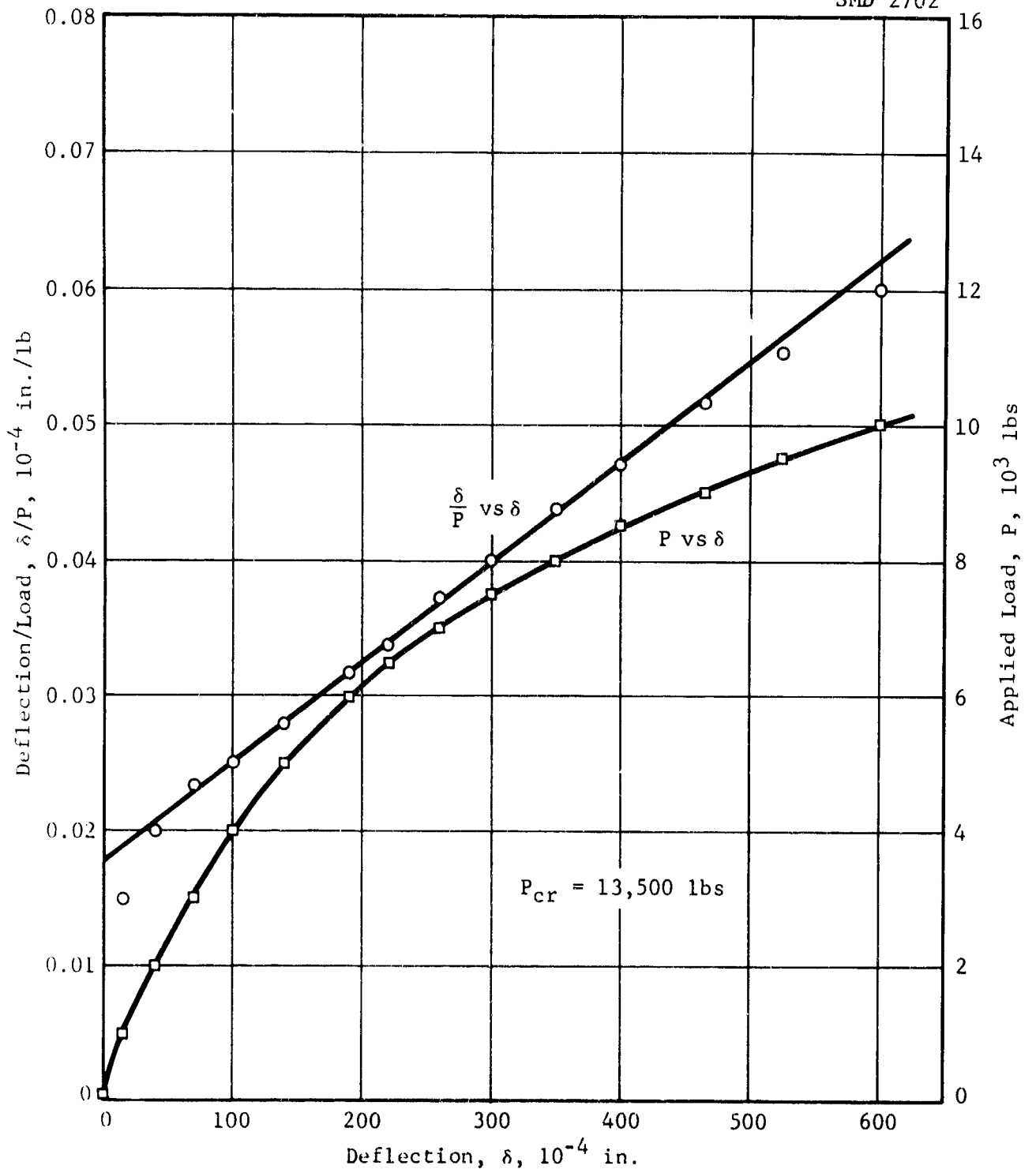


Figure 144 Load-Deflection Curve and Southwell Plot for Panel No. 3, Clamped-Clamped

SMD 2703

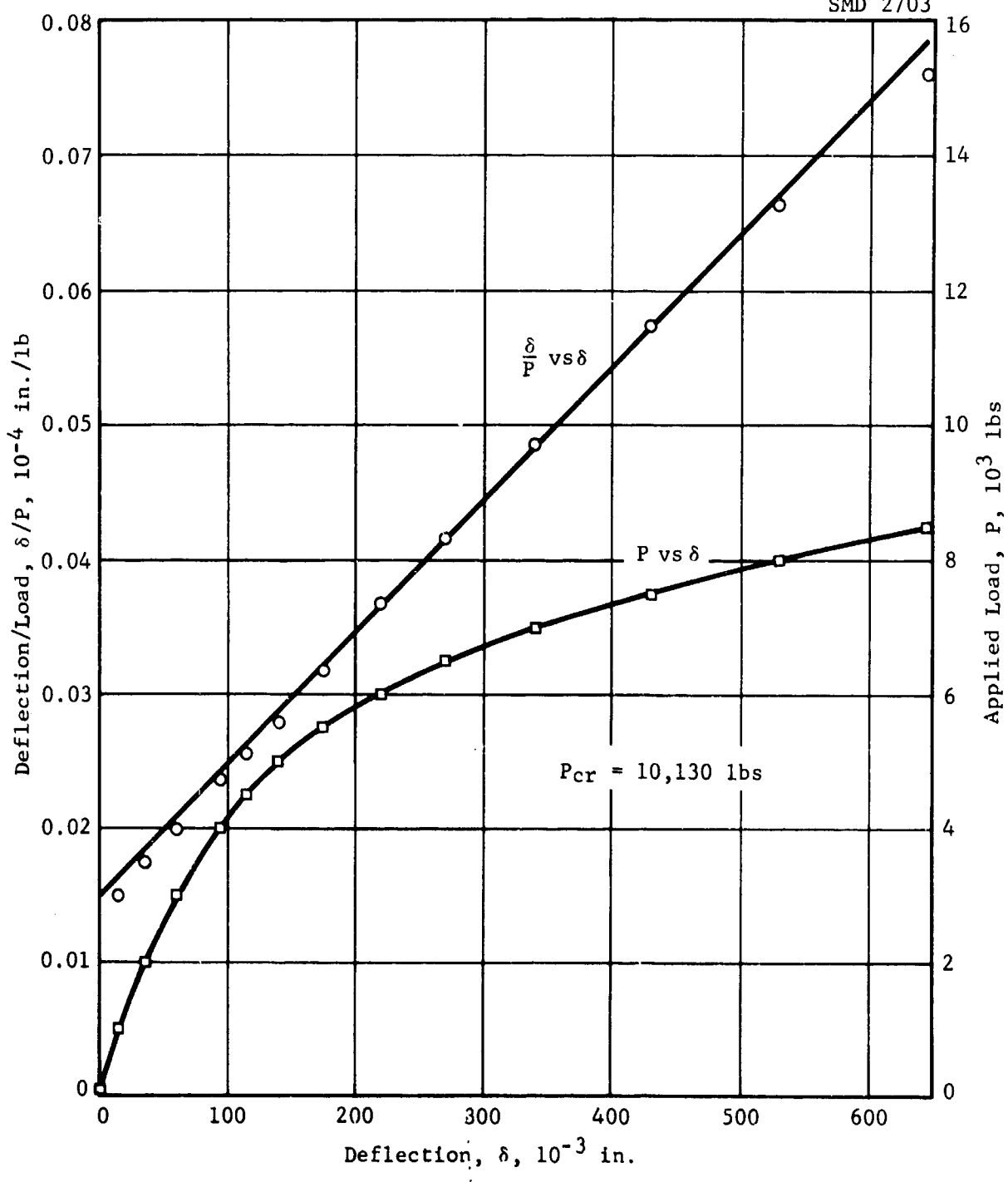


Figure 145 Load-Deflection Curve and Southwell Plot for Panel No. 3, Clamped-Simple

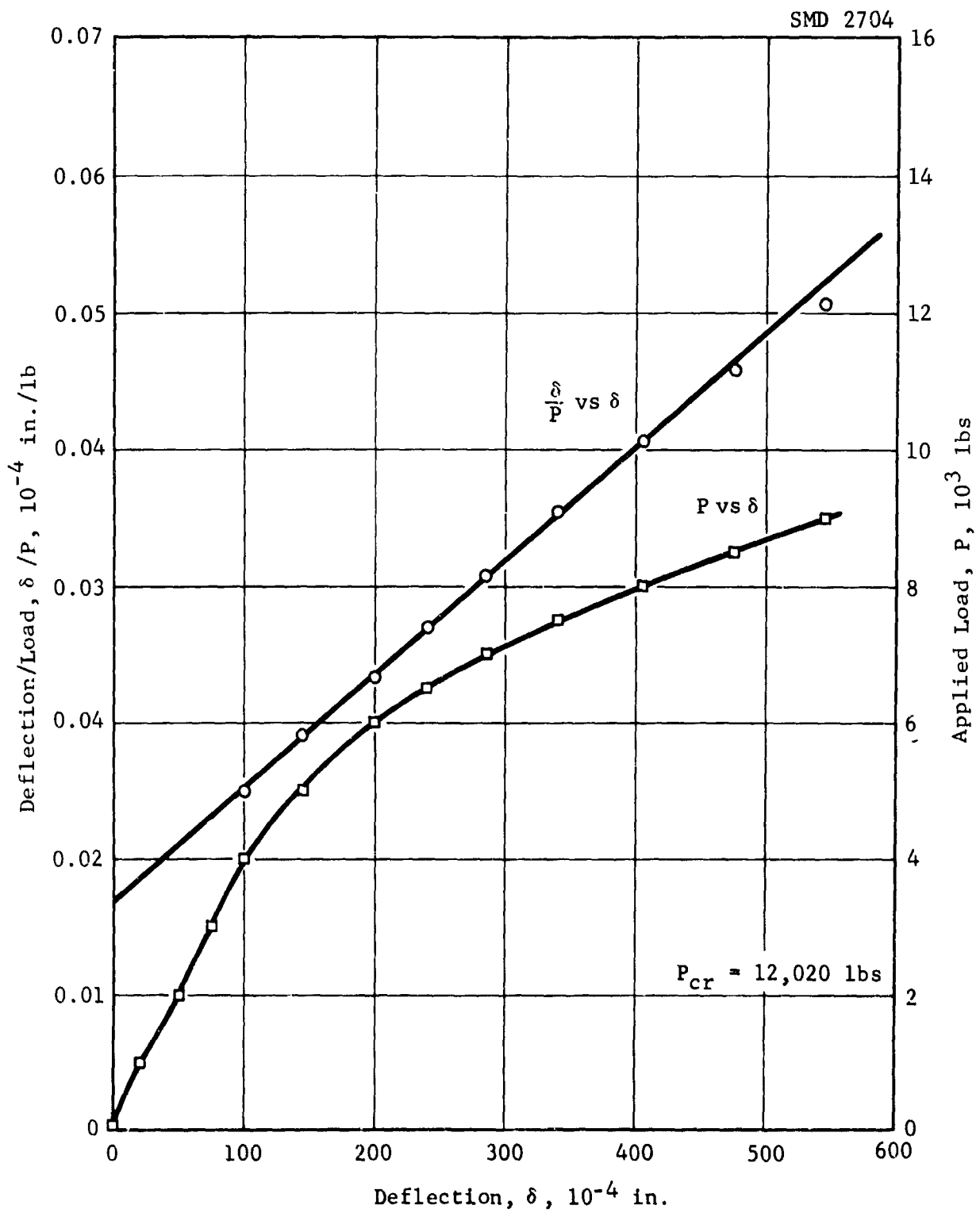


Figure 146 Load-Deflection Curve and Southwell Plot for Panel No. 5, Clamped-Clamped

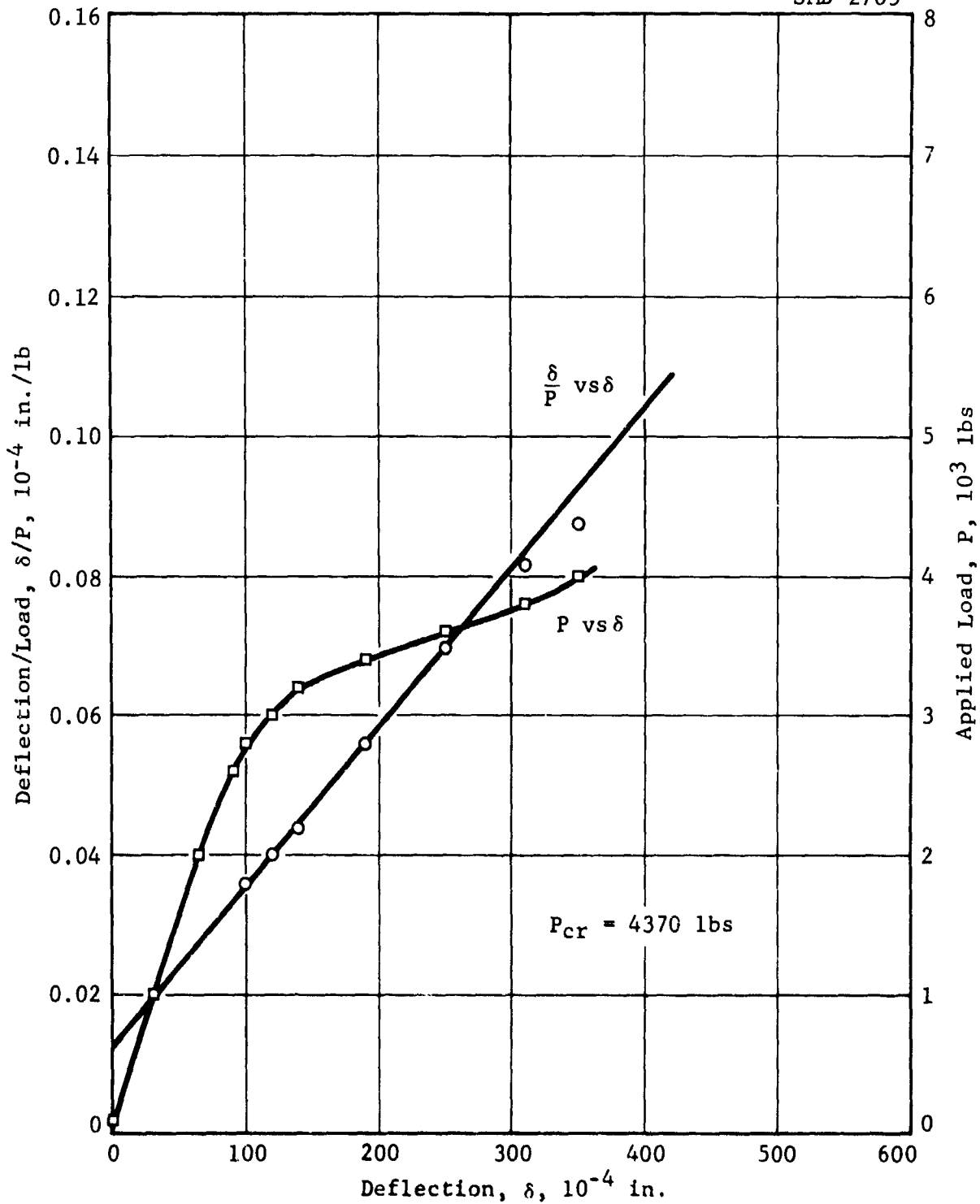


Figure 147 Load-Deflection Curve and Southwell Plot for Panel No. 5, Clamped-Clamped, Turned 90°

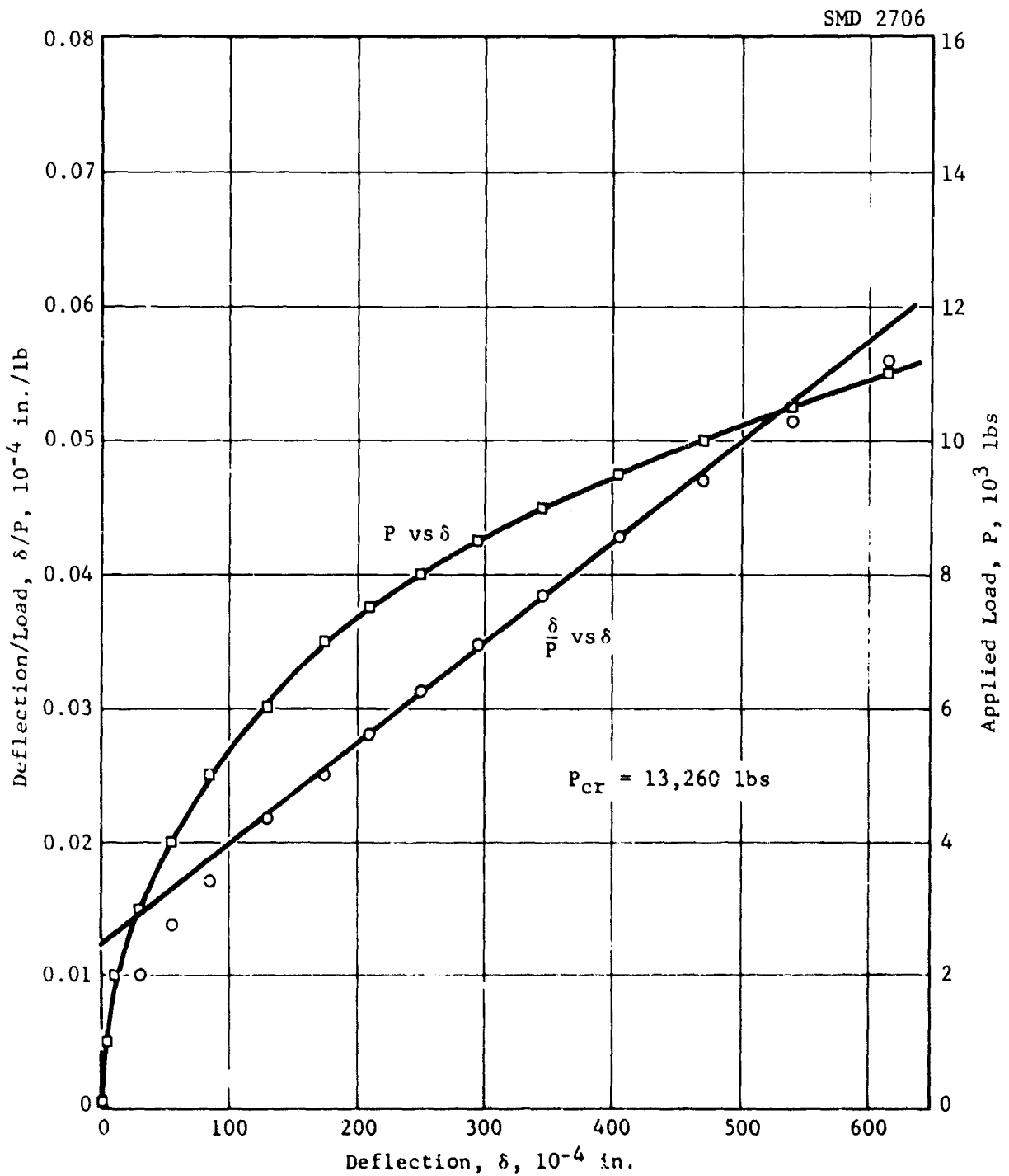


Figure 148 Load-Deflection Curve and Southwell Plot for Panel No. 5, Clamped-Simple

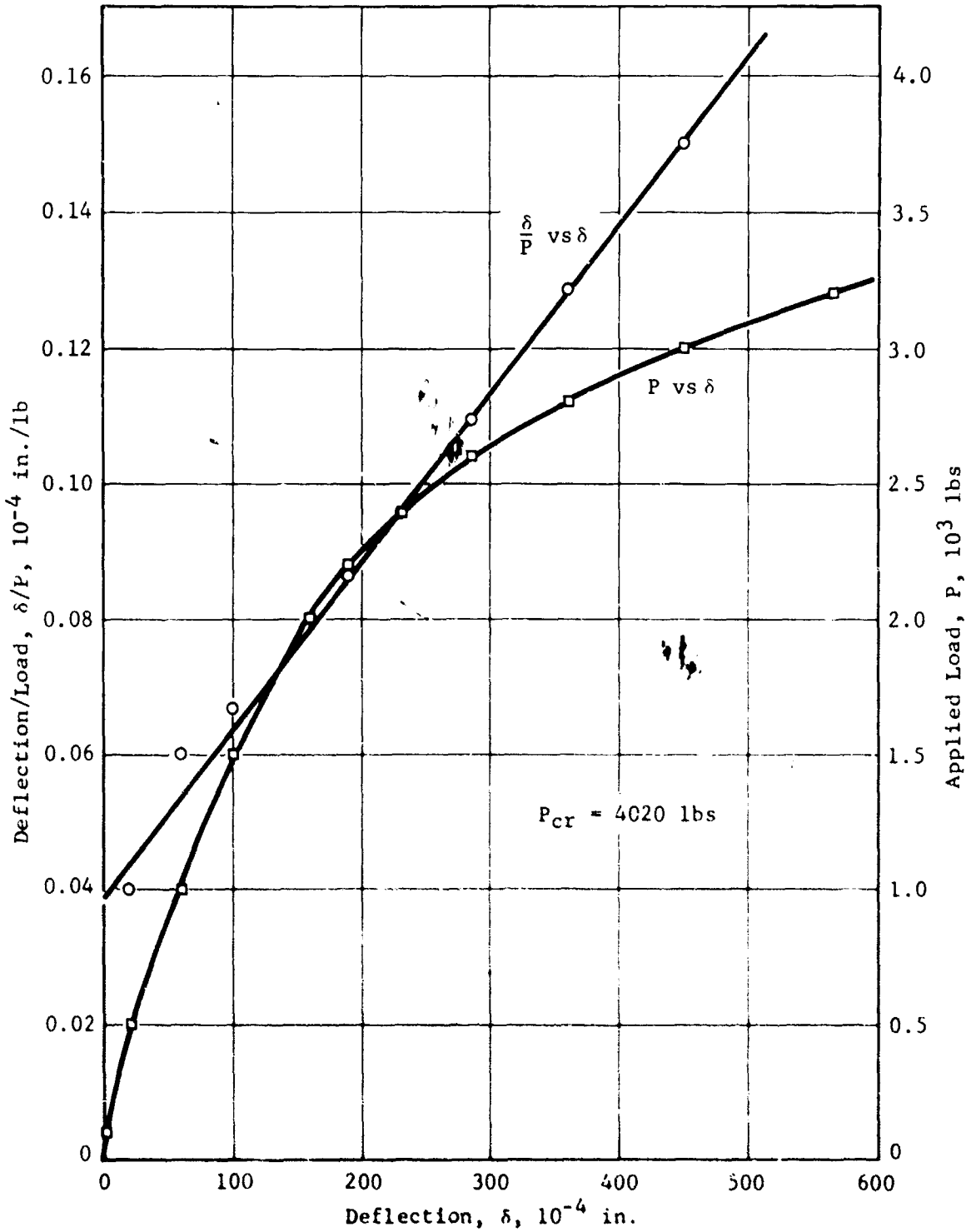


Figure 149 Load-Deflection Curve and Southwell Plot for Panel No. 5, Clamped-Simple, Turned 90°

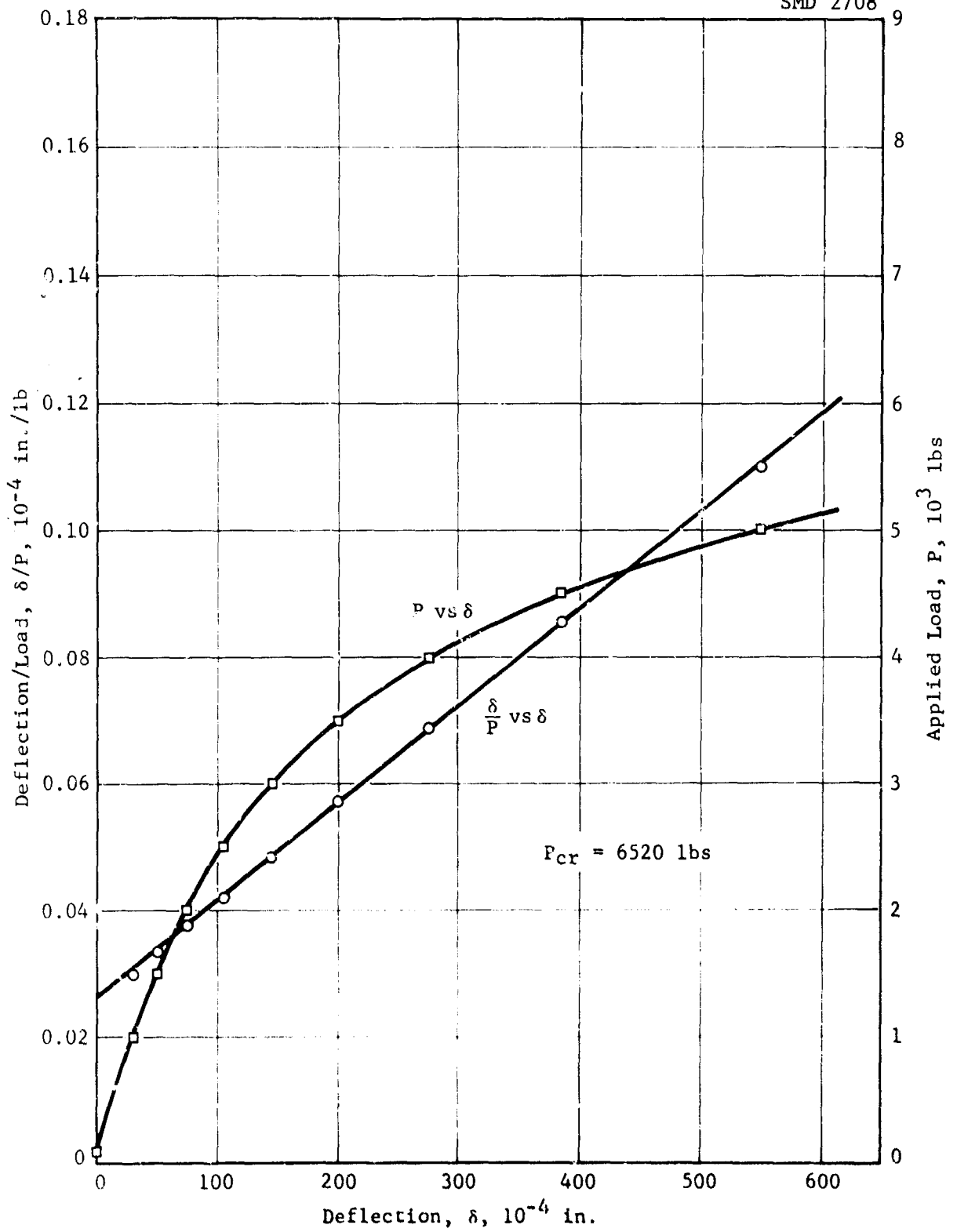


Figure 150 Load-Deflection Curve and Southwell Plot for Panel No. 7, Clamped-Clamped

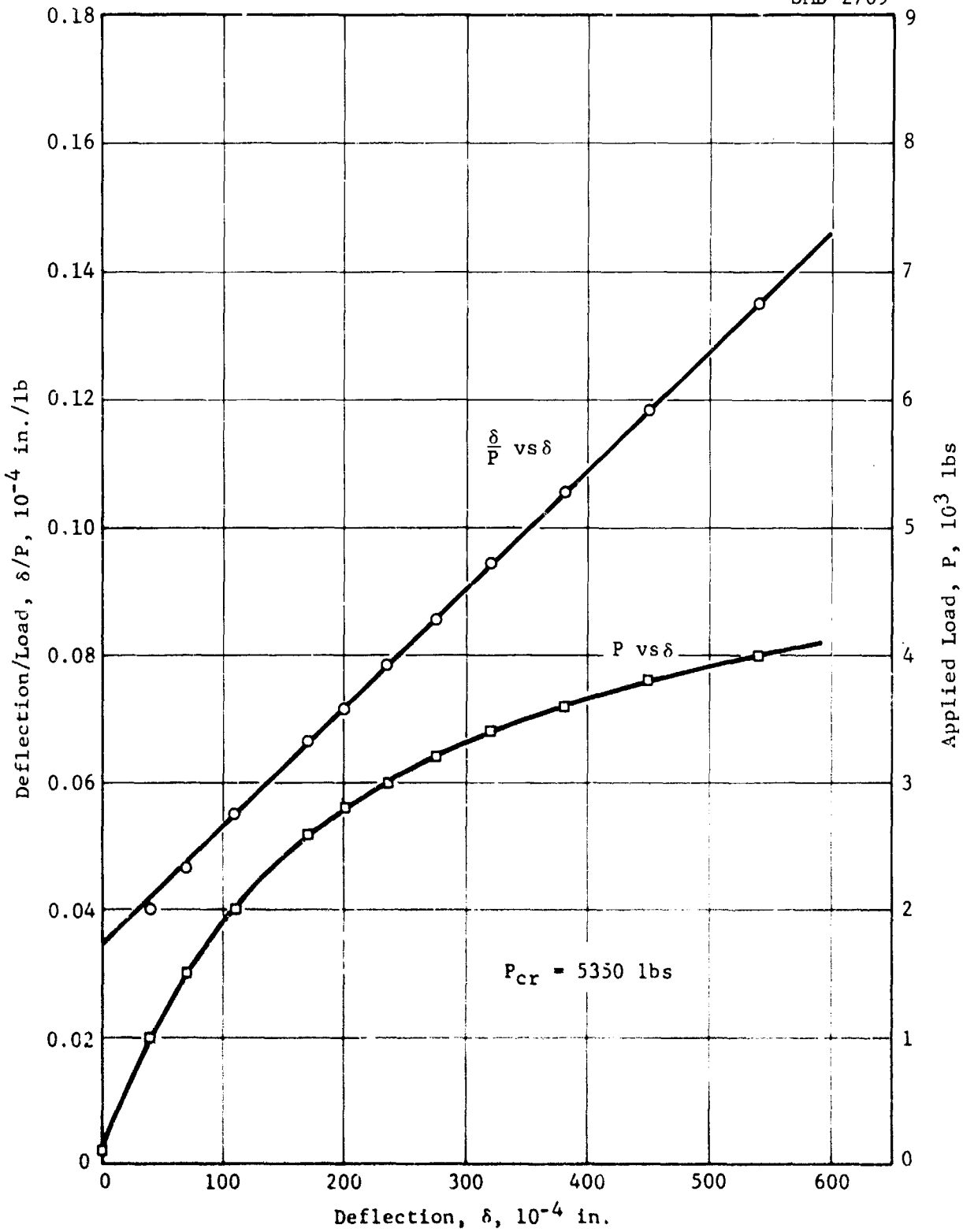


Figure 151 Load-Deflection Curve and Southwell Plot for Panel No. 7, Clamped-Simple

SMD 2710

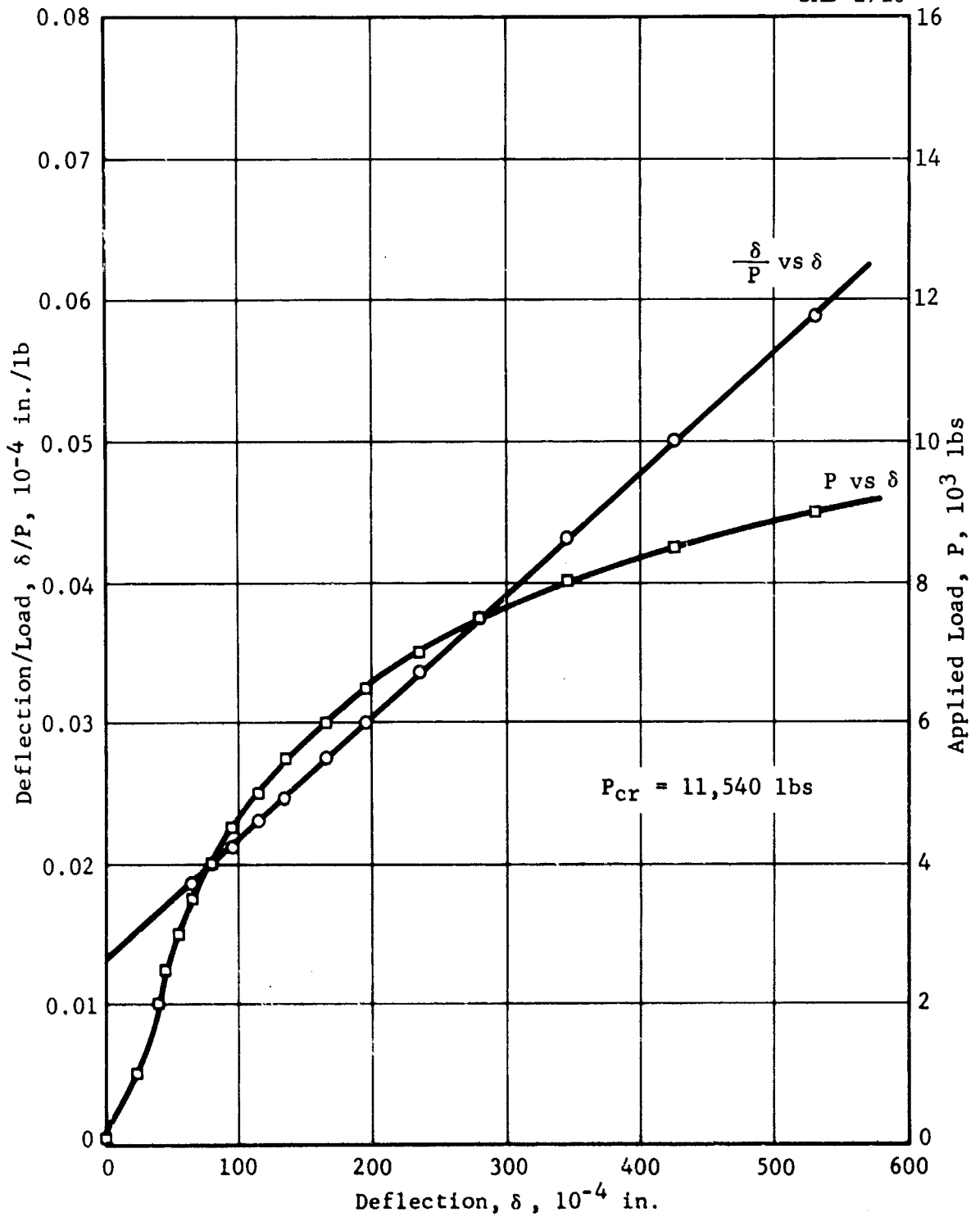


Figure 152 Load-Deflection Curve and Southwell Plot for Panel No. 9, Clamped-Clamped

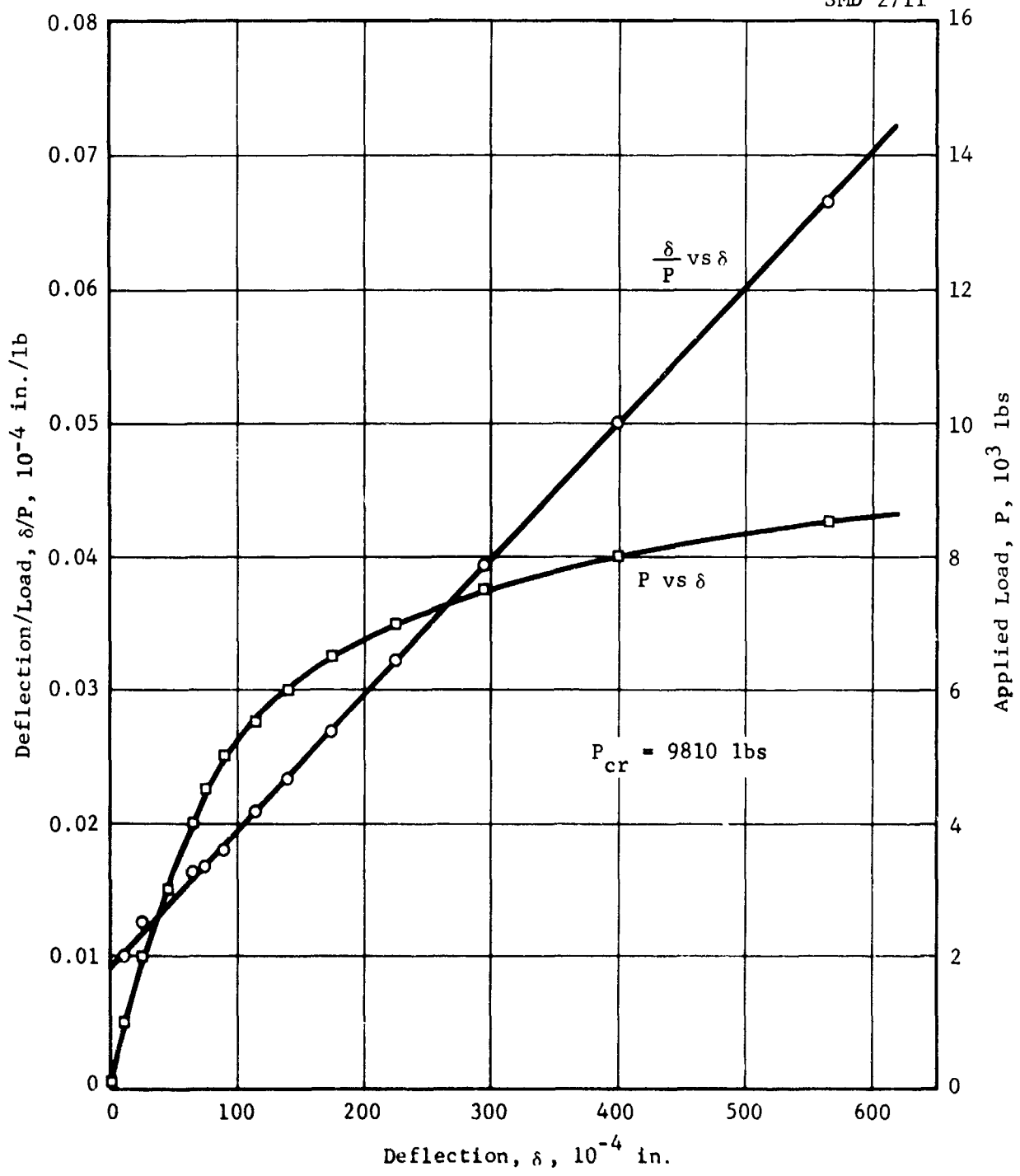


Figure 153 Load-Deflection Curve and Southwell Plot for Panel No. 9, Clamped-Simple

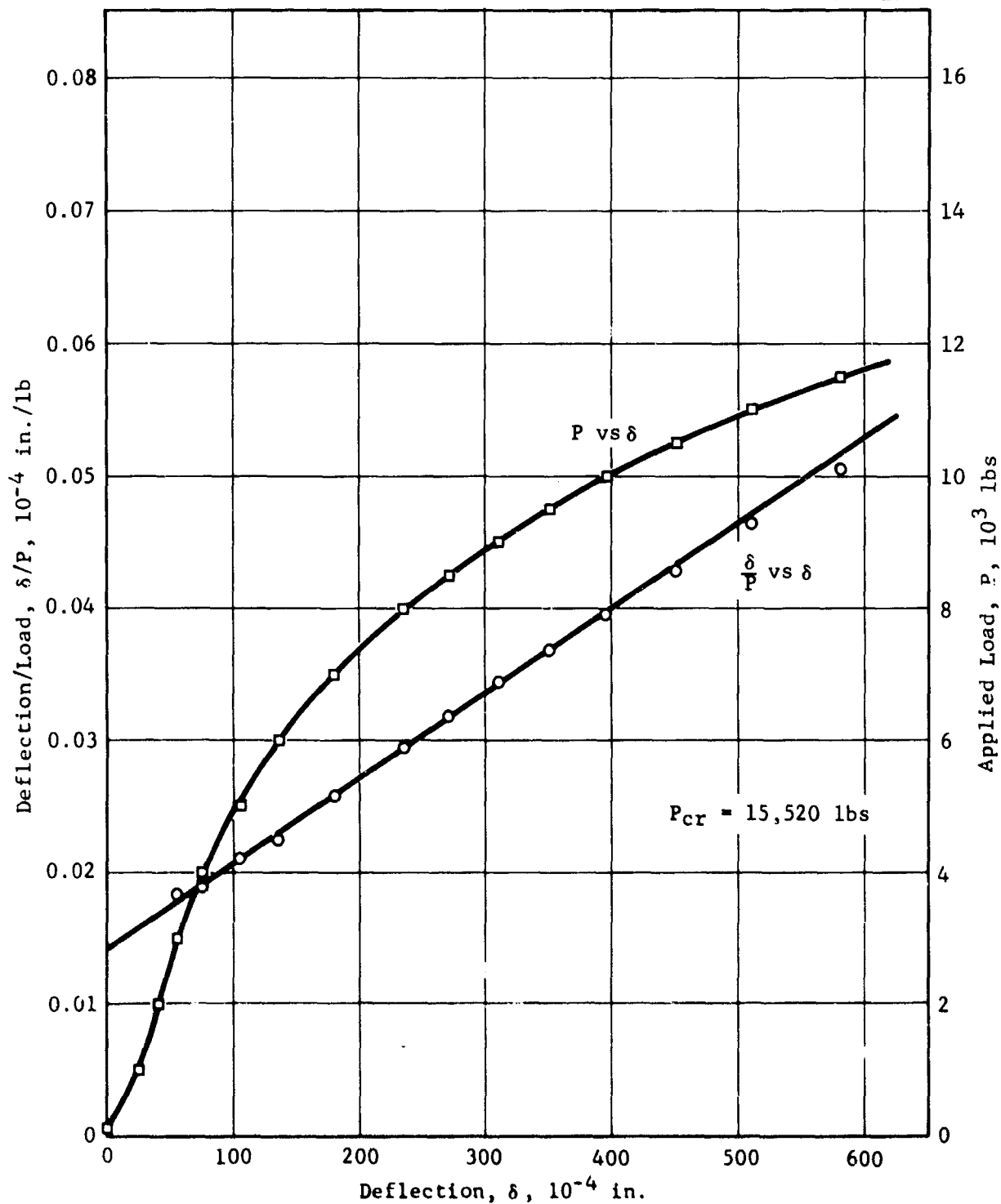


Figure 154 Load-Deflection Curve and Southwell Plot for Panel No. 12, Clamped-Clamped

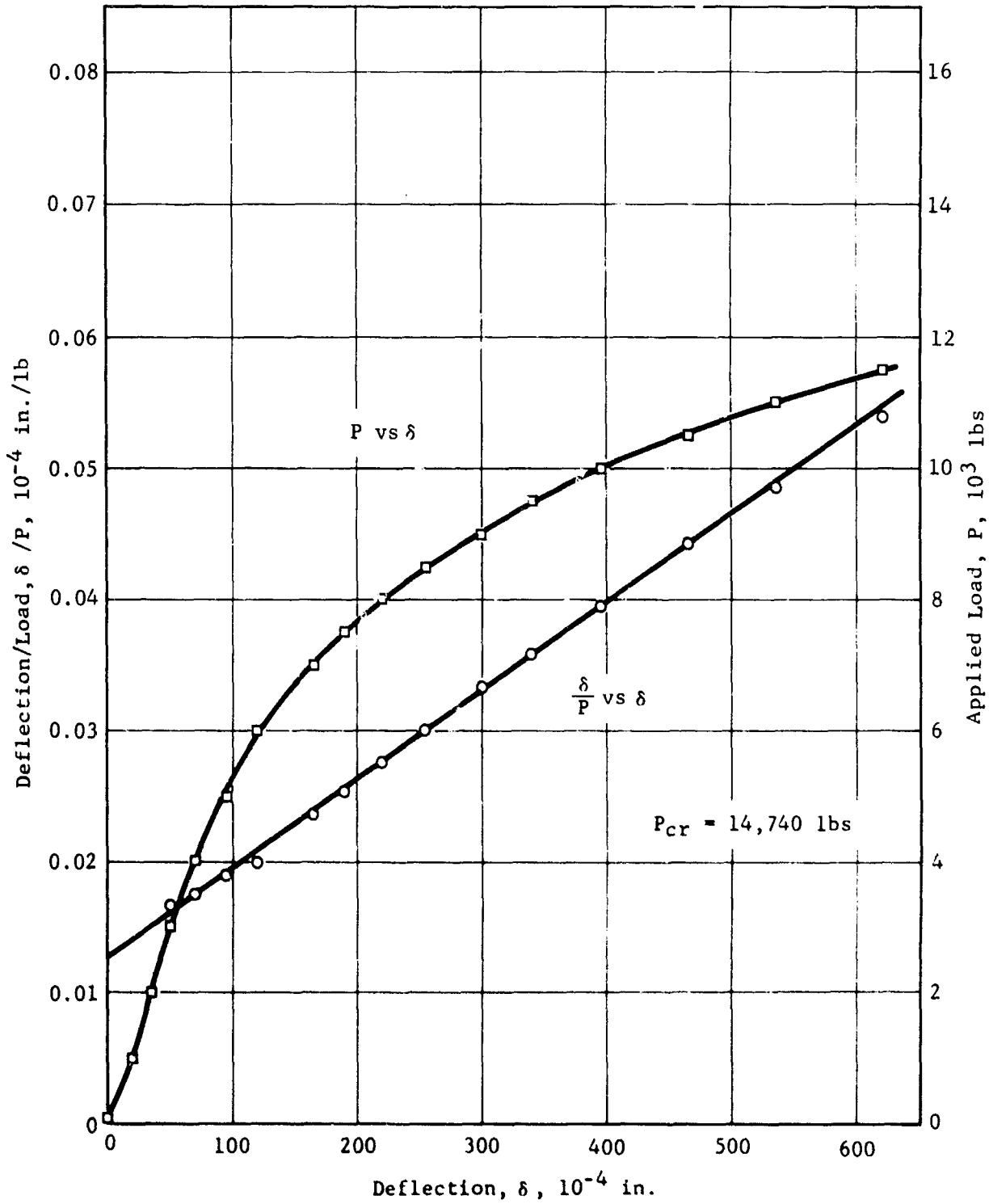


Figure 155 Load-Deflection Curve and Southwell Plot for Panel No. 12, Clamped-Simple

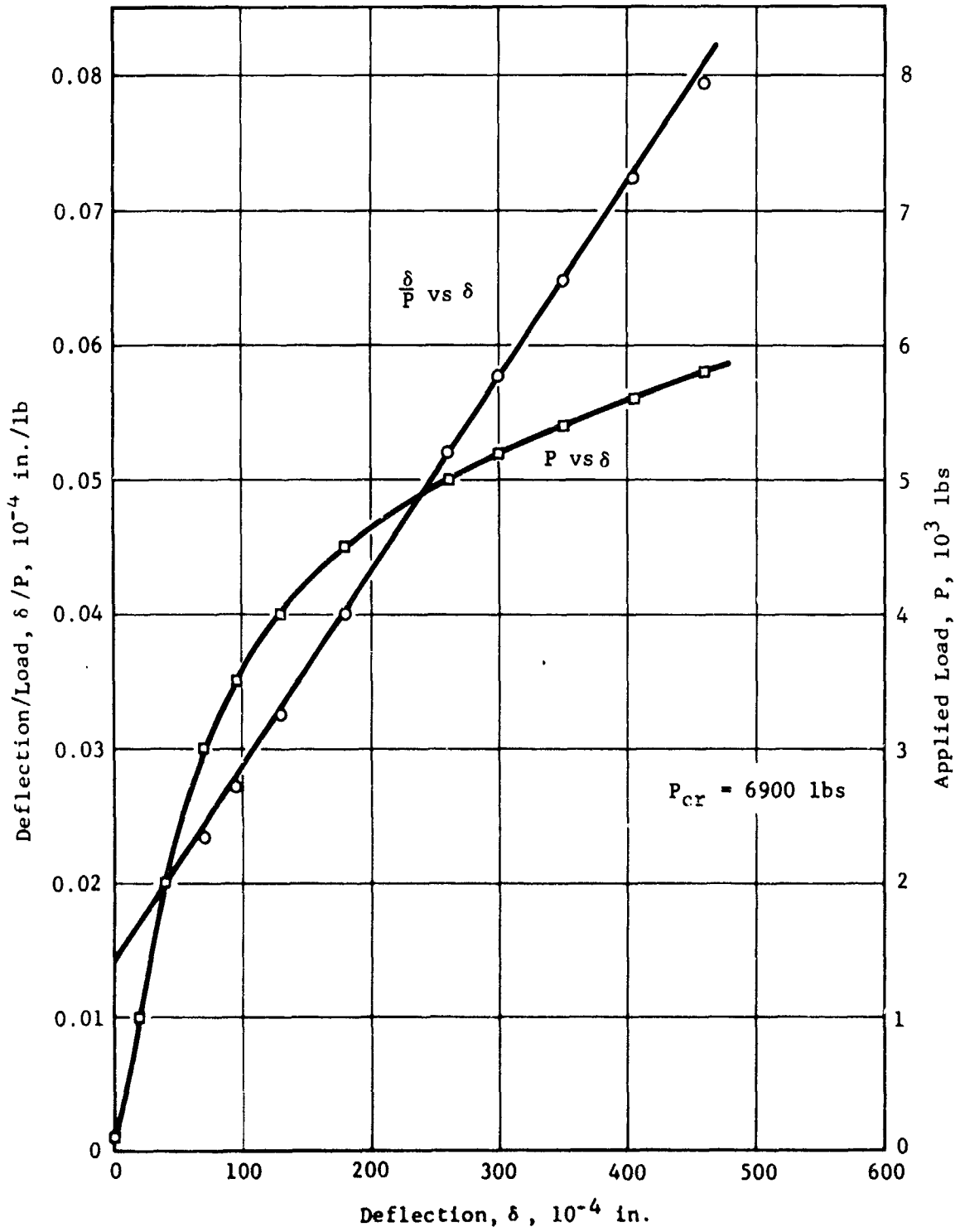


Figure 156 Load-Deflection Curve and Southwell Plot for Panel No. 16, Clamped-Clamped

SMD 2715

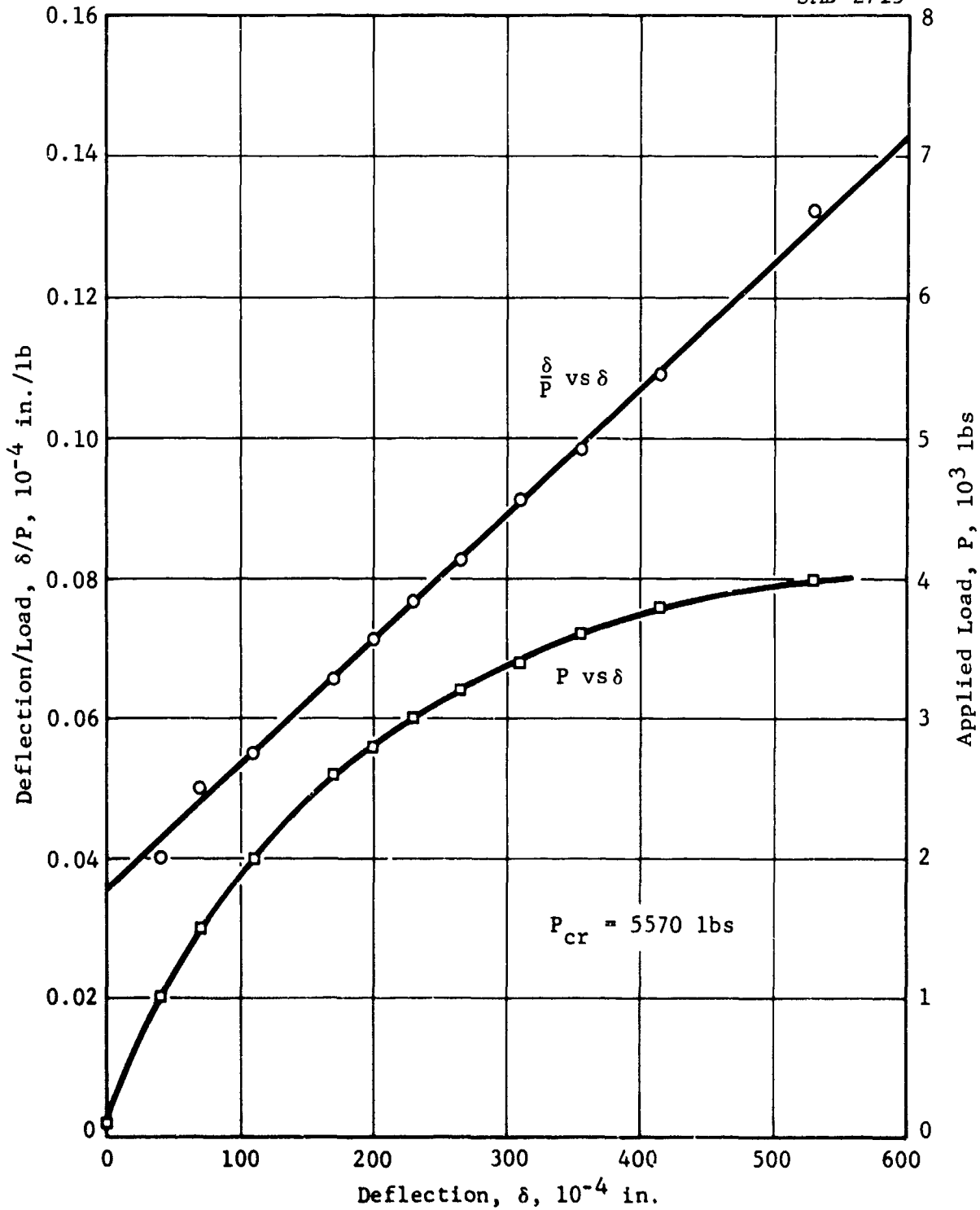


Figure 157 Load-Deflection Curve and Southwell Plot for Panel No. 16, Clamped-Simple

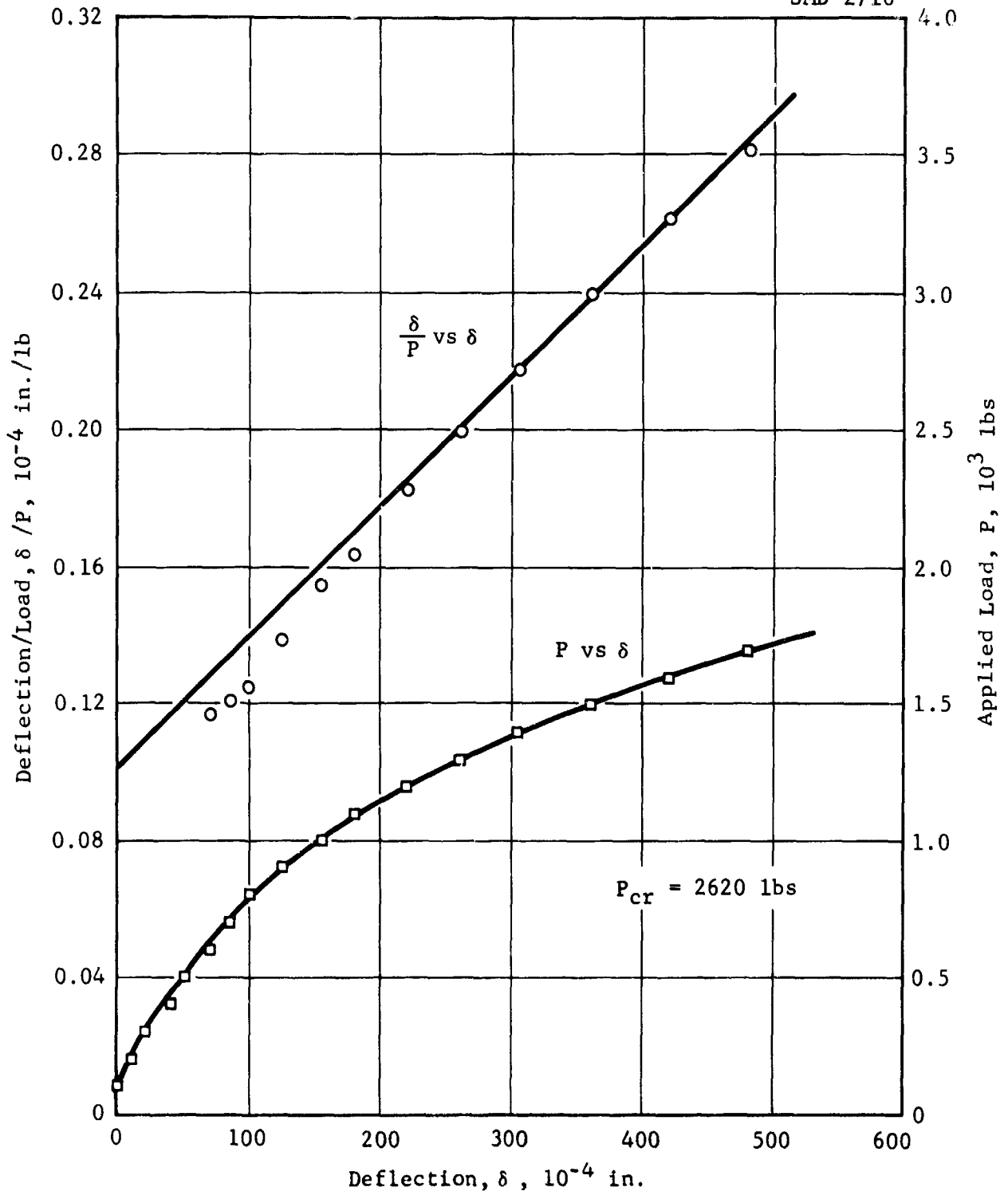


Figure 158 Load-Deflection Curve and Southwell Plot for Panel No. 19A, Clamped-Clamped

SMD 2717

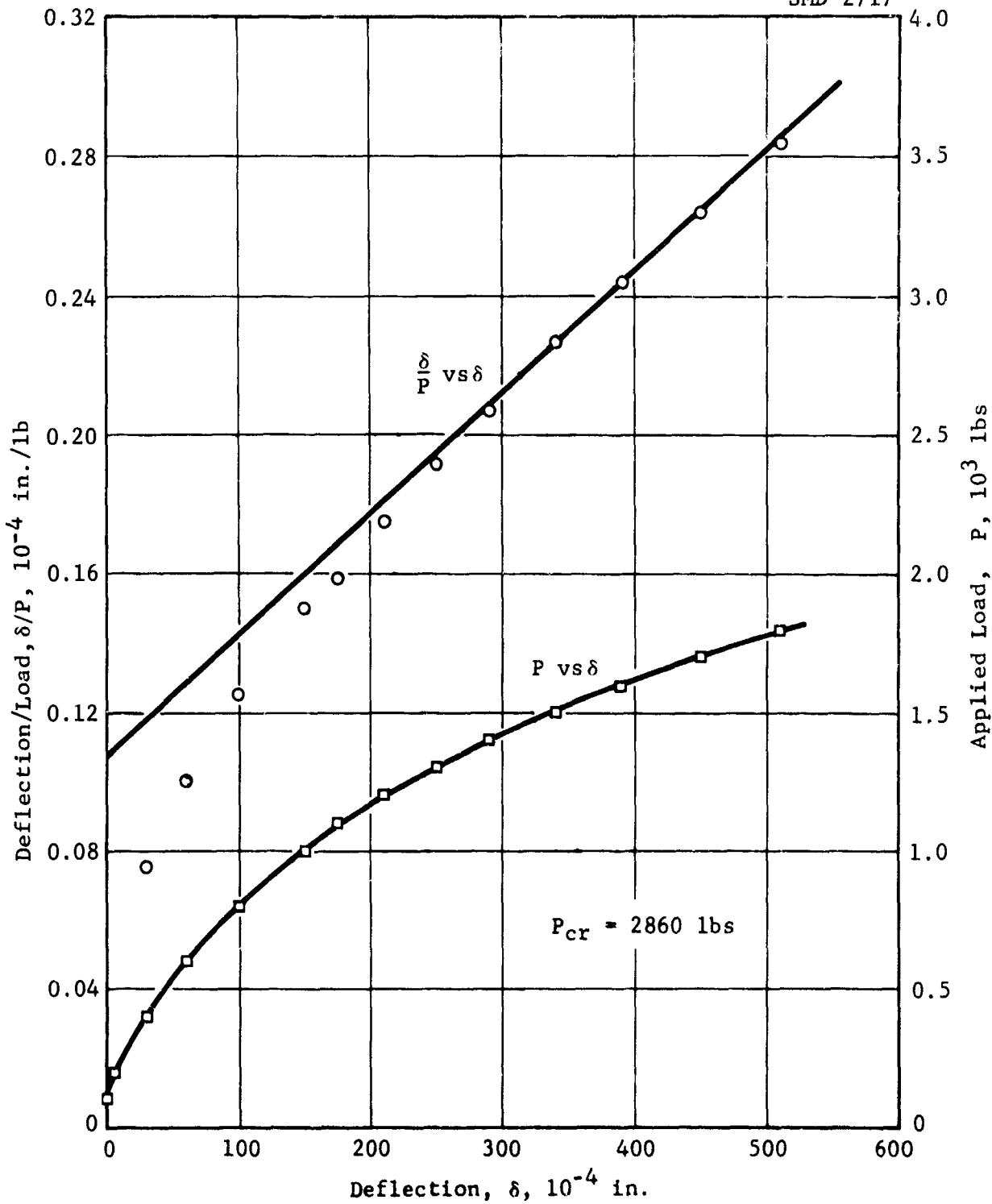


Figure 159 Load-Deflection Curve and Southwell Plot for Panel No. 19A, Clamped-Clamped, Turned 90°

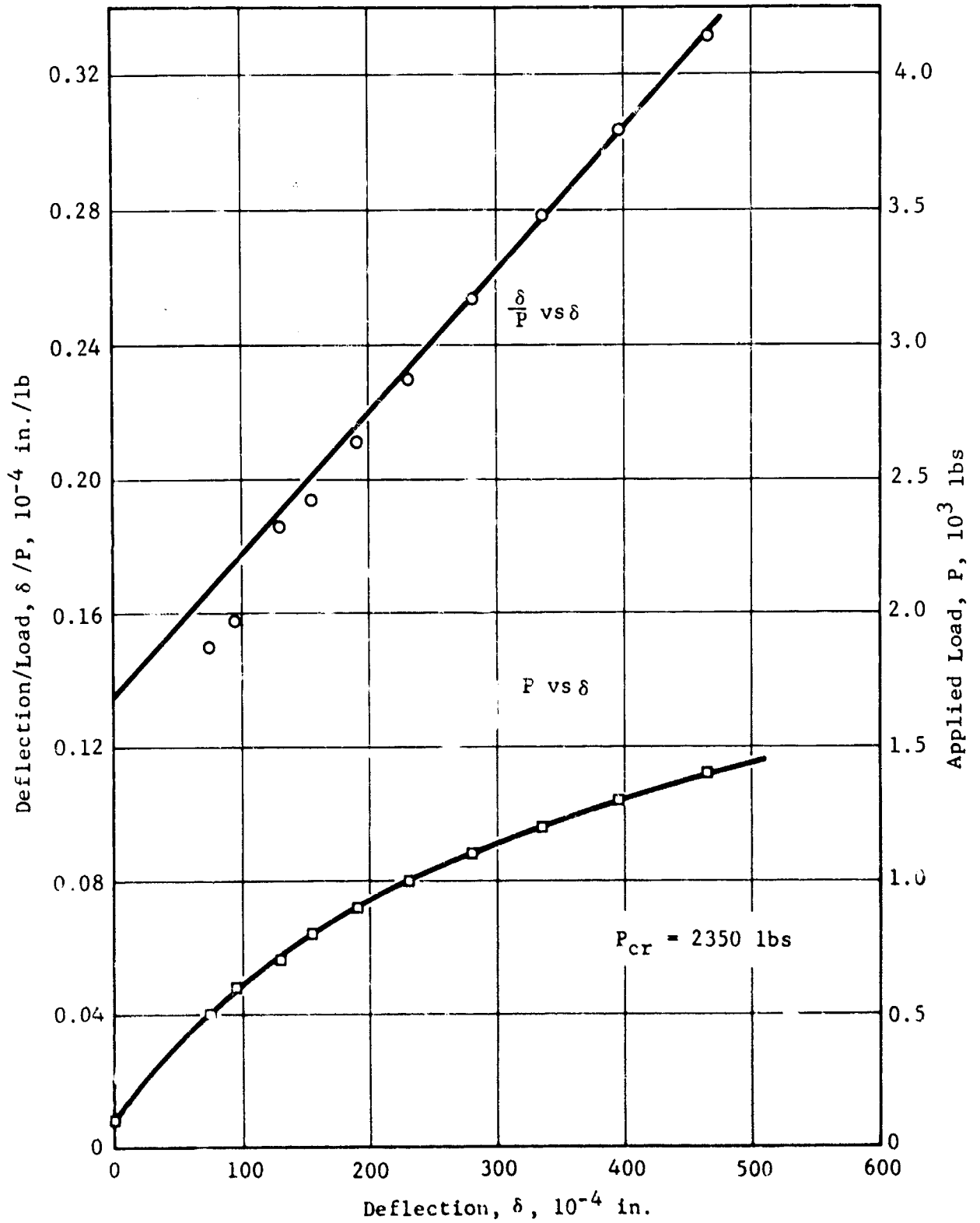


Figure 160 Load-Deflection Curve and Southwell Plot for Panel No. 19A, Clamped-Simple

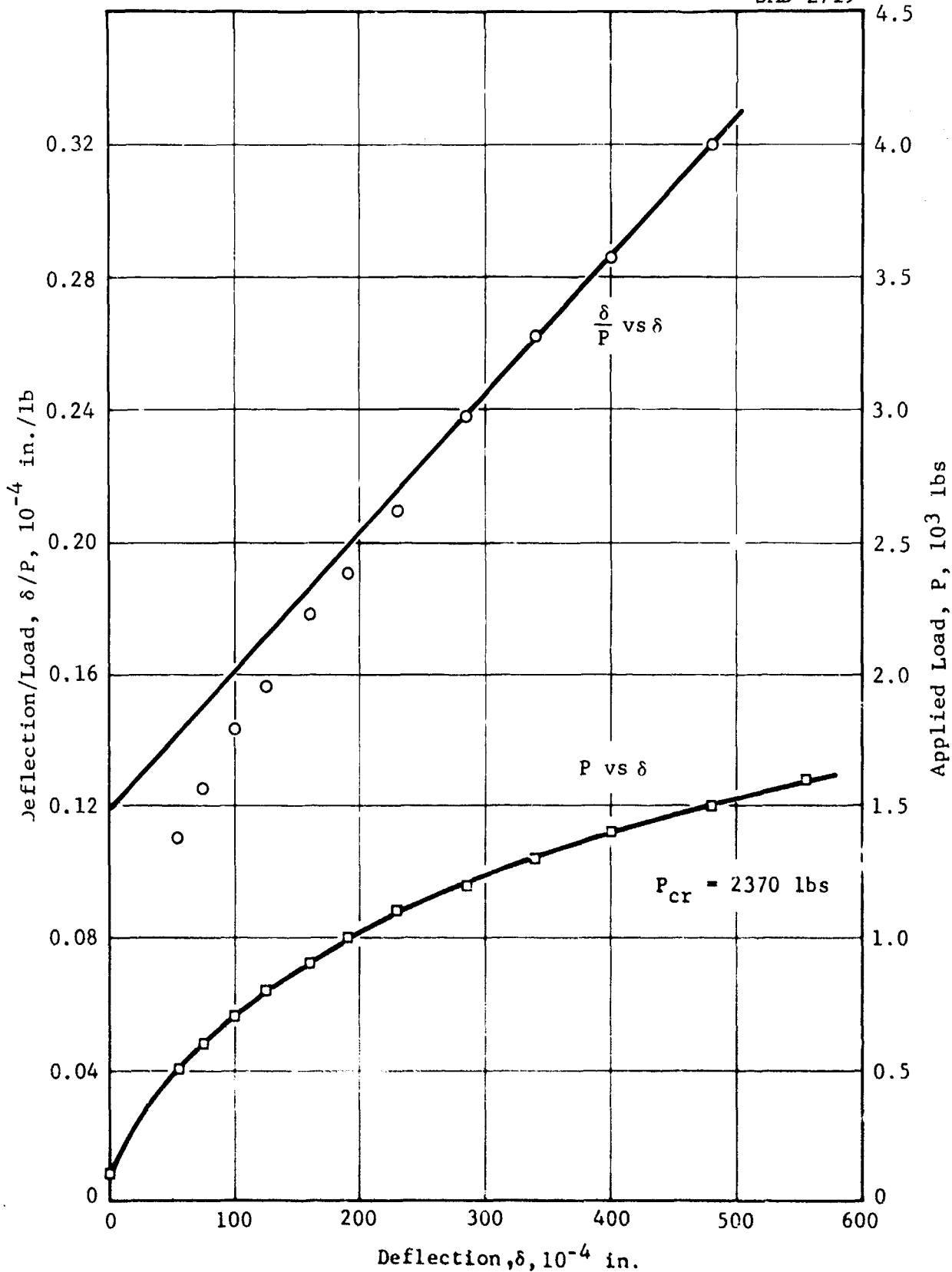


Figure 161 Load-Deflection Curve and Southwell Plot for Panel No. 19A, Clamped-Simple, Turned 90°

A P P E N D I X I I I

B I A X I A L B U C K L I N G D A T A

The load-deflection curves and Southwell plots used to generate the biaxial buckling data described in Section VI and summarized in Table IX are presented in this appendix, Figure 162 through 253.

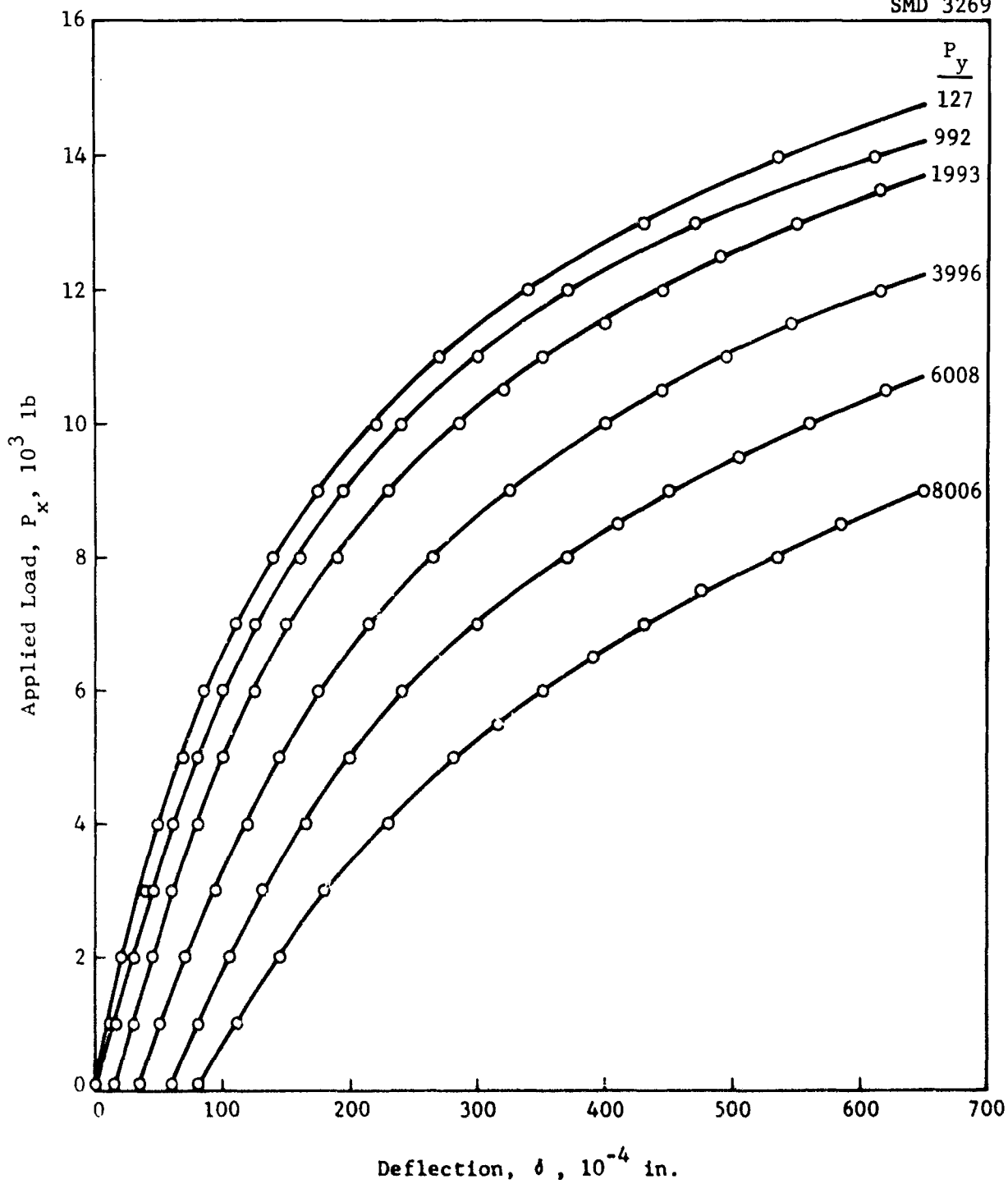


Figure 162 Load-Deflection Curves for Aluminum Panel No. 1

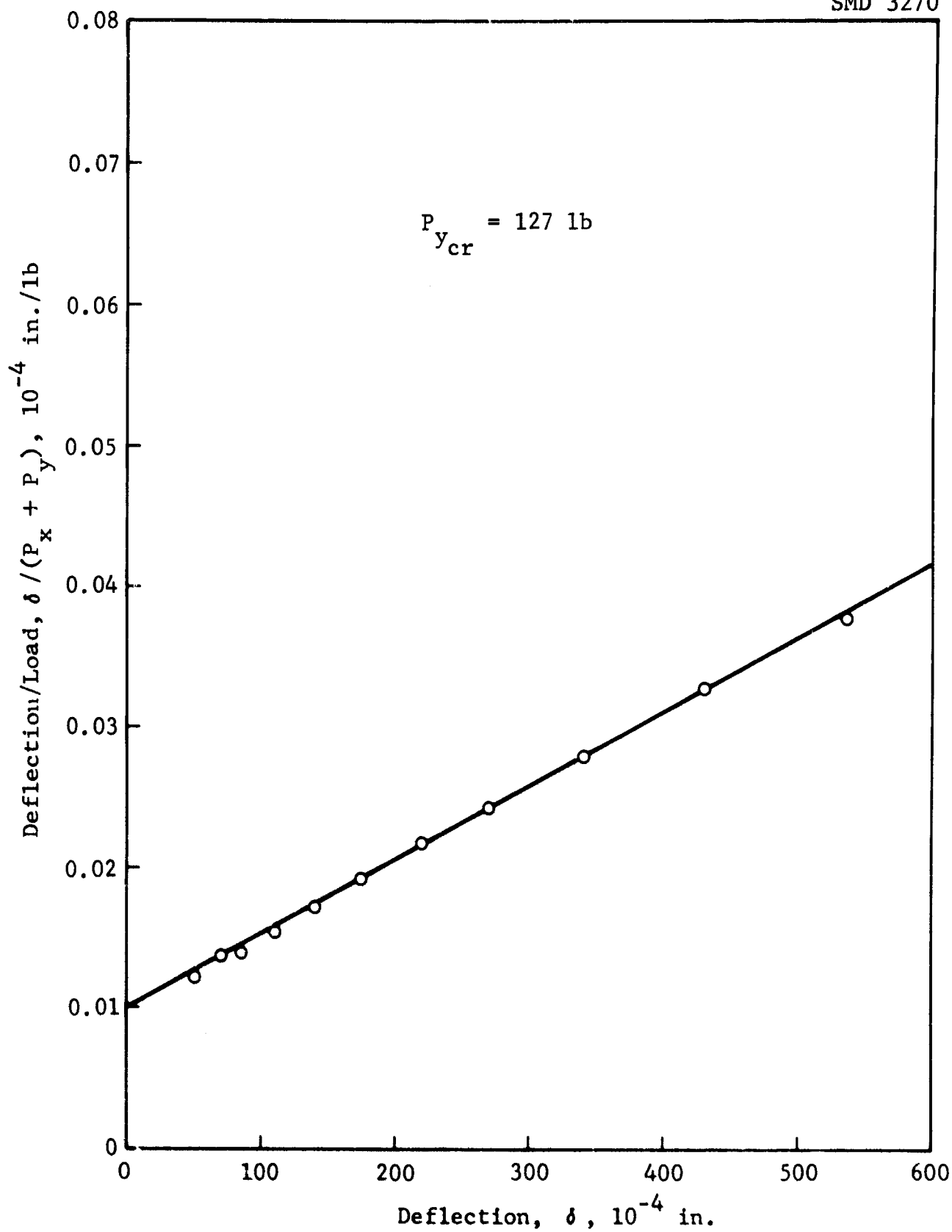
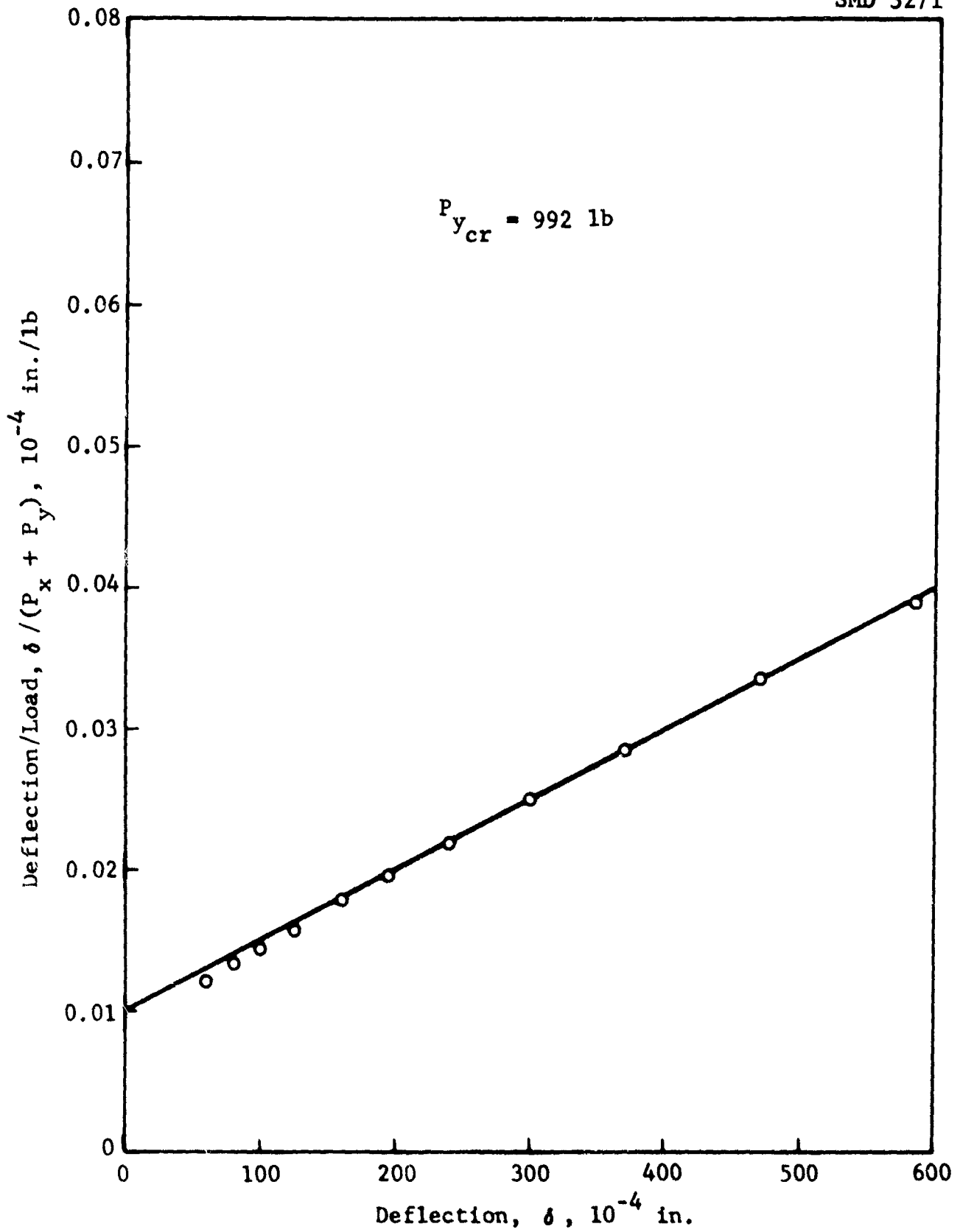


Figure 163 Southwell Plot for Aluminum Panel No. 1, $N_y/N_x = 0.0068$

Figure 164 Southwell Plot for Aluminum Panel No. 1, $N_y/N_x = 0.053$

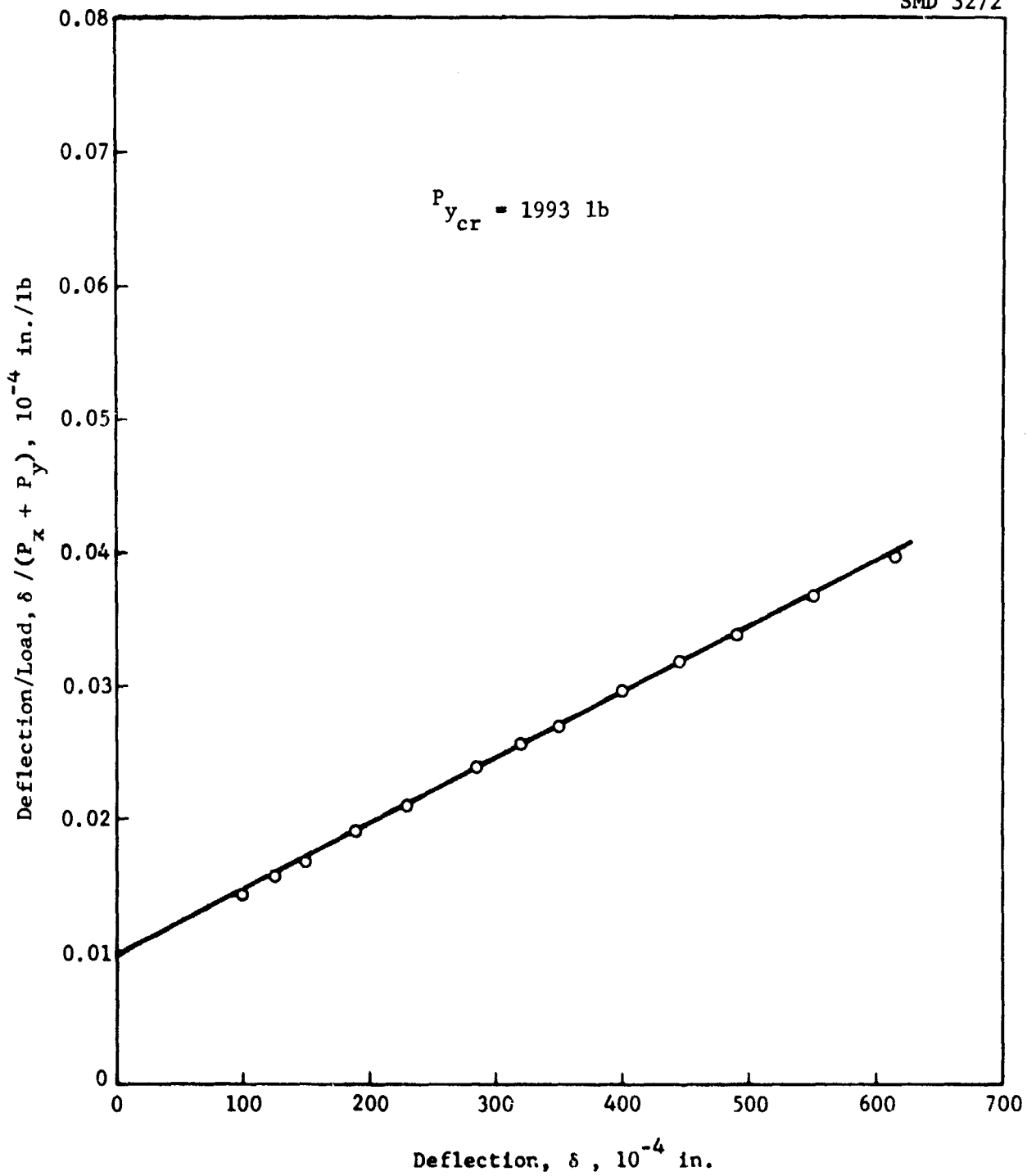


Figure 165 Southwell Plot for Aluminum Panel No. 1, $N_y/N_x = 0.110$

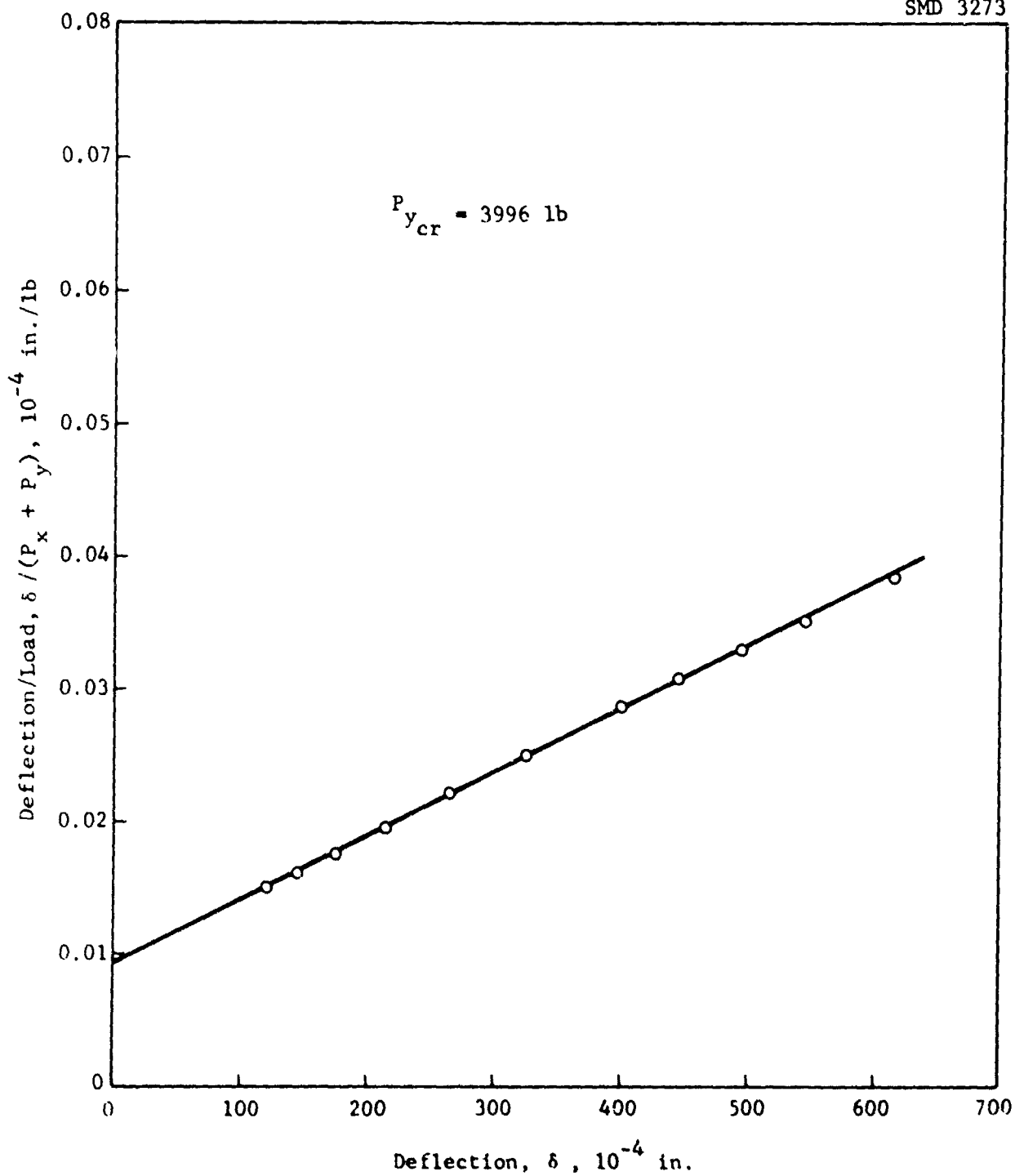


Figure 166 Southwell Plot for Aluminum Panel No. 1, $N_y/N_x = 0.239$

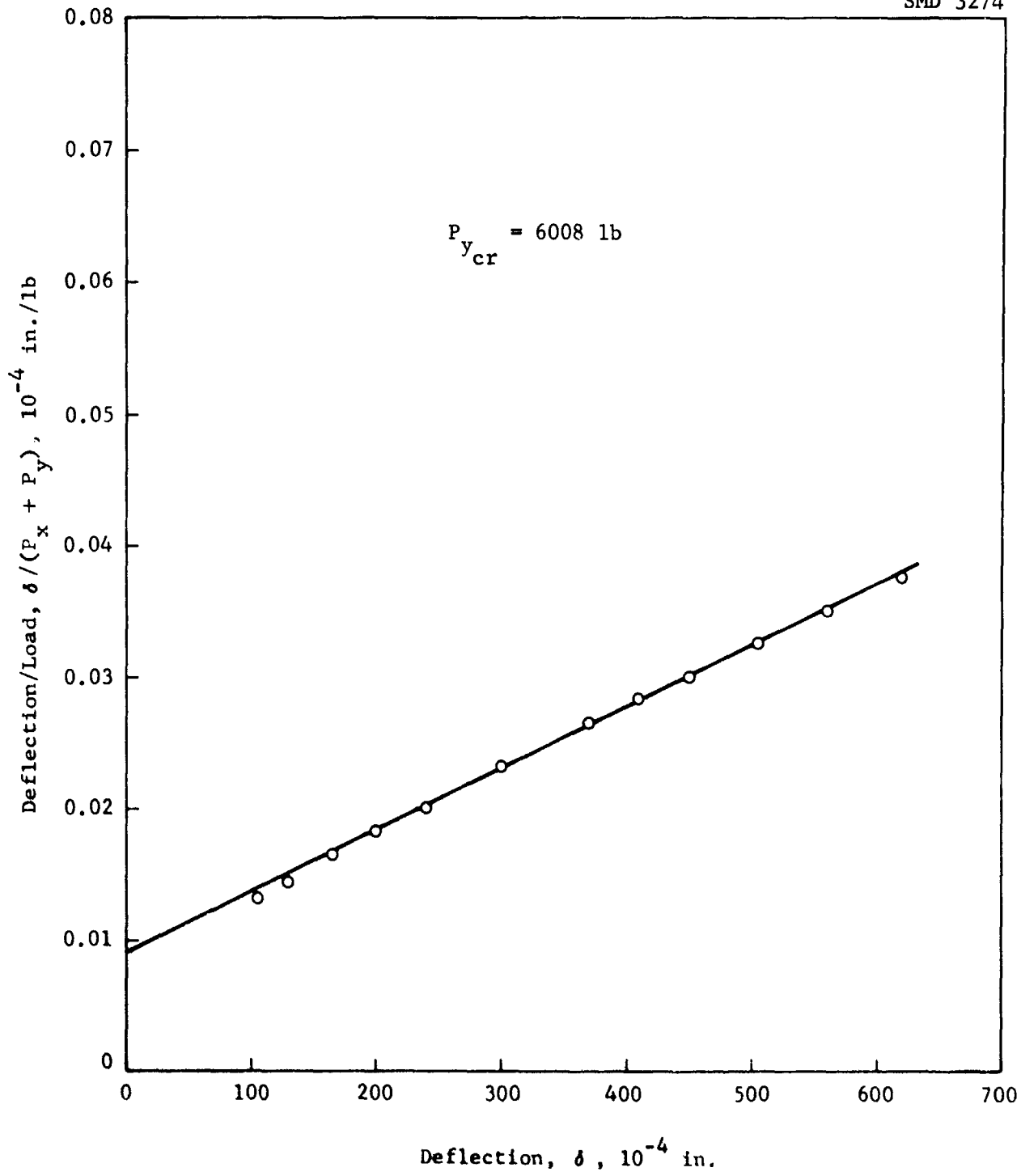
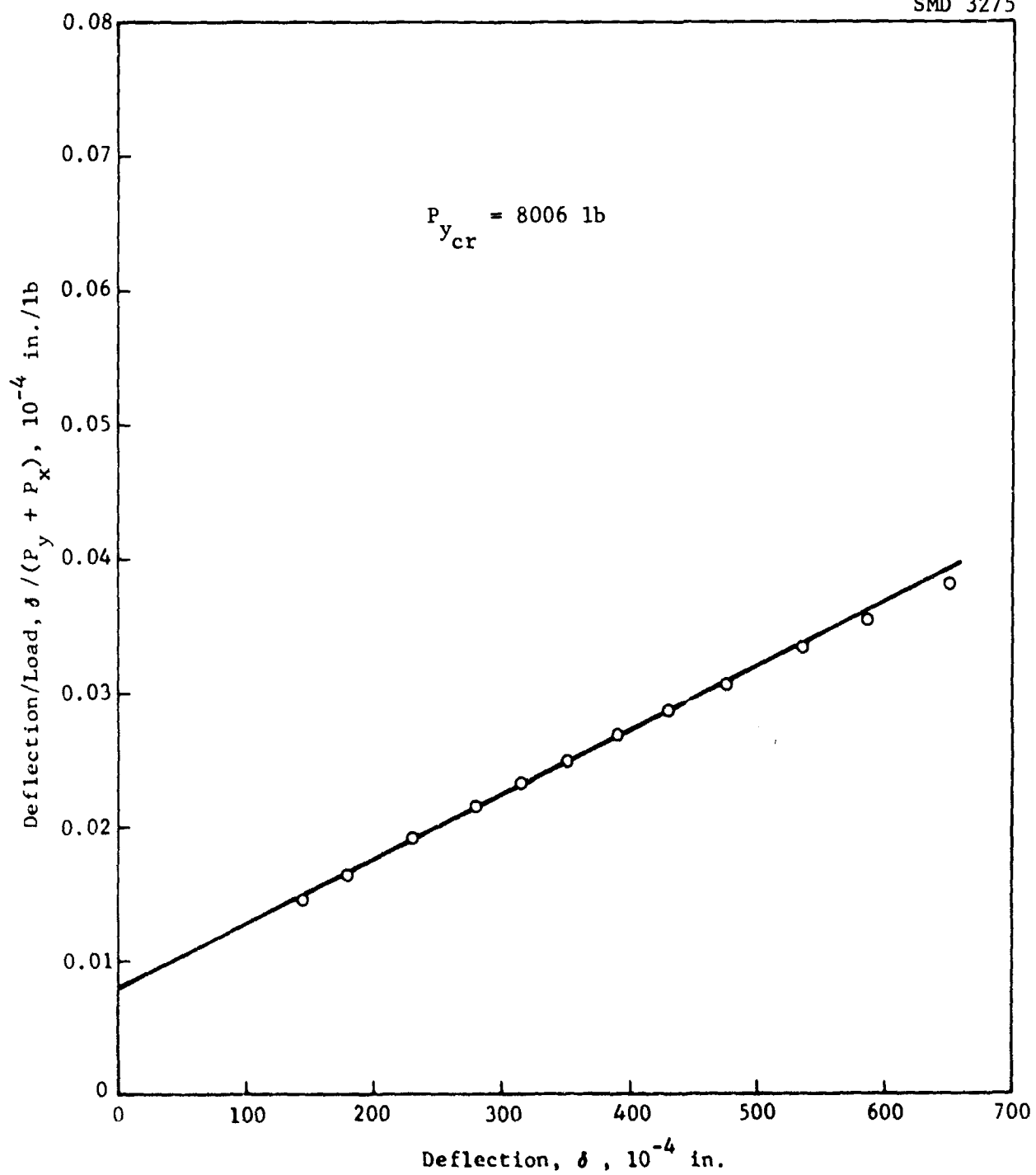


Figure 167 Southwell Plot for Aluminum Panel No. 1, $N_y/N_x = 0.402$

Figure 168 Southwell Plot for Aluminum Panel No. 1, $N_y/N_x = 0.627$

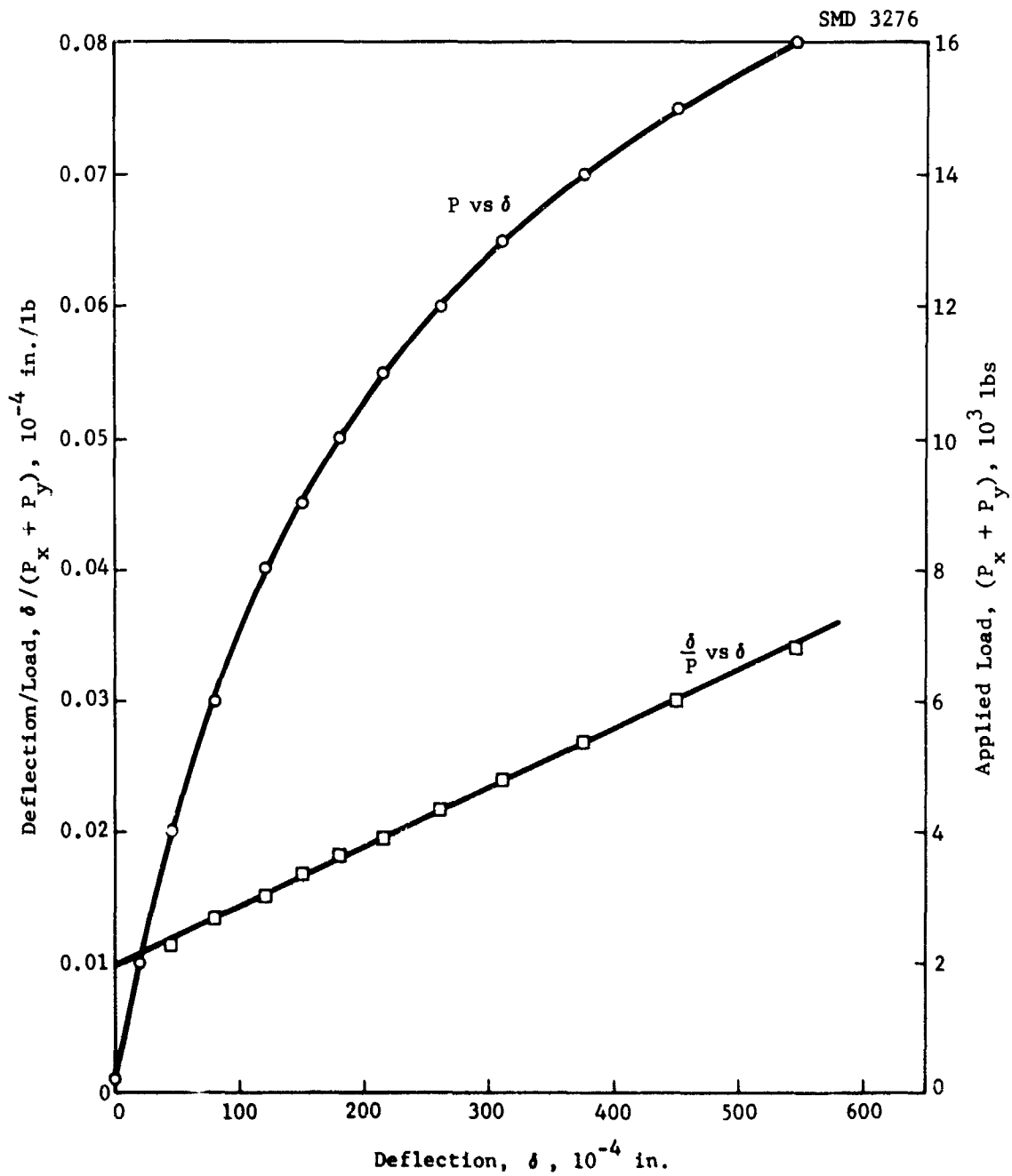


Figure 169 Load-Deflection Curve and Southwell Plot for Aluminum
 Panel No. 1, $N_y/N_x = 1.000$

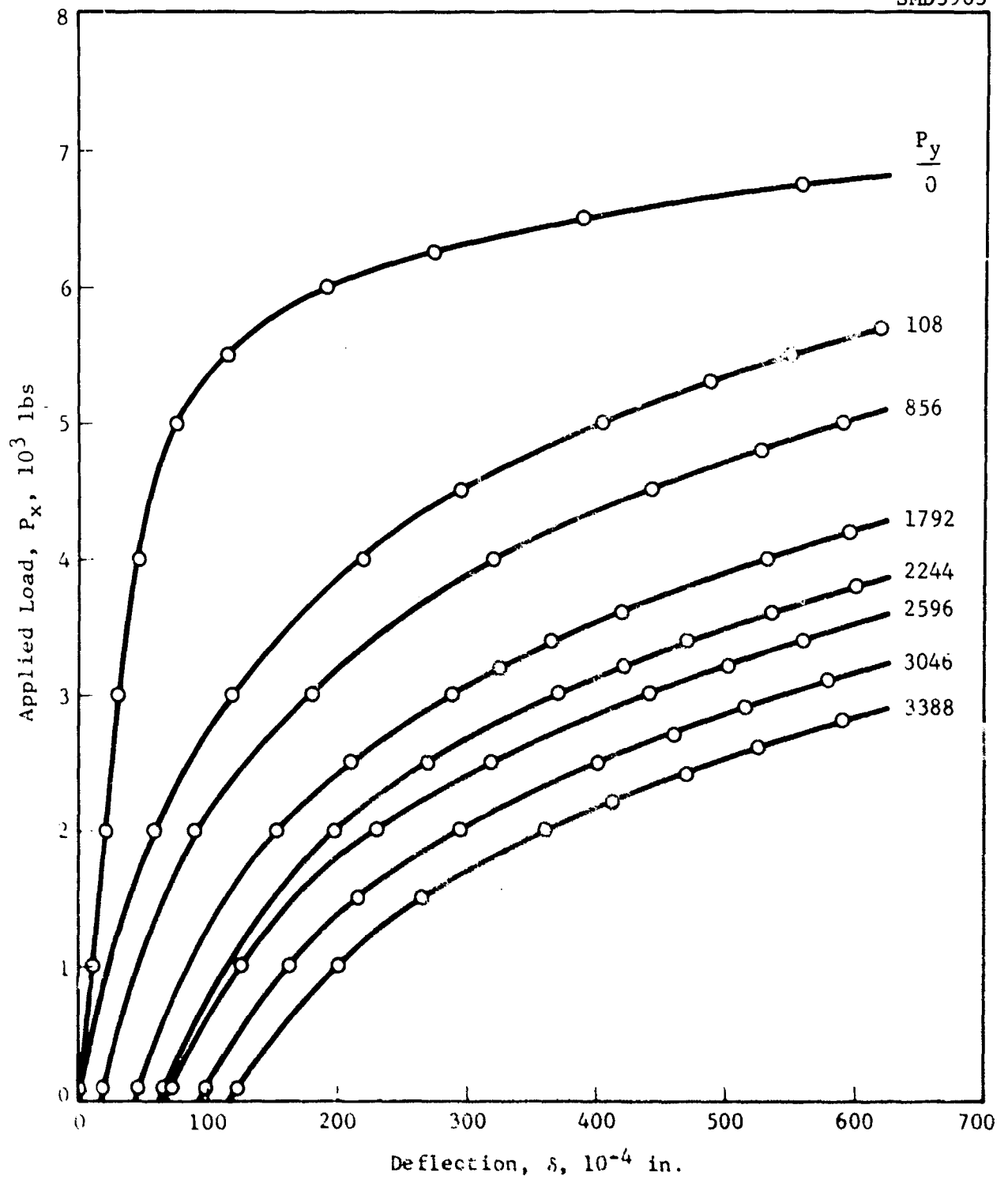
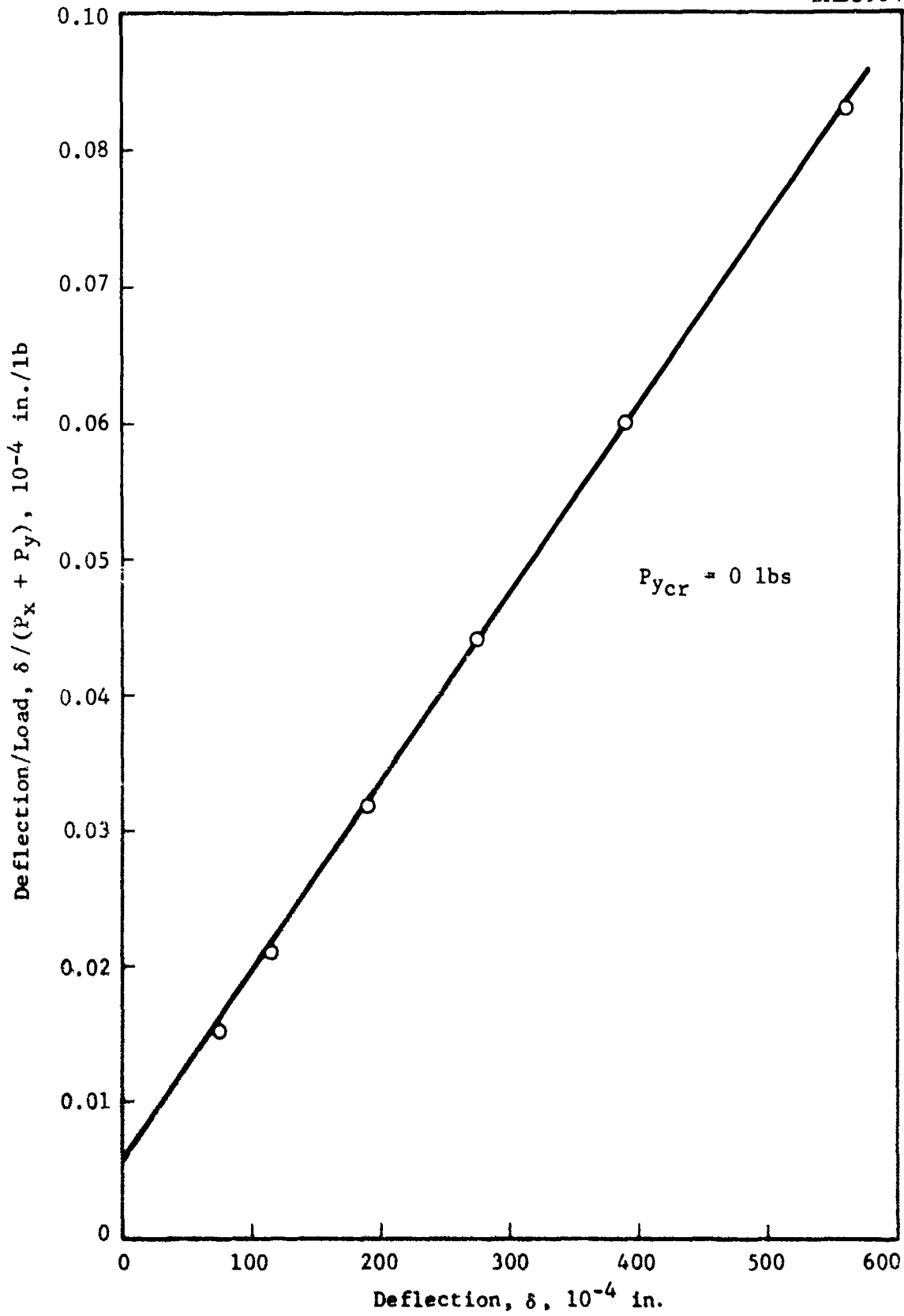


Figure 170 Load Deflection Curves for Panel No. 2

Figure 171 Southwell Plot for Panel No. 2, $N_y/N_x = 0$

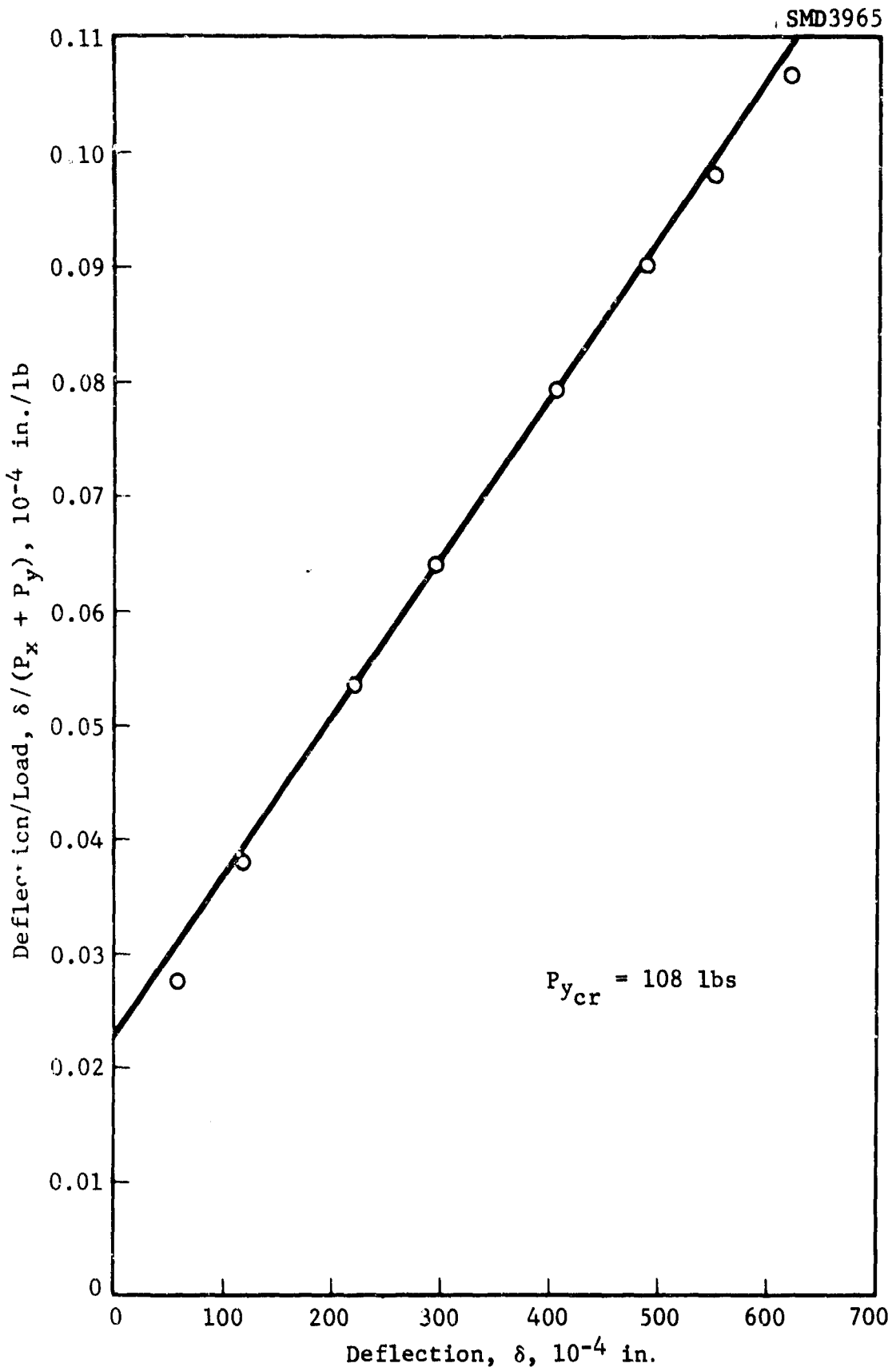


Figure 172 Southwell Plot for Panel No. 2, $N_y/N_x = .015$

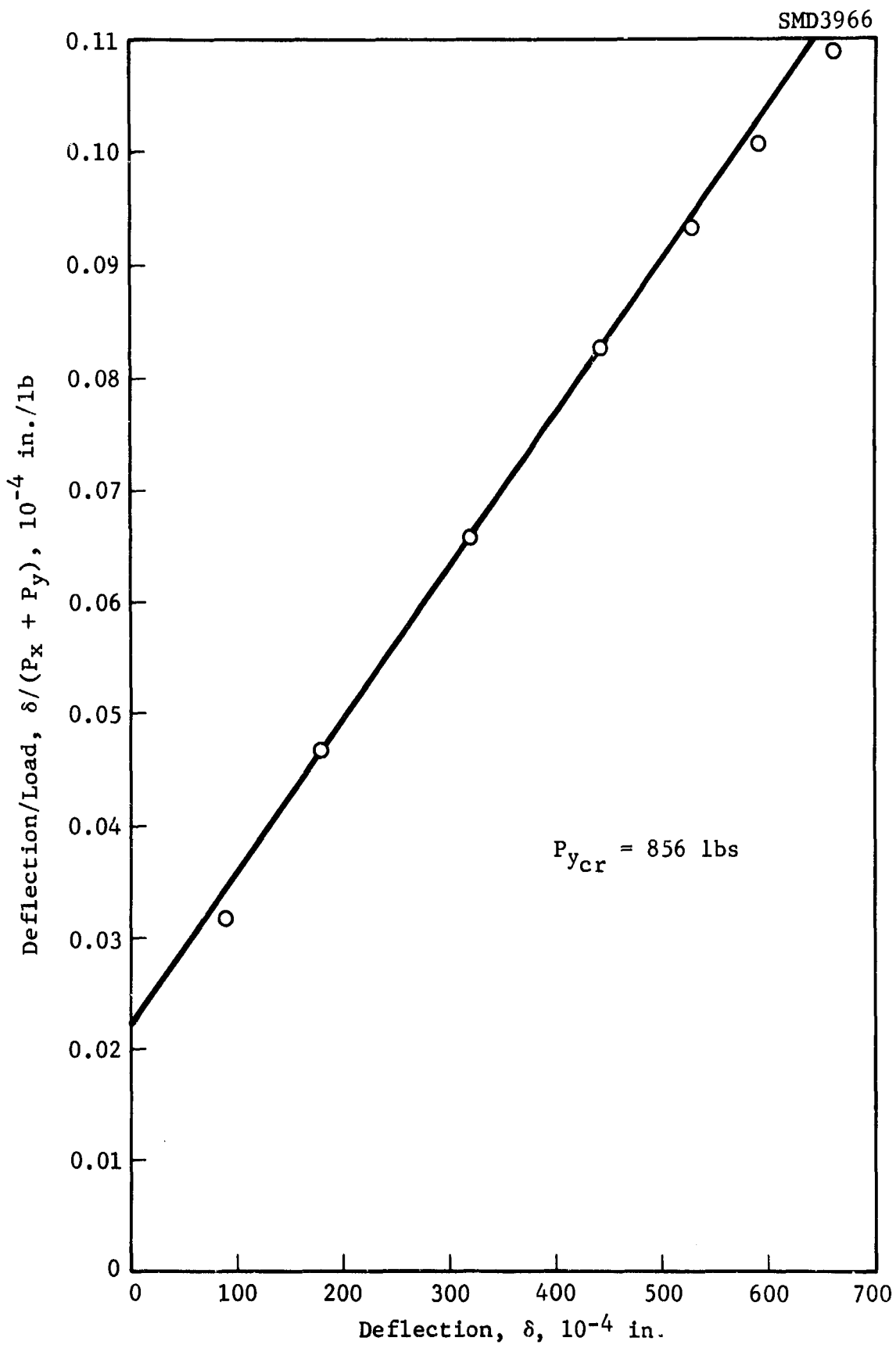
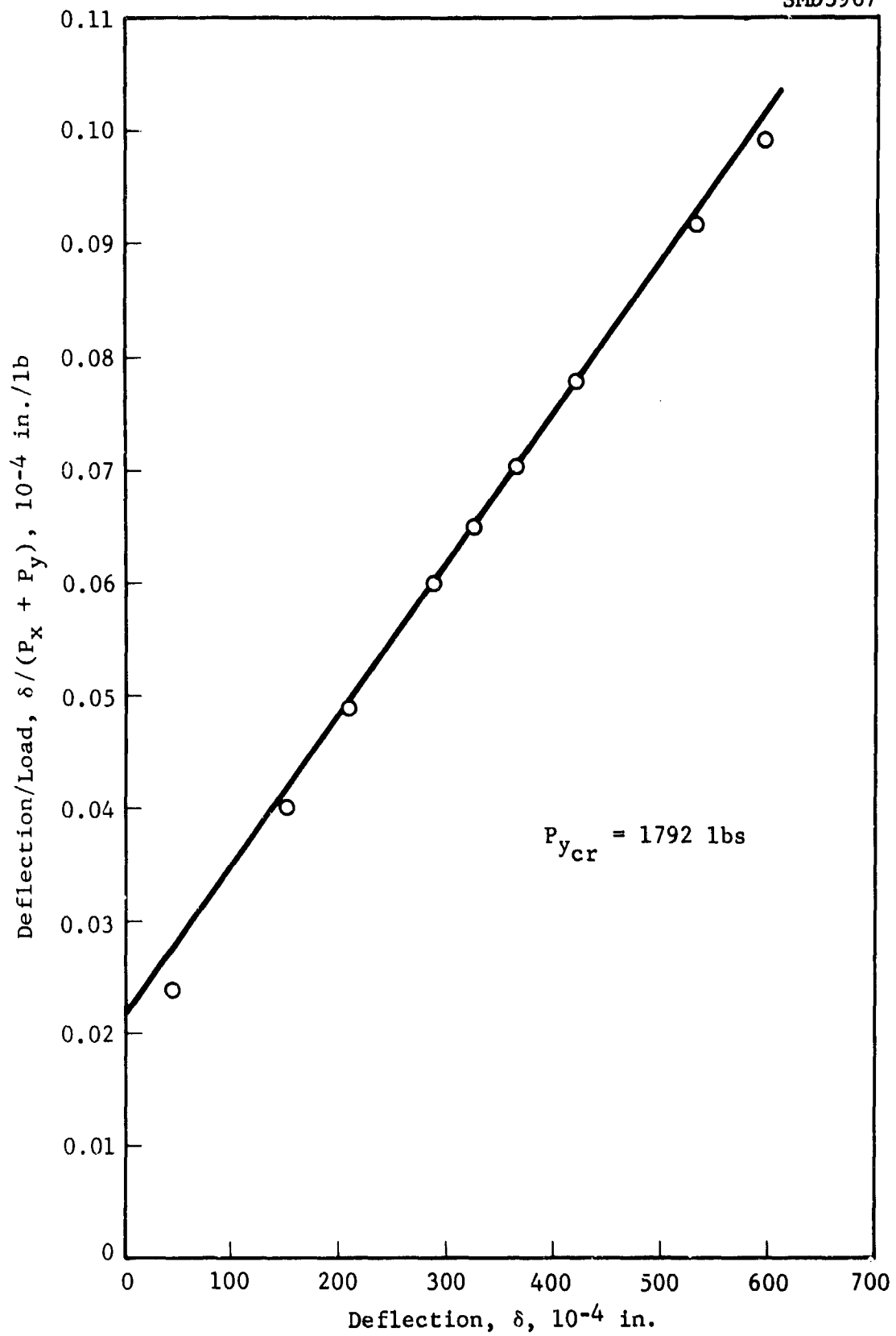


Figure 173 Southwell Plot for Panel No. 2, $N_y/N_x = .133$

Figure 174 Southwell Plot for Panel No. 2, $N_y/N_x = .319$

SMD3968

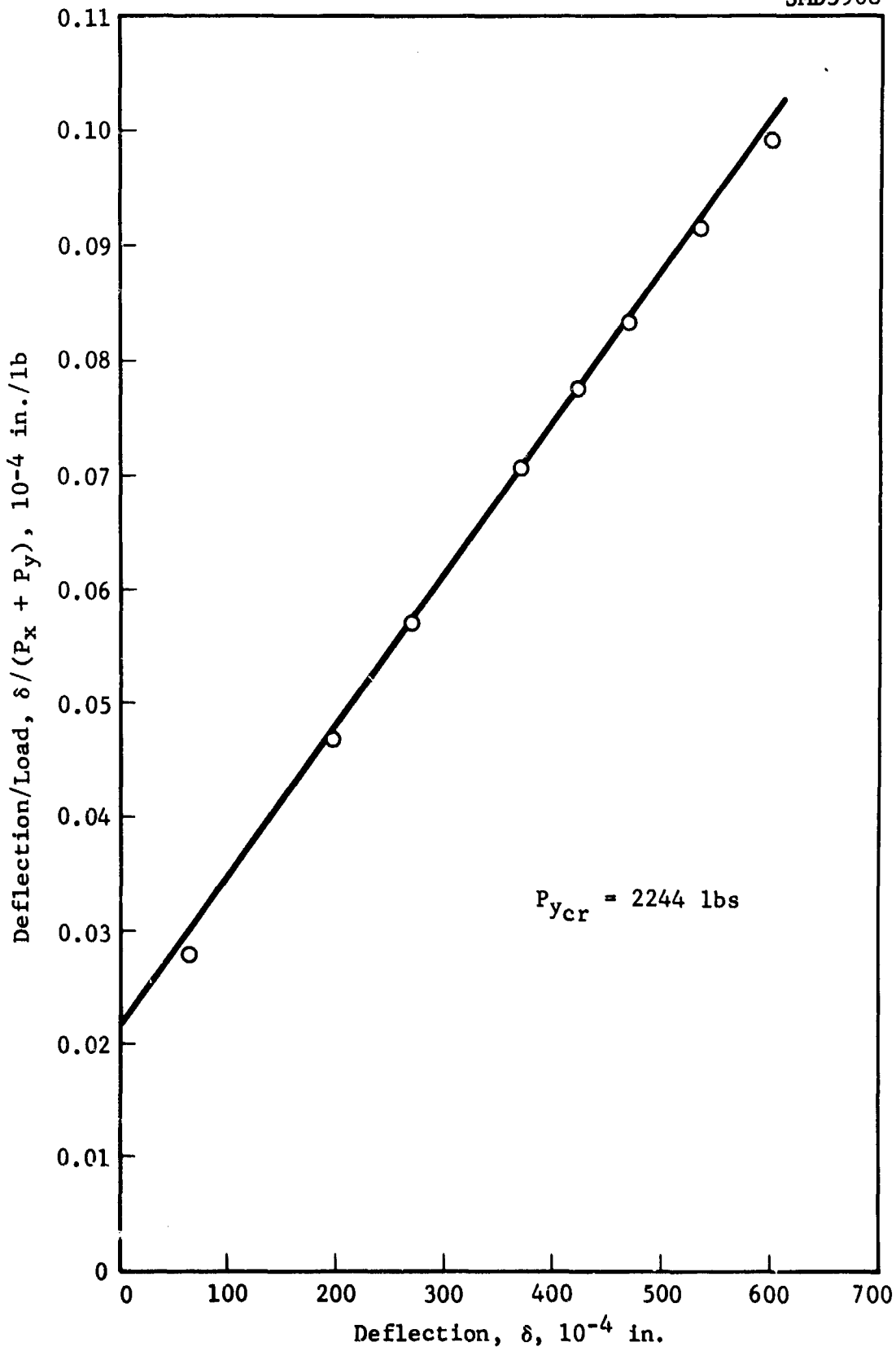


Figure 175 Southwell Plot for Panel No. 2, $N_y/N_x = .445$

SMD3969

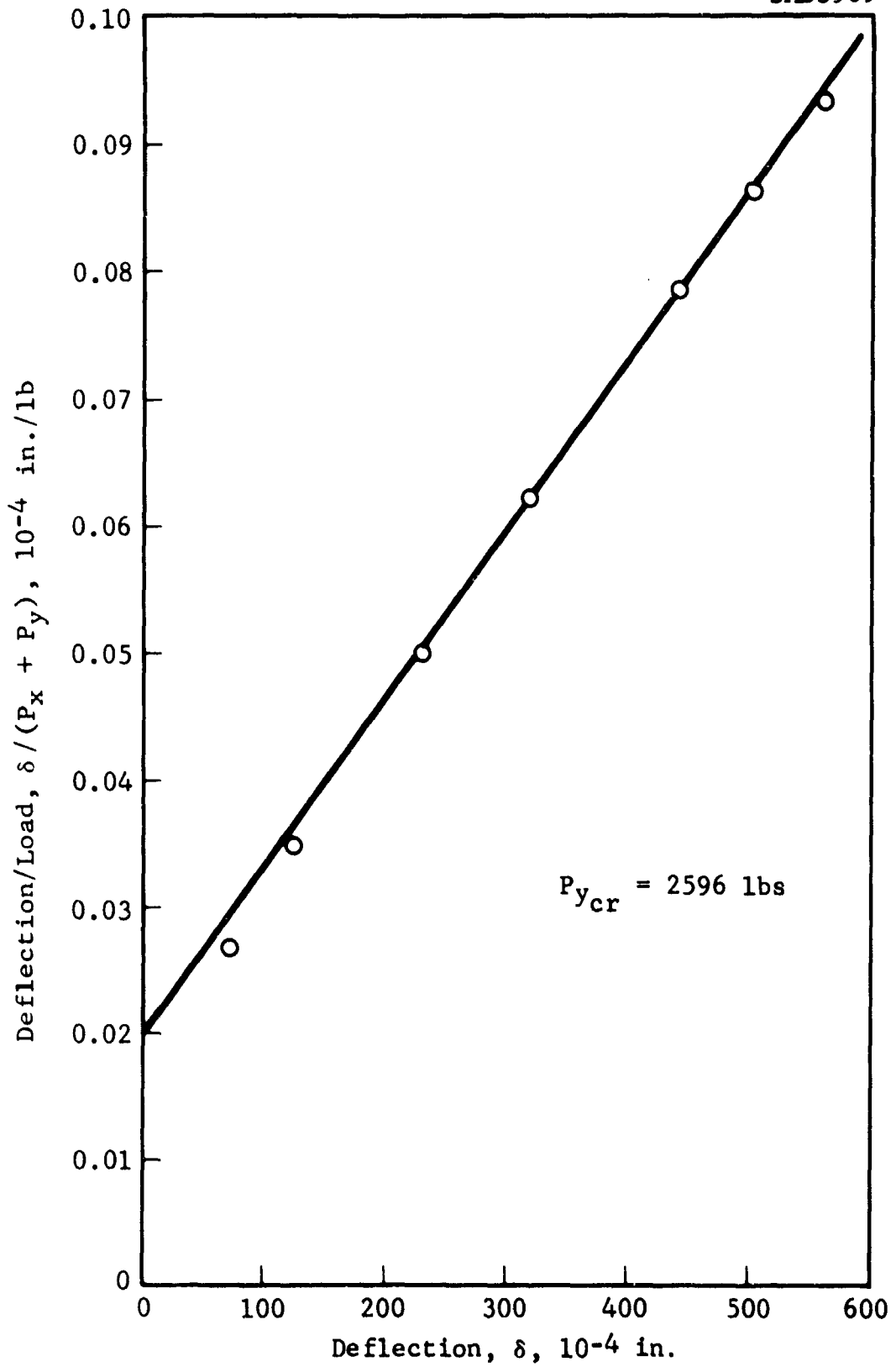


Figure 176 Southwell Plot for Panel No. 2, $N_y/N_x = .531$

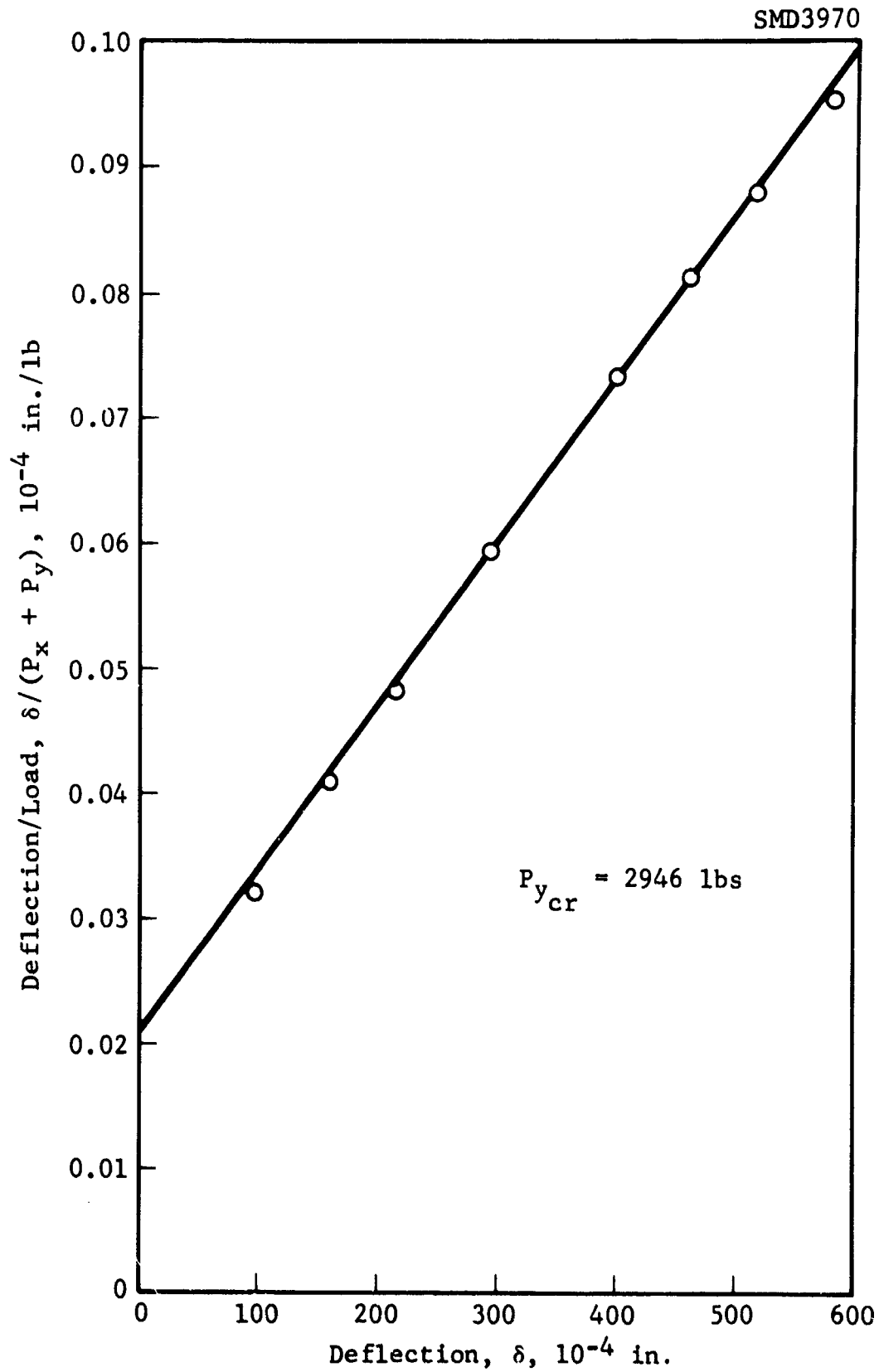


Figure 177 Southwell Plot for Panel No. 2, $N_y/N_x = .634$

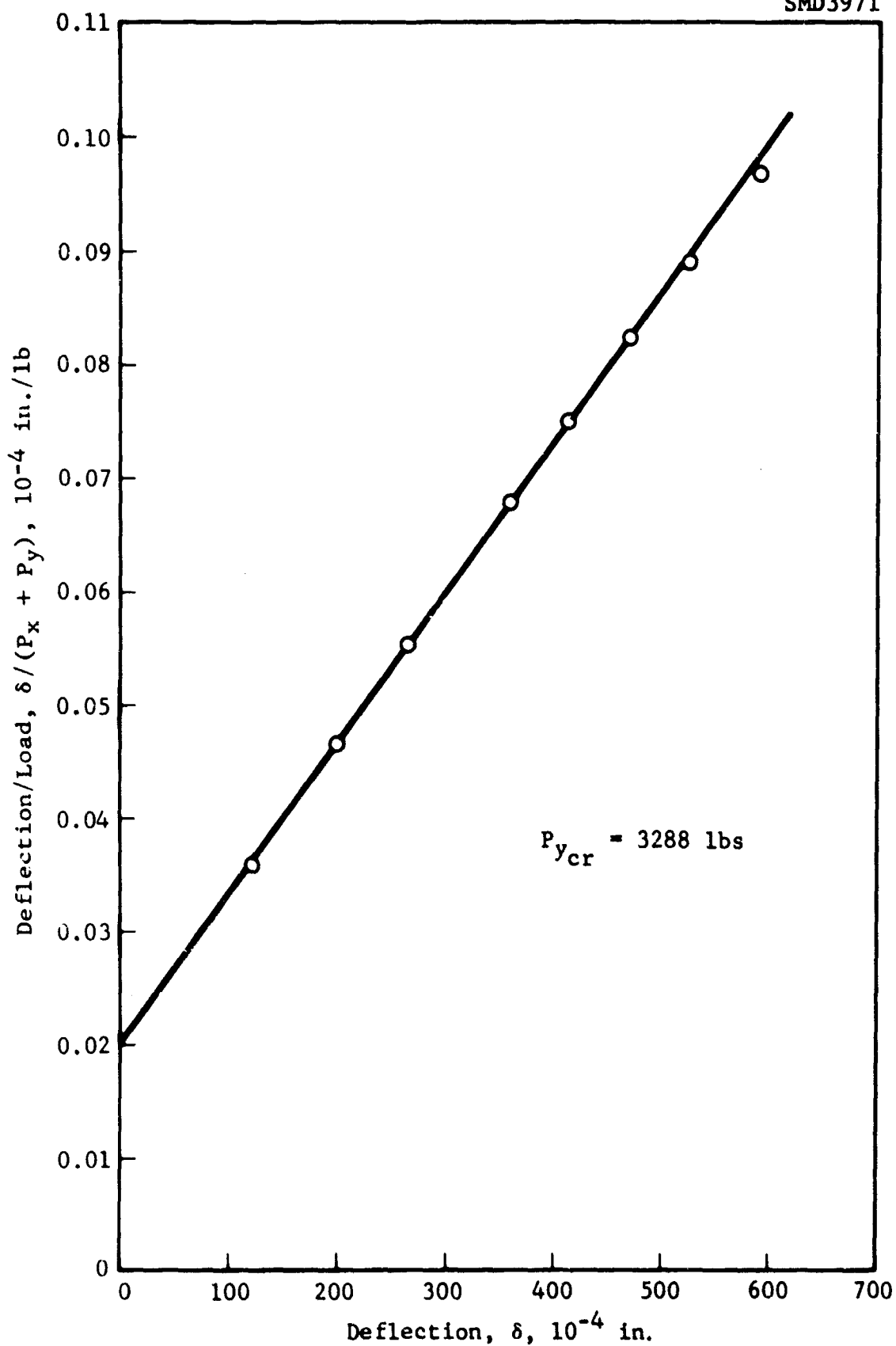


Figure 178 Southwell Plot for Panel No. 2, $N_y/N_x = .774$

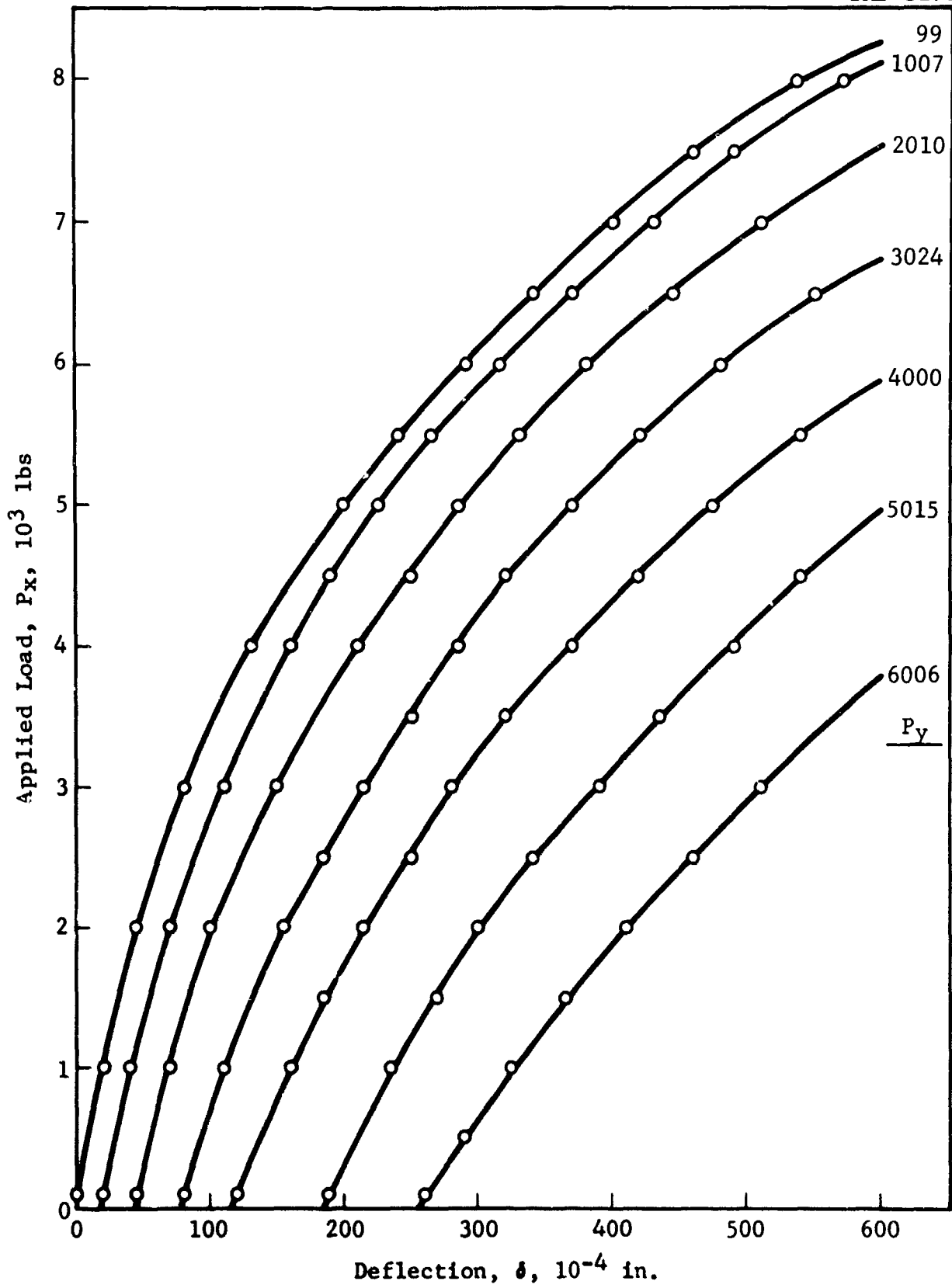


Figure 179 Load-Deflection Curves for Panel No. 3

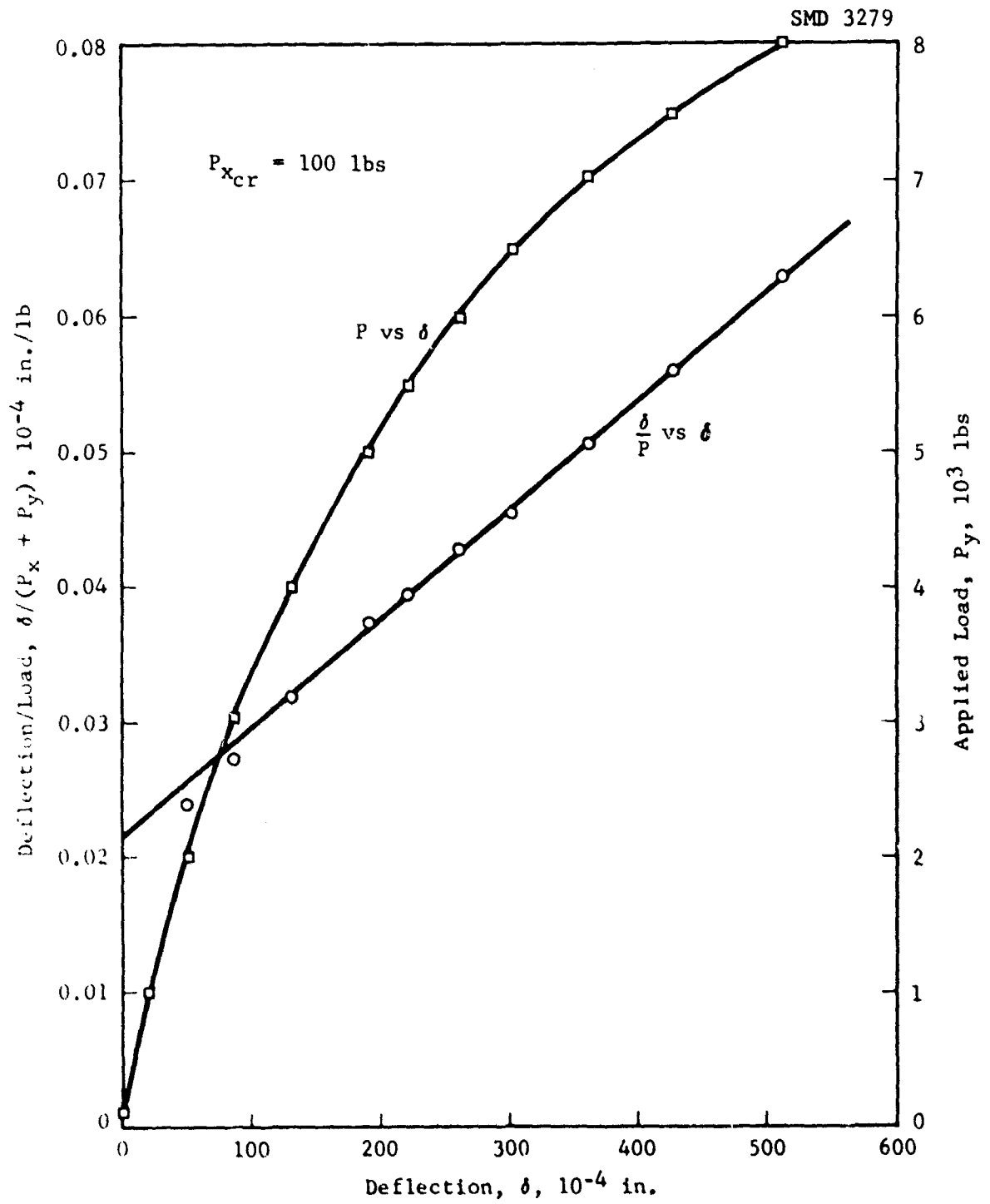


Figure 180 Load-Deflection Curve and Southwell Plot for Panel No. 3, $N_y/N_x = 123.0$

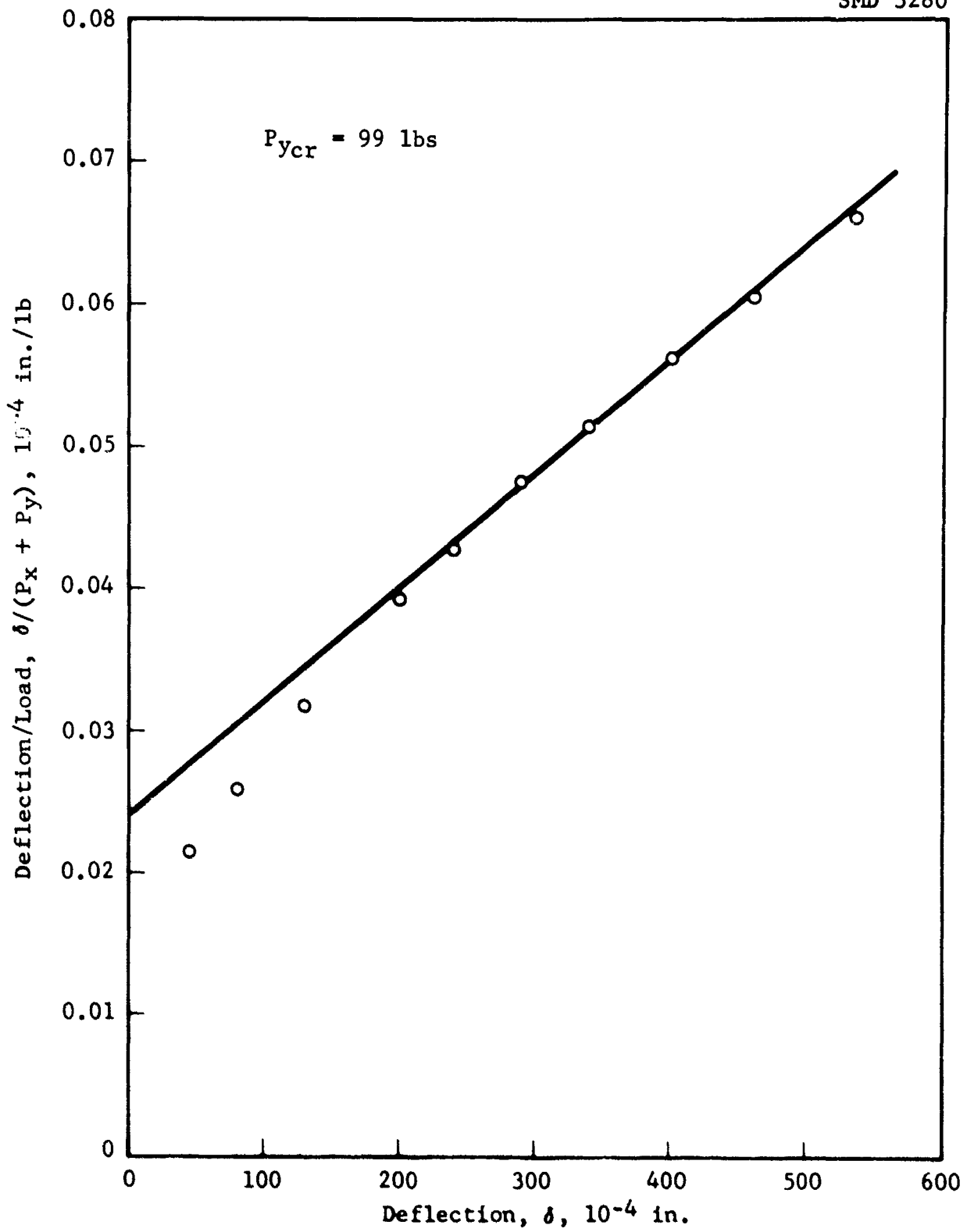
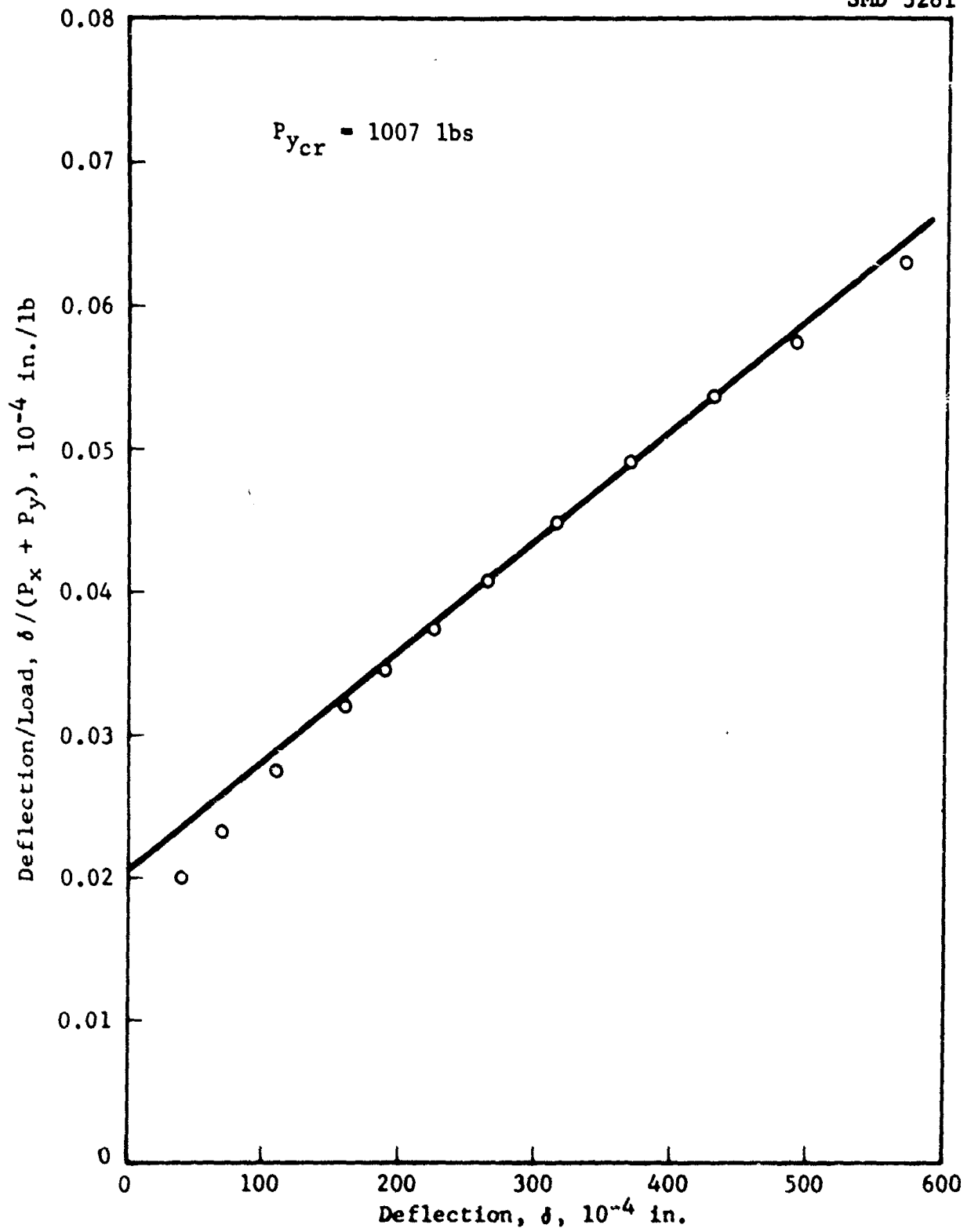
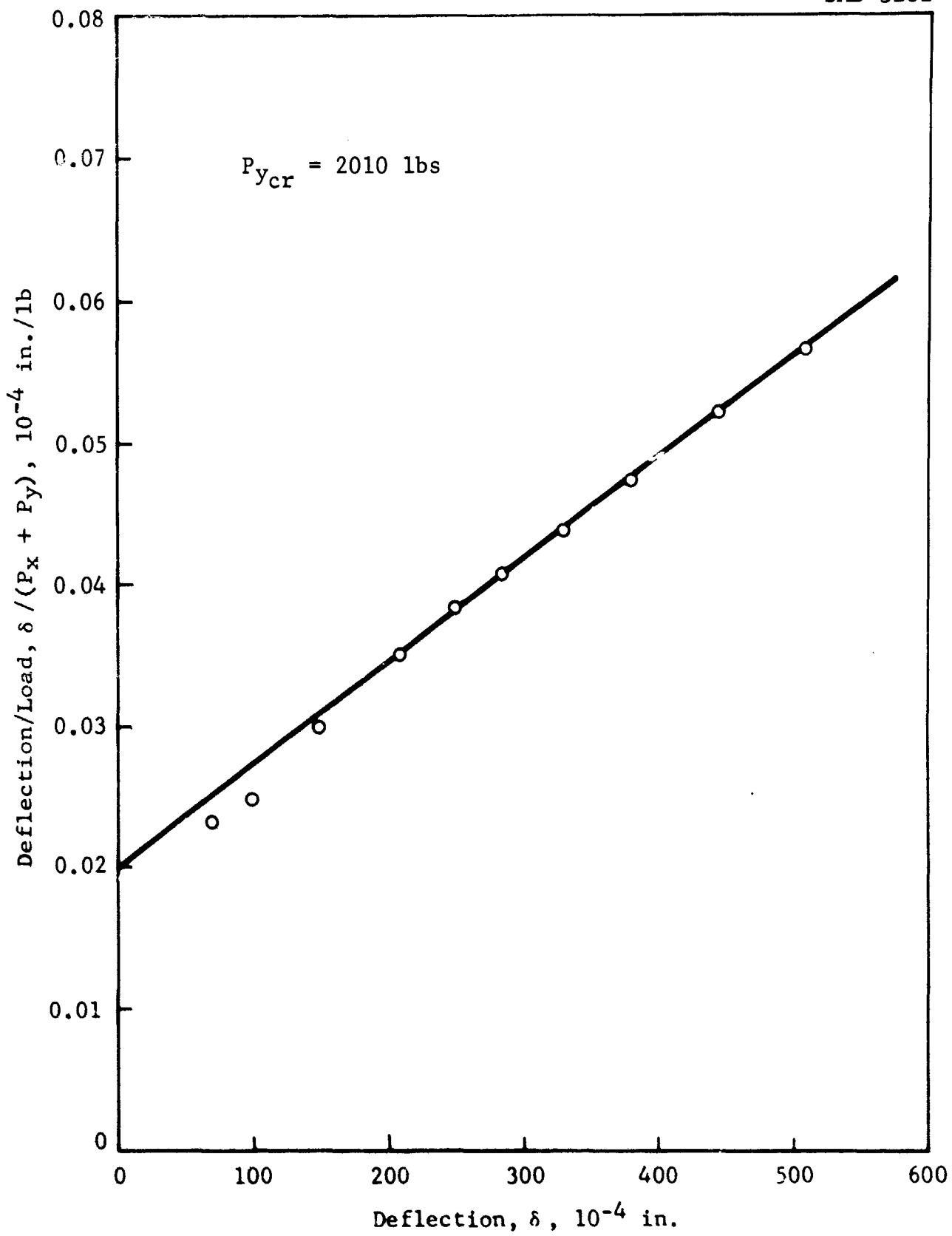
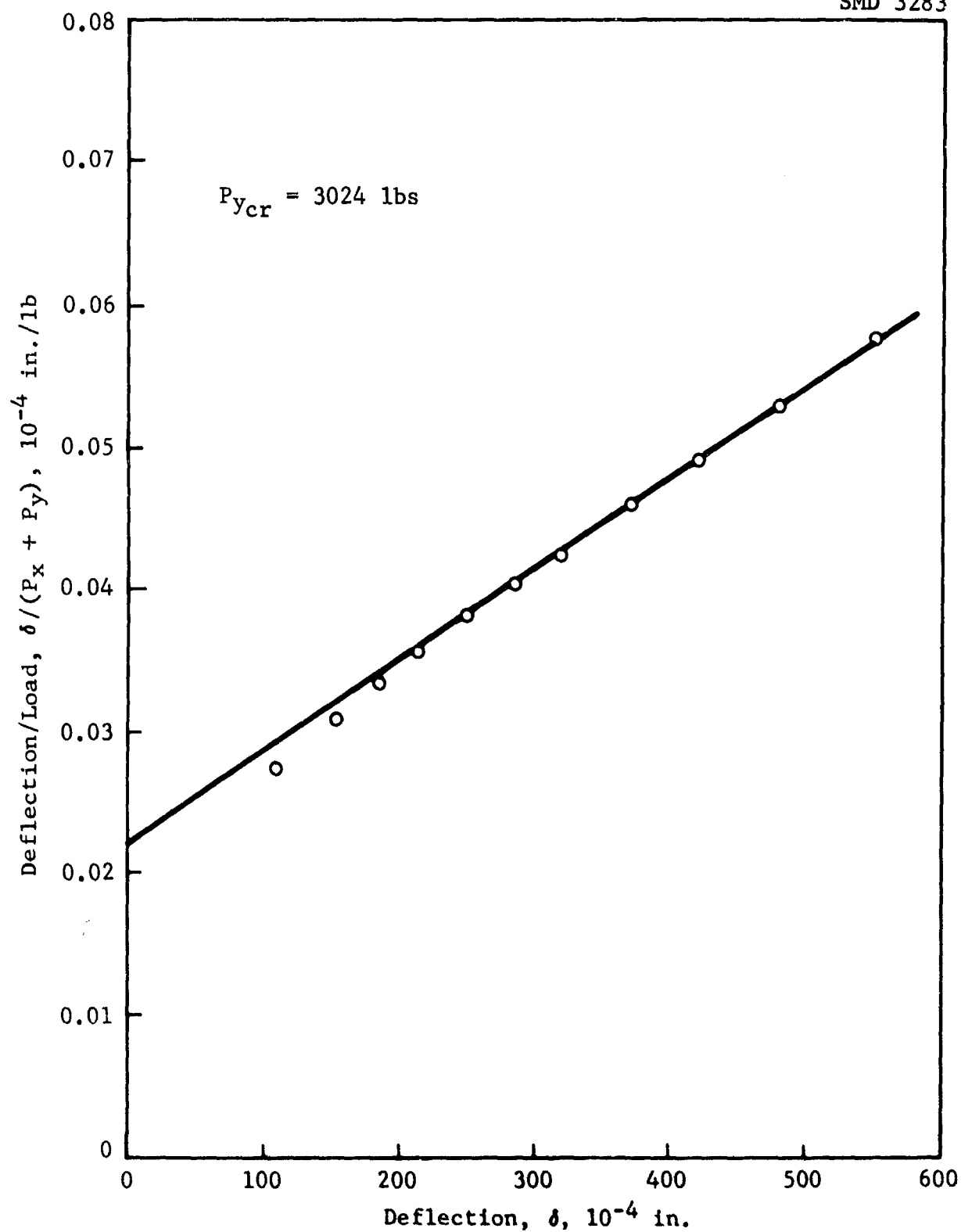


Figure 181 Southwell Plot for Panel No. 3, $N_y/N_x = .0081$

Figure 182 Southwell Plot for Panel No. 3, $N_y/N_x = .086$

Figure 183 Southwell Plot for Panel No. 3, $N_y/N_x = .171$

Figure 184 Southwell Plot for Panel No. 3, $N_y/N_x = .244$

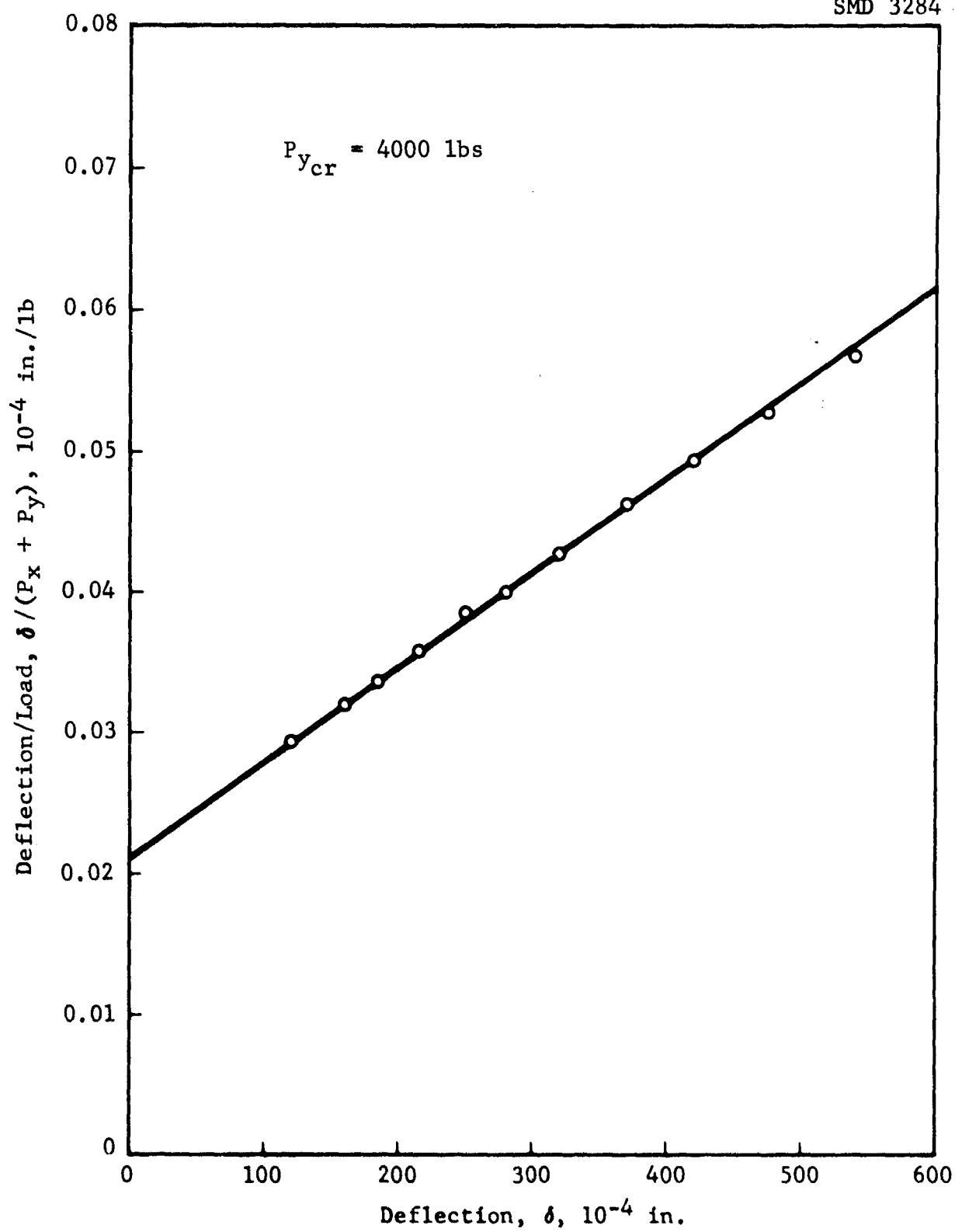
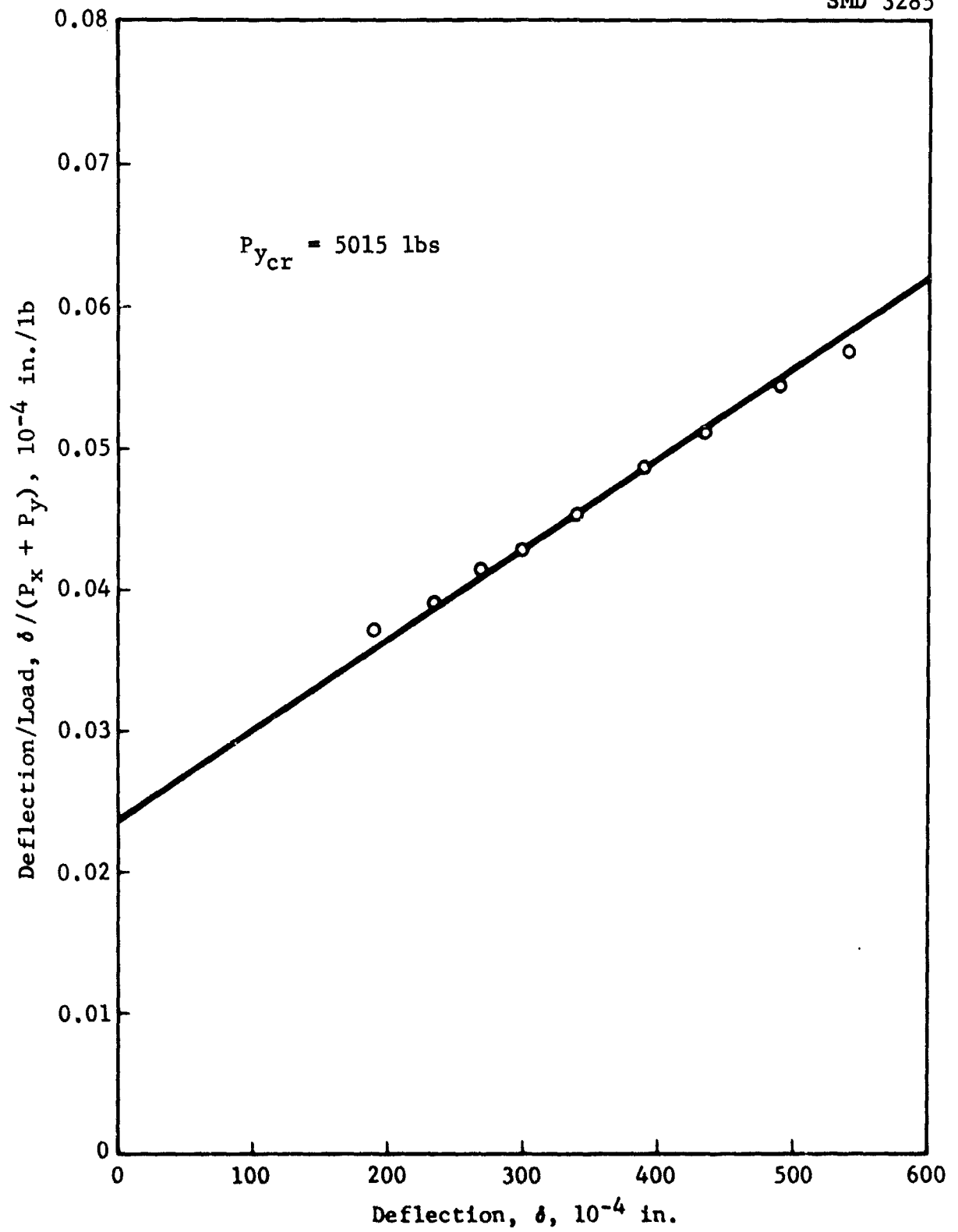


Figure 185 Southwell Plot for Panel No. 3, $N_y/N_x = .367$

Figure 186 Southwell Plot for Panel No. 3, $N_y/N_x = .475$

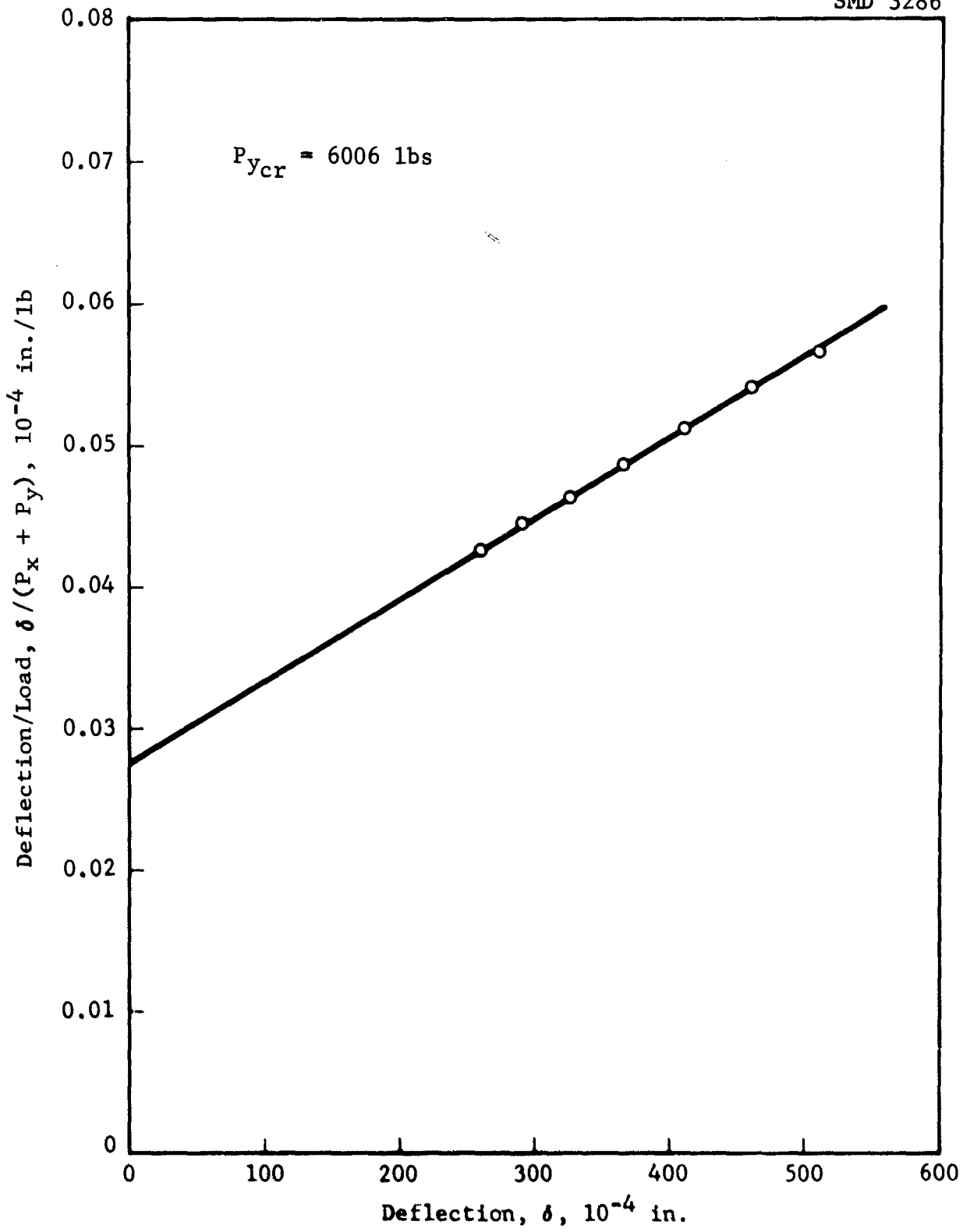


Figure 187 Southwell Plot for Panel No. 3, $N_y/N_x = .532$

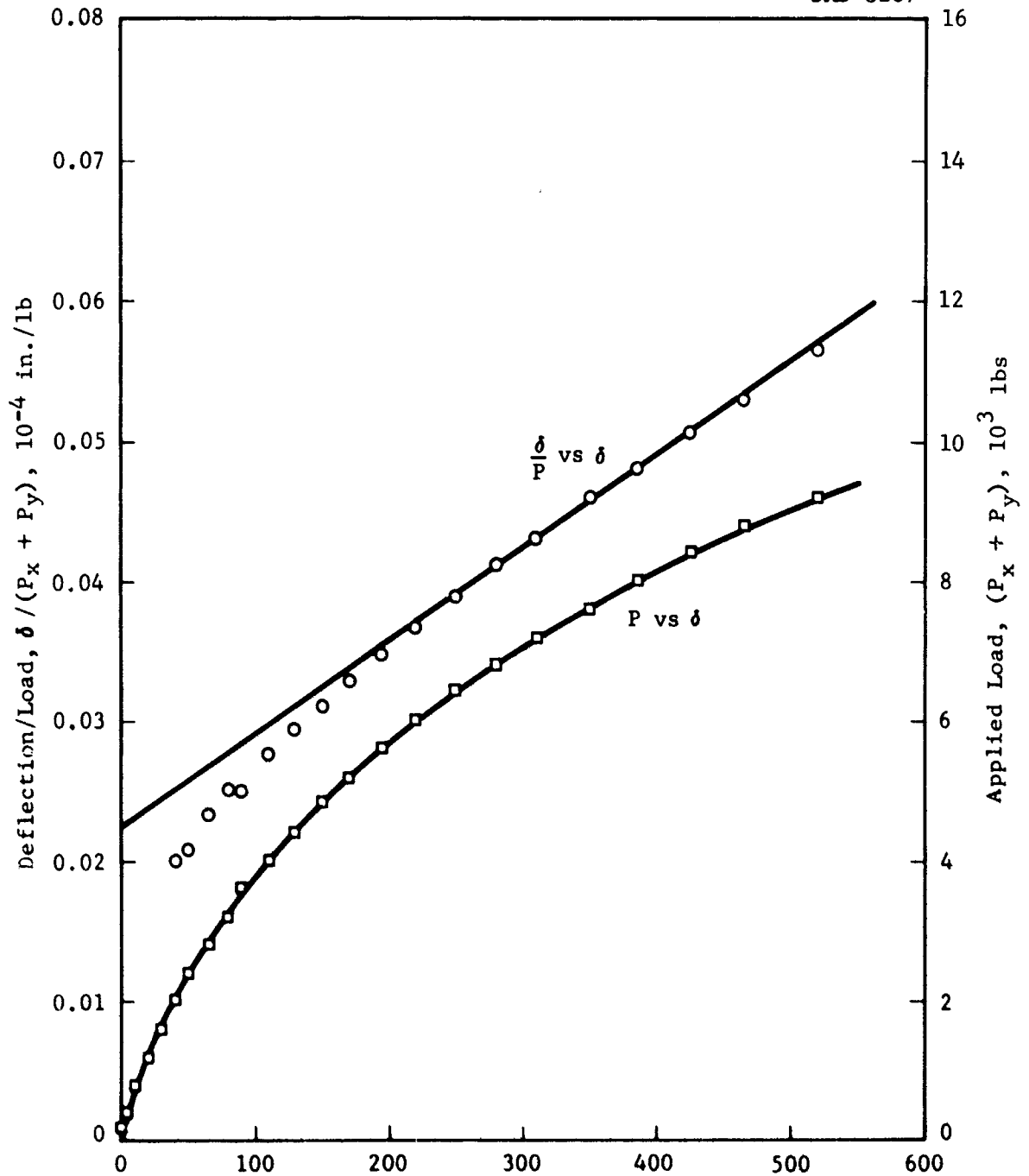


Figure 188 Load-Deflection Curve and Southwell Plot for Panel No. 3, $N_y/N_x = 1.000$

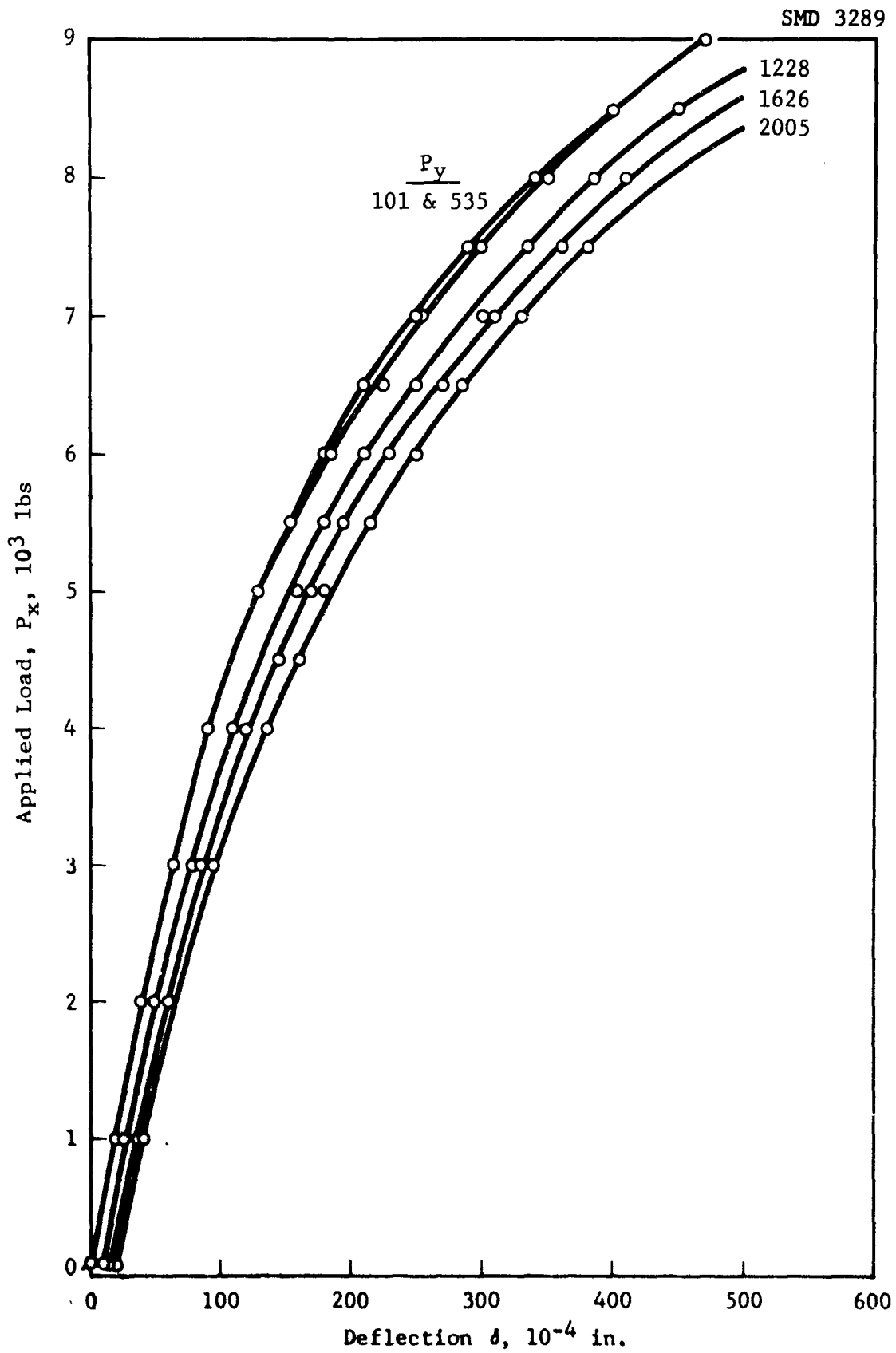
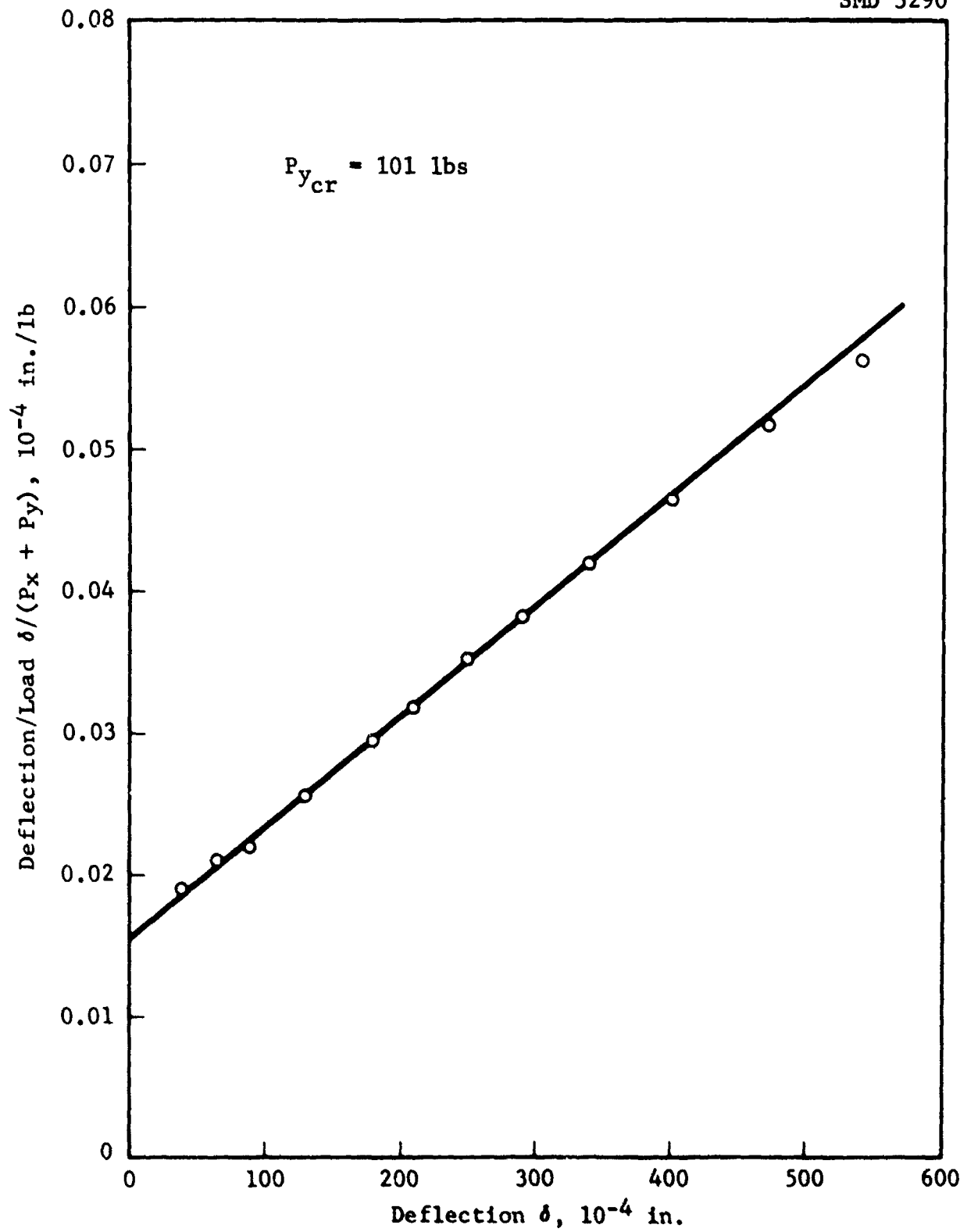
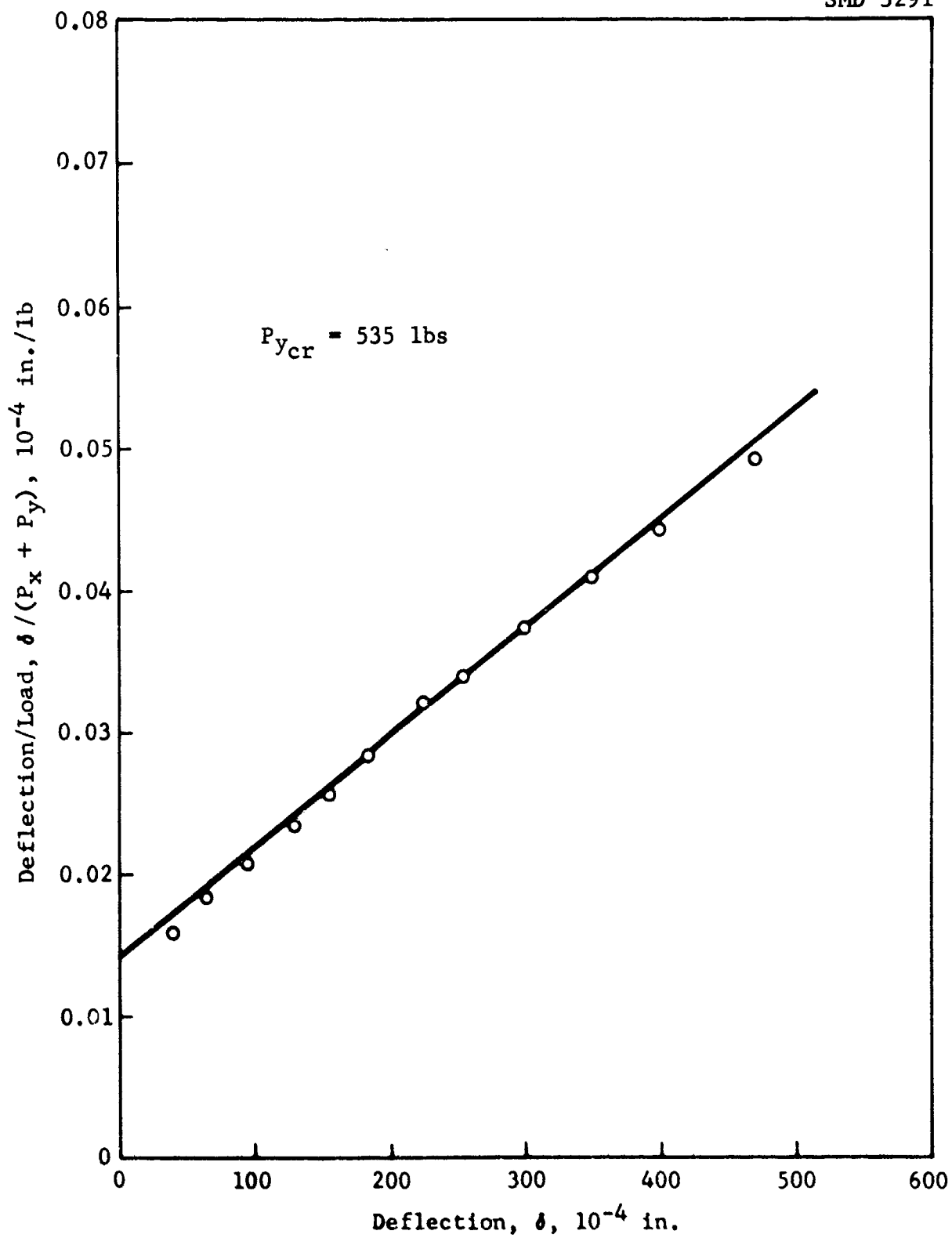
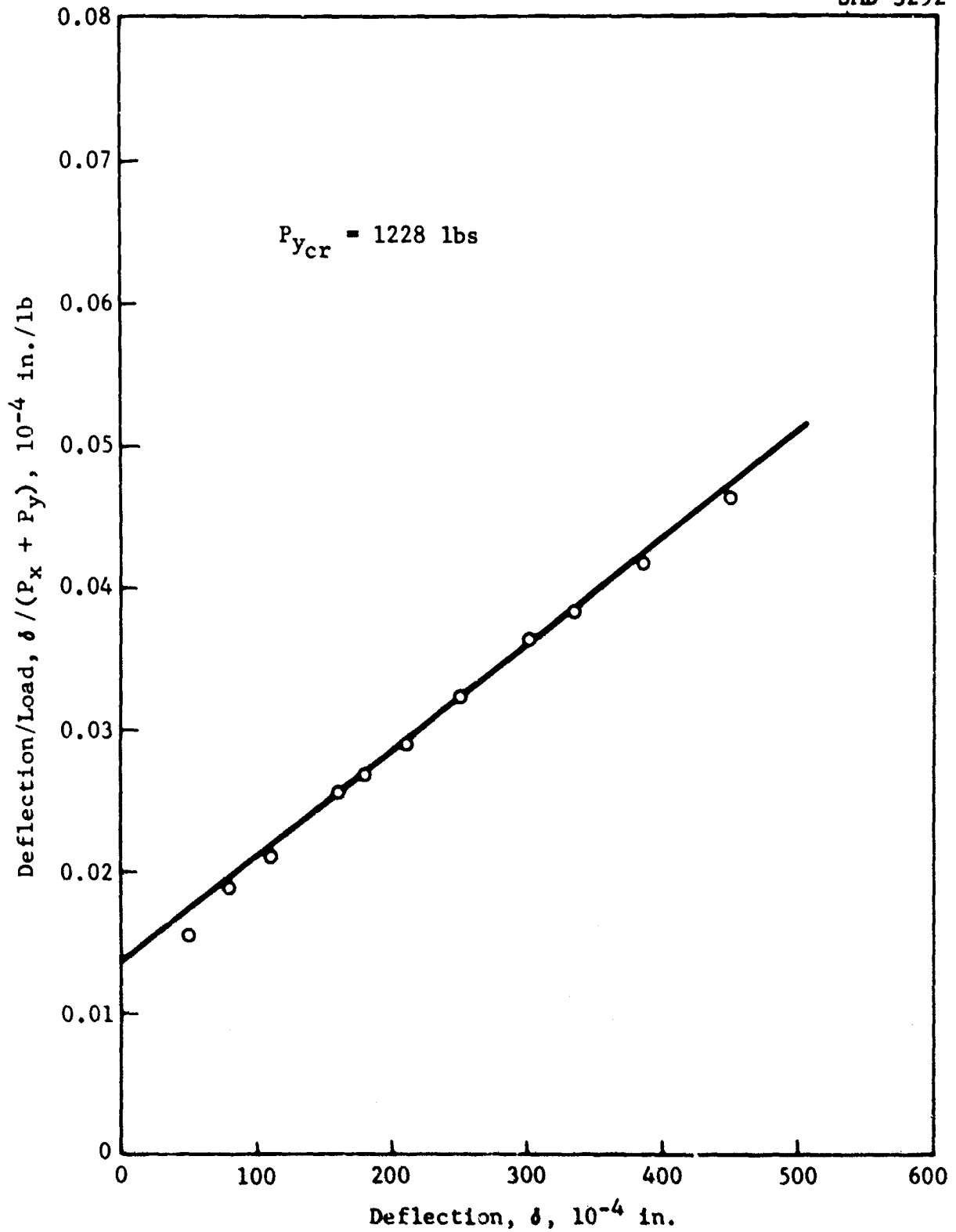
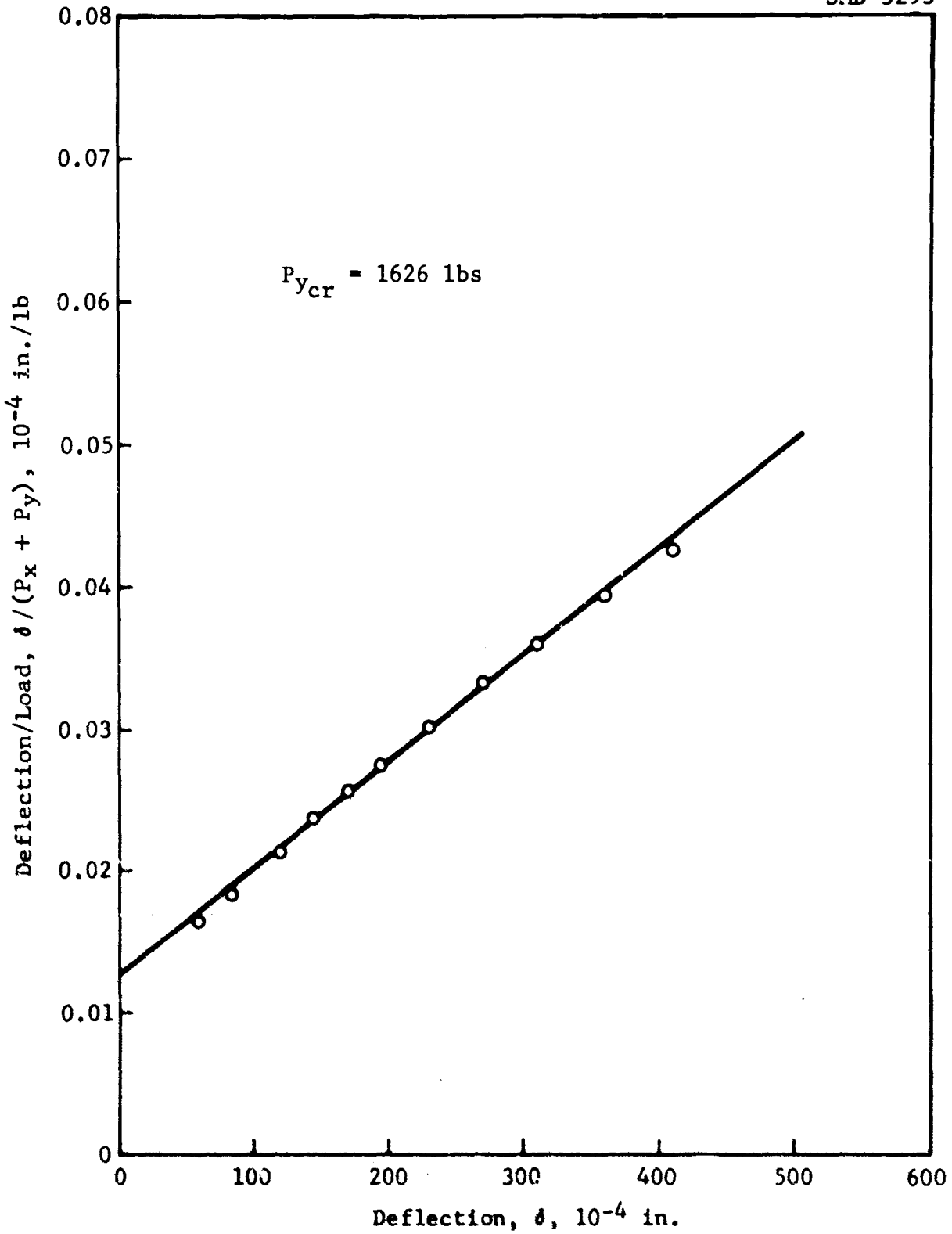


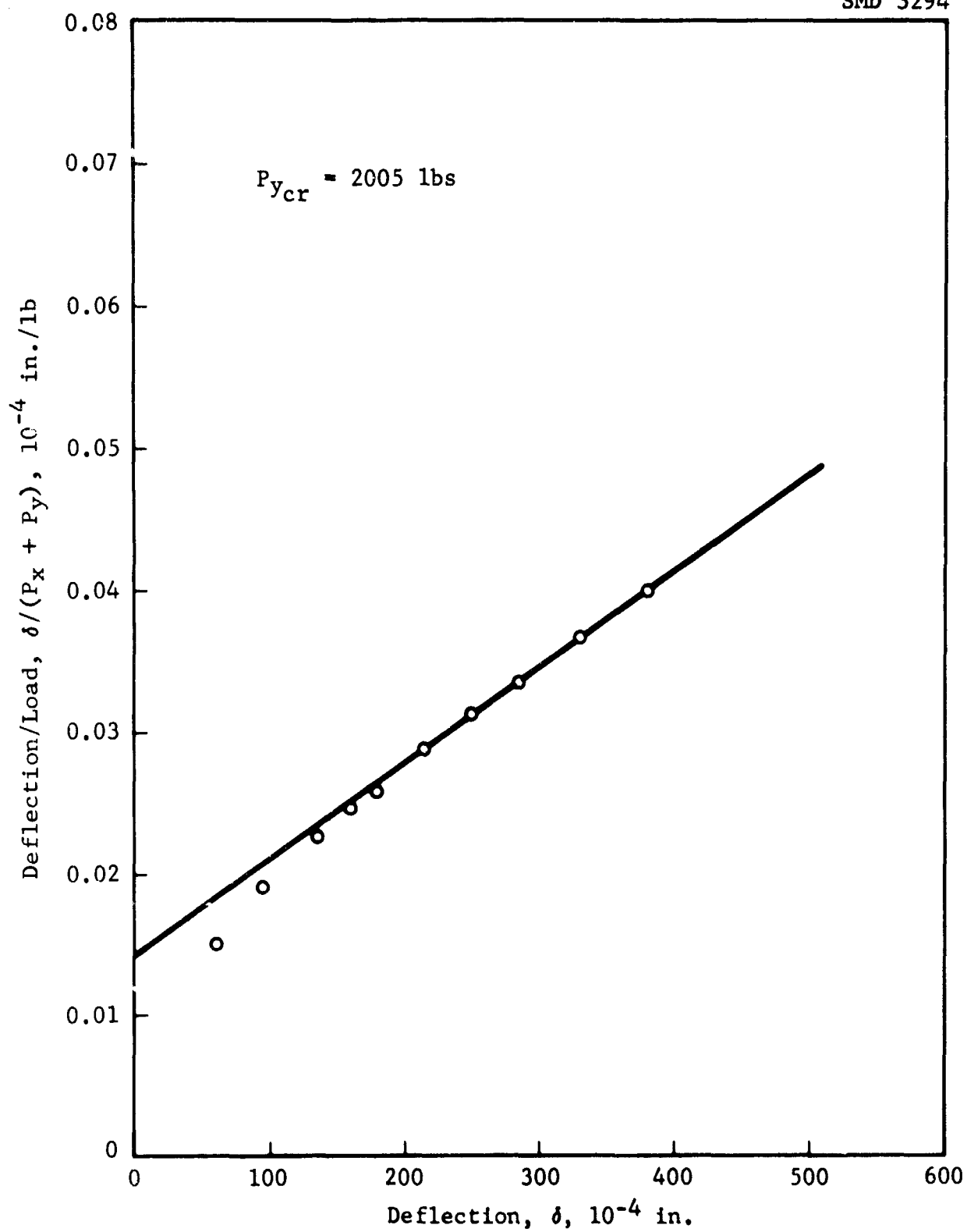
Figure 189 Load-Deflection Curves for Panel No. 5

Figure 190 Southwell Plot for Panel No. 5, $N_y/N_x = .0079$

Figure 191 Southwell Plot for Panel No. 5, $N_y/N_x = .043$

Figure 192 Southwell Plot for Panel No. 5, $N_y/N_x = .101$

Figure 193 Southwell Plot for Panel No. 5, $N_y/N_x = .140$

Figure 194 Southwell Plot for Panel No. 5, $N_y/N_x = .158$

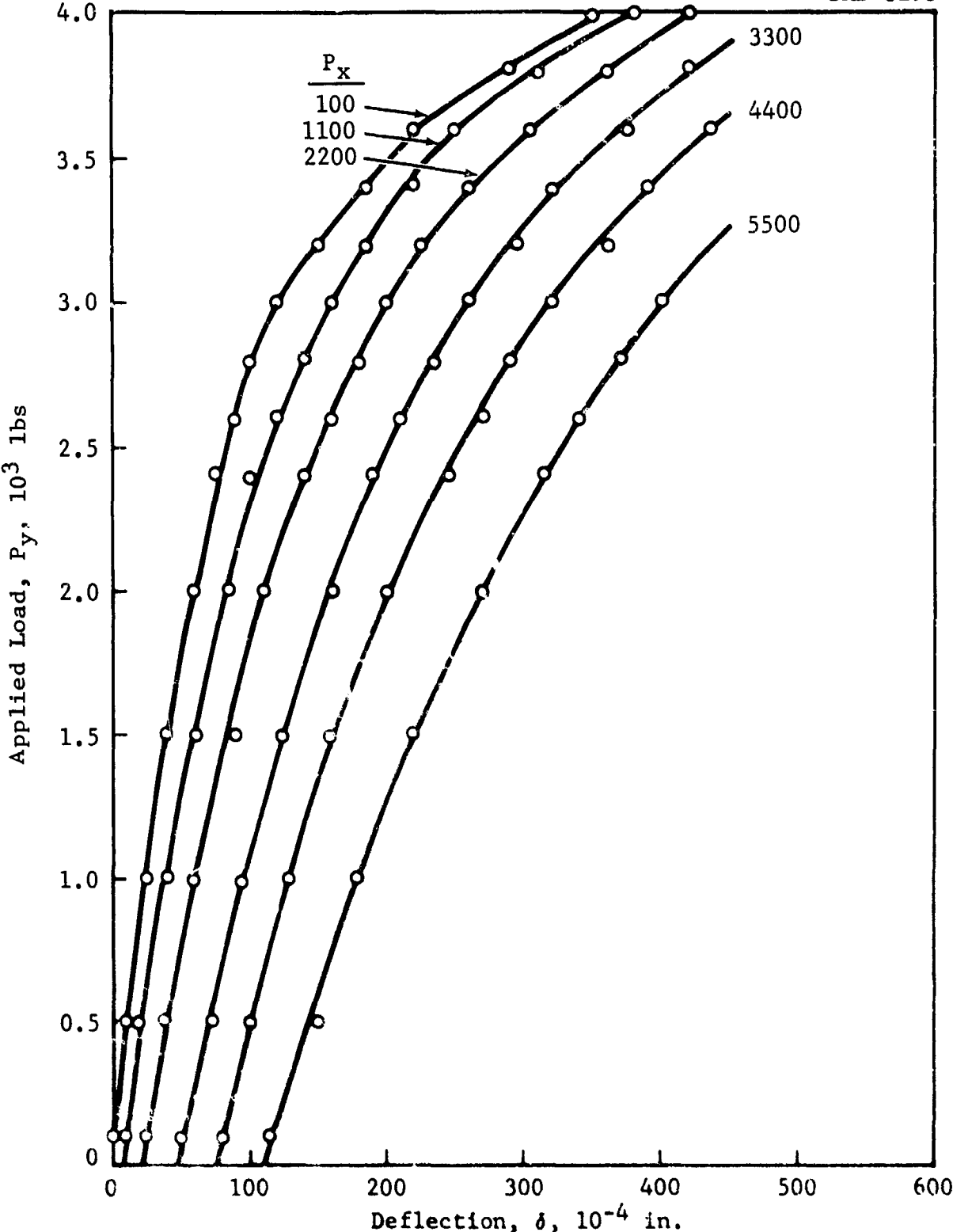
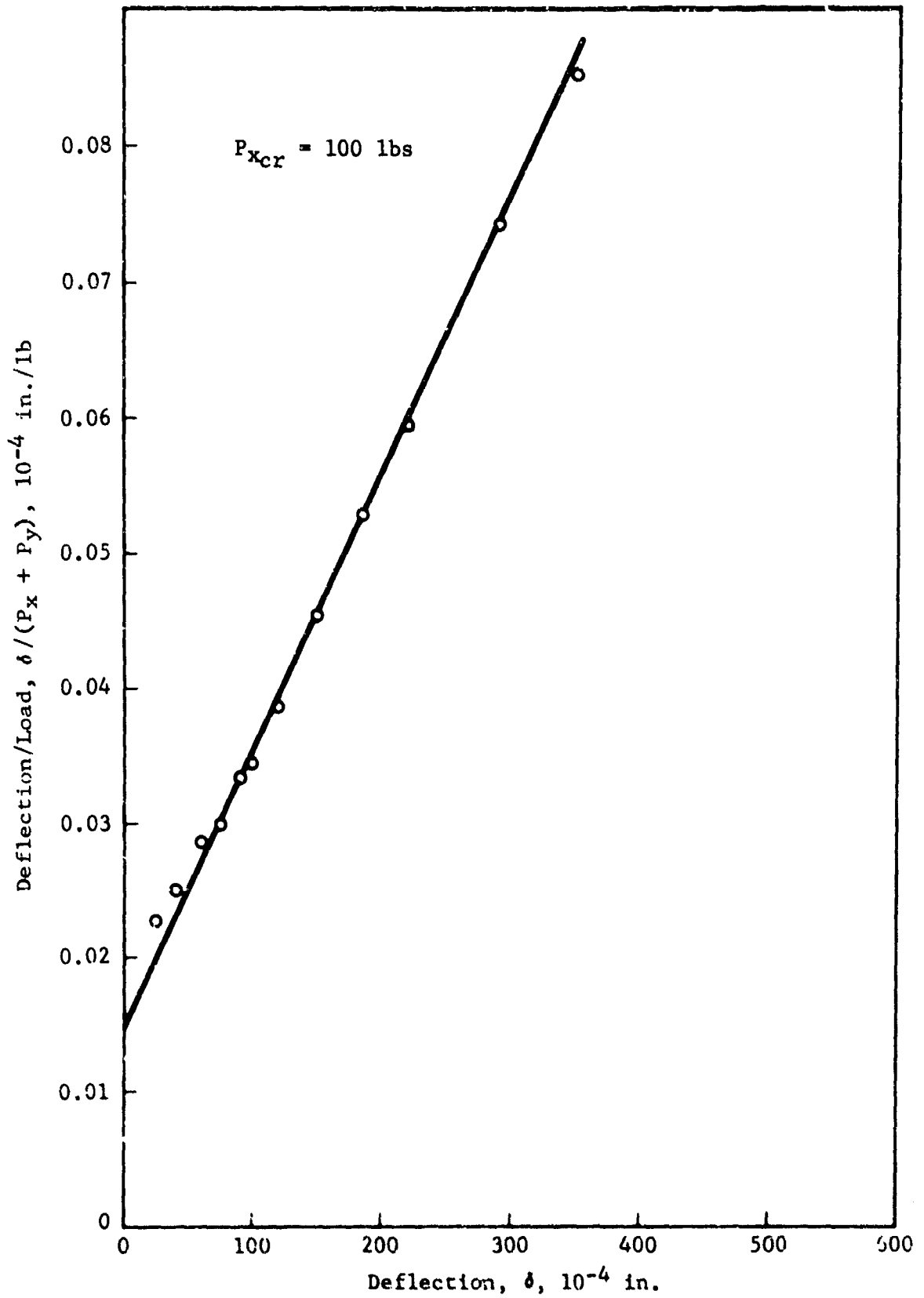
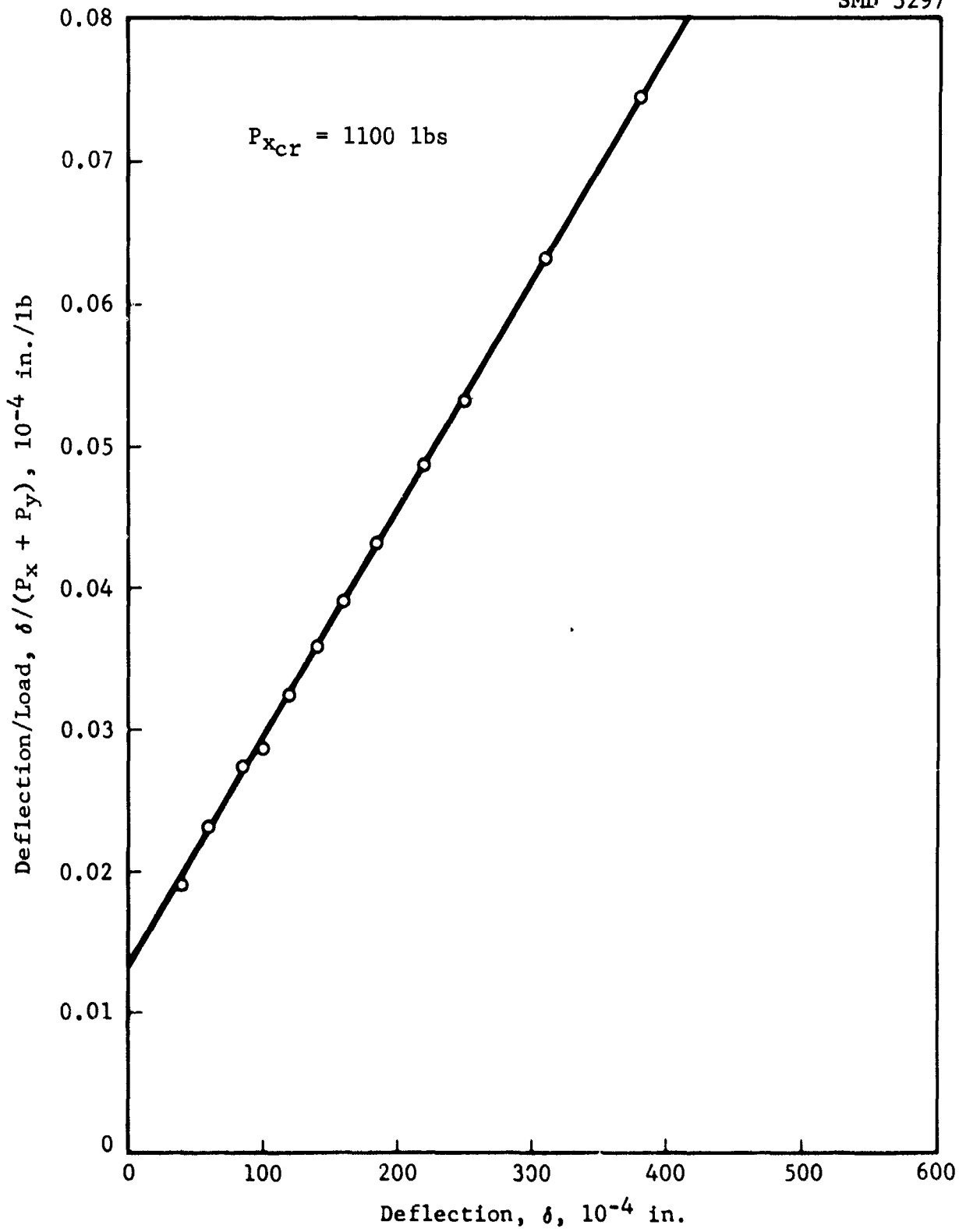
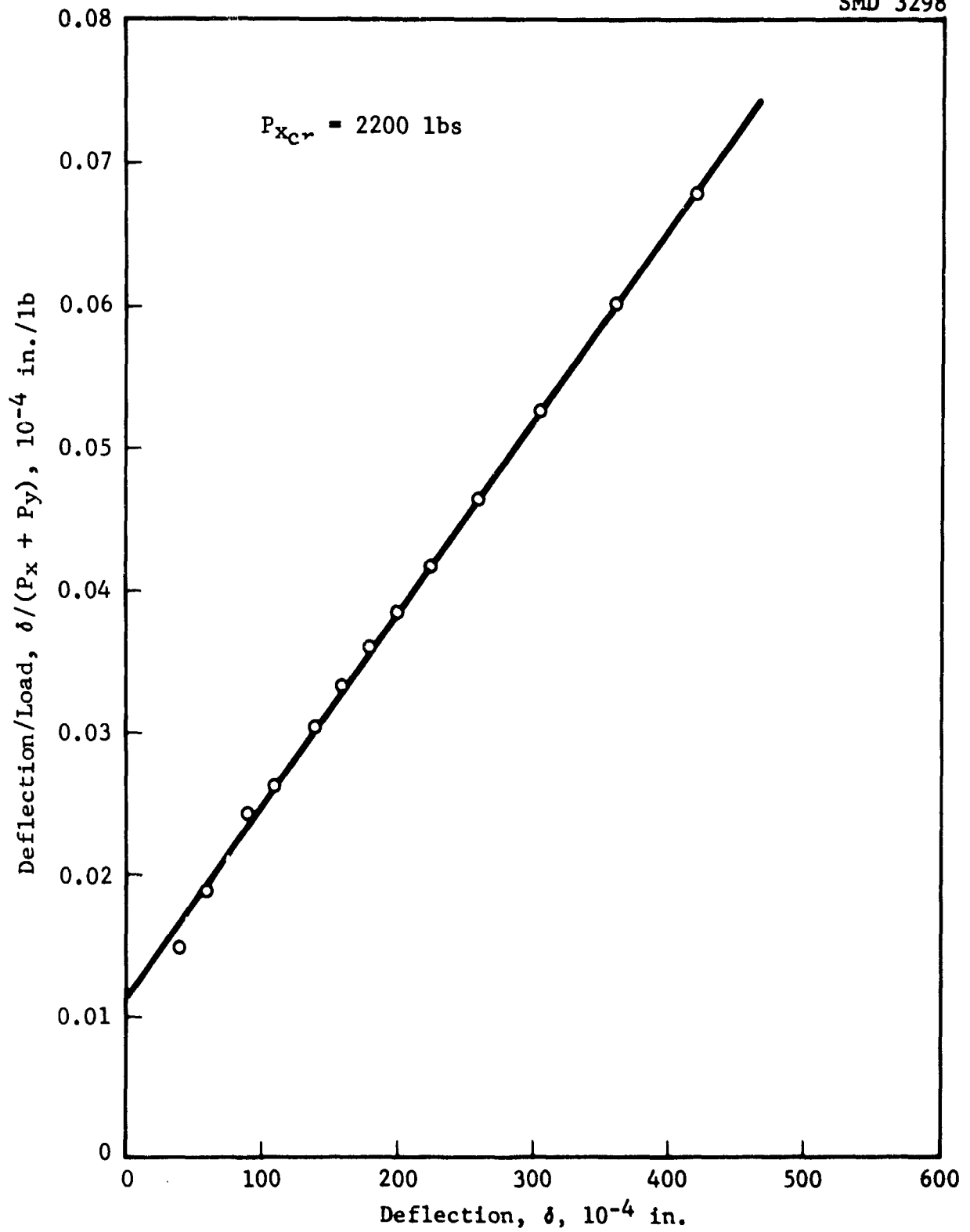
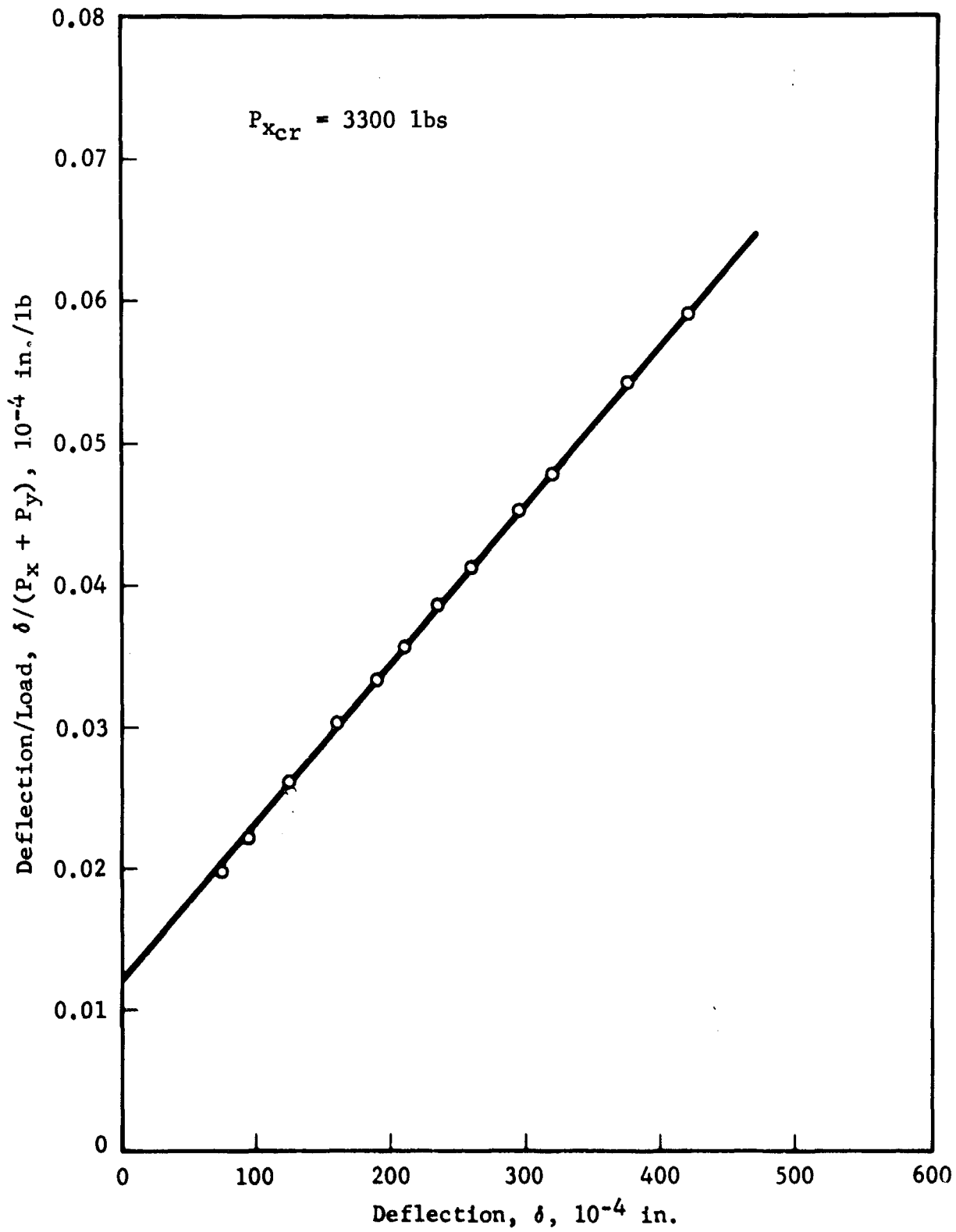


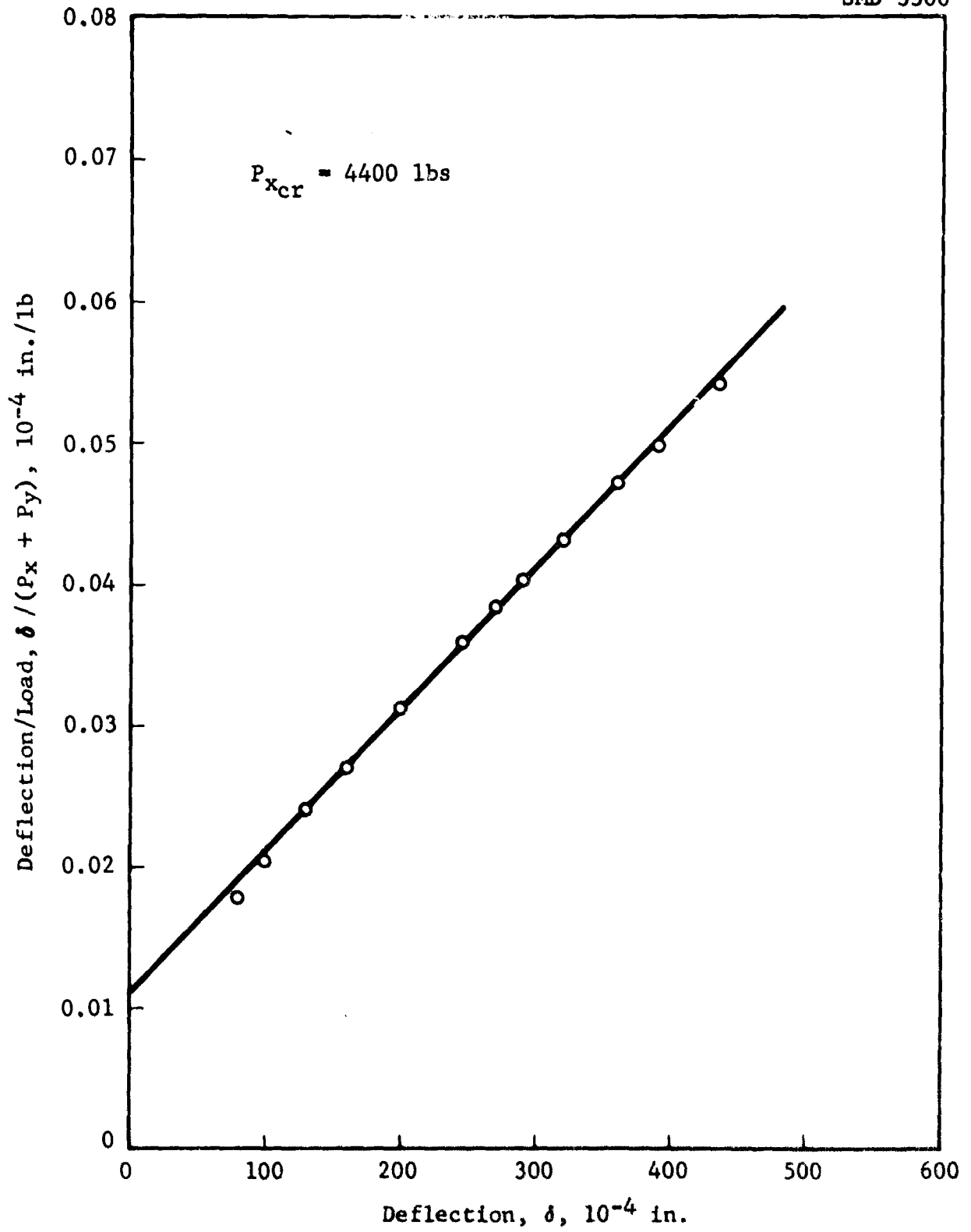
Figure 195 Load-Deflection Curves for Panel No. 5, Turned 90°

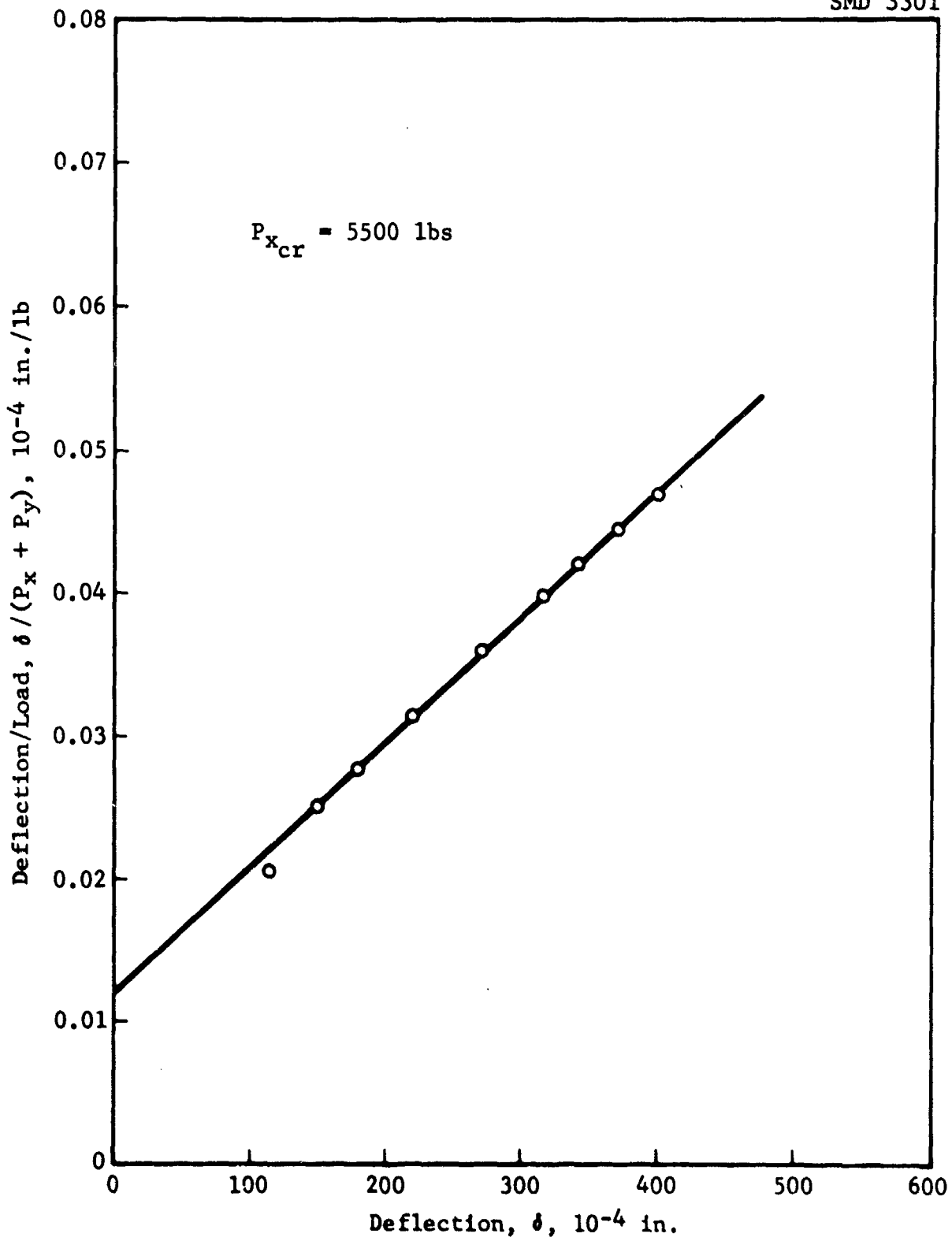
Figure 196 Southwell Plot for Panel No. 5, $N_y/N_x = 47.250$

Figure 197 Southwell Plot for Panel No. 5, $N_y/N_x = 4.620$

Figure 198 Southwell Plot for Panel No. 5, $N_y/N_x = 2.350$

Figure 199 Southwell Plot for Panel No. 5, $N_y/N_x = 1.703$

Figure 200 Southwell Plot for Panel No. 5, $N_y/N_x = 1.255$

Figure 201 Southwell Plot for Panel No. 5, $N_y/N_x = 1.060$

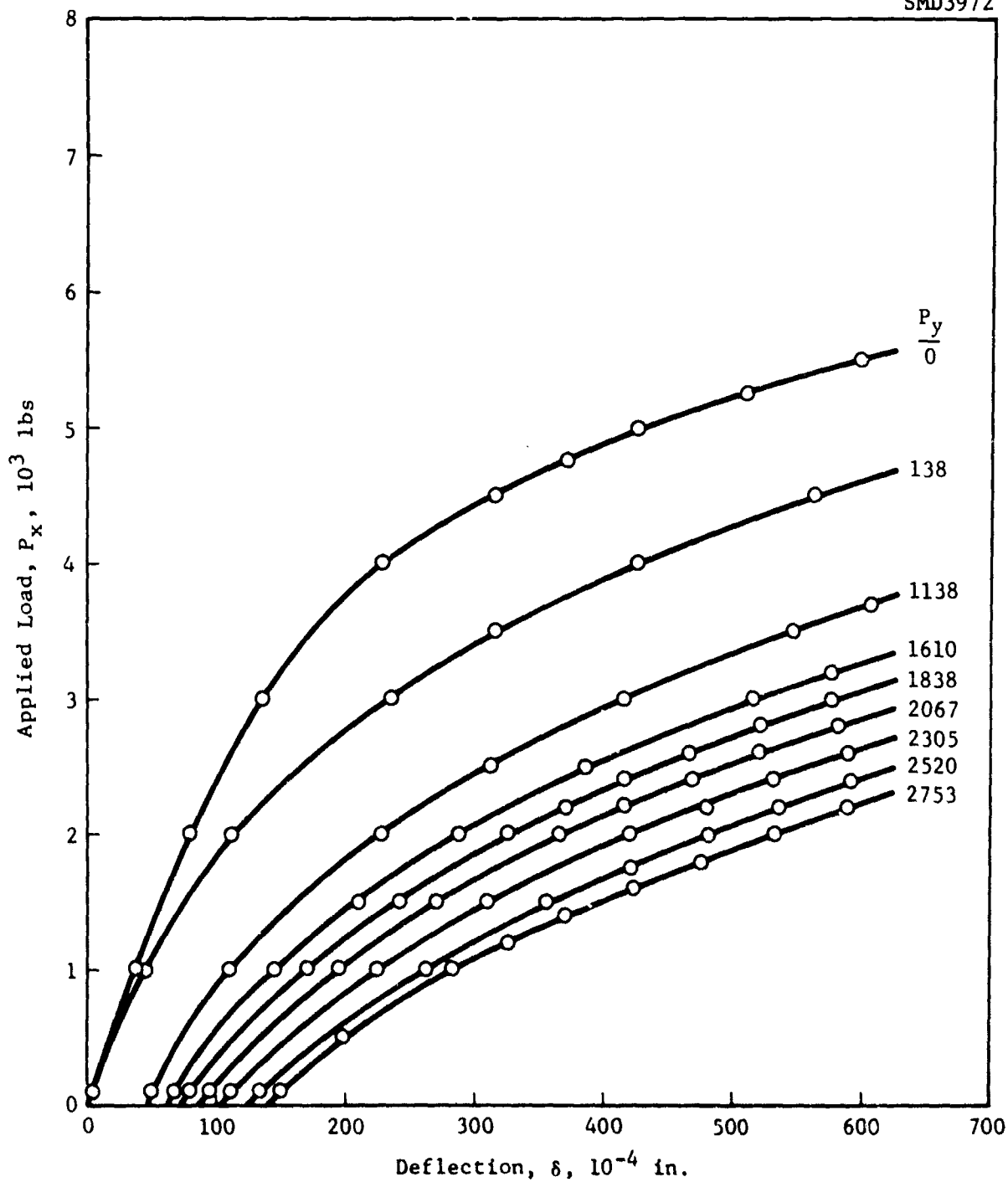


Figure 202 Load Deflection Curves for Panel No. 7

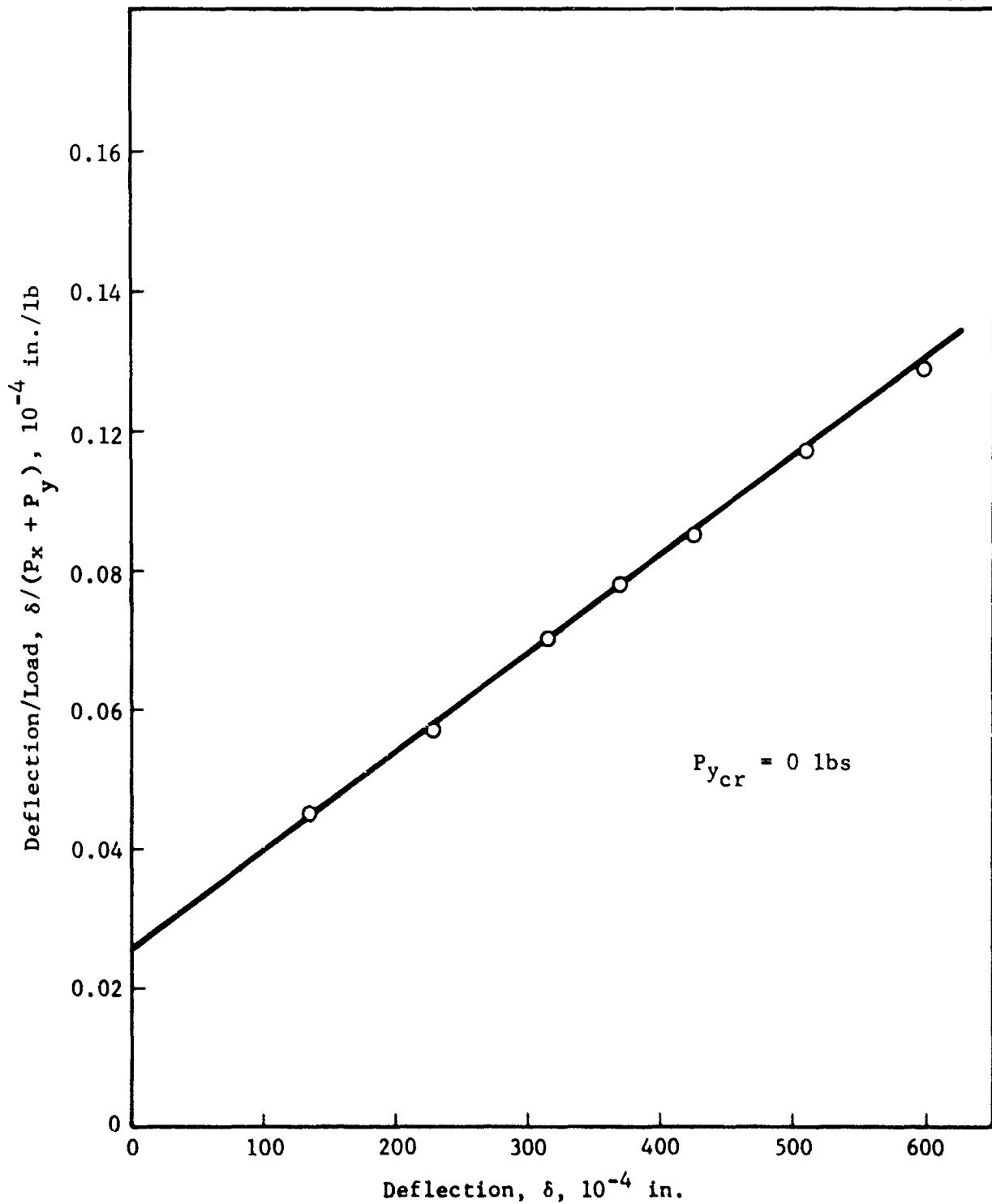


Figure 203 Southwell Plot for Panel No. 7, $N_y/N_x = 0$

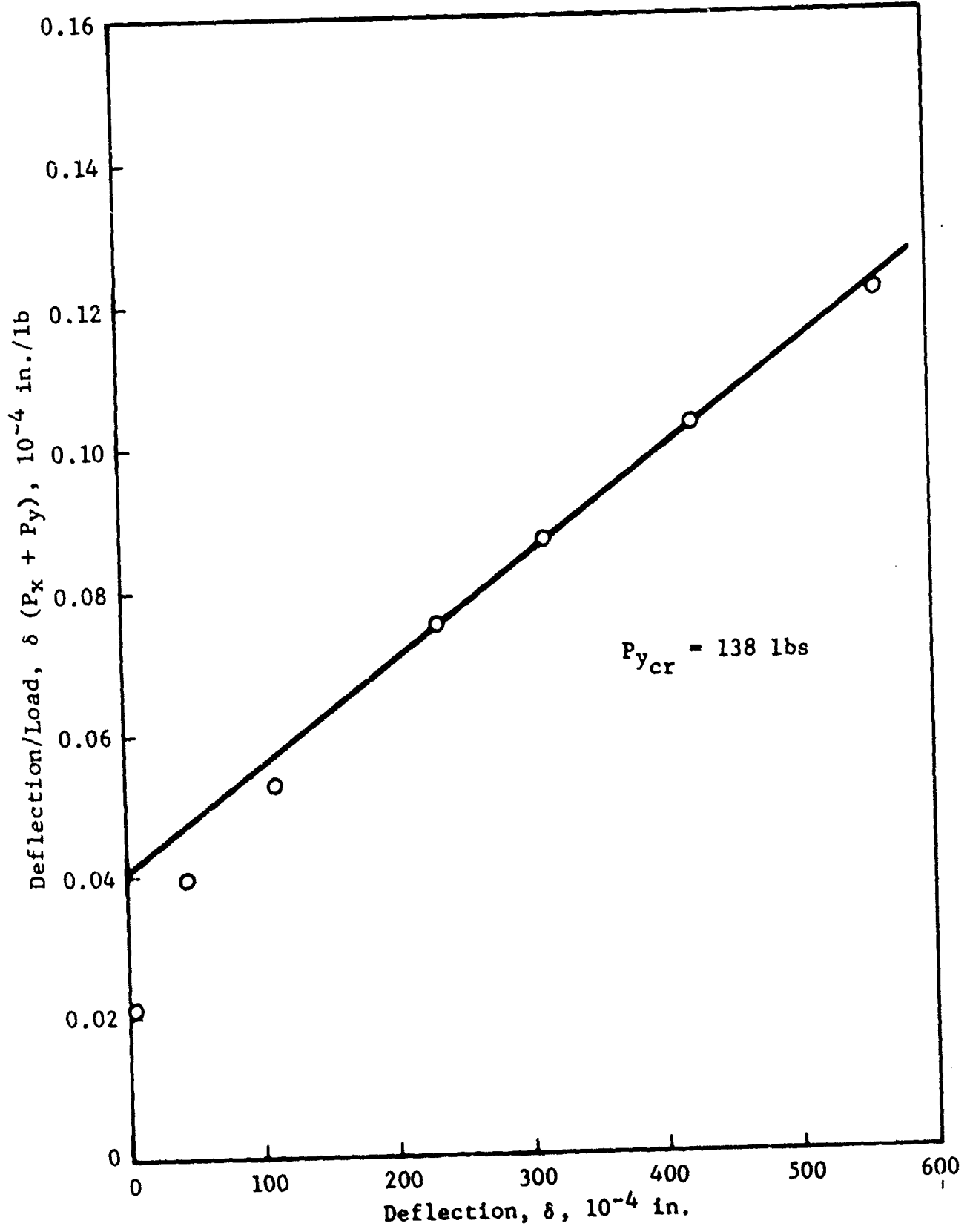


Figure 204 Southwell Plot for Panel No. 7, $N_y/N_x = .021$

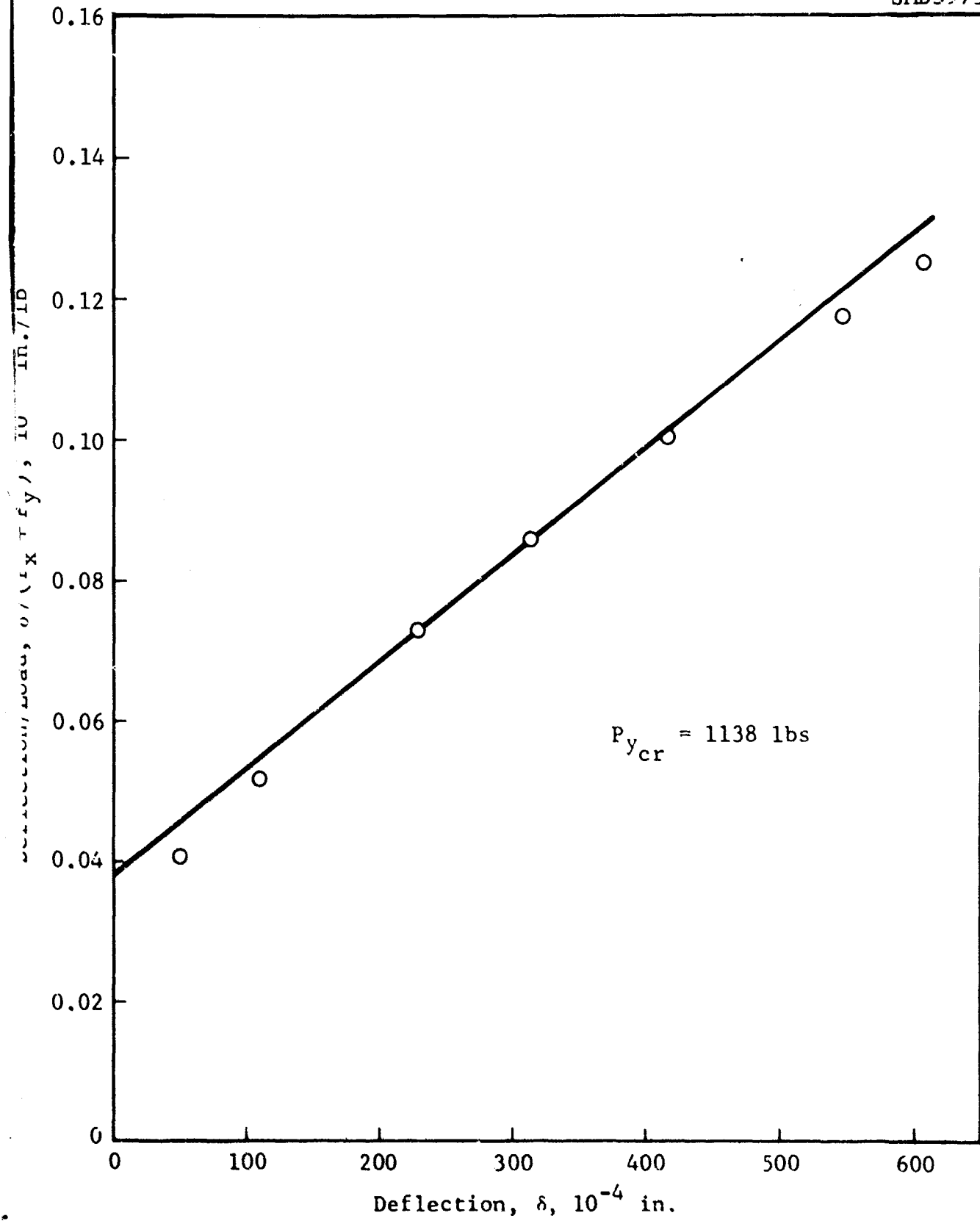
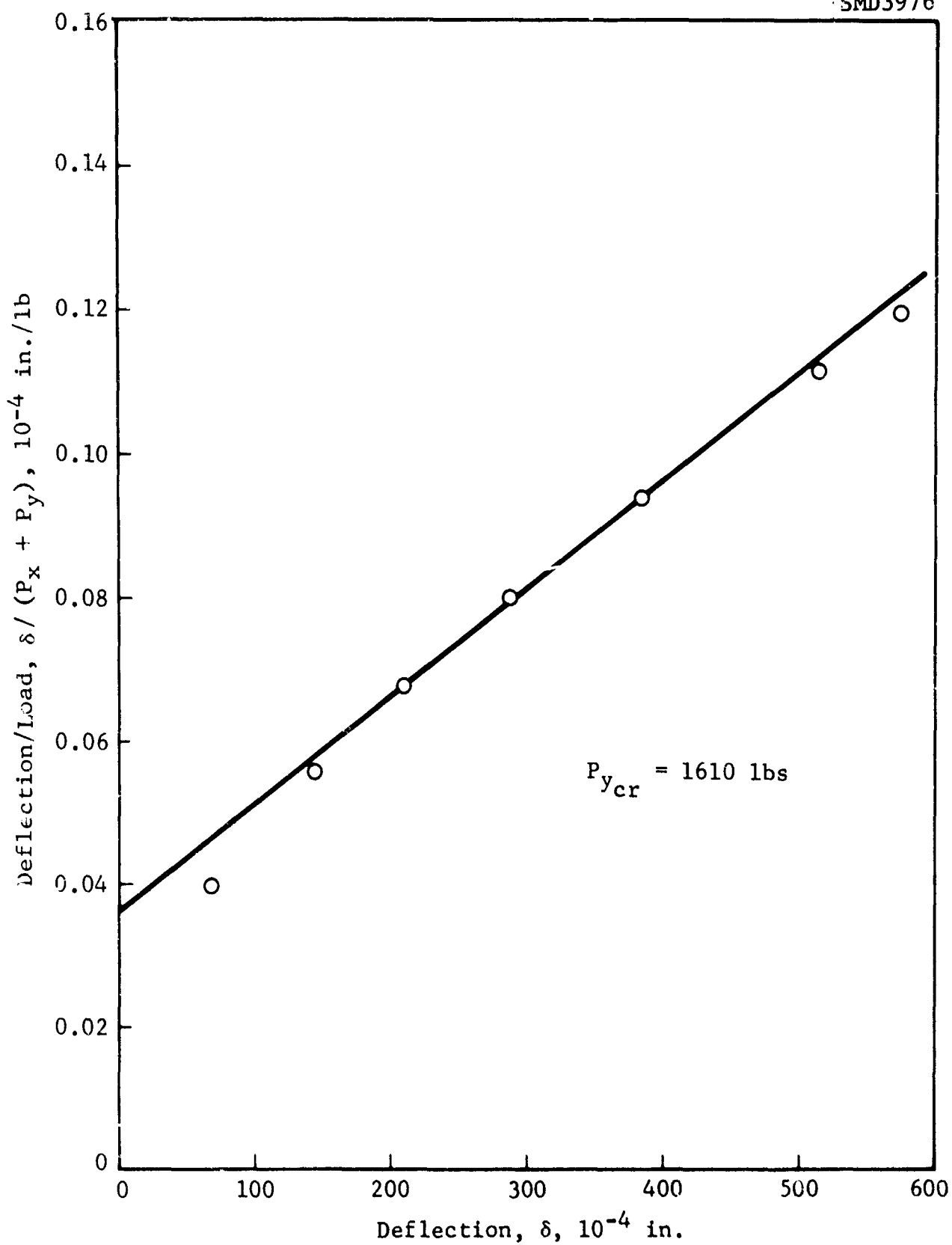


Figure 205 Southwell Plot for Panel No. 7, $N_y/N_x = .212$

Figure 206 Southwell Plot for Panel No. 7, $N_y/N_x = .312$

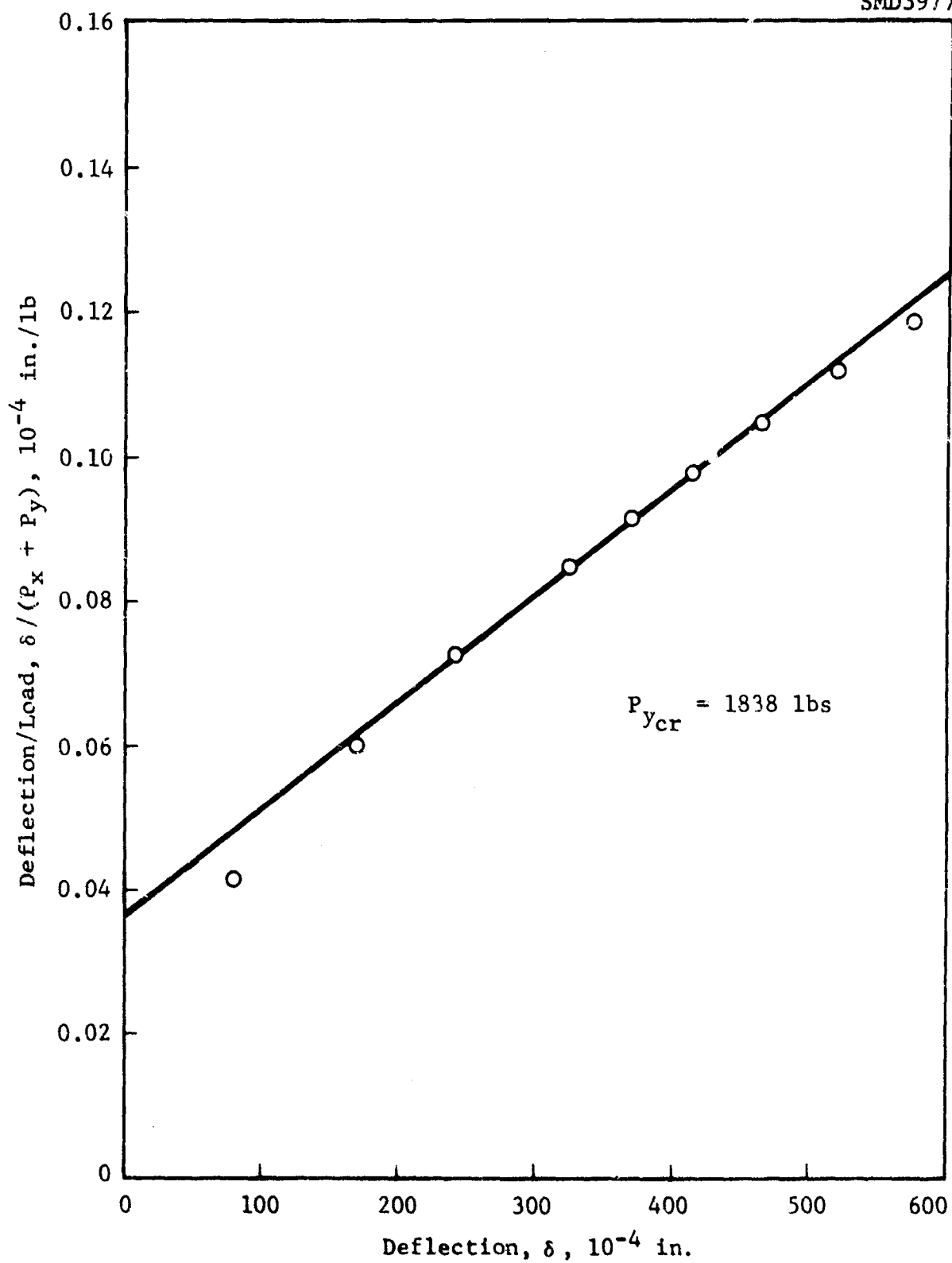
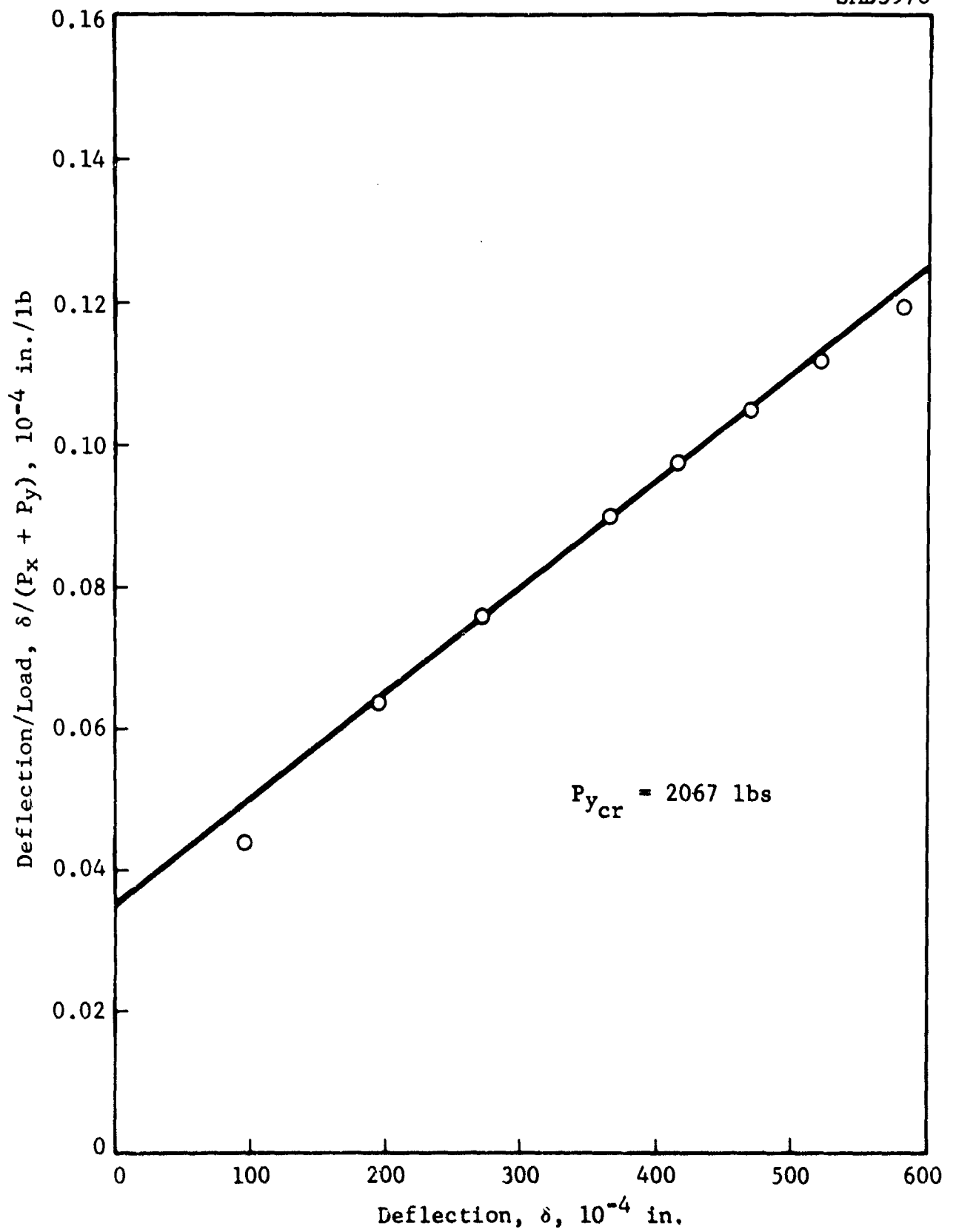


Figure 207 Southwell Plot for Panel No. 7, $N_y/N_x = .376$

Figure 208 Southwell Plot for Panel No. 7, $N_y/N_x = .448$

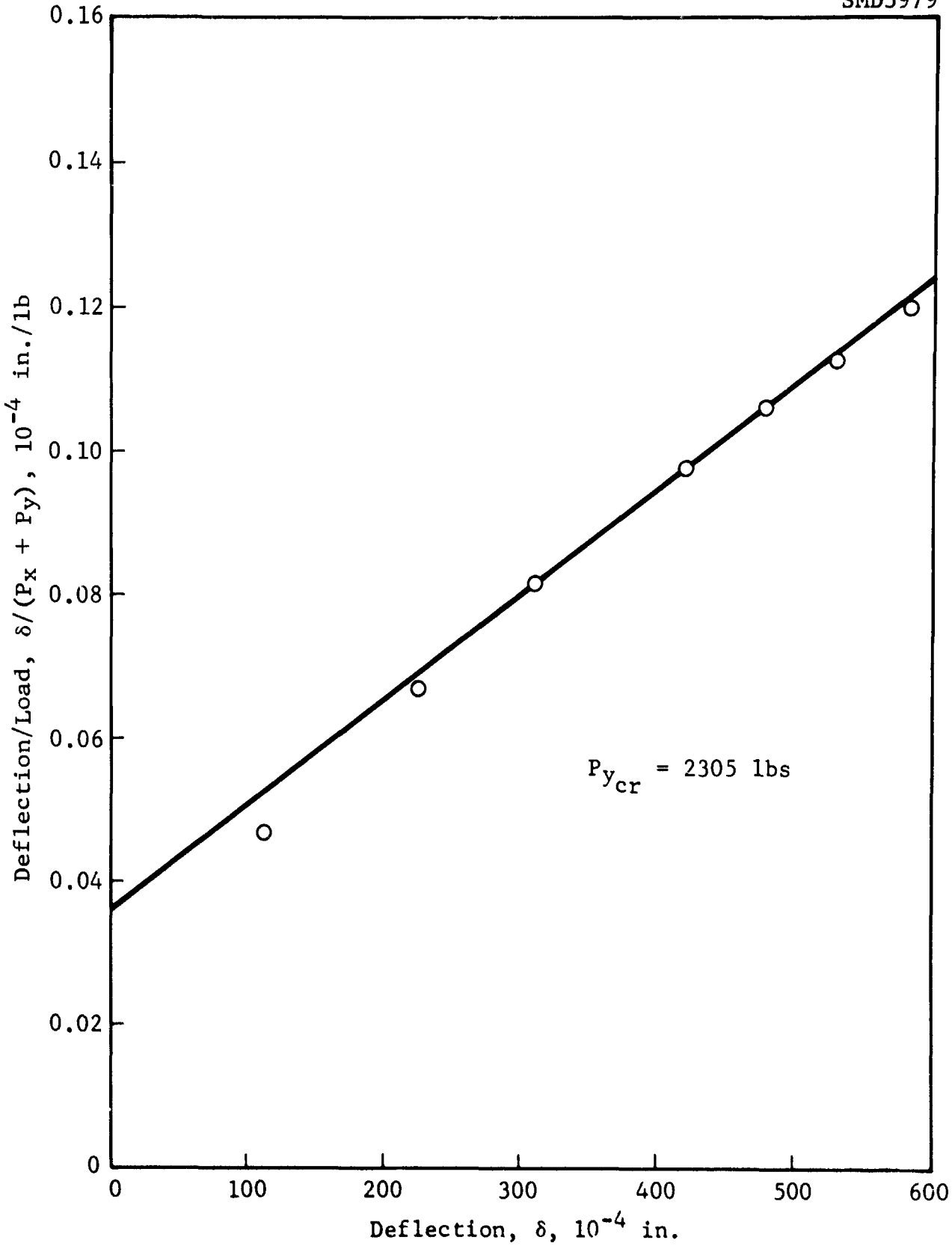
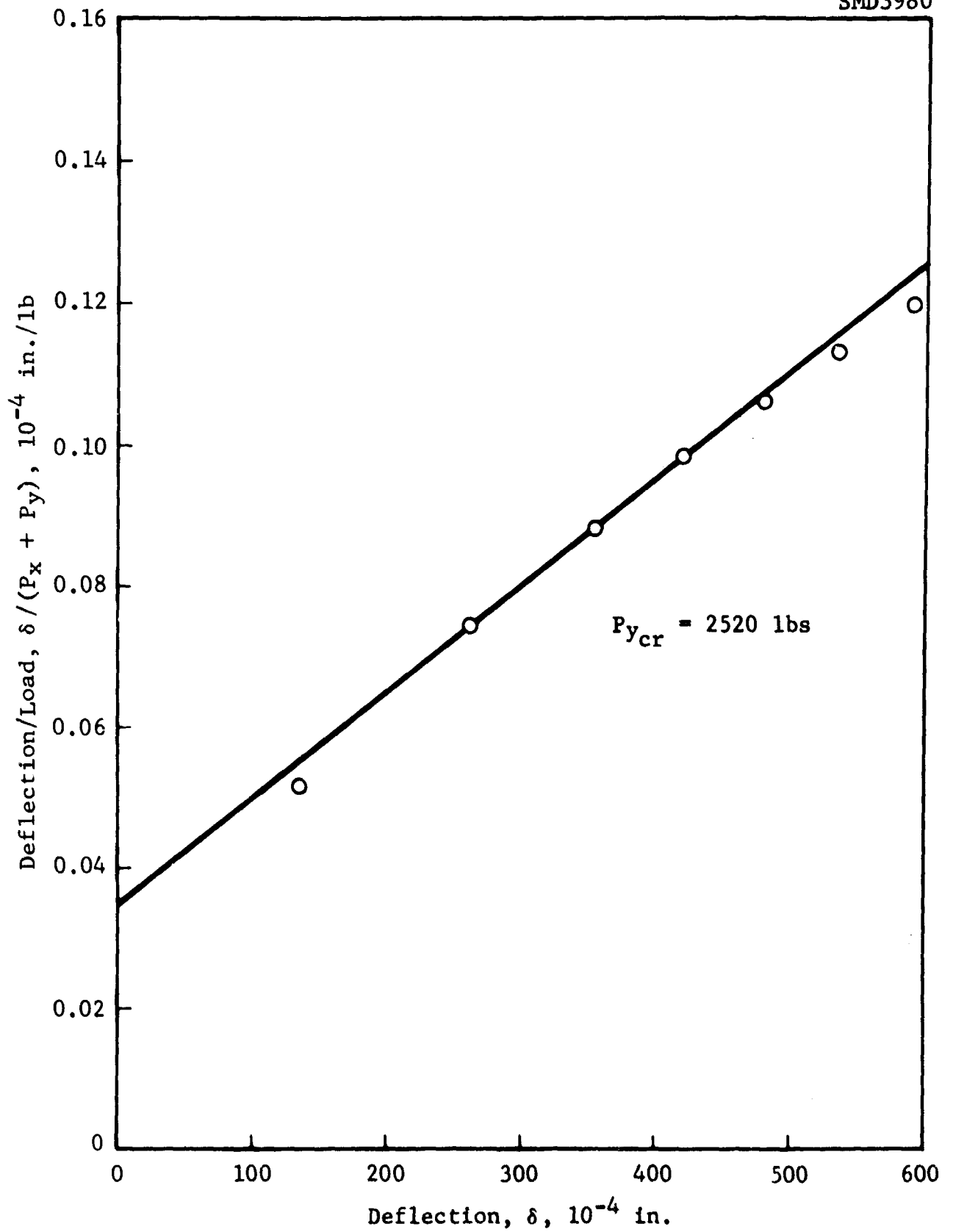


Figure 209 Southwell Plot for Panel No. 7, $N_y/N_x = .509$

Figure 210 Southwell Plot for Panel No. 7, $N_y/N_x = .614$

SMD3981

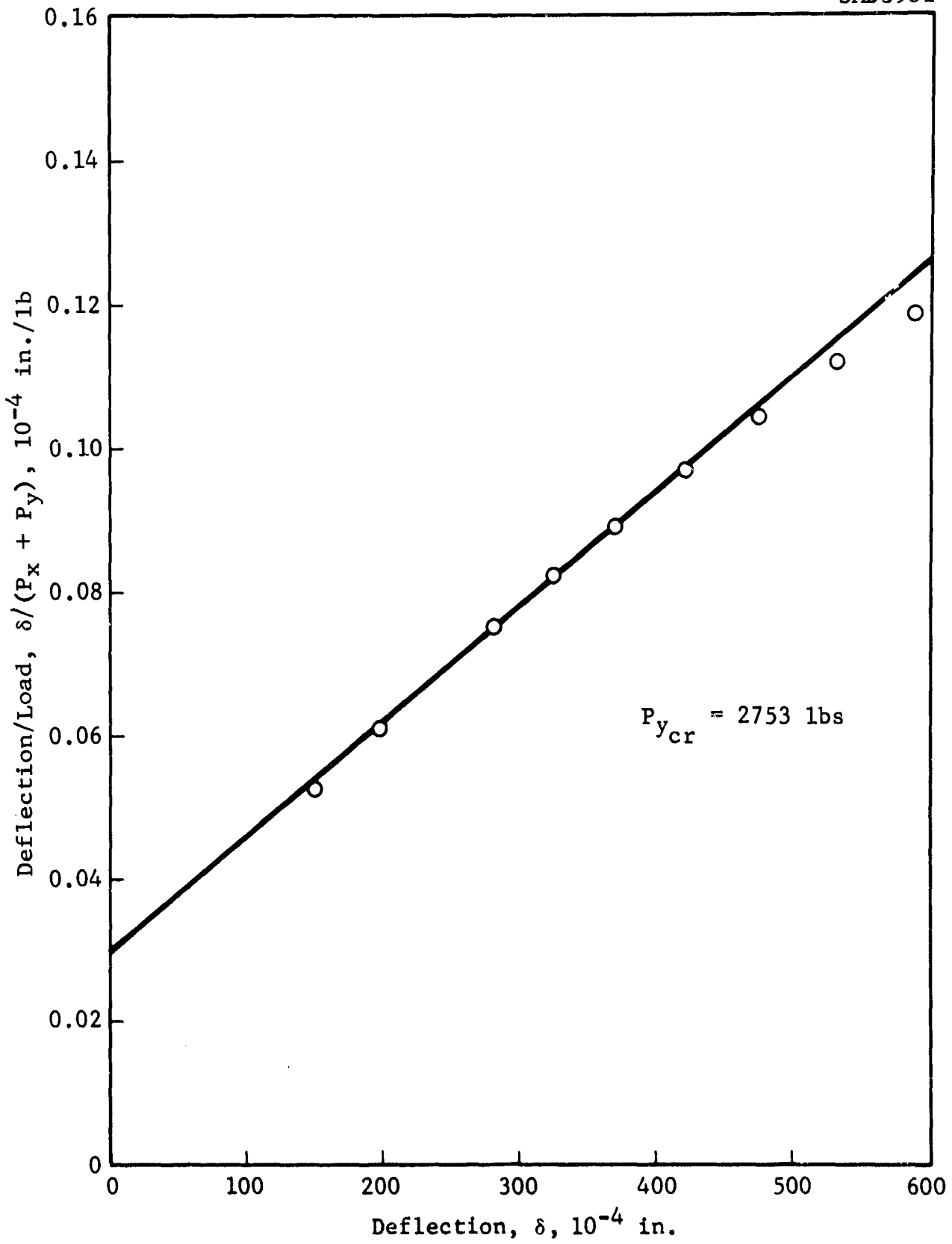


Figure 211 Southwell Plot for Panel No. 7, $N_y/N_x = .787$

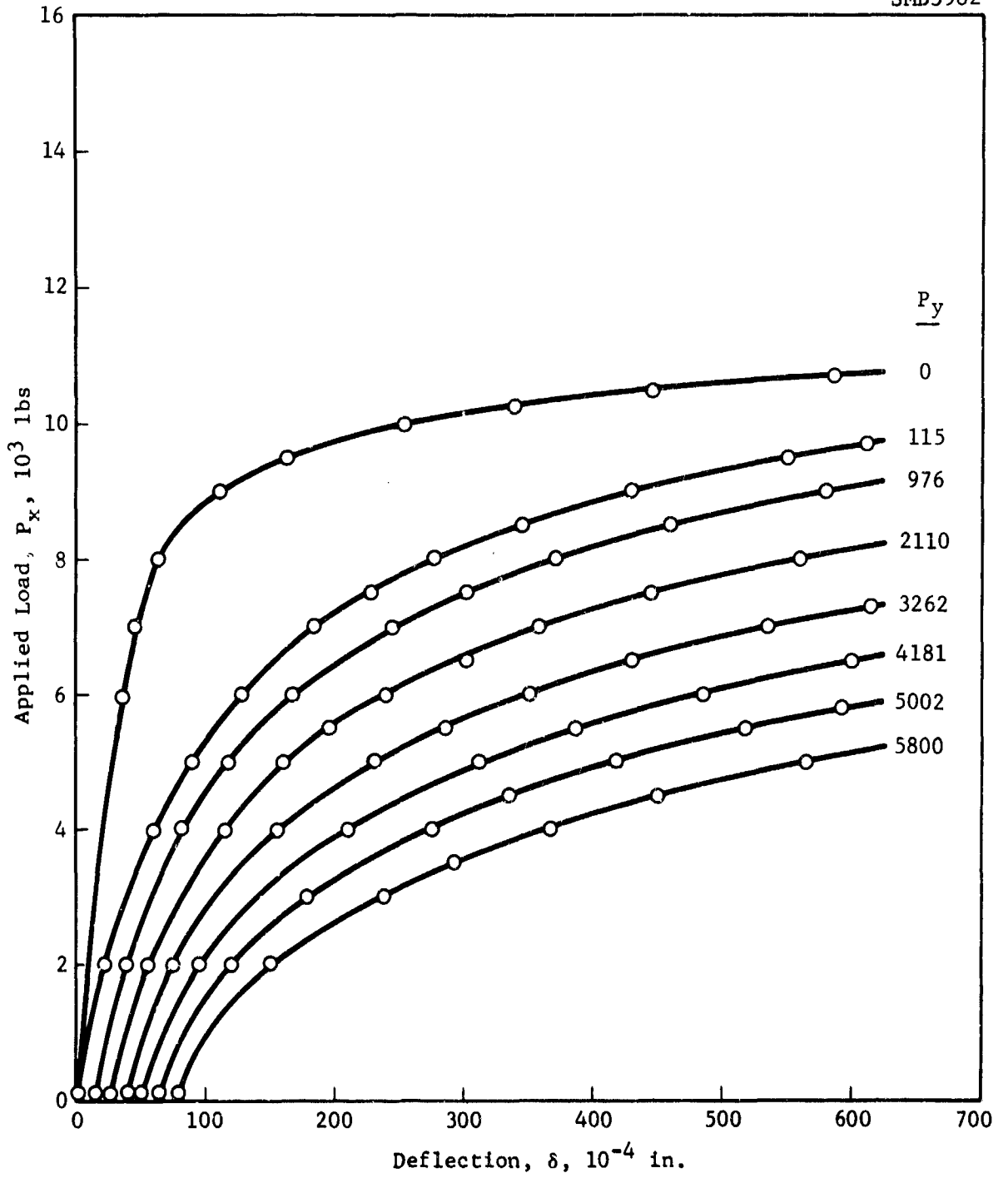
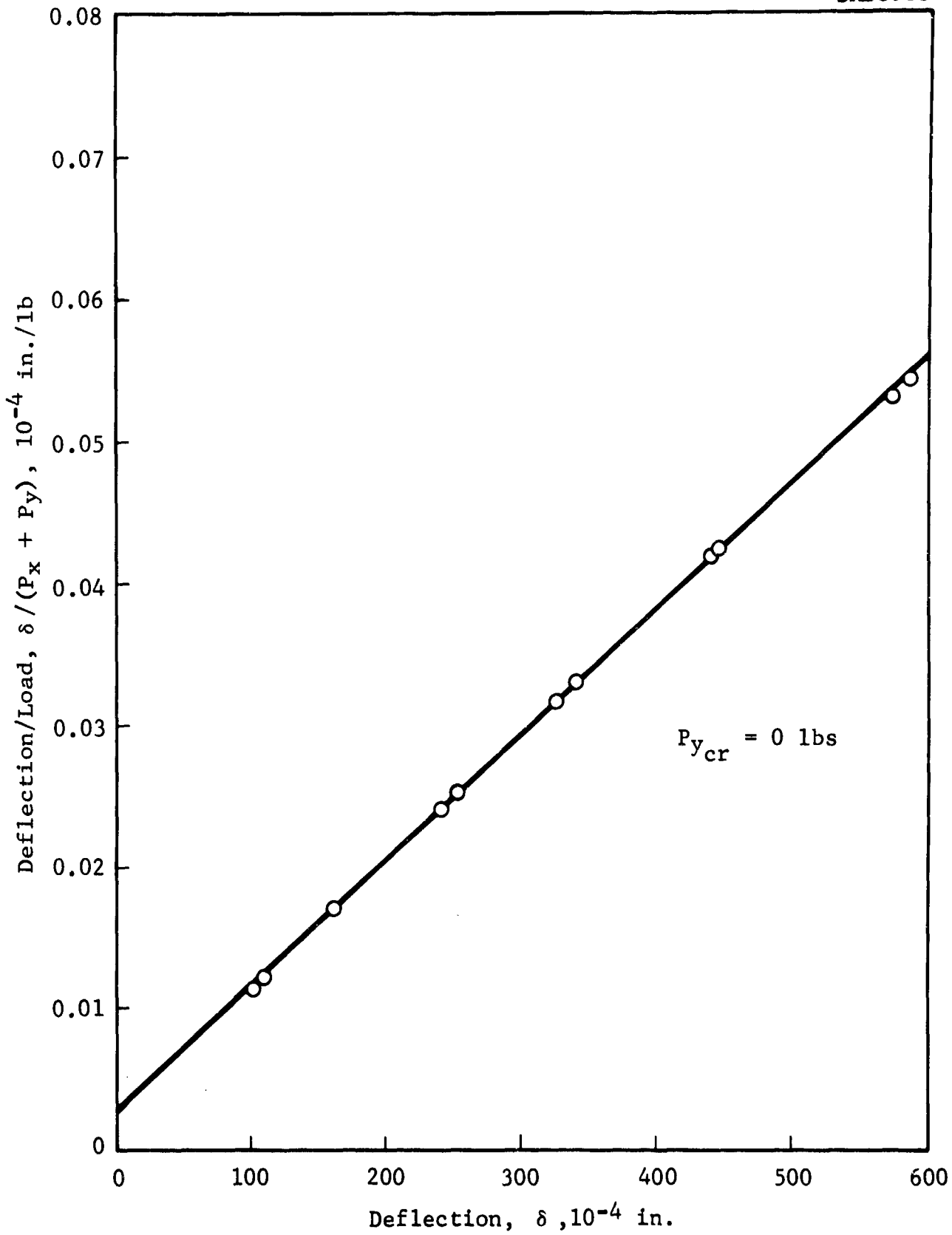
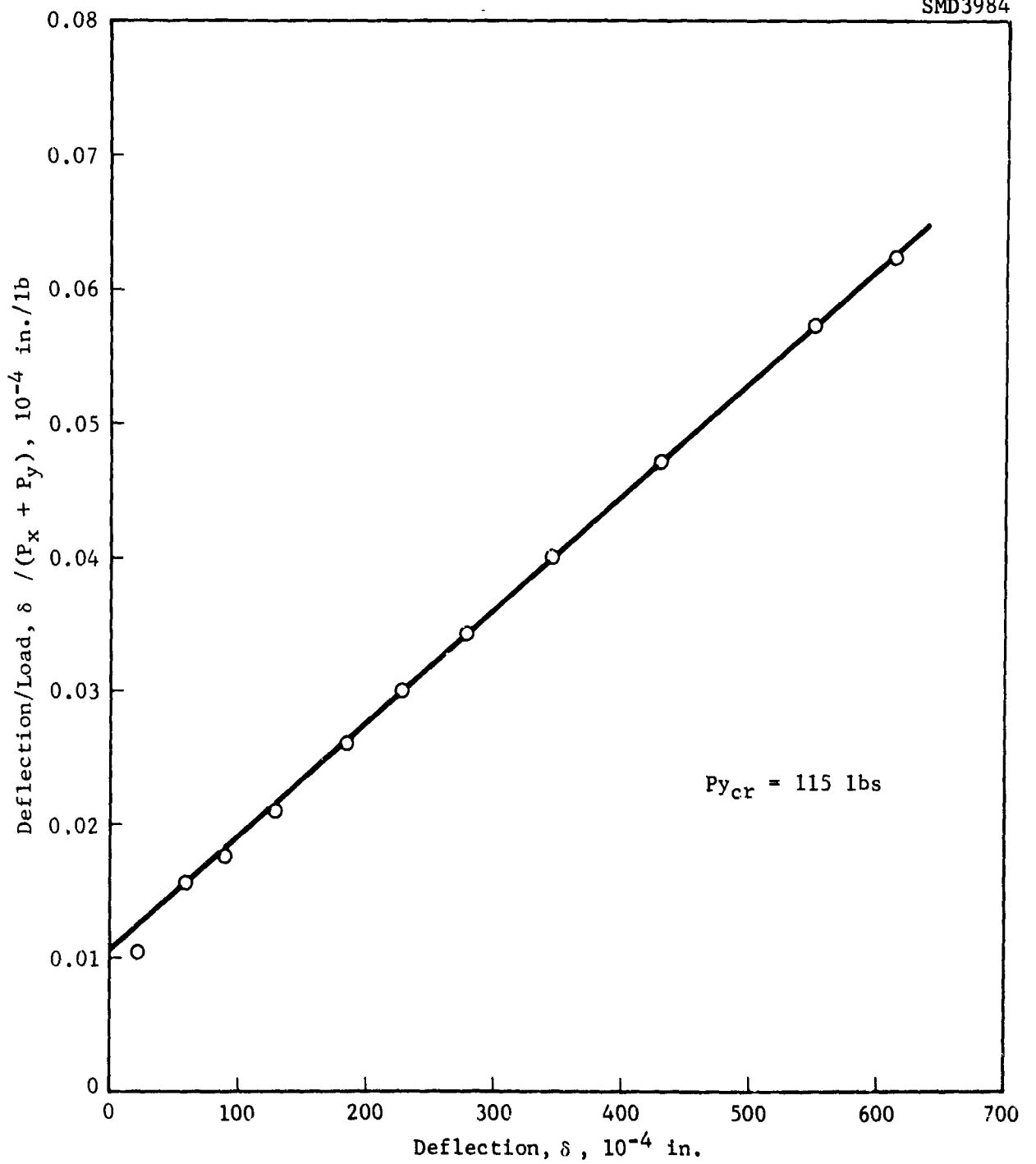
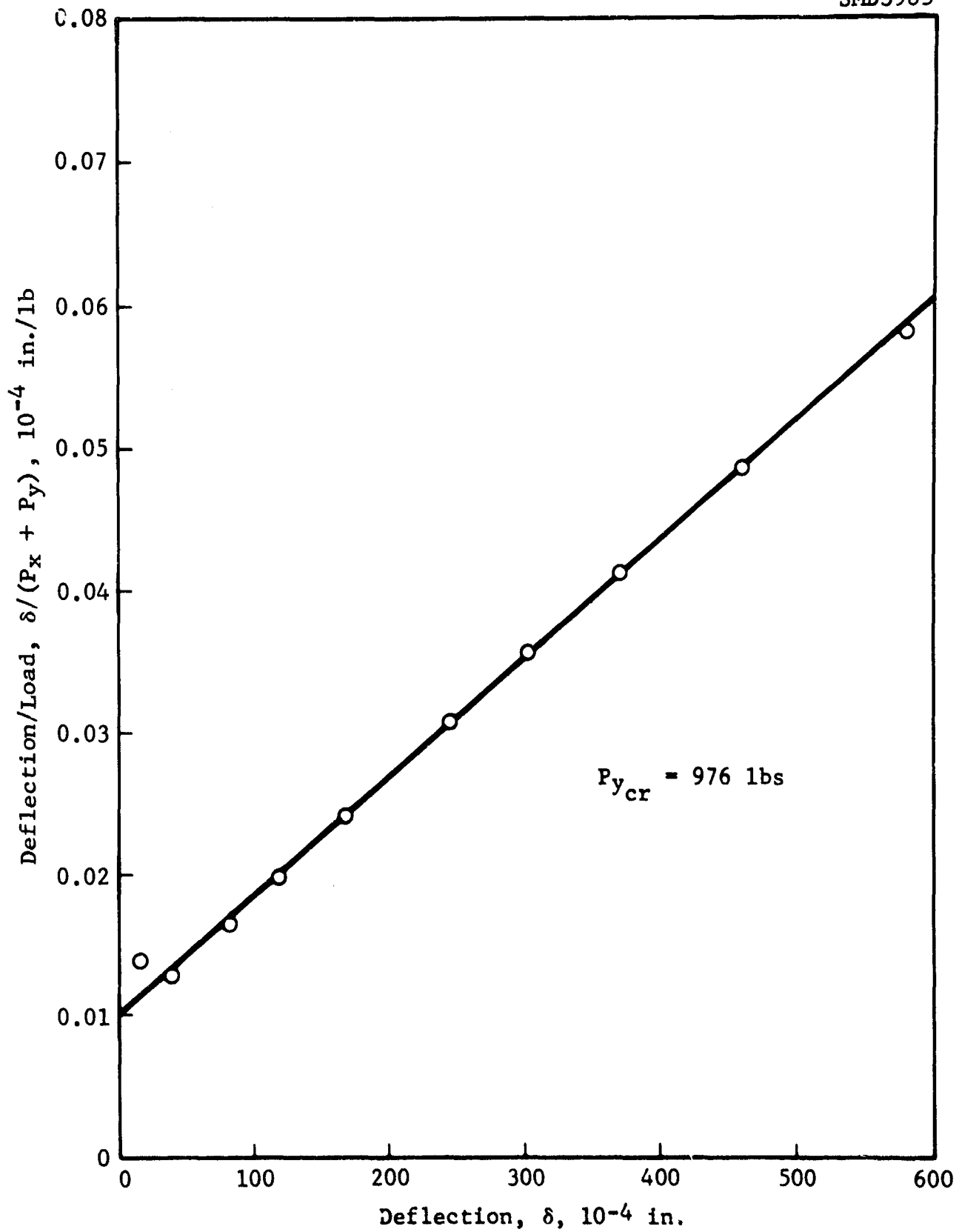
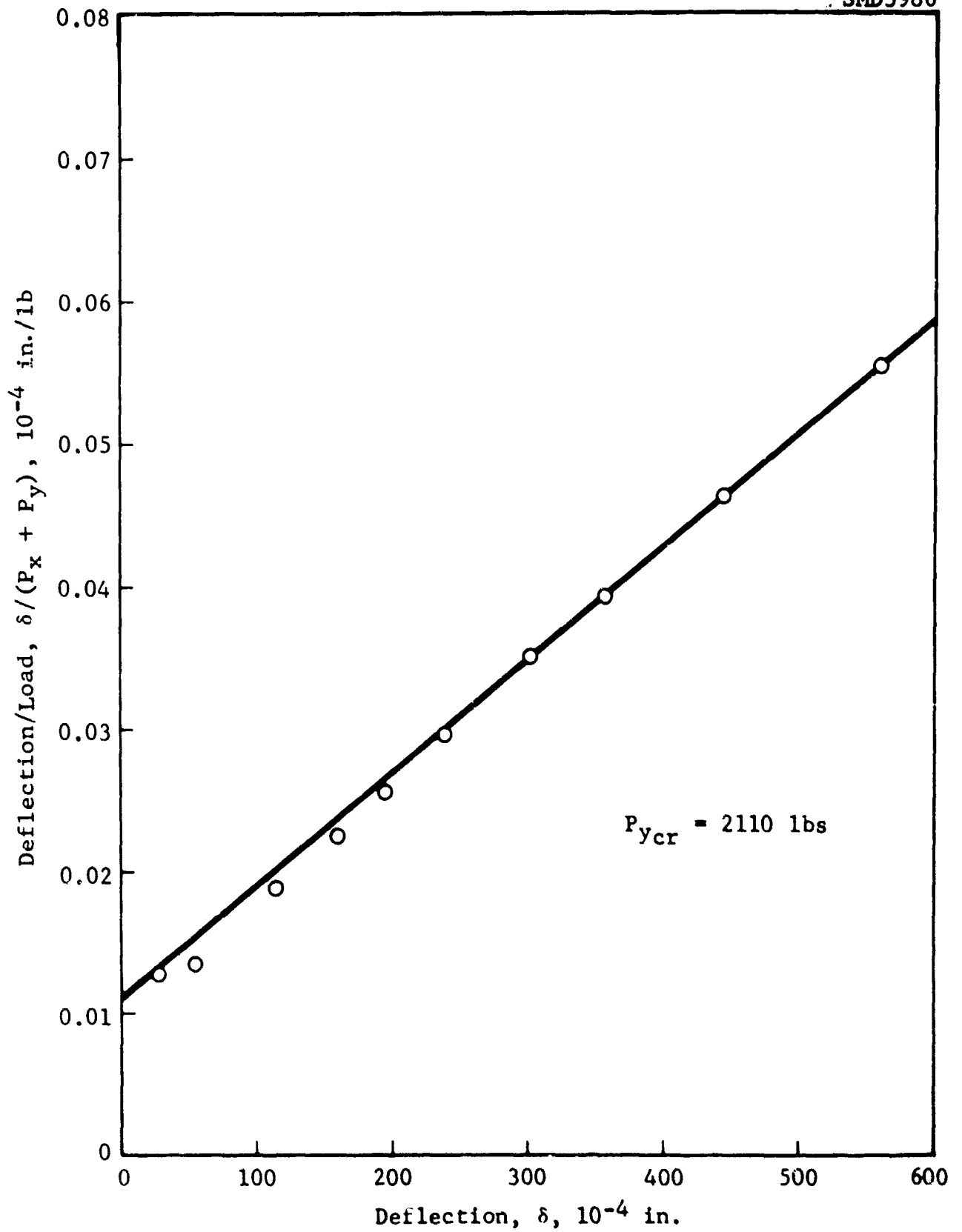


Figure 212 Load Deflection Curves for Panel No. 9

Figure 213 Southwell Plot for Panel No. 9, $N_y/N_x = 0$

Figure 214 Southwell Plot for Panel No. 9, $N_y/N_x = .013$

Figure 215 Southwell Plot for Panel No. 9, $N_y/N_x = .089$

Figure 216 Southwell Plot for Panel No. 9, $N_y/N_x = .201$

SMD3987

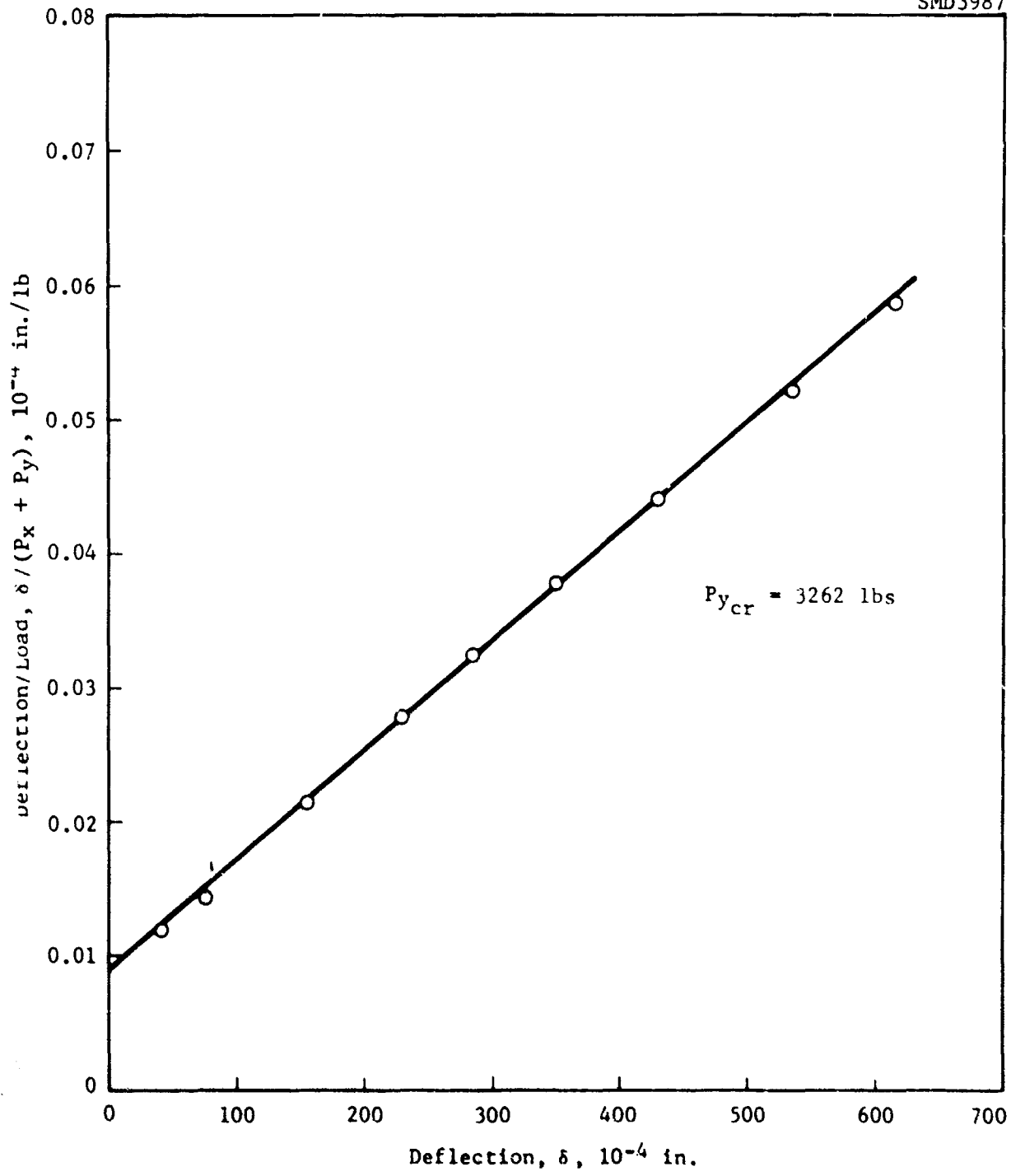
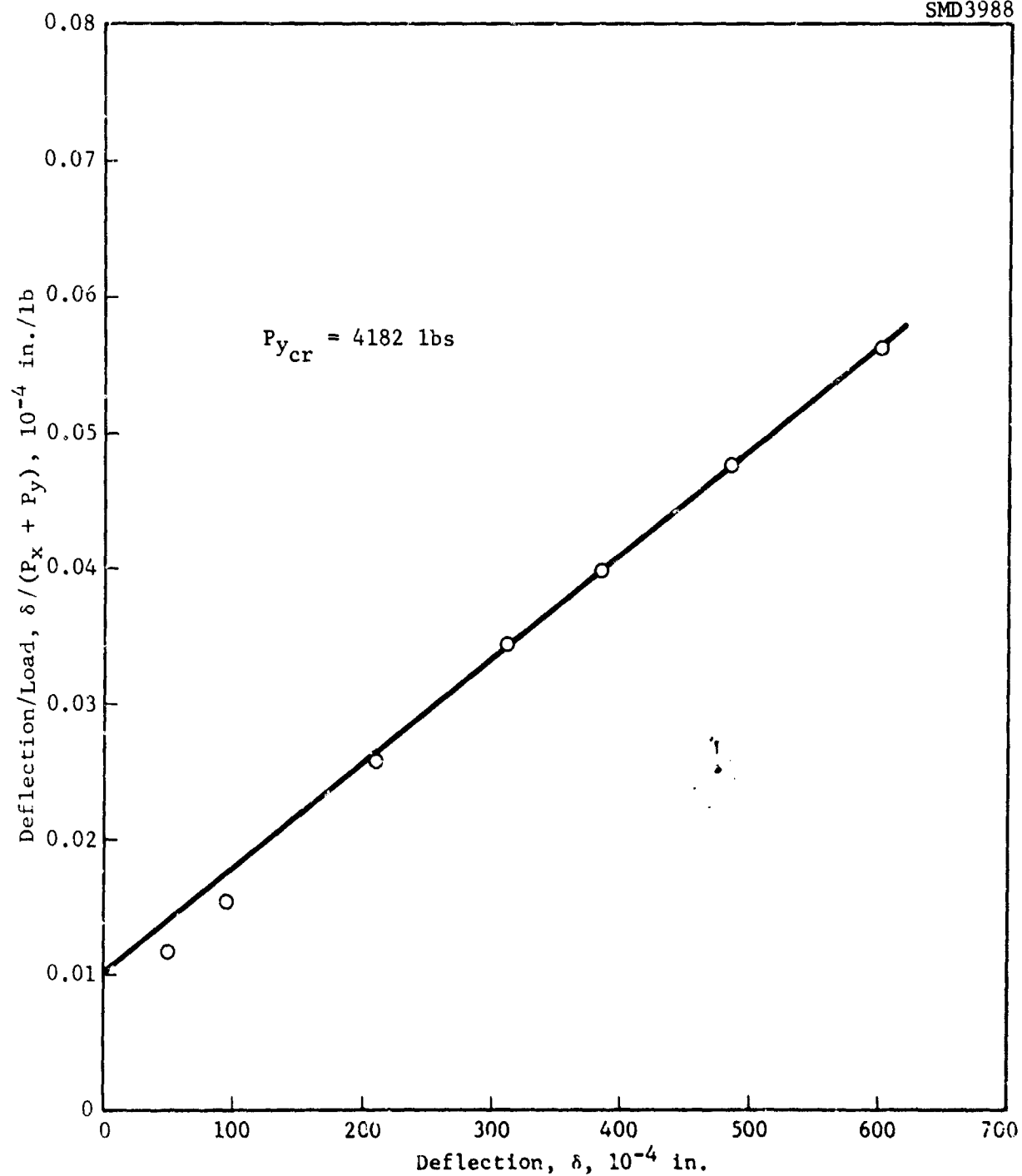
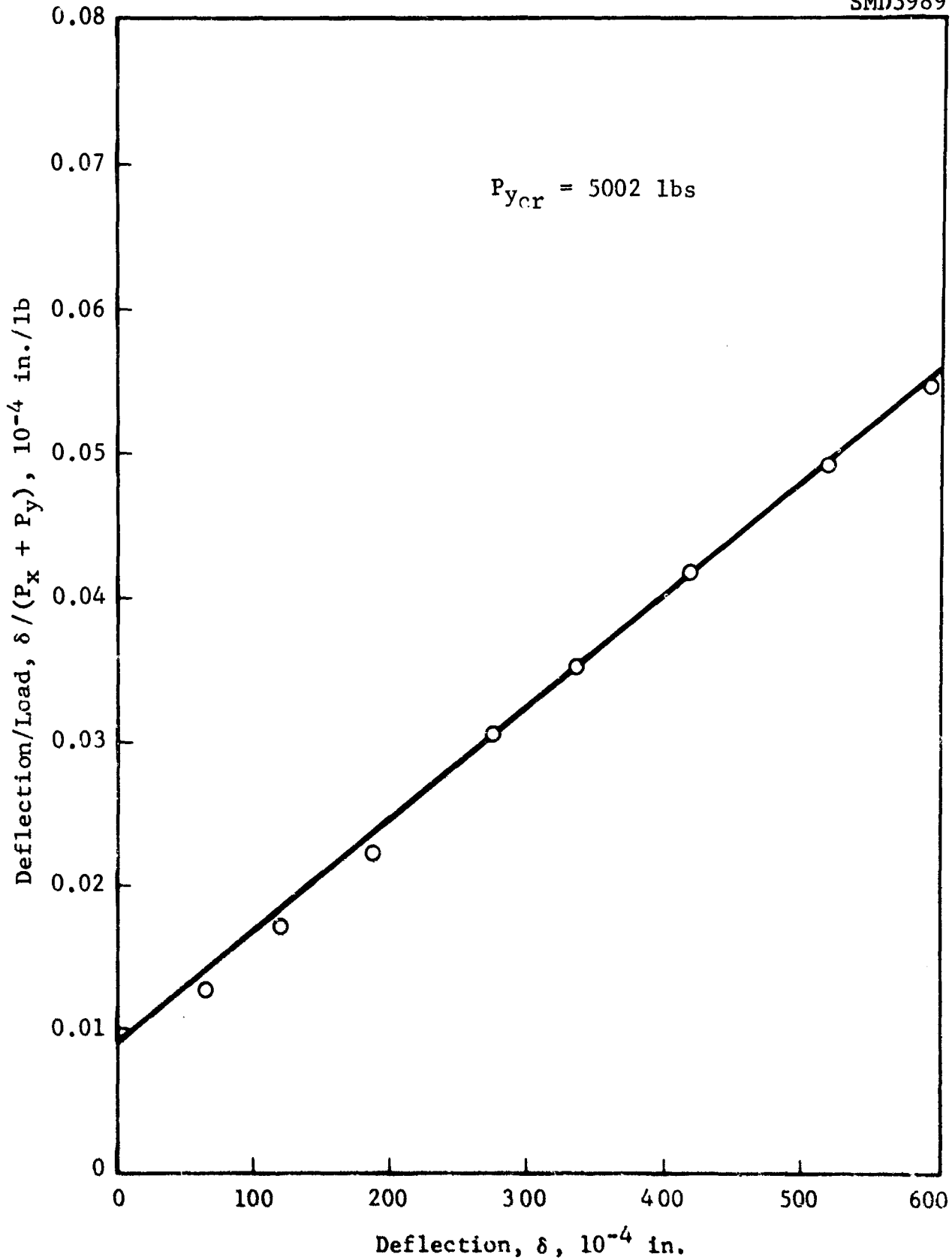
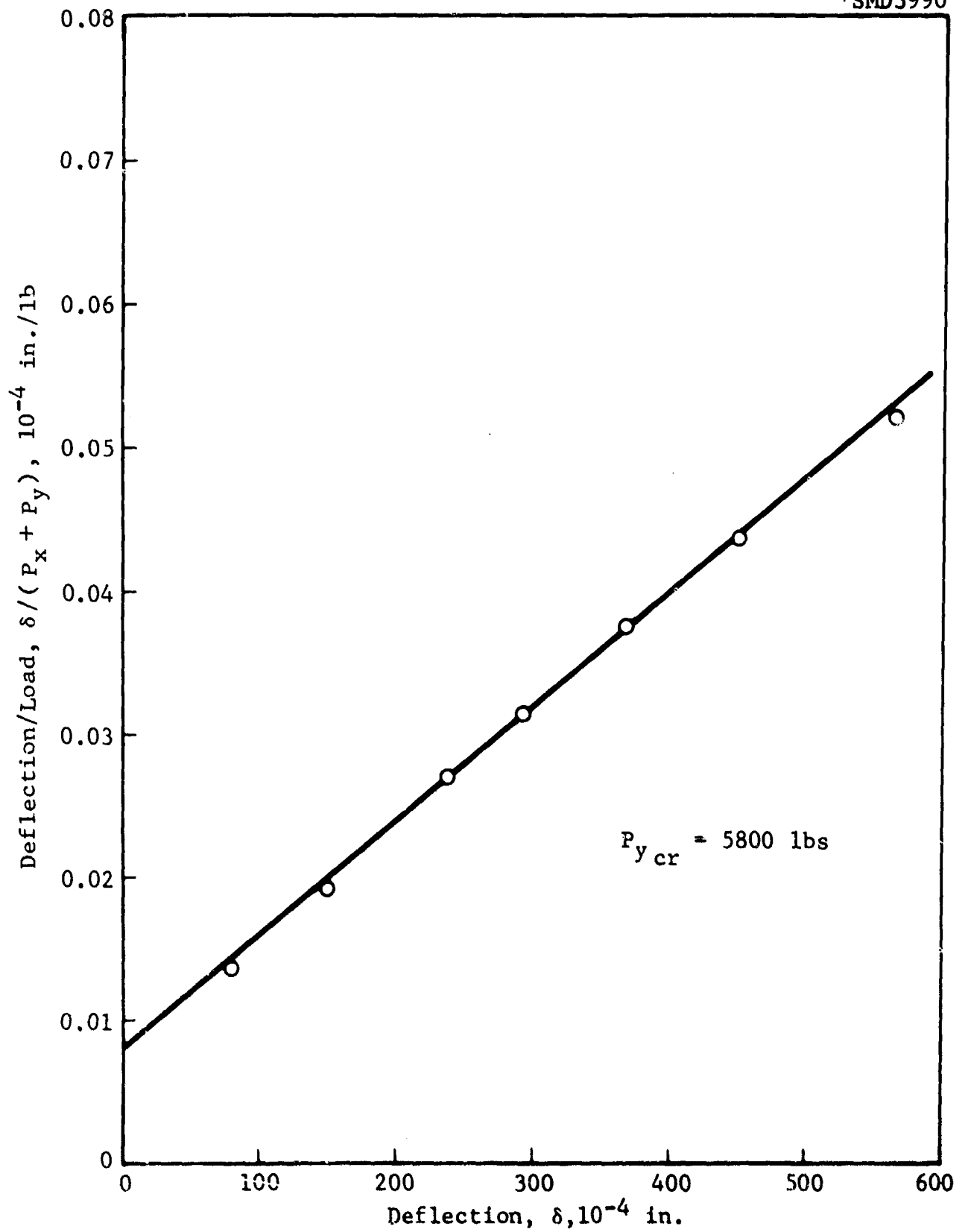


Figure 217 Southwell Plot for Panel No. 9, $N_y/N_x = .364$

Figure 218 Southwell Plot for Panel No. 9, $N_y/N_x = .475$

Figure 219 Southwell Plot for Panel No. 9, $N_y/N_x = .643$

Figure 220 Southwell Plot for Panel No. 9, $N_y/N_x = .867$

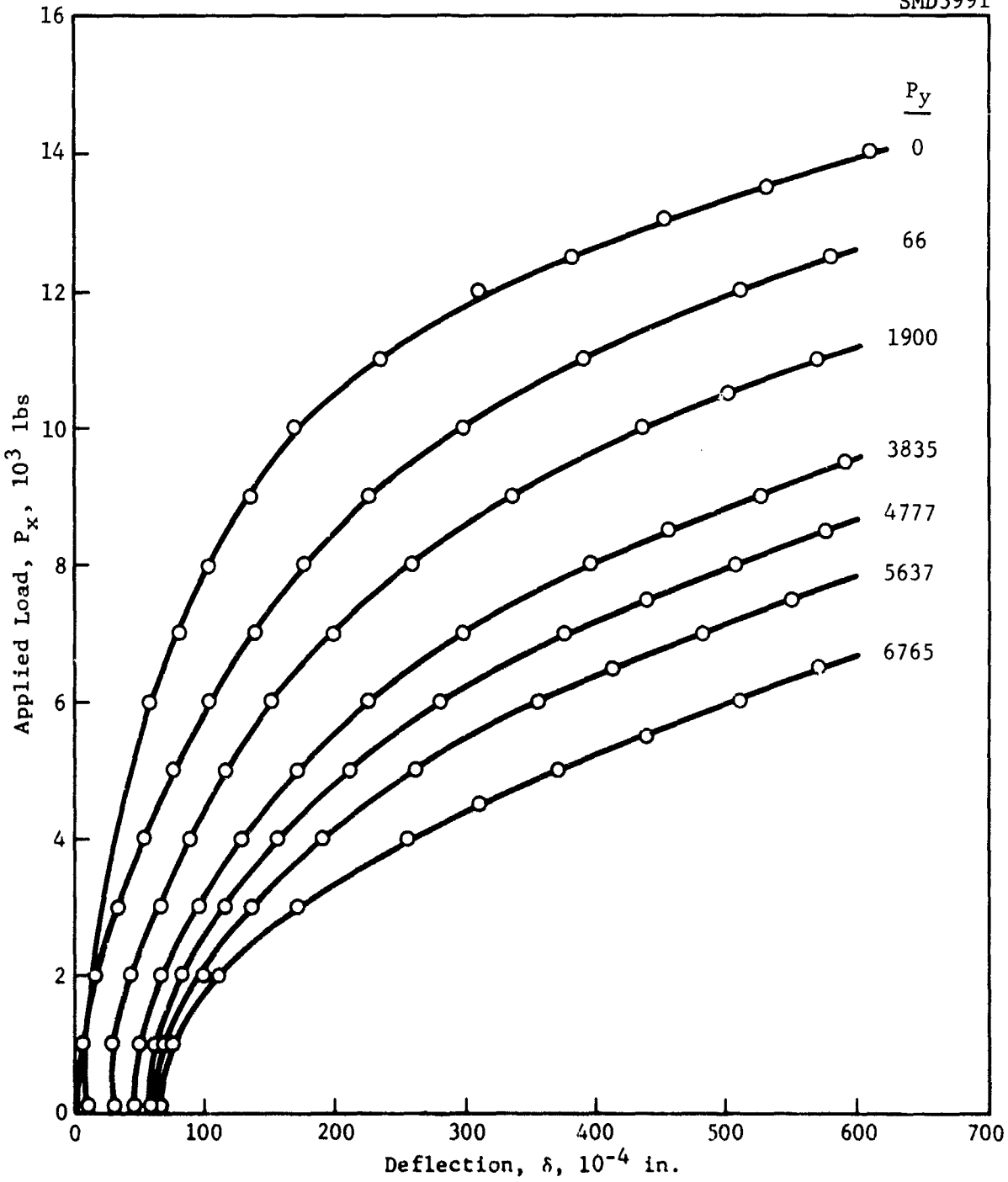
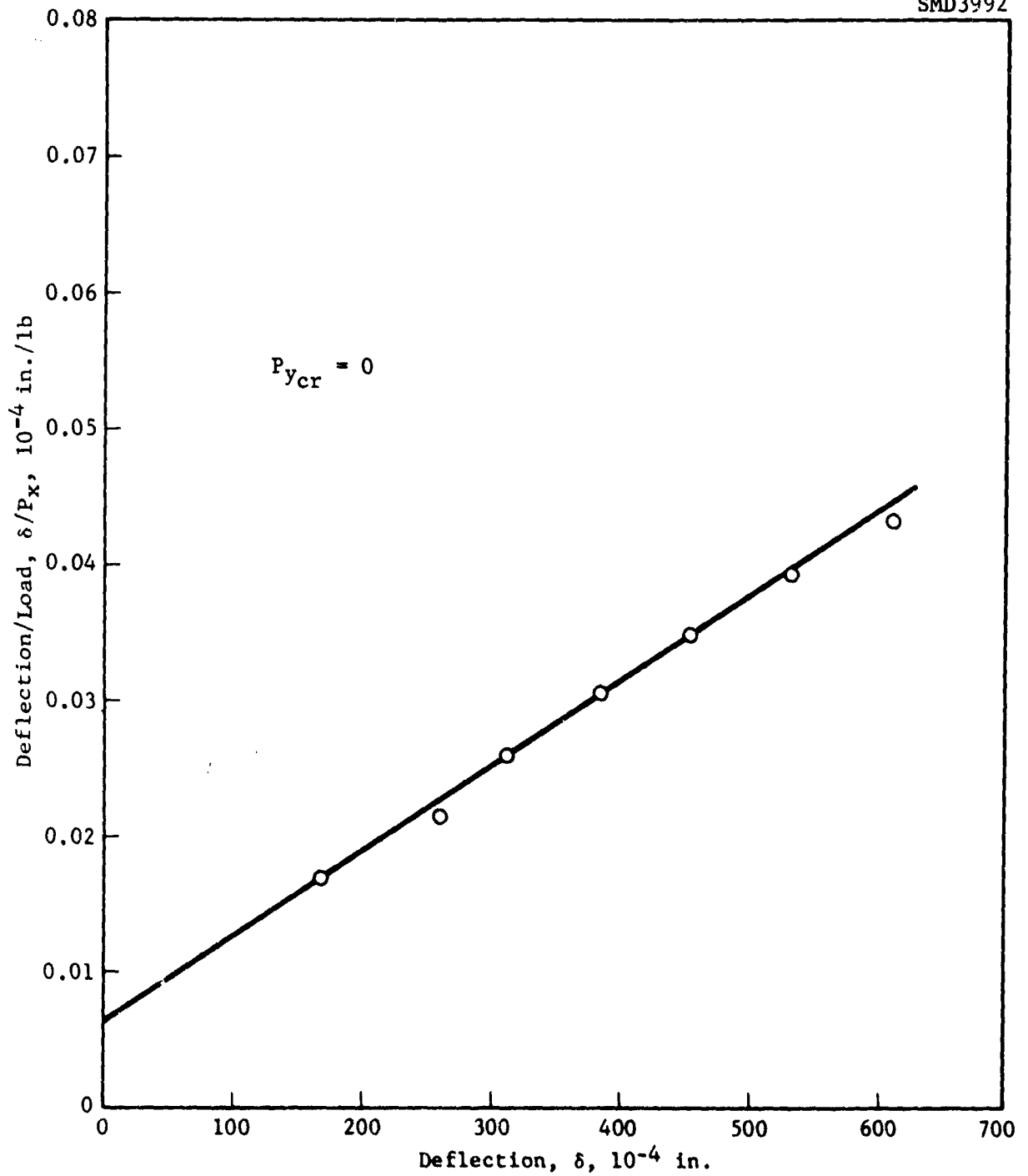


Figure 221 Load Deflection Curves for Panel 12

Figure 222 Southwell Plot for Panel No. 12, $N_y/N_x = 0$

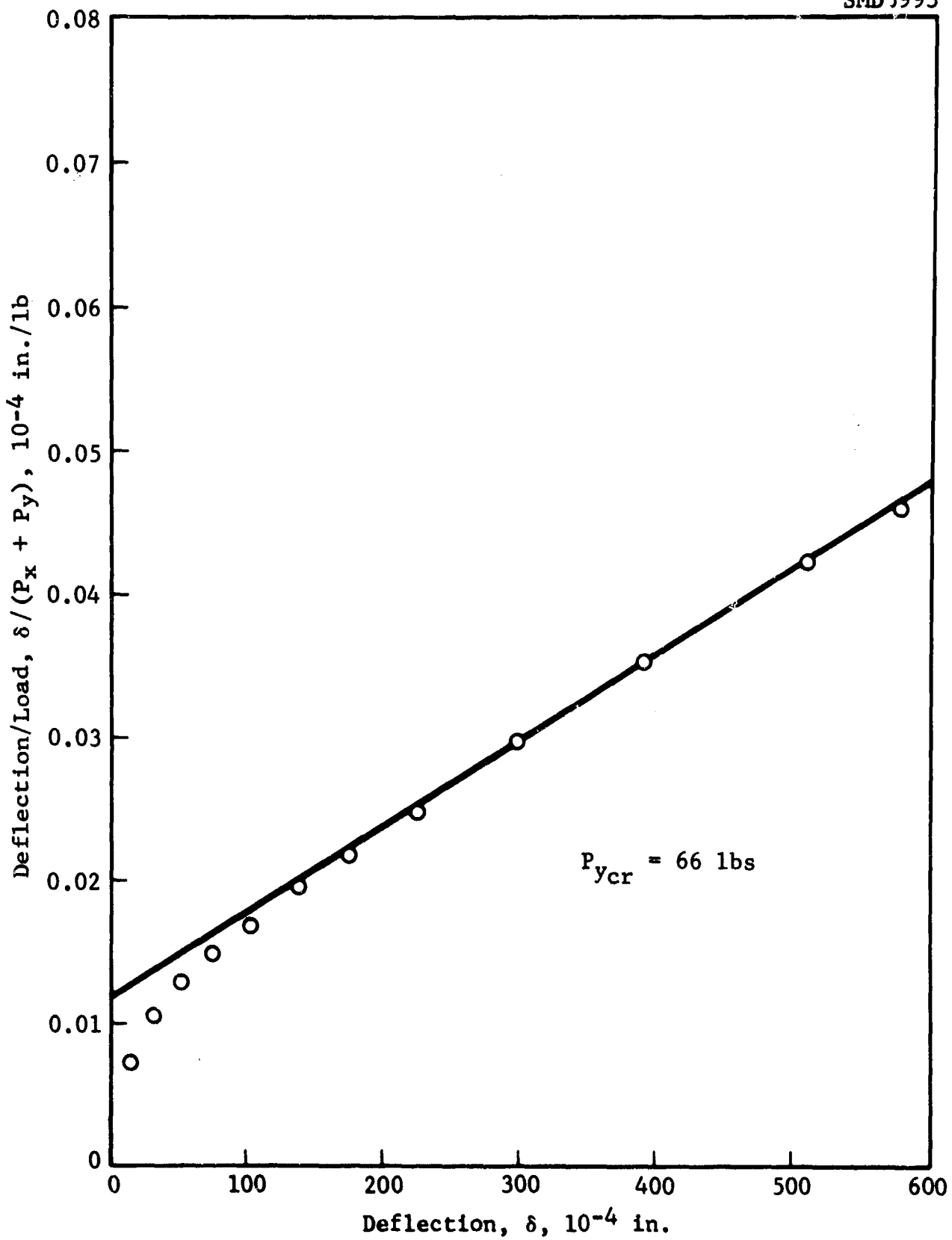
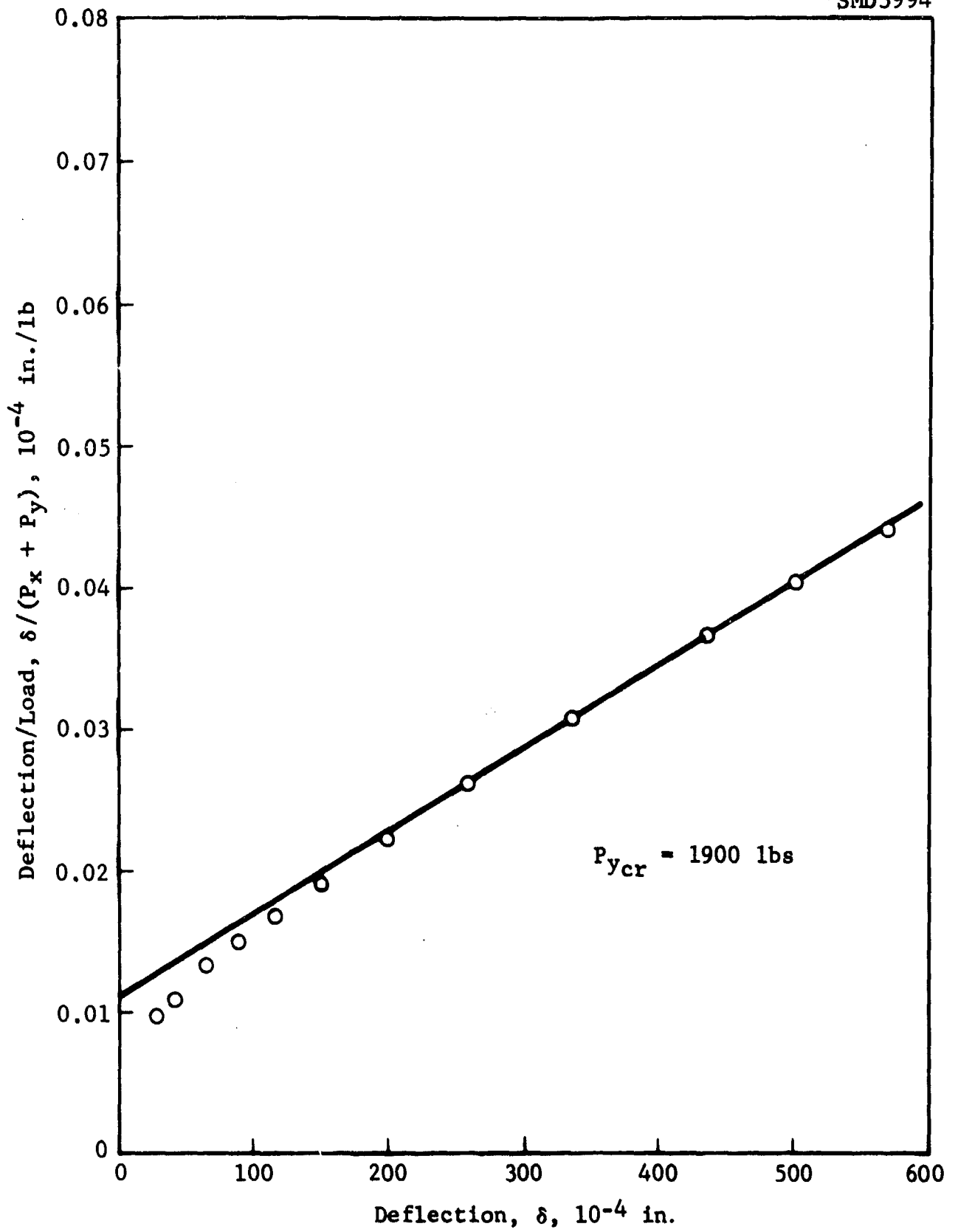


Figure 223 Southwell Plot for Panel No. 12, $N_y/N_x = .004$

Figure 224 Southwell Plot for Panel No. 12, $N_y/N_x = .125$

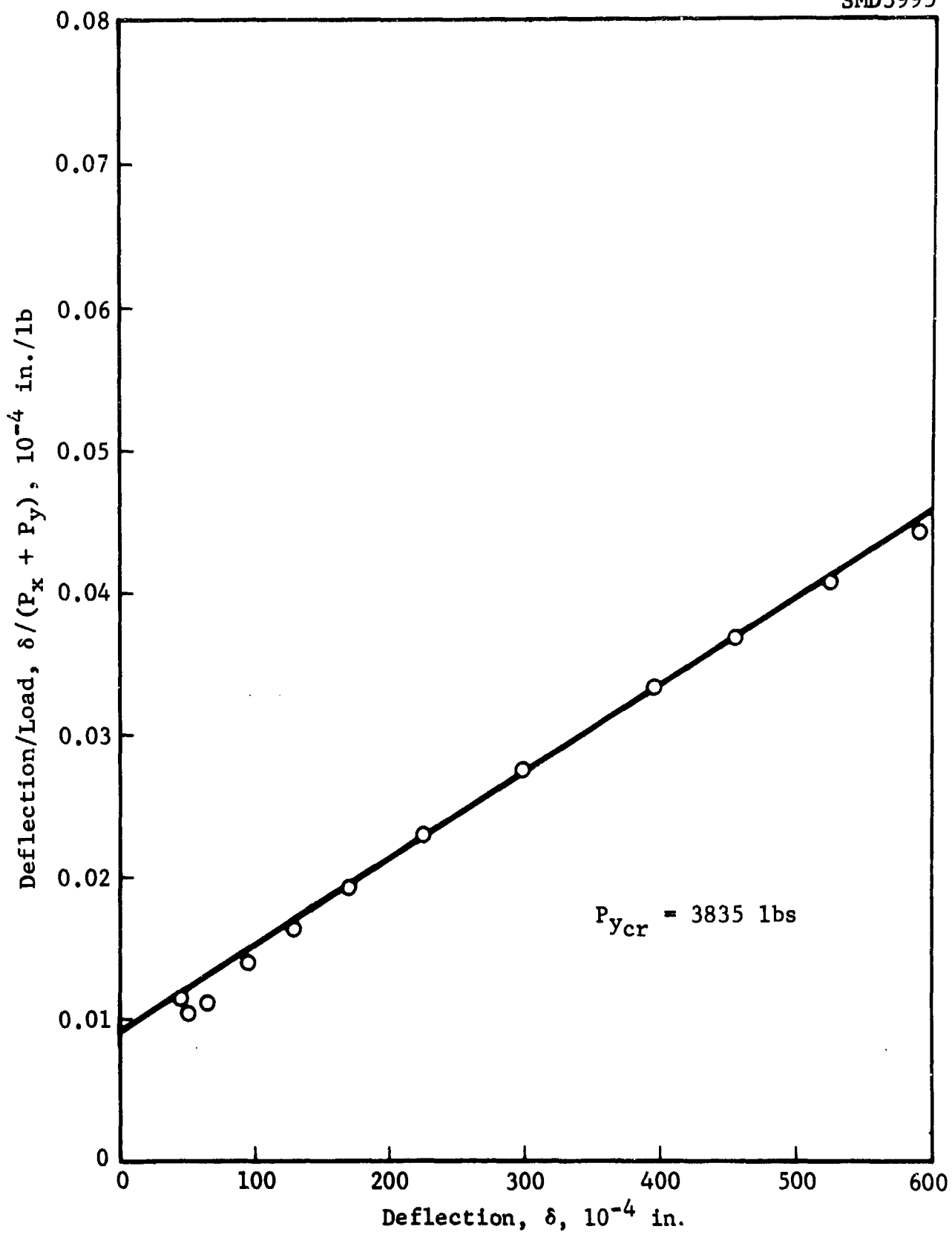
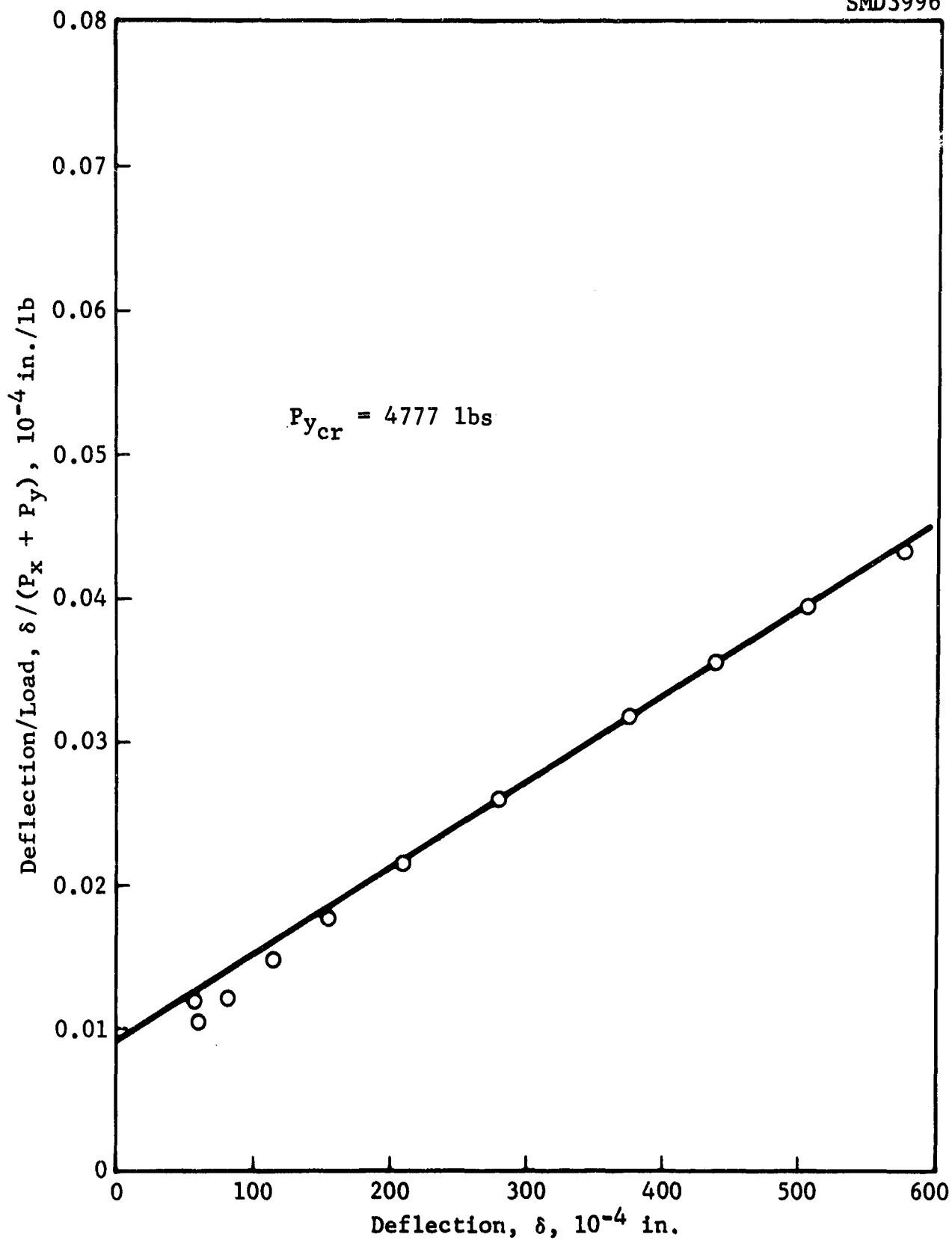


Figure 225 Southwell Plot for Panel No. 12, $N_y/N_x = .306$

Figure 226 Southwell Plot for Panel No. 12, $N_y/N_x = .406$

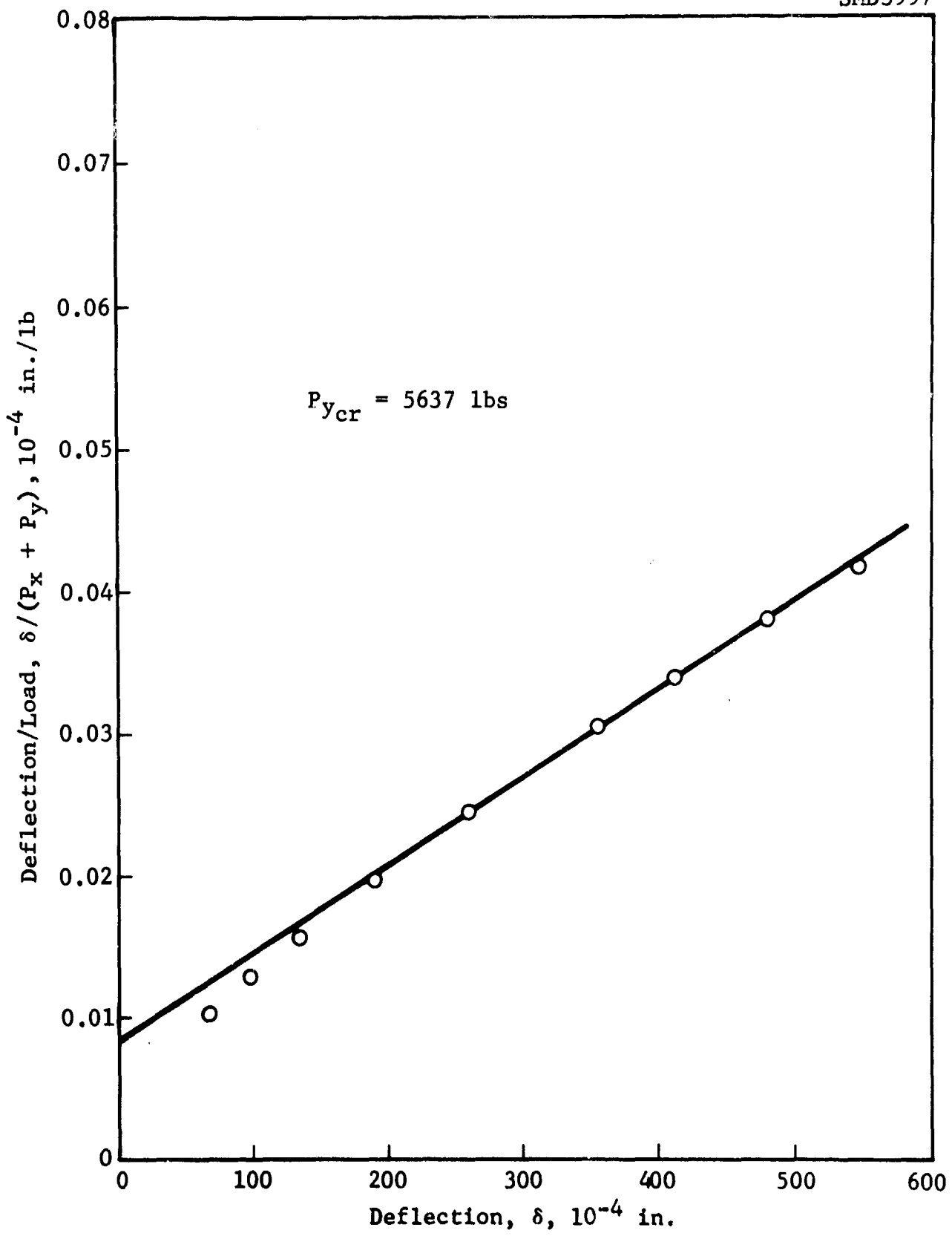


Figure 227 Southwell Plot for Panel No. 12, $N_y/N_x = .537$

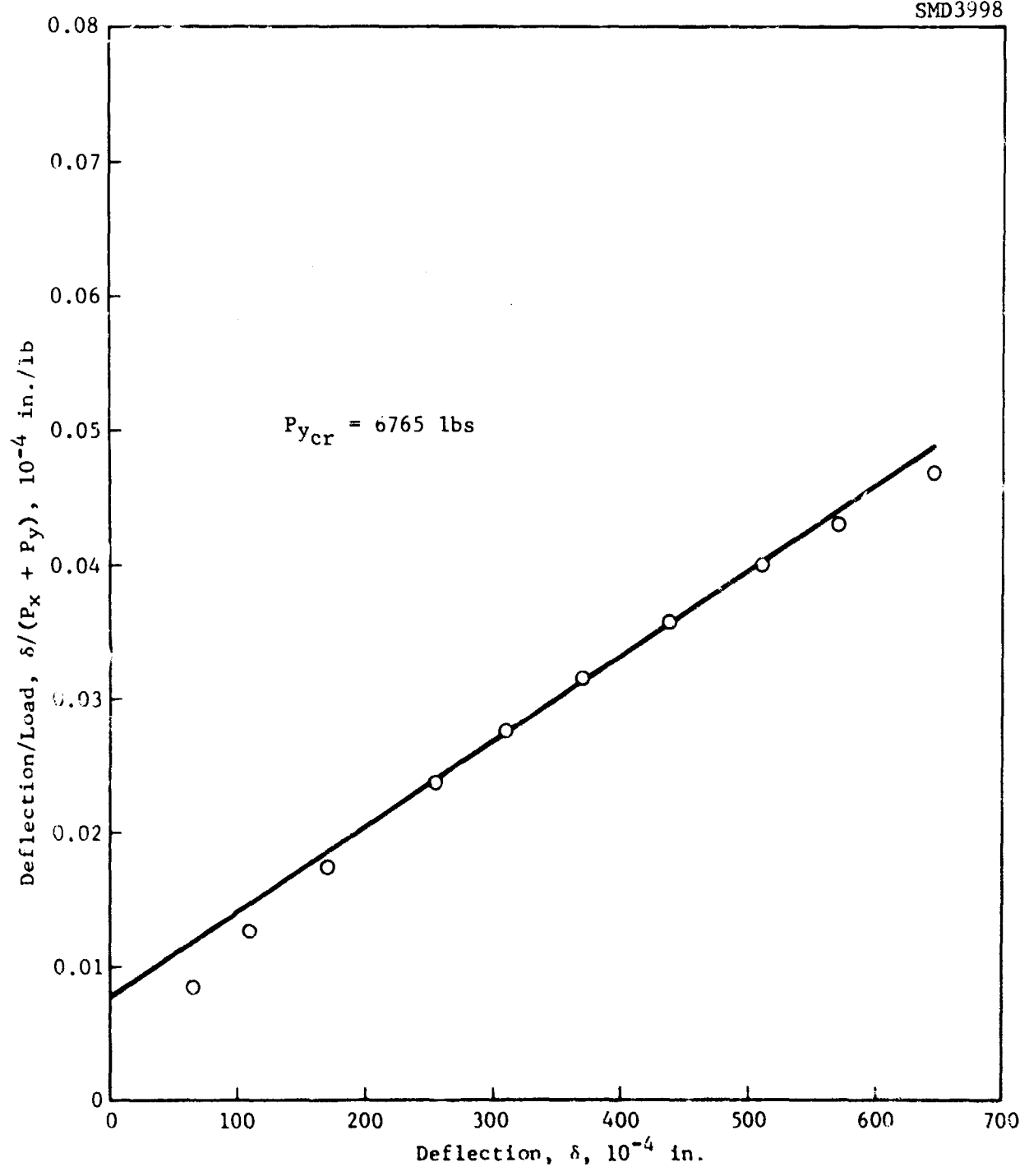


Figure 228 Southwell Plot for Panel No. 12, $N_y/N_x = .762$

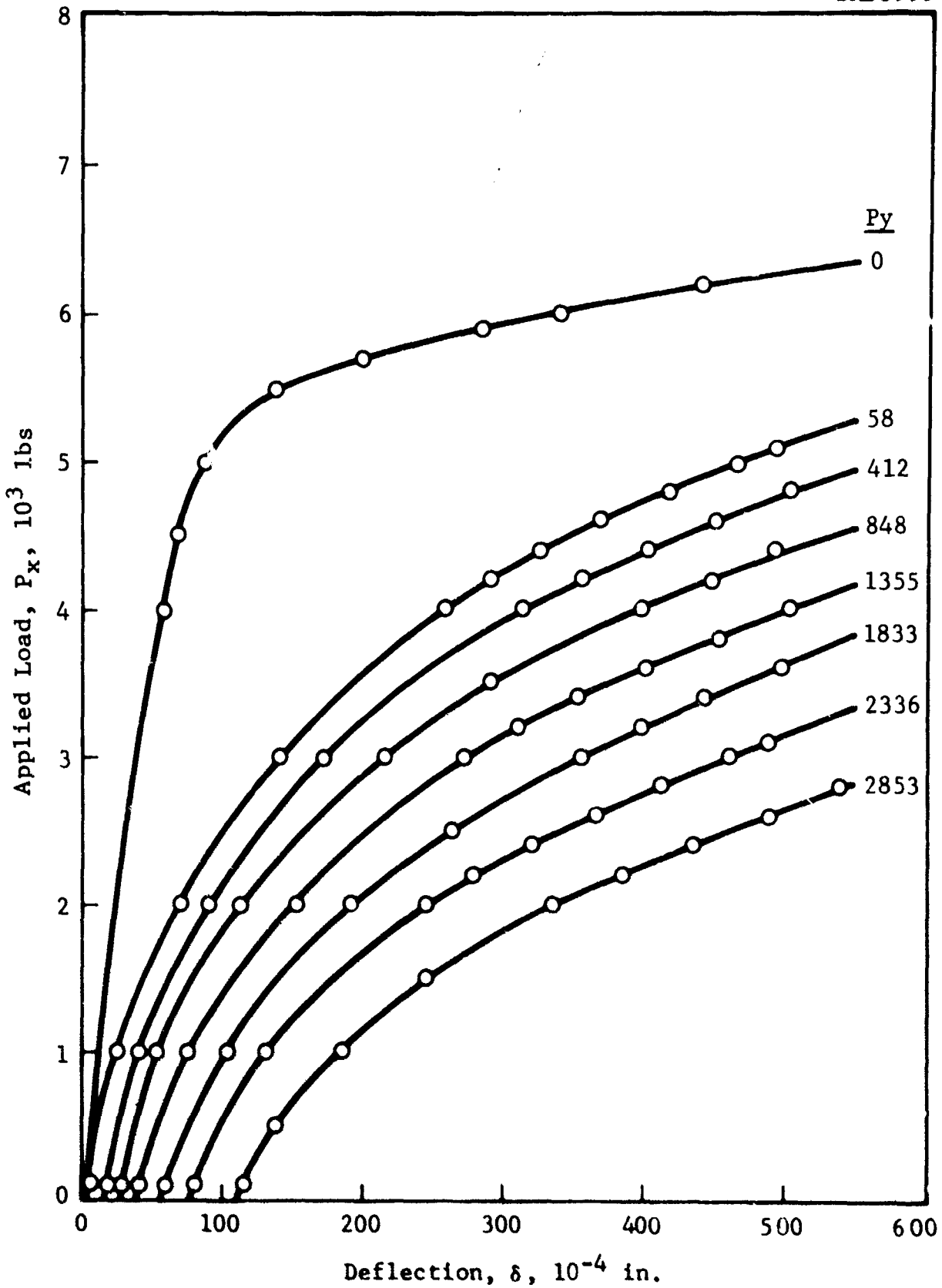


Figure 229 Load Deflection Curves for Panel No. 16

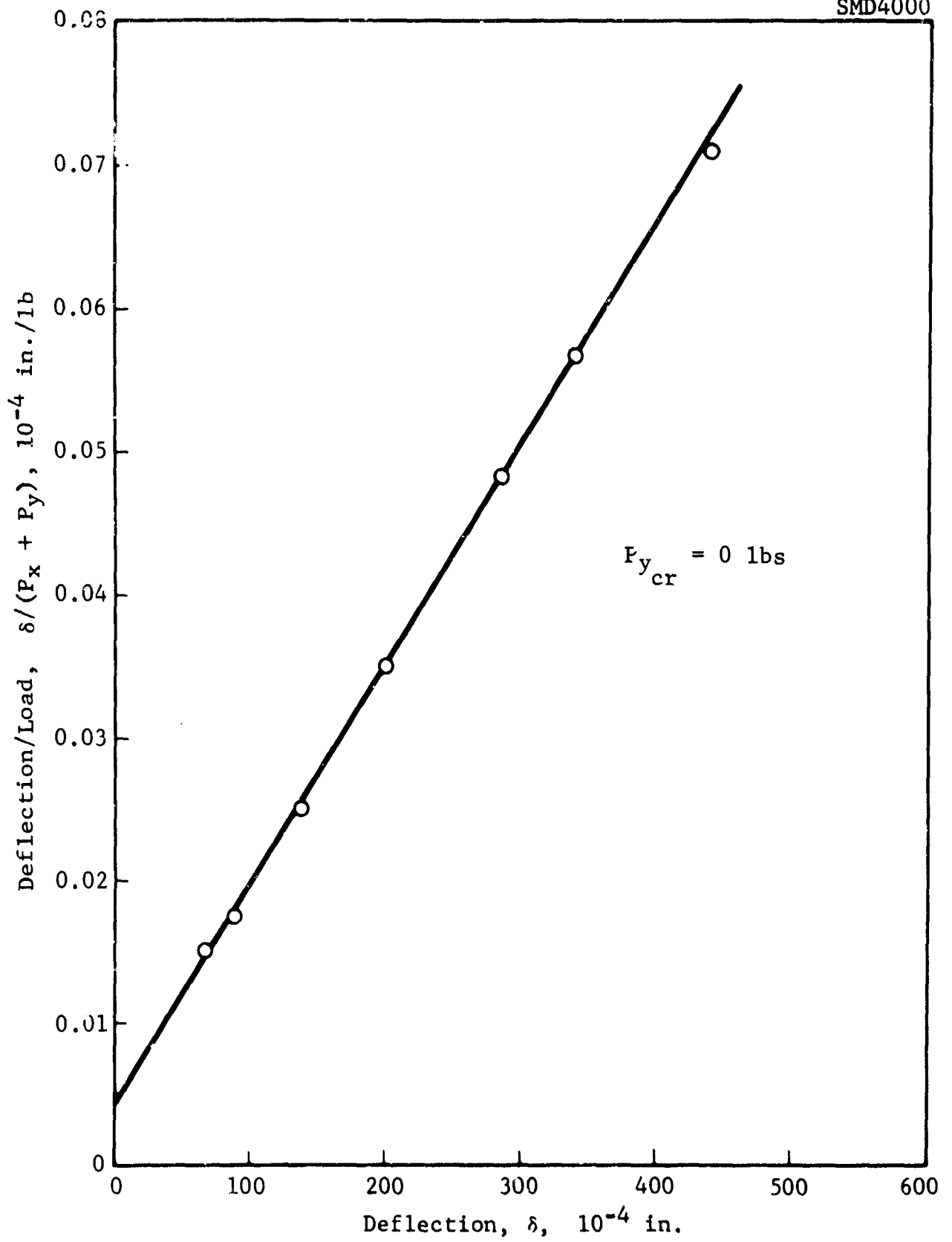


Figure 230 Southwell Plot for Panel No. 16, $N_y/N_x = 0$

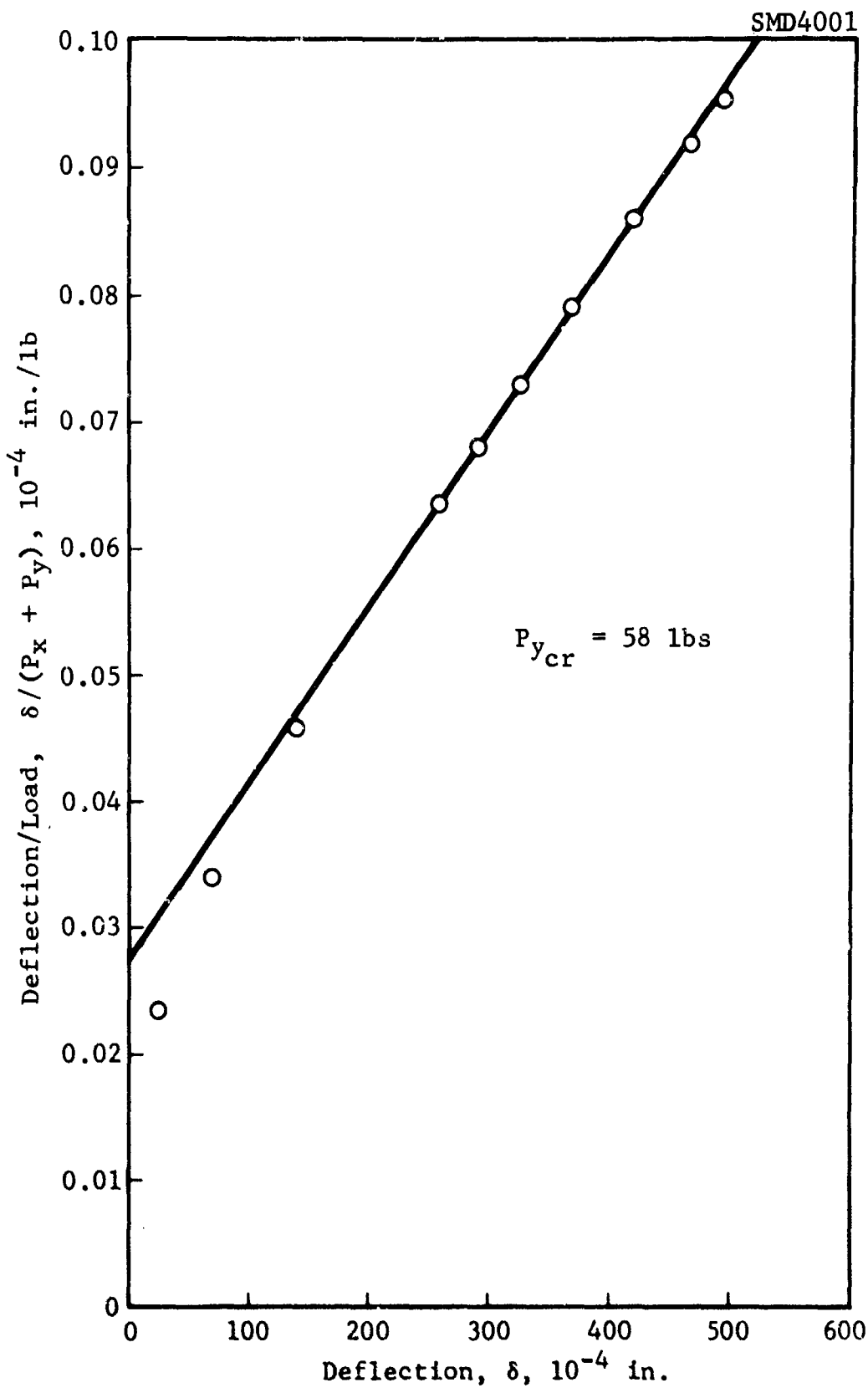


Figure 231 Southwell Plot for Panel No. 16, $N_y/N_x = .008$

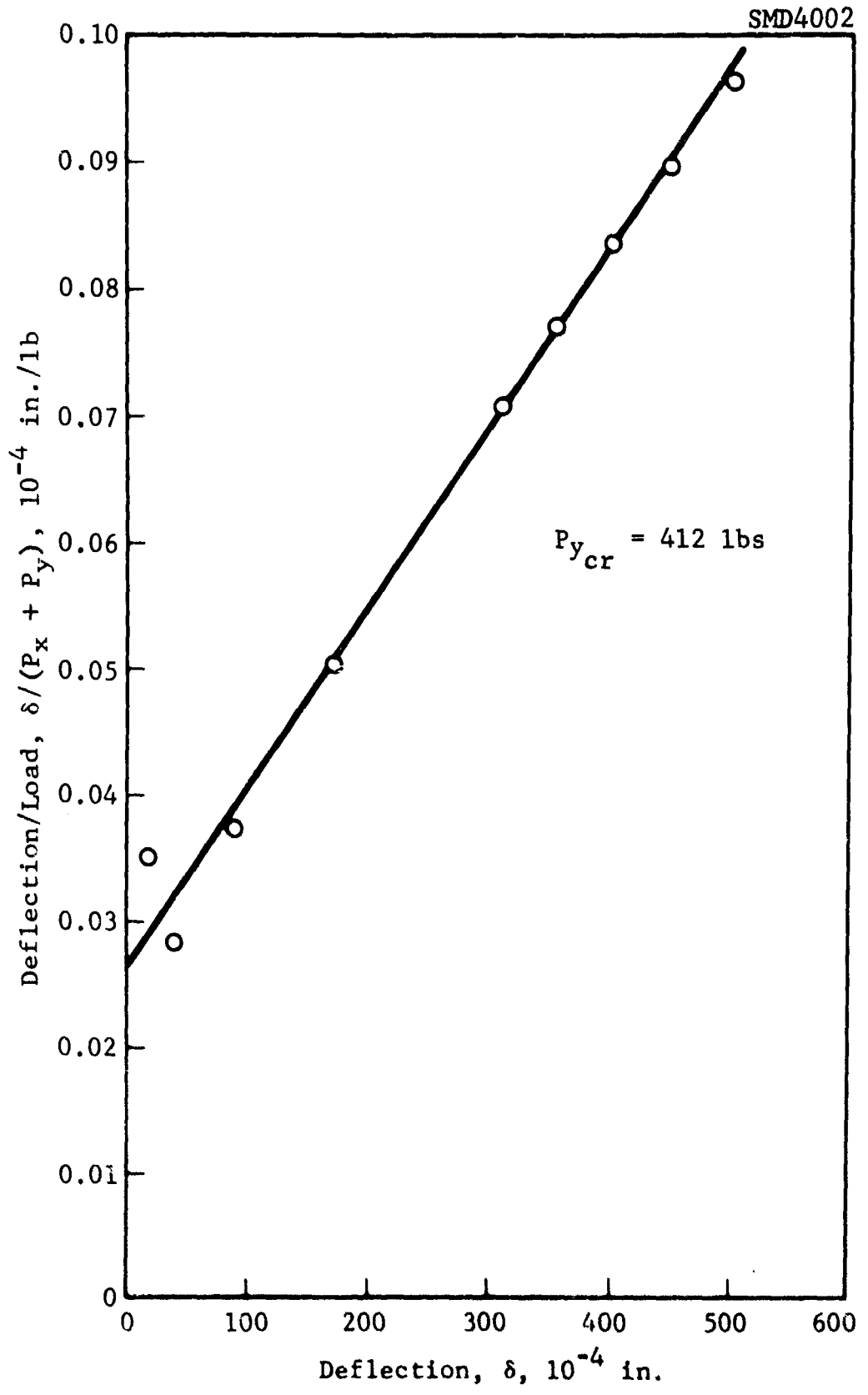


Figure 232 Southwell Plot for Panel No. 16, $N_y/N_x = .062$

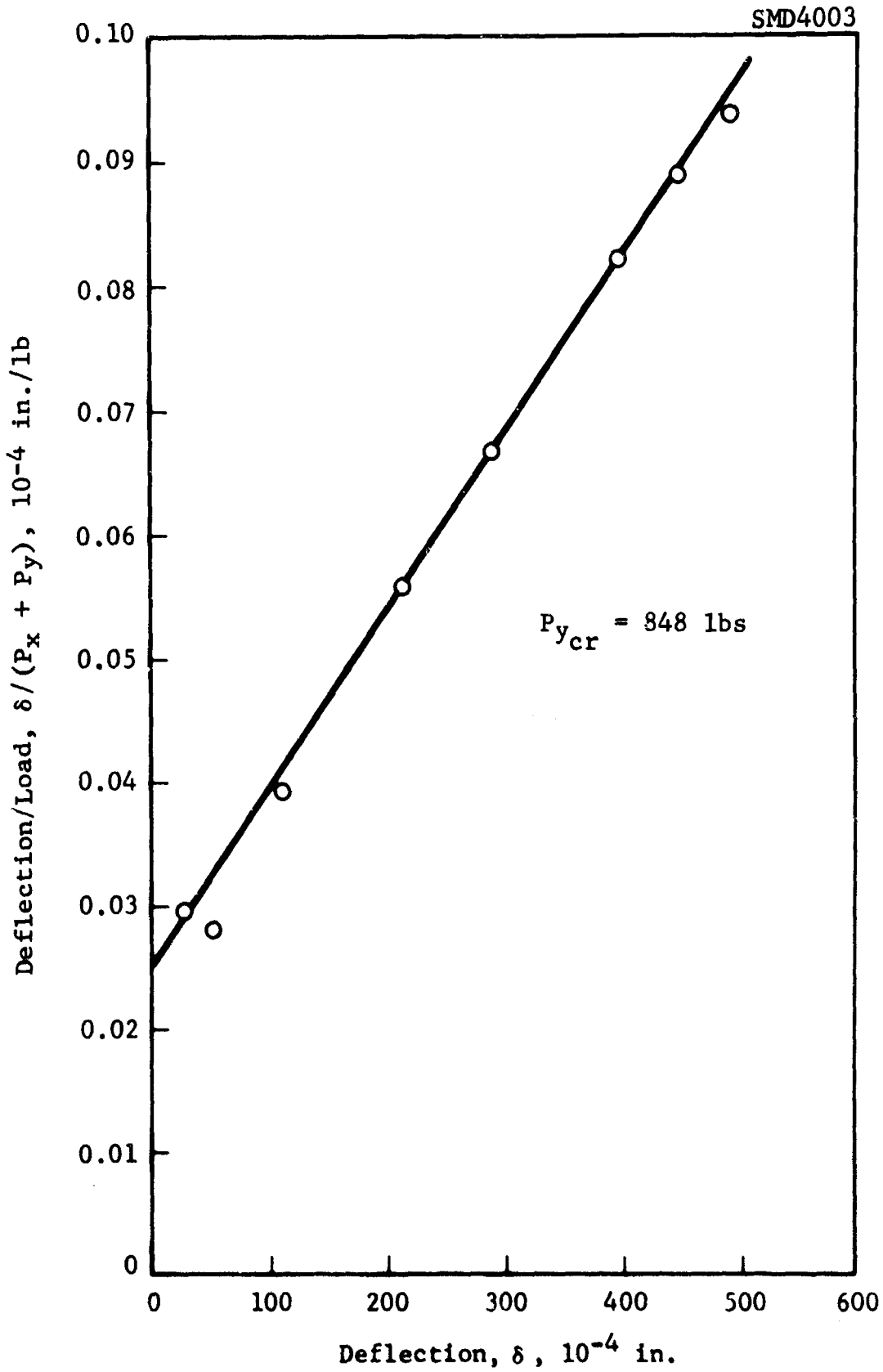


Figure 233 Southwell Plot for Panel No. 16, $N_y/N_x = .139$

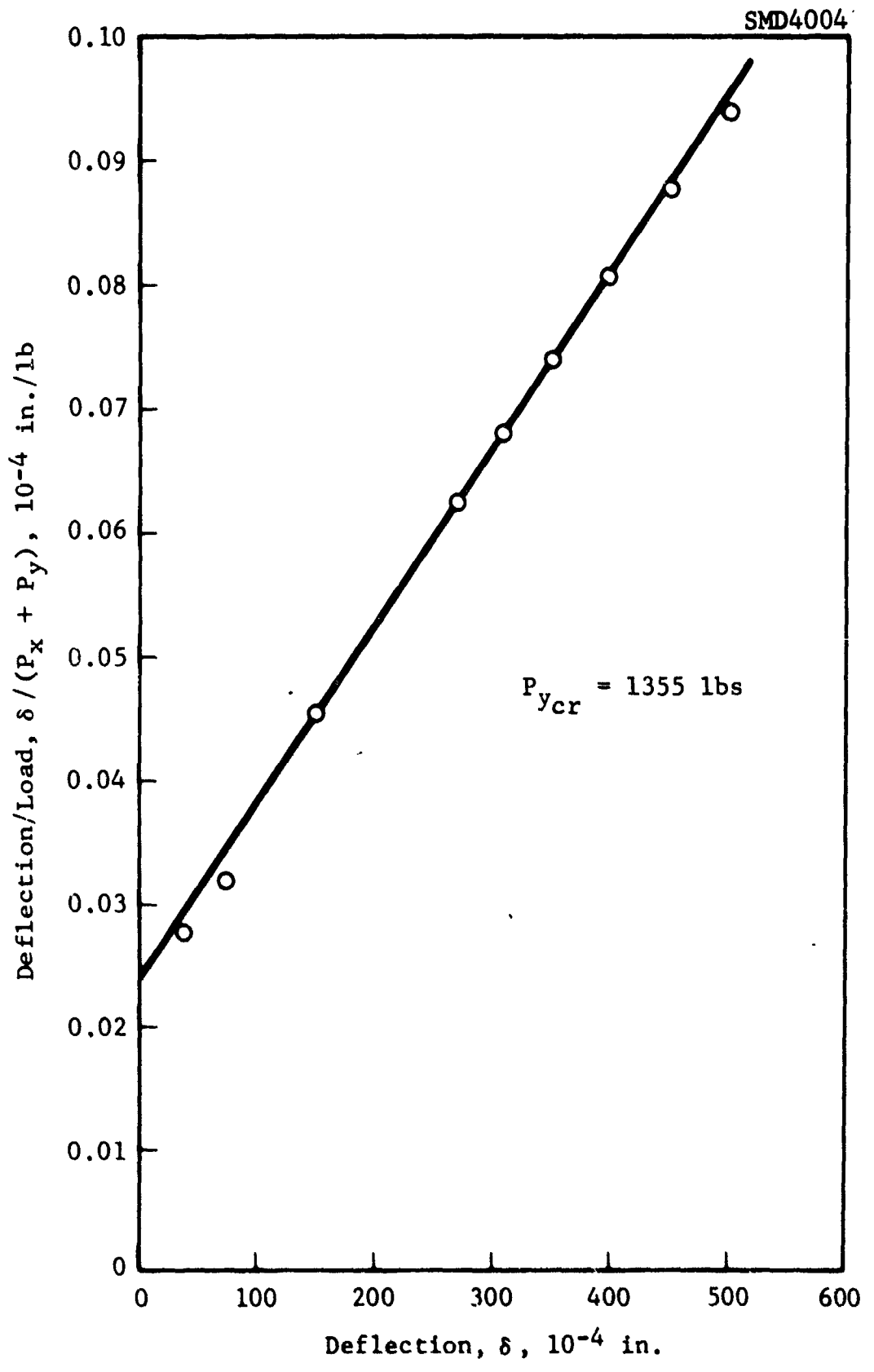


Figure 234 Southwell Plot for Panel No. 16, $N_y/N_x = .240$

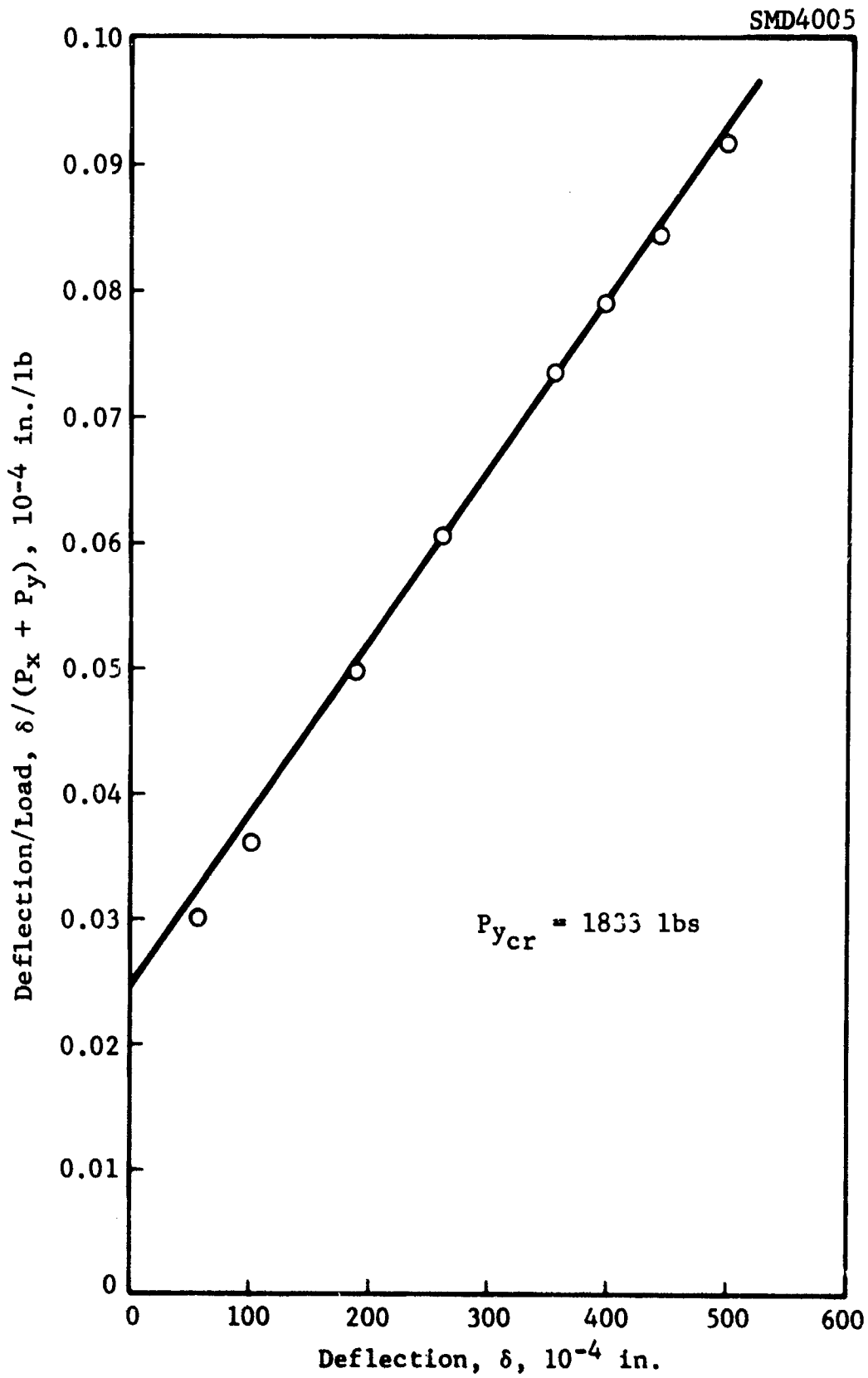


Figure 235 Southwell Plot for Panel No. 16, $N_y/N_x = .405$

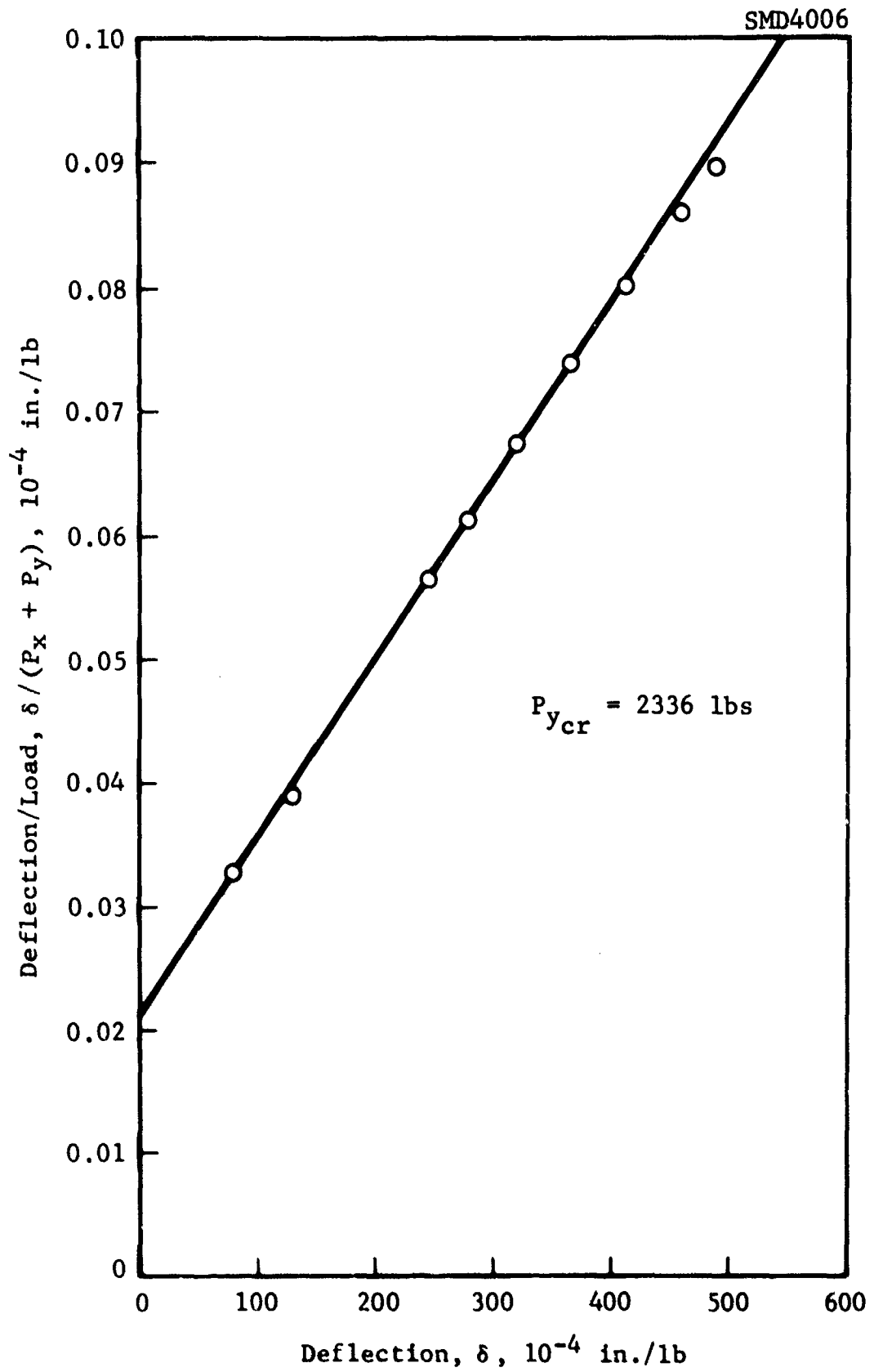


Figure 236 Southwell Plot for Panel No. 16, $N_y/N_x = .517$

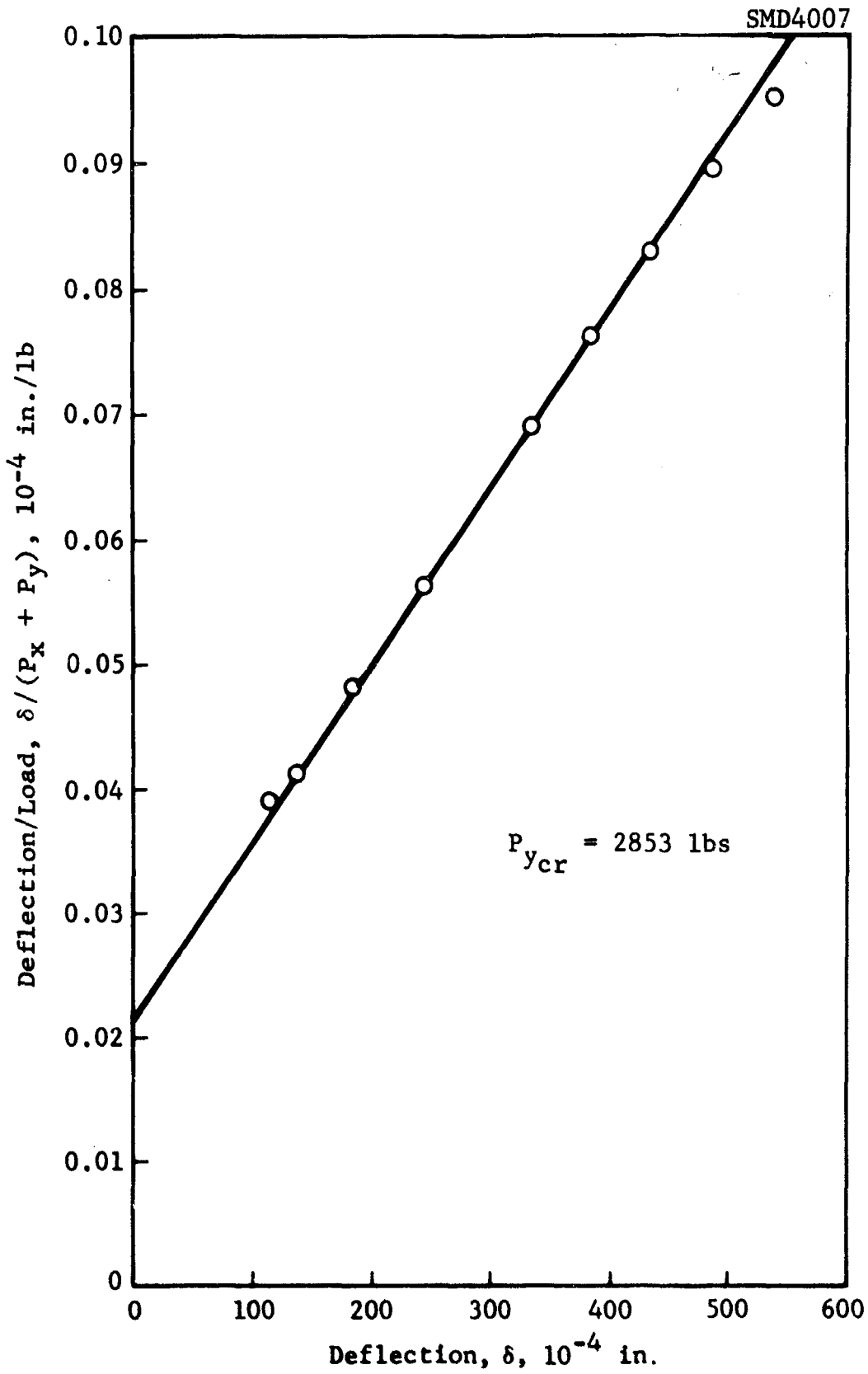


Figure 237 Southwell Plot for Panel No. 16, $N_y/N_x = .678$

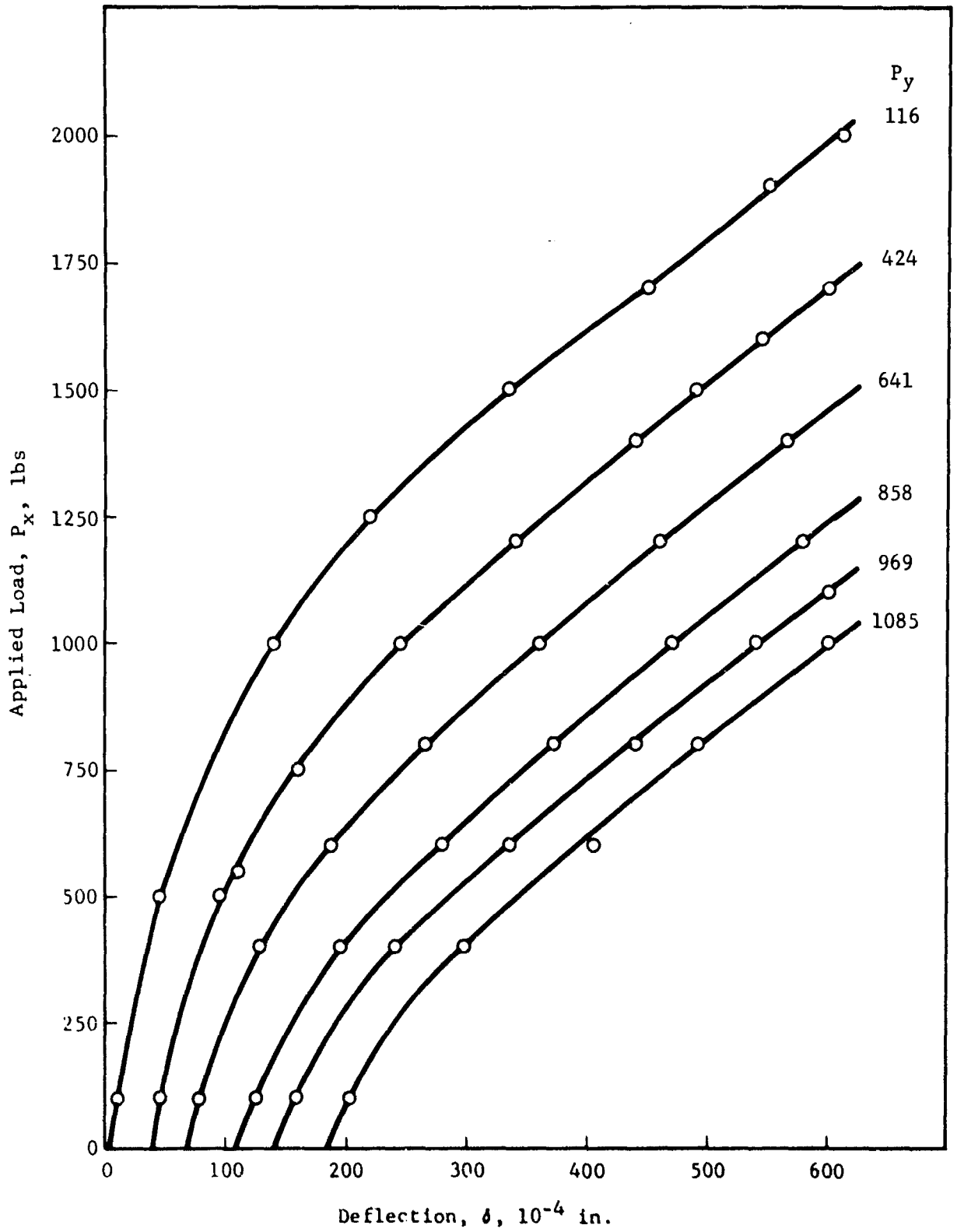


Figure 238 Load-Deflection Curves for Panel 19A

SMD1350

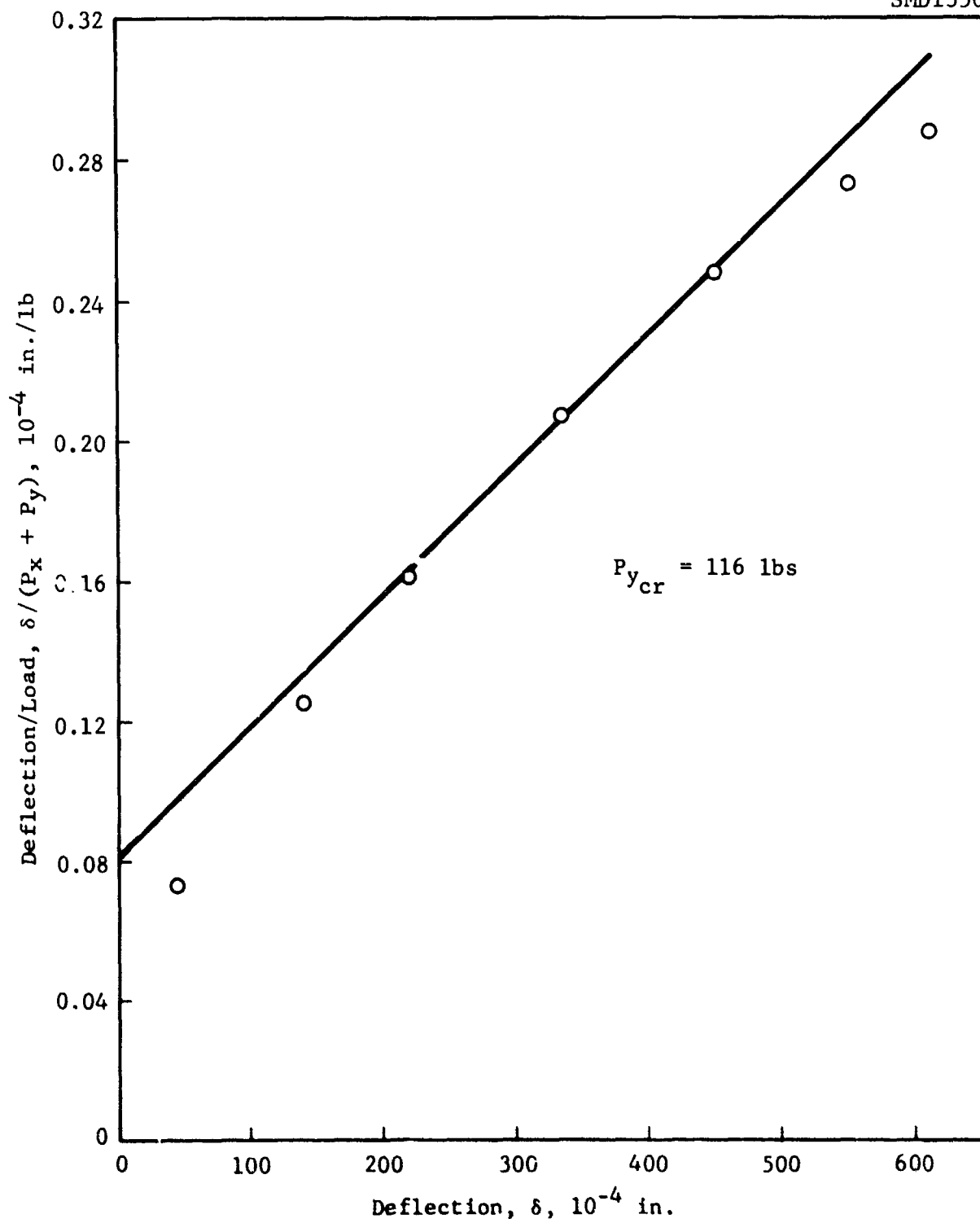


Figure 239 Southwell Plot for Panel No. 19A, $N_y/N_x = .047$

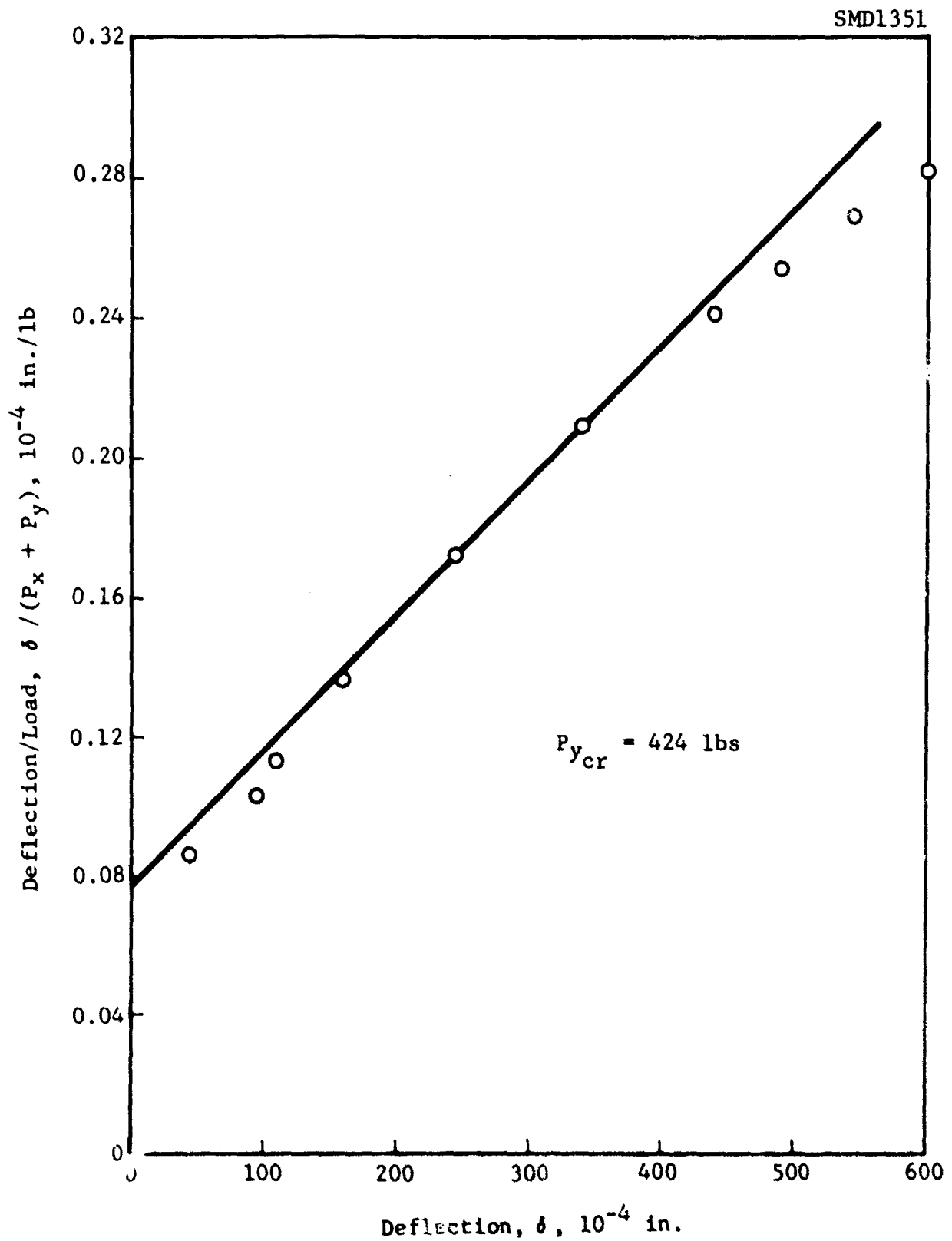


Figure 240 Southwell Plot for Panel No. 19A, $N_y/N_x = .194$

SMD1352

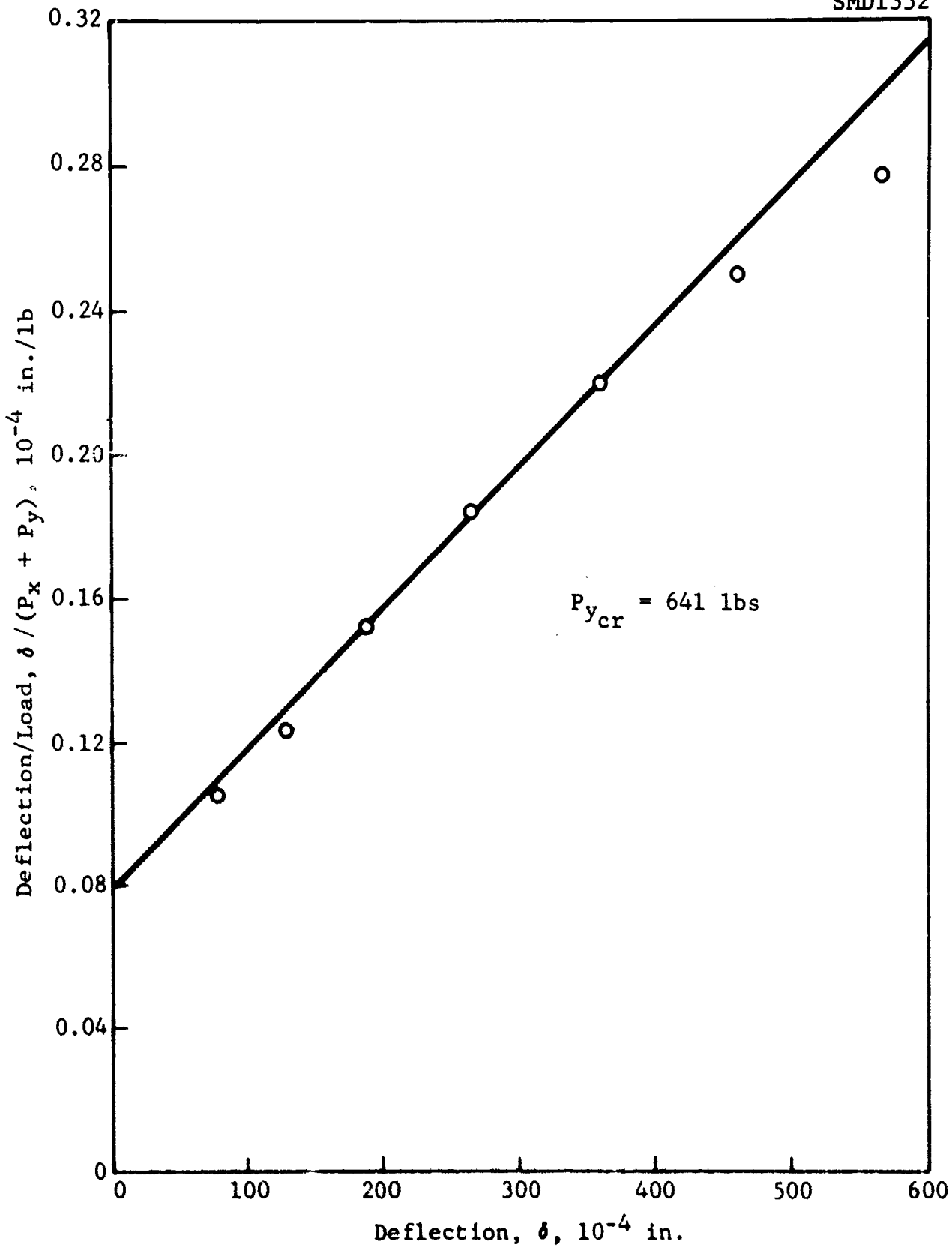


Figure 241 Southwell Plot for Panel No. 19A: $N_y/N_x = .335$

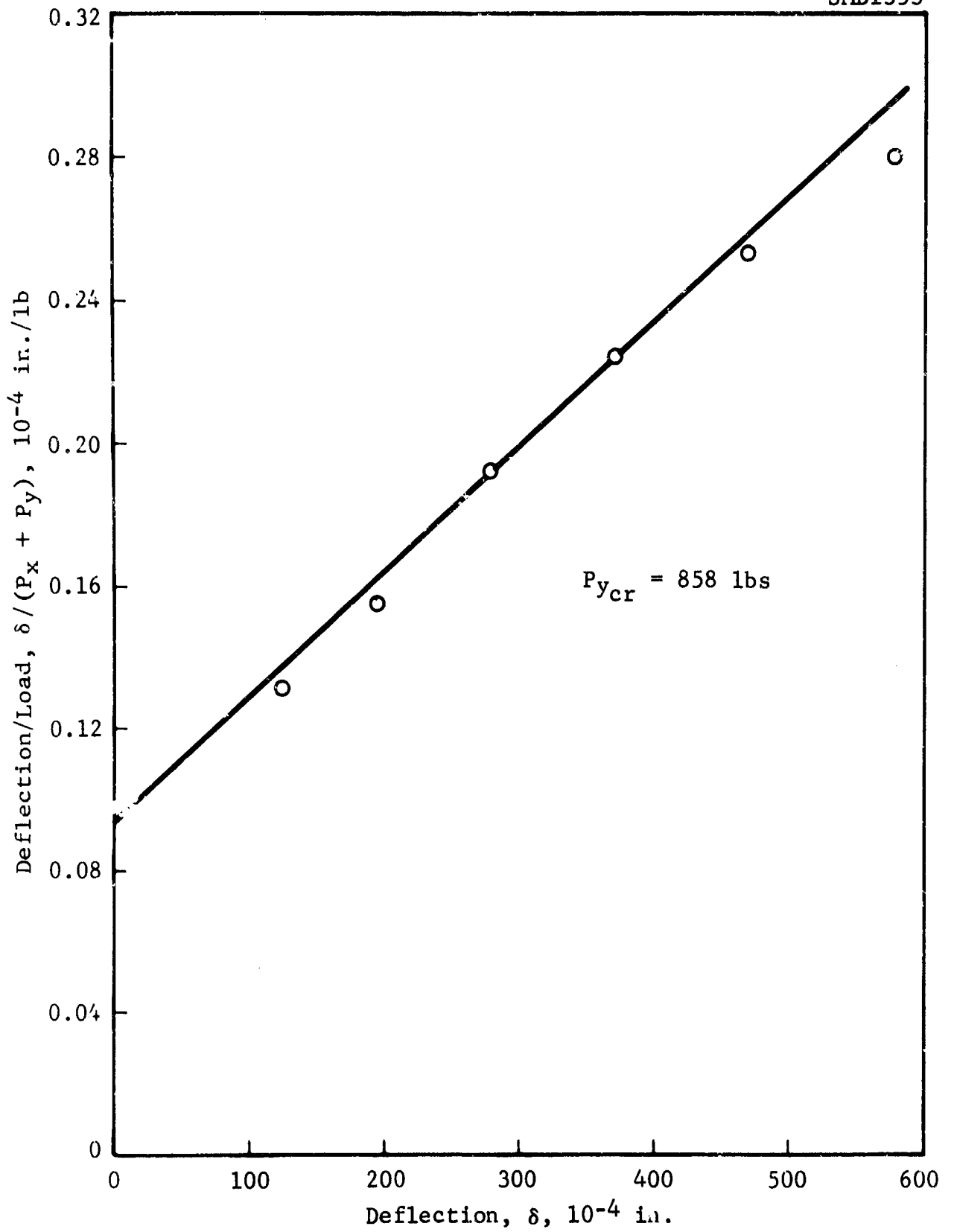


Figure 242 Southwell Plot for Panel No. 19A, $N_y/N_x = .428$

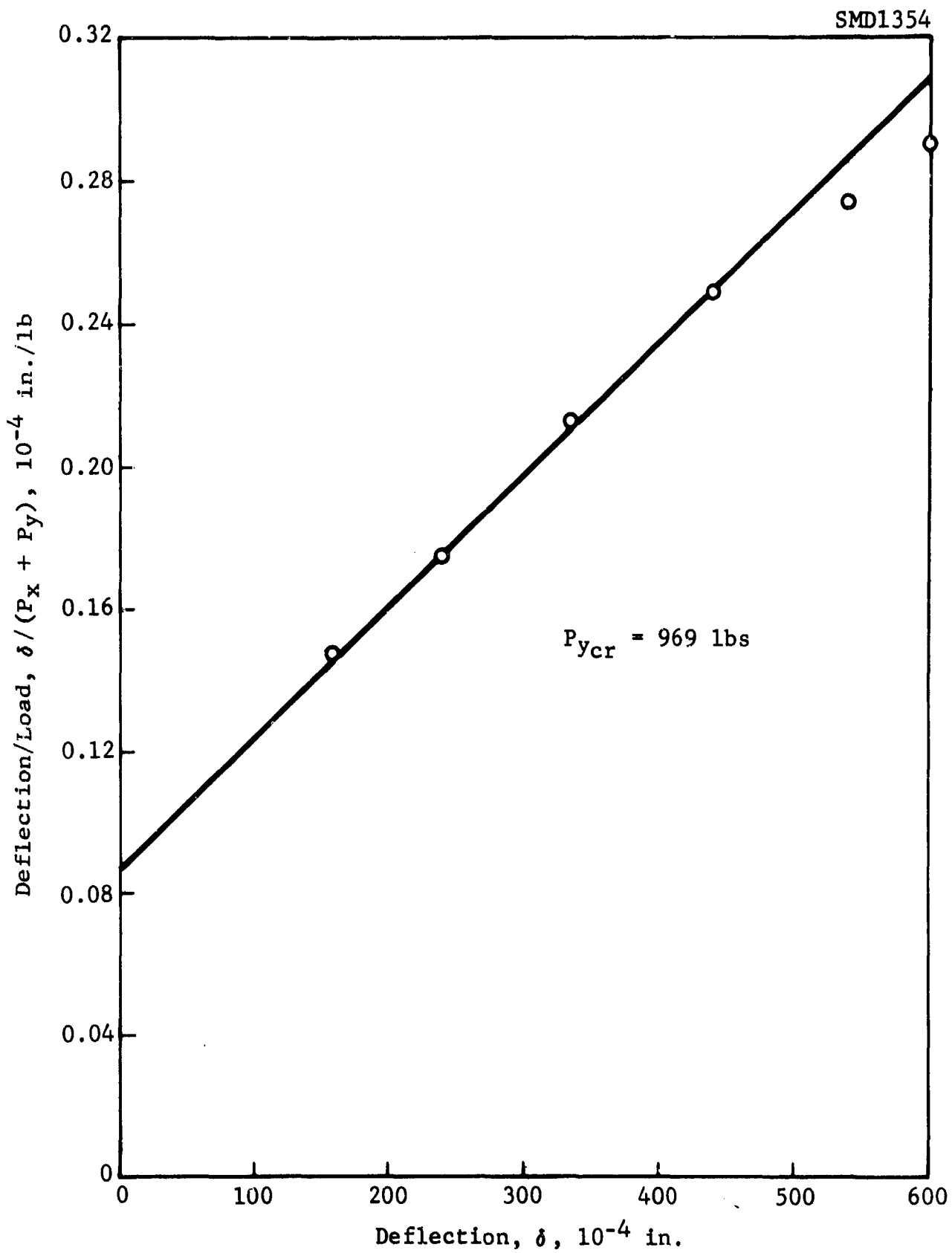


Figure 243 Southwell Plot for Panel No. 19A, $N_y/N_x = .560$

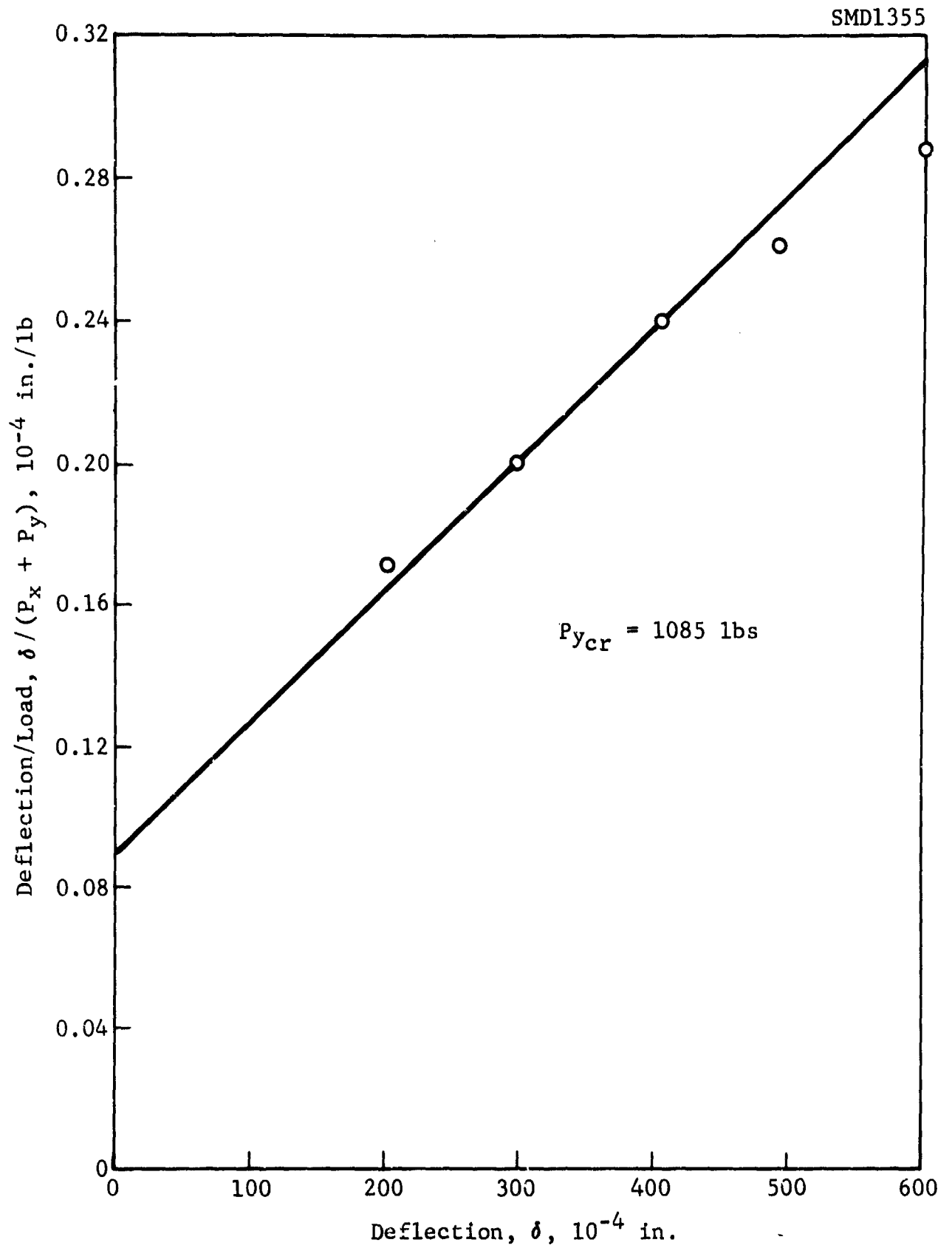


Figure 244 Southwell Plot for Panel No. 19A, $N_y/N_x = .678$

SMD1356

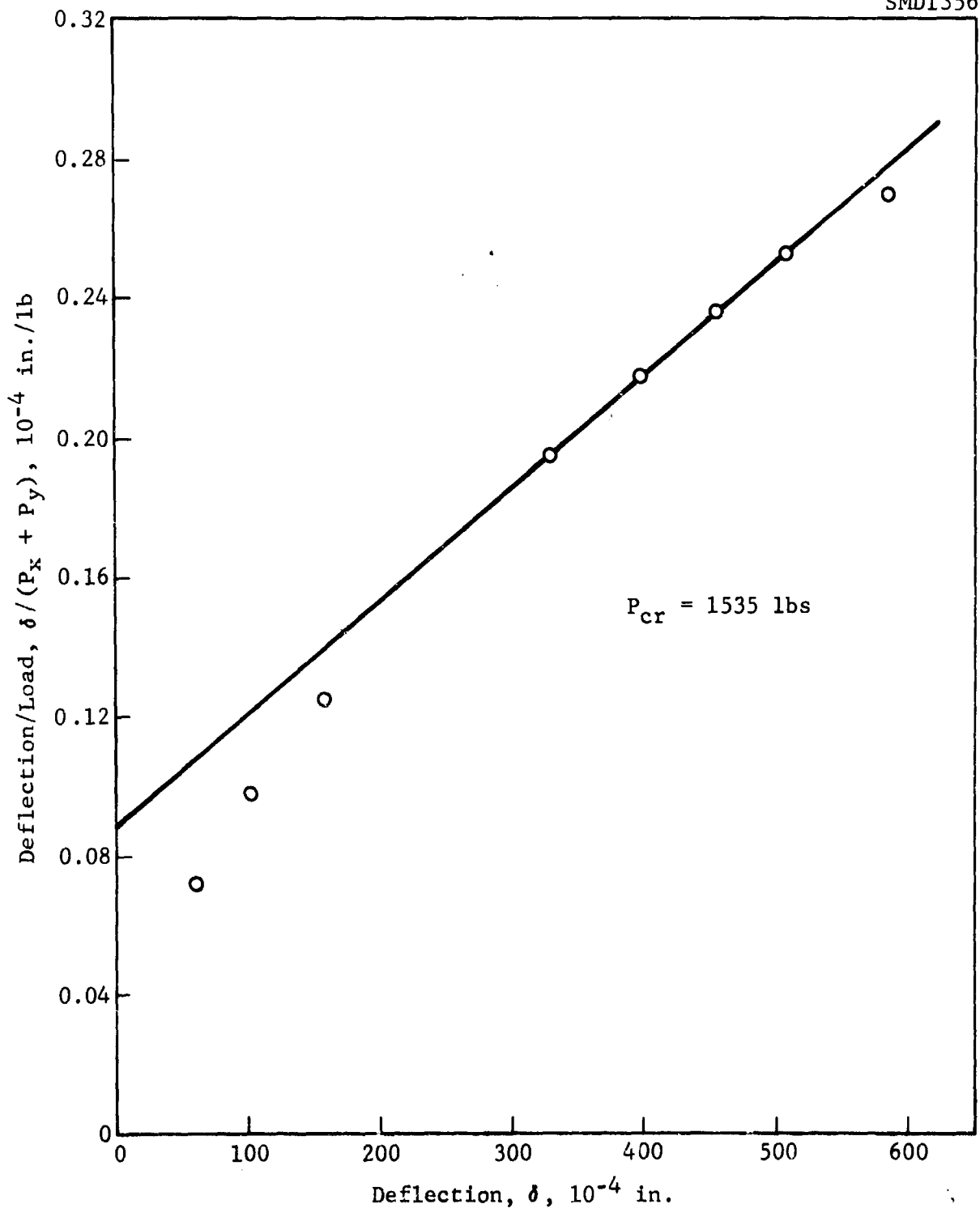


Figure 245 Southwell Plot for Panel No. 19A, $N_y/N_x = 1.00$

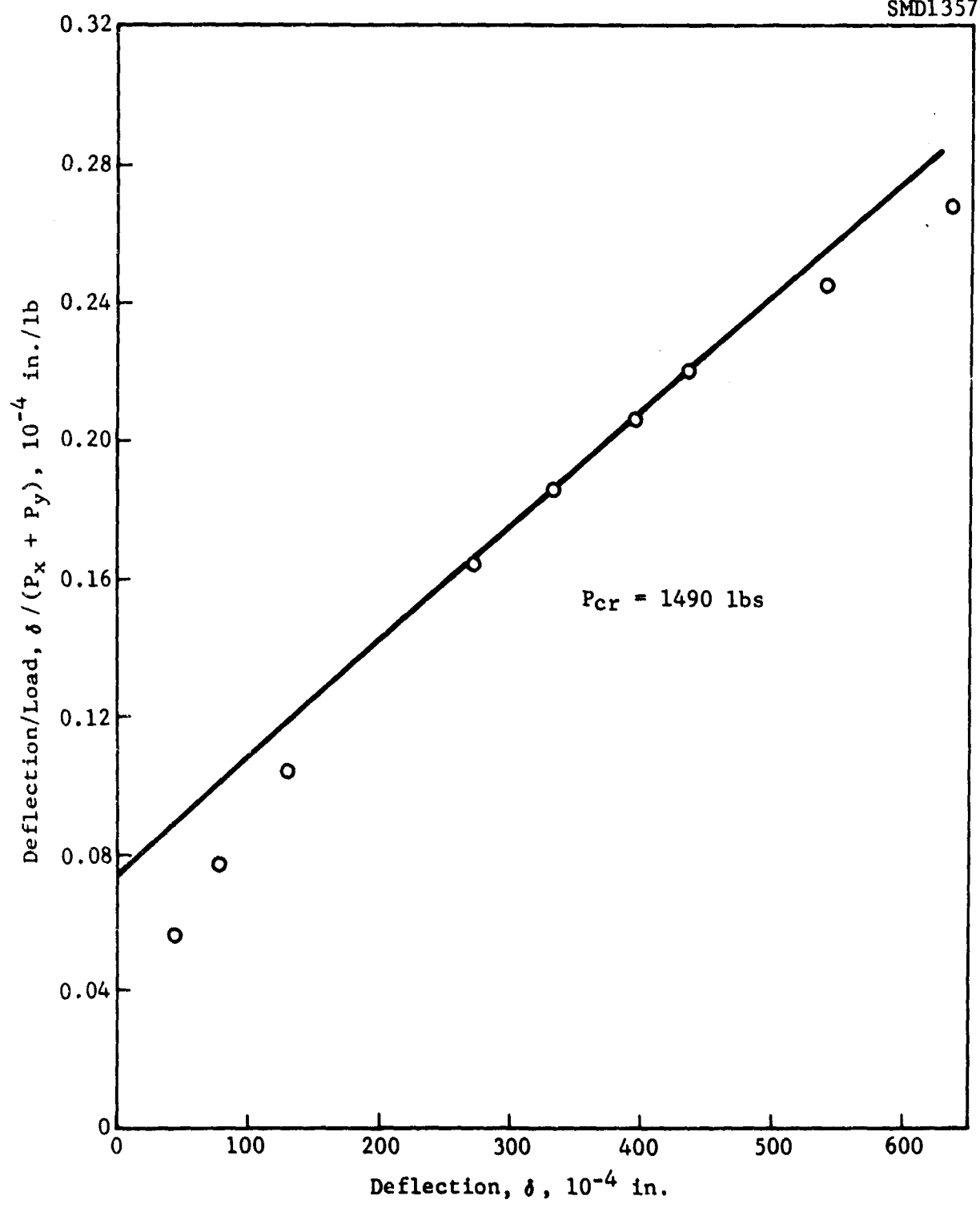


Figure 246 Southwell Plot for Panel No. 19A, $N_y/N_x = 1.00$, Turned 90°

SMD1358

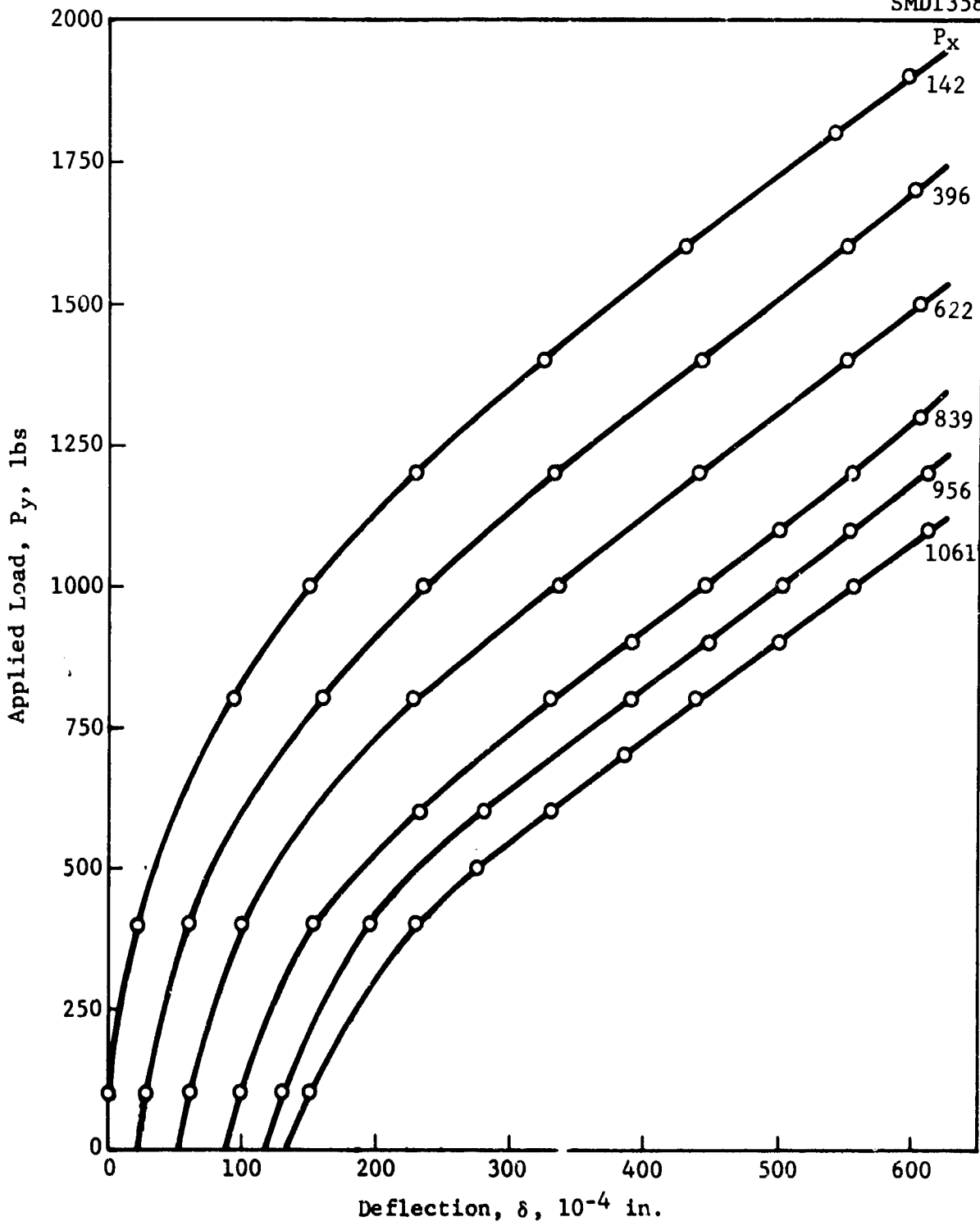


Figure 247 Load-Deflection Curves for Panel No. 19A, Turned 90°

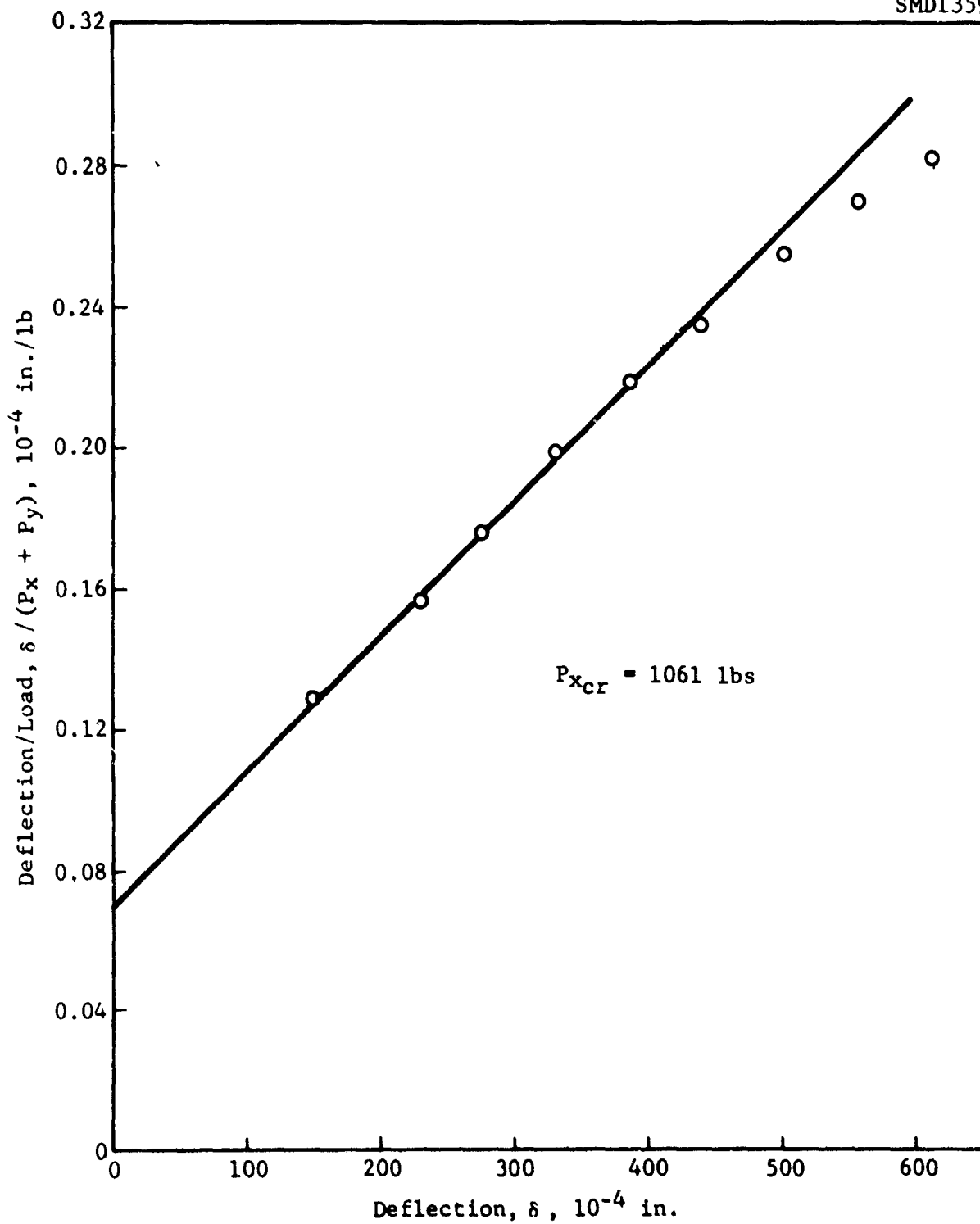


Figure 248 Southwell Plot for Panel No. 19A, $N_y/N_x = 1.448$

SMD1360

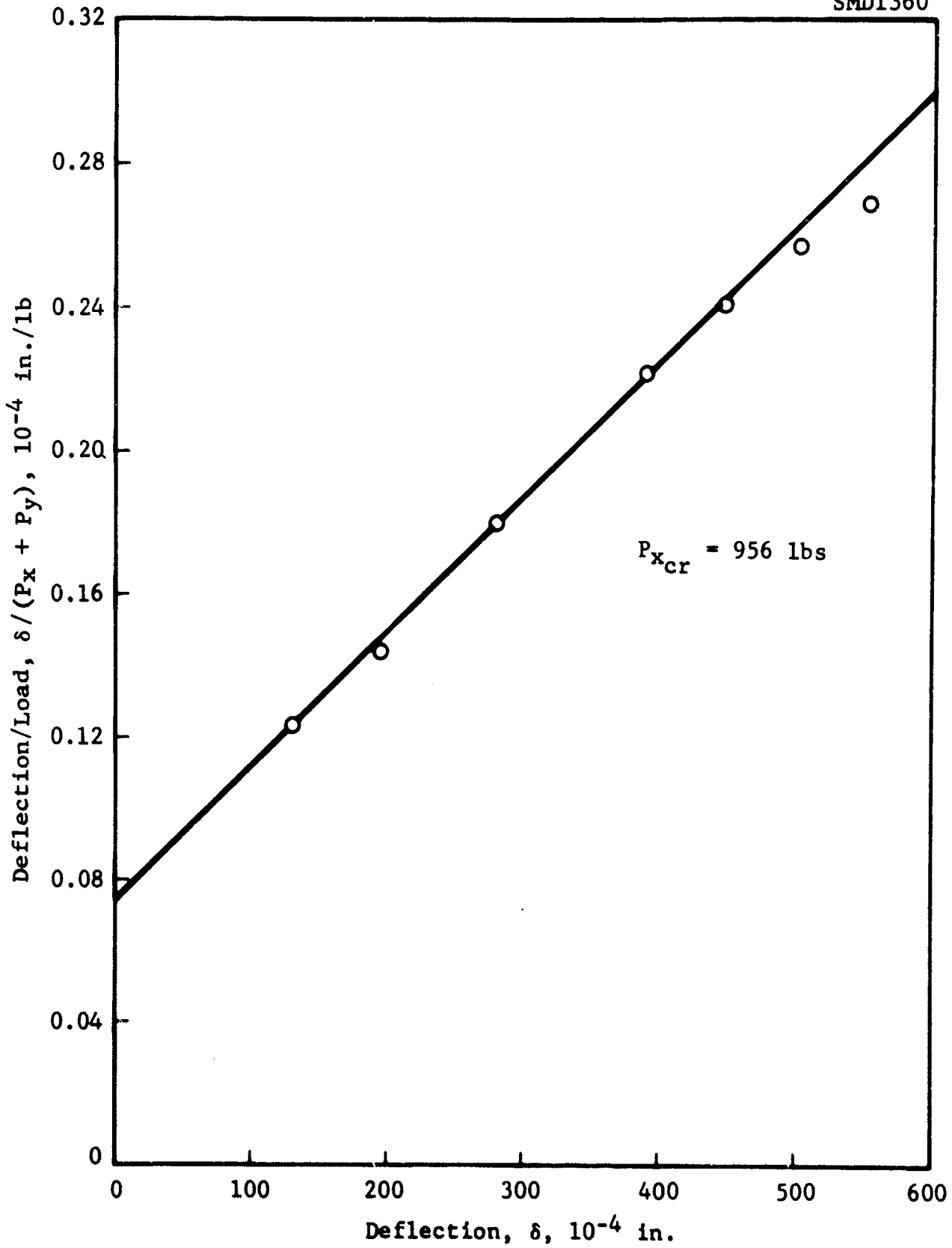


Figure 249 Southwell Plot for Panel No. 19A, $N_y/N_x = 1.759$

SMD1361

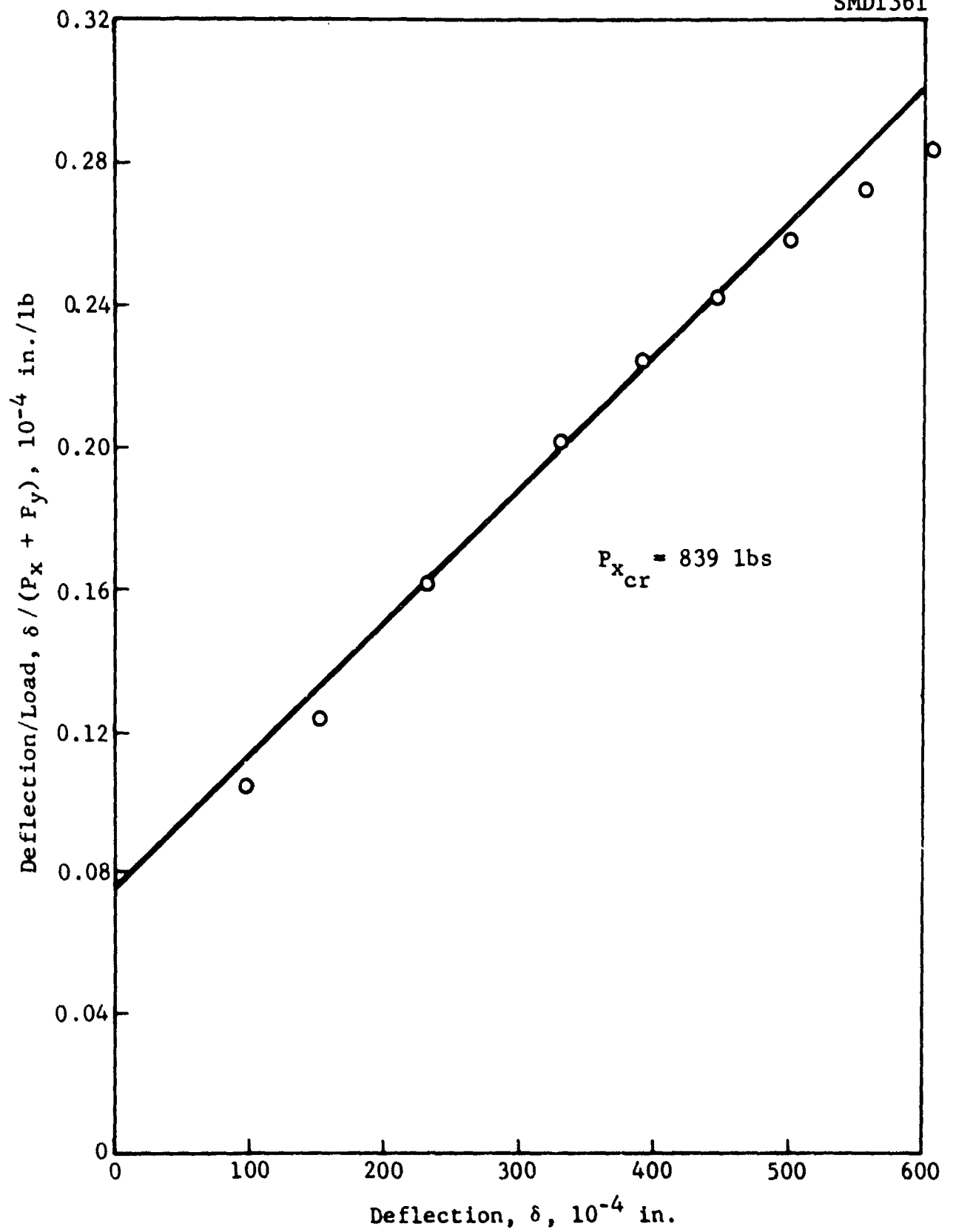


Figure 250 Southwell Plot for Panel No. 19A, $N_y/N_x = 2.171$

SMD1362

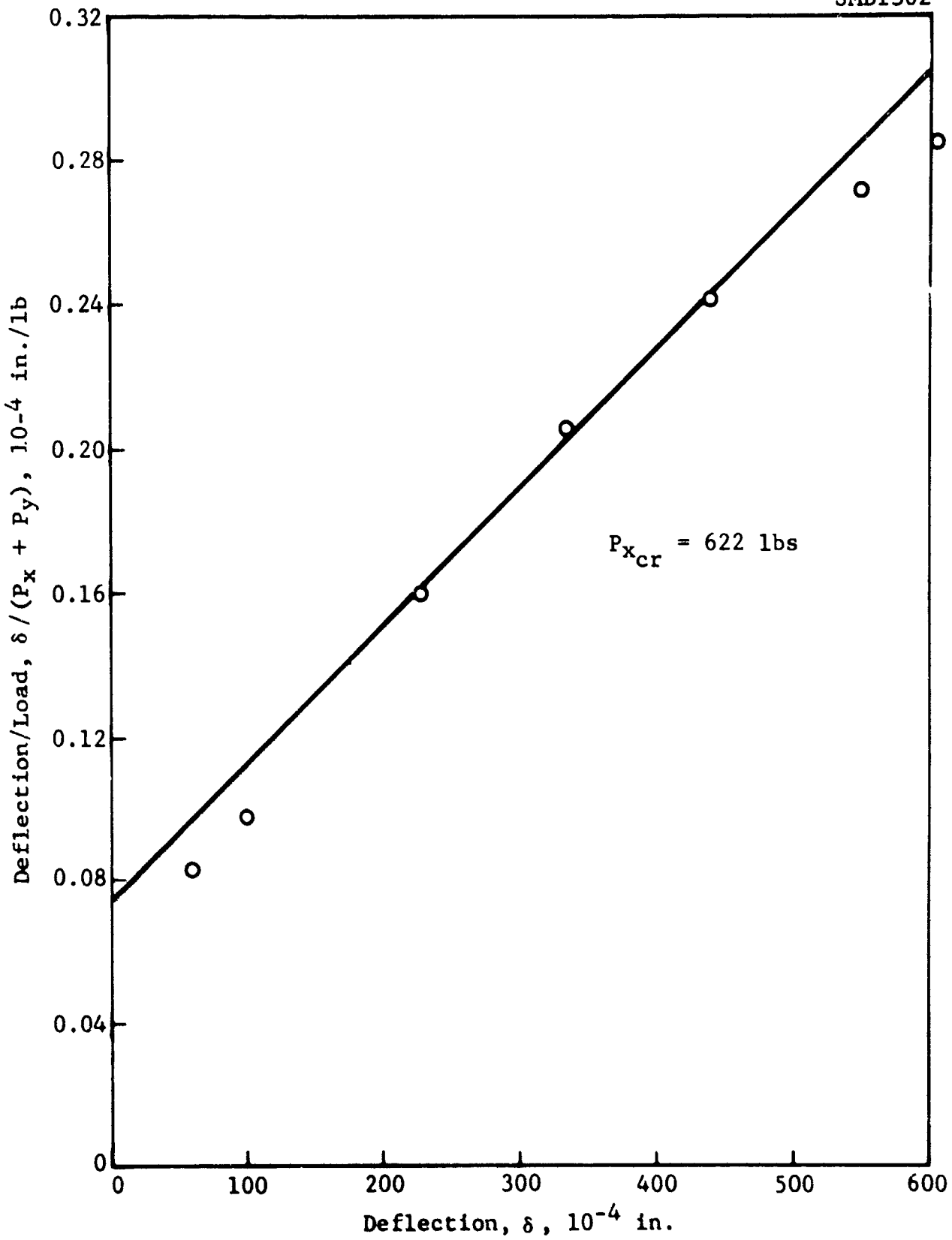


Figure 251 Southwell Plot for Panel No. 19A, $N_y/N_x = 3.214$

SMD1363

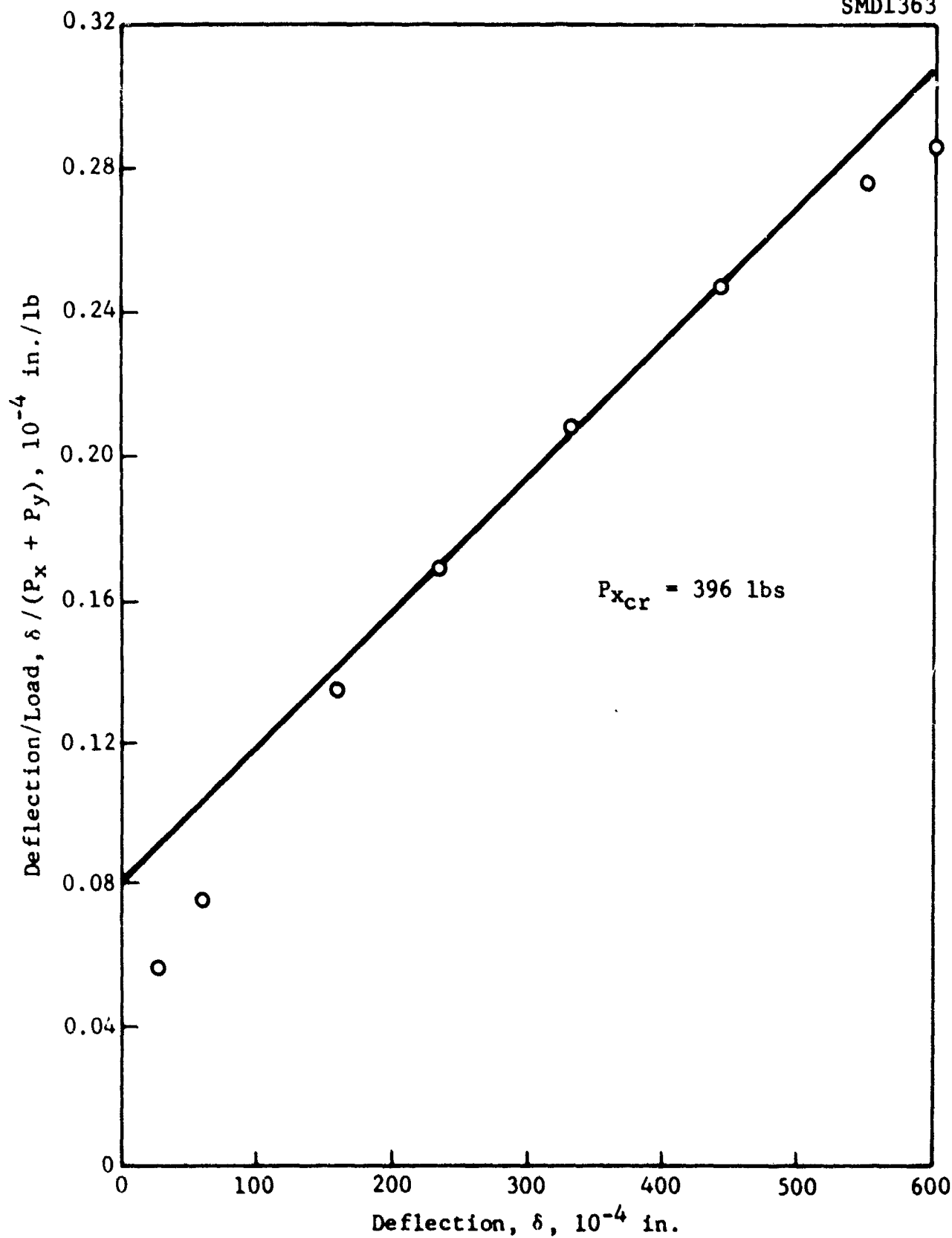


Figure 252 Southwell Plot for Panel No. 19A, $N_y/N_x = 5.611$

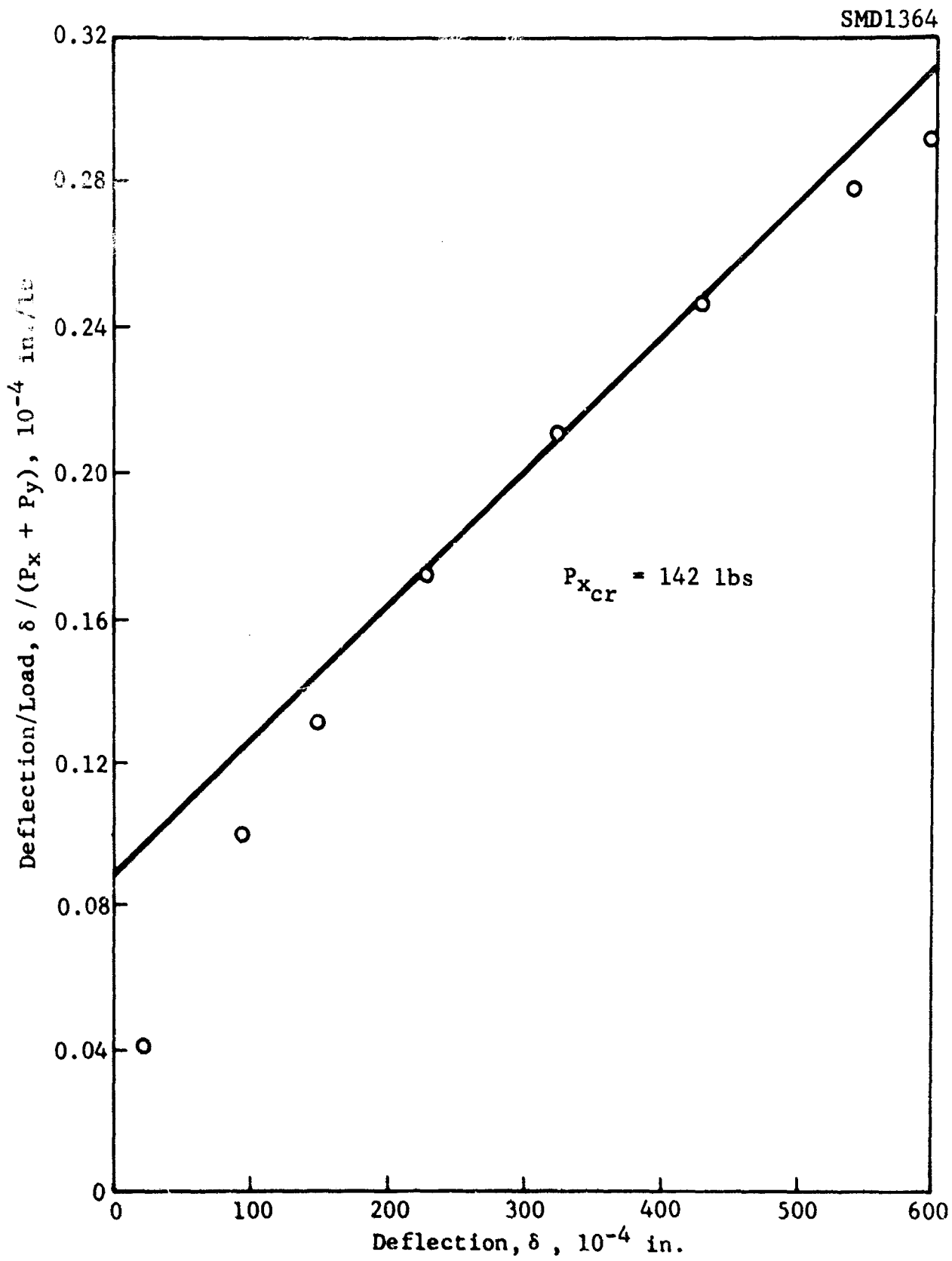


Figure 253 Southwell Plot for Panel No. 19A, $N_y/N_x = 17.769$

REFERENCES

1. Ashton J. E., "Anisotropic Plate Analysis - Boundary Conditions," J. Composite Materials, Vol. 4, 1970, p. 162.
2. Timoshenko, S., and Woinowsky-Krieger, S., Theory of Plates and Shells, McGraw-Hill, 1959.
3. Lekhnitski, S. G., Anisotropic Plates, 2nd Edition., OGIZ, Moscow-Leningrad, 1947, English edition translated by S. W. Tsai and T. Cheron, Gordon and Breach, 1968.
4. Ashton, J. E., and Love, T. S., "Experimental Study of the Stability of Composite Plates," J. Composite Materials, Vol. 3, 1959, p. 230.
5. Structural Design Guide for Advanced Composite Applications, Air Force Materials Laboratory, 1969.
6. Southwell, R. V., Proceedings of the Royal Society, London, Series A, Vol. 135, p. 601, 1932.
7. Thomson, W. T., Mechanical Vibrations, 2nd Edition, Prentice-Hall, 1953.
8. Ashton, J. E., and Anderson, J. D., "The Natural Modes of Vibration of Boron-Epoxy Plates," The Shock and Vibration Bulletin, Part 4, Bulletin 39, 1969.
9. Waddoups, M. E., McCullers, L. A., Olson, F. O., Ashton, J. E., "Structural Synthesis of Anisotropic Plates," AIAA/ASME 11th Structures, Structural Dynamics, and Materials Conference, Denver, Colorado, April 1970.
10. Ashton, J. E., "Approximate Solutions for Unsymmetrically Laminated Plates," J. Composite Materials, Vol. 3, p. 189, 1969.
11. Roorda, J., "Some Thoughts on the Southwell Plot," A.S.C.E. Journal of the Engineering Mechanics Division, Vol. 93, No. EM6, December, 1967.

N O N E

Security Classification

DOCUMENT CONTROL DATA - R & D

(Security classification of title, body of abstract and indexing annotation must be entered when the overall report is classified)

1. ORIGINATING ACTIVITY (Corporate author) General Dynamics Fort Worth Division		2a. REPORT SECURITY CLASSIFICATION None	
		2b. GROUP None	
3. REPORT TITLE Development of Engineering Data for Advanced Composite Materials			
4. DESCRIPTIVE NOTES (Type of report and inclusive dates)			
5. AUTHOR(S) (First name, middle initial, last name) Benjamin E. Kaminski			
6. REPORT DATE August, 1970		7a. TOTAL NO. OF PAGES 320	7b. NO. OF REFS 13
8a. CONTRACT OR GRANT NO. F33615-68-C-1474		9a. ORIGINATOR'S REPORT NUMBER(S) Volume III	
b. PROJECT NO.		9b. OTHER REPORT NO(S) (Any other numbers that may be assigned this report)	
c.			
d.			
10. DISTRIBUTION STATEMENT This document is subject to special export controls and each transmittal to foreign governments or foreign nationals may be made only with the prior approval of AFML(MAC) WPAFB, Ohio 45433			
11. SUPPLEMENTARY NOTES		12. SPONSORING MILITARY ACTIVITY AFML	
13. ABSTRACT Volume III covers the anisotropic plate evaluation--bending, dynamics, and stability--of the Narmco 5505 boron-epoxy material system. The primary objective was to determine the small deflection and post-buckling behaviors of boron-epoxy flat plates subject to transverse, uniaxial, biaxial, and diagonal tension loading configurations. These studies were conducted to verify an existing anisotropic plate analysis. A secondary objective was to observe the mode of failure of laminated anisotropic flat plates under uniaxial compression and shear.			

DD FORM 1473
1 NOV 68

N O N E

Security Classification

N O N E

Security Classification

14.	KEY WORDS	LINK A		LINK B		LINK C	
		ROLE	WT	ROLE	WT	ROLE	WT
	Plates, anisotropic, tests, analysis; bending, dynamics, stability, post-buckling.						

N O N E

Security Classification